ANTARES search for high-energy neutrinos from TeV-emitting blazars, Markarian 421 and 501, in coïncidence with HAWC gamma-ray tiares

Mukharbek Organokov

Université de Strasbourg

UNIVERSITÉ DE STRASBOURG

IPHC Institut Pluridisciplinaire Hubert CURIEN STRASBOURG

ÉCOLE DOCTORALE DE PHYSIQUE ET CHIMIE-PHYSIQUE

Institut Pluridisciplinaire Hubert Curien (IPHC), UMR 7178

THÈSE présentée par :

Mukharbek ORGANOKOV

soutenue le : **30 septembre 2019**

pour obtenir le grade de : **Docteur de l'Université de Strasbourg**

Discipline/Spécialité : Physique des particules élémentaires

ANTARES search for high-energy neutrinos from TeV-emitting blazars, Markarian 421 and 501, in coincidence with HAWC gamma-ray flares

THÈSE dirigée par :

M.	**PRADIER Thierry**	Maître de Conférences, Université de Strasbourg, IPHC, CNRS

RAPPORTEURS :

M.	**ERNENWEIN Jean-Pierre**	Directeur de recherche, Universite d'Aix Marseille, CPPM
M.	**VALLAGE Bertrand**	Ingénieur chercheur, Université Paris-Saclay, CEA

AUTRES MEMBRES DU JURY :

M.	**SALESA GREUS Francisco**	Adjunct Professor, Institute of Nuclear Physics, PAN
Mme.	**LANÇON Ariane**	Directeur de recherche, Observatoire Astronomique de Strasbourg, CNRS
M.	**GOERLACH Ulrich**	Directeur de recherche, Université de Strasbourg, IPHC, CNRS

Mukharbek Organokov

ANTARES search for high-energy neutrinos from TeV-emitting blazars, Markarian 421 and 501, in coincidence with HAWC gamma-ray flares

September 30th, 2019

Supervisor: Thierry Pradier

Université de Strasbourg

Groupe neutrino

Institut Pluridisciplinaire Hubert Curien (IPHC), UMR 7178

Département Recherches Subatomiques

23 rue du Loess, BP 28. 67037, Strasbourg

Abstract

Neutrinos are unique messengers for detecting violent phenomena in the Universe. Potential sources of cosmic neutrinos are, for example, Active Galactic Nuclei (AGNs) or Gamma-Ray Bursts (GRBs). In the case of hadronic cosmic rays acceleration, the production of neutrinos is possibly accompanied by high-energy gamma-ray emissions. The search for coincidences between high-energy neutrinos detected by the ANTARES neutrino telescope and gamma-rays detected by the HAWC gamma-ray observatory is presented. Searching in a particular time window significantly reduces the background noise in the neutrino data and thus increases the discovery potential. In this thesis, the results of a search for neutrinos detected in correlation with a gamma-ray signal from two particular AGNs, Markarian 421 and Markarian 501, are presented. As the blazars closest to Earth, they are excellent sources for testing the blazar-neutrino connection scenario, especially during the increase of their activities (flares) in which the search for neutrinos may have a higher detection probability.

Keywords: High-energy neutrinos, Multi-messenger astronomy, Active Galactic Nuclei, blazars, Markarian, ANTARES, HAWC

Résumé

Les neutrinos sont des messagers uniques pour détecter les phénomènes violents de l'Univers. Les sources potentielles de neutrinos cosmiques sont, par exemple, les Noyaux Actifs de Galaxie (NAGs), ou les sursauts gammas. Dans le cas d'un accélérateur astrophysique de rayons cosmiques hadroniques, la production de neutrinos s'accompagne éventuellement d'émissions gammas de haute énergie. La recherche des coïncidences entre des neutrinos de haute énergie détectés avec le télescope à neutrinos ANTARES et des photons gamma captés par l'observatoire HAWC est présentée. La recherche dans une fenêtre temporelle particulière réduit le bruit de fond de manière significative dans les données du télescope à neutrinos et augmente donc le potentiel de découverte. Dans cette thèse, les résultats de la recherche de neutrinos détectés en corrélation avec un signal gamma en provenance de 2 NAG particulier, Markarian 421 et Markarian 501, sont présentés. En tant que blazars les plus proches de la Terre, ils constituent d'excellentes sources pour tester le scénario de connexion blazar-neutrinos, en particulier lors de leurs "bouffées" d'activités (flares) pour lesquelles la recherche de neutrinos en fonction du temps peut présenter une probabilité de détection plus élevée.

Mots-clés: Neutrinos de haute énergie, Astronomie multimessager, Noyaux Actifs de Galaxies, blazars, Markarian, ANTARES, HAWC

Си анэм папщIэ

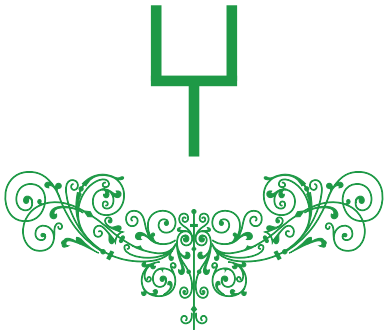

Acknowledgements

> *Alice: Where I come from, people study what they are not good at in order to be able to do what they are good at.*
> *Mad Hatter: We only go around in circles in Wonderland, but we always end up where we started. Would you mind explaining yourself?*
> *Alice: Well, grown-ups tell us to find out what we did wrong, and never do it again.*
> *Mad Hatter: That's odd! It seems to me that in order to find out about something, you have to study it. And when you study it, you should become better at it. Why should you want to become better at something and then never do it again? But please continue.*
> *Alice: Nobody ever tells us to study the right things we do. We're only supposed to learn from the wrong things. But we are permitted to study the right things other people do. And sometimes we're even told to copy them.*
> *Mad Hatter: That's cheating!*
> *Alice: You're quite right, Mr. Hatter. I do live in a topsy-turvy world. It seems like I have to do something wrong first, in order to learn from what not to do. And then, by not doing what I'm not supposed to do, perhaps I'll be right. But I'd rather be right the first time, wouldn't you?*
>
> **— Lewis Carroll**
> (Alice's Adventures in Wonderland, 1865)

NONE of the PhD can be completed without the assistance of other scientists, the complicity of the friends and the support of the family. Therefore, I would like to render homage to all people without the involvement of whom this work might never have been accomplished.

I would like to take this opportunity to thank my supervisor Thierry Pradier, without whom this work would not have been possible. My deep gratitude and sincere appreciation for the guidance, encouragement, and assistance I got during my PhD. Thanks also for being available every time I needed help and for generously sharing your expertise. My warmest thanks also for the time and endless patience. Likewise, I would like to express my gratitude for introducing me to ANTARES and suggesting an intriguing topic to work with. Thanks also for creating an enabling working environment at IPHC - Institut Pluridisciplinaire Hubert Curien, where I spent an exciting time searching for the elusive particles from the most violent and energetic objects in the Universe.

My deepest appreciation for the jury members of my dissertation committee: Jean-Pierre Ernenwein, Bertrand Vallage, Francisco Salesa-Greus, Ariane Lançon, and Ulrich Goerlach for generously offering their time and rigorous review of this document.

Working in large collaborations such as ANTARES or KM3NeT assumes close interactions with colleagues from various laboratories, cities, and even countries. I would like to thank Agustín Sánchez Losa for the warm welcome during my stay in Bari at INFN - Istituto Nazionale di Fisica Nucleare, and for his invaluable help in my understanding of time-dependent search concept. A big part of collaboration is coordination. Therefore, I would like to express my appreciation to Damien Dornic and Alexis Coleiro as the coordinators of the group for the unbiased and rigorous referee of my analysis. Apart from them, I would like to thank Bruny Baret, Thomas Eberl, Dorothea Samtleben for being the referees of my analysis and aspirations and willingness to help for its improvements. Also, I would like warmly thank Maurizio Spurio, Fabian Schüssler, Rosa Coniglione and Véronique Van Elewyck for constant attention to my analysis, presentations, and proceedings. I would like to thank all of them mentioned above for their fruitful discussions, helpful suggestions and comments that I have had the privilege to receive.

A special thanks go to Luigi Antonio Fusco for his help on data and Monte Carlo issues, crucial for this work. I would like also to warmly thank Alexandre Creusot for his invaluable help and guidance toward KM3NeT calibration. My sincere appreciation to Alexander Enzenhöfer, Arnauld Albert and Doriane Drouhin for their assistance and support during shifts on ANTARES. Along with this, I would like to emphasize the inconceivable reachability of Alexander Enzenhöfer at any time when the help was urgently needed.

I would not like to miss out on the chance to thank all the members of the ANTARES & KM3NeT collaborations for such a supportive, inspiring, and friendly atmosphere and for a pleasant time we spent together during collaboration meetings and conferences. In no particular order, among them especially warm thanks to Simon Bourret, Nafis Rezwan Khan Chowdhury, Marta Colomer Molla, Alba Domi, Giulia Illuminati, Giovanna Ferrara, Tamas Gal, Steffen Hallmann, Vladimir Kulikovskiy, Massimiliano Lincetto, Moritz Lotze, Karel Melis, Liam Quinn, Dmitry Zaborov. I apologize for those colleagues I forgot to mention.

I had a great opportunity to work with HAWC collaboration, which people I would also like to mention and warmly thank. I would like to thank Ignacio Taboada for encouraging my initiative to receive HAWC data as part of an agreement between HAWC and ANTARES collaborations. I would like to appreciate the enthusiasm and help from Robert Lauer and Israel Martinez-Castellanos who introduced me to HAWC data. My warm thanks also to Sara Coutiño De León for her patience during discussions about the spectra of HAWC sources. And special thanks to Alberto Carramiñana, Andrés Sandoval Espinosa, and Henrike Fleischhack for very valuable comments and constructive critiques.

I would also like to express appreciation to people who willingly helped me: David Paneque for a generously sharing the SED of Mrk 421 taken during the multifrequency campaign in 2009; René Reimann for kindly providing IceCube upper limits on neutrino emission from Mrk 421; and Maria Petropoulou for her goodwill, initiative, and willingness to help in my understanding of model prediction for neutrino emission from Mrk 421.

Some parts of this thesis have been written in several places outside Strasbourg during some business trips, be it a collaboration meeting, conference, or summer school. In this regard, I would especially like to express my sincere appreciation to Alexander Pizzuto from the University of Wisconsin-Madison & IceCube for kindly offering me his office during my stay in Madison at ICRC 2019 that allowed me to finalize one of the chapters of this thesis. And of course, thanks to Madison, WI for its pleasant summer atmosphere that made the thesis writing much nicer.

And finally, last but by no means least, I would like to express very special gratitude to Khasanbi Erganokov who strongly influenced my career choice as a physicist and supported me much at the final stages of my PhD I would also like to express my warmest thanks to all the people who supervised me during my previous studies and made the entry to PhD easier: Jean-François Glicenstein at IRFU, CEA-Saclay; Andrei Bykov and Gennady Vasilyev at Ioffe Institute; Vladimir Gavrin and Valery Gorbachev at Baksan Neutrino Observatory; Murat Khokonov and Azamat Khokonov at Kabardino-Balkarian State University.

Family is important in my life and I would never find the courage to overcome all the difficulties and obstacles during this work and in my life without the presence of some people. My special highest thanks to Khusen, Khasen and Zaur Kabardovs without the help of whom my life would have been harder. My sincere and heartfelt thanks to my wife Asiiat for her continuous caring, spiritual support, and encouragement to me throughout this journey. And also thanks to little Berzeg for his great contribution.

Contents

Préface

Le $20^{20ème}$ siècle a été fécond pour l'astronomie et a donné lieu à de nombreuses découvertes révolutionnaires. À partir de l'utilisation de photons optiques uniquement, les différentes bandes du spectre électromagnétique ont été maîtrisées, telles que les ondes radio, l'infrarouge, le visible, l'ultraviolet, les rayons X et jusqu'aux rayons gamma, passant progressivement à l'astronomie multi-longueurs d'onde. Le progrès scientifique a mené à un ensemble de découvertes fondamentales en astronomie comme les premières observations de: l'expansion de l'Univers, les quasars, les objets extrêmement lumineux et très éloignées de nous tel que les noyaux actifs de galaxie, le fond diffus cosmologique en 1964, les pulsars en 1968 dans le spectre des ondes radio, les sursauts gamma, les exoplanètes, les neutrinos de haute énergie d'origine extrasolaire en 2013, les ondes gravitationnelles en 2015 résultant de la fusion d'une binaire de trous noirs, la fusion des étoiles à neutrons en 2017, et enfin récemment la possible identification d'une source de neutrinos de haute énergie, TXS0506+056, un blazar de la famille des noyaux de galaxies actives. Ces succès d'un domaine si récent tel que l'astronomie neutrino l'a établi comme un domaine mature de la physique, maturité confirmée par la construction de télescopes de tailles kilométriques. Cela offre une occasion sans précédent de poursuivre une étude approfondie des phénomènes les plus énergiques et violents de l'Univers tel que les noyaux actifs de galaxie ou les sursauts gammas.

La Terre est continuellement bombardée par les rayons cosmiques, en grande majorité des particules chargées, essentiellement des protons. Pendant longtemps, les sources de rayons cosmiques sont restées un mystère pour les scientifiques. Les sources potentielles de ces particules cosmiques sont, par exemple, les noyaux actifs de galaxie, ou les sursauts gammas. Les particules chargées émises dans les noyaux actifs de galaxie ou les sursauts gammas sont déviées par les champs magnétiques cosmiques et il est donc impossible de déterminer leur origine après leur détection sur Terre. Les neutrinos n'ont pas ce problème car ils ne possèdent pas de charge électrique; de plus ils n'interagissent pas sur leur trajet jusqu'à la Terre, à cause de leur faible section efficace d'interaction. Par ailleurs, les neutrinos sont produits dans les mêmes régions denses et énergétiques que les rayons cosmiques, ils sont donc des messagers uniques pour détecter et étudier les phén. les plus énergétiques et violents de l'Univers que sont les NAG, potentiels sites d'accélération de rayons cosmiques. Ces neutrinos "cosmiques" peuvent interagir dans la Terre et produire des particules telles que les muons, qui vont se propager dans la roche et l'eau sur de grandes distances, en émettant de la lumière Tcherenkov, détectable si le milieu est transparent.

ANTARES (Astronomy with a Neutrino Telescope and Abyss environmental RESearch) est un télescope à neutrinos de haute énergie situé dans la mer Méditerranée au large de Toulon et construit pour capter cette faible lumière Tcherenkov dans l'eau de mer. Etant données les sections efficaces d'interaction, le volume instrumenté est nécessairement important (de l'ordre du km^3); par ailleurs pour se prémunir du bruit de fond atmosphérique, le détecteur doit être immergé à de grandes profondeurs, si l'on veut mettre en évidence un faible flux d'origine cosmique. L'objectif du projet ANTARES, en opération depuis 2008, est la detection des neutrinos cosmiques avec des énergies supérieures à 100 GeV environ. Dans le cas d'un accélérateur astrophysique de rayons cosmiques hadroniques, tel qu'un noyau actif de galaxie, la production de neutrinos s'accompagne éventuellement d'émissions gammas de haute énergie. Ainsi, il peut être recherché des coïncidences entre les neutrinos de haute énergie détectés avec un télescope à neutrinos et les photons gammas captés par un observatoire dédié à ces messagers. HAWC (High Altitude Water Cherenkov Experiment), situé dans l'État de Puebla, au Mexique, est un observatoire de rayons gammas de très hautes énergies couvrant une plage d'énergie allant de 100 GeV à 100 TeV. Ainsi, un tel télescope peut fournir des informations important sur la source gamma, telles que le spectre et flux, et détecter une augmentation du flux pouvant déclencher la recherche par ANTARES de l'émission de neutrinos correspondante dans cette région et à cette heure particulier. La recherche dans une fenêtre temporelle particulière réduit le bruit de fond de manière significative dans les données du télescope à neutrinos et augmente donc le potentiel de découverte.

Les résultats de la recherche de neutrinos détectés en corrélation avec un signal gamma en provenance de deux noyaux actifs de galaxie particuliers, Markarian 421 et Markarian 501, sont présentés. En tant que blazars les plus proches de la Terre, ils constituent d'excellentes sources pour tester le scénario de connexion blazar-neutrinos, en particulier lors de leurs "bouffées" d'activités (ou *flares*) pour lesquelles la recherche de neutrinos en fonction du temps peut présenter une probabilité de détection plus élevée.

Dans cette thèse, la disposition des chapitres est la suivante:

Chapitre 1: Messagers Cosmiques et avénement de l'astronomie des neutrinos.

Chapitre 2: Les télescopes à neutrinos.

Chapitre 3: Le télescope à neutrinos ANTARES.

Chapitre 4: L'observatoire de rayons gamma HAWC.

Chapitre 5: Simulation et reconstruction de traces de muons dans ANTARES.

Chapitre 6: La méthode de recherche dépendante du temps.

Chapitre 7: Recherche de neutrinos en provenance de Mrk 421 et Mrk 501.

Ensuite, la conclusion résume les résultats et l'importance de ce travail et discute de certaines possibilités de travaux futurs. Par ailleurs, il comprend une annexe, qui décrit les unités et définitions astronomiques, les constantes mathématiques, physiques et astrophysiques utilisées dans cette analyse ainsi que des matériaux supplémentaires pour l'analyse tels que les carte du ciel des événements sélectionnés.

Dans **le premier chapitre**, un aperçu général et concis de l'astronomie multimessager sera donné. Avant de se concentrer sur les neutrinos (voir le paraghraphe 1.4 pour plus de détails) et leurs sources possibles (voir les détails au paragraphe 1.6), une revue des trois autres messagers en astronomie (rayons cosmiques (voir le paraghraphe 1.1), rayons gamma (voir le paraghraphe 1.2), ondes gravitationnelles (voir le paraghraphe 1.3)) sera faite. Dans cette partie, l'accent sera mis sur l'origine (voir le paraghraphe 1.1.4) et les sites d'accélération (voir le paraghraphe 1.1.3 pour plus de détails) des rayons cosmiques qui, jusqu'à présent, restent un mystère et restent l'un des problèmes non résolus les plus importants en astrophysique. Ceci est particulièrement important car les neutrinos peuvent être produits dans les mêmes environnements extrêmes que les rayons cosmiques (voir les détails au paragraphe 1.5). À cet égard, une petite excursion dans l'histoire de l'étude de la composition et de l'énergie des rayons cosmiques sera donnée (voir le paraghraphe 1.1.1 pour plus de détails). Les rayons cosmiques, d'abord vus comme des rayonnements provenant de l'espace extra-atmosphérique, ont ensuite été identifiés comme des noyaux chargés. La composition des rayons cosmiques va des éléments les plus légers aux plus lourds du tableau périodique, ainsi que les leptons de haute énergie (électrons et positrons) et d'autres particules subatomiques. Les rayons cosmiques sont approximativement composés de: protons, c'est-à-dire, des noyaux d'hydrogène (~85%); particules alpha, c'est-à-dire, noyaux d'hélium (~12%); noyaux d'éléments plus lourds (~1%); électrons et positrons (~2%). Les rayons cosmiques couvrent une large gamme d'énergie et de flux, couvrant plus de 10 décades de flux et des décades d'énergie (voir la figure 1.4). Les mesures de la composition des rayons cosmiques contraignent les théories de l'accélération et de la propagation des rayons cosmiques. Le spectre des rayons cosmiques est bien décrit par une loi de puissance brisée qui indique les processus d'accélération non thermiques. Ainsi, les mécanismes responsables de l'accélération des rayons cosmiques jusqu'aux énergies extrêmes, qui ont été un défi théorique vital pendant des décennies, ainsi la production d'un spectre de loi de puissance brisé et la propagation dans l'espace seront discutées (voir les détails au paragraphe 1.1.3). Les interactions des rayons cosmiques dans leur propagation dans l'espace pourraient produire des neutrinos. Les rayons gamma produits dans les mêmes interactions que les neutrinos suggèrent ces processus. Ainsi, les phénomènes extrêmement puissants de l'Univers qui alimentent l'accélération et sont à l'origine des rayons cosmiques accompagnés de neutrinos et/ou de rayons gamma seront également discutés (voir le paraghraphe 1.1.4 pour plus de détails).

Les supernovae sont considérées comme les accélérateurs de la majeure partie des rayons cosmiques dans notre galaxie depuis près d'un siècle (voir les détails au paragraphe 1.1.4), au

moins jusqu'aux énergies $10^{14}-10^{15}$ eV (décrit par l'équation 1.15). Les chocs d'explosions de supernovae se propageant à travers le milieu interstellaire peuvent expliquer l'accélération des rayons cosmiques galactiques (voir la figure 1.12). La propagation par diffusion des particules chargées de haute énergie dans le milieu dissipatif sans collision leur permet de traverser le front de choc plusieurs fois avant de finalement dériver dans la région derrière l'onde de choc. La nature physique essentielle du processus d'accélération dans l'explosion d'une supernova réside dans le fait que dans chaque traversée du front d'onde (nombre de cycles indiqué par un coefficient de diffusion) se traduit une augmentation de l'énergie de la particule. La propagation des rayons cosmiques dans la galaxie peut s'expliquer par le modèle simple (voir la figure 1.13) qui décrit le confinement des rayons cosmiques au sein de la galaxie en raison des champs magnétiques ($B \geq 3\mu G$) pendant une durée de vie donnée, appelée temps d'évasion. Ainsi, pour acquérir des énergies supérieures à $10^{14}-10^{15}$ eV, les particules doivent être confinées dans la région d'accélération pendant un temps beaucoup plus long car lorsque les particules s'échappent de la région d'accélération, elles ne seront plus capables de gagner de l'énergie. Cela impose une limite à l'énergie maximale que la particule est capable d'atteindre. L'énergie maximale qu'une particule d'une charge donnée peut atteindre peut être calculée indépendamment du mécanisme d'accélération. Le rayon de Larmor (gyroradius) de la particule est considéré comme plus petit que la taille de la région d'accélération, ce qui implique une accélération efficace d'une particule par un processus de diffusion répété au sein d'une source astrophysique. Ces estimations donnent également des énergies d'environ $10^{14}-10^{15}$ eV. Il est suggéré que l'origine des rayons cosmiques au-dessus de ces énergies soit de nature extragalactique en raison des grandes échelles et des champs magnétiques nécessaires pour accélérer et confiner les particules chargées de telles énergies. Dessus de ces énergies est généralement supposé en raison du fait qu'au-dessus de ces énergies, le rayon de Larmor d'un proton dans le champ magnétique galactique augmente avec l'énergie et devient comparable ou dépasse la taille de la galaxie. Par conséquent, afin de fournir une explication de la transition des rayons cosmiques galactiques aux rayons cosmiques extragalactiques, plusieurs modèles seront mis en évidence et discutés (voir le paraghraphe 1.1.4 pour plus de détails) pour résoudre le problème de transition. Remarquons que l'observation des neutrinos TeV à partir de restes de supernovae peut être une signature claire pour l'accélération hadronique dans les supernovae, signature qui n'a pas été mise en évidence jusqu'à présent.

Après une brève introduction à l'astronomie des rayons gamma (voir le paraghraphe 1.2.1), télescopes passés et actuels utilisés pour la recherche de rayons gamma de haute énergie, les neutrinos seront discutés. L'astronomie gamma permet d'étudier les objets astrophysiques les plus énergétiques, compacts et violents de l'Univers. Pourtant, l'astronomie extragalactique des rayons gamma est quelque peu limitée par l'absorption des rayons gamma sur leur chemin vers la Terre par la lumière d'arrière-plan extragalactique lorsque l'énergie du centre de masse de la réaction des rayons $\gamma + p$ permet la production d'une paire électron-positron. Cet effet d'absorption a été observé sur les rayons gamma TeV provenant de sources extragalactiques en raison de la lumière de fond infrarouge et optique. La lumière

d'arrière-plan extragalactique empêche les rayons gamma de se propager sur des distances cosmologiques. Contrairement à cela, les neutrinos portant une seule charge faible se propagent sans déflexion ni absorption et remontent à leur source, faisant de l'astronomie avec des neutrinos un instrument puissant pour révéler les processus physiques derrière les phénomènes astrophysiques extrêmes dans l'Univers. En outre, la combinaison de plusieurs messagers, tels que les neutrinos, les rayons gamma, les rayons cosmiques, les ondes gravitationnelles augmentent considérablement les chances d'obtenir des informations sur les phénomènes astrophysiques les plus extrêmes et élargissent ainsi considérablement nos connaissances sur ces objets (voir les détails au paragraphe 1.7). La corrélation entre les rayons gamma et l'astronomie des neutrinos est très importante et utilisé dans ce travail, d'où la description de ce domaine.

À cet égard, une grande attention sera accordée à la discussion sur le début et les progrès dans l'astronomie multimessager (voir le paraghraphe 1.7). Les observations multimessagers ont commencé avec l'observation des neutrinos solaires (voir le paraghraphe 1.4.1 pour plus de détails), aboutissant en 1987 (voir les détails au paragraphe 1.4.3) à l'observation de neutrinos et de photons coïncidents de la supernova SN1987A (voir la figure 1.39). Depuis la première détection d'un flux extragalactique diffus de neutrinos de haute énergie en 2013 (voir le paraghraphe 1.5.6 pour plus de détails), le mystère de l'origine de ces neutrinos n'est toujours pas résolu. Des efforts importants ont été déployés ces dernières années pour dévoiler le mystère de l'origine de ces neutrinos. En particulier, IceCube qui est situé sous le pôle Sud a implémenté un outil où les événements de suivi des neutrinos avec une forte probabilité d'être d'origine cosmique sont sélectionnés en temps réel et transmis aux télescopes pour des observations électromagnétiques de suivi immédiates. Le cadre d'analyse en temps réel mis en œuvre visait à aider à l'identification d'une contrepartie électromagnétique d'une source qui s'estompe rapidement et pour localiser les objets astrophysiques responsables des signaux neutrinos en 2013. Les informations sur les neutrinos sont distribués par le réseau d'observation astrophysique multimessager (AMON en Anglais) via le réseau des coordonnées des rayons gamma (GCN en Anglais) (voir les détails au paragraphe 1.7). Partager les informations sur les observations avec d'autres expériences encourage et aide la recherche d'événements astrophysiques à la limite du bruit qui ne pas pourraient perçu par un instrument individuellement. Le projet AMON a été créé pour relier les observatoires mondiaux de haute énergie et multimessagers en un seul réseau, dans le but de permettre la découverte de sources multimessagers, d'exploiter ces sources à des fins d'astrophysique, de physique fondamentale et de cosmologie et d'explorer de données d'archives pour l'étude des populations de sources multimessagers. Actuellement, les contributions d'AMON incluent les alertes rapides GCN pour les neutrinos probablement cosmiques, plusieurs campagnes de suivi pour les neutrinos probablement cosmiques, y compris l'événement IceCube-170922A (voir le paraghraphe 1.7.1), et plusieurs recherches d'archives sur les sources multimessagers de neutrinos avec de rayons gamma transitoires et avec les "bouffées" d'activités et neutrinos avec rayons cosmique. En ce moment, AMON reçoit des données en temps réel d'ANTARES dont le décommissionnement devrait avoir

lieu en 2020, et avec l'avènement de la nouvelle génération de détecteurs de neutrinos télescopes comme KM3NeT (Cubic Kilometre Neutrino Telescope), qui sera de taille kilométrique, davantage de sources de neutrinos devraient être détectées.

Dans **le deuxième chapitre**, l'historique et la situation actuelle des télescopes à neutrinos seront présentés. Une brève revue des télescopes à neutrinos modernes et de leurs prédécesseurs sera donnée (voir le paraghraphe 2.4 pour plus de détails). Ici, les principes de détection des télescopes à neutrinos sous-marins seront aussi présentés (voir les détails au paragraphe 2.3). En plus de cela, une description des interactions des neutrinos (voir le paraghraphe 2.3.1) et des différentes topologies d'événements créées (voir le paraghraphe 2.3.2 pour plus de détails) dans de telles interactions sera discutée. Aussi, la propagation des neutrinos (voir le paraghraphe 2.3.3) et des muons (voir le paraghraphe 2.3.4) sera discutée. L'effet Tcherenkov rayonnement important pour les télescopes à neutrinos sera également présenté (voir le paraghraphe 2.3.5 pour plus de détails). Trois télescopes à neutrinos fonctionnent actuellement dans le monde: un télescope à neutrinos Baïkal-GVD (voir le paraghraphe 2.4.2) déployé dans le lac Baïkal en Fédération de Russie, ANTARES dans la mer Méditerranée (avec la construction en cours de KM3NeT (voir le paraghraphe 2.4.4) qui remplacera ANTARES) et IceCube (voir le paraghraphe 2.4.3) qui est situé dans la glace antarctique sous le pôle Sud. Ainsi, le réseau mondial de neutrinos (GNN en Anglais) sera composé de trois télescopes à neutrinos de taille kilométrique. En général, un télescope à neutrinos est composé de plusieurs structures semi-rigides appelées "lignes" intégrées profondément dans l'eau ou la glace et équipées sur toute leur longueur par un réseau des tube photomultiplicateurs qui détectent la lumière Tcherenkov émise par les particules générés dans les interactions des neutrinos avec la matière à proximité ou dans le détecteur (voir la figure 2.1). Le principe de détection des télescopes à neutrinos consistant à utiliser l'eau comme cible pour les neutrinos remonte aux physiciens russes Moisey Markov et Igor Zheleznykh dans les années 1960. L'idée de "mettre en place un appareil dans un lac souterrain ou au fond de l'océan afin de séparer les directions des particules chargées par le rayonnement Tcherenkov" a été suggérée par Markov en 1960. Les preuves de fonctionnement du concept ont été faits par la collaboration DUMAND (Deep Underwater Muon And Neutrino Detector Project) qui a été le pionnier des technologies pour les télescopes à neutrinos sous-marins (voir le paraghraphe 2.4.1 pour plus de détails). L'idée principale d'un télescope à neutrinos est de construire une matrice de détecteurs de lumière à l'intérieur d'un milieu transparent comme l'eau profonde ou la glace afin de (voir le paraghraphe 2.2):

- Fournir un grand volume instrumenté d'une cible libre pour les interactions neutrino dont les sections efficaces sont très petites;

- Fournir un blindage contre les particules secondaires produites par les rayons cosmiques qui peuvent améliorer la sensibilité à un très faible flux de neutrinos de haute énergie provenant de sources astrophysiques, réduisant considérablement le bruit de fond. Le pluie de particules secondaires généré par les collisions des rayons

cosmiques avec l'atmosphère de la Terre produisent les muons atmosphériques et les neutrinos. Le blindage est nécessaire en raison des muons atmosphériques qui peuvent pénétrer dans l'atmosphère et jusqu'à plusieurs km de eau/glace. De plus, le flux des muons atmosphériques descendants dépasse le flux induit par les interactions des neutrinos atmosphériques de plusieurs ordres de grandeur (voir la figure 2.14), diminuant avec l'augmentation de la profondeur du détecteur.

- Fournir une transmission lumineuse efficace de la lumière Tcherenkov (voir le paraghraphe 2.3.5) émise par des particules secondaires relativistes induites par l'interaction des neutrinos;

- Assurer une longévité qui joue un rôle décisif en raison de l'inaccessibilité des composants du détecteur en cas de problème et de la collecte de données pour la détection d'événements extrêmement rares ou exceptionnels.

Le neutrino ne porte pas de charge électrique et ne peut donc interagir que via la force faible ou via la gravité. Les neutrinos sont détectés par leurs interactions avec un nucléon via l'interaction faible (voir le paraghraphe 2.3.1 pour plus de détails). Il existe deux types d'interaction faible, en fonction des bosons vecteurs intermédiaires échangés, le W ou le Z, impliqués dans la médiation de la force. Les réactions de courant chargé sont induites par $W^{\pm}$ boson (avec une masse $M_W \sim 80.379$ GeV):

$$\nu_l + N \xrightarrow{W^-} l^- + X,$$
$$\bar{\nu}_l + N \xrightarrow{W^+} l^+ + X.$$

Les réactions de courant neutre sont induites par le boson Z^0 (de masse $M_Z \sim 91.188$ GeV):

$$\nu_l + N \xrightarrow{Z^0} \nu_{l'} + X.$$

Ici, l désigne un lepton chargé, N est le noyau cible et X indique une cascade hadronique. Il n'y a pas de lepton chargé dans l'état final pour le canal de courant neutre. La connaissance de la section efficace des neutrinos dans la région des hautes énergies devient de plus en plus importante en raison des récentes découvertes de neutrinos astrophysiques. En tant que télescope axé sur la détection des neutrinos extraterrestres de haute énergie, l'ANTARES s'intéresse principalement à la diffusion des neutrinos muoniques par les noyaux de matière en raison de la probabilité de détection plus élevée pour les neutrinos muoniques (et les anti-neutrinos muoniques): la plus longue longueur d'absorption des muons produits dans les interactions de courant chargées conduit à des taux d'événements plus élevés. Différents processus de diffusion doivent être pris en compte lors de la génération d'interactions des neutrinos avec la matière: diffusion inélastique profonde (DIS en Anglais), diffusion de nucléons quasi-élastique (QE en Anglais), plusieurs résonances nucléon N et Δ (RES en Anglais). La diffusion QE est prédominante dans les interactions neutrino pour les énergies neutrino inférieures à ~2 GeV. Ainsi, les canaux QE et RES sont souvent négligés car

leur contribution n'est significative qu'à basse énergie ($E \leq 10$ GeV). En conséquence, le canal DIS est dominant pour les interactions des neutrinos avec la matière dans la gamme d'énergie d'intérêt pour les télescopes à neutrinos modernes, c'est-à-dire pour ($E \geq 10$ GeV). Il y a aussi une résonance dite de Glashow, un pic de désintégration du boson W^- à l'énergie $E^{res}_{\bar{\nu}_e} \sim 6.3$ PeV, dont la section efficace dépasse les sections efficaces de courant chargées et de courant neutre de 50 et 100 fois respectivement (voir la figure 2.4).

Les différentes signatures de neutrinos (voir le paraghraphe 2.3.2) correspondent à différents types d'interaction (courant chargé, courant neutre ou résonance de Glashow) et les saveurs de neutrinos impliquées (électronique, muonique et tauique) sont observées par un télescope à neutrinos (voir la figure 2.5):

- Interactions des courant neutre des neutrinos de toutes les saveurs. Produit uniquement une gerbe hadronique, et aucun lepton chargé capable de laisser une trace détectable. Dans ce travail, il n'est pas utilisé.

- Interactions à courant chargé des neutrinos électroniques. Produisent une gerbe électromagnétique et hadronique. Les deux gerbes se combinent, et leur somme d'énergie est égale à l'énergie des neutrinos entrants. Contrairement à l'interaction des courant neutre des neutrino électronique, le neutrino dans l'interaction de courant chargé de neutrino électronique se transforme en un électron, qui initie une cascade leptonique. Dans ce travail, il n'est pas utilisé.

- Interactions à courant chargé des neutrinos muoniques. Produit une gerbe hadronique et un muon. La signature du muon sortant générée dans les interactions de courant neutre des neutrino muonique est appelée une trace. Un tel muon, traversant le milieu à une vitesse relativiste, le polarise, produisant le rayonnement Tcherenkov le long de sa trajectoire. La lumière Tcherenkov émise par les muons est alors détectée. Pour les neutrinos muoniques, une résolution angulaire médiane que 0.4° est obtenue. Ainsi, cela donne un avantage dans la recherche de neutrinos en provenance de sources ponctuelles. Dans ce travail, de tels événements, appelés de muons, sont sélectionnés.

- Interactions à courant chargé des neutrinos tauique. Produit une gerbe hadronique et trace différentes signatures d'événements telles que "double bang", "lollipop", "inverted lollipop", "sugar daddy", et tautsie pop. Ces signatures seront discutées en détail. Dans ce travail, il n'est pas utilisé.

Les neutrinos muoniques sont particulièrement intéressants dans la recherche de sources ponctuelles cosmiques de neutrinos avec des énergies supérieures à ~1 TeV. Dans cette gamme d'énergie, l'interaction des neutrinos muoniques peut se produire en dehors du volume du détecteur ANTARES, alors que dans la plupart des cas, les muons sont suffisamment énergétiques pour traverser complètement le détecteur. Cela donne un signal expérimental propre qui permet une reconstruction précise de la direction des muons, étroitement corrélée avec la direction des neutrinos. La relation entre les directions des neutrinos et des muons

est essentielle pour le concept d'un télescope à neutrinos. Puisque les neutrinos ne sont pas déviés par les champs magnétiques (extra-) galactiques, il est possible de remontrer à la source de neutrinos, ce qui équivaut à l'astronomie traditionnelle où les photons pointent vers leur source. Lors de sa propagation dans la roche, la glace ou l'eau, le muon subit de multiples diffusions. Malgré la diffusion multiple de Coulomb lors de la traversée d'une roche, de glace ou d'eau, la déviation de la direction du muon due au processus de diffusion est d'un ordre de grandeur inférieur à l'angle de diffusion entre le neutrino incident et le muon sortant dans le canal de courant chargé. En conséquence, la direction du muon peut être reconstruite avec une estimation précise de la direction du neutrino car le muon conserve sa direction d'origine avec une très bonne approximation. Ceci, à son tour, conduit à une localisation précise de la source de neutrinos dans le ciel, ce qui est essentiel pour l'astronomie des neutrinos. Le muon perd de l'énergie en raison de plusieurs processus, notamment l'ionisation, la production de paires, la rayonnement de freinage (ou "bremsstrahlung") et les interactions photonucléaires (voir les détails au paragraphe 2.3.4). L'ionisation devient dominante sur les processus radiatifs (production de paires, bremsstrahlung et interactions photonucléaires) à des énergies inférieures à ∼1 TeV, tandis que la production de paires, bremsstrahlung et les interactions photonucléaires deviennent dominantes sur l'ionisation à des énergies supérieures à ∼1 TeV (voir la figure 2.11). Les muons avec des énergies supérieures à ∼1 TeV peuvent se propager dans l'eau sur de grandes distances telles que des dizaines de kilometres (voir la figure 2.11), ce qui explique qu'un télescope à neutrinos tel qu'ANTARES y soit le plus sensible.

L'utilisation d'eau ou de glace comme milieu de détection permet la détection des particules chargées induites par les neutrinos via la détection du rayonnement Tcherenkov (voir le paraghraphe 2.3.5 pour plus de détails). La particule chargée traversant le milieu polarisable excite les molécules et les atomes en créant des dipôles (voir la figure 2.12). Tant que la vitesse de la particule $u < c/n$, les dipôles sont disposés symétriquement autour du trajet des particules, de sorte que le champ dipolaire intégré sur tous les dipôles disparaît et qu'aucun rayonnement ne se produit. Si, cependant, la particule se déplace avec $u > c/n$, la symétrie est rompue, ce qui entraîne un moment dipolaire qui ne disparaît pas, ce qui conduit au rayonnement. Lorsque la perturbation est passée, les molécules reviennent rapidement à leur état fondamental et réémettent un rayonnement électromagnétique, connu sous le nom de rayonnement Tcherenkov. Ce rayonnement peut être mesuré dans des détecteurs de photons. Une particule voyageant à travers un milieu transparent à une vitesse supérieure à celle à laquelle la lumière se propage dans le même milieu, $u > c/n$, émet des ondes sphériques de lumière le long de sa trajectoire. Les ondes émises s'additionnent de manière constructive conduisant à un rayonnement cohérent à un angle dit de Tcherenkov θ_C par rapport à la direction des particules:

$$cos\theta_C = \frac{1}{\beta n}.$$

Ici, $\beta = u/c$ désigne le facteur de Lorentz de la particule, c est la vitesse de la lumière dans le vide, n est l'indice de réfraction du milieu ($n = 1.33$ pour l'eau). L'angle de Tcherenkov pour une trace relativiste ($\beta \approx 1$) est $\approx 41.2°$. La mesure du temps d'arrivée de la lumière Tcherenkov permet la reconstruction de la direction des particules, et la quantité de lumière collectée peut être utilisée pour estimer la particule énergie. Dans l'intensité du rayonnement Tcherenkov, les courtes longueurs d'onde sont dominées et les intensités sont principalement réparties dans les bandes ultraviolettes et bleues du spectre, où les tubes photomultiplicateurs sont les plus sensibles. Par conséquent, ces détecteurs de lumière sont utilisés dans les télescopes à neutrinos tels que ANTARES.

Dans **le troisième chapitre**, une brève description du télescope à neutrinos ANTARES est donnée suivi de la description (voir le paraghraphe 3.1) et des caractéristiques de la disposition et des composants du détecteur (voir le paraghraphe 3.2), du système d'acquisition de données (DAQ en Anglais) (voir le paraghraphe 3.3), des propriétés du site du détecteur (voir le paraghraphe 3.4) et de l'étalonnage (en temps, en charge et en position) du détecteur (voir le paraghraphe 3.5) et se termine par une description des principales étapes de construction et le statut du détecteur (voir le paraghraphe 3.6). ANTARES est le premier télescope à neutrinos sous-marin et actuellement le plus grand détecteur Tcherenkov d'eau en fonctionnement de l'hémisphère Nord. ANTARES est une collaboration internationale impliquant plus d'une centaine de physiciens, ingénieurs et experts en sciences de la mer de dizaines d'instituts de nombreux pays. ANTARES est principalement conçu pour rechercher des neutrinos de haute énergie à partir de sources astrophysiques en détectant l'émission de lumière Tcherenkov de particules chargées induites par les neutrinos dans les eaux très profondes de la mer Méditerranée et les plus sensibles au neutrino énergies 100 GeV $< E_\nu <$ 100 TeV. ANTARES s'est révélé être un instrument très efficace pour effectuer un large éventail d'analyses physiques, des oscillations des neutrinos atmosphériques à l'annihilation de la matière noire ou à des particules exotiques tels que les nucléites et les monopôles magnétiques. En tant que détecteur situé dans l'hémisphère Nord. ANTARES bénéficie de sa latitude et est capable d'explorer le ciel austral, offrant une sensibilité sans précédent à la région centrale de notre galaxie, où des candidats sources de neutrinos sont attendus. Le programme de recherche comprend également des analyses multimessagers sur la base de coïncidences temporelles et/ou spatiales avec d'autres particules cosmiques telles que les noyaux actifs de galaxie, les sources les plus brillantes de notre Univers. Comparé à un expérience du Pôle Sud tel que IceCube, le télescope ANTARES donne la possibilité supplémentaire d'étudier des sources galactiques comme les étoiles binaires, rémanents de supernova ou microquasar et rechercher l'accumulation de matière noire au centre de la galaxie. Cependant, la vue donnée par les télescopes du Sud et du Nord est complémentaire à la fois dans la carte du ciel potentielle et les objets qui peuvent être étudiés.

Le détecteur est constitué d'un réseau de 885 photomultiplicateurs sensibles à la lumière Tchérenkov répartis sur 12 lignes de détection (voir la figure 3.3) de 450 m de hauteur (voir le paraghraphe 3.2). Chaque ligne est équipée de 25 étages de 3 modules optiques, à

l'exception de la ligne 12 avec seulement 20 étages des modules optiques complétés par un dispositif dédié à la détection acoustique. Les lignes sont disposées dans une configuration octogonale, l'espacement horizontal entre les lignes est ~60 m, tandis que l'espacement vertical entre les étages est de 14.5 m à 100 m du fond marin. Les distances entre des modules optiques sont optimisés par rapport à la longueur d'absorption dans l'eau, qui a un maximum environ ~60 m. Le détecteur est installé sur une surface d'environ 0.1 km^2 à 2475 mètres de profondeur. Chaque ligne est ancrée sur le fond marin et est maintenue verticale par une bouée immergée. Chaque module optique (voir la figure 3.4) est une sphère de verre qui héberge un photomultiplicateur, le tube de 10 pouces de Hamamatsu, dont l'axe pointe 45° vers le bas (voir la figure 3.6) afin d'optimiser la détection de la lumière des muons montants. Le module optique, l'œil du détecteur, est un composant clé du détecteur ANTARES, car il détecte en fait la lumière Tcherenkov des particules secondaires chargées créées dans les interactions neutrinos à proximité ou à l'intérieur du détecteur. Les modules optiques sont regroupés en triplets pour la réduction essentielle du fond optique environnemental des eaux profondes comme les désintégrations radioactives de ^{40}K ou la bioluminescence en utilisant des coïncidences sur le même étage dans un court intervalle de temps. Chaque ligne est instrumentée avec plusieurs conteneurs électroniques contenant en particulier l'équipement acoustique de positionnement et le système de calibration (voir le paraghraphe 3.2.3). Au bas de chaque ligne les informations transitent sur des câbles électro-optiques de 40 km de long qui sont connectés, à l'aide d'un sous-marin, vers une boîte de jonction. De cette boîte de jonction part le câble qui relie le détecteur à la côte. Tout cela sera expliqué en détail dans le troisième chapitre ainsi que l'électronique du détecteur tel que le système d'acquisition des données (DAQ). Le but principal de la DAQ est de convertir les signaux analogiques des photomultiplicateurs dans un format adapté à l'analyse physique. Pour y parvenir, le système DAQ a pour tâche de préparer le détecteur pour la prise de données, de convertir les signaux analogiques des PMT en données numériques, de transporter les données vers le côte, de filtrer les différents signaux physiques de fond, de stocker les données filtrées sur disque et archiver les paramètres du run. La stratégie choisie pour le système DAQ en ANTARES est basée sur le concept "all-data-to-shore" (voir le paraghraphe 3.3). Cette stratégie nécessite le transfert de toutes les données brutes au-dessus d'un certain seuil donné vers le rivage, où différents déclencheurs logiciels sont appliqués pour le filtrage avant le stockage. La numérisation des signaux photomultiplicateurs analogiques, la charge totale de l'impulsion et l'heure d'arrivée sont effectuées par une électronique dédiée. Il y a différents déclencheurs (voir le paraghraphe 3.3.3 pour plus de détails) tels que les déclencheurs de niveau 0 (L0), de niveau 1 (L1), de niveau 2 (L2), de niveau 3 (L3). Tous les signaux des photomultiplicateurs qui dépassent un seuil de 0.3 photoelectron (p.e.), appelés hits, sont numérisés et envoyés à la station à la côte. Lorsque le signal franchit le seuil défini, une impulsion de déclenchement L0 est envoyée à la carte DAQ. L'activité optique due à la désintégration des isotopes radioactifs de ^{40}K dans l'eau de mer et les bactéries bioluminescentes peut déclencher le seuil L0. Afin de réduire le fond aléatoire, les coïncidences de hit entre deux PMT voisins du même étage, dites coïncidences locales, dans une fenêtre de temps réglable (20 ns par défaut) sont nécessaires ou hits avec une

amplitude dépassant une certaine valeur (ajustables à partir de 3 p.e. à 10 p.e. en fonction de la période de temps) dans un seul photomultiplicateur. Ces coups sont étiquetés comme coups L1 et une telle logique de déclenchement basée sur les coïncidences locales est appelée déclencheur L1. Un groupe de L1 hits satisfait la relation causale (décrit par l'équation 3.3) comme dans les 20 ns afin de tenir compte des photons diffusés et des incertitudes dues à l'étalonnage et contient un nombre minimum de coups (généralement 5 hits, donc $N_{L1} \geq 5$) est appelé un cluster. Cet ensemble de hits L1 qui forme un cluster est considéré comme un événement candidat qui est l'entrée pour les stratégies de reconstruction. La formation de clusters permet de supprimer le taux d'événements du fond. Tous les hits qui satisfont une ou plusieurs conditions de déclenchement sont sélectionnés comme L2 hits. L'inclusion de hits éventuellement produits par un signal physique et non précédemment ajoutés dans le cluster se fait au niveau L3. Le système DAQ de ANTARES exécute plusieurs déclencheurs en même temps. Les déclencheurs principaux, basés sur des coïncidences locales et directionnelles, incluent K40, 3N, T3, 2T3, GC, TQ. Tous ces déclencheurs seront décrits dans le troisième chapitre.

L'environnement extrême, incontrôlable et hostile des grands fonds, où se trouve le détecteur ANTARES, nécessite des études d'évaluation de site approfondies et détaillées pour garantir le succès du déploiement d'un détecteur à grande échelle et que les éléments du détecteur résisteront à ses conditions difficiles (voir le paraghraphe 3.4 pour plus de détails). La sélection d'un site approprié pour un télescope à neutrinos nécessite une profondeur suffisante afin de fournir un blindage contre les muons atmosphériques, des conditions météorologiques acceptables, la proximité de la côte et une infrastructure développée pour le soutien à terre, un déploiement facile et une réduction substantielle des coûts d'électricité et connexion des signaux au rivage. En outre, la force des courants profonds, l'encrassement des surfaces optiques, la transparence de l'eau (par exemple pour les longueurs d'absorption et de diffusion souhaitables), le fond optique et le niveau de bioluminescence doivent être examinés avec attention et rigueur. Le site ANTARES a été choisi après une évaluation détaillée des sites candidats au cours de la phase R&D du projet et des mesures in situ des propriétés optiques et environnementales pertinentes pour la performance du détecteur. Certains des problèmes les plus importants sont abordés dans le troisième chapitre.

Dans **le quatrième chapitre**, une brève description de observatoire de rayons gammas de très hautes énergies HAWC est donnée suivie de la description (voir le paraghraphe 4.1) et des caractéristiques de la disposition du détecteur (voir le paraghraphe 4.2), le fonctionnement du détecteur (voir le paraghraphe 4.3), aussi les objectifs scientifiques (voir le paraghraphe 4.4), sources astrophysiques détectées (voir le paraghraphe 4.5) et l'extension possible du détecteur (voir le paraghraphe 4.6). HAWC est constitué d'un ensemble de 300 réservoirs d'eau purifiée couvrant une superficie de 22 000 m^2 (la surface active est de 12 000 m^2) (voir la figure 4.2). Chaque réservoir rempli de 190 000 litres d'eau hautement purifiée et équipé de quatre photomultiplicateurs dirigés vers le haut pour détecter la lumière Tcherenkov des particules chargées dans une gerbe atmosphérique. Les réservoirs font 7.5

mètres de diamètre et 5 mètres de hauteur (voir la figure 4.3). Au bas de chaque réservoir, trois photomultiplicateurs Hamamatsu de 8 pouces sont ancrés dans un triangle équilatéral de 3.2 mètres de long, avec un Hamamatsu à efficacité quantique élevée de 10 pouces ancré au centre, conçu pour augmenter l'efficacité de l'observatoire à faible energies. Cet observatoire est conçu pour détecter les cascades électromagnétiques produites lors de l'interaction de particules hautement énergétiques avec l'atmosphère terrestre. HAWC est optimisée pour la détection de gerbes atmosphérique par des rayons gamma entre ~0.1 et ~100 TeV, la sensibilité maximale étant atteinte à quelques TeV, selon les spectres de la source. Les objectifs scientifiques de HAWC s'inscrivent dans le contexte de l'astronomie gamma et de l'astronomie multimessager, qui tentent d'étudier les phénomènes astrophysiques les plus énergétiques et le plus puissant de l'Univers. L'avantage de HAWC par rapport à la technique de télescope à imagerie Tcherenkov atmosphérique (IACT en Anglais) est que les gerbe à photons peuvent être détectées sur l'ensemble du champ de vue de 2 stéradians de l'instrument, de jour comme de nuit, quelles que soient les conditions météorologiques avec cycle utile >95%. Les IACT ont un champ de vue de quelques degrés et ne peuvent fonctionner que par nuits claires. Tout cela fait que HAWC est particulièrement adapté pour étudier les courbe de lumières de longue durée des objets et pour rechercher des sources avec les "bouffées" d'activités. Les informations temporelles des "bouffées" d'activités gamma de HAWC sont en mesure d'améliorer sensiblement l'efficacité de la recherche d'une contrepartie neutrino avec ANTARES et augmente le potentiel de découverte en réduisant le bruit de fond de manière significative dans les données. HAWC a publié le résultat de son première recherche de source réalisée avec 507 jours de données dans le catalogue 2HWC. Dans ce catalogue, 39 sources ont été trouvées, dont 19 étaient nouvelles. Les seules sources qui ont confirmé des associations extragalactiques dans le catalogue sont Markarian 421 (2HWC J1104+381) et Markarian 501 (2HWC J1653+397) (voir la figure 4.10). Ces deux blazars sont les deux sources extragalactiques les plus proches et les plus brillantes de la gamma d'énergie du TeV et présentent un intérêt particulier pour ce travail. D'autres sources HAWC seront également décrites en détail dans le quatrième chapitre. Remarquons que la plupart des sources détectées par HAWC sont des sources de neutrinos plausibles et sont dans la visibilité du télescope ANTARES.

Dans **le cinquième chapitre**, la chaîne de simulation ANTARES et la reconstruction d'événements sont décrites. Les simulations sont nécessaires pour comprendre la réponse du détecteur aux événements physiques et pour valider les techniques d'analyse telles que l'optimisation des coupures de sélection pour assurer un rejet correct des événements de fond (voir le paraghraphe 5.1 pour plus de détails). La chaîne de simulation peut être divisée en différentes étapes mais peut être résumée en deux sous forme de simulation physique et de simulation de la réponse de détecteur. La simulation physique comprend la simulation des neutrinos (voir les détails au paragraphe 5.1.1), des muons atmosphériques (voir les détails au paragraphe 5.1.2) et de la lumière induite par les particules chargées via l'effet Tcherenkov lors de leur propagation dans l'eau (voir les détails au paragraphe 5.1.3). Après cela, la réponse du détecteur est simulée (voir les détails au paragraphe 5.1.4). Une variété

d'algorithmes de reconstruction d'événements ont été développés dans ANTARES pour obtenir les informations les plus pertinentes sur les signatures d'événements produites dans le neutrino ou les interactions des muons atmosphériques (voir le paraghraphe 5.2 pour plus de détails). Les algorithmes de reconstruction d'événements ANTARES en mettant l'accent sur ceux qui ont été utilisés dans ce travail seront décrits dans le cinquième chapitre. La stratégie de simulation Monte Carlo utilisée pour ANTARES est appelée run-by-run (rbr). Pour chaque analyse physique, un fichier Monte Carlo est produit en extrayant des informations concernant les conditions d'acquisition des données directement à partir des données, ce qui permet de rendre compte de la variabilité des conditions environnementales et de l'état du détecteur ANTARES. Comme mentionné ci-dessus, la chaîne de simulation, développée dans ANTARES, peut être divisée en deux étapes principales et résumée comme suit:

- Simulation physique: les neutrinos et les muons atmosphériques sont générés à proximité du détecteur. Les particules se propagent à travers le détecteur et la lumière provenant de l'effet Tcherenkov est simulée et propagée aux photomultiplicateurs.

- Simulation DAQ: le comportement des photomultiplicateurs et de l'électronique d'acquisition de données est simulé. Des algorithmes de filtrage et de déclenchement sont appliqués qui prennent en charge l'ajout de l'optique fond des hits générés par les événements physiques et du déclenchement des événements. Le fond optique dû à la lumière de l'environnement (principalement les organismes bioluminescents et la désintégration du sel radioactif ^{40}K) est ajouté aux photomultiplicateurs en fonction des taux de comptage réellement observés dans les données de chaque photomultiplicateur. Les pphotomultiplicateurs non fonctionnels sont désactivés et la perte d'efficacité des photomultiplicateurs en fonction du temps peut également être prise en considération.

Aux fins de la génération d'interactions avec les neutrinos, le volume instrumenté du détecteur est traité comme un cylindre qui contient tous les photomultiplicateurs et entouré d'un plus grand cylindre, appelé *can* (voir la figure 5.1). La *can* définit le volume nécessaire pour que la lumière Tcherenkov atteigne le volume instrumenté où elle peut être détectée. Dans ANTARES, la *can* a été choisie de manière à ce que sa surface soit à une distance d'environ ~200 m autour du volume instrumenté, soit environ trois fois la plus longue longueur d'absorption de lumière dans l'eau (~60 m). La *can* est la base du volume de génération, qui est une extension dépendante de l'énergie de la *can*, au sein de laquelle des interactions neutrino sont générées. Il est défini pour assurer la génération de toutes les interactions possibles qui pourraient produire un muon qui pourrait traverser la détecteur. Sa taille est déterminée à partir de la énergie maximale de muons associée à l'énergie neutrino la plus élevée qui est générée, généralement $E_{max} = 10^8$ GeV, et correspond à un cylindre de 25 km de rayon et de hauteur autour du détecteur. En dehors de ce volume, seules les pertes d'énergie des particules en propagation sont prises en considération. Dans ANTARES, les interactions neutrinos à haute énergie sont générées à l'aide du générateur

d'événements Monte Carlo GENHEN développé par ANTARES (voir le paraghraphe 5.1.1). Ce générateur sera décrit en détail dans le cinquième chapitre. Outre les neutrinos, les muons atmosphériques, comme fond principal des neutrinos, sont également simulés (voir le paraghraphe 5.1.2). Dans ANTARES, les muons atmosphériques sont générés à l'aide du logiciel MUPAGE qui sera également décrit en détail dans le cinquième chapitre. L'émission de lumière de Tcherenkov peut provenir de la propagation de muons et d'électrons chargés dans l'eau. La sortie ASCII fichier de GENHEN est traitée avec KM3 basé sur GEANT et avec les packages logiciels GEASIM, pour simuler la production de lumière Tcherenkov et sa propagation vers les photomultiplicateurs du détecteur (voir le paraghraphe 5.1.3), où les hits sont générés. Un modèle de l'eau de mer, qui contient des informations sur la composition, la densité et la longueur d'atténuation, sur le site d'ANTARES est fourni en entrée à KM3. Enfin, le détecteur est simulé (voir le paraghraphe 5.1.4).

Une variété d'algorithmes de reconstruction d'événement ont été développés dans ANTARES pour obtenir les informations sur la direction, la position et l'énergie de l'événement en utilisant les temps et les amplitudes d'arrivée des hits. Les algorithmes de reconstruction, en ligne (BBfit) et hors ligne (AAfit), seront discutés (voir le paraghraphe 5.2.1 pour plus de détails) en mettant l'accent sur ceux utilisés pour ce travail. AAfit, plus avantageux et précis que BBfit a été développé par ANTARES à des fins d'analyse de données. Il a une meilleure efficacité de détection et une résolution angulaire ce qui le rend AAfit avantageux dans les recherches des neutrinos de sources ponctuelles, en particulier avec son excellente résolution angulaire, et est utilisé dans ce travail. En bref, l'algorithme de reconstruction de piste AAfit se compose de quatre procédures d'ajustement consécutives. Il comprend un préfit linéaire utilisant un χ^2, un estimateur M, un ajustement de vraisemblance maximale (sans et avec des hits de fond) lors de l'ajustement des hits dans une piste de muons. La description complète de l'algorithme de reconstruction AAfit sera donnée dans le cinquième chapitre. Dans l'algorithme de reconstruction, deux variables sont introduites qui peuvent être utilisées pour rejeter des événements mal reconstruits, par example, muons atmosphériques reconstruits à tort comme ascendants. Ceci est crucial pour les analyses dépendantes du temps en tant que telles effectuées dans ce travail. Le premier paramètre qui peut être obtenu est le paramètre de qualité Λ qui est utilisé pour sélectionner les événements bien reconstruits. Le paramètre Λ caractérise la qualité de l'ajustement. Le deuxième paramètre est l'estimation de l'erreur angulaire sur la direction de la piste de muons reconstruite, β, qui est obtenue à partir des estimations d'erreur du zénith σ_θ de la trace et des angles d'azimut σ_ϕ comme suit:

$$\beta = \sqrt{\sigma_\theta^2 + sin^2\theta\sigma_\phi^2}.$$

Ces deux variables, Λ et β, peuvent être utilisées pour sélectionner des muons bien reconstruits parmi des muons ascendants mal reconstruits. Les mêmes paramètres sont utilisés pour rejeter du fond des muons atmosphériques mal reconstruits, qui forment du fond plus dangereux que les muons ascendants. Cela permet la suppression du fond et améliore le

rapport signal/bruit. Pour la reconstruction de l'énergie des muons (voir le paraghraphe 5.2.2 pour plus de détails), la quantité de lumière détectée sur le photomultiplicateur est utilisée. Deux méthodes indépendantes sont utilisées pour estimer l'énergie des muons. La première - désignée ci-après comme *la méthode de vraisemblance énergétique* - maximise l'accord de la quantité de lumière attendue dans les photomultiplicateurs avec la quantité de lumière réellement observée. La deuxième méthode d'estimation de l'énergie des muons - désignée ci-après comme *la méthode de la perte d'énergie* - repose sur les pertes d'énergie des muons le long de sa trajectoire. Les deux méthodes seront décrites en détail dans le cinquième chapitre. Les neutrinos générés dans l'atmosphère ont un spectre d'énergie beaucoup plus doux ($\propto E^{-3.7}$) que les neutrinos du flux astrophysique attendu (par exemple, $\propto E^{-2.0}$). Par conséquent, les informations de l'estimateur d'énergie sont utilisées selon la probabilité de distinguer davantage le signal cosmique et le fond atmosphérique. Divers estimateurs d'énergie ont été développés dans ANTARES: *nhit*, *dE/dX*, *ANNr*. Le plus simple est *nhit*, qui est le nombre total de hits dans les photomultiplicateurs sélectionnés par la reconstruction de la trace, qui devrait être proportionnel à l'énergie des particules incidentes. Ce nombre dépend fortement de la géométrie du détecteur et de la localisation de l'événement neutrino en son sein. Cependant, jusqu'à présent, l'estimateur *nhit* a servi dans de nombreuses analyses de estimateur énergétique generale et de critère de sélection pour les événements de neutrinos bien reconstruits, de sorte qu'il est adopté pour ce travail.

Dans **le sixième chapitre**, les méthodes statistiques qui seront exploitées dans l'analyse sont introduites. L'algorithme de recherche utilisé dans cette analyse est basé sur une méthode de maximisation du rapport de vraisemblance (voir le paraghraphe 6.1 pour plus de détails). Les ingrédients de la vraisemblance tels que la direction, l'énergie et le temps seront également discutés (voir les détails au paragraphe 6.2). La fonction de distribution de probabilité de temps du bruit de fond et la fonction de distribution de probabilité de temps du signal seront présentées. La simulation de pseudo-expériences et la systématique possible seront discutées (voir le paraghraphe 6.3 pour plus de détails). La statistique de test sera également expliquée brièvement (voir le paraghraphe 6.4). La stratégie d'optimisation sera décrite et le potentiel de découverte du modèle sera présenté (voir les détails au paragraphe 6.5). Enfin, la façon dont les limites supérieures sont fixées sera donnée (voir le paraghraphe 6.5.2). L'avantage de l'analyse en fonction du temps par rapport à la recherche de source ponctuelle standard est que les informations de temps supplémentaires provenant de "bouffées" dans l'activité des sources améliorent l'analyse en restreignant les données à une période d'intérêt et donc en réduisant les fond atmosphériques de neutrinos et de muons; elle nécessite donc un nombre inférieur d'événements de signal pour une découverte. Les courbes de lumières des "bouffées" d'activité peuvent être utilisées comme une fonction de distribution de probabilité temporelle dans la vraisemblance. De ce fait, les informations de synchronisation de "bouffées" dans l'activité gamma fournies par HAWC et impliquées dans la méthode de recherche seront discutées dans le sixième chapitre. Ces informations peuvent améliorer l'efficacité de la recherche d'une contrepartie neutrino avec ANTARES. Les sources avec le "bouffées" d'activité gamma sont intéressantes d'un point de vue physique car les processus

requis pour la production de "bouffées" peuvent impliquer les processus hadroniques dans lesquels les neutrinos peuvent également être produits. La bonne résolution angulaire dans ANTARES, inférieure à 1^0, permet de rechercher des corrélations spatiales avec des sources astrophysiques connues. Dans ce travail, les deux sources ciblées pour la recherche temporelle sont les blazars, Markarian 421 et Markarian 501.

L'échantillon de données ANTARES est un mélange à deux composantes, de signal (S) et de bruit de fond (B):

$$\ln(\mathcal{L}) = \left(\sum_{i=1}^{N} \ln[N_S S_i + N_B B_i] \right) - [N_S + N_B]$$

Les S_i et B_i sont définies comme les Fonctions de densité de probabilité (PDFs) respectivement pour le signal et le bruit de fond d'un événement i, au temps t_i, énergie E_i, déclinaison (direction d'origine) δ_i:

$$S_i = P_s(\alpha_i) \cdot P_s(E_i) \cdot P_s(t_i)$$
$$B_i = P_b(\sin(\delta_i)) \cdot P_b(E_i) \cdot P_b(t_i)$$

Ici,

- Les fonctions de distribution de probabilité directionnelle: $P_S(\alpha_i)$ (signal) et $P_B(\delta_i)$ (fond). Le paramètre α_i représente la distance angulaire entre la direction de l'événement i et la direction de la source δ_i.

- Les fonctions de distribution de probabilité d'énergie: $P_S(E_i)$ (signal) et $P_B(E_i)$ (fond). L'estimateur *nhit* est adopté pour ce travail. Le terme en énergie de la fonction de densité de probabilité pour les événements de signal est construit en fonction du spectre d'énergie étudié: $E^{-2.0}$, $E^{-2.5}$, $E^{-1.0} \exp(-E/1\,\mathrm{PeV})$ pour les deux sources, en ajoutant un spectre $E^{-2.25}$ pour Mrk 501 seulement (en regard du spectre gamma observé).

- Les fonctions de distribution de probabilité temporelle: $P_S(t_i)$ (signal) and $P_B(t_i)$ (fond). Les courbes de lumière pour chaque source dérivées de HAWC montrent les périodes d'intérêt pour la recherche de neutrinos coïncidents et utilisées comme fonction de distribution de probabilité temporelle. Les fonctions de distribution de la probabilité de temps de fond $P_B(t_i)$ est la probabilité d'avoir un événement de fond à un moment donné t_i. Il est construit en utilisant la distribution dans le temps des événements ANTARES avec les critères suivants: coupure sur le paramètre de qualité $\Lambda > -5.6$, le nombre de hits dans les photomultiplicateurs *nhit*>5 sur plus d'une ligne *nline*>1, et une incertitude angulaire estimée sur la direction de la trajectoire du muon $\beta < 1.0°$.

Les paramètres N_S et N_B représentent le nombre d'événements de signal inconnus et le nombre d'événements de bruit de fond connu (a priori lors de la construction de L) respectivement. Le N_S est ajusté en maximisant la vraisemblance $\mathcal{L}$. Le but de la méthode est de déterminer dans une direction donnée dans le ciel et à un instant donné la contribution relative du signal et du fond.

Comme discuté ci-dessus, les "courbes de lumière" gamma mesurées pour ces sources sont utilisées pour l'analyse en tant que terme temporelle de la fonction de densité de probabilité, en supposant la proportionnalité entre les flux gamma et les flux neutrinos. Afin de trouver la période de recherche optimale, plusieurs conditions de sélection sur le flux ont été prises en compte tel que les états d'émission qui dépassent les seuils *flux moyen*, *flux moyen+1*σ, *flux moyen+2*σ. En plus de cela, la situation où la courbe de lumière complète est utilisée est prise en compte. En fait, l'utilisation de ce seuil fournit un meilleur pouvoir de découverte et de meilleures sensibilités sur la fluence neutrino, bien que de meilleures sensibilités sur les flux neutrino sont données par l'utilisation de toutes les états d'émission disponibles.

Le but de la méthode de maximisation du rapport de vraisemblance est de déterminer, dans une direction donnée du ciel et à un instant donné, la contribution relative du signal et du bruit de fond. Pour différencier ces deux hypothéses, en présence d'une petite quantité de signal et en présence du bruit de fond seulement, nous construisons une statistique de test (TS) équivalente à un rapport de vraisemblance :

$$\mathrm{TS} = 2(\ln(\mathrm{L}_{s+b}^{max}) - \ln(\mathrm{L}_b))$$

La TS est évaluée en générant des pseudo-expériences simulant le bruit de fond et le signal autour de la source considérée. Dans cette analyse, 30 000 pseudo-expériences sont effectuées pour chaque événement de signal injecté et 300 000 pour le bruit de fond. Avec les pseudo-expériences simulées, les paramètres de la recherche sont optimisés.

Pour améliorer le rapport signal-sur-bruit et obtenir la meilleure sensibilité au flux des sources en rejetant le bruit de fond de de muons atmosphériques mal reconstruits, plusieurs sélections sont appliquées, telles que: coupures sur le cosinus de l'angle zénithal des événements reconstruits $\cos(\theta) > -0.1$ ($\cos(\theta) = 0$ représentant la direction horizontal, et $\cos(\theta) = 1$ la verticale ascendante), coupure sur l'erreur sur la direction des événements reconstruits $\beta < 1.0°$ et coupure sur la qualité du paramètre de reconstruction des traces Λ (l'intervalle [-5,8; -5,0] a été testé, et il a été observé que [-5,6; -5,0] s'avère suffisante pour l'analyse). La coupure sur Λ est optimisée pour chaque source et chaque spectre de neutrinos sur la base de l'optimisation du potentiel de découverte du modèle (MDP), c'est-à-dire la probabilité d'effectuer une découverte.

Dans **le septième chapitre**, les résultats du travail de thèse seront exposés. Ce travail est dédié à la recherche de recherche avec le télescope ANTARES de neutrinos de haute énergie en provenance des blazars proches Markarian 421 et Markarian 501 en corrélation avec des

émissions gamma détectés par l'observatoire HAWC (voir le paraghraphe 7.1 pour plus de détails). Les blazars sont les premières sources identifiées de neutrinos astrophysiques de haute énergie, qui motivent à chercher les neutrinos de haute énergie des deux blazars les plus proches et les plus brillants, Markarian 421 et Markarian 501. En tant que premier et deuxième objets extragalactiques découverts dans la bande d'énergie TeV, Markarian 421 et Markarian 501 sont de un très bons candidats pour une contrepartie neutrino. Notons que ces deux blazars ont confirmé des associations extragalactiques dans le catalogue 2HWC et font l'objet de campagnes de surveillance à long terme par l'observatoire à rayons gamma HAWC TeV.

L'échantillon de données d'ANTARES utilisé dans dans cette analyse correspond à la période de recherche d'observation par HAWC et couvrant les données collectées entre novembre 2014 et décembre 2017 (voir le paraghraphe 7.3 pour plus de détails). Dans les courbes de lumière variables, des algorithmes bayésiens sont utilisés pour trouver la segmentation optimale des données dans des régions bien représentées par un flux constant. L'algorithme utilisé dans l'analyse (voir les détails au paragraphe 7.1.2) est basé sur celui utilisé par HAWC pour ses propres données. Les états de flux stables et les "points de changement" lors du passage d'un état de flux à un autre sont identifiés. L'algorithme de blocs bayésien n'a pas été appliqué pour la première partie de l'analyse car les états de flare déjà calculés par HAWC avaient été utilisés. Pour la deuxième partie de l'analyse, l'analyse prolongée avec l'inclusion de l'année 2017, les blocs bayésiens sont appliqués (voir la figure 7.4).

Aucun excès significatif n'est trouvé dans cette analyse (voir le paraghraphe 7.4 pour plus de détails). Jusqu'à présent, aucune émission neutrino par ces 2 objets n'a pu être mise en évidence. Les valeurs-p obtenues (probabilité pour un modèle statistique donné sous l'hypothèse nulle d'obtenir la même valeur ou une valeur encore plus extrême que celle observée) pour les sources sont supérieures à 10% et ne présentent donc aucun intérêt particulier pour une discussion plus approfondie. Avec ces valeurs-p, on peut considérer que les données plaident contre l'hypothèse de la présence de signal. En prenant en compte les facteurs d'essai, les valeurs-p finales sont supérieures à 50%, ce qui est tout à fait compatible avec l'hypothèse selon laquelle notre échantillon de données est composé uniquement d'événements de bruit de fond. Ainsi, les limites supérieures à 90% de niveau de confiance ont été déterminées pour les flux à 90% CL pour Mrk 421 et Mrk 501 pour le spectre E^{-2}:

$$E^2\Phi_{90\%} = 4.96 \times 10^{-11} \text{ TeV cm}^{-2} \text{ s}^{-1} \quad \text{[Mrk 421]}$$
$$E^2\Phi_{90\%} = 9.79 \times 10^{-11} \text{ TeV cm}^{-2} \text{ s}^{-1} \quad \text{[Mrk 501]}$$

Plus de détails sur les résultats et les discussions pour d'autres spectres seront donnés dans le septième chapitre. Et la conclusion finale sera faite et les perspectives seront discutées dans le chapitre de conclusion.

1 Cosmic Messengers and the rise of Neutrino Astronomy

> *In an ordinary way I might say that I do not believe in neutrino... But I have to reflect that a physicist may be an artist, and you never know where you are with artists. My old-fashioned kind of disbelief in neutrinos is scarcely enough. Dare I say that experimental physicists will not have sufficient ingenuity to make neutrinos? Whatever I may think, I am not going to be lured into a wager against the skill of experimenters under the impression that it is a wager against the truth of a theory. If they succeed in making neutrinos, perhaps even in developing industrial applications of them, I suppose I shall have to believe – though I may feel that they have not been playing quite fair.*
>
> **— Sir Arthur Stanley Eddington**
> The Philosophy of Physical Science:
> Tarner Lectures, 1938

THE discovery of Cosmic Rays (CRs) by Victor Hess [1] dates back to a more than a century. This discovery had an immediate impact on particle physics: the use of CRs as a source of high-energy particles led to the discovery of a large number of particles, such as positrons in 1932 [2], muons in 1936 [3], kaons and pions in 1947 [4]. Soon, the relation between CR's, Gamma Rays (γ-rays) and neutrinos has been understood: the high-energy γ-rays and neutrinos dominantly are the result of the processes where CR particles are involved.

The 20$^{\text{th}}$ century was fruitful for astronomy and resulted in many revolutionary discoveries. Starting from the usage of only optical photons, different bands across the electromagnetic spectrum have been mastered, progressively moving to *multiwavelength* astronomy. The impetuous scientific progress leads to a set of fundamental discoveries in astronomy such as the first observations of: the Universe expansion in [5], the Quasars, an extremely luminous Active Galactic Nuclei (AGNs) [6], the Cosmic Microwave Background (CMB) in 1964 [7], pulsars in 1968 [8] in the radio-wave spectrum, the Gamma-Ray Bursts (GRBs) [9], the exoplanets [10], the high-energy neutrinos of extrasolar origin in 2013 [11], the Gravitational

Waves (GWs) in 2015 as a result of the merger of a pair of Black Holes (BHs) [12], the Neutron Star (NS) merger in 2017 [13], the identification of the source of high-energy neutrinos in 2017 [14, 15, 16]. The success of the relatively young field of neutrino astronomy by several breakthroughs established it as a mature domain of physics initiating the construction of km^3 scale neutrino telescopes. This provides unprecedented opportunity to pursue a deep study of the most violent and energetic phenomena in the Universe.

The hadronic acceleration of CRs is an open question for γ-ray despite a wealth of electromagnetic data. There was no viable explanation of blazar radiation mechanisms with leptonic and lepto-hadronic scenarios. Detection of neutrinos produced in the vicinity of cosmic accelerators, able to prove where the CRs acceleration takes place. Since blazars are proposed sites of CRs acceleration, the hadronic acceleration issue in such sources has substantial implications and the message conveyed by high-energy neutrinos is crucial for resolving these issues. The recent detection of first high-energy neutrinos with correlated γ-rays from blazars was vital to resolve this challenge [15, 16] (see Section 1.7).

Neutrinos which carry only a weak charge and thus able to propagate indefinitely without neither deflection neither absorption can point back to their sources. This makes neutrinos as the most advantageous messenger among CRs, γ-rays, GWs to carry information from the most violent environments in the Universe.

Before focusing on neutrinos and their possible sources, the brief reviews of the three other messengers in astronomy (CRs, γ-rays, GWs) are given. The CRs are discussed in Section 1.1, where the overview of the composition and energy spectrum of CRs is given in Section 1.1.1, the mystery of extreme energies are described in Section 1.1.2, the acceleration mechanisms and the origin of CRs are discussed in Section 1.1.3 and Section 1.1.4 respectively. The γ-rays are discussed in Section 1.2. The GWs are discussed in Section 1.3. The neutrinos are discussed in Section 1.4. The CR-γ-ν connection is discussed in Section 1.5. The potential high-energy neutrino source candidates, galactic and extragalactic origin, are discussed in Section 1.6. Finally, Section 1.7 focuses on multimessenger astronomy.

1.1 Cosmic rays: particles from outer space

Cosmic rays are high-energy charged particles constantly hitting the Earth's upper atmosphere from all directions and producing showers of secondary particles (see Fig. 1.1 and Fig. 2.13) that reaches the ground. Despite being discovered in 1912 by V. Hess [1], more than a century ago, many features about CRs remain a mystery so far, among which the origin and acceleration sites of the CRs still remains one of the most important unresolved problems in astrophysics. It is known that the CRs of the lowest energies come from the Sun. Most scientists suspect supernovae (star explosions) to be the accelerators of the CRs within our Galaxy (see Section 1.1.4) and other mechanisms proposed for CRs of the highest energies arriving from outside of the Galaxy (see Section 1.1.4).

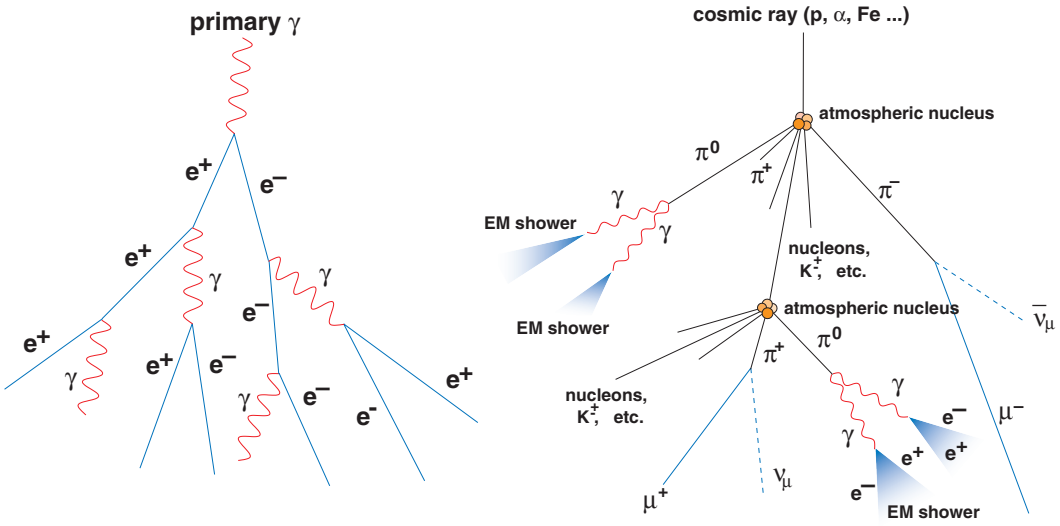

Fig. 1.1.: Schematic description of *Extensive Air Showers*, or EAS. *Left:* Electromagnetic shower generated by a primary γ-ray and purely composed of electron-positron (e^+e^-) pairs and photons. *Right:* Hadronic shower generated by a CR (hadronic particle, proton or nucleus) producing a large variety of secondary particles: pions, kaons, muons, photons and neutrinos. The figure is taken from [17].

1.1.1 Composition and energy spectrum

Back in 1930, Bruno Rossi predicted [18] that the CRs as charged particles would be affected by the presence of the Earth's magnetic field giving preference in their arrival direction to be from the West. This asymmetry is a so-called "East-West" effect proved by the variety observations in the 1930s starting with the first evidence made by Johnson and Street in 1933 [19] (with the most survey undertaken in 1935 [20]) and followed by Alvarez and Compton in 1933 [21], Rossi in 1934 [22, 23], Bhattacharya in 1942 [24]; other studies were performed in [25, 26]. The "East-West" effect showed that CRs are mainly composed of positively charged particles (e.g., protons). In balloon measurements performed by Hess, he observed an electroscope discharged more rapidly when increasing an altitude. And the CRs, first seen as radiation coming from outer space, later in 1948 [33,

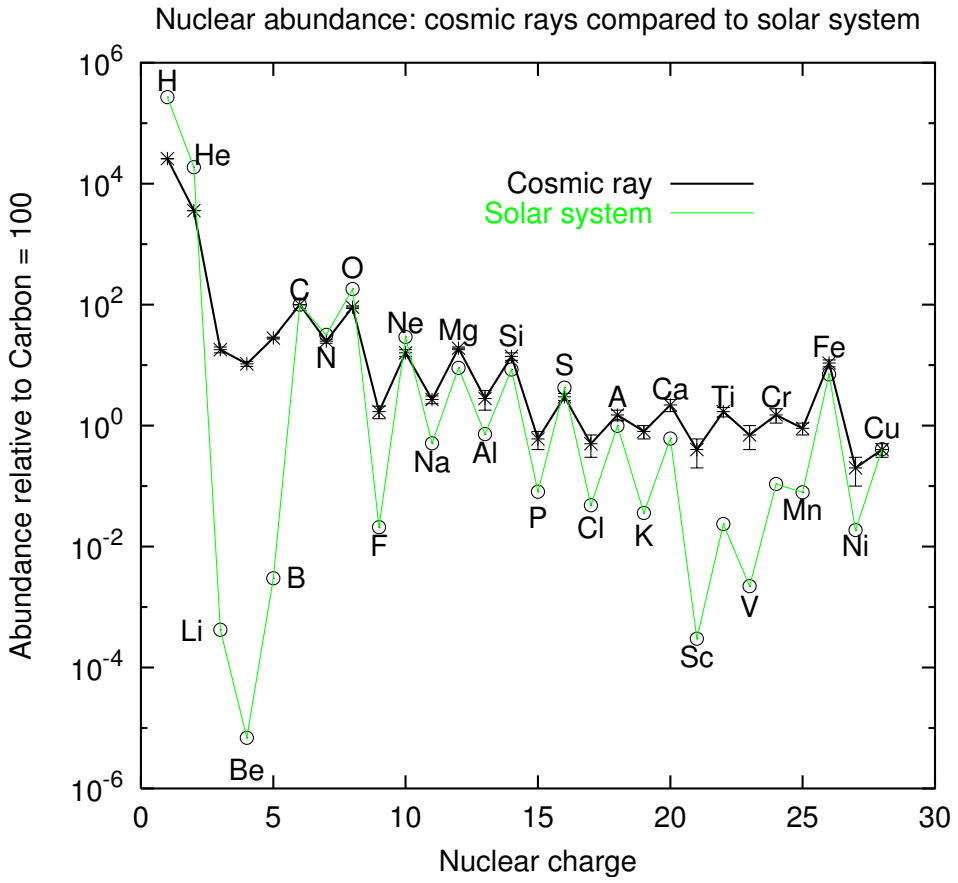

Fig. 1.2.: Comparison of Solar system [27] and CR elemental abundances, all relative to carbon. The shown nuclear abundances are from [28]; protons and helium abundances are from [29, 30, 31]. The figure is taken from [32].

34] were identified as charged nuclei in observations with nuclear emulsions which were carried by balloons. The CRs composition ranges from the lightest to the heaviest elements in the periodic table together with the high-energy leptons (electrons and positrons) and other subatomic particles. The CRs are approximately composed of: protons, i.e., hydrogen (H) nuclei (~85%); α particles, i.e., helium (He) nuclei (~12%); nuclei of heavier elements (~1%); electrons and positrons (~2%) [35]. The distributions of element abundances in CRs are not so different from those of the Solar system as shown in Fig. 1.2. As can be seen, the hadronic component of CRs demonstrates similar abundance as for Solar system except for lithium (Li), beryllium (Be), boron (B) nuclei and for sub-iron nuclei, i.e., that between calcium (Ca) and iron (Fe) [36, 37]. This is due to the fragmentation of heavier nuclei in primary CRs after the interaction with interstellar matter, called *spallation*. The *spallation* of abundant elements plays a major role, especially for the light elements, where spallation and subsequent ionization loss in collisions with ambient interstellar gas can even explain the abundances of the light elements in the Interstellar Medium (ISM) [36]. Thus, the overabundance of Li, Be, B relative to their interstellar abundances can be explained by the spallation of carbon (C) and oxygen (O), while the overabundance of sub-iron nuclei can be explained by the spallation of iron into lighter elements during the propagation of

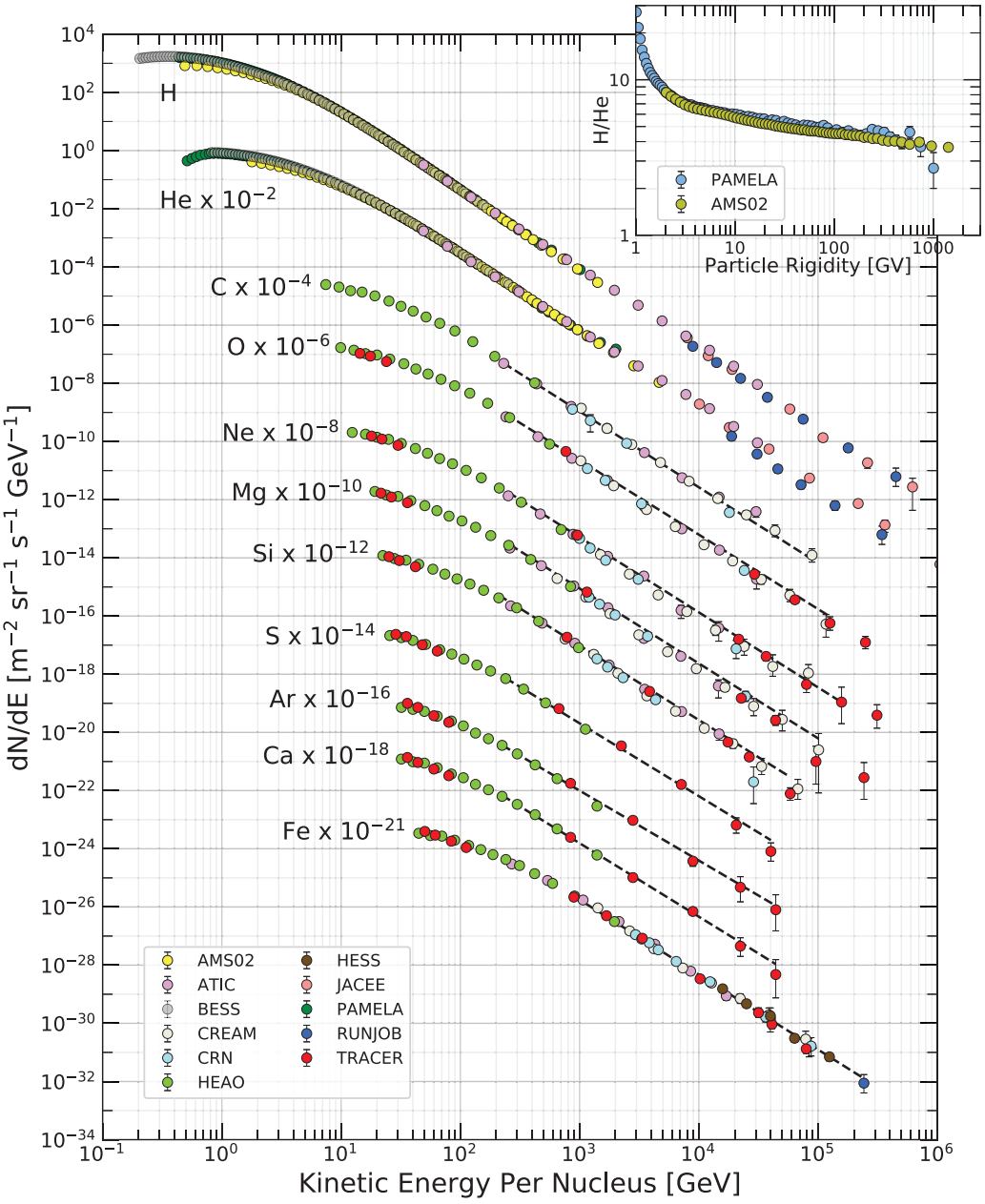

Fig. 1.3.: Fluxes of nuclei of primary cosmic radiation as measured by the variety of the experiments. Plotted in particles per energy-per-nucleus vs energy-per-nucleus. The inset displays the H/He ratio at constant rigidity. The figure is taken from [39].

CRs through the Galaxy. Primary CRs are those accelerated by some astrophysical source, while those created by the spallation of primary CRs are referred to as secondary CRs.

Interactions of the CRs in propagation could produce neutrinos. The accompanying γ-rays produced in the same interactions as neutrinos suggest toward these processes.

The fractions in CR composition vary over the CRs energy range [38] as shown in Fig. 1.3 which represents the nuclei abundances in primary CRs as a function of energy (see [39] for the reference to the experiments whose data were used). The composition of CRs up to

$E < 10^{14}$ eV (see Fig. 1.3) is directly accessible in the so-called *direct* experiments such as balloon experiments at high altitude or experiments by onboard satellites; at higher energies $E > 10^{14}$ eV, the CRs composition, flux and arrival direction are measured in the so-called *indirect* experiments by *extensive air shower* (EAS) experiments, which detect the cascades of secondary particles produced by the high-energy CRs in the Earth's atmosphere (see Fig. 1.4). Figure 1.5 indicates the energy ranges accessible by the *direct* and *indirect* methods. The EAS was first discovered by Bruno Rossi in 1934 [23] and independently, in 1937, by Pierre Auger and collaborators [40, 41] who performed a deep survey of the air showers. Both discovered that many events reach the detector simultaneously and can be associated with a single event. Auger estimated the primary energy to be around 10^{15} eV and various mechanisms exist which can explain such energies (see Section 1.1.3). The discovery of EAS was a crucial milestone in the study of the high-energy CRs, because it yielded a new way to study CRs at the high energies.

The CRs span a broad range of energy and flux, covering over 10 decades in flux and 11 decades in energy [44, 38]. The CR flux steeply falling at increasing energies. The CR flux decreases from more than 1000 particles per second and m^2 at GeV energies to about one particle per m^2 and year at a PeV, and further to less than one particle per km^2 and century above 100 EeV[1] [43]. As seen in Fig. 1.4, the CRs composed of mostly protons in $\approx 1-3$ 10^6 GeV energy range with the spectral index ≈ 2.7; this part of the spectrum carries most of the CR. The electrons constitute a few % of CRs composition while the positrons are even one order of magnitude less. The steeper slope of the electron spectrum relative to the proton spectrum is explained by the importance of radiative losses, and the E^2 dependence of synchrotron and inverse Compton radiative emission rates [45]. Measurements of CR composition constrain theories of CR acceleration and propagation [45]. The acceleration mechanisms and propagation of CRs are discussed in Section 1.1.3.

The spectrum of CRs (see Fig. 1.4) is well described by a broken power law, , indicating non-thermal acceleration processes:

$$\frac{dN}{dE} \propto E^{-\gamma} \tag{1.1}$$

where N is the number of observed events, E is the energy of the primary particle and γ is the spectral index. The spectral index γ is an energy-dependent (see Fig. 1.6) such as that:

$$\gamma \approx \begin{cases} 2.7 & \log(E/eV) < 15.5 & [46, 47] \\ 3.3 & 15.5 < \log(E/eV) < 18.7 & [46, 48, 49, 47] \\ 2.7 & 18.7 < \log(E/eV) < 19.8 & [46, 49, 47] \\ 5 & 19.8 < \log(E/eV) & [48, 49, 47] \end{cases} \tag{1.2}$$

[1] 1 EeV = 10^{18} eV, see units in Table A.1 in Appendix A.1.2.

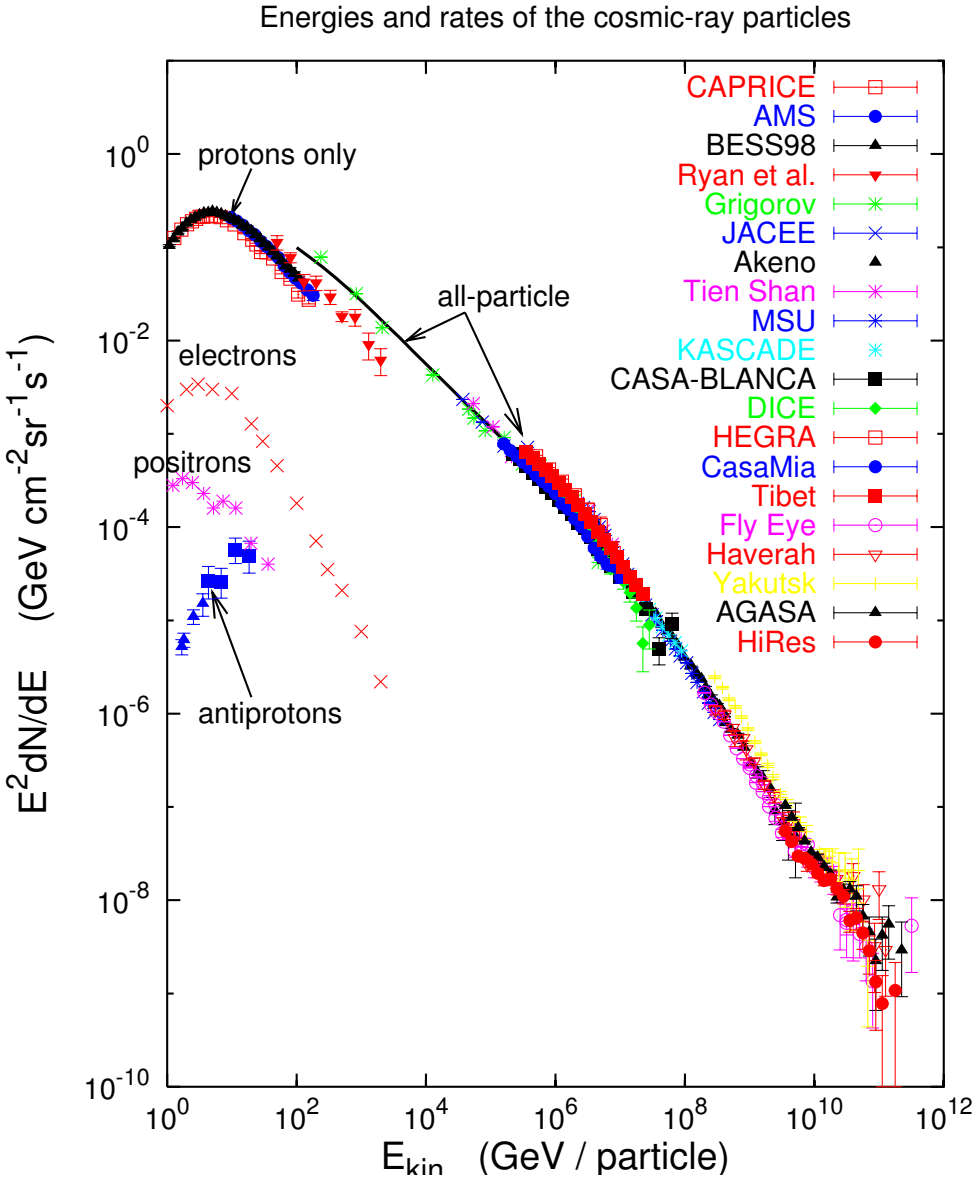

Fig. 1.4.: Many measurements of the CR flux from 10^9 to 10^{21} eV as measured on Earth (assembled by Gaisser). The figure is taken from [42].

In $15.5 < \log(E/eV) < 18.7$ energy range, the spectrum index changes from 2.7 to 3.0 at $\log(E/eV) \approx 15.5$ [46, 44] known as "*knee*" and then from 3.0-3.1 to 3.3 at $\log(E/eV) \approx 17.7$ [46, 44] with transition to 2.7 again at $\log(E/eV) \approx 18.7$ [44, 49, 47] known as "*ankle*".

Figure 1.6 demonstrates the "*all-particle*" spectrum (see [39] for the reference to the experiments whose data were used). The steepening that occurs at several PeV (10^{15} eV) with a well-recognized kink in the spectrum (see Fig. 1.6) is referred to as the "*knee*" of the spectrum [43]. The "*knee*" may represent a transition in the acceleration or confinement mechanism, and/or in elemental composition [45]. A further steepening occurs at about

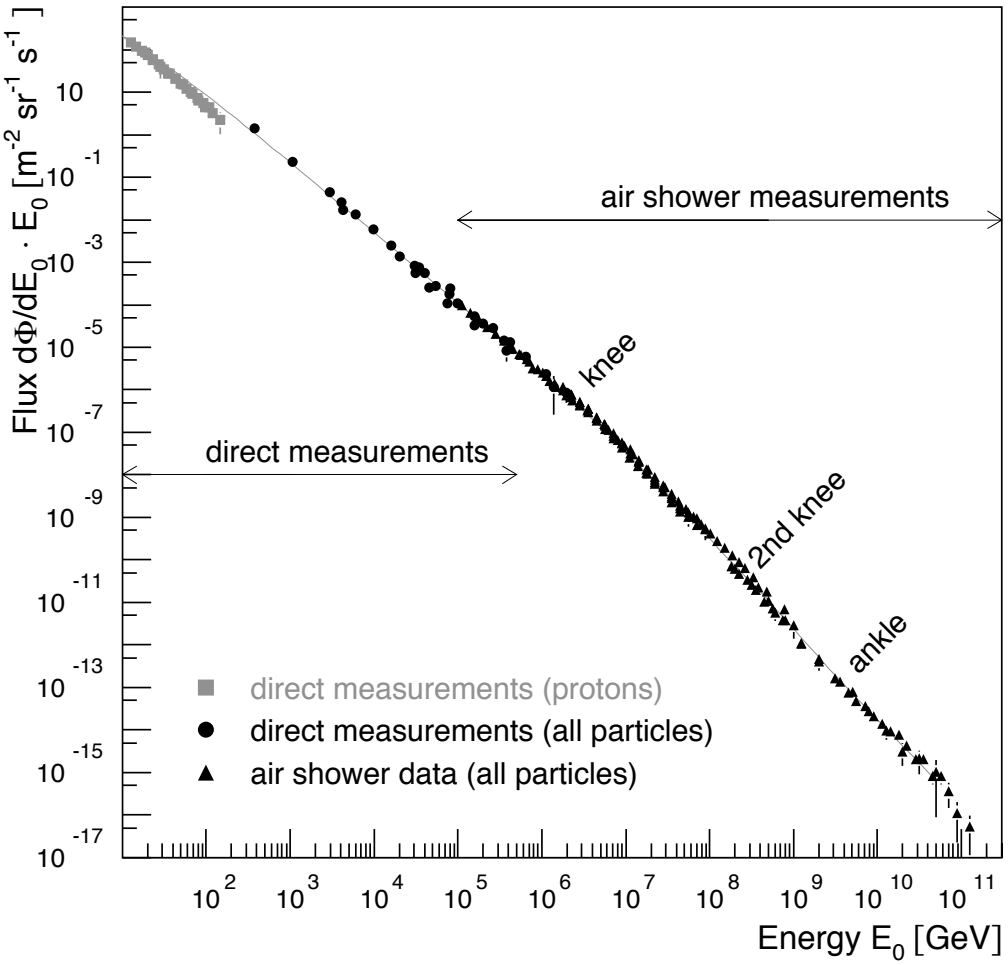

Fig. 1.5.: The "*all-particle*" energy spectrum of CRs as measured directly with detectors above the atmosphere and with air shower detectors. At low energies, the flux of primary protons is shown. See explanations of the "*knee*", "*second knee*" and "*ankle*" features of the spectrum in the text. The figure is taken from [43].

4×10^{17} eV (0.4 EeV) is known as the "*second knee*" [43]. Finally, at about 4×10^{18} eV (4 EeV), at the so-called "*ankle*" (or *dip*), the spectrum flattens again [43].

The "*ankle*" has been first discussed in the early 1960s [50] and firmly established in the early 1990s [51, 52] with Fly's Eye [53, 54], the predecessor of High-Resolution Fly's Eye (HiRes)[2] [55, 56], and Akena [57], the predecessor of Akeno Giant Air Shower Array (AGASA)[3] [58], EAS experiments. Furthermore, Fly's Eye detected a 51-joule ($3.2\pm0.9\times10^{20}$ eV) CR [59], the highest-energy CR with substantially greater energy than of any previously reported CR; and the achievement is not beaten so far.

[2] HiRes Collaboration, http://www.cosmic-ray.org/
[3] AGASA Collaboration, http://www-akeno.icrr.u-tokyo.ac.jp/AGASA/

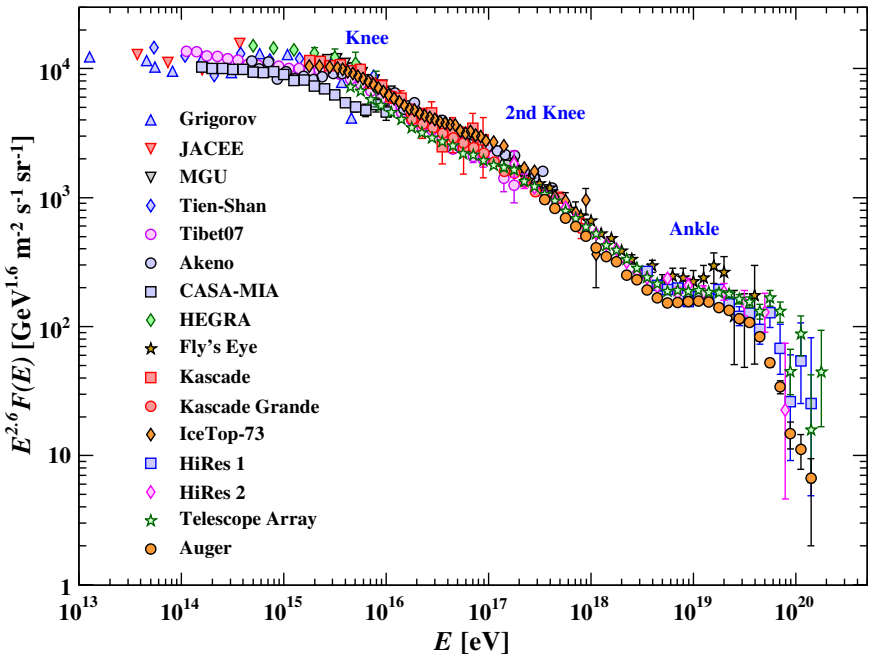

Fig. 1.6.: The all-particle spectrum of primary CRs as a function of E (energy-per-nucleus) as measured by the variety of air shower experiments. The differential energy spectrum has been multiplied by $E^{2.6}$ in order to display the features of the steep spectrum that are otherwise difficult to discern. The figure is taken from [39].

1.1.2 GZK effect

In 1966, Greisen [60], and Zatsepin & Kuzmin [61], proposed an upper limit to the CR energy spectrum known as Greisen-Zatsepin-Kuzmin (GZK) cutoff [60, 61] (not a real cutoff, but rather a suppression, i.e., a sharp steepening of the spectrum). These authors predicted a strong suppression in the spectrum at ~5×10^{19} eV due to the interaction of CRs with photons of the CMB [62, 63, 7] radiation. The CMB was predicted by George Gamow and Ralph Alpher in 1948 [62, 63] and accidentally discovered by two radioastronomers, Arno Penzias and Robert Woodrow Wilson, at the Bell Telephone Laboratory[4] in 1964 [7]. The CMB corresponds to the remnant photons of the Big Bang and acts like a black body spectrum being characterized by a temperature T~2.73° K and a density of n_γ~411 photons cm^{-3} [5] [39]. In [62, 63] the background temperature found to be of the order of 5° K. The value measured by Penzias and Wilson was 3.5°±1.0° K [7].

The CRs lose part of their energy interacting with the CMB photons. The basic process for protons is pion photoproduction which occurs if the proton energy is larger than the

[4] Crawford Hill Radiotelescope, Holmdel, New Jersey, USA
[5] see Table A.4 in Appendix A.2.3.

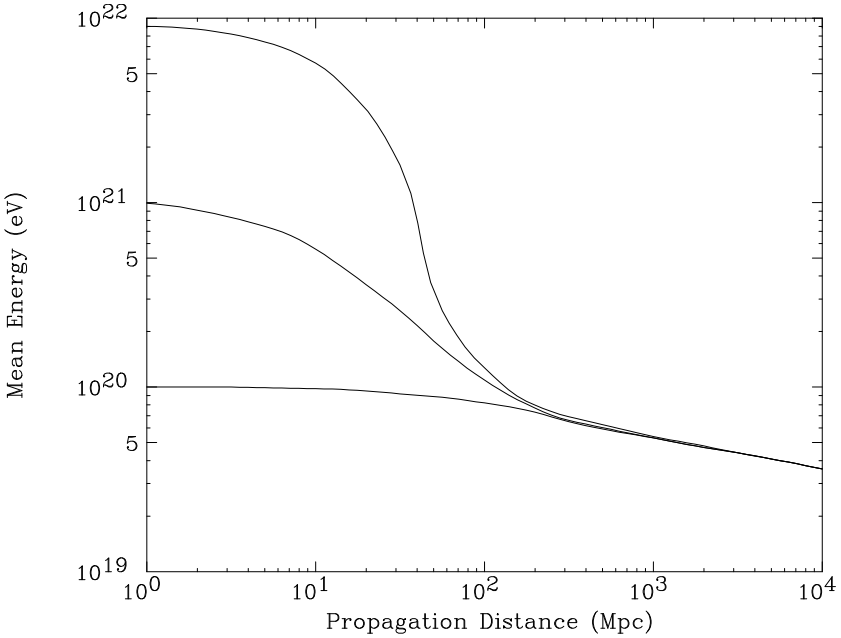

Fig. 1.7.: Mean energy of protons as a function of propagation distance through the CMB. Curves are for energy at the source of 10^{22} eV, 10^{21} eV, and 10^{20} eV. Notice that, independently of the initial energy of the proton, the mean energy values approach to 100 EeV after a distance of ≈100 Mpc. The figure is taken from [65].

threshold for the resonant production of the Δ+ resonance at 1.232 MeV, that undergoes a prompt decay [64]:

$$p + \gamma_{CMB} \rightarrow \Delta^{+}(1232) \rightarrow \begin{cases} p + \pi^{0} \\ n + \pi^{+} \end{cases} \tag{1.3}$$

The proton loses ∼20% [66, 64, 67, 68] of its energy in such interaction and so the distance from which high-energy (HE) particle can have traveled before detection is limited to ∼100 Mpc[6] [68, 69]. The limit for a CR with mass A is raised by a factor A. The neutron mean decay length is 1 Mpc at 10^{20} eV so on the Mpc scale it quickly becomes a proton again [65]. Figure 1.7 illustrates the energy degradation of ultra-high-energy CRs (UHECRs) in terms of their propagation distance through the CMB. As seen, a proton with energy above ∼10^{20} eV loses most of its initial energy in about ≈100 Mpc until it gets below the GZK energy threshold. Such a distance somewhat defines the "GZK volume" (or "GZK horizon") and one might suspect that the sources of particles above GZK cutoff energy would lie within this volume [68]. The "GZK horizon" at which the CRs can be observed is limited to a distance that depends on the mass of the primary particle. The mean free path for the reaction in Eq. 1.3 is only ≃6 Mpc [67, 70]. Indeed, using the the photo-pion cross-section (taken beyond the Δ resonance production) and the CMB photon density n_γ the interaction length for GZK effect can be estimated from [71]:

$$L = \frac{1}{\sigma_{p\gamma} n_\gamma} \simeq 2.0 \times 10^{25} \text{ cm} \simeq 6 \text{ Mpc} \tag{1.4}$$

[6] 1 Mpc ∼3.26×10^6 ly ∼3×10^{19} km, see Table A.4 in Appendix A.2.3.

for $n_\gamma = 411$ cm^{-3} and $\sigma_{p\gamma} = 120$ μb[7] (the cross-section of the photopion process in high-energy limit is constant with the value $\sigma_{p\gamma} \simeq 120$ μb [64, 70]).

Another mechanism is pair production in the interaction with CMB photons [64]:

$$p + \gamma_{CMB} \rightarrow p + e^- + e^- \tag{1.5}$$

It occurs at a much lower threshold (around $5{\times}10^{17}$ eV) but the cross-section is orders of magnitude smaller and together with a smaller inelasticity the overall interaction length stays around 1 Gpc [71].

In addition, using the proton mass m_p and target CMB photon energy ϵ, the GZK cutoff threshold for collisions between protons (photopion production) and CMB can be expressed in the CMB "rest" frame as [71]:

$$E_{th} \simeq \frac{E_\gamma m_p}{2\epsilon} \simeq \frac{7{\times}10^{16}}{\epsilon} \tag{1.6}$$

For an energetic CMB photon with $\epsilon = 10^{-3}$ eV, E_{th} is $7{\times}10^{19}$ eV which is somewhat the GZK cutoff is expected to start. If a sufficient number of particles at these energies are detected, then one might observe a steepening in the spectrum at these energies, which can provide the information about sources out to $\sim$70$-$200 Mpc, depending on the energy [68].

Experimental evidence

Forty years after its initial prediction, the HiRes experiment has observed for the first time the GZK cutoff with a statistical significance of 5 standard deviations [48]. It has been measured that the energy of the GZK cutoff to be $(5.6{\pm}0.5(\text{stat}){\pm}0.9(\text{syst})){\times}10^{19}$ eV ($19.75{\pm}0.04$ at logE as shown in Fig. 1.8) [48] and consistent with a suppression of protons. This result was supported by the observation in Pierre Auger Observatory (Auger)[8] [72, 73] where the hypothesis that the CR spectrum continues with a constant slope above $4{\times}10^{19}$ eV was rejected with a statistical significance of 6 standard deviations [74]. Both experiments measure EAS induced by UHECRs in the atmosphere by using of air fluorescence detectors (HiRes) and giant arrays of particle detectors (Auger) on the ground [75]. More recent measurements by the Telescope Array (TA)[9] [76, 77, 78] give a steepening at $(5.4{\pm}0.6){\times}10^{19}$ eV which is consistent with the expectation from the GZK cutoff [47]. TA is a hybrid detector system which combines the two techniques of ground array detectors and air-fluorescence detectors (used by the AGASA and HiRes experiments) in order to obtain a consistent energy spectrum for UHECRs from both techniques and to resolve the disagreement (see Fig. 1.8) between the AGASA results (observed no GZK cutoff [79, 80]) and those of HiRes (claimed that the GZK cutoff may be present [81] and later witnessed the suppression [48]).

[7] 1 b = 1 barn = 10^{-24} cm^2
[8] Pierre Auger Collaboration, https://www.auger.org/
[9] Telescope Array Collaboration, http://www.telescopearray.org/

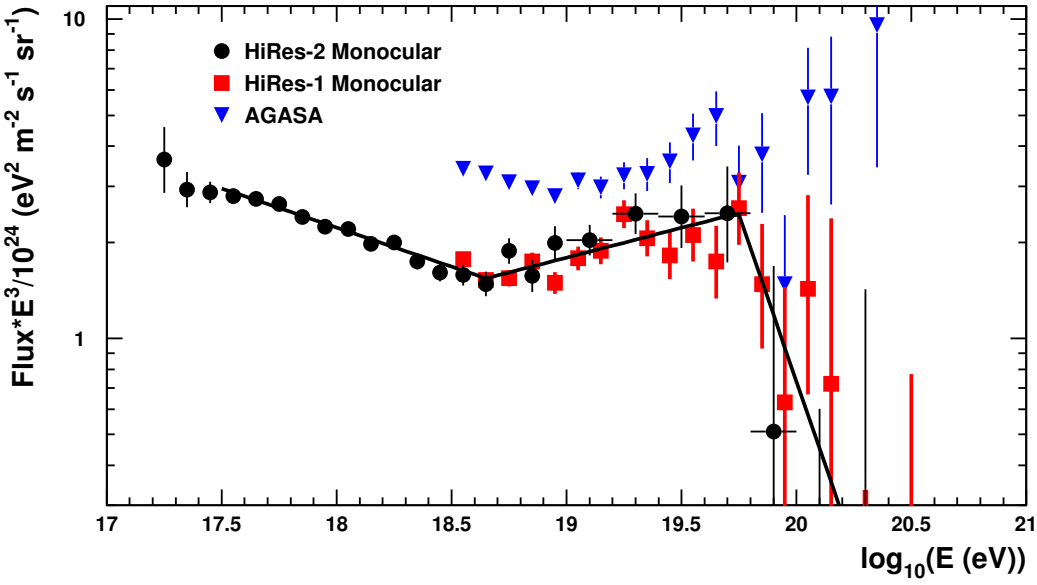

Fig. 1.8.: The CR energy spectrum measured by the HiRes detectors operating in monocular mode (HiRes-I and HiRes-II). The highest two energy bins for each detector are empty, with the 68% C.L. bounds shown. The spectrum of the AGASA experiment is also shown. The "*ankle*" and the GZK cutoff at the highest energies are clearly visible. The figure is taken from [48].

The Auger and TA are the two largest facilities to detect CRs built so far and cover 3000 km^2 [72, 73] and 700 km^2 [77, 78] areas on the ground respectively [75].

In addition to GZK observation, the HiRes also observed the "*ankle*" feature [48]: a hardening of the spectrum, at an energy of 4.5±0.05±0.8 EeV (18.65±0.05 at logE as shown in Fig. 1.8) [48, 47] as expected for cosmic protons. The TA finds the "*ankle*" at an energy of 4.6±0.3 EeV [47], which is compatible with HiRes results. The power-law index measured by HiRes is 3.25±0.01 below the "*ankle*", 2.81±0.03 between the "*ankle*" and the GZK cutoff, and 5.1±0.7 above the GZK cutoff [48, 86]. The TA finds the power-law to be 3.34±0.04 below the "*ankle*", 2.67±0.03 between the "*ankle*" and the GZK cutoff, and 4.6±0.6 above the GZK cutoff [47, 86], which agrees very well with HiRes results.

The combined results from Auger and TA experiments are presented in Fig. 1.9. Both observatories clearly exhibit the "*ankle*" at ~5 EeV and a flux suppression above ~40 EeV in the CRs energy spectra and are compared to simplified astrophysical scenarios with parameters are given in the figure caption [85]. As seen in Fig. 1.9, the "*ankle*" occurs at an energy which is compatible with the *dip*-model under the assumption of a pure proton composition and the flux suppression at the highest energies is in accordance with the energy loss processes of the GZK-effect [85, 60, 61].

Even though Auger clearly observes the steepening of the spectrum, but its position and shape are not much consistent with that predicted for the GZK cutoff. The suppression starting at lower energies can be described by assuming pure iron emission from the

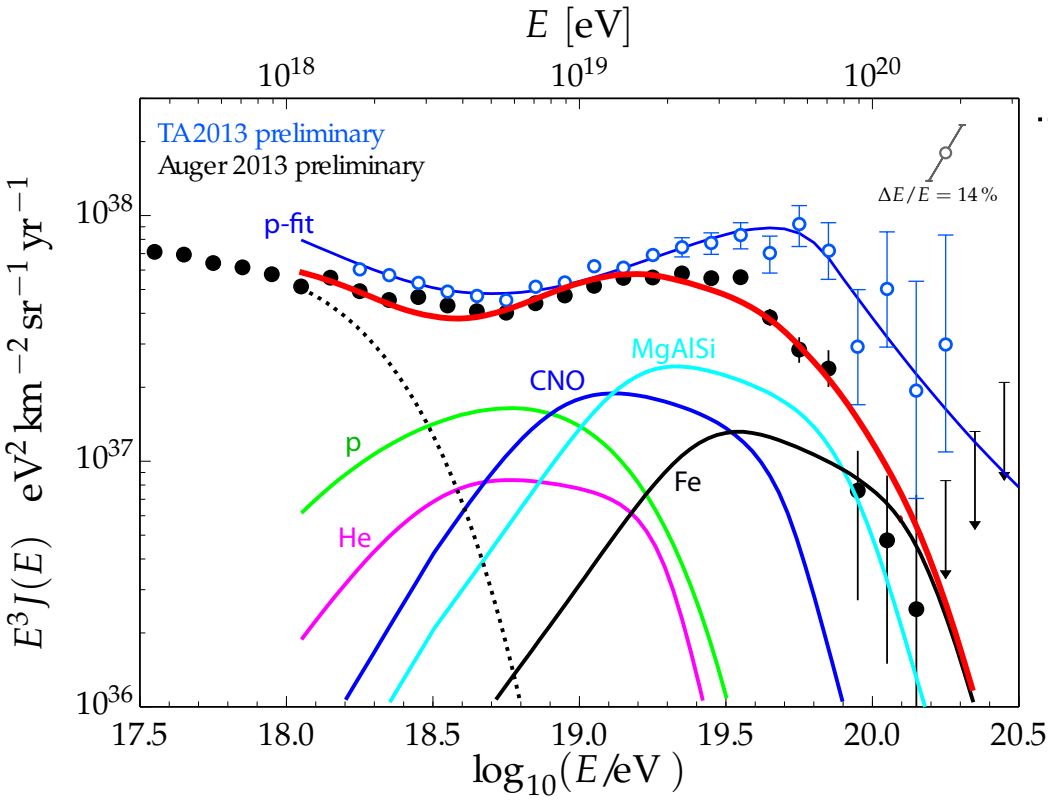

Fig. 1.9.: Measurements of the flux of CRs at the highest energies by the Auger and Telescope Array collaborations [82, 83]. The Telescope Array data are fitted to a model of extragalactic proton sources, distributed cosmologically according to $(1+z)^{4.4}$ and injecting a power-law distribution at the sources according to the best-fit expected energy spectrum $E^{-2.39}$ (blue line) [82]. The Auger data are compared to a model assuming a maximum acceleration energy $E_{max} = Z{\times}10^{18.7}$ eV with injection spectra $\gamma = 1$ and an enhanced Galactic Cosmic Ray (GCR) composition from [84]. An additional Galactic component is plotted as a dotted black line. The figure is taken from [85].

sources [85] (black line). In this case, however, the "*ankle*" would require another component of CRs to contribute to the flux at lower energies [85] (black dots). Several models have been developed to explain the Auger data such as the "*disappointing*" model [87] with the assumption that the flux suppression is primarily caused by the limiting acceleration energy at the sources rather than by the GZK-effect [85]. A good description of the Auger all-particle energy spectrum is obtained for $E_{max,p} \simeq 10^{18.7}$ eV, with a mix of protons and heavier nuclei being accelerated up to the same rigidity, so that their maximum energy scales like $E_{max,Z} \propto Z{\times}E_{max,p}$ (colored lines in Fig. 1.9) [85].

The different interpretations of the Auger and TA energy spectra demonstrate the ambiguity left by the all-particle energy spectrum and they underline the importance of understanding the absolute CR energy scales to a high level of precision [85]. Despite the high level of precision reached, the all-particle energy spectrum by itself does not allow one to conclude about the origin of the spectral structures and thereby about the origin of CRs from the "*ankle*" to the highest energies [85]. Additional key information is obtained from the mass composition of CRs. As seen in Fig. 1.10, the breaks in the CRs energy spectrum coincide with the turning points of changes in the mass composition of CRs: the mean mass becomes increasingly heavier above the "*knee*", reaches a maximum near the "*second knee*" (or "*iron knee*"), another minimum at the "*ankle*" before it starts to modestly rise again towards the highest energies [85].

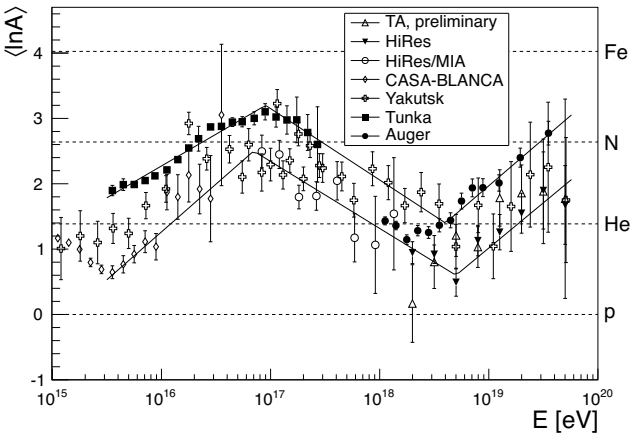

Fig. 1.10.: Average logarithmic mass of the CR composition as a function of energy derived from electromagnetic shower maximum X_{max} (the depth at which the particle cascade reaches its maximum in terms of the number of particles) measurements with optical detectors for the EPOS 1.99 hadronic interaction model. Lines are estimates of the experimental systematics, i.e. upper and lower boundaries of the data presented [88]. The figure is taken from [85].

1.1.3 Acceleration mechanisms

Identification of the processes that are responsible for CR acceleration up to the extreme energies was a vital theoretical challenge for decades.

Second-order Fermi mechanism

In 1949, Enrico Fermi proposed a mechanism [89] for the acceleration of relativistic CR particles by means of their collision and repeated scatters with magnetized interstellar clouds. Such clouds act as magnetic mirrors for CRs, so that the particle reflects off them and get energized (see Fig. 1.11). After dozens of such collisions and stochastic scattering, particles are able to gain significant energy. This mechanism was later dubbed as second-order Fermi acceleration mechanism. Let us derive the average energy the accelerated particle gain via this mechanism. For simplicity, we assume the particle to be initially relativistic, i.e. $E \approx pc$ [90]. If we consider the energy of the particle in the Galaxy's frame is E_1, and a cloud with Lorentz factor γ and speed $u = \beta c$, then in the cloud's reference frame the particle's energy is [90]:

$$E_1^{'} = \gamma E_1 (1 - \beta cos\theta_1), \tag{1.7}$$

where θ_1 is the angle between the particle's and cloud's velocities. After the interaction, the energy in the cloud's frame remains unchanged, namely $E_2' = E_1'$, while the final energy in the Galaxy's frame is [90]:

$$E_2 = \gamma E_2^{'}(1 + \beta cos\theta_2^{'}), \tag{1.8}$$

where $\theta_2^{'}$ is the exit angle in the cloud's frame. Hence after a single encounter the energy gain is [90]:

$$\frac{\Delta E}{E_1} = \frac{1 - \beta cos\theta_1 + \beta cos\theta_2' - \beta^2 cos\theta_1 cos\theta_2'}{1 - \beta^2} - 1. \tag{1.9}$$

The mean energy gain can be obtained averaging over the incoming and the outcoming directions and because the scattering in the cloud frame is isotropic, one can find that $\langle cos\theta_2' \rangle = 0$ [90]. On the other hand, the mean incoming direction can be computed averaging over the particle flux, which is proportional to the relative velocity, such as $\beta_r = 1 - \beta cos\theta_1$ [90]. Hence, if the particle distribution is isotropic in the Galaxy's frame [90]:

$$\langle cos\theta_1 \rangle = \frac{\int d\Omega \beta_r cos\theta_1}{\int d\Omega \beta_r} = -\frac{1}{3}\beta. \tag{1.10}$$

Consequently, assuming that $\beta \ll 1$ the average energy gain become [90]:

$$\frac{\Delta E}{E_1} = \frac{1 + \frac{1}{3}\beta^2}{1 - \beta^2} - 1 \simeq \frac{4}{3}\beta^2. \tag{1.11}$$

In spite of the fact that in each interaction a particle can either gain or lose energy, the average energy gain is positive simply because the cloud is moving, hence the flux of particle crossing the cloud in front is greater then the one leaving the cloud from behind [90]. The proportionality of the energy gain to the second power of the speed Eq. 1.11 justifies the name of second-order Fermi mechanism and this is exactly the reason why it cannot explain the CR spectrum [90]. In fact, the random velocities of clouds are relatively small, $v/c \approx 10^{-4}$ and, for a particle with a mean free path of 0.1 pc, the collisions occur only a few times per year hence the final energy gain is really modest [90].

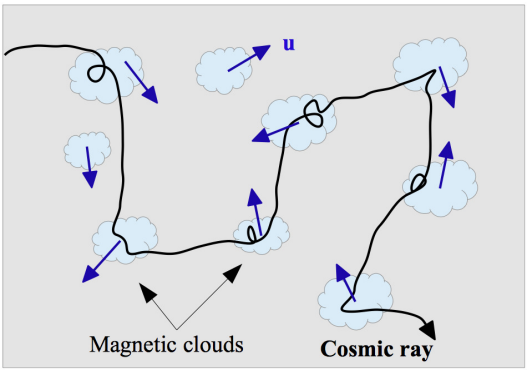

Fig. 1.11.: Schematic representation of the original Fermi idea to energize CRs through repeated scatters with magnetic clouds randomly moving in the Galaxy. The figure is taken from [90].

First-order Fermi mechanism

In the 1970s, Bell [91, 92], Blandford and Ostriker [93], and other authors [94, 95, 96, 97] independently realized that when Fermi's idea is applied to particles in the vicinity of a shock wave, the result changes dramatically [90]. In this case, the magnetic turbulence in the plasma provides the scattering centers needed to confine particles around the shock wave, allowing them to cross the shock repeatedly [90]. Each time a particle crosses the shock front, it always suffers head-on collisions with the magnetic turbulence on the other side of the shock, gaining a bit of energy which is subtracted from the bulk motion of the plasma [90]. In contrast to the second-order mechanism, in which not every interaction increases energy and only head-on collisions encounter, the current mechanism results in an increase in energy in every interaction.

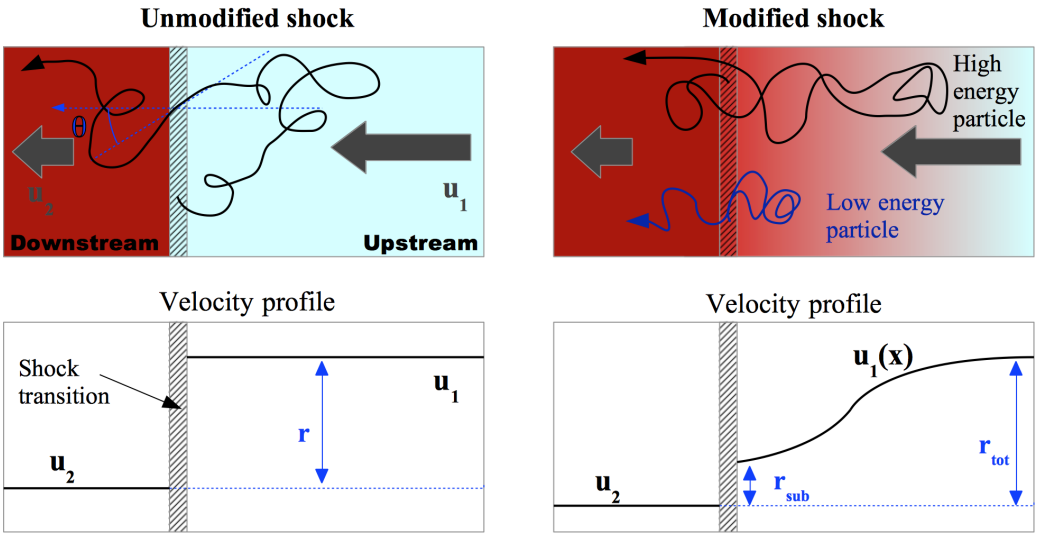

Fig. 1.12.: *Left:* Structure of an unmodified plane shock wave. Particle diffusing from upstream towards downstream suffers the compression factor r in the velocity of the plasma, which is the same at all energies. *Right:* . Shock structure modified by the presence of accelerated particles. The pressure exerted by accelerated particles diffusing upstream slows down the plasma creating a "precursor". High-energy particles, which propagate farther away from the shock, suffer now a larger compression factor with respect to low energy particles which diffuse closer to the shock. The figure is taken from [90].

Let us derive the average energy the accelerated particle gain via this mechanism. Consider a plane shock moving with velocity u_{sh}, then in the frame where the shock is at rest, the upstream plasma moves towards the shock with velocity $u_1 \equiv u_{sh}$, while the downstream plasma moves away from the shock with velocity u_2 [90] (see Fig. **??**, left panel). The situation is similar to what happens in the case of a moving cloud described above but in this case, the relative velocity between downstream and upstream plasma is $u_r \equiv \beta_r c = u_1 - u_2$ [90]. Assuming that the density of the particles, n, is isotropic, the flux of particle crossing the shock from the downstream region towards the upstream one is [90]:

$$J_{-} = \int \frac{d\Omega}{4\pi} n c \cos\theta = \frac{1}{4} n c, \tag{1.12}$$

where the integration is performed in the interval $-1 \leqslant cos\theta \leqslant 0$. Hence, the average value of the incoming angle is [90]:

$$\langle cos\theta_1 \rangle = \frac{1}{J_-} \int \frac{d\Omega}{4\pi} nccos^2\theta_1 = -\frac{2}{3}, \tag{1.13}$$

while for the outcoming direction, with the integration performed in the interval $0 \leqslant cos\theta \leqslant 1$, we have $\langle cos\theta_1 \rangle = 2/3$ [90]. According to Eq. 1.9, the average energy gain in a single cycle downstream-upstream-downstream is [90]:

$$\frac{\Delta E}{E} = \frac{1 + \frac{4}{3}\beta_r + \frac{4}{9}\beta_r^2}{1 - \beta_r^2} - 1 \sim \frac{4}{3}\beta_r. \tag{1.14}$$

Compared to the collision with clouds, the shock acceleration is more efficient, resulting in an energy gain proportional to the relative velocity between upstream and downstream plasmas [90]. Thus, the mechanism is called the first-order Fermi process. It is worth noting, that the first- and second-order Fermi acceleration mechanisms are also known as diffusive and stochastic acceleration processes relatively.

Particle spectrum

The most remarkable property of the first-order Fermi mechanism consists in the production of a particle spectrum which is a universal power-law $f(E) \propto E^{-2}$, which is a consequence of the balance between the energy gain and the escape probability from the accelerator [90]. Hence, $f(E) \propto E^{-2}$ means $f(p) \propto p^{-4}$ expressed in momentum rather than energy [90]. Such a universal spectrum is based on two ingredients: 1) the energy gained in a single acceleration cycle is proportional to the particle's energy and 2) the escaping probability is energy independent [90]. Both these properties are direct consequences of the underlying assumption that the particle transport is diffusive, even if the details of the scattering process never enter the calculation; for this reason, the first-order Fermi mechanism is also called Diffusive Shock Acceleration (DSA) [90]. From a mathematical point of view the diffusion guarantees the isotropization of the particle distribution both in the upstream and downstream reference frames [90]. If this is not the case, Eq. 1.14 do not hold anymore. On the other hand, from a physical point of view the scattering process between particles and magnetic turbulence is the real responsible for the energy transfer between the plasma bulk kinetic energy and the non-thermal particles [90].

1.1.4 Origin of Cosmic Rays

Since the discovery more than a century ago [1], significant advancements have been achieved in understanding the CRs. Despite on the comprehension of the acceleration and propagation processes, the key questions about the source and origin of CRs remain open even after a century since their discovery. The extremely powerful phenomena in the Universe that powers the acceleration and be the origin of CRs are still to be confidently revealed. The *Fermi* Large Area Telescope (*Fermi*-LAT)[10] [98, 99, 100] interpreted the measured γ-ray emission to be produced mainly by CRs interacting with the shocked clouds inside SNRs [101]. The characteristic pion-decay feature as evidence that a significant fraction of primary CRs originate from the SN explosions of stars has been detected [101]. Also, based on observations of neutrinos and γ-rays from blazar TXS 0506+056 in 2018 [15, 16], the AGNs appear to produce CRs. The neutrino alert [15] prior to γ-ray flare from TXS 0506+056 and the multimessenger observation performed by γ-ray telescopes [16] are discussed in Section 1.7.1 and Section 1.7.2 respectively.

Supernova Remnants

Supernovae (SNe) are believed to be the accelerators of the bulk of CRs in our Galaxy since 1930s [102]. A few decades later the origin of CRs is discussed [103, 104, 105, 106, 107, 108, 109] with hardly any doubt that Supernova Remnants (SNRs) energetically completely can be the accelerators of CRs in our Galaxy, at least up to energies $E \sim 10^{14}-10^{15}$ eV [110], i.e. up to the so-called "*knee*" with a distinct spectral feature at such energies.

Shocks from SN explosions propagating through the ISM can account for the acceleration of GCRs [93]. The mechanical energy E_{SN} released in a SN explosion in the initial stage of evolution is represented by the kinetic energy of the expanding shell of ejected matter [110]. The powerful shock wave in the surrounding ISM is generated by the motion of the ejected shell [110]. The diffusive propagation of high-energy charged particles in the collisionless dissipative medium enables them to cross the shock front many times before they finally drift into the region behind the shock wave [110]. The essential physical nature of the regular acceleration process in SN explosion lies in the fact that in every pair of consecutive crossings of the shock front (number of cycles shown by a diffusion coefficient k) is resulted in an increase of the energy of the particle [97, 91, 110]. The maximum energy of CRs attained by the acceleration in SNR can be estimated from the expression [110]:

$$E_{max} = 5\times10^{4} Z \left(\frac{E_{SN}}{10^{51}\ \mathrm{erg}}\right)\left(\frac{M_{ej}}{1.4 M_{\odot}}\right)^{-1/6}\left(\frac{N_H}{3\times10^{-3}\ \mathrm{cm}^{-3}}\right)^{1/3}\left(\frac{B_0}{3\mu\mathrm{G}}\right)\ \mathrm{eV}, \tag{1.15}$$

where

- E_{SN} is the mechanical energy released in a SN explosion;

[10] Fermi Collaboration, https://fermi.gsfc.nasa.gov/

- $M_\odot$ is the solar mass ($\sim 2 \times 10^{30}$ kg[11] [39]);
- M_{ej} is the mass of the ejected shell;
- N_H is the density of hydrogen atoms in the ISM;
- B_0 is the magnetic field in the ISM.

The typical parameters of the SN type Ia: explosion energy $E_{SN} = 10^{51}$ erg, mass of the ejected shell $M_{ej} = 1.4 M_\odot$ and the CR diffusion coefficient $k = 7$ [93, 110]. It is shown in [110] using Eq. 1.15 that the maximum energy of CRs accelerated in SNRs is about 10^{15} eV.

The CR propagation in the Galaxy can be explained by the "*leaky box*" model [111]. This simple model describes the confinement of CRs within the Galaxy (see Fig. 1.13) due to the magnetic fields ($B \geq 3 \mu G$) during a given livetime, called escape time. The CRs are accelerated in the Galactic plane and propagate freely within a cylindrical box of size H and radius R_d and reflected at the boundaries as shown in Fig. 1.13.

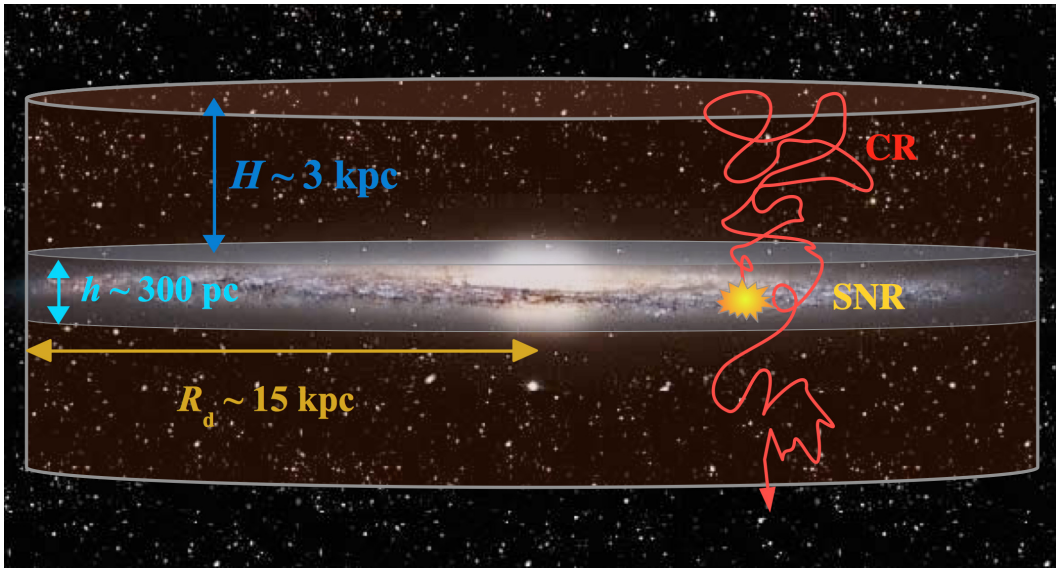

Fig. 1.13.: Schematic representation of the "*leaky box*" model: CRs are produced by sources in the Galactic disk and diffuse in the magnetic halo above and below the disk, before escaping in the intergalactic medium. The figure is taken from [90].

[11] see Table A.3 in Appendix A.2.2.

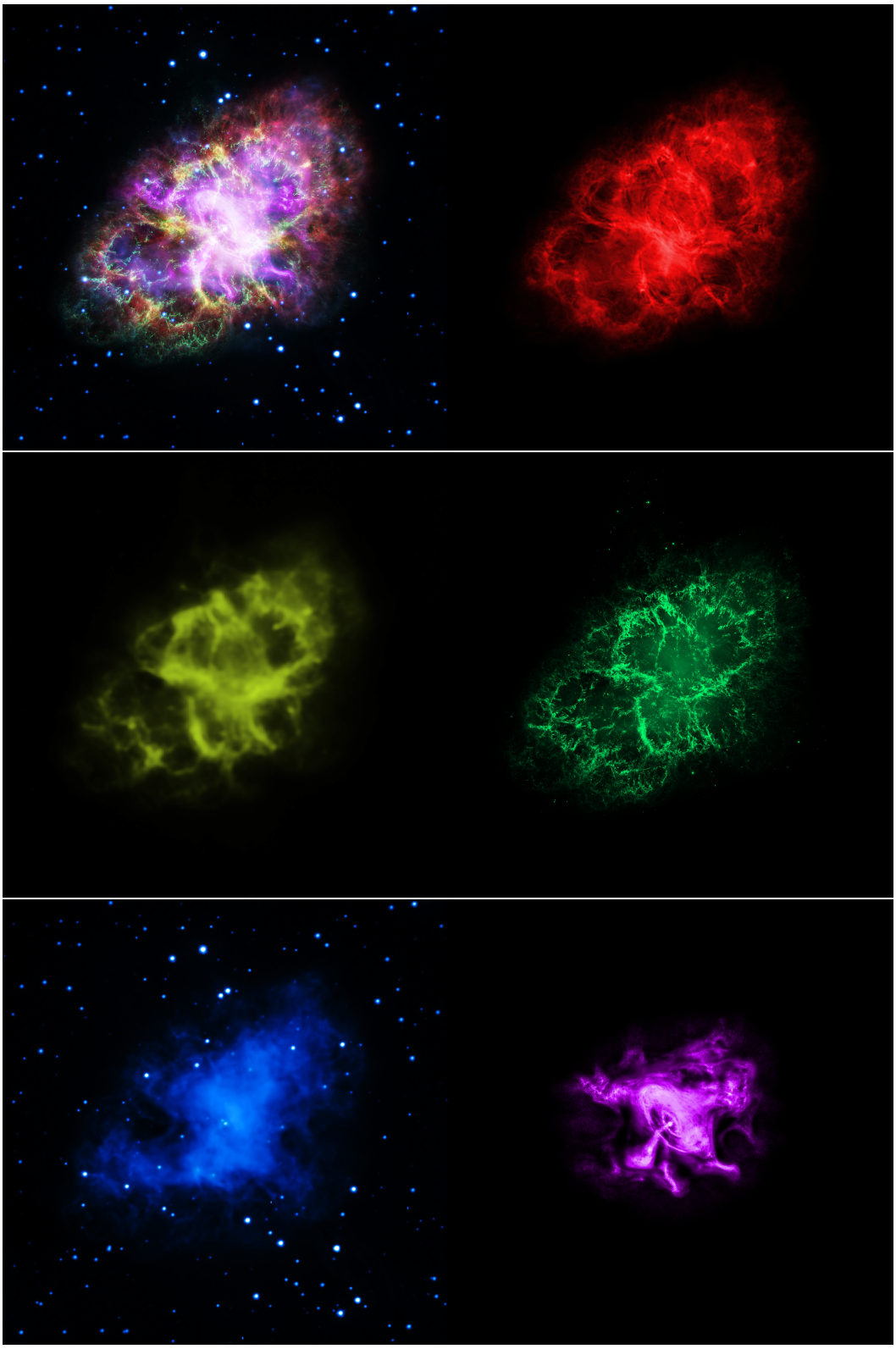

Fig. 1.14.: Multiwavelength Crab Nebula. The VLA (radio) in red; Spitzer Space Telescope (IR) in yellow; Hubble Space Telescope (optical) in green; XMM-Newton (UV) in blue; and Chandra X-ray Observatory (X-ray) in purple. Image credit: NASA, ESA, G. Dubner (IAFE, CONICET-University of Buenos Aires) et al.; A. Loll et al.; T. Temim et al.; F. Seward et al.; Radio: VLA/NRAO/AUI/NSF; X-ray: Chandra/CXC; IR: Spitzer/JPL-Caltech; UV: XMM-Newton/ESA; and Hubble/STScI; Optical: NASA/STScI.

Over the last decades, galactic plane surveys with space- and ground-based detectors revealed a number of HE and VHE CR sources associated with SNRs (see TevCat[12] online catalog [112]) with fluxes consistent with the standard scenario of the origin of CRs through the process of diffusive shock acceleration in SNRs [113]. The interpretation of CR data from several SNRs within the so-called "hadronic models" demands hard proton spectra extending to 100 TeV, and the total energy released in accelerated protons and ions $E_{CR} \gtrsim 10^{50}$ erg, which can be treated as a support of the SNR paradigm of GCRs [113]. Notable that the observation of TeV neutrinos from SNRs can be a clear signature for the hadronic acceleration in SNe and is not detected so far.

A highly detailed multiwavelength image of the Crab Nebula is shown in Fig. 1.14, which combined data from five different telescopes [114] spanning nearly the entire breadth of the electromagnetic spectrum from radio to UV (includes radio, IR, optical, UV, X-ray). The Crab Nebula is the remnant of supernova 1054 (SN 1054), located at a distance of 2 kpc [115]. The bright SN explosion, the result of which the Crab Nebula is, has been observed by Chinese and other astronomers far back in 1054, and now it is one of the most famous and carefully observed objects in the sky. A detailed analysis of the morphological properties of the Crab Nebula has been done in [114]. The SN 1054 was a core-collapse SN primarily due to the presence of a super-dense NS (pulsar). In a simplified picture, there are three different components from inside out [114]: (i) the 33 millisecond Crab pulsar PSR B0531 21 (J0534 2200) powering the nebula, (ii) the synchrotron-emitting shocked pulsar's wind, highly dynamic and with a wealth of fine-scale structure, and (iii) a network of thermal filaments from the ejecta (and possibly some material from the precursor stellar wind) compressed by the Pulsar Wind Nebula (PWN).

Galactic-Extragalactic transition

To acquire higher energies, particles must be confined for a longer time in the acceleration region. When particle escapes from the acceleration region it will be no more able to gain energy. This imposes a limit on the maximum energy that the particle able to reach. Hillas [116] derived the maximum energy which a particle of a given charge can reach, independently of the acceleration mechanism [117]. The Larmor radius (gyroradius) of the particle R_L is considered to be smaller than the size R of the acceleration region, which implies an efficient acceleration of a particle by a repeated scattering process within an astrophysical source. Hence, the maximum energy acquired by a particle of charge Ze traveling in a medium with magnetic field B is given by [116]:

$$E_{max} \sim ZeRBU, \tag{1.16}$$

where U stands for the speed of the magnetic scattering centers.

[12] TevCat, http://tevcat.uchicago.edu/

The Eq. 1.16 shows a relationship between the sources' magnetic field strength and its size and known as "*Hillas criterion*" [116]. The geometrical arguments are conveniently depicted in the "*Hillas diagram*" (see Fig. 1.15), first produced by Hillas (1984) [116].

With the typical values of SN Type II, it yields to maximum energy $E_{max} \approx Z \times 10^{14}$ eV [118]. Indeed, with $B = 3$ μG, $R = 5$ pc[13], the Eq. 1.16 can be simplified as:

$$E_{max} \approx 5 \times 10^5 Z \left(\frac{R}{5\text{pc}}\right)\left(\frac{B}{3\mu\text{G}}\right) U[\text{cm/s}] \text{ eV}, \tag{1.17}$$

Finally, the Eq. 1.17 gives $E_{max} \approx Z \times 10^{14}$ eV if the velocity $U = 3 \cdot 10^8$ cm/s [118] assumed. Later estimates [119] for a maximum energy of CRs accelerated in SNR gives one order of magnitude larger energies if the CR acceleration efficiency is high enough, being as large as $E_{max} \approx Z \times 10^{15}$ eV. This gave a strong argument that GCR spectrum at least up to the "*knee*" energy 3×10^{15} eV is produced in SNRs by diffusive shock acceleration processes if the CR diffusion coefficient is as small as the Bohm limit [119]. As seen, the energy limit of heavy nuclei is a factor of Z higher, e.g., for an iron $Z = 26$. Thereby, assuming the nuclei being fully ionized via acceleration, an iron nucleus can be accelerated to ~30 times higher energies, i.e., up to $E_{max} \approx 3 \times 10^{16}$ eV.

It has been also proposed [120] the mechanism for the CRs to be accelerated to even higher energies with the assumption of the efficient transfer of CR streaming energy to the perturbed magnetic field of the Alfvén waves. The streaming CRs excite Alfvén waves [95, 94]. Indeed this is an essential part of the diffusive shock acceleration mechanism, and in [91, 92], it is these CR-excited Alfvén waves that scatter the CRs downstream of the shock, allowing them to re-cross the shock and gain energy (see Fig. 1.12) (see Section 1.1.3). Thus, the increased magnetic field of the Alfvén waves reduces the acceleration time of the CRs and so increases the maximum CR energy. Such magnetic field amplification mechanism, driven by the CRs themselves, refines the highest energy GCR problem via a simple and elegant solution where the CRs themselves provide the fields necessary for their acceleration to the highest energies.

As "Hillas diagram" suggests (see Fig. 1.15), above 10^{20} eV there is a lack of objects that satisfy the condition in Eq. 1.16, and very few sites remain as possibilities. Radio Galaxies, Colliding Galaxies, Active Galactic Nuclei, Gamma-Ray Bursts and perhaps Galactic Clusters might host the right conditions but other objects such as SNRs are incapable of accelerating particles to this energy [68, 116] and has to be excluded.

For a long time, the "*ankle*" in the CR energy spectrum has been generally interpreted as the signature for the transition between Galactic and Extragalactic CRs [121, 122] and the origin of CRs above the "*ankle*" is suggested to be of extragalactic nature due to the large scales and magnetic fields required to accelerate and confine charged particles above 10^{18} eV. The transition is described as an intersection of a steep galactic component

[13] see units in Table A.4 in Appendix A.2.3.

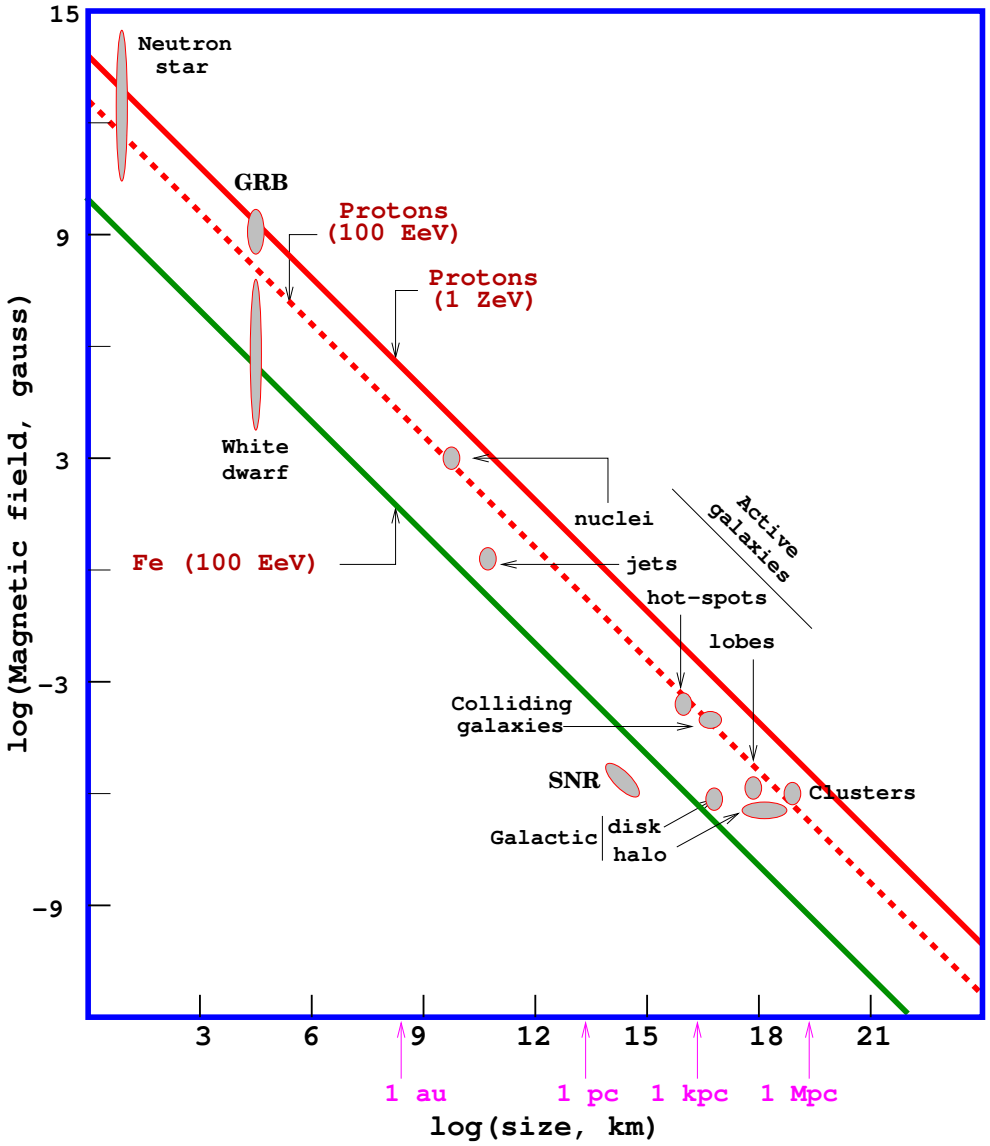

Fig. 1.15.: Hillas diagram [116] (drawn by Murat Boratav). Proposed plausible sites for CR acceleration with their size and magnetic field strength. The diagonal lines show the required magnetic field strength vs gyroradii for the acceleration of protons (solid and dashed red) and irons (solid green) and derived from Hillas criterion (see Eq. 1.16). The objects below the dashed red line cannot accelerate protons to 10^{20} eV. Some sources candidates are still controversial (1 EeV=10^{18} eV, 1 ZeV=10^{21} eV). The figure is taken from [117].

with a flat extragalactic one [123, 124]. Thus, the "*knee*" is associated with the upper limit of acceleration by galactic SNe, while the "*ankle*" is associated with the onset of an extragalactic population that is less intense but has a harder spectrum that dominates at sufficiently high energy [32]. In such a scenario, Extragalactic CRs (EGCRs) dominate the flux above about 10^{19} eV [43]. The onset of the extragalactic component in the CR spectrum above the "*ankle*" is generally assumed due to the fact that above such energies the

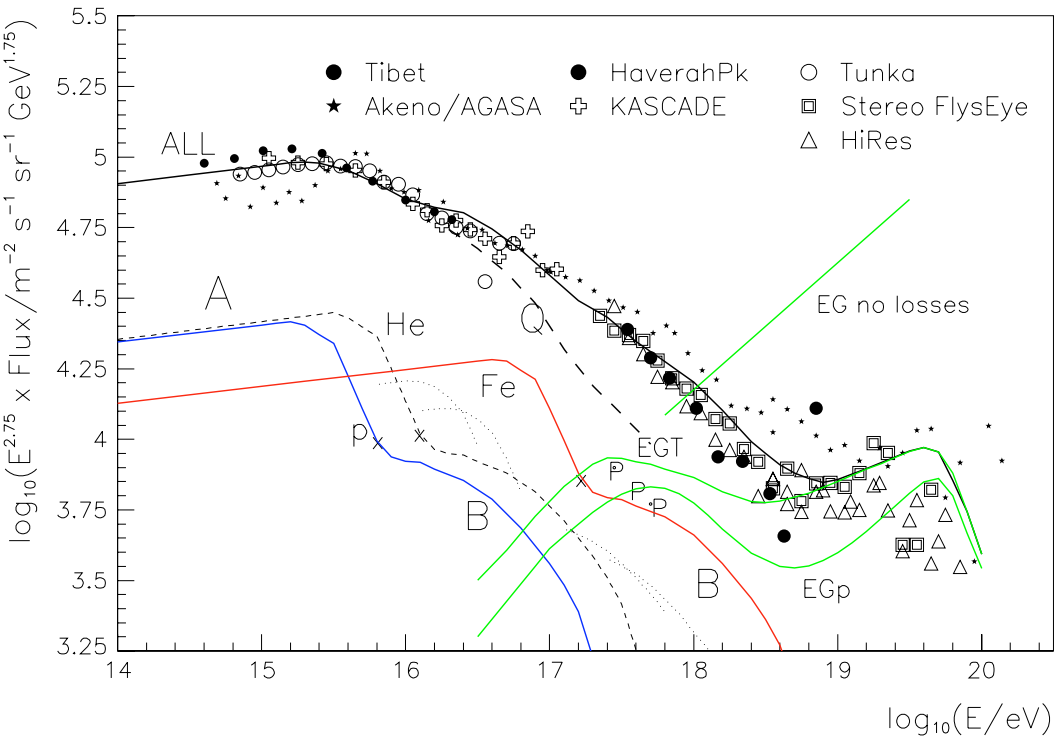

Fig. 1.16.: The CR spectrum turn-down according to a Hillas model [121] as the sum of galactic H, He, CNO, Ne-S and Fe components with the same rigidity dependence, and extragalactic H+He (marked as "EGT") having a spectrum $\propto E^{-2.3}$ before suffering losses by CMB and starlight interactions. The galactic components were given a turn-down shape based on KASCADE "*knee*" shape as far as the point marked x. The dashed line Q is the total of the galactic flux if the extended tail (galactic flux component "B") is omitted. The figure is taken from [121].

Larmor radius of a proton in the galactic magnetic field increases with energy and becomes comparable or exceeds the size of the Galaxy [116]:

$$R_L = 1.08 \frac{E[\text{PeV}]}{ZB[\mu\text{G}]}\text{pc} \tag{1.18}$$

The picture of the transition to EGCRs was supported by Fly's Eye's pioneering observations of the composition change at about 1 EeV [51, 125] (a *dip* at $\sim 10^{18.5}$ eV in [51, 126]) and suggested that near such energies the galactic sources are not effective in producing particles through the "*knee*" region and the composition is at least partly due to CRs of extragalactic origin [125].

In order to properly fill the gap between the CRs population accelerated by SNRs and the onset of the CRs of extragalactic origin, it has been proposed an extragalactic component (see Fig. 1.16) at higher energies known as the "*Hillas model*" [121].

Exploring the properties of CRs accelerated in SNRs and using the fluxes as derived by the KASCADE experiment, marked as component "A" in Fig. 1.16, Hillas faced with insufficiency of obtained all-particle flux (dashed line, marked with Q in the figure) to explain the observed total flux [121]. Then, Hillas proposed a second (galactic) component,

marked as component "B" in the figure, to be added to the KASCADE component "A" in order to make up the well-measured total CR flux at several times 10^{17} eV [121]. An extragalactic component, marked as "EGT" in fugure, has been suggested being present at the highest energies and dominates the all-particle spectrum above 10^{19} eV [121].

Let us summarize the models of transition from Galactic to Extragalactic CRs: *ankle*, *dip* and *mixed composition* models [124]:

In the *ankle* models [127, 121, 42, 122] it is assumed that the transition occurs at the flat part of the observed spectrum in the energy interval $E_a^{trans} \sim (3-10)$ EeV [124]. This is the traditional model based on the interpretation of the "*ankle*" as the spectrum feature where the transition occurs and the transition energy is given by the intersection of a flat extragalactic spectrum and a very steep galactic one [124]. In the majority of *ankle* models [121, 42, 122], the large fraction of the observed CRs have a Galactic origin at $E \gtrsim 10$ EeV [124]. To facilitate the acceleration problem, a pure proton composition is not enough, thus one should assume a heavy-nuclei composition of the new component [124].

In the *mixed composition* model [128, 129, 130, 131] it is assumed that the extragalactic component consists of nuclei of various types with the transition occurred from Iron to lighter nuclei of *mixed composition*; it can occur at the "*ankle*" or nearby it [124]. The main concept of the *mixed composition* model is based on the argument that any acceleration mechanism operating in gas involves different species of nuclei in the acceleration process and thus the primary flux must have a mixed composition [124].

In the *dip* model [132, 133], the transition begins at the second knee and is completed at the beginning of the *dip*, at $E \approx 1$ EeV and the "*ankle*" in this model appears as an intrinsic part of the *dip* [124]. The *dip* model is based on the assumption that UHECRs at $E \gtrsim 1$ EeV are mostly extragalactic protons and his assumption is confirmed by the HiRes and TA data (mass composition and observation of pair-production dip and GZK cutoff), but contradicts to PAO mass composition data [124]. Like in the *ankle* model, the transition here also occurs as an intersection of the flat EG component (this flatness is especially prominent in the case of diffusive propagation) with the steep Galactic spectrum [124]. In contrast to the "*ankle*" and *mixed composition* models, the *dip* model predicts an almost pure proton composition above $E \approx 1$ EeV and a pure Iron composition below this energy [124].

1.2 Gamma-rays

Gamma rays represent the most energetic photons of the electromagnetic spectrum. The γ-rays, as an extremely high-energy form of electromagnetic radiation, denotes photons with energies above 100 keV [134] and are the subject of γ-ray astronomy (see Section 1.2.1). The photons with energies below 100 keV are conventionally defined as X-rays and are the subject of X-ray astronomy. To date, γ-ray astronomy ranges from about 100 keV to about 100 TeV [135], the energies of the highest-energy photons currently detected. Thus, γ-ray astronomy covers about 9 orders of magnitude in photon energy, extending the window by 3 orders of magnitude if X-rays are also considered (see Fig. 1.17).

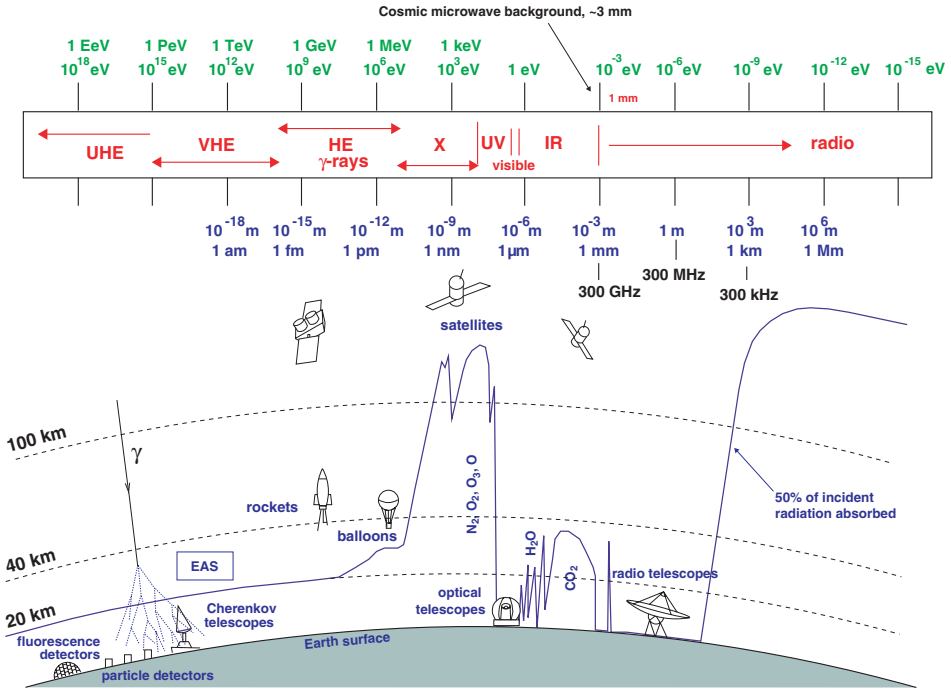

Fig. 1.17.: Atmospheric windows for the observation of the Universe via electromagnetic radiation. The continuous line indicates the height at which a detector can receive half of the total incoming electromagnetic radiation for every wavelength (50% absorption level). The different ranges of electromagnetic radiation are labeled in red. The figure is taken from [17].

As seen in Fig. 1.17, the Earth's atmosphere is mostly transparent for the visible and the radio part of the spectrum and this range is accessible by the telescopes on the ground. In turn, X-rays are completely absorbed by the atmosphere and this part of the electromagnetic spectrum is accessible only by satellite (space-based) experiments. The IR radiation is also highly absorbed by the atmosphere and this part of the electromagnetic spectrum is also studied by the space-based telescopes. Regarding the γ-rays, which are also highly absorbed by the atmosphere, the detection of γ-rays at the highest energies becomes possible from the ground by Imaging Atmospheric Čherenkov Telescopes (IACTs) or detectors based on fluorescence. In such telescopes, the cascades of secondary particles, EAS (see Fig. 1.1), produced by the by energetic primary photons are detected.

1.2.1 Gamma-ray Astronomy

The photoelectric effect is dominant <100 keV, Compton scattering between 100 keV and 10 MeV, and pair production into e^+e^- pairs is the dominant interaction mechanism for photons at energies above 10 MeV [136, 134]. Since γ-ray fluxes decrease rapidly with increasing energy, satellite experiments can only efficiently explore the energy band below about 100 GeV, called the HE γ-ray domain as opposed to the VHE, for which ground-based detectors are required [137]. The conventional energy windows of γ-ray astronomy in Table 1.1.

Tab. 1.1.: The conventional energy windows of γ-ray astronomy

Low Energy (LE)	MeV range	0.1 - 100 MeV
High Energy (HE)	GeV range	0.1 - 100 GeV
Very High Energy (VHE)	TeV range	0.1 - 100 TeV
Ultra High Energy (UHE)	PeV range	0.1 - 100 PeV
Extremely High Energy (EHE)	EeV range	0.1 - 100 EeV

The first observation [138, 139, 140] of a γ-ray source has been performed by the OSO-3[14] satellite in 1967-1968, providing the first clear evidence that the Milky Way was a bright source of γ-rays above ~50 MeV [137]. Less than a year later, the first [9] GRB was detected during the mission of the United States Vela satellite. The Vela satellite originally was designed to detect a flash of γ radiation during covert nuclear weapons tests and was declassified and published only in 1973 [9].

The first catalog of detected high-energy γ-ray sources have been performed by COS-B[15] [141] mission of European Space Agency (ESA)[16], which operated in 1975-1982 years and was first ESA's mission to study γ-ray sources. COS-B provided the first complete map of the Galaxy in γ-rays. Starting with tens of high-energy sources in the Second COS-B Gamma catalog (2CG Catalog) detected by COS-B satellite, this number was significantly increased to hundreds [142, 143, 144] in the 1990s by NASA's[17] Energetic Gamma Ray Experiment Telescope (EGRET)[18] [145] satellite on board of Compton Gamma Ray Observatory (CGRO)[19]. The Third EGRET Catalog [143] of high-energy γ-ray sources, 3EG Catalog, containing 271 sources (E>100 MeV) collected between 1991 and 1995 years is shown in Fig. 1.18. The EGRET telescope covered the energy range from 30 MeV to over 20 GeV recording γ-ray photons individually as e^+e^- pair production events, which were processed automatically to provide the arrival direction and energy of each photon [143].

[14] Third satellite of the Orbiting Solar Observatory (OSO-3) Program, https://heasarc.gsfc.nasa.gov/docs/heasarc/missions/oso3.html.
[15] COS-B Mission, http://www.esa.int/Our_Activities/Space_Science/Cos-B_overview2, https://heasarc.gsfc.nasa.gov/docs/cosb/cosb_about.html
[16] European Space Agency (ESA), https://www.esa.int/ESA/
[17] National Aeronautics and Space Administration (NASA), https://www.nasa.gov/
[18] Energetic Gamma Ray Experiment Telescope (EGRET), https://heasarc.gsfc.nasa.gov/docs/cgro/egret/
[19] Compton Gamma Ray Observatory (CGRO) Mission, https://heasarc.gsfc.nasa.gov/docs/cgro/index.html

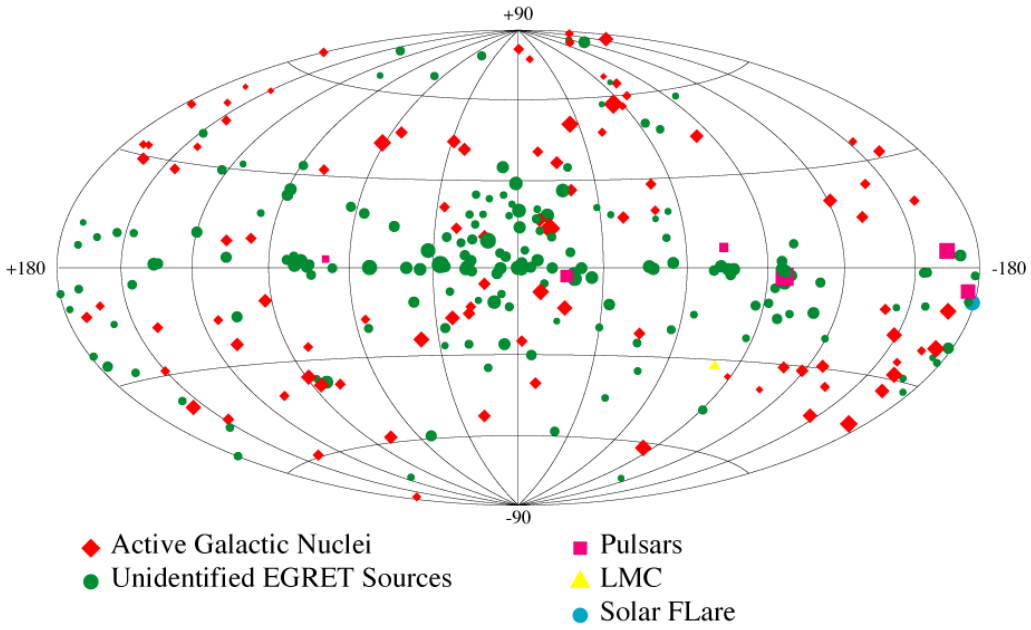

Fig. 1.18.: Third EGRET source catalog [143], in Galactic coordinates. The size of the symbol represents the highest intensity seen for this source by EGRET. Image credit: NASA/GSFC/EGRET Collaboration.

Currently, the *Fermi*-LAT [98, 99, 100] observatory monitors the γ-ray sky in the energy range 20 MeV to more than 1 TeV, measuring the arrival times, energies, and directions of γ-rays [146]. The latest published *Fermi*-LAT source catalog (fourth FGL catalog, or 4FGL) catalog [146] includes 5065 high-energy γ-ray sources (see Fig. 1.19) detected in the first eight years of the *Fermi*-LAT. The 4FGL catalog includes the sources detected above 4γ significance and for each source, the localization and spectral properties have been provided. More than 3130 of the identified or associated sources are active galaxies of the blazar[20] class [146]. Compared to the third catalog, 3FGL [149], which is given in 100 MeV - 300 GeV energy range, the 4FGL [146] catalog benefits from a number of improvements with respect to the 3FGL. The lower bound of the energy range was set to 50 MeV, down from 100 MeV in 3FGL, and the upper bound was raised from 300 GeV to 1 TeV [146]. With the eight years of science data in the energy range from 50 MeV to 1 TeV, the 4FGL catalog is the deepest yet in this energy range [146]. Also, the number of sources presented in the 4FGL catalog is increased by about two thousand with respect to the 3FGL. Blazars, the most extreme type of active galaxies, make up more than ~60% in the 4FGL catalog. The γ-ray sky of blazars seen by *Fermi*-LAT after 5 years of operation is shown in Fig. 1.20. The two closest blazars to Earth, Mrk 421 and Mrk 501, are clearly visible. The key advantage of ground-based instrumentation over space-based GeV instruments such as EGRET or current *Fermi*-LAT is a collection area [150]. So far, the IACT technique has proven to be the most powerful approach in the VHE energy regime with the typical effective collection area of

[20] The term "blazar" was coined in 1978 astronomer Edward Spiegel [147, 148] to denote the contraction of the names of two classes of active galaxies, BL Lacertae objects and Flat-Spectrum Radio Quasars (FSRQ), the latter exhibits less extreme behavior.

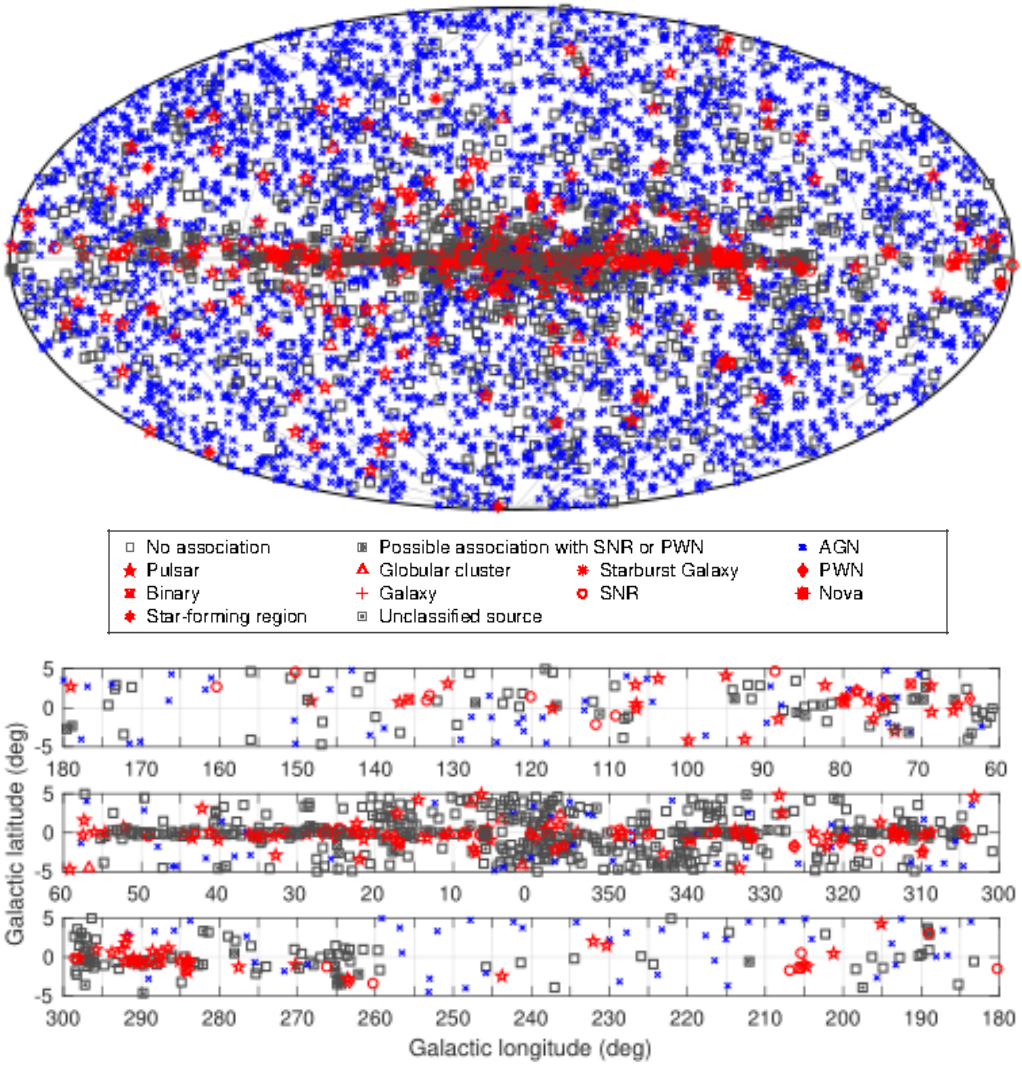

Fig. 1.19.: Full skymap in equatorial coordinates (*Top*) and blow-up of the Galactic plane split into three longitude bands (*Bottom*) showing sources by source class (see [146] for details, no distinction is made between associations and identifications). All AGN classes are plotted with the same blue symbol for simplicity. Other associations to a well-defined class are plotted in red. Unassociated sources and sources associated to counterparts of unknown nature are plotted in black. The figure is taken from [146].

a single Čherenkov telescope is 10^5 m^2, almost five orders of magnitude larger than can realistically be achieved via direct detection in space [150]. The exploit of IACT technique resulted in the first VHE detection of the Crab Nebula (now the standard candle in VHE astronomy) in 1989 [151] by Fred Lawrence Whipple Observatory (FLWO)[21] [152, 153], proving the existence of a steady source of TeV γ-rays and having important consequences for the field. The limitations of the IACT technique in comparison to the air-shower particle detectors are a limited Field of View (FOV) about 5° and a relatively poor duty cycle, with about 1000 hours of useful observations obtainable per year [150].

[21] Whipple Collaboration, http://www.sao.arizona.edu/FLWO/whipple.html

Despite the fact that most of the observations in the TeV band have been performed with IACTs, which provide very useful data for in-depth studies of the astrophysical objects but have limited capabilities for regular monitoring and can only operate during clear nights and typically monitor only one source in the FOV at any time [154]. In contrast, the wide FOV TeV instruments with high duty cycles such as the High Altitude Water Cherenkov (HAWC) Observatory[22] [155, 156] have substantial advantages. Its wide field of view of 2 steradians (sr) and duty cycle of >95% are unique features compared to other TeV observatories and allow observing every source that transits over HAWC for up to ~6 hours each sidereal day [154]. The HAWC is the successor of the Milagro [157, 158] γ-ray observatory which successfully operated during 2000-2008 years. The HAWC telescope is discussed in details in Section 4. Several instruments based on space and on the ground have been observed hundreds of TeV γ-ray sources so far. Current VHE observatories, based on IACT technique and which effectively complements the NASA's *Fermi*-LAT mission include High Energy Stereoscopic System (H.E.S.S.)[23] [159, 160, 161], Major Atmospheric Gamma Imaging Cherenkov Telescopes (MAGIC)[24] [162, 163, 164], Very Energetic Radiation Imaging Telescope Array System (VERITAS)[25] [165, 166, 167]. Soon will come into operation the Cherenkov Telescope Array (CTA)[26] [168, 169], a new facility, with capabilities well beyond those of conceivable upgrades of existing instruments [169] such as H.E.S.S., MAGIC or VERITAS. Building on the technology of the current generation ground-based γ-ray telescopes, it will be the largest such kind observatory in the world, with more than 100 telescopes in both hemispheres, providing unprecedented accuracy and being about a factor of 10 times more sensitive [169] than existing instruments.

Astronomy with γ-rays allows studying the most energetic, compact and violent astrophysical objects in the Universe. Nevertheless, the extragalactic γ-ray astronomy is limited somewhat by the absorption of γ-rays on their path to the Earth by the Extragalactic Background Light (EBL) when the center-of-mass energy of the γ + photon reaction allows for the production of a e^+e^- pair [137]. This absorption effect has been observed on TeV γ-rays from AGNs due to the IR and optical background light [137]. The diffuse EBL prevents γ-rays to propagate over cosmological distances [170] (see Fig. 1.40). In contrast to that, neutrinos carrying an only weak charge propagate indefinitely without neither deflection neither absorption and trace back to their source [171], making astronomy with neutrinos a powerful instrument for disclosure the physical processes behind extreme astrophysical phenomena in the Universe (see Section 1.5). Furthermore, combining several messengers, such as neutrinos, γ-rays, CRs, GWs significantly increases chances to get information about such astrophysical phenomena and thus substantially extends our knowledge them as discussed in Section 1.7.

[22] HAWC Collaboration, https://www.hawc-observatory.org/
[23] H.E.S.S. Collaboration, https://www.mpi-hd.mpg.de/hfm/HESS/
[24] MAGIC Collaboration, https://wwwmagic.mpp.mpg.de/
[25] VERITAS Collaboration, https://veritas.sao.arizona.edu/
[26] CTA Consortium, https://www.cta-observatory.org/

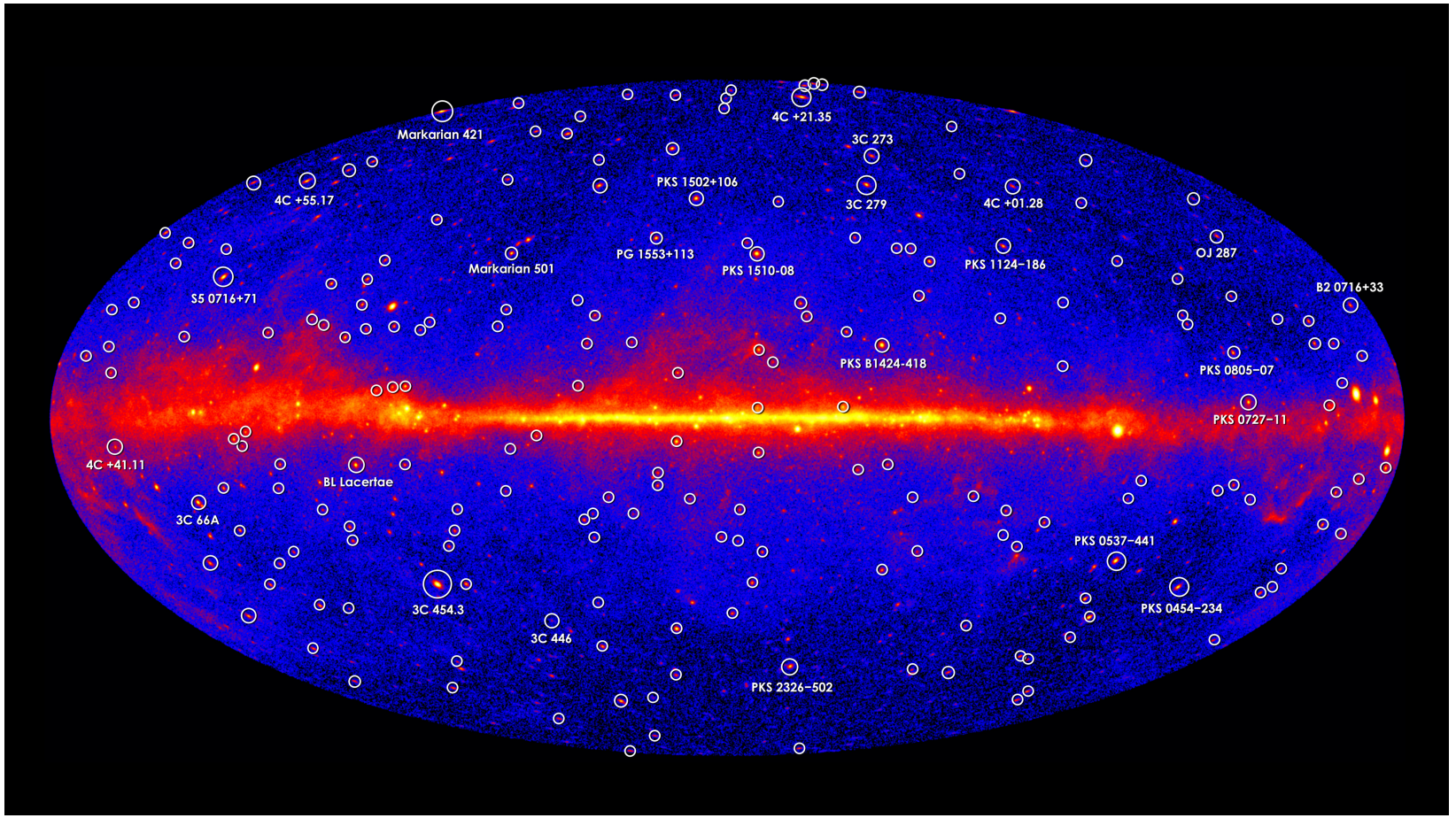

Fig. 1.20.: The γ-ray sky of blazars, the most extreme type of active galaxies, seen by *Fermi*-LAT. Image credit: NASA/DOE/*Fermi*-LAT Collaboration.

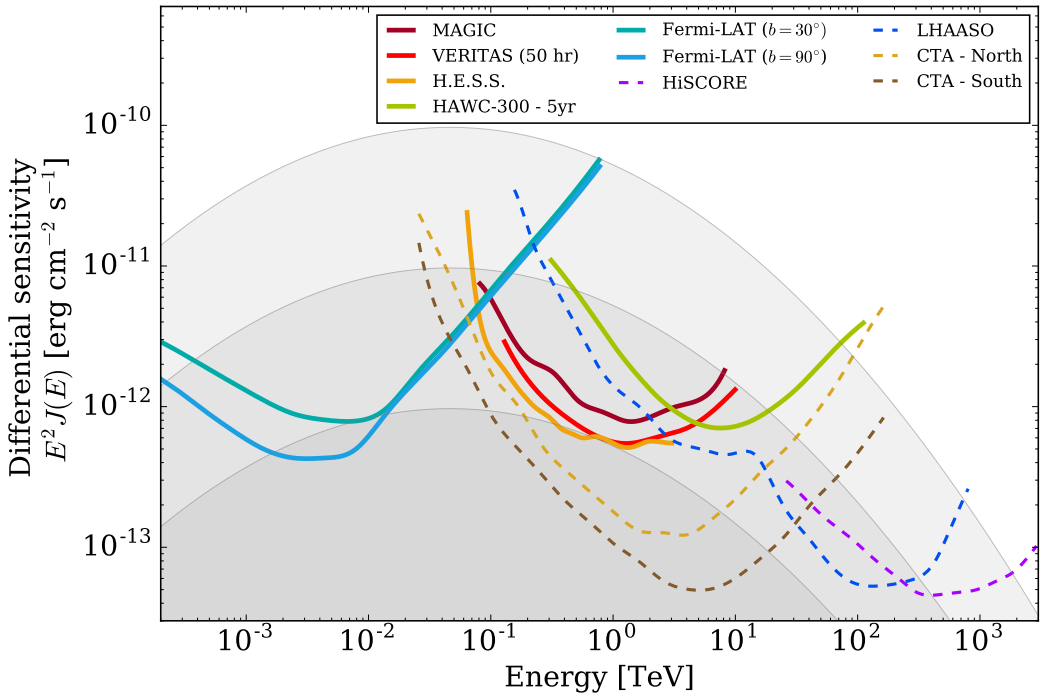

Fig. 1.21.: Differential 5σ sensitivity of current (solid lines) and future (dashed lines) gamma-ray observatories. The *Fermi*-LAT sensitivity curve is given for a 10-year exposure at two galactic latitudes (30° and 90°). The *Fermi*-LAT and HAWC curves are given for quarter-decade energy bins. The VERITAS, MAGIC, H.E.S.S., and CTA curves are given for 50 hours of observation and 5 energy bins per decade. The HAWC 300 sensitivity, and that of HiScore and LHAASO arrays, is given for a five-year exposure. For reference, the shaded grey regions indicate, from the top, 100%, 10%, and 1% levels of the Crab γ-ray spectrum. See [172] for references to the data used. The figure is taken from [172].

High-energy neutrinos can be searched in correlations with sources of extragalactic γ-rays at GeV-TeV energies, using the data from the main instruments in this band: the space-based *Fermi*-LAT telescope; the ground-based telescopes such as the H.E.S.S., MAGIC, VERITAS, and the HAWC array. The link between γ-rays and neutrinos are explained in Section 1.5. The sensitivities [172] of current and future[27] γ-ray telescopes are shown in Fig. 1.21. As more facilities go online in the coming years, a drastic increase in the sensitivity of these searches is expected, which may finally reveal these elusive sources [172], encouraging the search with renewed vigor after the very recent discovery of the correlation between neutrino (IceCube-170922A neutrino event (see Section 1.7.1) and γ-rays (TXS 0506+056 γ-ray flare (see Section 1.7.2) on September 22, 2017 [16]. An extensive multiwavelength campaign followed, ranging from radio frequencies to γ-rays, which characterized the variability and energetics of the TXS 0506+056 blazar and include its first detection in VHE γ-rays [16]. This observation of a neutrino in spatial coincidence with a γ-ray emitting blazar during an active phase suggests that blazars may be a source of high-energy neutrinos [16].

[27] As of 2016.

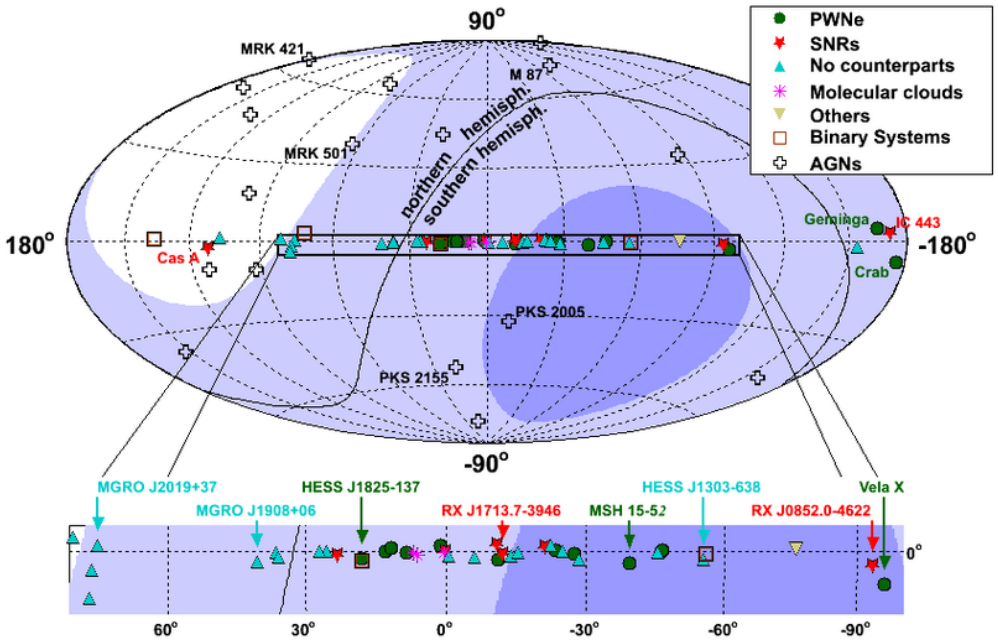

Fig. 1.22.: Skymap of high-energy γ-ray sources at the energy range 100 GeV $< E_\gamma <$ 100 TeV, in Galactic coordinates. The source types are represented by different symbols. The shaded areas indicate 25-75% (light violet) and >75% (dark violet) visibility for a detector in the Mediterranean sea with 2π downward coverage while the white color represents the region which is not observable. The solid curve indicates the extent of the visibility of a South Pole detector (IceCube). *Inset:* A zoomed view of the area between $-100°$ and $+28°$ in the Galactic longitude and about $-3.5°$ and $+0.8°$ in the Galactic latitude and covers the Galactic center region. The figure is taken from [179].

The KM3NeT neutrino telescope [173, 174, 175] with a unique design of multi-PMT optical modules and of a multi-km^3 instrumented volume will have surpassed ANTARES in the sensitivity by the time of the scheduled decommissioning of the ANTARES telescope in 2019. As a neutrino telescope builds in the Mediterranean Sea, KM3NeT will complement the IceCube in its FOV surveying the entire sky. The searches for galactic and extragalactic neutrino sources with such coverage, good angular resolution, and sensitivity will lead to a lot of exciting discoveries such as that in 2017. The skymap of high-energy γ-ray sources seen by neutrino telescope build in the Mediterranean Sea are shown in Fig. 1.22. The advantage of the telescope in the Mediterranean Sea, such as ANTARES or KM3NeT, with respect to the IceCube detector, is a better exposure to the Galactic center region, and a much better angular resolution on the measurement of the neutrino direction [117]. As also seen, Mrk 421 and Mrk 501 are located almost at the edge of visibility for the telescope build in the Mediterranean Sea such as ANTARES or KM3NeT. Thereby, the search for neutrinos from such sources can be performed by accepting a small amount of down-going neutrino events [176], such as done in [177, 178]. The KM3NeT and ANTARES telescopes are described in detail in Section 2.4.4 and Section 3 respectively.

1.3 Gravitational Waves

The idea of GWs was already implicit in the 1905 special theory of relativity, with its finite limiting speed for information transfer [180]. The explicit formulation for GWs in general relativity were put forward by Albert Einstein in a decade later [180]. He showed that the acceleration of masses generates time-dependent gravitational fields that propagate away from their sources at the speed of light as warpages of spacetime, which is called a GW [180] (see artist's illustration in Fig. 1.23). Einstein predicted the existence of GWs in 1916, the year after the final formulation of the field equations of general relativity [12]. He found [181, 182] that the linearized weak-field equations had wave solutions: transverse waves of spatial strain that travel at the speed of light, generated by time variations of the mass quadrupole moment of the source [12]. He also understood that the amplitudes of the GWs would be remarkably small [12]; moreover, until the Chapel Hill Conference in 1957, there was significant debate about the physical reality of GWs [183]. The current understanding of the physical nature of GWs took a giant step forward at that conference where some insights on GWs were achieved and the question of the reality of GWs was resolved by a recognition that one could, in principle, construct a detector for such waves [183]. An essential part of creating a modern understanding of GWs was played by Josh Goldberg, through whose patronage the Chapel Hill Conference actually was organized [183]. In his work in 1955 [184], Goldberg investigated the existence of gravitational radiation and showed that EIH (Einstein, Infeld, and Hoffman) [185] approximation method does not exclude the possibility of radiation [184] and a previous claim that binary star systems could not radiate GWs was untrue [183]. That was a crucial step toward understanding the applicability of the quadrupole formula for binaries, the most promising astrophysical source of GWs and one of the most important prospective sources for modern interferometers [183] such as LIGO and Virgo. The Laser Interferometer Gravitational-Wave Observatory (LIGO)[28] [186, 180, 187] and Virgo[29] [188, 189, 190] are interferometers designed to detect GWs that predicted by the general relativity. The discovery of the binary pulsar system by Hulse and Taylor [191] and subsequent observations of its energy loss by Taylor and Weisberg [192] demonstrated the existence of GWs [12].

1.3.1 Gravitational-Wave Astronomy

Experiments to detect GWs began [12] with Weber and his resonant mass detectors in the 1960s [193], followed by an international network of cryogenic resonant detectors [194], while interferometric detectors were first suggested in the early 1960s by Gertsenshteĭn and Pustovoĭt [195] and the 1970s by Moss, Miller, and Forward [196]. By the early 2000s, a set of initial detectors was completed, including TAMA 300[30] [197] in Japan, GEO 600[31] [198] in Germany, LIGO [187] in the United States, and Virgo [190] in Italy [12]. Combinations

[28] LIGO Collaboration, https://www.ligo.caltech.edu/
[29] Virgo Collaboration, http://www.virgo-gw.eu/
[30] TAMA interferometer, https://gwpo.nao.ac.jp
[31] GEO Collaboration, https://www.geo600.org/

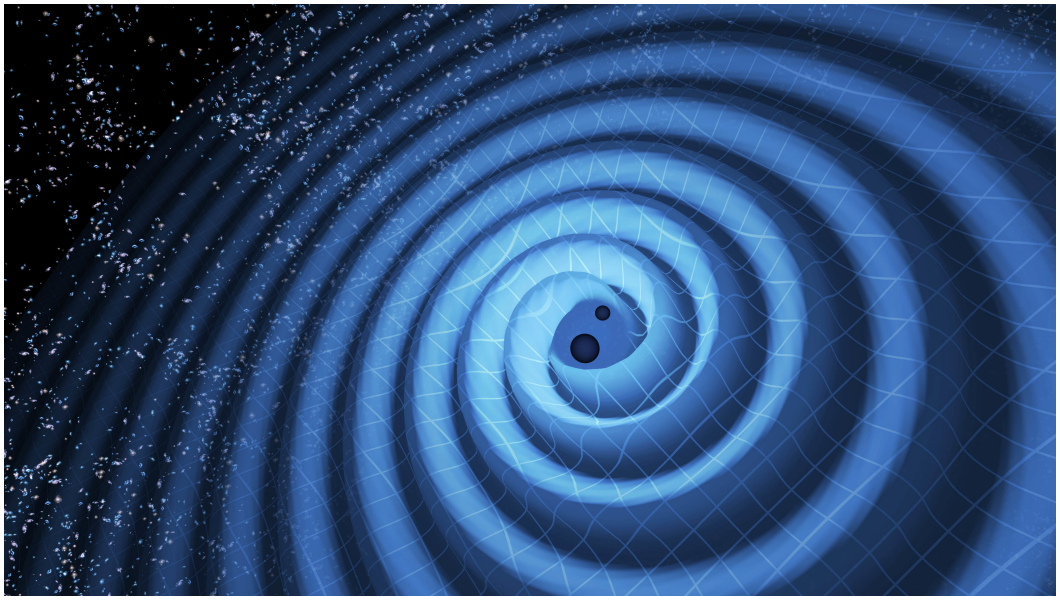

Fig. 1.23.: Illustration of the merger of two BHs and the GWs that ripple outward as the BHs spiral toward each other. Image credit: LIGO/T. Pyle.

of these detectors made joint observations from 2002 through 2011, setting upper limits on a variety of GW sources while evolving into a global network. In 2015, Advanced LIGO became the first of a significantly more sensitive network of advanced detectors [199, 200, 190, 187] to begin observations [12]. Currently, Japan constructs the next-generation GW detector, the KAmioka GRAvitational Wave Detector (KAGRA)[32] [199], to be the world's first GW observatory in Asia. In addition, a concept proposal for a new advanced GW detector to be located in India as part of the worldwide network of advanced GW interferometric detectors, LIGO-India[33] [201], is now under active consideration in India and the USA. The timeline for construction, upgrades, and data-taking for modern and future GW detectors are discussed briefly in Section 1.3.1.

A century after the fundamental predictions of Einstein and Schwarzschild, on September 14, 2015 the first direct detection of GWs and the first direct observation of a Binary Black Hole (BBH) system merging to form a single BH was made during its first observing run (O1) [12]. It turned out that at the time of the event, the Virgo detector was being upgraded, and GEO 600, though not sufficiently sensitive to detect this event, was operating but not in observational mode; thus, only the LIGO detectors were observing [12]. This GW150914[34] event was a breakthrough of the [35] and became a remarkable accomplishment of the LIGO and for entire GW astronomy in recent decades. The GW150914 event marked the birth of a new branch of astronomy, GW astronomy, and is described in detail in Section 1.3.1. Soon, in the same year on December 26, 2015, at 03:38:53 UTC, during O1 run the twin

[32] KAGRA Collaboration, https://gwcenter.icrr.u-tokyo.ac.jp/
[33] LIGO-India interferometer, https://www.ligo-india.in/
[34] From "**G**ravitational **W**ave" and the date of observation 20**15**-**09**-**14**.
[35] Science's 2016 Breakthrough of the Year, http://www.sciencemag.org/news/2016/12/ripples-spacetime-sciences-2016-breakthrough-year.

detectors of the LIGO observed a GW signal produced by the coalescence of two stellar-mass BHs [202]. The final $20.8^{+6.1}_{-1.7} M_\odot$ is a result of the coalescence of two BHs with masses $14.2^{+8.3}_{-3.7} M_\odot$ and $7.5^{+2.3}_{-2.3} M_\odot$ [202]. This event, GW151226, became the second-ever detected in GW astronomy. LIGO undertook O1 run from September 12, 2015, to January 19, 2016 [202]. In addition to two unambiguously (with a significance of greater than 5σ over the observing period) identified signals, GW150914 and GW151226, a third possible signal, LVT151012[36], has been identified but with substantially lower significance however with an 87% probability of being of astrophysical origin [203, 204]. A few years later, the results of LVT151012 event has been revised. With the improved methods employed in [205], the false alarm rate of the LVT151012 candidate improves by an order of magnitude and it was considered a true astrophysical event. The probability that LVT151012 is astrophysical in origin was estimated to be 97.59% [205].

Following a commissioning break, LIGO undertook a second observing run (O2) from November 30, 2016, to August 25, 2017, with the Advanced Virgo detector [190] joining the run on August 1, 2017 [206]. Several important discoveries have been made including:

On January 4, 2017, at 10:11:58.6 UTC, during O2 run the twin detectors of the Advanced LIGO measured a GW signal produced by the coalescence of a pair of stellar-mass BHs with masses $31^{+8.4}_{-6.0} M_\odot$ and $19.4^{+5.3}_{-5.9} M_\odot$ [207]. This GW170104 signal was the third GW event confirmed, after GW150914 and GW151226, and fourth overall. On June 8, 2017, at 02:01:16.49 UTC, during O2 run the two Advanced LIGO detectors observed a GW signal from the merger of two stellar-mass BHs with masses $12^{+7}_{-2} M_\odot$ and $7^{+2}_{-2} M_\odot$ [206].

On August 14, 2017, at 10:30:43 UTC, the Advanced Virgo detector and the two Advanced LIGO detectors coherently observed a transient GW signal produced by the coalescence of two stellar-mass BHs with masses $30.5^{+5.7}_{-3.0} M_\odot$ and $25.3^{+2.8}_{-4.2} M_\odot$ [208]. It was the first BBH merger detected by both LIGO and Virgo (see Section 1.3.1 for details). Moreover, for the first time, the LIGO-Virgo network has allowed probing the nature of GW signal polarizations, thus enabled a new class of phenomenological tests of gravity [208].

On August 17, 2017, at 12:41:04 UTC the Advanced LIGO and Advanced Virgo detectors made another breakthrough[37], the first observation of a Binary Neutron Star (BNS) merger [13]. A GW signal, GW170817, from the inspiral of two low-mass compact objects consistent with a BNS merger [13] (see Section 1.3.1 for details).

[36] Such probable low significance GW detections are designated LVT ("LIGO-Virgo trigger").
[37] Science's 2017 Breakthrough of the Year, https://vis.sciencemag.org/breakthrough2017/

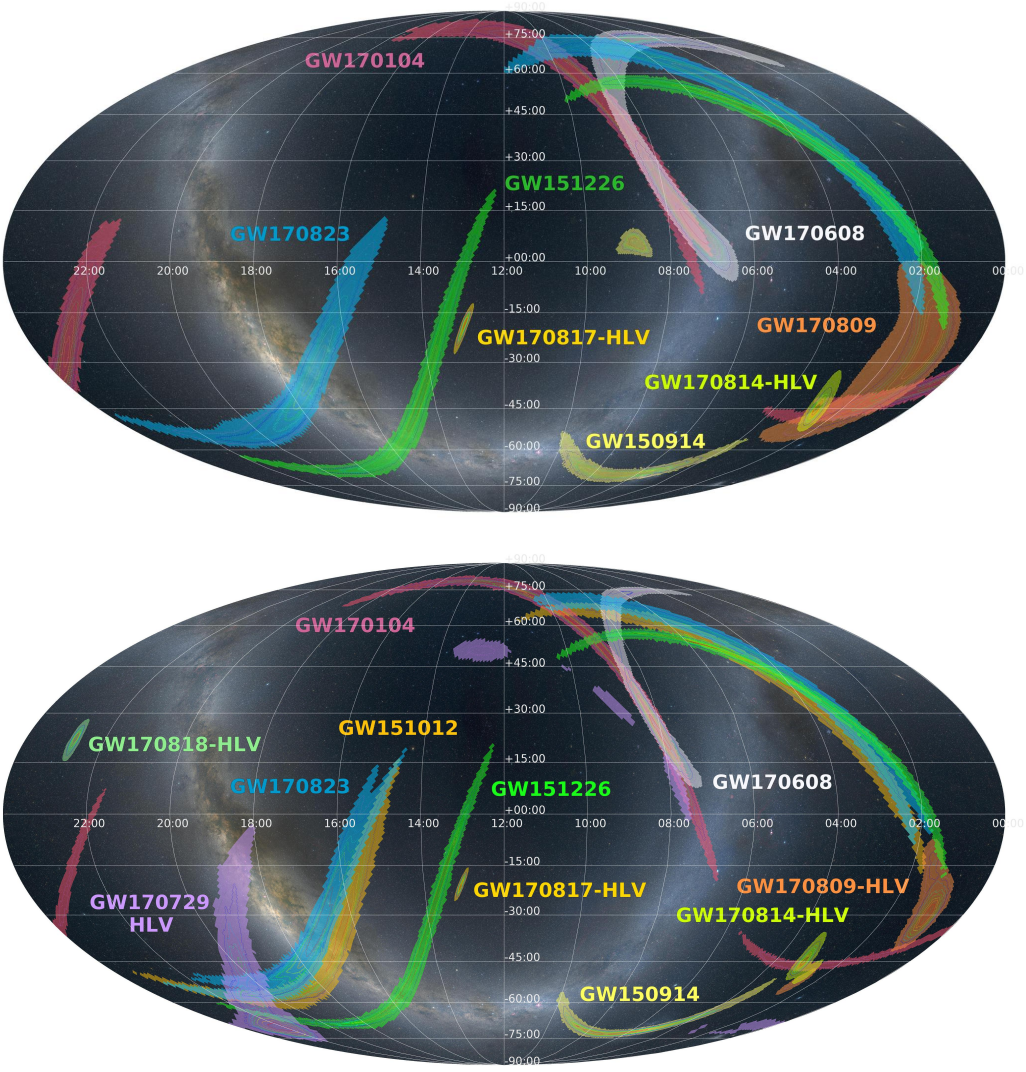

Fig. 1.24.: Sky locations of GW events confidently detected in O1 and O2. *Top:* Initial sky location released in low-latency to the astronomers [212, 213, 211]. *Bottom:* Refined sky location including updated calibration and final choice of waveform models [210]. Three events (GW151012, GW170729, GW170818) among the 11 confident detections were identified offline and were not shared in low-latency. The shaded areas enclose the 90% credible regions of the posterior probability sky areas in a Mollweide projection. The inner lines enclose regions starting from the 10% credible area with the color scheme changing with every 10% increase in confidence level. The localization is shown in equatorial coordinates (RA in hours, and declination in degrees). The HLV label indicates events for which both the LIGO and Virgo data were used to estimate the sky location. The figure is taken from [209].

The sky localization of GW events confidently detected during O1 and O2 and sent in low-latency and refined sky localization obtained offline are shown in Fig. 1.24. The offline analyses exploit [209] refined instrumental calibration, noise subtraction, updated estimates of the amplitude power spectral density, etc [210, 211].

GW interferometers

The GW astronomy exploits multiple, widely separated detectors to distinguish GWs from local instrumental and environmental noise, to provide source sky localization, and to measure wave polarizations [12]. Since the full science of ground-based GW detectors is broad, only a brief overview of the interferometers will be given with a particular focus on the LIGO, the telescope which for the first time detected GWs. The LIGO consists of two detectors identical in design and located in the USA at Livingston, LA (L1) and Hanford, WA (H1) [187] (see Fig. 1.25). The LIGO sites each operate a single Advanced LIGO detector [187], a modified Michelson interferometer (see Fig. 1.26) with 4 km long arms that measure GW strain as a difference in length of its orthogonal arms [12]. Each arm is formed by two mirrors, acting as test masses, separated by $L_x = L_y = L_z$ km [12]. The Fabry-Perot resonant cavity in each arm is to build up the phase shift produced by an arm length change [12]. A passing GW effectively alters the arm lengths such that the measured difference is [12]:

$$\Delta L(t) = \delta L_x - \delta L_y = h(t)L, \tag{1.19}$$

where h is the GW strain amplitude projected onto the detector. This differential length variation alters the phase difference between the two light fields returning to the beam splitter, transmitting an optical signal proportional to the GW strain to the output photodetector [12]. To achieve sufficient sensitivity to measure GWs, the detectors include several enhancements to the basic Michelson interferometer [12].

Fig. 1.25.: The LIGO detector. *Left:* Livingston, LA (L1). *Right:* Hanford, WA (H1). Images credit: Caltech/MIT/LIGO Lab.

The LIGO's interferometry techniques are designed to maximize the conversion of strain to an optical signal, thereby minimizing the impact of photon shot noise (the principal noise at high frequencies) [12]. High strain sensitivity also requires that the test masses have low displacement noise, which is achieved by isolating them from seismic noise (low frequencies) and designing them to have low thermal noise (intermediate frequencies) [12]. To minimize additional noise sources, all components other than the laser source are mounted on vibration isolation stages an in ultrahigh vacuum [12]. The detector output is calibrated in strain with two methods, one referenced to the main laser wavelength and the other to

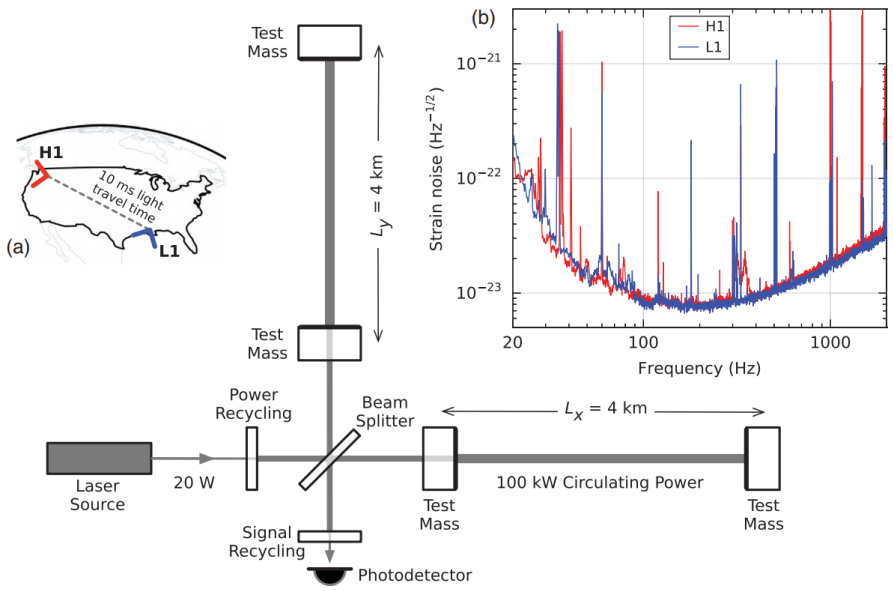

Fig. 1.26.: Simplified diagram of an Advanced LIGO detector (not to scale). A GW wave propagating orthogonally to the detector plane and linearly polarized parallel to the 4-km optical cavities will have the effect of lengthening one 4-km arm and shortening the other during one half-cycle of the wave; these length changes are reversed during the other half-cycle. The output photodetector records these differential cavity length variations. While a detector's directional response is maximal for this case, it is still significant for most other angles of incidence or polarizations (GWs propagate freely through the Earth). *Inset (a)*: Location and orientation of the LIGO detectors at H1 and L1. *Inset (b)*: The instrument noise for each detector near the time of the signal detection; this is an amplitude spectral density, expressed in terms of equivalent GW strain amplitude. The sensitivity is limited by photon shot noise at frequencies above 150 Hz, and by a superposition of other noise sources at lower frequencies. Narrow-band features include calibration lines (33-38, 330, and 1080 Hz), vibrational modes of suspension fibers (500 Hz and harmonics), and 60 Hz electric power grid harmonics. The figure is taken from [12].

a radio-frequency oscillator [12]. Additionally, the detector response to GWs is tested by injecting simulated waveforms with the calibration laser [12]. To monitor environmental disturbances and their influence on the detectors, each observatory site is equipped with an array of sensors [12]: seismometers, accelerometers, microphones, magnetometers, radio receivers, weather sensors, ac-power line monitors, and a CR detector [214]. Data collection is synchronized to Global Positioning System (GPS) time to better than $10\mu s$ and the timing accuracy is verified with an atomic clock and a secondary GPS receiver at each observatory site [12]. In the most sensitive frequency region around 100 Hz (see Fig. 1.26), the design strain sensitivity for Advanced LIGO is a factor of 10 better than the initial LIGO due to improved frequency response [187]. The detectors respond proportionally to GW amplitude, thus at low redshift the volume of space to which they are sensitive increases as the cube of strain sensitivity [12]. Since the probed volume of the universe scales in that way, being 10 times better represents an enormous increase (of order 10^3x) in the number of potential astrophysical sources detectable by these instruments [187]. To minimize additional noise sources, all components other than the laser source are mounted on vibration isolation stages in an ultrahigh vacuum.

GW150914

The signal, GW150914, was confidently detected by two different types of searches [12]:

> **Binary coalescence search** recover signals from the coalescence of compact objects, using optimal matched filtering with waveforms predicted by general relativity.
>
> **Generic transient search** target a broad range of generic transient signals, with minimal assumptions about waveforms.

These searches use independent methods, and their response to detector noise consists of different, uncorrelated, events [12]. Each search identifies candidate events that are detected at both observatories consistent with the intersite propagation time. Events are assigned a detection-statistic value that ranks their likelihood of being a GW signal [12].

The GW150914 was initially detected by low-latency searches for generic GW transients [215] (see Fig. 1.27). Designed to operate without a specific waveform model, this search identifies coincident excess power in time-frequency representations of the detector strain data, for signal frequencies up to 1 kHz and durations up to a few seconds [12]. The generic transient search reconstructs signal waveforms consistent with a common GW signal in both detectors using a multidetector maximum likelihood method. Each event is ranked according to the detection statistic $\eta_c = \sqrt{2E_c/(1 + E_{n/E_c})}$, where E_c is the dimensionless coherent signal energy obtained by cross-correlating the two reconstructed waveforms, and E_n is the dimensionless residual noise energy after the reconstructed signal is subtracted from the data [12]. Also, based on their time-frequency morphology, the events are divided into three mutually exclusive search classes [215]: events with time-frequency morphology of known populations of noise transients (class C1), events with frequency that increases with time (class C3), and all remaining events (class C2) [12]. The GW150914 event was found in the C2+C3 class (see Fig. 1.27) with $\eta_c = 20.0$ (see Fig. 1.27) and with 4.6σ significance [12].

Subsequently, matched-filter analyses by the binary coalescence search (see Fig. 1.27) that use relativistic models of compact binary waveforms [203] recovered GW150914 as the most significant event from each detector [12]. Occurring within the 10-ms intersite propagation time, the events have a combined signal-to-noise ratio $\rho_c = 23.6$ (see Fig. 1.27) and a false alarm rate estimated to be less than 1 event per 203 000 years, equivalent to a significance greater than 5.1σ [12]. The binary coalescence search [12] targets GW emission from binary systems with individual masses from 1 to $99M_\odot$, total mass less than $100M_\odot$, and dimensionless spins up to 0.99 [203]. The search calculates the matched-filter signal-to-noise ratio $\rho(t)$ for each template in each detector and identifies maxima of $\rho(t)$ with respect to the time of arrival of the signal [12].

The basic features of GW150914 pointed out that it was produced by the coalescence of two BHs - i.e., their orbital inspiral and merger, and subsequent final BH ringdown [12].

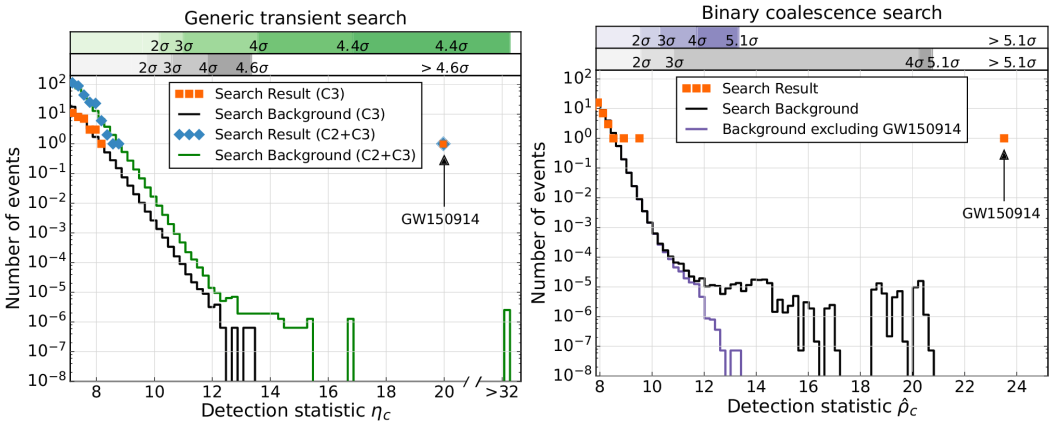

Fig. 1.27.: Search results from the generic transient search (left) and the binary coalescence search (right). The histograms show the number of candidate events (orange markers) and the mean number of background events (black lines) in the search class (denoted as C) where GW150914 was found as a function of the search detection statistic and with a bin width of 0.2. The scales on the top give the significance of an event in Gaussian standard deviations based on the corresponding noise background. The significance of GW150914 is greater than 5.1σ and 4.6σ for the binary coalescence and the generic transient searches, respectively. For generic transient search (right) along with the primary search (C3), the results (blue markers) and background (green curve) for an alternative search (C2+C3 that treats events independently of their frequency evolution, are also shown. The tail in the black-line background of the binary coalescence search (right) is due to random coincidences of GW150914 in one detector with noise in the other detector (it is practically absent in the generic transient search background because they do not pass the time-frequency consistency requirements used in that search). The purple curve is the background excluding those coincidences, which is used to assess the significance of the second strongest event. The figure is taken from [12].

Over 0.2 s, the signal increased in frequency and amplitude in about 8 cycles from 35 to 150 Hz (see Fig. 1.28), where the amplitude reached a maximum[38] [12]. The most plausible explanation for this evolution was the inspiral of two orbiting masses, m_1 and m_2, due to GW emission [12]. At the lower frequencies, such evolution is characterized by the chirp mass [216]:

$$\mathcal{M} = \frac{(m_1 m_2)^{3/5}}{(m_1 + m_2)^{1/5}} = \frac{c^3}{G}\left[\frac{5}{96}\pi^{-8/3} f^{-11/3} \dot{f}\right]^{3/5}, \tag{1.20}$$

where f and $\dot{f}$ are the observed frequency and its time derivative and G and c are the gravitational constant and speed of light [12]. Estimating f and $\dot{f}$ from the data in Fig. 1.28, a chirp mass $\mathcal{M} \simeq 30 M_\odot$ can be obtained, implying that the total mass $M = m_1 + m_2$ is $\gtrsim 70 M_\odot$ in the detector frame [12]. This bounds the sum of the Schwarzschild radii of the binary components to $2GM/c^2 \gtrsim 210$ km [12]. To reach an orbital frequency of 75 Hz (half the GW frequency) the objects must have been very close and very compact; equal Newtonian point masses orbiting at this frequency would be only $\simeq$ 350 km apart [12]. A pair of NSs, while compact, would not have the required mass, while a BH NS binary with the deduced chirp mass would have a very large total mass, and would thus merge at much

[38] The waveform shown is SXS:BBH:0305, available for download at http://www.black-holes.org/waveforms

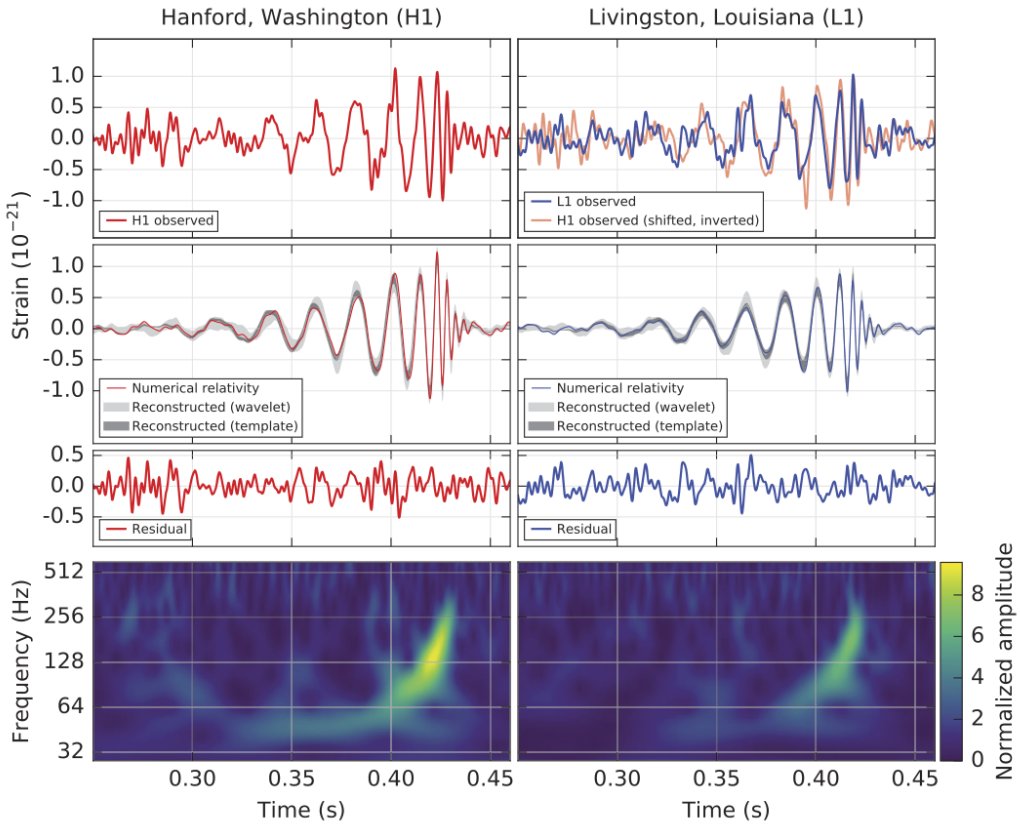

Fig. 1.28.: The GW event GW150914 observed by the LIGO Hanford (H1, left column panels) and Livingston (L1, right column panels) detectors. Times are shown relative to September 14, 2015 at 09:50:45 UTC. For visualization, all time series are filtered with a 35-350 Hz bandpass filter to suppress large fluctuations outside the detectors' most sensitive frequency band, and band-reject filters to remove the strong instrumental spectral lines seen in Fig. 1.26 spectra. *Top row, left:* H1 strain. *Top row, right:* L1 strain. GW150914 arrived first at L1 and $6.9^{+0.5}_{-0.4}$ ms later at H1; for a visual comparison, the H1 data are also shown, shifted in time by this amount and inverted (to account for the detectors' relative orientations). *Second row:* GW strain projected onto each detector in the 35-350 Hz band. Solid lines show a numerical relativity waveform for a system with parameters consistent with those recovered from GW150914 [217] confirmed to 99.9% by an independent calculation based on [218]. Shaded areas show 90% credible regions for two independent waveform reconstructions. One (dark gray) models the signal using BBH template waveforms [219]. The other (light gray) does not use an astrophysical model, but instead calculates the strain signal as a linear combination of sine-Gaussian wavelets [220, 215].These reconstructions have a 94% overlap, as shown in [219]. *Third row:* Residuals after subtracting the filtered numerical relativity waveform from the filtered detector time series. *Bottom row:* A time-frequency representation [221] of the strain data, showing the signal frequency increasing over time. The figure is taken from [12].

lower frequency. This leaves BHs as the only known objects compact enough to reach an orbital frequency of 75 Hz without contact [12]. Furthermore, the decay of the waveform after it peaks is consistent with the damped oscillations of a black hole relaxing to a final stationary Kerr configuration [12]. Figure 1.29 shows the calculated waveform using the resulting source parameters [12].

Several analyses have been performed [222] to determine whether or not GW150914 is consistent with a BBH system in general relativity [12]. A first consistency check involves the mass and spin of the final BH since, in general relativity, the end product of a BH binary coalescence is a Kerr BH, which is fully described by its mass and spin [12]. For quasicircular inspirals, these are predicted uniquely by Einstein's equations as a function of the masses and spins of the two progenitor BHs. Using fitting formulas calibrated to numerical relativity simulations [223], it has been verified [12] that the remnant mass and spin deduced from the early stage of the coalescence and those inferred independently from the late stage are consistent with each other, with no evidence for disagreement from general relativity. Within the post-Newtonian formalism, the phase of the GW during the inspiral can be expressed as a power series in $f^{1/3}$ [12]. The coefficients of this expansion can be computed in general relativity; thus, the consistency with general relativity can be tested by allowing the coefficients to deviate from the nominal values, and seeing if the resulting waveform is consistent with the data [12]. In this check [223], the constraints on these deviations were placed, finding no evidence for violations of general relativity [12].

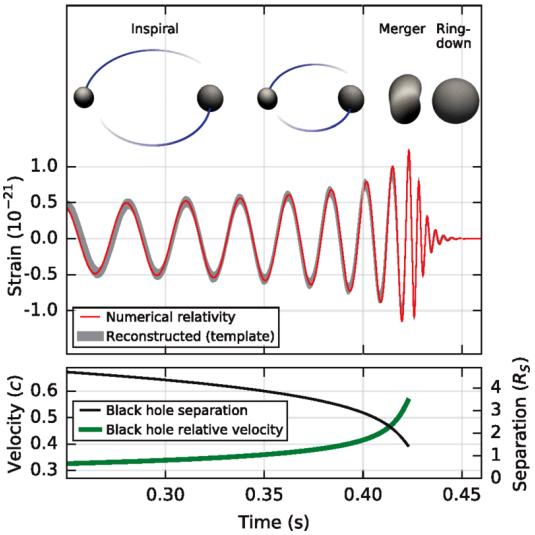

Fig. 1.29.: *Top:* Estimated GW strain amplitude from GW150914 projected onto H1. This shows the full bandwidth of the waveforms, without the filtering used for Fig. 1.28. The inset images show numerical relativity models of the BH horizons as the BHs coalesce. *Bottom:* The Keplerian effective BH separation in units of Schwarzschild radii ($R_S = 2GM/c^2$) and the effective relative velocity given by the post-Newtonian parameter $v/c = (GM\pi f/c^3)^{1/3}$, where f is the GW frequency calculated with numerical relativity and M is the total mass. The figure is taken from [12].

The source of GW150914 lies at a luminosity distance of 410^{+160}_{-180} Mpc corresponding to a redshift $z = 0.09^{+0.03}_{-0.04}$ [12]. In the source frame, the initial BH masses are $36^{+5}_{-4}M_\odot$ and $29^{+4}_{-4}M_\odot$, and the final BH mass is $62^{+4}_{-4}M_\odot$, with $3.0^{+0.5}_{-0.5}M_\odot$ radiated in GWs [12]. Also, GW150914 demonstrated the existence of stellar-mass BHs more massive than $25M_\odot$, and established that BBHs could form in nature and merge within a Hubble time [12].

GW170814

The signal, GW170814, was observed with a three-detector network matched-filter signal-to-noise ratio of 18 and a false-alarm rate of $\lesssim$1 in 27 000 years [208]. The first three-detector signal was the first observed at the LIGO Livingston detector at 10:30:43 UTC, and at the LIGO Hanford and Virgo detectors with a delay of ~8 ms and ~14 ms, respectively [208] (see Fig. 1.30). A network of three detectors improved the sky localization of the source, reducing the area of the 90% credible region from 1160 deg^2 using only the two LIGO detectors to 60 deg^2 using all three detectors. Adding the data from the new detector into coherent analysis significantly improves the inference of parameters describing the binary's position relative to the Earth since those parameters are predominantly determined by the relative amplitudes and arrival times observed in the detector network [208]. With the expected five-detector network after 2025 (see details in (see Section 1.3.1)), sky localization will improve [209] even more.

The inferred masses of the initial BHs were $30.5^{+5.7}_{-3.0}M_\odot$ and $25.3^{+2.8}_{-4.2}M_\odot$ [208]. The source of GW170814 lies at a luminosity distance of 540^{+130}_{-210} Mpc corresponding to a redshift $z = 0.11^{+0.03}_{-0.04}$ [208]. The BH characteristics of GW170814 are similar to GW150914 and are found to be consistent with the astrophysical population and merger rate determined with previous detections [208].

In addition, three detectors with different orientation allowed, for the first time, to test the nature of GW polarizations, enabling a new class of phenomenological tests of gravity [208]. In general relativity, GWs are characterized by two tensors (spin-2) [224, 225] polarizations only, whereas generic metric theories may allow up to six polarizations [208]. Two tensor degrees of freedom predicted by general relativity are only a subset of the six independent modes allowed by generic metric theories of gravity, which may in principle predict [208] any combination of the tensor (spin-2), vector (spin-1), or scalar (spin-0) polarizations [224, 225]. As the two LIGO instruments have similar orientations, little information about polarizations can be obtained using the LIGO detectors alone, while the addition of Advanced Virgo, the GW polarizations could be probed geometrically by projecting the wave's amplitude onto the three detectors [208]. As an illustration, it has been performed [208] a test comparing the tensor-only mode with scalar-only and vector-only modes. And it has been found that purely tensor polarization is strongly favored over purely scalar or vector polarizations [208]. With that and additional tests, it has been concluded [208] that GW170814 is consistent with general relativity.

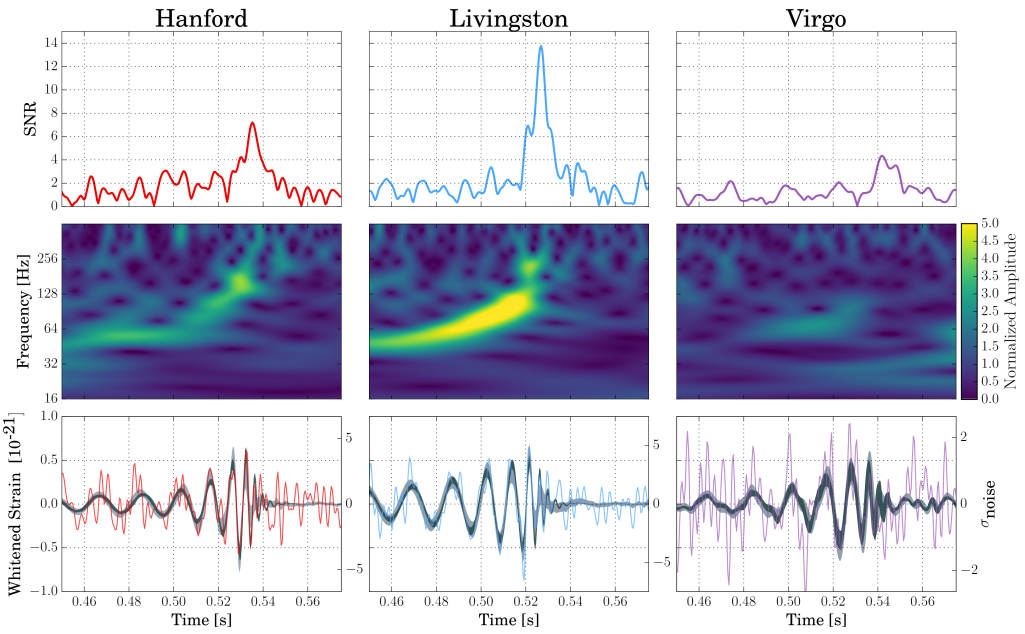

Fig. 1.30.: The GW event GW170814 observed by LIGO Hanford, LIGO Livingston, and Virgo. Times are shown from August 14, 2017, 10:30:43 UTC. *Top row:* Signal-to-noise ratio time series (here denoted as SNR) produced in low latency and used by the low-latency localization pipeline on August 14, 2017. The time series were produced by time shifting the best-match template from the online analysis and computing the integrated signal-to-noise ratio at each point in time. The single-detector signal-to-noise ratios in Hanford, Livingston, and Virgo are 7.3, 13.7, and 4.4, respectively. *Middle row:* Time-frequency representation of the strain data around the time of GW170814. *Bottom row:* Time-domain detector data (in color), and 90% confidence intervals for waveforms reconstructed from a morphology-independent wavelet analysis [220] (light gray) and BBH models (dark gray), whitened by each instrument's noise amplitude spectral density between 20 Hz and 1024 Hz. For this figure the data were also low passed with a 380 Hz cutoff to eliminate out-of-band noise. The whitening emphasizes different frequency bands for each detector, which is why the reconstructed waveform amplitude evolution looks different in each column. The left ordinate axes are normalized such that the physical strain of the waveform is accurate at 130 Hz. The right ordinate axes are in units of whitened strain, divided by the square root of the effective bandwidth (360 Hz), resulting in units of noise standard deviations. The figure is taken from [208].

GW170817

The signal, GW170817, was detected with a combined signal-to-noise ratio of 32.4 and a false-alarm-rate estimate of less than one per 8.0×10^4 years [13]. The source was localized within a sky region of 28 deg^2 (90% probability) and had a luminosity distance of 40^{+8}_{-14} Mpc, the closest and most precisely localized GW signal yet [13]. The component masses of the binary to be between 0.86 and 2.26 $M_\odot$, in agreement with masses of known NSs [13]. Restricting the component spins to the range inferred in BNSs, it has been found that the component masses to be in the range 1.17 to 1.60 $M_\odot$, with the total mass of the system $2.74^{+0.04}_{-0.01}M_\odot$ [13]. This discovery was made almost four decades since the discovery of the first BNS, PSR B1913+16 by Hulse and Taylor [191]. The association electromagnetic counterpart GRB 170817A [226, 227], detected by *Fermi*-GBM 1.7 s after the coalescence, corroborates the hypothesis of an NS merger and provides the first direct evidence of a link between the BNS merger and short GRBs (sGRBs) [13]. Subsequent identification of transient counterparts across the electromagnetic spectrum in the same location further supports the interpretation of this event as an NS merger [13]. [13].

Detailed analyses of the GW data, together with observations of electromagnetic emissions, are providing new insights into the astrophysics of compact BSs and GRBs, dense matter under extreme conditions, the nature of gravitation, and independent tests of cosmology [13]. Less than two years after the debut of GW astronomy, GW170817 marks the beginning of a new era of discovery [13]. The multimessenger astronomy's significant detections are summarized in (see Section 1.7) with the particular emphasis on γ-ray/neutrino connection on which this work is based. While a brief attention on recently detected GWs and their follow-ups are also given in (see Section 1.7.3) with a particular discussion of the multimessenger observations of a BNS merger [228] in the GW170817 event [13]. The prospects for GW astronomy with modern and future GW detectors and the outlined improvements in the sensitivity with the growth of the GW detectors networks (see Fig. 1.32) are discussed in the next section.

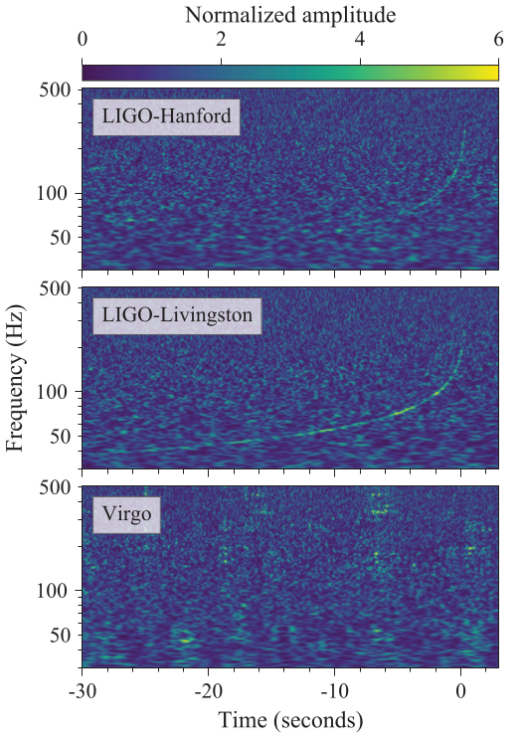

Fig. 1.31.: Time-frequency representations of data containing the GW event GW170817, observed by the LIGO-Hanford (*Top*), LIGO-Livingston (*Middle*), and Virgo (*Bottom*) detectors. Times are shown relative to August 17, 2017, 12:41:04 UTC. The amplitude scale in each detector is normalized to that detector's noise amplitude spectral density. In the LIGO data, independently observable noise sources and a glitch that occurred in the LIGO-Livingston detector have been subtracted. The figure is taken from [13].

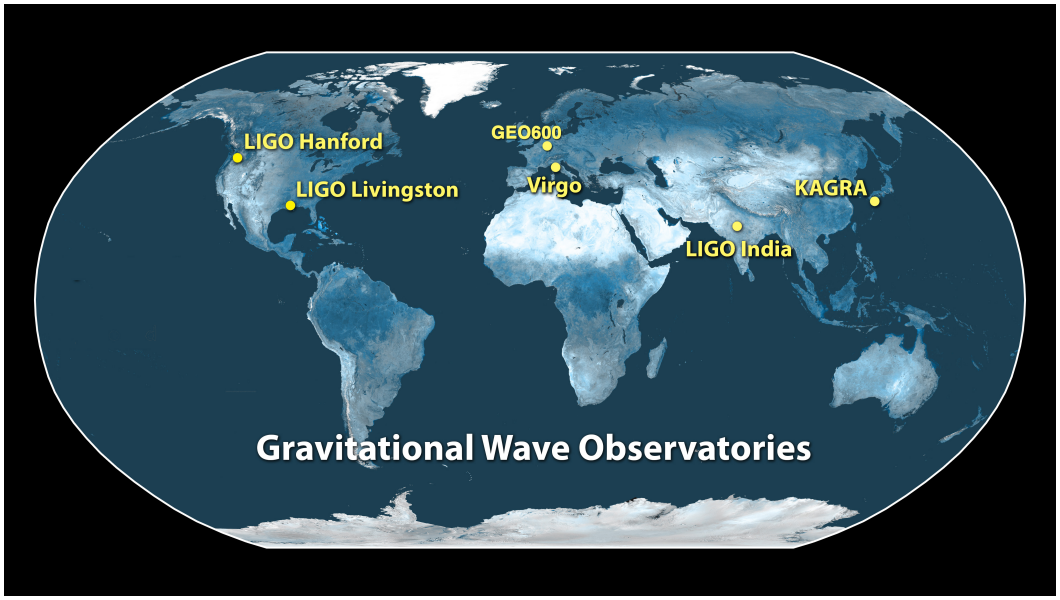

Fig. 1.32.: A map of the global ground-based GW detector network. The figure is taken from [229].

Prospects for GW Astronomy

The past few years have witnessed the birth of observational GW astronomy [229], starting with the first detection of a BBH merger September 14 2015 [12], followed by discoveries of nine more in the first and second LIGO/Virgo Observing runs [210], and the spectacular multimessenger observation of a merger of NSs on August 17, 2017 [227, 228]. These detections were enabled by a nearly three-decade-long effort to build Advanced LIGO [187, 230] comprising two lasers interferometric GW detectors with suspended mirrors, laser beams traveling in vacuum through 4 km perpendicular arms in each detector, to detect sub-nuclear distance scale changes in the distance [229]. In the next few years, the Advanced LIGO and Virgo detectors will continue to observe and analyze data together and are expected to reach the sensitivity to which they were designed [209, 229]. The LIGO works closely with the Virgo and KAGRA collaborations operating GW detectors to ensure coordinated observations by the global network [229] (see Fig. 1.32).

The timeline for construction, upgrades, and data-taking for modern and future GW detectors and the estimation of the sensitivity of the global network of GW detectors to transient GW signals for the third (O3), fourth (O4) and fifth observing (O5) runs, including the planned upgrades of the Advanced LIGO (aLIGO) and Advanced Virgo (AdV) detectors [209], are shown in Fig. 1.33. The plausible observing scenarios for the upcoming observing runs includes KAGRA and the upgrades of the aLIGO and AdV detectors, called A+ and AdV+, respectively [209] (see Fig. 1.33). After the first two observing runs, the LIGO and Virgo detectors have been upgraded and the O3 run started on April 1, 2019 [209]. A one-month commissioning break for the LIGO and Virgo instruments is scheduled in 2019, thus to preserve the 12 month O3 observing period, the end date for O3 is planned to be April 30, 2020 [209]. Possible extensions of the run will be limited so that O3 will end

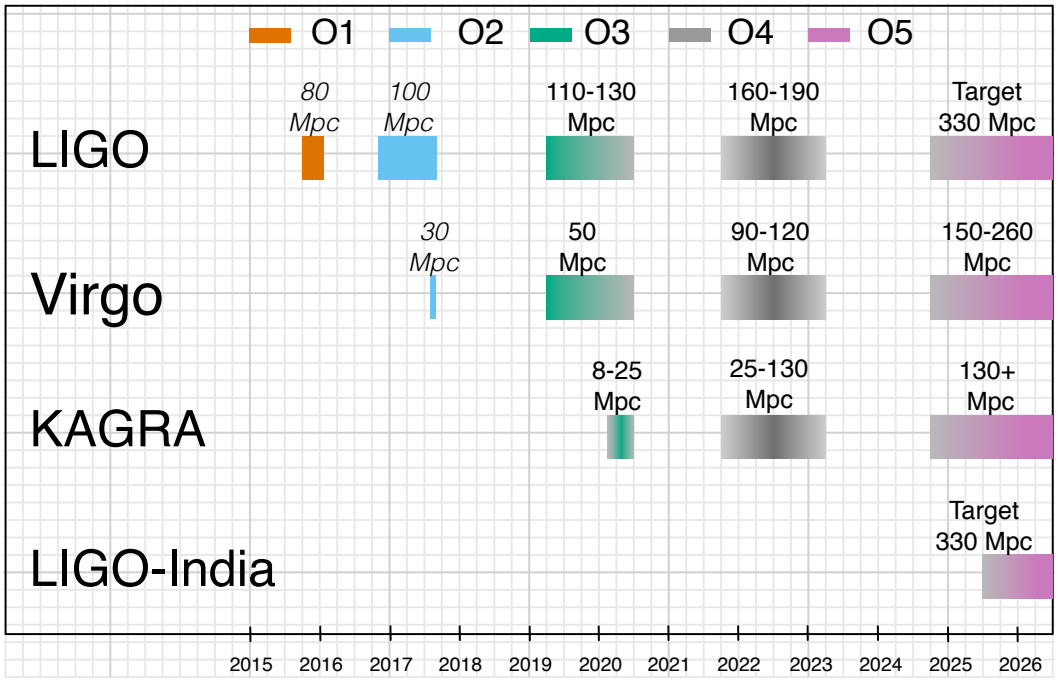

Fig. 1.33.: Planned sensitivity evolution and observing runs of the aLIGO, AdV and KAGRA detectors over the coming years. The colored bars show the observing runs, with achieved sensitivities in O1, O2 and O3, and the expected sensitivities for future O4 and O5 runs. There is significant uncertainty in the start and end times of the planned observing runs, especially for those further in the future, and these could move forward or backwards relative to what is shown above. Uncertainty in start or finish dates is represented by shading. A range of potential sensitivities for aLIGO during O4, depending on which upgrades and improvements are made after O3, is indicated. The figure is taken from [229].

no later than June 30, 2020 [209]. The O4 run includes a four-detector network with the two aLIGO instruments at 160-190 Mpc; Phase 1 of AdV+ at 90-120 Mpc and KAGRA at 25-130 Mpc [209]. The O5 run will begin with a four-detector network incorporating the A+ upgrade for the aLIGO instruments and the AdV+ Phase 2 upgrade for Virgo [209]. The target range for aLIGO is 330 Mpc and for AdV it is 150-260 Mpc, while KAGRA will operate at or above its O4 sensitivity of 130 Mpc [209]. After 2025, with the addition of an upgraded aLIGO interferometer in India [201] a five-detector network is expected: three aLIGO detectors with a design sensitivity of 330 Mpc, AdV at 150-260 Mpc and KAGRA at 130+ Mpc [209]. As the network grows, sky localization will improve [209]. While the median sky localization area is expected to be a few hundreds of square degrees for all types of binary systems in O3, it will improve to be a few tens of square degrees during O4 [209]. By 2025 a five-detector network is expected to operate at sensitivities approaching twice that of their predecessors, and a median sky localization area of a few degrees [209]. Detection of BBHs will become routine, while BNSs are expected to be detected with a rate from a few per year, to a few per month. Associated electromagnetic counterparts will probe properties of relativistic jets and sub-relativistic dynamical ejecta, the nucleosynthesis of heavy elements, and will enable precise cosmology [209]. Follow-up observations by km^3-sized neutrino detectors such as KM3NeT are also expected.

1.4 Neutrino

Neutrinos are fundamental fermionic particles of a Standard Model (SM) of particle physics. Neutrinos have a zero charge, thus unlike charged leptons, neutrinos only interact via weak or gravitational interactions. As a consequence of the presence of only left-handed neutrinos ν_L in SM, neutrinos are considered to be massless particles, but the existence of neutrino oscillation contradicts that. The SM contains three types (flavors) of neutrinos each one corresponding to a charged lepton: electron neutrino ν_e, muon neutrino ν_e, and tau neutrino ν_e.

In 1930 [231], Wolfgang Pauli hypothesized the existence of a new particle, electrically neutral and with a small mass, called the *neutron*, in order to prevent the law of energy conservation violation and explain the continuous spectrum of β decay instead of the expected monoenergetic one. Two years later, James Chadwick discovered a neutral particle [232], that we know now as the neutron. After that, Enrico Fermi incorporated the particle [233], which he called a neutrino (in Italian, means "the little neutral object'), into his theory of β decay. The discovery of a neutrino happened two decades later in the experiments of Clyde Cowan and Frederick Reines, at Hanford nuclear reactor in 1953 [234] and at Savannah River nuclear reactor [235] in 1956 where a more definitive conclusion has been made. The neutrino hypothesis suggested by Pauli and incorporated in a quantitative theory of β decay by Fermi has been verified [235]. The neutrinos were detected via inverse β reaction [234, 235]:

$$\bar{\nu}_e + p \rightarrow e^+ + n. \tag{1.21}$$

The neutrino was detected by using an intense beam of $\bar{\nu}_e$ from a powerful nuclear reactor. The detector was set up in the vicinity of the face of a reactor and was surrounded on all sides by a shield of lead (Pb) [234]. The intense neutrino flux from fission-fragment decay in a large reactor was incident on a detector containing many target protons in a hydrogenous liquid scintillator [235].

Neutrinos carrying an only weak charge thus propagating indefinitely without neither deflection neither absorption are unique messengers of the physical processes behind extreme astrophysical phenomena in the Universe (see Section 1.5). Thus, astronomy with neutrinos is a powerful instrument to disclose the mystery of such phenomena.

1.4.1 Solar Neutrinos: the neutrino deficit

At all times, people have been always intrigued by the fact that Sun shines. Since the middle of the 19-s century, scientists challenged by the questions what makes the Sun shine and on how does the Sun produce a vast amount of energy necessary to support life on Earth [236]?

The mechanism of nuclear fusion processes in stars as a source of a star's energy has been suggested far back in the 1920s by Sir Arthur Stanley Eddington [237]. The demonstration that the mass of the helium atom is less than the sum of the masses of the 4 hydrogens in the 1920s by Francis Aston [238] immediately prompted Sir Arthur Stanley Eddington that the difference in mass cannot be annihilated and that the energy liberated in the nuclear fusion of hydrogen into helium in stars is sufficed to explain how stars got their energy [237].

The answer to what makes the Sun shine is given by the thermonuclear fusion reactions similar to those envisioned for terrestrial fusion reactors and the basic solar process is the fusion of four protons ($4p$) to form an α particle (^{4}He), two positrons ($2e^+$), and two neutrinos (2ν) [239]:

$$4p \rightarrow {}^4\mathrm{He} + 2e^+ + 2\nu. \tag{1.22}$$

The combination of four protons and two electrons can occur essentially only in two ways and the first mechanism starts with the combination of two protons to form Deuteron (D or ^{2}H) with positron emission [240]:

$$p + p \rightarrow {}^2\mathrm{H} + e^+ + \nu_e. \tag{1.23}$$

The Deuteron is then transformed into ^{4}He by further capture of protons; these captures occur very rapidly compared with the process in Eq. 1.23 [240]. This fusion reaction has been proposed independently in 1937-1938 by Carl von Weizsäcker [241, 242] and in 1939 by Hans Bethe [243, 240] to explain what supplies the energy in the stars, and known as *proton-proton* or *pp*-chain. The second mechanism uses Carbon (C) and Nitrogen (N) as catalysts to convert hydrogen into helium, and known as Bethe-Weizsäcker cycle, or Carbon-Nitrogen-Oxygen (CNO) cycle [243, 240]. Due to the fact that the mean free path for photons emitted in the center of a star is negligible compared to the radius of the star, only neutrinos, with their extremely small interaction cross-sections, could enable to see into the interior of a star and thus verify directly the hypothesis of nuclear energy generation in stars [244]. A theoretical calculation of solar neutrino fluxes from the Sun carried out by John Bahcall in 1964 [245]. In the same year, Raymond Davis Jr. put forward the proposal of the experiment for solar neutrino detection [246] (see discussion in Section 1.4.2). The solar neutrino fluxes are predicted by the calculations based on the Standard Solar Model (SSM), which describes the internal solar structure and follows its evolution from zero age to the present [39]. The neutrino fluxes predicted by SSM are shown in Fig. 1.34. The solar energy is produced through sequences of nuclear reactions that convert hydrogen into helium, starting from the fusion of two protons (*pp*-chain) [247]. The Sun and lower-mass stars are predominantly powered by the *pp*-chain [247], which constitutes about 99% of the energy production in the Sun, the rest ~1% is due the CNO cycle. As seen, neutrinos can be produced in different reactions in the Sun such as *pp*-chain and CNO cycle. In addition to the standard fluxes, the so-called ecCNO neutrinos are produced by electron capture reactions on ^{13}N, ^{15}O, and ^{17}F [248, 249].

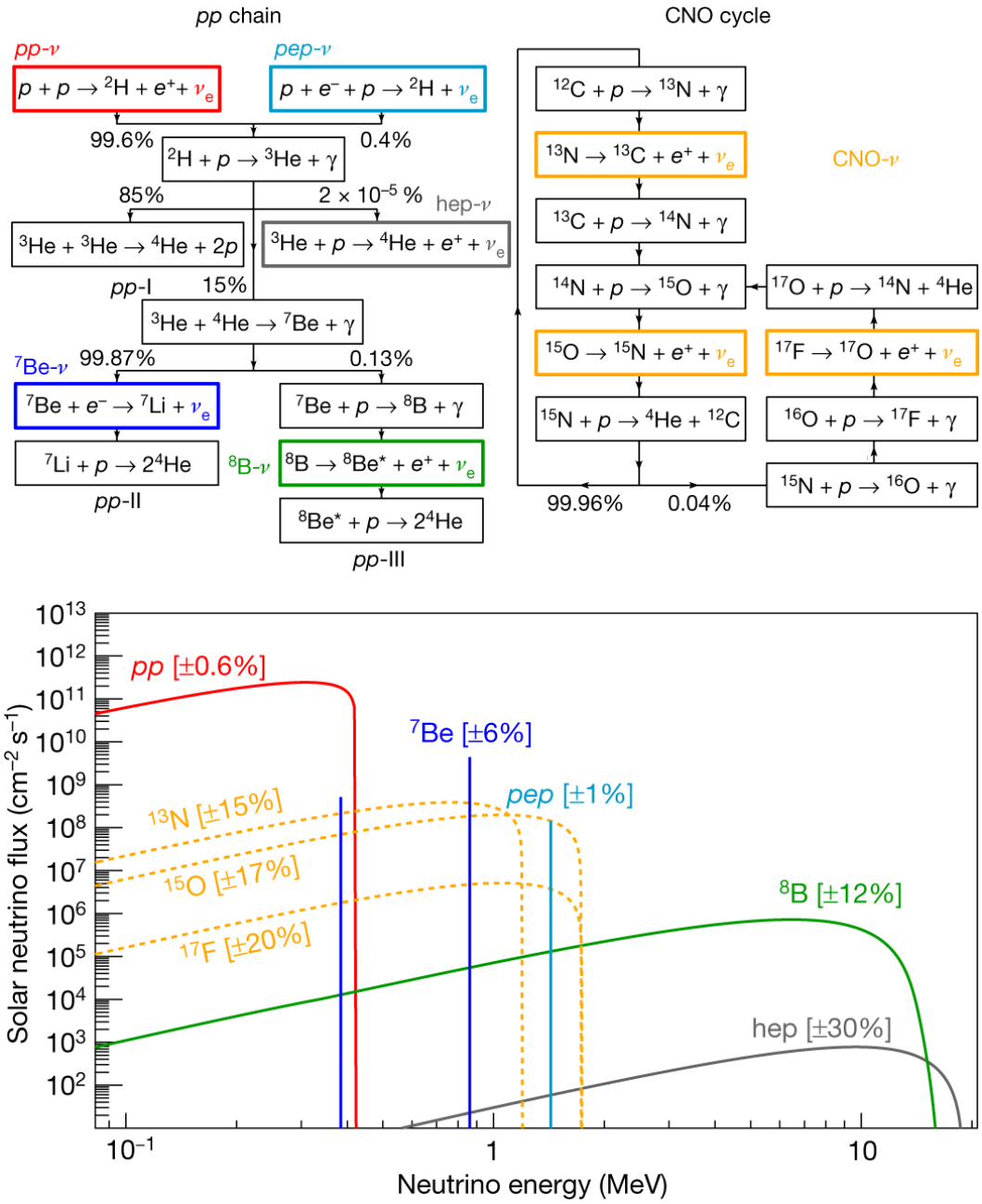

Fig. 1.34.: *Top:* Schematic view of the *pp* and CNO nuclear fusion sequences. *Bottom:* The solar neutrino energy spectrum. The neutrino fluxes are given in units of $\mathrm{MeV}^{-1}\,\mathrm{cm}^{-2}\,\mathrm{s}^{-1}$ for continuous spectra and $\mathrm{cm}^{-2}\,\mathrm{s}^{-1}$ for line spectra from monoenergetic sources. The numbers associated with the neutrino sources show theoretical errors of the fluxes. The figure is taken from [247].

Solar neutrino experiments observed fluxes smaller than the expectations from the SSM and this deficit is known as the "Solar Neutrino Problem". The first confirmation of the existense of thermonuclear reactions in the Sun came from the pioneering solar neutrino experiment in Homestake[39] [246]. The measurements of neutrino flux [250, 251] carried out by Kamiokande II (currently, Super-Kamiokande)[40] [252] and SNO[41] [253] experiments, in Japan and Canada respectively, have also demonstrated that the solar neutrino problem is due to neutrino oscillations. The neutrino oscillation is discussed in Section 1.4.2.

1.4.2 Neutrino oscillations

Oscillations of neutrinos are a consequence of the presence of flavor neutrino mixing, or lepton mixing, in vacuum [39]. The first ideas of neutrino oscillations was put forward by Bruno Pontecorvo [254] impressed by the idea of $K^0 \rightleftharpoons \overline{K^0}$ oscillations proposed by Gell-Mann and Pais in 1955 [255] and interesting consequences which follow from the fact that K^0 and $\overline{K^0}$ are not identical particles, such as the necessity of superposition and mixing. At that time only one neutrino type was known and possible oscillations, in this case, are $\nu_L \rightleftharpoons \bar{\nu}_L$ and $\bar{\nu}_R \rightleftharpoons \nu_R$, where ν_L and ν_R are left- and right-handed neutrinos respectively [256]. But for one neutrino type the states $\bar{\nu}_L$ and ν_R do not exist[42], while a left-handed neutrino ν_L and right-handed antineutrino $\bar{\nu}_R$ exist according to the two-component neutrino theory [257, 258, 259]. After the discovery of the second neutrino ν_μ in the Brookhaven[43] experiment in 1962 [260], Pontecorvo generalized his idea for the case of the two-component neutrino in 1967 [261]. Earlier in 1962, Maki, Nakagawa, and Sakata (MNS) [262] proposed the idea with two neutrino mixing considering the existence of two kinds of neutrinos, ν_e and ν_μ, but did not consider neutrino oscillations [263].

The modern three-neutrino mixing has the form [39]:

$$|\nu_l\rangle = \sum_j U_{lj}^{PMNS} \left|\nu_j\right\rangle, \tag{1.24}$$

where $l = e, \mu, \tau$. Here $\left|\nu_j\right\rangle$ is the state of neutrino with mass m_j (mass eigenstates) and the flavor neutrino ν_l is a coherent superposition of states of neutrinos with definite masses (see Eq. 1.24) [264].

The 3×3 unitary mixing matrix U in Eq. 1.24 is called Pontecorvo-Maki-Nakagawa-Sakata (PMNS) mixing matrix and named after the scientists who pioneered the courageous ideas of neutrino mixing and neutrino oscillations. The U_{lj}^{PMNS} term can be parameterized by mixing

[39] Homestake Chlorine Detector, https://www.bnl.gov/bnlweb/raydavis/research.htm
[40] Super-Kamioka Neutrino Detection Experiment Super-Kamiokande, http://www-sk.icrr.u-tokyo.ac.jp/sk/index-e.html
[41] Sudbury Neutrino Observatory (SNO), https://www.snolab.ca/
[42] In the two-component neutrino theory they are noninteracting "sterile" particles and neutrino is considered as a massless particle.
[43] Brookhaven National Laboratory (BNL), https://www.bnl.gov/

angles, θ_{ij}, the Dirac CP violation phase, δ_{CP}, and two Majorana CP violation phases, α_{21} and α_{31} [39]:

$$U^{PMNS} = \begin{pmatrix} 1 & 0 & 0 \\ 0 & c_{23} & s_{23} \\ 0 & -s_{23} & c_{23} \end{pmatrix} \begin{pmatrix} c_{13} & 0 & s_{13}\Delta^{-} \\ 0 & 1 & 0 \\ -s_{13}\Delta^{+} & 0 & c_{13} \end{pmatrix} \begin{pmatrix} c_{12} & s_{12} & 0 \\ -s_{12} & c_{12} & 0 \\ 0 & 0 & 1 \end{pmatrix} \begin{pmatrix} 1 & 0 & 0 \\ 0 & e^{i\frac{\alpha_{21}}{2}} & 0 \\ 0 & 0 & e^{i\frac{\alpha_{31}}{2}} \end{pmatrix} \tag{1.25}$$

where $c_{ij} = \cos\theta_{ij}$, $s_{ij} = \sin\theta_{ij}$, $\Delta^{\pm} = e^{\pm i\delta_{CP}}$ and $\theta_{ij} = [0, \pi/2)$, $\delta_{CP} = [0, 2\pi]$. In the case of massive Dirac neutrinos, the neutrino mixing matrix U is similar, in what concerns the number of mixing angles and CP violation phases, to the Cabibbo-Kobayashi-Maskawa (CKM) matrix [39], which describes the quark flavor mixing. The PMNS mixing matrix elements determine the flavor content of the mass eigenstates. Hence, from this matrix, the probability to find a given neutrino flavor in a given eigenstate in a matter can be obtained. Accordingly, the PMNS matrix elements determine the flavor composition of the mass eigenstates in a vacuum [265].

Neutrino oscillation data allow to determine only neutrino mass-squared differences $\Delta m^2_{ij} = m^2_i - m^2_j$ and the absolute values of the neutrino masses at present are unknown [264]. Which ν_j is the lightest/heaviest, or equivalently, what is the sign of neutrino mass-squared differences Δm^2_{ij} is unknown. Thus, the relative ordering of the three neutrino mass eigenstates ("mass ordering") is currently an open question. Two neutrino mass ordering is possible and are not distinguishable from the existing neutrino oscillation data [264]:

normal ordering (NO): $m_1 < m_2 < m_3$, Δm^2_{12} ("solar") $\ll \Delta m^2_{23}$ ("atmospheric")

inverted ordering (IO): $m_3 < m_1 < m_2$, Δm^2_{12} ("solar") $\ll |\Delta m^2_{13}|$ ("atmospheric")

In the same paper in 1967 [261], Pontecorvo first introduced the notion of "sterile" neutrino, when discussed all possible transitions between active neutrinos ν_μ and ν_e, $\nu_\mu \rightleftharpoons \nu_e$, and between ν and $\bar{\nu}$, $\nu \rightleftharpoons \bar{\nu}$, with the oscillations of the active neutrinos into particles that are, from the point of view of the ordinary weak interactions, sterile, i.e., cannot be detected [261]. So, the transitions $\nu_{eL} \rightleftharpoons \bar{\nu}_{eL}$ and $\nu_{\mu L} \rightleftharpoons \bar{\nu}_{\mu L}$, were considered. In addition, Pontecorvo pointed out that from an observational point of view the ideal object is the sun [261]. Finally, the effect of neutrino oscillations for solar neutrinos discussed by Pontecorvo in 1967 [261], has been observed by Raymond Davis Jr. in the first results of his pioneering solar neutrino experiment at Homestake [246].

The radiochemical method of detecting the neutrino used in Homestake was originally suggested by Pontecorvo in 1946 [266]. This Cl-Ar method was based on the possibility to observe the inverse β process induced by neutrino [266]:

$$\nu + (A, Z) \rightarrow e^{-} + (A, Z + 1). \tag{1.26}$$

From several reactions, the most promising one has been chosen [266]:

$$\nu + {}^{37}\mathrm{Cl} \rightarrow e^{-} + {}^{37}\mathrm{Ar}. \tag{1.27}$$

Pontecorvo's radiochemical method was used in two gallium-germanium radiochemical experiments, Soviet–American Gallium Experiment (SAGE) [267, 268] and GALLium EXperiment (GALLEX) [269, 270]. The SAGE experiment is being conducted in Gallium-Germanium Neutrino Telescope (GGNT) at the Baksan Neutrino Observatory (BNO)[44] of INR RAS[45], which is located in the Northern Caucasus Mountains, Russian Federation. The GALLEX detector, continued under a new name Gallium Neutrino Observatory (GNO), is located at the LNGS[46] laboratory in Gran Sasso, Italy.

In the gallium-germanium experiments, the following reaction was used:

$$\nu_e + {}^{71}\mathrm{Ga} \rightarrow e^{-} + {}^{71}\mathrm{Ge}. \tag{1.28}$$

In 2014 the SAGE experiment was upgraded to perform a very short-baseline neutrino oscillation experiment with an intense artificial neutrino source,^{51}Cr, with activity ~3 Megacurie (MCi) to search for transitions of active neutrinos to sterile states with $\Delta m^2 \sim 1$ eV^2 [271]. Recently, another neutrino source,^{65}Zn, has been proposed [272]. The project is called the Baksan Experiment on Sterile Transitions (BEST) [273] and based on the existing SAGE experiment with an upgraded GGNT at BNO INR RAS.

In contrast to radiochemical experiments, the SNO detector was designed to detect solar neutrinos through their interactions with a large tank of ultra-pure heavy water, D_2O (deuterium oxide), in a spherical volume of one kilotonne as a target [253]. The Super-Kamiokande is a water Čherenkov detector which consists of a welded stainless-steel tank, 39 m diameter and 42 m tall, with a total nominal water capacity of 50 000 tons [252]. Neutrino interactions are detected by an inward-facing array of ~11000 PMTs via the Čherenkov light emitted by the charged particles produced'[252]. The main neutrino source for the Homestake, Kamiokande II, and SNO experiments was ^{8}B neutrinos as the most energetic ones despite its low intensity (<0.01%) [247] (see Fig. 1.34) with respect to the total solar flux. The Super-Kamiokande observed almost pure ^{8}B solar neutrinos through ν_e Elastic Scattering (ES) and a clear deficit of ^{8}B solar neutrino flux have been reported [39]. In 2001, the initial SNO CC result combined with the Super-Kamiokande's high-statistics ν_e ES result [274] provided direct evidence for flavor conversion of solar neutrinos [275], this conclusion further strengthened by NC measurements [251] in SNO [39]. The results from radiochemical solar-neutrino experiments are summarized in Table 1.2. The Solar Neutrino Unit (SNU) is defined as 10^{-36} neutrino captures per atom per second.

[44] Baksan Neutrino Observatory (BNO), http://www.inr.troitsk.ru/eng/ebno.html
[45] Institute for Nuclear Research (INR) of the Russian Academy of Sciences (RAS), http://www.inr.troitsk.ru/english.html
[46] Laboratori Nazionali del Gran Sasso (LNGS), http://www.lngs.infn.it/

Tab. 1.2.: Results from radiochemical solar-neutrino experiments [39]. The predictions of the SSM [BPS08(GS)] [276] are also shown. The first and the second errors in the experimental results are the statistical and systematic errors, respectively.

	^{37}Cl→^{37}Ar (SNU)	^{71}Ga→^{71}Ge (SNU)
Homestake [277]	2.56±0.16±0.16	–
GALLEX [278]	–	$77.5\pm6.2^{+4.3}_{-4.7}$
GNO [279]	–	$62.9^{+5.5}_{-5.3}\pm2.5$
GNO+GALLEX [279]	–	69.3±4.1±3.6
SAGE [280]	–	$65.4^{+3.1+2.6}_{-3.0-2.8}$
SSM [BPS08(GS)] [276]	$8.46^{+0.87}_{-0.88}$	$127.9^{+8.1}_{-8.2}$

Figure 1.35 shows the SNO's salt phase results [281] of non-electron flavor active neutrinos ($\phi_{\mu\tau}$) versus the flux of electron neutrinos ϕ_e with the 68%, 95%, and 99% joint probability contours.

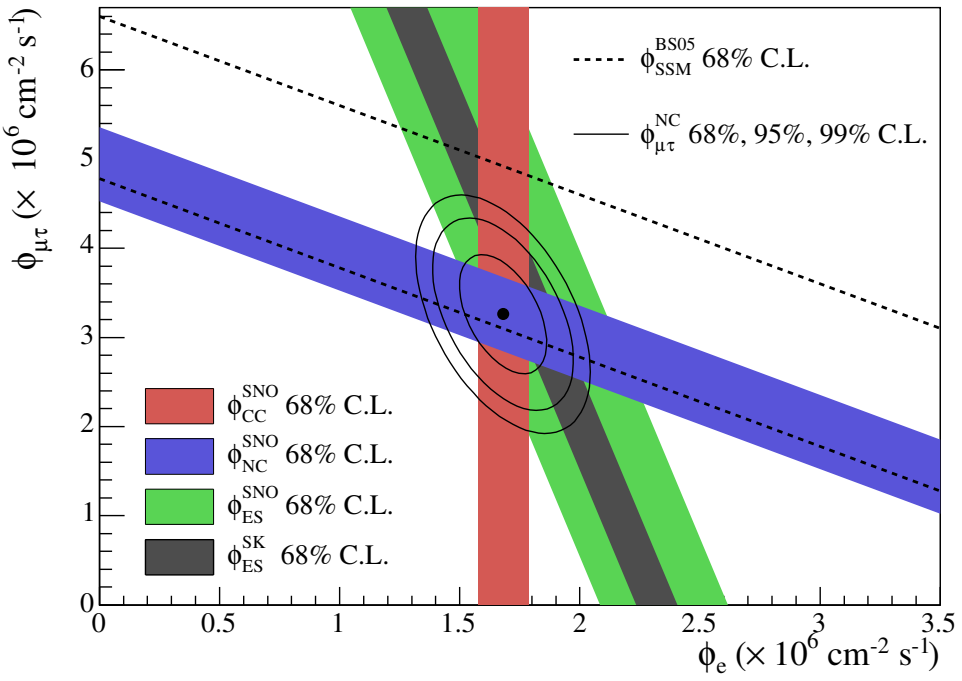

Fig. 1.35.: Fluxes of ^{8}B solar neutrinos, $\phi_{\mu\tau}$ versus ϕ_e, in the SNO's salt phase measurement [281]. CC, NC and ES flux measurements are indicated by the filled bands. The Super-Kamiokande result in [282] is represented by the narrow band parallel to the SNO ES result. The total ^{8}B solar neutrino flux predicted by the SSM [283] (BS05(OP) solar model) is shown as dashed lines, and that measured with the NC channel is shown as the solid band parallel to the model prediction. The intercepts of these bands with the axes represent the $\pm1\sigma$ uncertainties. The non-zero value of $\phi_{\mu\tau}$ provides strong evidence for neutrino flavor transformation. The point represents ϕ_e from the CC flux and $\phi_{\mu\tau}$ from the NC-CC difference with 68%, 95%, and 99% C.L. contours included. The figure is taken from [281].

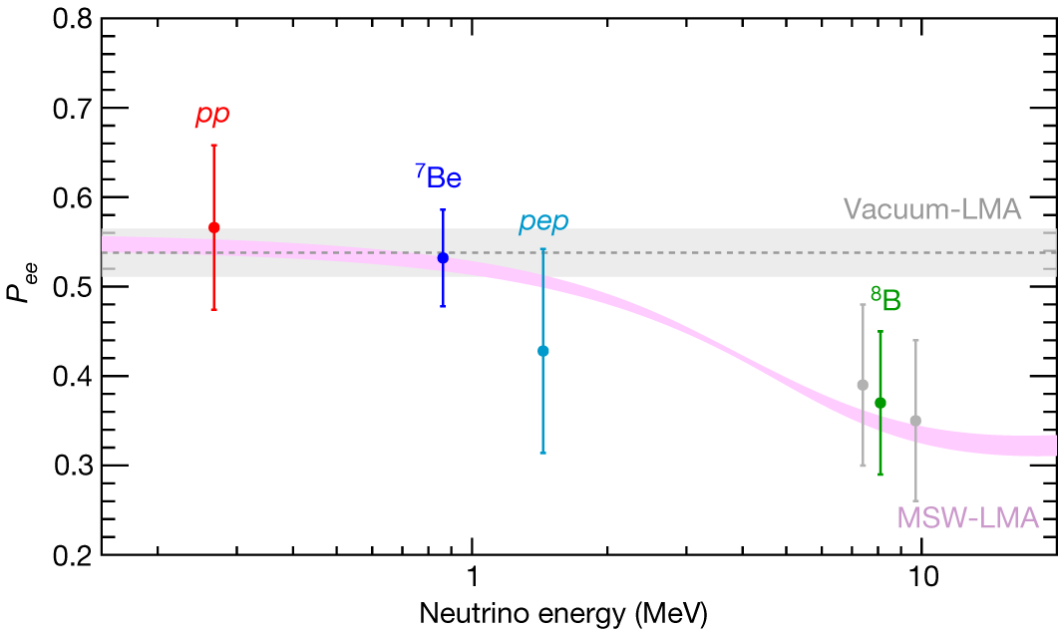

Fig. 1.36.: Electron neutrino survival probability as a function of neutrino energy. The pink band is the $\pm 1\sigma$ prediction of MSW-LMA with oscillation parameters determined from [284]. The grey band is the Vacuum-LMA case with oscillation parameters determined from refs 38,39. Data points represent the Borexino results for *pp* (red), ^{7}Be (blue), *pep* (cyan) and ^{8}B (green for the HER range, and grey for the separate HER-I and HER-II sub-ranges), assuming HZ-SSM. ^{8}B and *pp* data points are set at the mean energy of neutrinos that produce scattered electrons above the detection threshold. The error bars include experimental and theoretical uncertainties. The figure is taken from [247].

The long distance to the Sun makes the search for neutrino mass sensitive to much smaller mass splittings than can be studied with terrestrial sources [253]. During propagation, the vacuum oscillations can change the ratio of neutral-current (NC) to charged-current (CC) interactions, produce spectral distortions and introduce time dependence in the measured rates [253]. Thus, with the sufficiently large matter density in the Sun, the small mixing effects between neutrino flavors ν_e and ν_μ in the Sun's matter can be enhanced [253, 247] through the so-called Mikheyev-Smirnov-Wolfenstein (MSW) mechanism [285, 286]. For a long time, a short mixing angle (SMA) MSW effect was the favored ("non-adiabatic") solution of the solar neutrino problem and a large mixing angle MSW effect (LMA) was considered as a non-excluded possibility ("adiabatic" solution) [287, 288]. Things changed in 1998 when Super-Kamiokande [289] has testified against SMA (the flatness of spectrum and the absence of a peak in the zenith angle distribution of events in the Earth core bin) [287]. An MSW-LMA has been selected as the most favorable solution of the solar neutrino problem based on neutrino mass and mixing [290, 287, 291].

Borexino[47] (the Italian diminutive of BOREX (BORon solar neutrino EXperiment)) [292] experiment at the LNGS laboratory in Gran Sasso, Italy is the only one that can simultaneously test neutrino flavor conversion both in the vacuum and in the matter-dominated regime [247]. Prior to the establishment of the Borexino project, only ^{8}B neutrinos (<0.01%

[47] Borexino Collaboration, http://borex.lngs.infn.it/

of the total flux) have been measured individually by Super-Kamiokande [250] and the SNO [251] to prove that neutrinos undergo leptonic flavor conversion in the Sun's matter, enhanced through the MSW mechanism [247]. Running continuously since 2007, the Borexino experiment has observed the neutrinos from *pp*, *pep*, ^{7}Be, and ^{8}B separately [247]. At higher energy, where flavor conversion is dominated by matter effects in the Sun, the Borexino results [247] are in agreement with the high-precision measurements performed by Super-Kamiokande [293] and SNO [294]. A likelihood ratio test has been performed [247] to compare Borexino data with the MSW-LMA and the Vacuum-LMA predictions (pink and grey bands in Fig. 1.36, respectively). Borexino data disfavor the Vacuum-LMA hypothesis at 98.2% C.L [247]. Overall, the results are in excellent agreement with the expectations from the MSW-LMA paradigm [247] with the oscillation parameters indicated in [284].

With the exception of possible short-baseline anomalies (such as LSND), current accelerator, reactor, solar and atmospheric neutrino data can be described within the framework of a 3x3 mixing matrix between the flavor eigenstates ν_e, ν_μ and ν_τ and mass eigenstates ν_1, ν_2 and ν_3 [39]. As a result, almost all neutrino oscillation experiments can be consistently described using three active neutrino flavors, i.e. two mass splittings and three mixing angles [39]. Thus, the transitions between flavors, i.e., neutrino oscillations, are well described with masses m_1, m_2, and m_3 [273] whose mass-squared differences Δm^2_{12} and Δm^2_{23} are of the order of $\sim 10^{-5}$ eV^2 and $\sim 10^{-3}$ eV^2 respectively. The existence of three neutrino generations has been proven (see Fig. 1.37) by four experiments at LEP[48] at CERN[49] on the decay of the Z^0 boson and shown 2.984±0.008 of light neutrinos [295]. The LSND's data was interpreted to show oscillations between muon and electron antineutrinos at $\Delta m^2 \sim 1$ eV^2 [271], but such a large value cannot be obtained with three neutrino generations since the maximal value

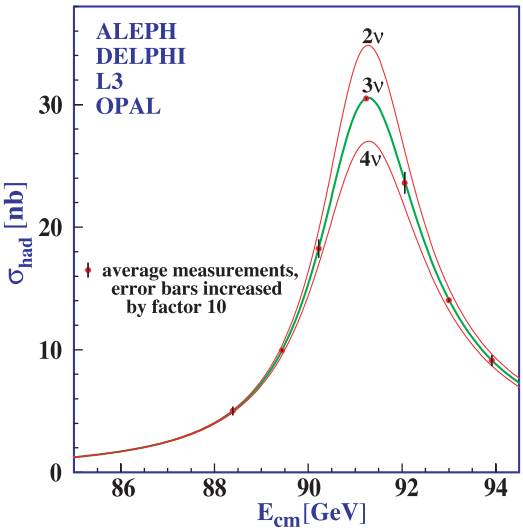

Fig. 1.37.: Combined data [295] from the ALEPH, DELPHI, L3, and OPAL collaborations for the cross-section in e^+e^- annihilation into hadronic final states as a function of the center-of-mass energy around the Z resonance. The curves indicate the predictions of the Standard Model with two, three, and four species of light neutrinos. The asymmetry of the curve is produced by initial-state radiation. Note that the error bars have been increased by a factor ten for display purposes. See [39] for references to the different experiments involved and the contributions provided. The figure is taken from [295, 39].

[48] Large Electron-Positron Collider (LEP), http://aleph.web.cern.ch/aleph/aleph/Public.html, http://delphi-www.web.cern.ch/delphi-www/, , http://l3.web.cern.ch/l3/, http://opal.web.cern.ch/Opal/

[49] Conseil Européen pour la Recherche Nucléaire (CERN), https://home.cern/

is $\Delta m^2 \approx \Delta m^2_{23}$ which is of the order of $\sim 10^{-3}$ eV^2 [273]. To comply with the results of LEP experiments (see Fig. 1.37) one must assume to add to the theory at least one light "sterile" neutrino, which interaction cross-section with matter is much less than the other three neutrino species [273, 271]. The currently available data on neutrino oscillations are

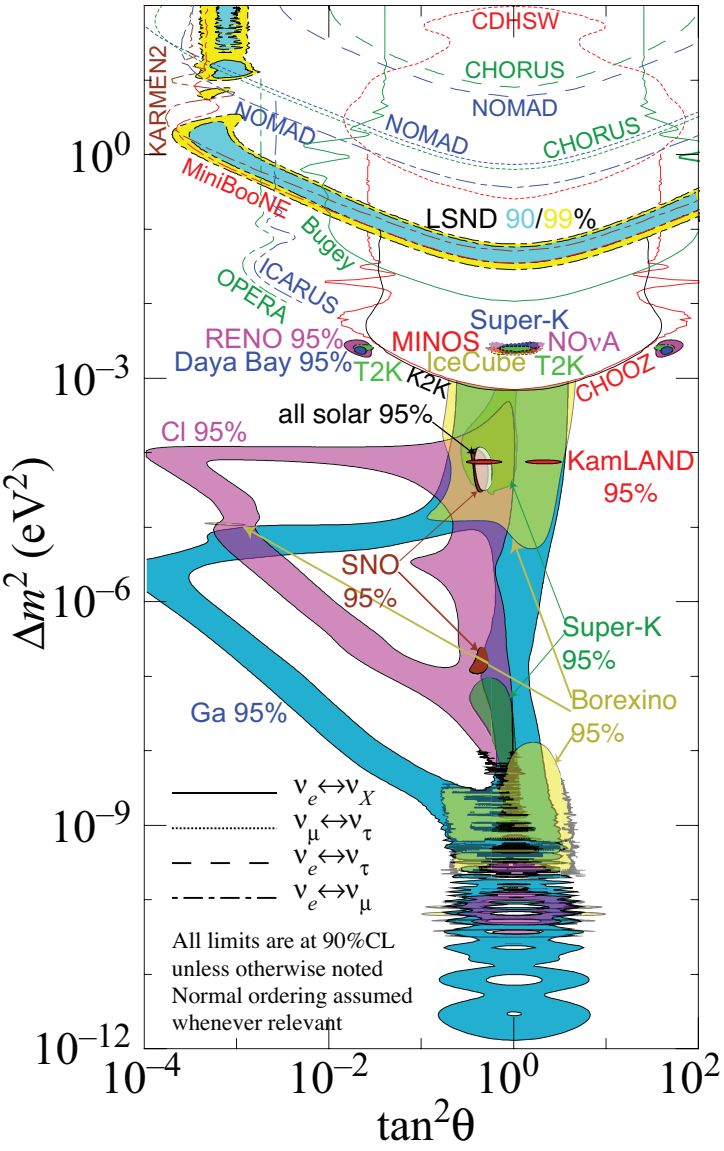

Fig. 1.38.: The squared-mass splittings Δm^2_{ij} and mixing angles θ_{ij} favored (solid regions) or excluded (open regions) by existing neutrino oscillation measurements. Results are categorized by channels: ν_e disappearance (solid lines), $\nu_\mu \rightleftharpoons \nu_\tau$ (dotted lines), $\nu_e \rightleftharpoons \nu_\tau$ (dashed lines), and $\nu_e \rightleftharpoons \nu_\mu$ (dashed-dotted lines). The normal mass ordering is assumed where relevant. The figure is taken from [39].

summarised in Fig. 1.38. In the coming years, a wealth of new data is expected which will shed light on the fundamental aspects of neutrino mixing: the nature of massive neutrinos, Dirac or Majorana, the type of spectrum the neutrino masses obey, the status of CP symmetry in the lepton sector, the absolute neutrino mass scale, the origin of the observed patterns of the neutrino masses and mixing, and, eventually, on the mechanism of neutrino mass generation [39].

1.4.3 Extra-Solar Neutrinos: SN 1987A

Extra-solar neutrino astronomy was born on February 23, 1987, when light and neutrinos arrived at Earth from the brightest SN in 383 years since the naked eye observation of SN 1604[50] [296]. The neutrino signal came from a core-collapse SN (SN 1987A) in the Large Magellanic Cloud (LMC), 50 kpc[51] away from Earth. In a very short time interval, approximately 3×10^{53} ergs of gravitational binding energy have been released in a burst consisting of about 10^{58} neutrinos [298, 299]. The fortunate detection of neutrinos and coincident photons became a start point for multimessenger astronomy.

The SN 1987A now is one of the most thoroughly studied object outside the Solar System [296]. Figure 1.39 (*Top*) shows the picture of the SN 1987A based on observations done with NASA's Hubble Space Telescope (HST)[52] [300, 301, 302]. The most prominent feature in the image is a ring with dozens of bright spots. A shock wave of material unleashed by the stellar blast is slamming into regions along the ring's inner regions, heating them up, and causing them to glow. The ring, about a light-year across, was probably shed by the star about 20 000 years before it exploded. Figure 1.39 (*Bottom*) shows the artist's impression with the different elements present in SN 1987A: two outer rings, one inner ring and the deformed, innermost expelled material.

Fig. 1.39.: *Top:* The entire region around SN 1987A. Image credit: NASA, ESA, K. France (University of Colordo, Boulder, USA), and P. Challis and R. Kirshner (Harvard-Smithsonian Center for Astrophysics, USA). *Bottom:* The artist's impression of the material around a recently exploded star, SN 1987A. Image credit: ESO/L. Calçada

The first hint, a burst of pulses, have been detected on February 23.12 (2 h 52 m 36 s UT[53]) [303] by the Liquid Scintillation Detector (LSD) of the Mount Blanc Underground Neutrino Observatory (UNO) [304]. About a week later, Kamiokande II [252] Collaboration reported similar evidence, a neutrino burst at 7h 35m 35s UT (±1 min) [299] during a time interval of 13 s. Another water Čerenkov detector, Irvine-Michigan-Brookhaven (IMB) [305], detected a neutrino signal at 7h 35m 41s UT [298]. In addition,

[50] This SN is known as Kepler's Supernova and occurred in the Milky Way Galaxy in 1604.
[51] The distance to SN 1987A is debated within the range of 50±5 kpc [297].
[52] Hubble Space Telescope (HST), https://hubblesite.org/
[53] Universal Time.

an event was found by Baksan Underground Scintillation Telescope (BUST) at BNO INR RAS at the time indicated by the Kamiokande II (7h 36 h 11±2 s UT) [306].

The data of Kamiokande II are not in contradiction with the burst detected at the Mont Blanc UNO almost five hours earlier, since the neutrinos detected in Kamiokande II may have been emitted in a delayed pulse from the NS already existing [307]. This interpretation seems to be a natural explanation of the two neutrino pulses, due to the formation of an NS and subsequently (2-9 hours later) to its collapse into a BH [307]. The two transitions could have originated the two pulses with the observed delay of 4.72 hours, which, because of the different energy spectra, have given different information in detectors of a different type [307].

Since the discovery of SN 1987A, a variety of experiments detected a lot of new SNe. The SNRs are included in the search of ANTARES and KM3NeT as the most promising acceleration sites of the CRs in our Galaxy, thus neutrinos are also expected. SNRs can be efficient high-energy hadron accelerators (~GeV-TeV neutrinos) [308]. As the neutrino telescopes in the Northern Hemisphere, ANTARES and KM3NeT explore the Southern Sky with unprecedented sensitivity to the central region of our Galaxy and have excellent visibility to most of the SNRs in our Galaxy [308]. Several analyses have been performed on the search for neutrinos from SNRs. It has been shown [309, 310, 311] that at least the most intense galactic ones such as the young shell-type SNR RXJ1713.7-3946 are within reach for KM3NeT. The SNR RXJ1713.7-3946 is visible for about 90% of the time by KM3NeT [312]. Some ANTARES results and KM3NeT perspectives for SNRs detection are summarized in [308].

In the recent combined search for neutrino sources in the Southern Sky using data from the ANTARES and IceCube detectors [313], no significant evidence of cosmic neutrinos from the direction of the SNR RXJ1713.7-3946 has been found. In the recent KM3NeT search for Galactic point-like neutrino sources [312], the detection perspectives of the telescope have been investigated. It has been shown [312] that the SNR RXJ1713.7-3946 can be observed by KM3NeT with a significance of 3σ within 5.5 years of operation. However, if no signal is observed after about 5 years, the hadronic contribution to the γ-ray emission can be constrained to be less than 50% for this source [312]. See Section 1.5 for details about the CR-γ-ν connection. The description of the KM3NeT and ANTARES detectors and discussion of their scientific goals can be found in Section 2.4.4 and Section 3 respectively.

1.5 The CR-γ-ν Connection: Neutrino Astronomy

With the discovery of neutrinos from SN 1987A [298, 299] (see Section 1.4.3) with the coincident photons led to a clear understanding that exploration of the Universe with different messengers is powerful thus different detectors have been constructed and placed on space, under ground, sea, and ice in last decades. This discovery became a start point for what is now called multimessenger, which is discussed in Section 1.7. It is known that neutrinos are tracers of CR acceleration and it became clear that there was a lot to learn from examining any type of particles and radiation coming from astrophysical objects, and that neutrino detector could give early alerts as in 2017 [14] Section 1.7.1 that would facilitate the observation of the evolution of such transients from the earliest stages [314]. The different wavelengths of γ-ray astronomy, neutrinos, CRs, and GWs provide complementary insight for the most energetic phenomena of the Universe.

The presence of a diffuse EBL, which is due to star light and reprocessed star light, prevents high-energy photons to propagate over cosmological distances [170] (see Fig. 1.40). Photons are highly attenuated by interaction with the CMB and IR background radiation limiting the horizon for TeV γ-rays to tens of megaparsecs [171] as seen in Fig. 1.40. Protons can penetrate larger distances but the observation of the Universe with high-energy protons is restricted by the existence of the GZK effect described in Section 1.1.2. Apart from it, protons at lower energies are undergoing magnetic deflection (is small for high energies) are not able to point back to their sources. Unlike these messengers, none of these problems arise for neutrinos which carry an only weak charge and thus can propagate indefinitely without neither deflection neither absorption and still point back to their source [171]. The shaded blue region in Fig. 1.40 represents the region opaque to photons but transparent to neutrinos.

Unlike these messengers, none of these problems arise for neutrinos which carry an only weak charge and thus can propagate indefinitely without neither deflection neither absorption and still point back to their source [171]. The shaded blue region in Fig. 1.40 represents the region opaque to photons but transparent to neutrinos.

Neutrinos should follow the energy spectrum of their parent CRs, $\propto E^{-\Gamma}$ with $\Gamma{\sim}2$ [316] according to the diffusive shock acceleration mechanism [91, 92, 93, 94, 95, 96, 97] (see Section 1.1.3). Under the assumption that neutrinos are produced in charged meson decays (see Section 1.5.1), the intrinsic flux at source assumed to have the $\Phi_{\nu_e}{:}\Phi_{\nu_\mu}{:}\Phi_{\nu_\tau} = (1{:}2{:}0)$ flavor composition, but after propagation over cosmic distances the flavor composition changes due to the oscillation to $\Phi_{\nu_e}{:}\Phi_{\nu_\mu}{:}\Phi_{\nu_\tau} = (1{:}1{:}1)$ at Earth (see Section 1.5.2).

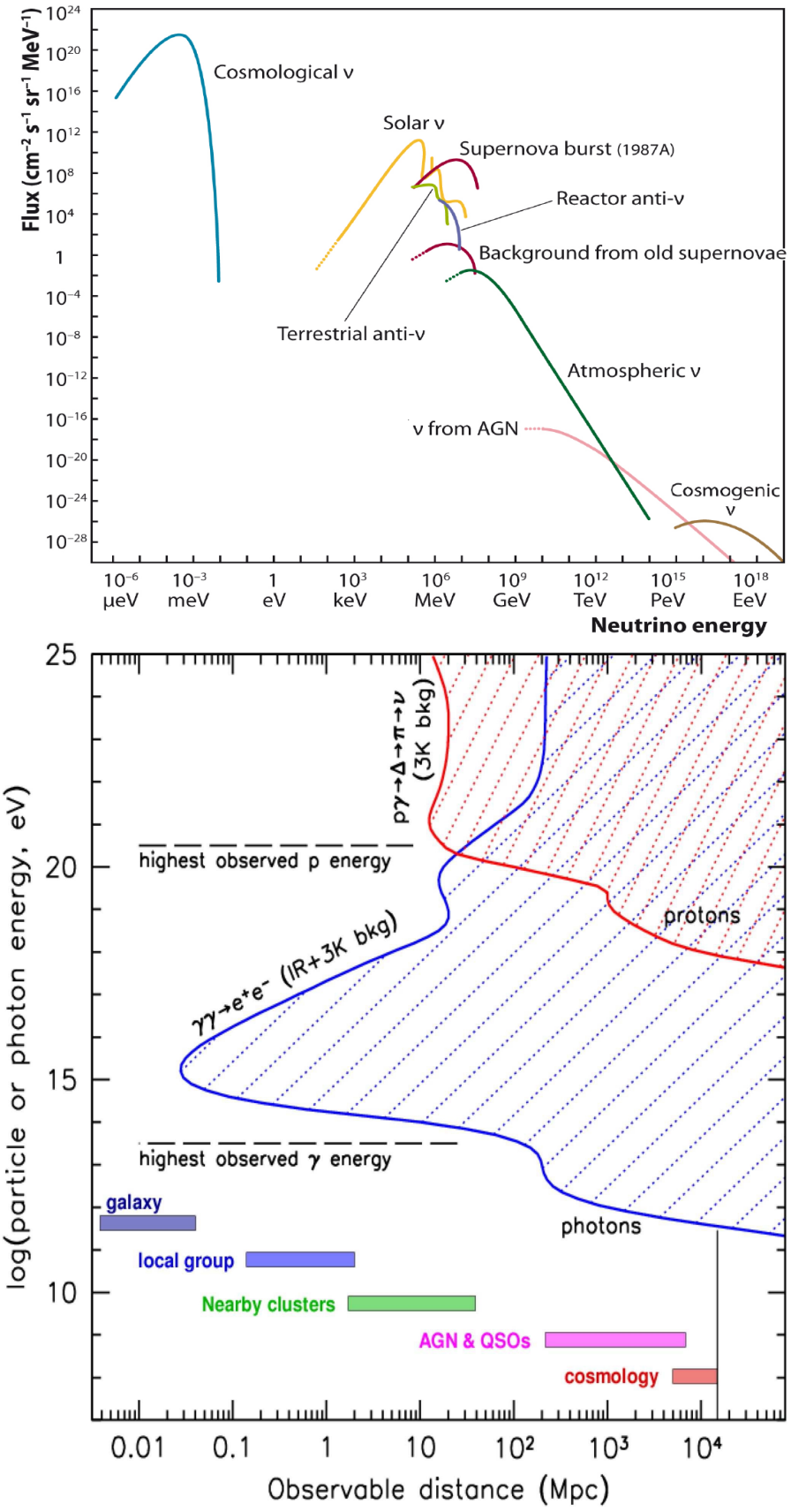

Fig. 1.40.: *Top:* Measured and expected fluxes of natural and reactor neutrinos versus energy. The figure is taken from [315]. *Bottom:* Observable energy versus distance for different astrophysical messengers such as protons (red) and γ-rays (blue). The shaded regions correspond to those invisible with the use of photons or protons. The figure is taken from [170].

1.5.1 Neutrino production mechanisms

For half a century it has been recognized [317, 318] that protons from cosmic accelerators would also generate neutrinos, via charged pion production in collisions with the ambient matter or radiation fields, in reactions such as [315]:

$$p + \text{nucleus} \rightarrow X + \pi \quad (\pi = \pi^{\pm}, \pi^{0}) \tag{1.29}$$

$$p + \gamma \rightarrow \Delta^{+} \rightarrow \begin{cases} p + \pi^{0} \\ n + \pi^{+} \end{cases} \tag{1.30}$$

with the subsequent decays [315]:

$$\begin{aligned} \pi^{0} &\rightarrow \gamma\gamma \\ \pi^{+} &\rightarrow \mu^{+} + \nu_{\mu} \\ &\hookrightarrow e^{+} + \nu_{e} + \bar{\nu}_{\mu} \\ \pi^{-} &\rightarrow \mu^{-} + \bar{\nu}_{\mu} \\ &\hookrightarrow e^{-} + \bar{\nu}_{e} + \nu_{\mu}. \end{aligned} \tag{1.31}$$

The resulting neutrino flavor ratio (see discussion in Section 1.5.2) is approximately ν_e:ν_μ:ν_τ = (1:2:0) at the sources [319, 320, 315]; neutrino oscillation turns this into a ratio of ν_e:ν_μ:ν_τ = (1:1:1) upon arrival at Earth [315] (see Section 1.4.2). Despite the fact that the production of pions dominate in photomeson interactions ($p + \gamma$), some other channels, in particular, the ones leading to the production of K- and η-mesons, contribute noticeably (up to 10 to 20 %) to the overall production of photons and leptons [321].

The energy escaping from the source is shared among high-energy protons (=CRs), γ-rays, and neutrinos produced by the decay of neutrons[54], π^0 and $\pi^{\pm}$ respectively [322]. To be observed, this energy partition between CRs, γ-rays and neutrinos requires the source to be transparent enough, i.e., to have a size much larger than that of the proton mean free path, but smaller than the meson interaction length in order to allow protons to interact and most secondary mesons to decay [322]. Thus, the mechanisms that produce CRs also produce neutrinos and high-energy photons as shown in Eq. 1.31, and the candidate neutrino sources are in general also γ-ray sources [322]. Such processes involving nucleons and mesons are often referred to as the "hadronic" model. In this model "hadronic" model, there is a strong relationship between the spectral index of the CR energy spectrum (α_{CR}) and that of γ-rays and neutrinos [117, 322]. The spectral index of secondary mesons (when their interaction processes can be neglected) is identical to that of the parent primary CRs [322]. The same

[54] While protons may remain trapped due to high magnetic fields, neutrons are not confined by magnetic fields; thus, neutrons can escape the acceleration region and turn into proton through the weak interaction decay $n- \rightarrow pe^{-}\bar{\nu}_e$ [322].

holds (in a transparent source, where interaction probability of secondary mesons is low) for the pion daughters, γ-rays and neutrinos, and thus [322]:

$$\alpha_{CR} \sim \alpha_{\gamma} \sim \alpha_{\nu}. \tag{1.32}$$

Hence, γ-ray measurements give crucial information on primary CRs, and make possible to constrain the expected neutrino flux from sources where γ-rays are detected [322].

Another model that can explain the production of γ-rays is the "leptonic" model, where the acceleration processes are induced by leptons, i.e., electrons and positrons. High-energy electrons and positrons interact with radiation fields [137]. In magnetic fields, they produce synchrotron photons whose energies can at most reach the domain of low-energy γ-rays [137]. But also they can interact with ambient low-energy photons from stellar or synchrotron origin and boost them to very high energies, i.e, by Inverse Compton (IC) effect [137, 315]:

$$e^- + \gamma_{\text{low energy}} \rightarrow e^- + \gamma_{\text{high energy}} \tag{1.33}$$

In fact, most of the measured spectra from TeV γ-ray sources are compatible with models based on IC scattering, and in many cases with the so-called Synchrotron-Self Compton (SSC) model where the photon gas is provided by synchrotron radiation from accelerated electrons [315] as illustrated in Fig. 1.41. Unnecessary to emphasize that pure SSC models are based on electron, not hadron acceleration and do not directly explain the origin of CRs [315]. Pure electron acceleration models are leptonic models [315]. In most realistic cases, both electrons and hadrons will be accelerated [315], and such a combined model is illustrated in Fig. 1.41. The synchrotron radiation from electrons serves as a target for IC scattering as well as for proton collisions [315]. Electrons are cooled by synchrotron emission and may boost synchrotron photons to the 10-100 TeV range but certainly not to PeV energies [315]. The observation of PeV γ-rays would, therefore, be a clear proof of hadron acceleration [315]. Unfortunately, the range of PeV photons does not exceed the size of our Galaxy, since they are absorbed by the process [315]: $\gamma_{PeV} + \gamma_{CMB} \rightarrow e^+e^-$ (see Fig. 1.40).

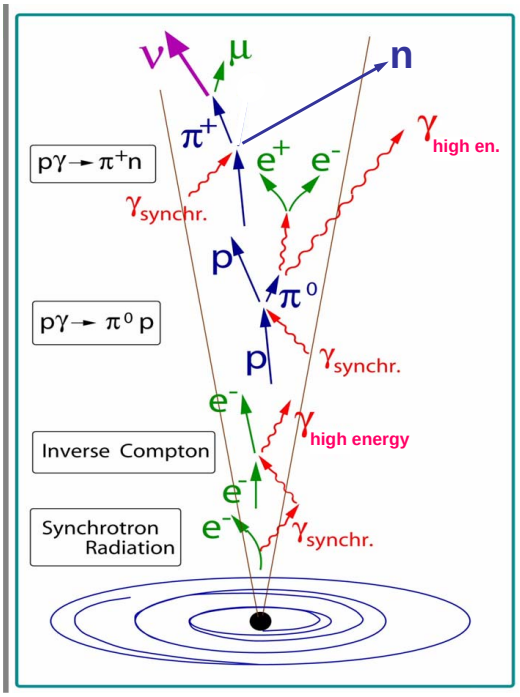

Fig. 1.41.: Generation of γ-rays and neutrinos in a jet emitted from an AGN, with both hadrons and electrons being accelerated along the jet. The figure is taken from [315].

Almost all observed objects emitting in the TeV γ-ray band are also sources of non-thermal X-rays, presumably of synchrotron origin, radiated by multi-TeV electrons [117]. Therefore, measurements of the synchrotron X-ray flux from a source with a similar signature in the TeV band is a signal that the accompanying γ-rays are likely produced by leptonic processes [117]. Since the same electrons can also radiate TeV γ-rays through IC scattering, this leptonic model represents a competitive process for TeV radiation; thus, only the coincident measurement of neutrinos from the source would give an uncontroversial proof of the discovery of the GCR acceleration sites [117]. Both models, leptonic and hadronic, could provide an adequate description of the present experimental situation [117]. If high-energy photons are produced in the hadronic models, high-energy neutrinos will be also produced [117]. Hadronic and leptonic components can in principle also be distinguished in the 50-200 MeV energy band, where they are expected to show different behaviors [323]. For the first time for an SNR, the γ-ray telescopes AGILE and *Fermi*-LAT have established the spectral continuum below 200 MeV for W44, which can be attributed to a π^0 emission [324, 325]; hence, confirming the hadronic origin of this γ-ray emission [323]. The leptonic-only model was disfavored to explain the γ-ray emission from W44, while the hadronic model with a non-smoothed broken power-law distribution was able to fit the observed γ-ray data [323]. The characteristic pion-decay feature in the γ-ray has been also detected for IC 443 [325], which is together with W44 one of the two highest-significance SNRs in the *Fermi*-LAT catalog [322].

The sources that can be responsible for the production of cosmic high-energy neutrinos (and joint γ-rays) are reviewed in Section 1.6.

1.5.2 Cosmic neutrino flavor

The decay of pions and their daughter muons (see Eq. 1.31) dominate the neutrino flux [326], resulting in a flavor ratio of $(\Phi_{\nu_e}{:}\Phi_{\nu_\mu}{:}\Phi_{\nu_\tau})_S = (1{:}2{:}0)_S$ at source [319, 320]. However, the composition could vary from $(0{:}1{:}0)_S$ to $(1{:}0{:}0)_S$ under scenarios such as muon energy loss in high matter density or magnetic fields [327, 328, 329, 330], muon acceleration [331], and neutron decay [332]. Propagating over astronomical distances, the flavor composition transforms according to the PMNS mixing matrix because of neutrino oscillation (see Section 1.4.2).

Taking global best-fit mixing parameters [333], a flavor ratio at Earth ($\oplus$) for the different flavor ratios at source (S) [326]:

$$\begin{aligned}
(1{:}2{:}0)_S &\xrightarrow{osc} (0.93{:}1.05{:}1.02)_\oplus \approx (1{:}1{:}1)_\oplus \\
(0{:}1{:}0)_S &\xrightarrow{osc} (0.6{:}1.3{:}1.1)_\oplus \\
(1{:}0{:}0)_S &\xrightarrow{osc} (1.6{:}0.6{:}0.8)_\oplus
\end{aligned} \tag{1.34}$$

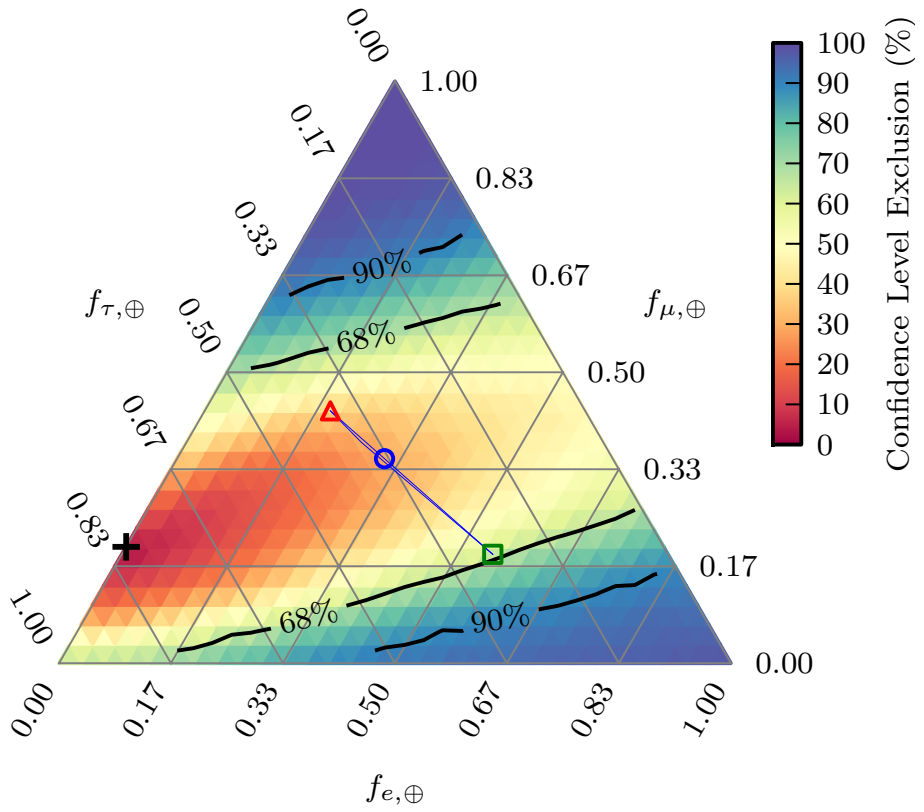

Fig. 1.42.: The exclusion regions for astrophysical flavor ratios (Φ_{ν_e}:Φ_{ν_μ}:Φ_{ν_τ}) at Earth. The labels for each flavor refer to the correspondingly tilted lines of the triangle. Averaged neutrino oscillations map the flavor ratio at sources to points within the extremely narrow blue triangle. The $\approx(1{:}1{:}1)_\oplus$ composition at Earth, resulting from a $(1{:}2{:}0)_S$ source composition, is marked with a blue circle. The compositions at Earth resulting from source compositions of $(0{:}1{:}0)_S$ and $(1{:}0{:}0)_S$ are marked with a red triangle and green square, respectively. Though the best-fit composition at Earth (black cross) is $\approx(0{:}0.2{:}0.8)_\oplus$, the limits are consistent with all compositions possible under averaged oscillations. The figure is taken from [326].

The flavor composition at Earth varies linearly from $(0{:}1{:}0)_S$ to $(0.6{:}1.3{:}1.1)_\oplus$ for a composition at Earth varying from $(0{:}1{:}0)_S$ to $(1{:}0{:}0)_S$ (see Eq. 1.34). Though expected to be negligible [319], even a large ν_τ contribution at sources causes only a small deviation from this range [326]. Such limited variation in the flavor ratio at Earth has consequences [326] for all possible source compositions, so that the observation of a ratio inconsistent with these expectations would signal new physics in the neutrino sector, such as neutrino decay [334, 335], sterile neutrinos [336], pseudo-Dirac neutrinos [337], Lorentz or CPT[55] violation [338], and quantum gravity-induced decoherence [339]. Thus, measuring the flavor ratio of astrophysical neutrinos is interesting both as a probe of the source of high-energy CRs and a test of fundamental particle physics [326]. Flavor ratio analysis of a diffuse flux detected by IceCube in 2013 [11] (see Section 1.5.6) shows the consistency with the ratio $(1{:}1{:}1)_\oplus$ (see Fig. 1.42).

[55] Charge, parity, and time symmetry.

1.5.3 The Waxman-Bahcall upper bound

Theoretical models set the upper bounds on the neutrino diffuse flux and constrain the emission from extragalactic sources using the observation of the diffuse fluxes of γ-rays and UHECRs [117]. The Waxman-Bahcall, shortened as W&B, limits the high-energy neutrino flux produced in astrophysical sources, in particular, from either AGN jets or GRBs, optically thin to photo-meson interactions on protons [340, 341]. Under the assumption of W&B, the diffuse neutrino flux follows the spectrum of the parent CRs at the acceleration site, i.e. proportional to E^{-2} as expected from the Fermi acceleration mechanism [89] (see Section 1.1.3 for details). The W&B uses the observation of CRs at energies $E_{CR}{\approx}10^{19}$ eV to constrain the neutrino diffuse flux. Indeed, a simple inspection of Fig. 1.4 one can see that $E^2dN/dE \approx 10^{-8}\,\mathrm{GeV\,cm^{-2}\,s^{-1}\,sr^{-1}}$ at 10^{19} eV. In addition injection spectrum $\propto E^{-2}$, there are few assumptions used to derive the W&B upper bound [340] such as that neutrons produced in photohadronic interactions can escape freely from the source[56] and that magnetic fields within the source and in the Universe do not affect the observed flux of EGCRs [340]. A model-independent W&B upper bound [340] on diffuse $\nu_\mu + \bar{\nu}_\mu$ flux is:

$$E_\nu^2 \Phi_\nu < 4.5 \times 10^{-8}\,\mathrm{GeV\,cm^{-2}\,s^{-1}\,sr^{-1}} \tag{1.35}$$

Figure 1.43 summarises the $\nu_\mu + \bar{\nu}_\mu$ limits obtained in the TeV-PeV region and only the best limit is shown for each experiment and each method. Remarkably, from the first limit derived from the underground experiment, Fréjus, in 1996 [342] to the IceCube-40 configuration limit obtained in 2010, a factor of 500 improvements have been achieved [315]. Moreover, the limit obtained with IceCube-40 configuration [343] has reached a sensitivity in the region of the W&B upper bound and the limit obtained with ANTARES [344] is close to that. Such achievement presaged the start of exciting times for neutrino astrophysics. Further improvements were achieved after the next years using more data with ANTARES and the full IceCube detector configuration and combining muon and cascade information. In IceCube three years search [345], it has been obtained the astrophysical flux of $E_\nu^2\Phi_\nu = 0.95 \pm 0.3 \times 10^{-8}\,\mathrm{GeV\,cm^{-2}\,s^{-1}\,sr^{-1}}$ rejecting a purely atmospheric explanation at 5.7σ. This measurement is compatible with W&B upper bound corrected by the cosmological evolutionary effects [340], where the redshift energy loss of neutrinos produced by CRs are not neglected and CR generation rate is not considered to be independent of cosmic time and may have been higher at an earlier time, i.e. at high redshift.

As also seen, several models can be excluded such as the blazar model of Stecker [346] indicated in Fig. 1.43. In addition to Stecker AGN core model [346], in analysis with IceCube-40 configuration [343], the AGN neutrino models derived by Mannheim [347] and for the radio galaxy from Becker, Biermann, and Rhode [348] were rejected at the 5σ C.L.

[56] A photo-meson interaction producing a charged pion also converts the proton to a neutron, which is not magnetically confined while proton is not and will escape a source with small photo-meson optical depth before decaying to a proton [340].

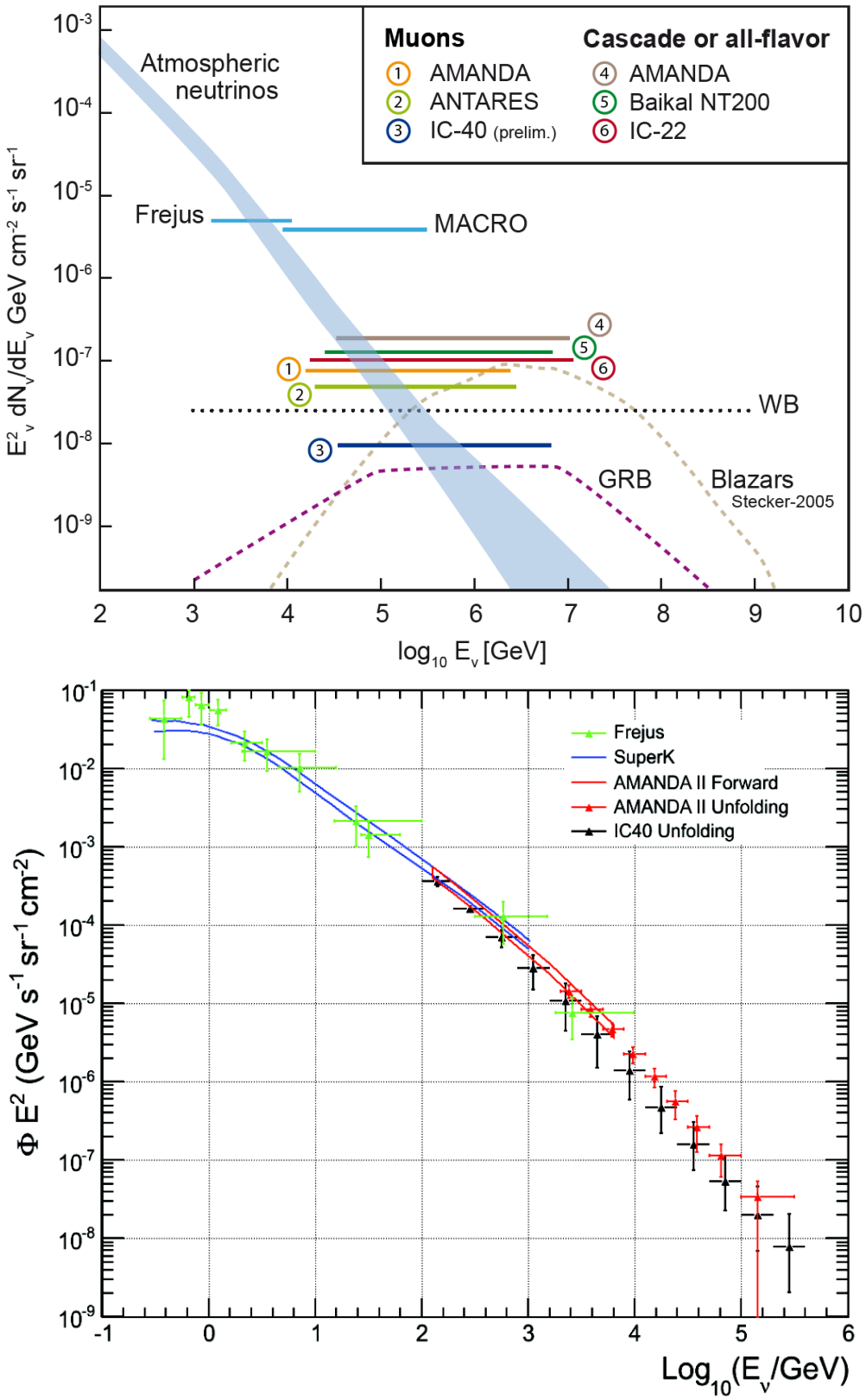

Fig. 1.43.: *Left:* 90% C.L. integral upper limits on the diffuse flux of extraterrestrial neutrinos (normalized to one flavor). The horizontal lines extend over the energy range which would cover 90% of the detected events from a E^{-2} source (5% below and 5% above the range). The measured flux of atmospheric neutrinos is indicated by the colored band, the broadening of which at higher energies reflects the uncertainties for prompt neutrinos. The muon neutrinos and cascade/all flavor limits are indicated. The W&B bound [340] is also shown. *Bottom:* The energy spectrum of atmospheric neutrinos. See [315] for the reference to the data was used. The figures are taken from [315].

1.5.4 The Mannheim-Protheroe-Rachen upper bound

The W&B limit was criticized as not completely model-independent, in particular, the main observation was about the choice of the spectral index $\gamma = 2$ [117]. It has been shown [349], that the W&B upper bound is not model-independent but rather relies on very special model assumptions and the only observational upper limits can be truly model-independent bounds [349]. In [350], the new model has been proposed, which imposed a stronger bound, called Mannheim-Protheroe-Rachen (MPR) upper bound.

As stated above, in [340] the sources are assumed to be transparent for neutrons of an energy $\approx 10^{19}$ eV. To justify that such an assumption is valid for AGN jets, W&B refers to the observed TeV emission from Markarian (Mrk) 421 and 501, both blazars to be transparent to the emission of neutrons. In [349], it is discussed that W&B [340] misinterpreted the TeV data in stating that the observed emission at 10 TeV proves that blazar jets are optically thin at this energy. The MPR model is more general, therefore less restrictive [350]. The MPR bound is about two orders of magnitude higher than the W&B bound [350] (see Fig. 1.44):

$$E_\nu^2 \Phi_\nu < 2 \times 10^{-6} \,\mathrm{GeV\,cm^{-2}\,s^{-1}\,sr^{-1}} \quad (1.36)$$

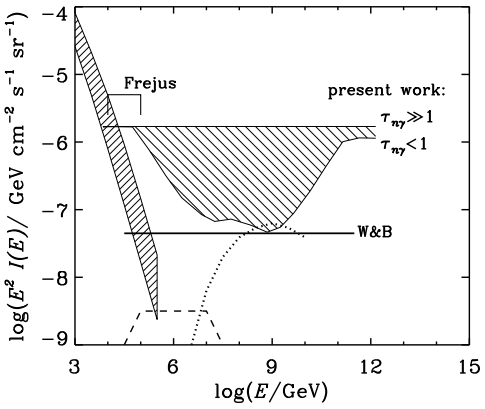

Fig. 1.44.: Muon neutrino upper bounds for optically thin pion photoproduction sources (curve labeled $\tau_{n\gamma}<1$) and optically thick pion photoproduction sources (curve labeled $\tau_{n\gamma}\gg 1$); the hatched range between the two curves can be considered the allowed region for upper bounds for sources with $\tau_{n\gamma}>1$. For comparison purposes, the W&B upper bound (for an evolving source distribution) is shown. Predictions for optically thin photoproduction sources are also shown: proton-blazar [347] (dotted curve); GRB sources [351] (dashed curve). Also shown is an observational upper limit from Fréjus [342] and the atmospheric background [352]. The figure is taken from [350].

It is indicated [350] that there may be other classes of sources, such as quasars, with a different spectral shape, and/or which are opaque to the emission of UHECRs, which can produce a higher neutrino flux than the source classes considered by W&B. Also, it is shown that hadronic processes in AGN which are optically thick to the emission of UHECRs could produce the Extragalactic γ-ray Background (EGRB) according to observational constraints and due to large photohadronic opacities at UHE, the MPR upper bound for the neutrino contribution from AGN is derived considering the effect of neutron opacity [350]. Models that predict neutrino emission mainly in the energy range of underwater/ice Čherenkov experiments are not rigorously bounded by CR data [350], because the effects of Extragalactic Magnetic Fields (EGMF) come into play, increasing/reducing the MPR bound [350]. At neutrino energies above 10^9 GeV, the upper limit rises up to the point where the energy flux of secondary γ-rays increases above the level of the observed EGRB, whose reason is that while CRs from evolving extragalactic sources above the nominal GZK cutoff reach us exponentially damped due to interactions with the CMB, neutrinos reach us essentially unattenuated [350].

1.5.5 Cosmogenic neutrinos

The detection of cosmogenic neutrinos [66], also known as "GZK neutrinos", in pion decays[57] (see Eq. 1.3) would point back to the direction of the UHECRs and help to determine the location and nature of the most powerful CR accelerators in the Universe. If however, the "*disappointing*" model would turn out to be true, then pion photoproduction on CMB photons in extragalactic space are absent and GZK cutoff in the spectrum does not exist; thus, a disappointing scenario with no cosmogenic neutrinos produced on CMB are expected in this case [87]. Furthermore, the fluxes of cosmogenic neutrinos produced on infrared - optical background radiation are too low for registration by existing detectors and projects [87]. Regarding the heavy nuclei, due to their deflection in Galactic magnetic fields, the correlation with nearby sources is absent even at the highest energies [87]. The IceCube searches for cosmogenic neutrinos have been so far fruitless [353, 354], and the origin of the flux suppression is still debated and remains one of the most challenging open questions of CR physics. The expected flux of cosmogenic neutrinos and differential limits on that flux

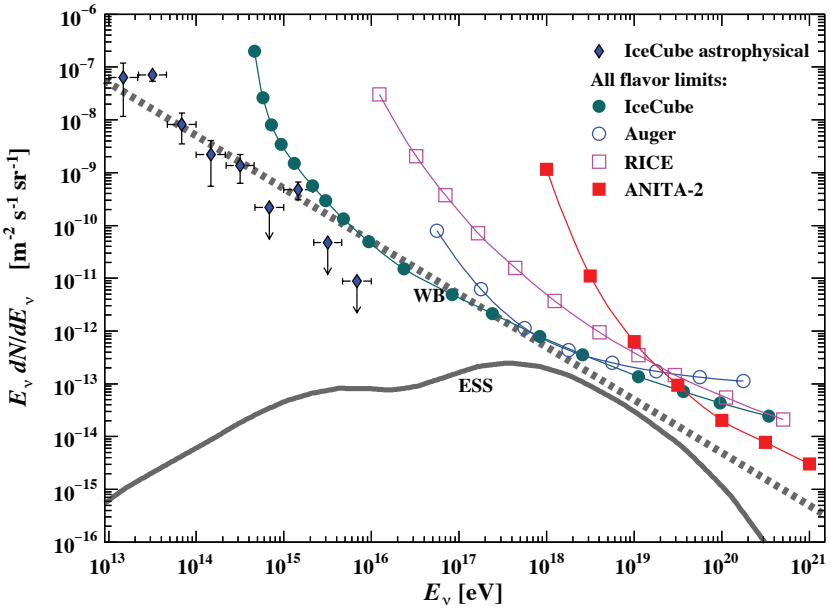

Fig. 1.45.: The best-fit IceCube astrophysical all-flavor neutrino flux [355]. The differential limits on the flux of cosmogenic neutrinos set by four experments are shown (see text for the details). The dotted and solid curves show the Waxman-Bahcall (W&B) bound [340, 341] and a representative "*mid-range*" model for the expected flux of cosmogenic neutrinos, Engel-Seckel-Stanev (ESS) [356], respectively. The expected flux is uncertain by over an order of magnitude in either direction. The figure is taken from [39].

set by IceCube [354], Auger [357], Radio Ice Cherenkov Experiment (RICE)[58] [358, 359] and ANtarctic Impulsive Transient Antenna (ANITA)[59] [360, 361] experiments together with a model for cosmogenic neutrino production (ESS) [356] are shown in Fig. 1.45.

[57] The neutral pion decays into two γ-rays such as $\pi^0 \rightarrow 2\gamma$ while in the charged pion decays three neutrinos and a positron are produced such as $\pi^+ \rightarrow \mu^+ + \nu_\mu \rightarrow e^+ + \nu_e + \bar{\nu}_\mu + \nu_\mu$

[58] The predecessor for Neutrino Array Radio Calibration (NARC) experiment

[59] ANITA Collaboration, https://www.phys.hawaii.edu/~anita/

1.5.6 First astrophysical neutrinos

The first strong evidence for high-energy neutrinos of extrasolar origin made by IceCube in 2013 [11]. With the 2-year dataset, 28 events with in-detector deposited energies more than 30 TeV were observed, two of which exceeding PeV energies [11]. The directions and energies of these 28 events found to inconsistent with those expected from the atmospheric muon and neutrino backgrounds rejecting a purely atmospheric origin at the 4σ level [11]. Nine were observed in the third year. In the full 988-day sample, the total 37 events have been detected, the expected background was of 8.4±4.2 atmospheric muon events and $6.6^{+5.9}_{-1.6}$ atmospheric neutrinos [345].

The two exceptional events in 28-events sample, #14 and #20, which exceeded PeV dubbed "Ernie" and "Bert"[60] by IceCube physicists. The deposited energies by "Ernie" and "Bert" are 1.04 PeV and 1.14 PeV respectively. The highest-energy neutrino ever observed, called "Big Bird" (event #35), within the 3-year HESE event sample of the 37 observed astrophysical neutrinos [345] is shown in Fig. 1.46. The size of the symbols in the skymap shown in Fig. 1.46 indicates the deposited energy of the events in the range of 30 TeV to 2 PeV, while the thin circles around cascade events indicate the angular reconstruction uncertainty [362]. The red-shaded regions reflects the 10% quantiles of neutrino Earth absorption at 30 TeV and increasing with neutrino energy [362]. The skymap shows 35 (7 track and 28 cascade events) out of 37 events originally detected, because two events, #28 and #32, have been omitted following the discussion in [345] due to strong evidence of a CR origin since they had coincident hits in the IceTop [363] surface array[61].

As seen in the plots below in Fig. 1.46, the data (black dots) are described well by the expected backgrounds (red and blue shaded regions for atmospheric muons and neutrinos respectively) and a hard astrophysical isotropic neutrino flux (gray lines), the hashed region shows uncertainties on the sum of all backgrounds [345]. Atmospheric neutrinos and uncertainties thereon (see Fig. 1.46) are derived [345] from the π/K and charm components of the atmospheric ν_μ spectrum [364]. The obtained best-fit per-flavor astrophysical flux ($\nu+\bar{\nu}$) in the energy range 60 TeV $< E_{dep} <$ 3 PeV is $E^2\phi(E) = 0.95 \pm 0.3 \times 10^{-8}$ GeV cm^{-2} s^{-1} sr^{-1} rejecting a purely atmospheric explanation at 5.7σ [345]. This flux is very similar to the lower bound of the W&B limit [69, 340, 341] discussed in Section 1.5.3 and describes the data well, with both the energy spectrum and arrival directions (see Fig. 1.46) of the events consistent with expectations for an origin in a hard isotropic 1:1:1 neutrino flux [345]. The corresponding range of best-fit astrophysical slopes (see Fig. 1.46) within 90% confidence band on the charm flux [364] is -2.0 to -2.3, and as the best-fit charm flux is zero, the best-fit astrophysical spectrum is on the lower boundary of this interval at -2.3 (solid line in Fig. 1.46)

[60] Bert and Ernie are two main characters of the popular children's television show, "Sesame Street".

[61] This fact implies that they are almost certainly produced in CR air showers. IceTop array is designed to extend IceCube's capabilities for CR physics and is discussed in details in Section 2.18.

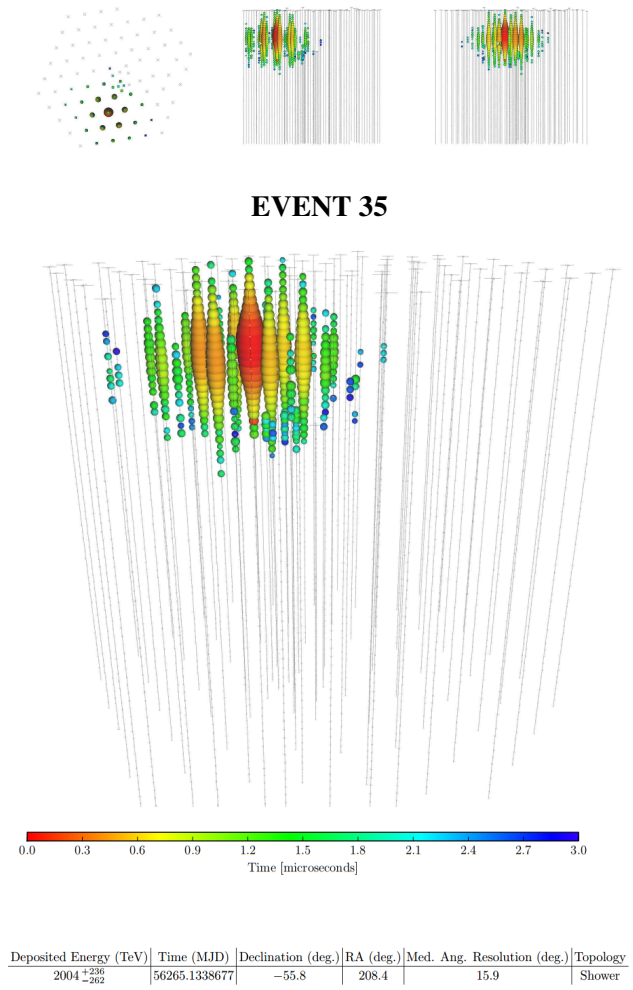

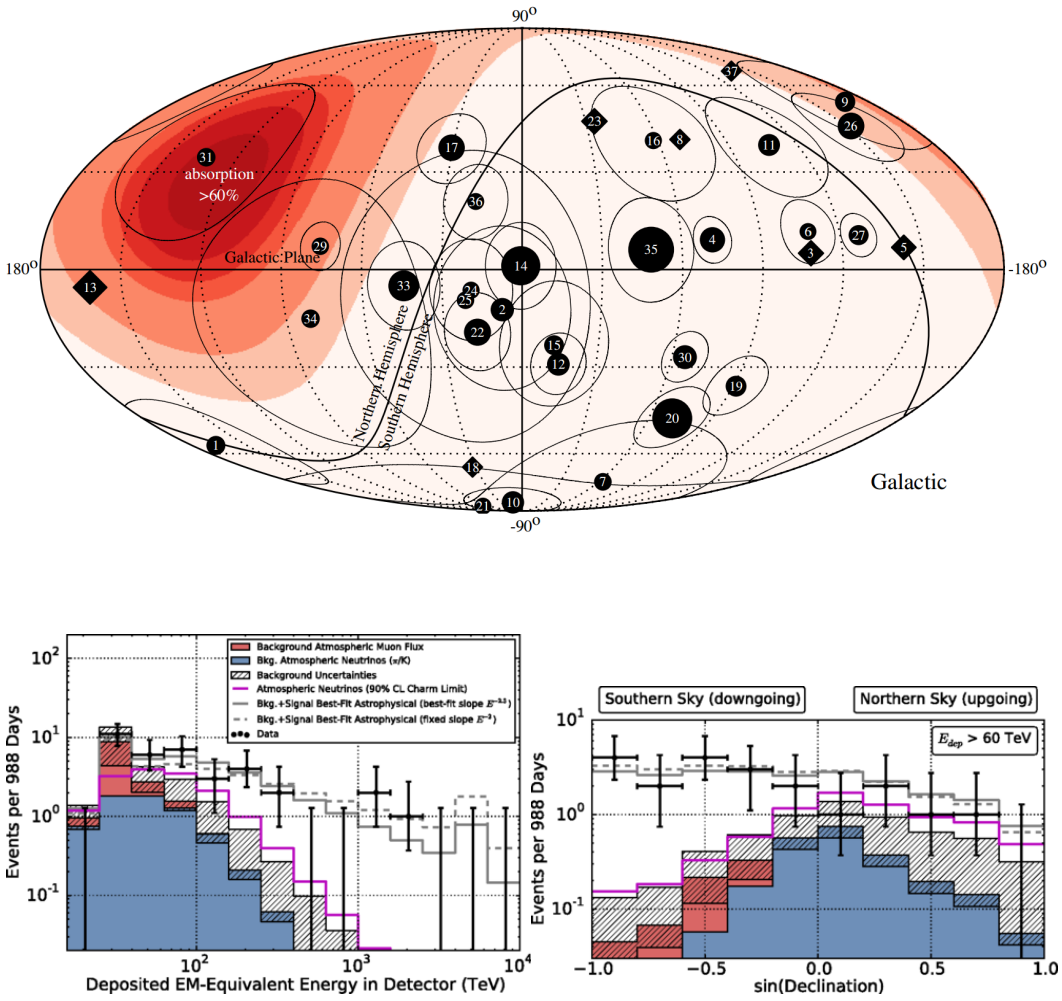

Fig. 1.46.: *Left:* The event #35 dubbed "Big Bird", the highest-energy neutrino ever observed, it deposited 2 PeV in IceCube. *Right:* Skymap (*Top*) of arrival directions of events of the 3-year HESE sample, in Galactic coordinates. Shower-like events are shown with filled circles and those containing muon tracks with diamond. The observed deposited energy E_{dep} distribution and arrival angles of events with E_{dep}>60 TeV compared with predictions (*Bottom*). See explanations in the text. The figures are taken from [345, 362].

The ANTARES search [365] for high-energy neutrinos from the direction of these events revealed six bright, variable blazars which are positionally coincident with two of the most energetic IceCube events, #14 and #20. Objects like these are prime candidates to be the source of the highest-energy CRs, and thus of associated neutrino emission [365]. The ANTARES [365] tested the hypothesis in [366] that the first two PeV neutrino events observed by IceCube are of blazar origin. The AGNs of all classes have long been proposed [367, 116, 368, 369] as sites of hadronic interaction, and are potential sources of the highest-energy CRs and, hence, neutrinos [365]. Predictions for the neutrino flux [370, 347, 341, 371, 372, 373, 374] depend on the nature of the AGN considered (more details about AGNs are in Section **??**), the CR composition and flux, and the assumed densities of target hadronic matter and magnetic and photon fields [365].

It is found [369], that Mrk 421, well-known, bright BL Lacertae (BL Lac) object, is respectively the strongest in the IceCube error circle of event #9. This blazar is the brightest and closest BL Lac objects known, at luminosity distance dL=134 Mpc with redshift z=0.031, which is the first [375] extragalactic objects discovered in the TeV energy band; thus, they are of a high good candidate for a neutrino counterpart [178]. Besides Mrk 421, there is only Mrk 501, the second [376] extragalactic objects discovered in the TeV energy band, that have confirmed extragalactic associations in the 2HWC catalog [377]. Several studies [176, 177, 178] have been focused on the search for space/time correlation between neutrinos detected by ANTARES and γ-ray flares detected by HAWC from these Markarians. The term "Markarian galaxies" came into use after the survey [378, 379, 380, 380] done by Benjamin Markarian in the 1960s, when who found tens and then extending this number to several hundreds of galaxies with UV excess, list of which, "First Byurakan Survey", was published in 1989 [381].

Massive efforts have been performed in order to find counterparts both, in γ-rays and CRs, for high-energy neutrino events detected in IceCube. The comparison of the TeV flux of Mrk 421 and the neutrino fluxes related to IceCube event #9 have been performed in [382]. The analysis in [383] focused on the steady-state emission of Mrk 421 in order to examine the resulting neutrino and neutron distributions in relation to the observed photon spectra and has been concluded, that neutrinos are far from being detectable from this source because of their low flux assuming the two models used (low pion production efficiency of Mrk 421 leading to difficulties in the production of the bright neutrino flux observed by IceCube). This goes against the conclusion made in [369], there Mrk 421 is found to be one of the most probable counterparts for the IceCube high-energy neutrino event #9 discussed above. Worth noticing, that there is another source, BL Lac object 1ES 1011+496, which also can be associated with IceCube event #9 in addition to Mrk 421. This blazar was detected in VHE by MAGIC in 2007 [384]. The search of counterparts for IceCube events has been performed for almost all known blazars coincident in position with the IceCube events. For instance, in [385], a major outburst of the blazar PKS B1424-418 found to be in temporal and positional coincidence with the 2 PeV neutrino event "Big Bird". And the only reason

for the particularly detailed discussion of Mrk 421 is due to that this thesis is focused on the search for high-energy neutrinos from Mrk 421 and Mrk 501 in association with γ-ray flares detected by HAWC.

After success in detection of first high-energy neutrinos of extraterrestrial origin in 2013 [11], a further challenge was to find the sources of such energetic neutrinos, what has been achieved a few years later in 2017 [14, 386]. The IceCube-170922A event alert is discussed in Section 1.7.1 whereas its γ-ray counterpart, blazar TXS 0506+056, is discussed in Section 1.7.2.

1.6 High-energy neutrino source candidates

In this section, a brief review of the candidate sources of high-energy neutrinos is given.

1.6.1 Galactic sources

Shell-type Supernova Remnants

Particles can be accelerated in the SNRs since the shock waves developing when SNe ejecta hit the ISM are prime candidates for hadron acceleration through the Fermi mechanism [117, 387] (see Section 1.1.3). If the final product of the SN is an NS, already accelerated particles can gain additional energy, due to the strong variable magnetic field of the NS [117]. Shell-type SNRs are considered to be the most likely sites of GCR acceleration and this hypothesis is supported by the observations from the TeV γ-ray IACT [117], such as, e.g., by the H.E.S.S. observation of TeV γ-ray emission from RX J1713.7-3946 [388] and RX J0852.0-4622 (Vela Jr) [389]. Several IACT observations support this hypothesis and disfavor the explanations of the γ-flux by purely electromagnetic processes. For instance, the hadronic acceleration provides a good explanation of the Vela Jr's hard and intense TeV γ-ray spectrum [389]. The detection of neutrinos from the SNRs would identify unambiguously specific cosmic accelerators [387]. It is worth noting that this is only possible with Northern-hemisphere neutrino telescopes such as ANTARES or KM3NeT which, in contrast to the South Pole detector IceCube, cover the relevant part of the Galactic plane in their FOV [387].

The SNRs are included in the search of ANTARES and KM3NeT as the most promising acceleration sites of the CRs in our Galaxy and efficient high-energy hadron accelerators with neutrinos to be expected. Several analyses have been performed on the search for neutrinos from SNRs with them.

Of particular interest for ANTARES and KM3NeT are the SNRs in the Vela Jr and RX J1713.7-3946, one of the brightest objects in the southern TeV sky [117]. The SNR RX J1713.7-3946 has been proposed [390, 391, 392] as a promising neutrino source candidate. For instance, an event rate of a few neutrinos per year (for $E_\nu > 1$ TeV is expected [390] for RX J1713.7-3946 and Vela Jr with KM3NeT. It has been shown [309, 310, 311] that at least the most intense one such as SNR RXJ1713.7-3946 is within reach for KM3NeT. The SNR RXJ1713.7-3946 is visible for about 90% of the time by KM3NeT, while Vela Jr is visible at around 100% [312] (see Fig. 1.47).

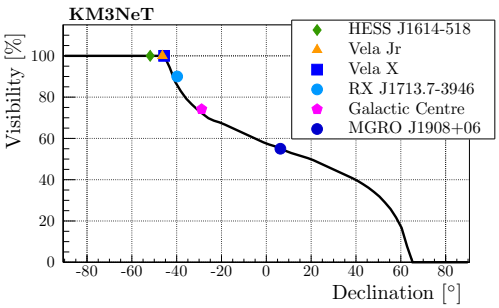

Fig. 1.47.: Source visibility for KM3NeT/ARCA as a function of declination for a zenith cut of 10° above the horizon (black line). The markers represent the visibility of the specific sources discussed in [312]. The figure is taken from [312].

Some ANTARES results and KM3NeT perspectives for SNRs detection are summarized in [308]. Search for neutrino sources in the Southern Sky using combined data from the ANTARES and IceCube detectors [313] shows no significant evidence of cosmic neutrinos from the direction of the SNR RXJ1713.7-3946. In addition, the recent ANTARES search (with 11 years of data) for neutrinos from various point-like sources including SNRs shows no significant excess in the direction of SNRs in the ANTARES candidate search list [393]. Among them are RXJ1713.7-3946 and Vela Jr. Despite no success in search, the competitiveness of the results achieved demonstrates the huge potential of the new, km^3-scale neutrino telescope KM3NeT (see Section 2.4.4), which is expected to make definite statements about a neutrino flux from several SNRs as good candidates of Galactic neutrino sources [393]. In the recent KM3NeT search for Galactic point-like neutrino sources [312], the detection perspectives of the telescope have been investigated. It has been shown [312] that the SNRs RXJ1713.7-3946 and Vela Jr can be observed by KM3NeT with a significance of 3σ within 5.5 and 6 years of operation (see Fig. 1.48) respectively. However, if no signal is observed after about 5 years, the hadronic contribution to the γ-ray emission can be constrained to be less than 50% for this source [312].

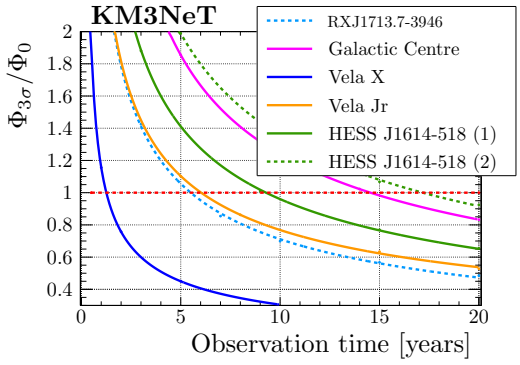

Fig. 1.48.: The ratio of the discovery potential at 3σ level to the expectation neutrino flux as a function of the observation time of KM3NeT/ARCA. The figure is taken from [312].

Pulsar Wind Nebulae

PWNe are a class of SNRs, whose broad-band emission is mostly non-thermal and powered by a fast-spinning magnetized NS, usually also observed as a pulsar [394]. Most of the rotational energy lost by such a star goes into the acceleration of a highly relativistic magnetized wind, with a particle content dominated by electron-positron pairs [394]. When the wind first impacts on the SNR, a reverse shock is launched towards the pulsar [394]. At this shock (the termination shock, TS hereafter) the wind is slowed down and its bulk energy is efficiently converted into an outflow of relativistic particles that are then responsible for the nebular emission [394]. So, the PWNe differ from the shell-type SNRs because there is a pulsar in the center that blows out equatorial winds and, in some cases, jets of very fast-moving material into the nebula [117]. The radio, optical and X-ray observations suggest a synchrotron origin for these emissions [117]. H.E.S.S. has also detected TeV γ-ray emission from the Vela PWN, named Vela X, which is likely to be produced by the IC mechanism [117]. A hadronic origin for the observed γ-ray spectrum, with the consequent flux of neutrinos, was also considered [117] and prediction for the neutrino emission is given [395]. Observations of neutrinos, which can only be expected in the case of hadronic origin, are key to discern the mechanism for the production of TeV γ-rays [395]. Among known TeV sources, the Vela X appears to be a favorable candidate [395]. Remarkable, that PWNe are the only Galactic sources in which we have direct evidence of PeV particles [394]. This fact makes them appealing for a search for neutrinos (and joint γ-rays). The youngest and most energetic PWN known is Crab Nebula (see Fig. 1.14), which has been studied with nearly all major telescopes since its discovery. It has been also detected by HAWC during its long-term monitoring campaigns but, in contrast to Mrk 421 and Mrk 501, no variability in the TeV band was found [154]; thereby, the source was not considered for this work. The recent ANTARES search (with 11 years of data) for neutrinos from various point-like sources including PWNe shows no significant excess in the direction of PWNe such as Vela X and Crab in the ANTARES candidate search list [393]. Despite no exsuccess found, the competitiveness of the results achieved demonstrates the huge potential of the new, km^3-scale neutrino telescope KM3NeT (see Section 2.4.4), which is expected to make definite statements about a neutrino flux from several PWNe as promising Galactic neutrino source candidates [393].

Microquasars

There is no clear definition of a microquasar, it can be characterized as a galactic X-ray binary system - constituted of a compact object (stellar-mass BH or NS) surrounded by an accretion disc and a companion star - emitting at high-energy and exhibiting relativistic jets [396]. The name is due to the fact that they result morphologically similar to the AGN since the presence of jets makes them similar to small quasars [117]. A schematic view of a microquasar, compared with quasars, is given in Fig. 1.49. Such quasar/microquasar analogy became rapidly very fruitful, the field of quasars benefitting of microquasars, and vice versa [396]. For instance, because accretion/ejection timescale is proportional to BH mass, it is easier (because faster) to observe accretion/ejection cycles in microquasars than in quasars [396]. On the other hand, the understanding of ejection phenomena in microquasars has largely benefitted from jet models developed for active galaxies [396]. Microquasars, as galactic jet sources, are among the best laboratories for high-energy phenomena [396] and have been proposed as galactic acceleration sites of charged particles up to $E{\sim}10^{16}$ eV [117]. The hypothesis was strengthened by the discovery of the presence of relativistic nuclei in microquasars jets like those of SS 433 [117]. The microquasar SS 433 is detected by HAWC [397] and a very detailed image is provided in Fig. 4.7 (see discussion in (see Section 4.5)).

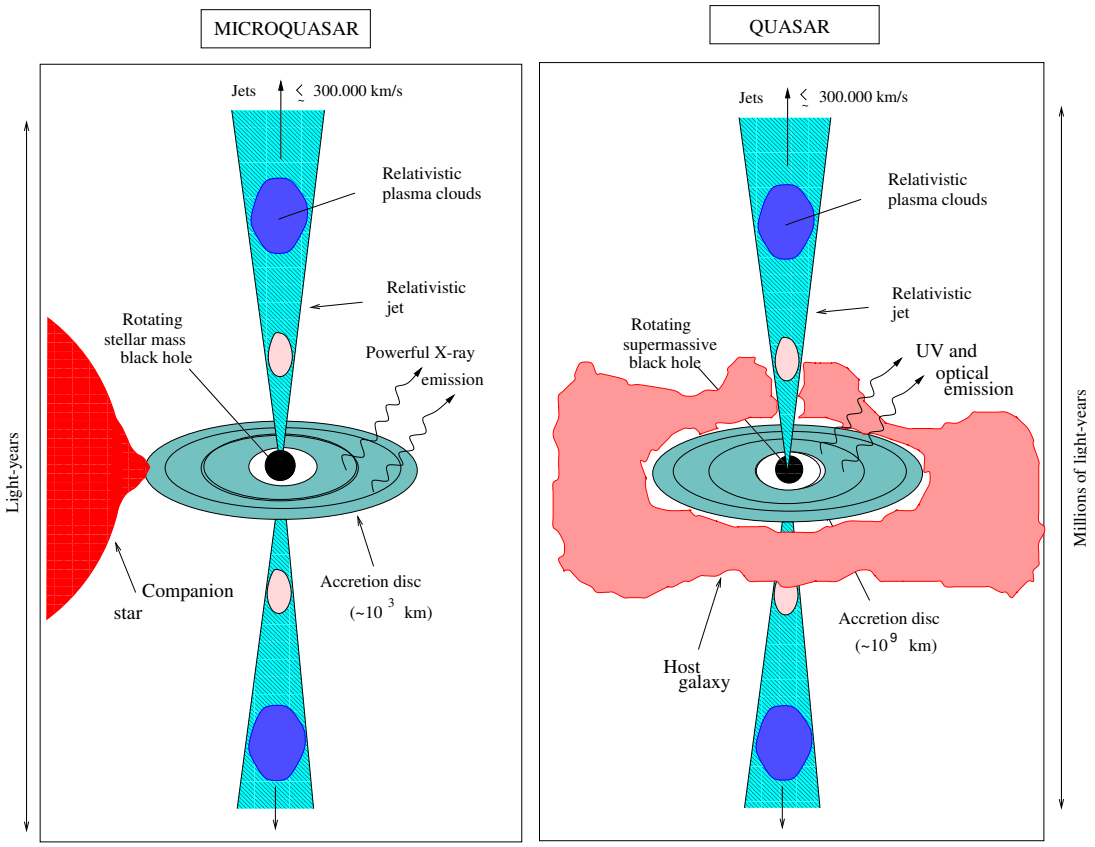

Fig. 1.49.: Schematic view illustrating analogies between microquasars (*Left*) and quasars (*Right*). Note the different mass and length scales between both types of objects. The figure is taken from [396].

Among the best candidates as neutrino sources are the steady microquasars SS433, GX339-4, LS I +61 303, and LS 5039 [173, 117]. Assuming reasonable scenarios for TeV neutrino production, a 1 km^3-scale neutrino telescope in the Mediterranean sea such as KM3NeT could identify microquasars in a few years of data taking, with the possibility of a 5σ level detection [117]. In the case of no-observation, the result would strongly constrain the neutrino production models and the source parameters [117]. The recent ANTARES search (with 11 years of data) for neutrinos from various point-like sources including microquasars shows no significant excess in the direction of microquasars in the ANTARES candidate search list [393]. Among them are SS 433, GX339-4 and LS 5039. But the competitiveness of the results achieved demonstrates the huge potential of the new, km^3-scale neutrino telescope KM3NeT (see Section 2.4.4), which is expected to make definite statements about a neutrino flux from several microquasars [393].

The Galactic Center

The Galactic center is probably the most interesting region of our Galaxy, also regarding the emission of neutrinos [117]. Particularly, due to the presence of the Supermassive Black Hole (SMBH) Sagittarius A (Sgr A) [398] and the SNR Sgr A East [117]. In addition, the region around the center of our Galaxy is known to have a high density of astrophysical objects such as shell-type and pulsar wind nebula SNRs, X-ray binaries, etc (see Fig. 1.22). A variety of IACT telescopes reported the existence of a diffuse γ-ray emission in the region of the Galactic center. In addition, H.E.S.S. observations of the Galactic center region showed a point-like source (HESS J1745-290 [399]) at the gravitational center of the Galaxy [117]. The Galactic center is especially appealing for these Mediterranean neutrino telescopes due to its location since it is within the sky view of a telescope located at such latitude [117]. Thus, it gives an advantage to ANTARES and KM3NeT to search for neutrino emission from this region compared to the South Pole detector IceCube. The recent ANTARES search (with 11 years of data) for neutrinos from the direction of the Galactic center shows slight excess (with 1.2 best-fit number of signal events and p-value = 0.10) [393]. Such results demonstrate the huge potential of the new, km^3-scale neutrino telescope KM3NeT with its better sensitivity (see Section 2.4.4).

The Galactic Plane

In addition to stars, the Galaxy contains interstellar thermal gas, magnetic fields, and CRs which have roughly the same energy density [117]. The inhomogeneous magnetic fields confine the CRs within the Galaxy [117]. Hadronic interactions of CRs with the ISM produce a diffuse flux of γ-rays and neutrinos (expected to be equal, within a factor of $\sim$2) [117]. It is expected that the fluence at Earth will be correlated to the gas column density in the Galaxy: the largest emission is expected from directions along the line of sight which intersects most matter [117]. The detected extended multi-TeV γ emission from the Cygnus

region is well correlated to the gas density and strongly supports the hadronic origin of the radiation [117]. With the assumption that the observed γ-ray emission comes from hadronic processes, it is possible to obtain an upper limit on the diffuse flux of neutrinos from the Galactic plane [117]. The observation of diffuse TeV γ-ray emission from the Galactic Plane [400, 401], which is expected to arise from the same hadronic processes that would produce high-energy neutrinos, strongly supports this hypothesis [175]. The diffuse fluxes of neutrinos are expected not only from the Galaxy but also from unresolved extragalactic sources [173]. The assumption that observed Galactic γ emission comes from hadronic processes thus yields an estimate of the diffuse Galactic neutrino flux [173]. In [173], the KM3NeT neutrino telescope estimated the diffuse flux from the inner part of the Galactic Plane. Recent ANTARES all flavor search [402] for Galactic diffuse neutrino emission shows no excess of events and put constraints on the prediction assuming the primary CR spectrum cut-off at 5 (50) PeV which disfavors the diffuse Galactic emission as the origin of the "spectral anomaly" [403], a non-negligible discrepancy between the measured neutrino Spectral Energy Distributions (SED) of the two hemispheres, observed by IceCube [402].

1.6.2 Extragalactic sources

Gamma-Ray Bursts

GRBs are short flashes of γ-rays, lasting typically from milliseconds to tens of seconds and carrying most of their energy in photons of the MeV scale [117]. The likely origin of the GRBs with a duration of tens of seconds is the collapse of massive stars to BHs [117]. The rapid variability time, ~1 ms, observed in some GRBs implies that the sources are compact, with a linear scale $r_0 \sim 10^2$ km [351]. GRBs are one of the most energetic phenomena in the universe and one of the candidates where both electrons and protons are accelerated up to very high energies [404]. If protons are accelerated up to very high energies, we can expect high energy neutrinos and γ-rays that are produced by the photomeson production process [404]. GRBs produce X-ray, optical and radio emission subsequent to the initial burst (the so-called "afterglow" of the GRB) [117]. The detection of the afterglow is performed with sensitive instruments that detect photons at wavelengths smaller than MeV γ-rays [117].

Leading models assume that a so-called "fireball" produced in the collapse, expands with a highly relativistic velocity (Lorentz factor $\Gamma \sim 10^{2.5}$) powered by radiation pressure [117]. Protons accelerated in the fireball internal shocks lose energy through photo-meson interaction with ambient photons (the same process as in Eq. 1.29 with Δ^+) [117]. In the observer frame, the condition required to the resonant production of the Δ^+ is $E_\gamma E_p = 0.2$ GeV$^2\Gamma^2$ [117]. For the production of γ-rays with energies ~1 MeV the characteristic proton energy required is $E_p = 10^{16}$ eV, if $\Gamma \sim 10^{2.5}$ [117]. The interaction rate between photons and protons is high due to the high density of ambient photons and yields a significant production of pions among which the charged ones decay in neutrinos, typically carrying

5% of the proton energy [117]. Thus, a burst of neutrinos with $E_\nu \sim 10^{14}$ eV is expected, created by photo-meson production of pions in interactions between the fireball γ-rays and accelerated protons [351]. Neutrinos with lower energies can also be produced in different regions or stages where GRB γ-rays are originated [117]. Depending on models, a different contribution of neutrinos is expected at every time stage of the GRB [117]. For instance, the neutrino emission from early afterglows of GRBs [404], due to dissipation made by the external shock with the surrounding medium or by the shock internal dissipation [117].

The existence of hadronic acceleration mechanisms in GRBs would be unambiguously proven by the identification of high-energy neutrinos in temporal and spatial coincidence with the prompt emission of the burst [405]. The detection of a single neutrino event would allow identifying GRB as a candidate for the UHECR production [405], whose origin is still under investigation [406]. In ANTARES searches for muon neutrinos in spatial and temporal coincidence with the emission of GRBs, no neutrino events have been detected [407, 405]. The connection between constraints in neutrinos and CR measurements indicates that a multi-messenger approach is a suitable strategy in the framework of testing the paradigm of GRBs as UHECR sources [405]. Current neutrino telescopes have a small probability to detect neutrinos from GRBs [405]; thus, further investigations will be possible with the incoming generation of km^3-scaled neutrino detectors, such as KM3NeT-ARCA [175] and IceCube-Gen2 [362].

Active Galactic Nuclei

AGNs are associated with the accretion of material on to SMBHs, of masses $M_{BH} > M_{\odot}$ [408], located near the centers of their host galaxies [409]. In order to be classified as an AGN, the Eddington ratio should exceed the limit of $L_{AGN}/L_{Edd} = 10^{-5}$, where L_{AGN} is the bolometric luminosity and $L_{Edd} = 1.5{\times}10^{38} M_{BH}/M_{\odot}$ s^{-1} erg[62] is the Eddington luminosity for a solar composition gas [408]. The unification scheme of AGN is generally accepted in order to explain the large diversity of observed AGN properties by a small number of physical parameters [410, 408]. The two main driving parameters are here the orientation of the AGN with respect to the line of sight, and the radio loudness [410]. The first one determines the detectability of the central engine and the broad-line region in the optical domain, the latter one indicates whether or not the AGN produces a significant jet [410].

Figure 1.50 shows a schematic diagram of the radio-loud AGNs, i.e. those with prominent radio jet and/or lobe emission, according to the unified model [411]. Surrounding the central BH is a luminous accretion disk [411]. Broad emission lines are produced in clouds orbiting above the disk and perhaps by the disk itself [411]. A thick dusty torus (or warped disk) obscures the broad-line region from transverse lines of sight; some continuum and broad-line emission can be scattered into those lines of sight by hot electrons that pervade the region [411]. A hot corona above the accretion disk may also play a role in producing the hard X-ray continuum [411]. Narrow lines are produced in clouds much farther from the central source [411]. Radio jets, shown in the scheme as the diffuse jets characteristic of low-luminosity, or FR I-type[63], radio sources, emanate from the region near the BH, initially at relativistic speeds [411].

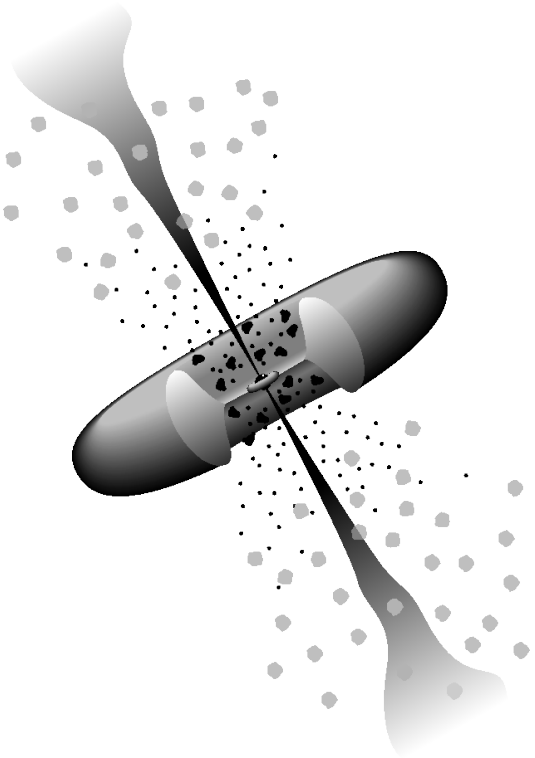

Fig. 1.50.: Schematic diagram of the unified model of radio-loud AGNs. The figure is taken from [411].

However, this simple unification scheme summarized also in Fig. 7.1 fails to explain all the different varieties of AGN phenomena that we observe [410]. Other important considerations may be the mass of the central BH, the accretion rate, or the specific geometry of the absorber [410].

[62] 1 erg $\equiv 10^{-7}$ J = 624.15 GeV [39].
[63] In turn, high-luminosity radio sources are of FR II-type, see Fig. 7.1 in Section 7.1.

The VHE extragalactic sky is dominated by emission from blazars, a class of non-thermal jet-powered AGN known as radio-loud AGN [412] with their jet axis aligned close to the line of sight of the observer (see Fig. 7.1). The SED of blazars can be described with two components: one low-energy from radio to X-ray and one high-energy from X-ray to TeV [176]. Contrary to the more commonly assumed leptonic scenarios, in which the two characteristic broad bumps of the non-thermal SED of blazars are described with electron-synchrotron and IC emission [413, 414], hadronic scenarios introduce relativistic protons to explain the high-energy bump that is generally seen from keV to GeV energies in FSRQs and in the MeV to TeV range for BL Lac objects [415]. In the hadronic framework, this high-energy component can be attributed to either proton-synchrotron emission or radiation from secondary products of $p\gamma$ or pp interactions [415, 416, 417]. Thus, these scenarios admit the possibility of a direct link between UHECRs and electromagnetic emission from blazars [415]. They also lead necessarily to the emission of high-energy neutrinos from the decay of proton-induced pions and muons [415]. This suggests that blazars, or more generally radio-loud AGNs, of which blazars are a sub-class, are potential sources of the PeV neutrinos [415] detected by IceCube in 2013 [11].

The largest source population in *Fermi*-LAT 4FGL catalog [146] (see Section 1.2.1) is that of AGNs, with 3137 blazars, 42 radio galaxies, and 28 other AGNs, so that blazars make up more than ~60% in the catalog. The blazar sample comprises 694 FSRQs, 1131 BL Lacs and 1312 Blazar Candidates of Uncertain type (BCUs) [146]. The γ-ray sky of blazars seen by *Fermi*-LAT after 5 years of operation is shown in Fig. 1.20. The two closest blazars to Earth, Mrk 421 and Mrk 501, neutrinos from which are searched for in this work, are clearly visible. The VHE spectrum of Mrk 421 has been successfully modeled with both leptonic and hadronic models and conclusive results have been achieved yet about the origin and both models are still under debate [418]. As the nearest blazars to Earth, both are excellent sources to test the blazar-neutrino connection scenario, especially during flares where time-dependent neutrino searches may have a higher detection probability [176] (see Section 6).

The recent detection of high-energy neutrinos [14, 386] (see Section 1.7.1) in correlation with γ-rays associated with TXS 0506+056 blazar (see Section 1.7.2), lead blazars to be the first identifiable sources of the high-energy astrophysical neutrino flux [15, 16]. This detection motivates a search for high-energy neutrinos from blazars with enhanced γ-ray activity performed in this work.

1.7 Multimessenger astronomy

Multimessenger observations started with the observation of the solar neutrinos resulting in 1987 in observation of coincident neutrinos and photons from supernova SN 1987A [299, 298]. Since the first detection of an extragalactic diffuse high-energy neutrino flux in 2013 [11] (see Section 1.5.6), the mystery of where those neutrinos originate was still unresolved. Significant efforts have been made in recent years to unveil the mystery of the origin of those neutrinos. To support this question to be resolved, IceCube has implemented a Target of Opportunity program (ToO), where neutrino track-events with a high probability of being of cosmic origin are selected in realtime at the South Pole [386] and forwarded to telescopes for immediate electromagnetic follow-up observations [419]. The implemented realtime analysis framework [386] aimed to help for the identification of an electromagnetic counterpart of a rapidly fading source and to locate the astrophysical objects responsible for the neutrino signals in 2013 [11]. Recently, two public neutrino streams existed which were distributed by the Astrophysical Multimessenger Observatory Network (AMON) [420, 421][64] via the Gamma-ray Coordinates Network (GCN)[65]: the High-Energy Starting Event (HESE) and Extremely High-Energy (EHE). Approximately four HESE and four EHE alerts were expected per year with an astrophysical purity of roughly 25% and 50% respectively [419], but in June 2019 both were replaced with new systems[66], ICECUBE_ASTROTRACK_BRONZE and ICECUBE_ASTROTRACK_GOLD, with the 16 and 12 alerts expected per year and to be at least 30% and 50% (Gold events) of astrophysical origin respectively. In addition, HAWC started to issue alerts from short timescale searches, looking for GRB-like events using HAWC_BURST_MONITOR system [422]. The AMON

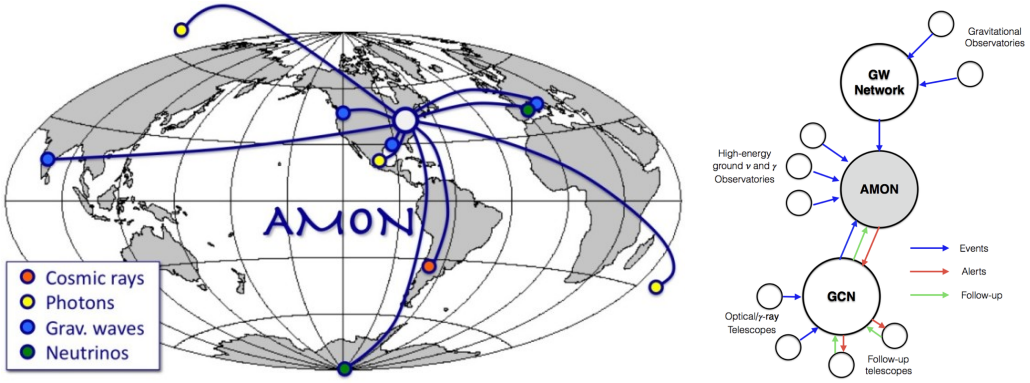

Fig. 1.51.: *Left:* The AMON network connecting collaborating observatories of different messengers. Image credit: AMON. *Right:* The AMON network. AMON receives information from triggering observatories which can be ground-based or space-based. Most of the space-based send their alerts through GCN, which AMON is subscribed to. Any alerts produced by AMON are sent to GCN for follow-up observations. Interesting followed-up observations are sent back to AMON for archival purposes. The figure is taken from [423].

system was founded to tie the world's high-energy and multimessenger observatories into a

[64] AMON system, https://www.amon.psu.edu/
[65] GCN circular, https://gcn.gsfc.nasa.gov/
[66] More information on https://gcn.gsfc.nasa.gov/amon.html

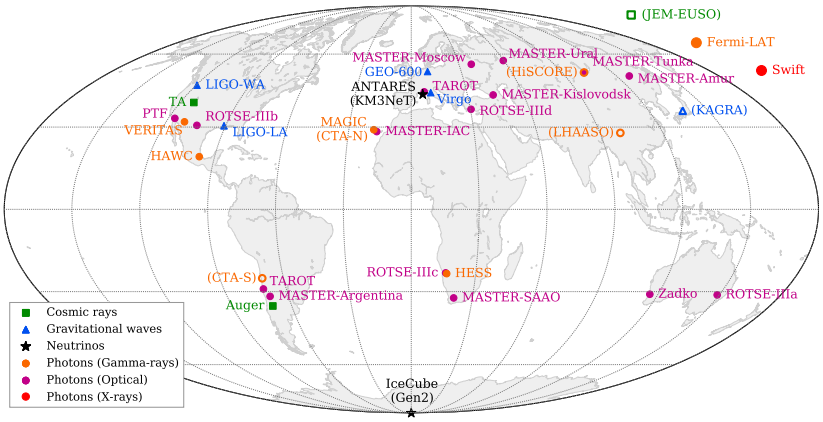

Fig. 1.52.: Global distribution of some of the observatories (past, present, and future) dedicated to multimessenger studies. Current and past facilities are shown with filled markers. Some representative future detectors are shown with empty markers with their names in parentheses. The figure is taken from [172].

single network, with the purpose to enable the discovering of multimessenger sources, to exploit these sources for purposes of astrophysics, fundamental physics, and cosmology, and to explore archival datasets for evidence of multimessenger source populations [423]. To date, AMON contributions include the GCN prompt alerts for likely-cosmic neutrinos, multiple follow-up campaigns for likely-cosmic neutrinos including the IceCube-170922A event, and several archival searches for transient and flaring γ plus neutrino and neutrino plus CR multimessenger sources [423]. Currently, AMON receives real-time data from ANTARES which decommissioning is expected to be at the end of 2019, and with the advent of the new generation of neutrino detectors such as KM3NeT [173, 174, 175], the more neutrino sources are expected to be detected. In recent work [424], the 7.3 years of ANTARES high-energy neutrino and *Fermi*-LAT γ-ray data have been analyzed in search of cosmic neutrino plus γ-ray transient sources or source populations. While no significant evidence of cosmic neutrino plus γ-ray coincidences found, the work with AMON and GCN is continued. The recent detection of a high-energy neutrino by IceCube [14] (see Section 1.7.1) associated with observations in γ-rays, by *Fermi*-LAT alert [425], and at other wavelengths, being for the first-ever detection of such correlation between the neutrino and γ-ray skies. Such convincing evidence for ν-γ association suggested to TXS 0506+056 blazar (see Section 1.7.2) possibly being an individually identifiable source of high-energy neutrinos, in turn, leading blazars to be the first identifiable sources of the high-energy astrophysical neutrino flux [15, 16]. The IceCube-170922A event was a breakthrough in multimessenger astrophysics and a giant leap forward in revealing the physical processes behind extreme astrophysical phenomena in the Universe. Neutrinos are tracers of CR acceleration: electrically neutral and traveling at nearly the speed of light, they can escape the densest environments and may be traced back to their source of origin [16]. Acting as ”messengers”, neutrinos, unaffected by magnetic fields and passing almost entirely through

matter, directly carry unique information about the regions where they are produced from the far reaches of the Universe. Hence, their detection is crucial for unraveling the CR origin and acceleration (see Section 1.1.3). Energetic and dense astrophysical environments in far Universe may be the sources of high-energy CRs, γ-rays, and neutrinos (see Section 1.6). Unlike the other particles, neutrinos trace a straight path all the way back to their source, while CRs are deflected by the intergalactic magnetic fields during propagation losing their directional information and photons undergo absorption by interstellar dust clouds with significant attenuation and also due to interactions with the CMB. Thus, the role of neutrinos as messengers in high-energy astrophysics is unique. The usage of such unique particles together with other messengers such as γ-rays, CRs, GWs, remarkably enhance the chance for detection and promises to yield crucial information on the mechanisms that power most energetic astrophysical phenomena, substantially extending our knowledge of the Universe.

Multimessenger astronomy aims for globally coordinated observations of CRs, GWs, neutrinos, and electromagnetic radiation across a broad range of wavelengths [16]. The production of neutrinos is accompanied by electromagnetic radiation from the source favors the chances of a multiwavelength identification; in particular, a measured association of high-energy neutrinos with a flaring source of γ-rays would elucidate the mechanisms and conditions for acceleration of the highest-energy CRs [16]. Combining several messengers simultaneously with neutrinos will increase chances to get information about the astrophysical sources as happened in the case of the IceCube-170922A event. The search for neutrino sources benefits from the boost in sensitivity provided by the multimessenger approach since over the last few years the large network of astrophysical observatories around the world (gathered in Fig. 1.52) provided the data which has been used to study correlations between neutrino events and other messenger signals [172]. This promises a brighter future for neutrino astronomy, where one of the main roles in the forthcoming discoveries will be played by KM3NeT, the multi-km^3-sized neutrino telescope [173, 174, 175] (see Section 2.4.4), which assures to be sensitive to astrophysical neutrino sources.

1.7.1 The IceCube-170922A event

On 22 September 2017 [14], IceCube detected a neutrino (IceCube-170922A) with high-energy and of astrophysical origin. The IceCube-170922A event was selected by the EHE online event filter [386], and reported as a public alert [14]. This event was coincident in direction and time with a γ-ray flare from the blazar TXS 0506+056 (see Section 1.7.2). Prompted by this association, the 9.5 years of IceCube data was investigated to search for excess emission at the position of the blazar [15]. An excess of high-energy neutrino events, with respect to atmospheric backgrounds, has been found at that position between September 2014 and March 2015 (see Fig. 1.53), which constitutes 3.5σ evidence for neutrino emission from the direction of TXS 0506+056, independent of and prior to the 2017 flaringepisode [15]. The results of the time-dependent analysis performed at the

coordinates of TXS 0506+056 are shown in Fig. 1.53 for each of the six data periods[67] made up the full 9.5-year data sample. The Gaussian time window is centered at 13 December 2014 [MJD 57004] with an uncertainty of ±21 days s and duration T_W=110$^{+35}_{-24}$ days [15]. Outside the 2012-2015 time period, the next most significant excess is found using the Gaussian window in 2017 (centered at 22 September 2017 with duration T_W=19 days) and includes the IceCube-170922A event with no other event besides the IceCube-170922A event contributes significantly to the best-fit [15]. The view of the IceCube-170922A neutrino

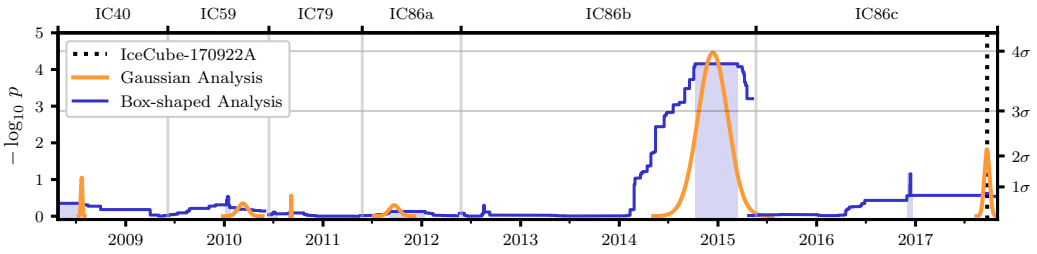

Fig. 1.53.: Time-dependent analysis results. The orange curve corresponds to the analysis using the Gaussian-shaped time profile. The central time T_O and width T_W are plotted for the most significant excess found in each period, with the P value of that result indicated by the height of the peak. The blue curve corresponds to the analysis using the box-shaped time profile. The curve traces the outer edge of the superposition of the best-fitting time windows (durations T_W) over all times T_O, with the height indicating the significance of that window. In each period, the most significant time window forms a plateau, shaded in blue. The large blue band centered near 2015 represents the best-fitting 158-day time window found using the box-shaped time profile. The vertical dotted line in IC86c indicates the time of the IceCube-170922A event. The figure is taken from [15].

event is shown in Fig. 1.54. After the alert was sent, further studies refined the directional reconstruction, with best-fitting coordinates found to be RA 77.43$^{+0.95}_{-0.65}$ and Dec +5.72$^{+0.50}_{-0.30}$ (degrees, J2000, 90% containment region) [15]. The most probable neutrino energy was estimated to be 290 TeV [15], assuming the best-fitting power-law energy spectrum for astrophysical high-energy muon neutrinos, $dN/dE \propto E^{-2.13}$, with a 90% C.L. lower limit of 183 TeV [16]. An energy of 23.7±2.8 TeV [16] was deposited in IceCube by the traversing muon. Figure 1.54 shows also the multimessenger follow-up by *Fermi*-LAT and MAGIC telescopes. The *Fermi*-LAT found a cataloged γ-ray source, TXS 0506+056, located at RA=77.36° and Dec= +5.69°, to be 0.1° from the neutrino direction and be in a flaring state at that time with enhanced γ-ray activity in the GeV range, while MAGIC revealed periods where the detected γ-ray flux from the blazar reached energies up to 400 GeV and detected above 100 GeV at 5σ significance level [15, 16]. The IceCube-170922A alert follow-up observations were performed by a variety of experiments at different wavelengths including γ-rays, X-rays, optical and radio (see Section 1.7.2).

[67] IC40: 5 Apr 2008 - 20 May 2009; IC59: 20 May 2009 - 31 May 2010; IC79: 31 May 2010 - 13 May 2011; IC86: 13 May 2011- 16 May 2012 (a); 16 May 2012 - 18 May 2015 (b); 18 May 2015 - 31 Oct 2017 (c).

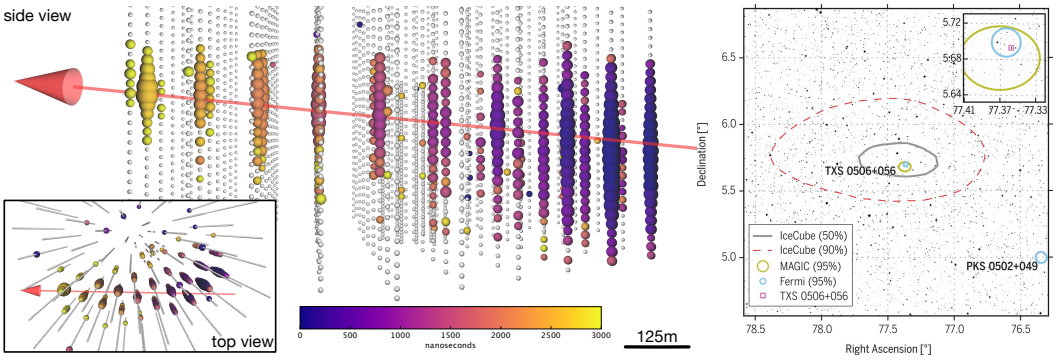

Fig. 1.54.: *Left:* Event display for neutrino event IceCube-170922A. The time at which a DOM observed a signal is reflected in the color of the hit, with dark blues for earliest hits and yellow for the latest. The size of a colored sphere is proportional to the logarithm of the amount of light observed at the DOM, with larger spheres corresponding to larger signals. The total time the event took to cross the detector and total charge recorded are ~3000 ns and ~5800 p.e. relatively. The inset is an overhead perspective view of the event. The arrow represent the best-fitting track direction. *Right:* Multimessenger observations of blazar TXS 0506+056. The 50% and 90% containment regions for the neutrino IceCube-170922A (dashed red and solid gray contours, respectively), overlain on a V-band optical image of the sky. The γ-ray sources in this region previously detected with the *Fermi* spacecraft are shown as blue circles, with sizes representing their 95% positional uncertainty and labeled with the source names. The IceCube neutrino is coincident with the blazar TXS 0506+056, whose optical position is shown by the pink square. The yellow circle shows the 95% positional uncertainty of VHE γ-rays detected by the MAGIC telescopes during the follow-up campaign. The inset shows a magnified view of the region around TXS 0506+056 on an R-band optical image of the sky. The figures are taken from [16].

1.7.2 The Blazar TXS 0506+056

Right after IceCube online system sent out an alert reporting a high-energy IceCube-170922A neutrino event, a variety of experiments simultaneously were triggered to perform a series of multiwavelength follow-up observations that revealed a flaring blazar being the origin of this event. Figure 1.55 shows the observatories that made follow-up observation of the IceCube-170922A alert, the number of which reaches almost 20. The follow-up observations were made across the electromagnetic spectrum including γ-rays (*Fermi*-LAT, H.E.S.S., MAGIC, VERITAS, HAWC, AGILE), X-rays (MAXI/GSC, Swift/XRT, NuSTAR), optical (ASAS-SN, SALT-HRS, SPRAT, Kanata, Subaru/FOCAS, VLT/X-Shooter) and radio (VLA) radiations. The direction of IceCube-170922A was spatially coincident with the location of BL Lac-type TXS 0506+056 blazar and coincident with a state of increased γ-ray activity observed since April 2017 [425] by the *Fermi*-LAT telescope. Several follow-up observations from different observatories have been reported (the timeline is shown in Fig. 1.56) in the Astronomer's Telegram (ATel) [426] and GCN circular such as (shown in order of appearance in ATel):

[ATel #10773] ANTARES [427]: no neutrino candidate events were recorded;

[ATel #10778] H.E.S.S. [428]: revealed no significant detection;

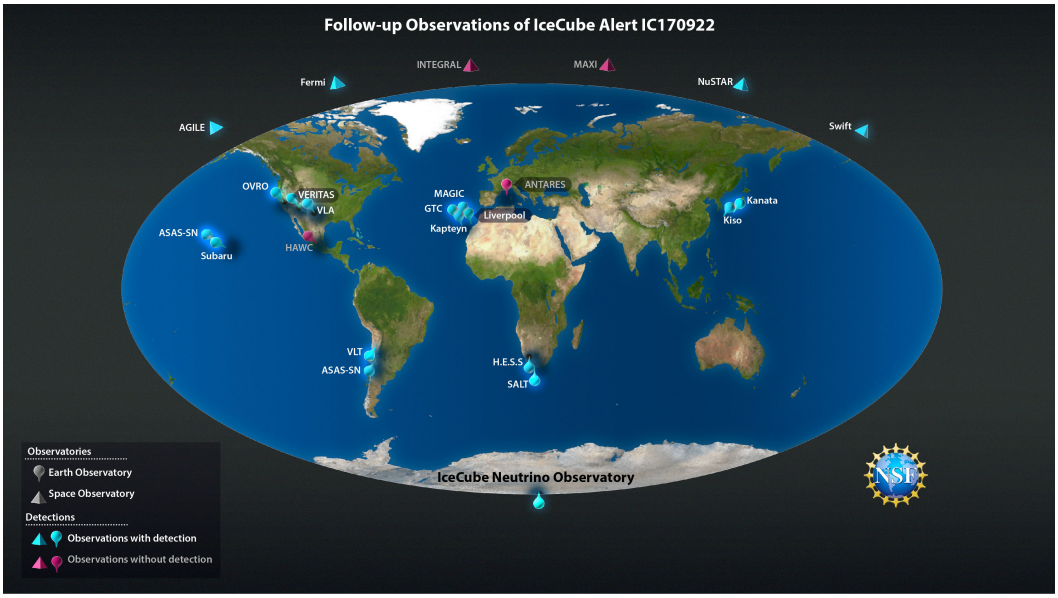

Fig. 1.55.: Observatories that made follow-up observation of IceCube-170922A high-energy neutrino event alert on 22 September 2017. Image credit: Nicolle R. Fuller/NSF/IceCube.

[ATel #10791] *Fermi*-LAT [425]: discover of increased γ-ray activity of TXS 0506+056, consistent with location of IceCube-170922A;

[ATel #10792] Swift-XRT [429]: stated the source brightening since the original observations and that it had undergone spectral evolution;

[ATel #10794] ASAS-SN[68] [431]: observation of a significant variability of TXS 0506+056 with the recent data of the time of IceCube-170922A alert were the brightest the TXS 0506+056 had been in several years;

[ATel #10799] SPRAT[69] [433]: indication of the considerably bluer optical spectrum, that in turn indicated a likely "bluer-when-brighter" behaviour;

[ATel #10801] AGILE[70] [435]: 4σ confirmation of γ-ray activity from the IceCube-170922A error region in less than 1 degree both from the IceCube centroid and from the position of 3FGL J0509.4+0541 with the detection to be within the period of increased γ-ray activity reported by *Fermi*-LAT [425];

[ATel #10802] HAWC [436]: no evidence for γ-ray emission found above 1 TeV;

[ATel #10817] MAGIC [437]: 5σ detection of γ-rays above 100 GeV;

[68] All-Sky Automated Survey for SuperNovae (ASAS-SN) Project [430], http://www.astronomy.ohio-state.edu/~assassin/
[69] SPectrograph for the Rapid Acquisition of Transients (SPRAT) [432], https://telescope.livjm.ac.uk/TelInst/Inst/SPRAT/
[70] Astro-Rivelatore Gamma a Immagini Leggero (AGILE) Mission [434], https://agile.asdc.asi.it/

[ATel #10830] SALT-HRS[71] [439]: observed visible NaD lines from Galactic absorption, which is consistent with observations of a non-thermally dominated blazar;

[ATel #10833] VERITAS [440]: no evidence for γ-ray emission found at blazar location;

[ATel #10838] MAXI/GSC[72] [442]: no significant X-ray enhancement detected;

[ATel #10840] VLT/X-Shooter[73] [444]: identification of absorption lines attributable to Galactic interstellar absorption, which is consistent with the spectrum of a non-thermally dominated blazar;

[ATel #10844] Kanata[74] [446]: detection of polarization in the R band;

[ATel #10845] NuSTAR[75] [448]: the source is well detected;

[ATel #10861] VLA[76] [451]: significant detection of TXS 0506+056 radio flux variability in all bands/epochs;

[ATel #10890] Subaru/FOCAS[77] [453]: observed the signal-to-noise ratios roughly about 350, also some weak emission lines;

and others.

[71] Southern African Large Telescope (SALT) [438],
https://www.salt.ac.za/
[72] Gas Slit Camera (GSC) of Monitor of All-sky X-ray Image (MAXI) Mission [441],
http://maxi.riken.jp/
[73] X-Shooter spectrograph [443] of Very Large Telescope (VLT),
https://www.eso.org/public/teles-instr/paranal-observatory/vlt/
[74] Kanata Telescope [445] ("Kanata" means a far away in Japanese),
http://hasc.hiroshima-u.ac.jp/telescope/kanatatel-e.html
[75] Nuclear Spectroscopic Telescope Array (NuSTAR) Mission [447],
https://www.nustar.caltech.edu/
[76] Karl G. Jansky Very Large Array (VLA) [449, 450],
http://www.vla.nrao.edu/
[77] Subaru telescope Faint Object Camera and Spectrograph (FOCAS) [452],
https://www.subarutelescope.org/Introduction/instrument/FOCAS.html

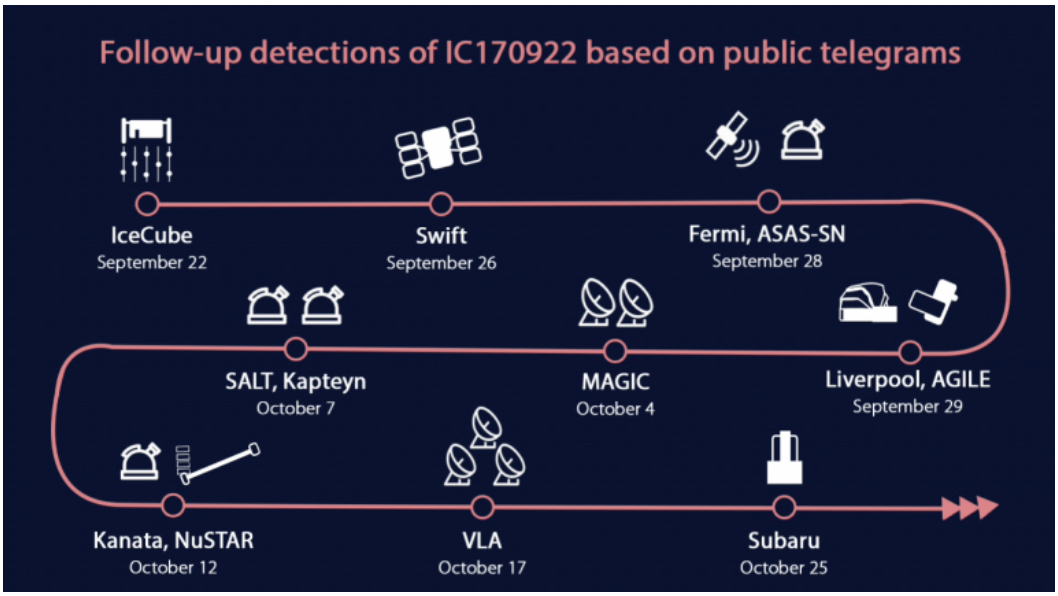

Fig. 1.56.: Timeline of the multimessenger ATel's reports of the follow-up observations triggered by the IceCube-170922A high-energy neutrino event alert. Image credit: IceCube Collaboration.

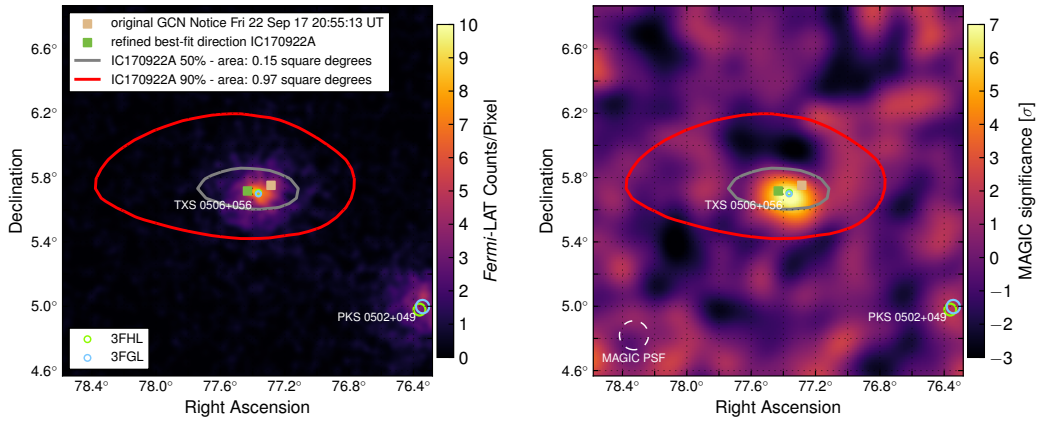

Fig. 1.57.: *Fermi*-LAT and MAGIC observations of IceCube-170922A's location. Sky position of IceCube-170922A in J2000 equatorial coordinates overlaying the γ-ray counts from *Fermi*-LAT above 1 GeV (**A**) and the signal significance as observed by MAGIC (**B**) in this region. The tan square indicates the position reported in the initial alert and the green square indicates the final best-fitting position from follow-up reconstructions [14]. Gray and red curves show the 50% and 90% neutrino containment regions, respectively, including statistical and systematic errors. *Fermi*-LAT data are shown as a photon counts map in 9.5 years of data in units of counts per pixel, using detected photons with energy of 1 to 300 GeV in a 2° by 2° region around TXS0506+056. The map has a pixel size of 0.02° and was smoothed with a 0.02°-wide Gaussian kernel. MAGIC data are shown as signal significance for γ-rays above 90 GeV. Also shown are the locations of a γ-ray source observed by *Fermi*-LAT as given in the *Fermi*-LAT source catalogs, 3FGL [149] and 3FHL [149] (hard), including the identified positionally coincident 3FGL object TXS 0506+056. For *Fermi*-LAT catalog objects, marker sizes indicate the 95% C.L. positional uncertainty of the source. The figure is taken from [16].

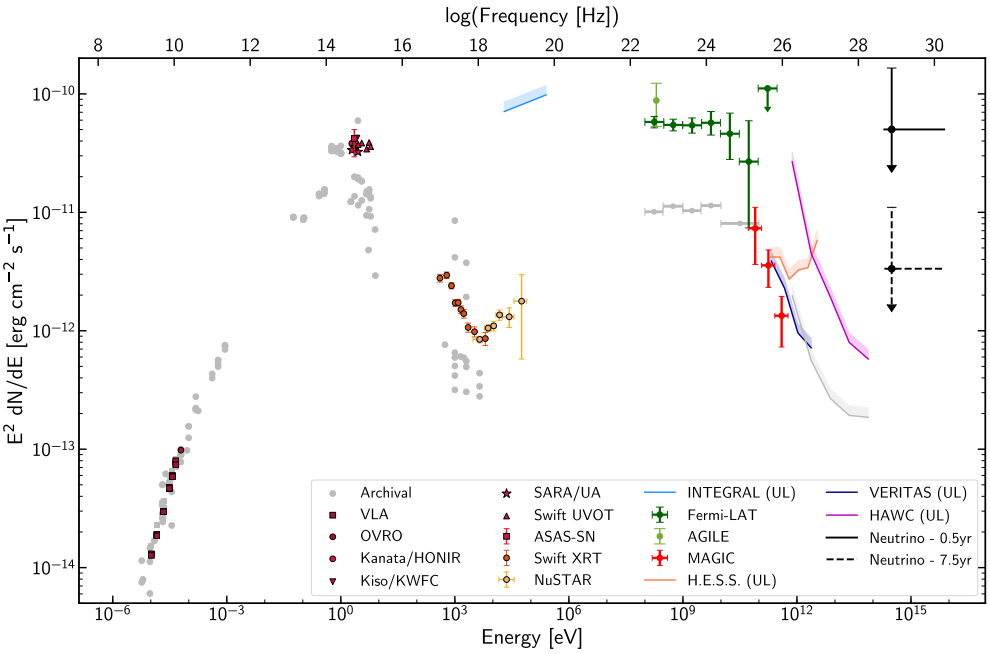

Fig. 1.58.: Broadband spectral energy distribution for the blazar TXS 0506+056. The SED is based on observations obtained within 14 days of the detection of the IceCube-170922A event. See [16] for references to the different instruments involved in the campaign and the contributions provided. Differential flux upper limits (shown as colored bands and indicated as "UL" in the legend) are quoted at the 95% C.L., while markers indicate significant detections. Archival observations are shown in gray to illustrate the historical flux level of the blazar in the radio-to-keV range as retrieved from the ASDC SED Builder [454], and in the γ-ray band as listed in the *Fermi*-LAT 3FGL catalog [149] and from an analysis of 2.5 years of HAWC data. The γ-ray observations have not been corrected for absorption owing to the EBL. Representative $\nu_\mu + \overline{\nu}_\mu$ neutrino flux ULs that produce on average one detection like IceCube-170922A over a period of 0.5 (solid black line) and 7.5 years (dashed black line) are shown, assuming a spectrum of $dN/dE \propto E^{-2}$ at the most probable neutrino energy (311 TeV). The figure is taken from [16].

As stated above, the *Fermi*-LAT found a known blazar, TXS 0506+056, to be only 0.1° from the best-fit neutrino position and well within the 50% containment region (see Fig. 1.57) and MAGIC made a 5σ discovery. The discovery was later confirmed by different space- and ground-based experiments. This discovery made blazars be the first identifiable sources of the high-energy astrophysical neutrino flux [15, 16]. The broadband SED for the blazar TXS 0506+056 based on multiwavelength observations is shown in Fig. 1.58. The electromagnetic SED displays a double-bump structure, one peaking in the optical-UV range and the second one in the GeV range, which is characteristic of the non-thermal emission from blazars [16]. The multiwavelength observations provide a mostly complete, contemporaneous picture of the TXS 0506+056 blazar emissions from 0.3 keV (Swift/XRT) to 400 GeV (MAGIC), more than nine orders of magnitude in photon energy [16]. The two benchmark cases of the average integrated energy flux of a source, that emits neutrinos over the whole observation period of IceCube (i.e., 7.5 years) and only during the 0.5-year period corresponding to the duration of the high-energy γ-ray flare, are also displayed in Fig. 1.58.

1.7.3 Multimessenger prospects with GWs

The discovery of the GW150914 event made by LIGO in September 2015, marked the birth of a new branch of astronomy, i.e., GW astronomy. As with other messengers, other experiments performed different follow-ups with such kinds of new signals. For GW150914, 63 teams participating in the memoranda of understanding (MoUs) were operational and covered the full electromagnetic spectrum [455]. Thorough checks were performed before the GW alert was released, resulting in latencies much greater than 1 hour and in 25 teams responding to it, spanning 19 orders of magnitude in electromagnetic wavelength [455]. Figure 1.59 shows the chronology of the GW detection alerts and follow-up observations. No significant electromagnetic counterpart and no afterglow emission was found [455] in optical, UV, X- or γ-rays [212]. Also, no neutrino candidates found in both temporal and spatial coincidence with the GW event [456]. Nevertheless, this first broadband campaign represented a milestone, highlighting the broad capabilities of the transient astronomy community and the observing strategies that have been developed to pursue BNS merger events [455]. Actually, no electromagnetic emission is expected for vacuum BBH mergers [457], but it is possible if there is surrounding material [458], e.g., remnants of mass lost from the parent star [455].

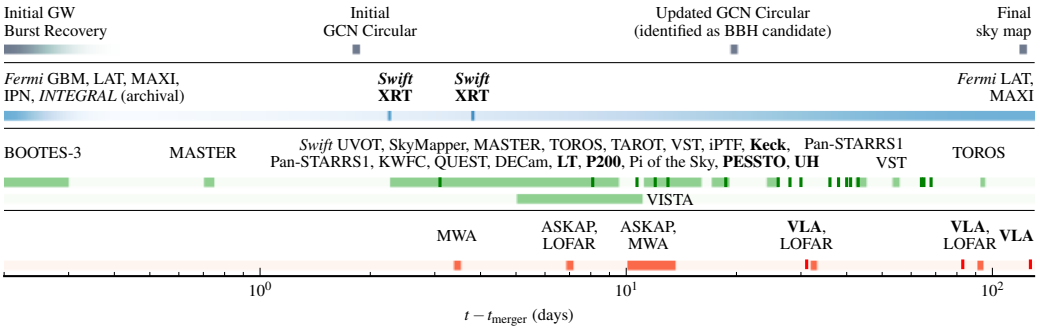

Fig. 1.59.: Timeline of observations of GW150914, separated by band and relative to the time of the GW trigger. The top row shows GW information releases. The bottom four rows show high-energy, optical, Near Infrared (NIR), and radio observations, respectively. Optical spectroscopy and narrow-field radio observations are indicated with darker tick marks and boldface text. See more detailed information on the times of observations made with each instrument in [212]. The figure is taken from [212].

The GW170817 was the first GW signal with association with another messenger such as CR, γ-ray or neutrino. The associated γ-ray burst GRB 170817A [226, 227], detected by *Fermi*-GBM, provides the first direct evidence of a link between the BNS mergers and sGRBs. An ~100 s long GW signal, GW170817, was followed by an sGRB, GRB 170817A, and also by an optical transient (SSS17a/AT 2017gfo) found in the host galaxy NGC 4993 (at ~ 40 Mpc) (see Fig. 1.60) less than 11 hours after the merger by the One-Meter, Two-Hemisphere (1M2H) team [459] using the 1 m Swope Telescope[78] [13, 228] (see Fig. 1.61). Also, GRB 170817A was detected by the INTErnational Gamma-Ray Astrophysics Laboratory

[78] Swope telescope at Las Campanas Observatory (LCO), http://www.lco.cl/

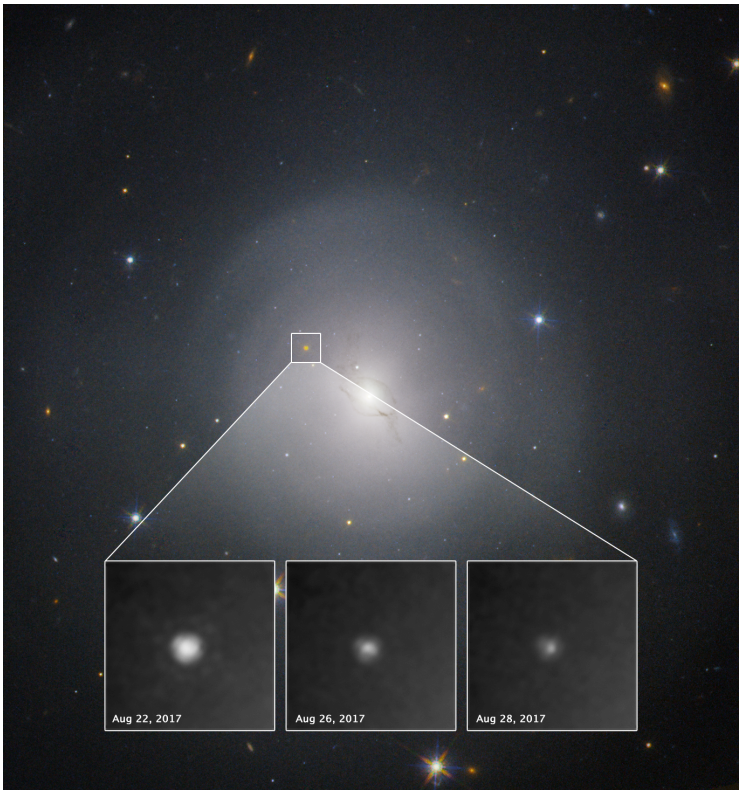

Fig. 1.60.: NGC 4993 and GRB 170817A afterglow as taken by Hubble Space Telescope. Within 12 hours, observatories had identified the source of the event within the galaxy NGC 4993 and located an associated stellar flare called a kilonova (in box). *Inset:* Hubble observed that flare of light from kilonova fade over the course of 6 days, as shown in these observations taken on August 22, 26, and 28. Image credit: NASA, ESA, A. Levan (U. Warwick), N. Tanvir (U. Leicester), and A. Fruchter and O. Fox (STScI).

(INTEGRAL)[79] [460, 461, 462] spacecraft using the Anti-Coincidence Shield (ACS) [463] of the SPectrometer on board INTEGRAL (SPI), through an offline search initiated by the LIGO-Virgo and Fermi-GBM reports [228]. The source of GW170817 was detected across the electromagnetic spectrum [226, 464, 465, 459, 466, 467, 468, 469, 470, 471] - in the X-ray, UV, optical, IR, and radio bands - over hours, days, and weeks [13]. These observations support the hypothesis that GW170817 was produced by the merger of two NSs in NGC4993, followed by an sGRB and a kilonova powered by the radioactive decay of r-process [472] nuclei synthesized in the ejecta [13]. The HAWC also participated in the follow-up [473], but no significant excess of counts was detected and the upper limits for energies >40 TeV assuming a $E^{-2.5}$ spectrum was derived [228].

Exploiting the difference in the arrival time of the γ-ray signals at *Fermi*-GBM and INTEGRAL SPI-ACS, additional significant constraints on the γ-ray localization area can be provided [228] (see Fig. 1.61). The InterPlanetary Network (IPN)[80] localization capability is especially important in the case of GW events that might be less well-localized by LIGO-Virgo [228].

[79] INTEGRAL Collaboration, https://sci.esa.int/web/integral/
[80] IPN Collaboration, http://www.ssl.berkeley.edu/ipn3/index.html

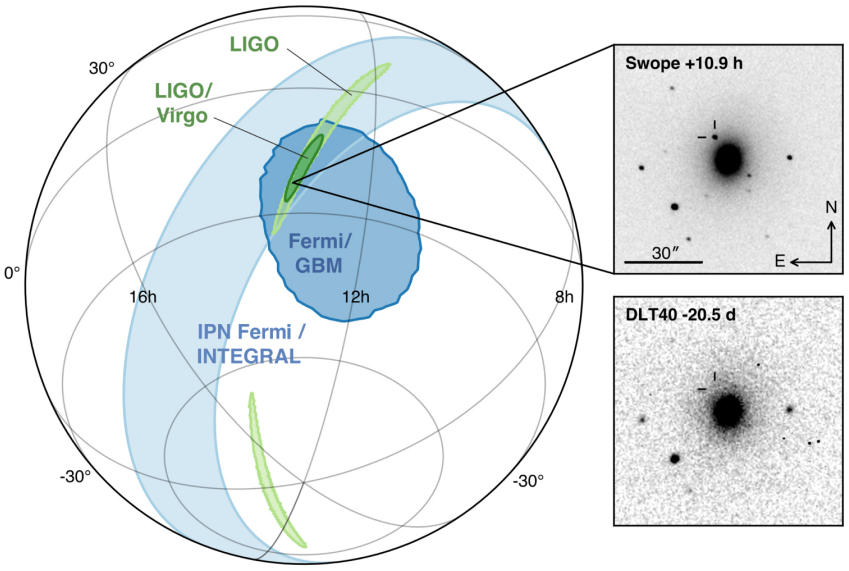

Fig. 1.61.: Localization of the GW, γ-ray, and optical signals. The left panel shows an orthographic projection of the 90% credible regions from LIGO (190 deg^2; light green), the initial LIGO-Virgo localization (31 deg^2; dark green), IPN triangulation from the time delay between Fermi and INTEGRAL (light blue), and *Fermi*-GBM (dark blue). *Inset:* Location of the apparent host galaxy NGC 4993 in the Swope optical discovery image at 10.9 hour after the merger (top right) and the DLT40 pre-discovery image from 20.5 days prior to merger (bottom right). The reticle marks the position of the transient in both images. The figure is taken from [228].

Upon the identification of the GW signal GW170817, preliminary information on this event was rapidly shared with partner observatories [228]. In response, ANTARES [474, 475], IceCube [465, 476, 477] and Auger [478] promptly searched for a neutrino counterpart, and shared their initial results (see Fig. 1.62) with partner observatories [479]. Subsequently, the three facilities carried out a more in-depth search for a neutrino counterpart in the GeV-EeV energy range using the precise localization of the source that was determined by optical detections of emission following the merger [479]. No up-going muon neutrino candidate events were found in a ~500 s time window centered on the GW event time - for an expected number of atmospheric background events of $\sim 10^{-2}$ during the coincident time window [479]. An extended online search during ±1 h also resulted in no up-going neutrino coincidences [479]. The precise direction of origin of GW170817 in NGC 4993 was above the ANTARES horizon at the detection time of the binary merger (see Fig. 1.62); thus, a dedicated analysis looking for down-going muon neutrino candidates in the online ANTARES data stream was also performed, but no neutrino counterparts were found [479]. The results of these low-latency searches were shared [474, 475] with follow-up partners within a few hours for the up-going search and a few days for the down-going search [479]. In IceCube, for source locations in the southern sky (predominantly muons generated by high-energy CRs interactions in the atmosphere above the detector), the sensitivity of the down-going event selection for neutrinos below 1 PeV weakens rapidly with energy due to the rapidly increasing atmospheric muon background at lower energies [479]. Events found by this track selection in the ±500 s time window are shown in Fig. 1.62. No events were

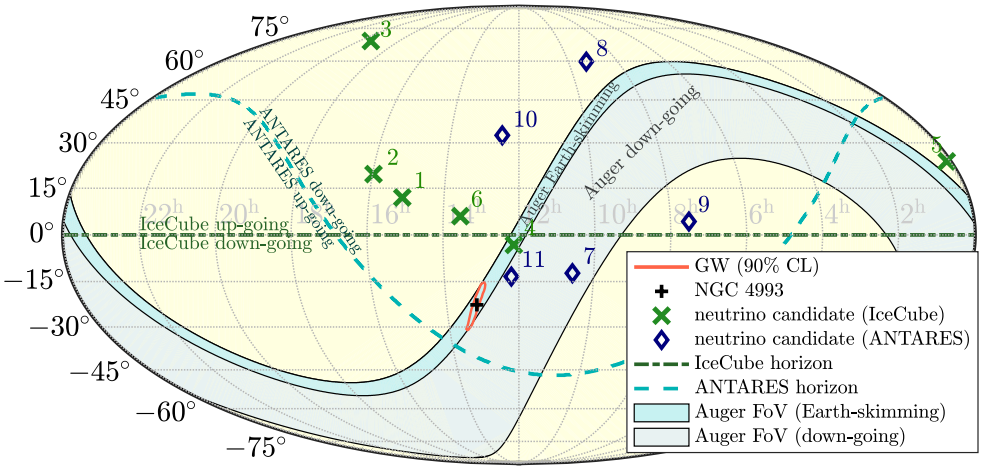

Fig. 1.62.: Localizations and sensitive sky areas at the time of the GW event in equatorial coordinates: GW 90% credible-level localization (red contour [227]), direction of NGC 4993 (black plus symbol [480]), directions of IceCube's and ANTARES's neutrino candidates within 500 s of the merger (green crosses and blue diamonds, respectively), ANTARES's horizon separating down-going (north of horizon) and up-going (south of horizon) neutrino directions (dashed blue line), and Auger's fields of view for Earth-skimming (darker blue) and down-going (lighter blue) directions. IceCube's up-going and down-going directions are on the northern and southern hemispheres, respectively. The zenith angle of the source at the detection time of the merger was 73.8° for ANTARES, 66.6° for IceCube, and 91.9° for Auger. The figure is taken from [479].

found to be spatially and temporally correlated with GW170817 [479]. No inclined showers passing the Earth-skimming selection (neutrino candidates) were found in Auger (see Fig. 1.62) in the time window ±500 s around the trigger time of GW170817 [479].

With the upcoming observation periods of Advanced LIGO-Virgo and with the gradual addition of KAGRA and LIGO-India detectors, the experience of the analyses carried by ANTARES (see Section 3) will be valuable for KM3NeT (see Section 2.4.4), a multi-km^3-sized neutrino telescope [173, 174, 175]. This can be substantially important for KM3NeT in the coming years for joint GW/neutrino searches.

The neutrino telescopes

2

> *The romance of science lies in its explorations. Equipped with his five senses, man explores the universe around him and calls the adventure Science.*
>
> **— Edwin Hubble**
> "The Exploration of Space",
> Harper's Magazine 158:732, 1929

The main focus of this chapter is the history and current situation of neutrino telescopes. The short review of the modern neutrino telescopes and their predecessors is done. Three neutrino telescopes are currently operating worldwide: Baikal-GVD neutrino telescope deployed in Lake Baikal in Russian Federation, ANTARES [481] in the deep Mediterranean Sea and IceCube [482] constructed at the South Pole deep in the Antarctic ice; with the decommissioning of ANTARES in 2019, even with the on-going construction of KM3NeT [175], the Global Neutrino Network (GNN)[1] will consist of three km^3-scale neutrino telescopes. In general, a neutrino telescope is composed of several semi-rigid structures called "strings" embedded deep in the water or ice and equipped along their entire length by an array of photomultiplier sensors detecting the Čherenkov light emitted by muons generated in neutrino interactions with matter near or in the detector. The detection principle to use water as a target for neutrinos goes back to Russian physicists Moisey Markov and Igor Zheleznykh in 1960-s [483, 484, 485]. The idea of "setting up apparatus in an underground lake or deep in the ocean in order to separate charged particle directions by Čerenkov radiation" (see Section 2.3.5) was suggested by Markov in 1960 [486]. The first step from conceptual ideas to large-scale experimental efforts was done by the DUMAND collaboration [487, 488, 489] that pioneered the technologies for underwater neutrino telescopes. The scientific goals and basic idea of the neutrino telescopes are given in Section 2.1 and Section 2.2 respectively. Section 2.3 introduces the detection principles of the underwater neutrino telescopes. In Section 2.3.1, the neutrino cross-section. In Section 2.3.2, the neutrino interactions and different event topologies is discussed. The propagation of neutrinos and muons are discussed in Section 2.3.3 and Section 2.3.4 respectively. The review of the important Čherenkov effect and radiation is given in Section 2.3.5. The brief description of the neutrino telescopes currently in operation such as Baikal/GVD, IceCube and KM3NeT is given in Section 2.4. The ANTARES detector design and its operation are described in detail in the next chapter.

[1] https://www.globalneutrinonetwork.org/

2.1 Scientific goals

Neutrinos at the UHE scale had to manifest themselves as confirmed observations; indeed, the modern multi-km^3-sized neutrino telescopes (completed and in construction) such as IceCube [482, 490, 491], KM3NeT [173, 174, 175] and Baikal-GVD [492, 493, 494] were remarkably close to dispelling that fact.

Before 2013, the highest energy neutrino recorded in the TeV energy range were neutrinos with several hundred TeV becoming the first atmospheric neutrino measurement to such high energies (up to 400 TeV) [495]. This has been surpassed later by the first-ever observation of PeV-energy neutrinos with IceCube, first-ever km^3-sized neutrino telescope, in 2013 [496] with the follow-up search of the existence of a diffuse flux of high-energy astrophysical neutrinos leading to the discovery of additional high-energy astrophysical neutrinos in the same year [11]. As the highest energy neutrinos ever observed and first of cosmic origin it satisfied the researchers' aspirations to set much higher, to energies above 1 PeV and opened the door for what can be called "neutrino astrophysics". A variety of astrophysical objects and mechanisms become accessible at the energies above 1 PeV, providing information that is complementary to that already obtained from electromagnetic or hadronic observations [497].

The recent detection of a high-energy neutrino by IceCube [14] associated with observations in γ-rays, by Fermi-LAT alert [425], and at other wavelengths, being for the first-ever detection of such a correlation between the neutrino and γ-ray skies. Such convincing evidence for ν-γ association suggested to TXS 0506+056 blazar possibly being an individually identifiable source of high-energy neutrinos, in turn, leading blazars to be the first identifiable sources of the high-energy astrophysical neutrino flux [15, 16].

2.2 Basic idea

The principal idea for a neutrino telescope is to build a matrix of light detectors inside a transparent medium such as deep water or ice in order to [117]:

- Provide large instrumented volume of a free target for neutrino interactions which cross-sections are very small (see Section 2.3.1);
- Provide shielding against secondary particles produced by CRs which can enhance the sensitivity to a very low flux of the high-energy neutrinos from astrophysical sources reducing remarkably the background. Showers induced by interactions of CRs with the Earth's atmosphere produce the atmospheric muons and atmospheric neutrinos. The shielding is required due to atmospheric muons that can penetrate the atmosphere and up to several km of ice/water. Moreover, the flux of down-going atmospheric muons exceeds the flux induced by atmospheric neutrino interactions by many orders

of magnitude (see Fig. 2.14) (see Section 2.3.6), decreasing with increasing detector depth.

- Provide efficient light transmission (see Section 3.4.1) of Čherenkov photons (see Section 2.3.5) emitted by relativistic secondary particles induced by the neutrino interaction;

- Provide longevity which plays a decisive role due to inaccessibility to the detector components in case of problems and in data collection for extremely rare or exceptional events detection.

2.3 Detection principle

The neutrino carries only a weak charge, and can therefore only interact via the weak force or via gravity. Neutrinos are detected by their interactions with a nucleon via the weak interaction. Figure 2.1 illustrates the detection principle of neutrino telescopes. There are two types of weak interaction, depending on the exchanged intermediate vector bosons, the W or the Z, involved to mediate the force. Charged current (CC) reactions are mediated by $W^{\pm}$ boson (see Eq. 2.1) (with mass M_W~80.379 GeV[2] [39]); neutral current (NC) reactions are mediated by Z^0 boson (see Eq. 2.2) (with mass M_Z~91.188 GeV[3] [39]).

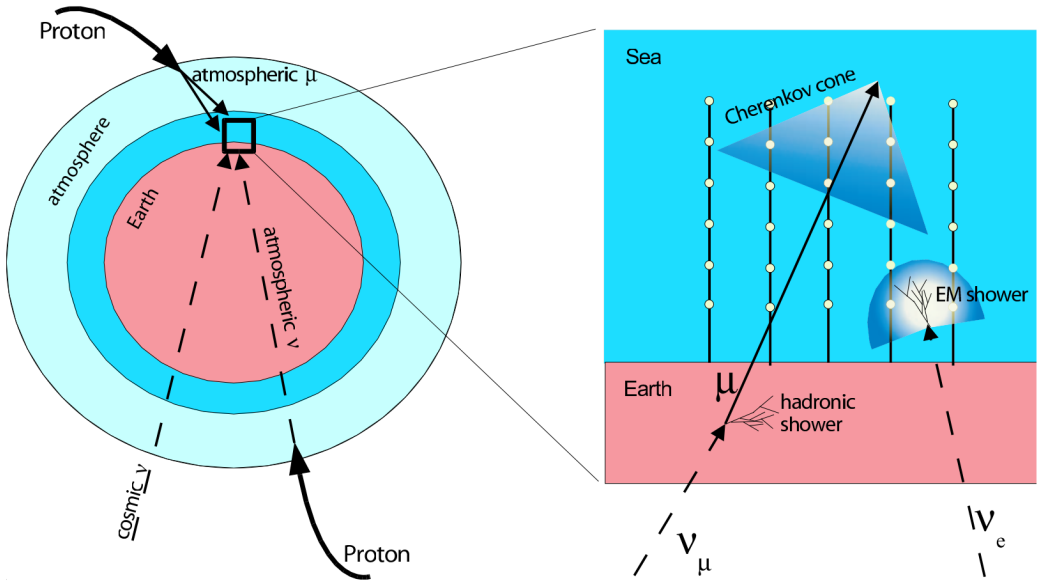

Fig. 2.1.: Detection principle of neutrino telescopes. After having traversed the Earth, neutrino interactions can produce up-going muons or electrons. The Čherenkov light they produce in the seawater is detected by an array of photomultiplier tubes. The main background consists of atmospheric muons. Up-going muons produced by atmospheric neutrinos also form a background. The figure is taken from [498].

[2] see Table A.3 in Appendix A.2.2.
[3] see Table A.3 in Appendix A.2.2.

$$\begin{aligned} \nu_l + N &\xrightarrow{W^-} l^- + X, \\ \bar{\nu}_l + N &\xrightarrow{W^+} l^+ + X, \end{aligned} \tag{2.1}$$

$$\nu_l + N \xrightarrow{Z^0} \nu_{l'} + X, \tag{2.2}$$

where l denotes a charged lepton, N is the target nucleus and X indicates a hadronic cascade. There is no charged lepton in the final state for the NC channel. Figure 2.2 shows the corresponding Feynman diagrams.

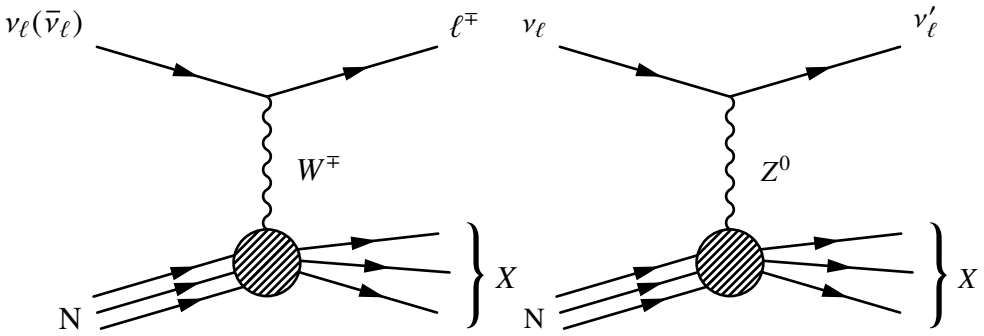

Fig. 2.2.: Feynman diagrams showing the Charged Current (CC) interaction, which produces a lepton in a final state (denoted as $l^\mp$), and a Neutral Current (NC) interaction, which keeps the neutrino unchanged except for the loss of energy (denoted as ν'. Both cases lead to energy being transferred to the quark in the nucleon, which recoils and produces a shower of hadronic particles denoted as X.

2.3.1 Neutrino cross-section

The knowledge of neutrino cross-section in the high-energy region is becoming increasingly important due to recent discoveries of astrophysical neutrinos (see Section 2.1). As a telescope focused on the detection of high-energy extraterrestrial neutrinos, the ANTARES is primarily interested in the CC muon neutrino scattering with matter nuclei because of the higher detection probability for the muon neutrinos (and muon anti-neutrinos): the longer absorption length of muons produced in the CC interactions leads to higher event rates [499, 500].

The differential cross-section for the neutrino CC interactions at leading order is given by [499]:

$$\frac{d^2\sigma_{\nu N}}{dxdy} = \frac{2G_F^2 M_N E_\nu}{\pi}\left(\frac{M_W^2}{Q^2+M_W^2}\right)^2\left[xq(x,Q^2) + x\bar{q}(x,Q^2)(1-y)^2\right], \tag{2.3}$$

where:

- G_F is Fermi coupling constant (~1.166×10^{-5} GeV^{-2}[4] [39]);

[4] see Table A.3 in Appendix A.2.2.

- M_N is the mass of the nucleon target;
- M_W is the mass of the mediator, an intermediate-boson W;
- E_ν is the incident (incoming) neutrino energy;
- $-Q^2$ is the invariant 4-momentum transfer between the incoming neutrino and outgoing lepton (e.g., a muon). So, $Q^2 = -q^2 > 0$, where $q = p_\nu - p_l$ and p_ν, p_l denote the 4-momenta of the incoming neutrino and outgoing lepton respectively (see Fig. 2.2);
- $x = \frac{Q^2}{2M_N\nu}$ is Bjorken scaling variable (scale is valid when $s = 2M_N E_\nu \gtrsim M_W^2$ [501], where s is the neutrino-nucleon center-of-mass energy squared), $\nu = E_\nu - E_l$ is the energy loss in the lab (target) frame (E_l is the energy of outgoing lepton) which characterizes the energy transfer to the outgoing lepton and to the final hadronic state, i.e., the energy of the hadronic system X (see Fig. 2.2);
- $y = \frac{\nu}{E_\nu}$ is Bjorken scaling variable (inelasticity, shows the relative energy transfer), $\nu = E_\nu - E_l$ is the energy loss in the lab (target) frame which characterizes the energy transfer to the outgoing lepton and to the final hadronic state, i.e., the energy of the hadronic system X (see Fig. 2.2). Also, $1-y$ can be expressed as the ratio between E_ν and E_l, i.e, $1-y = E_l/E_\nu$. In fact, one can readily see that the ratio between x and y is as follows: $xy = \frac{Q^2}{2M_N E_\nu}$;
- $q(x,Q^2)$ and $\bar{q}(x,Q^2)$ is the sum of quark and antiquark parton distribution functions [502] which represent the probability density for finding a particle with a certain longitudinal momentum fraction x and momentum transfer Q^2.

The quark parton distribution functions are expressed as [499]:

$$\begin{aligned} q(x,Q^2) =& \frac{u_v(x,Q^2) + d_v(x,Q^2)}{2} + \frac{u_s(x,Q^2) + d_s(x,Q^2)}{2} \\ &+ s_s(x,Q^2) + b_s(x,Q^2) \\ \bar{q}(x,Q^2) =& \frac{u_s(x,Q^2) + d_s(x,Q^2)}{2} + c_s(x,Q^2) + t_s(x,Q^2), \end{aligned} \tag{2.4}$$

where the subscripts v and s label valence and sea quarks contributions respectively, and u, d, c, s, t, b denote the distributions for various quark flavors in a proton. Due to the great mass of the top quark, $t\bar{t}$ pairs are a negligible component of the nucleon over the Q^2-range relevant to neutrino-nucleon scattering [499].

Using Bjorken scaling variables, x and y, the scattering angle, θ, i.e. angle of produced lepton relative to incoming neutrino can be expressed as [503]:

$$cos\theta = 1 - \frac{xy}{1-y}\frac{M_N}{E_\nu} \tag{2.5}$$

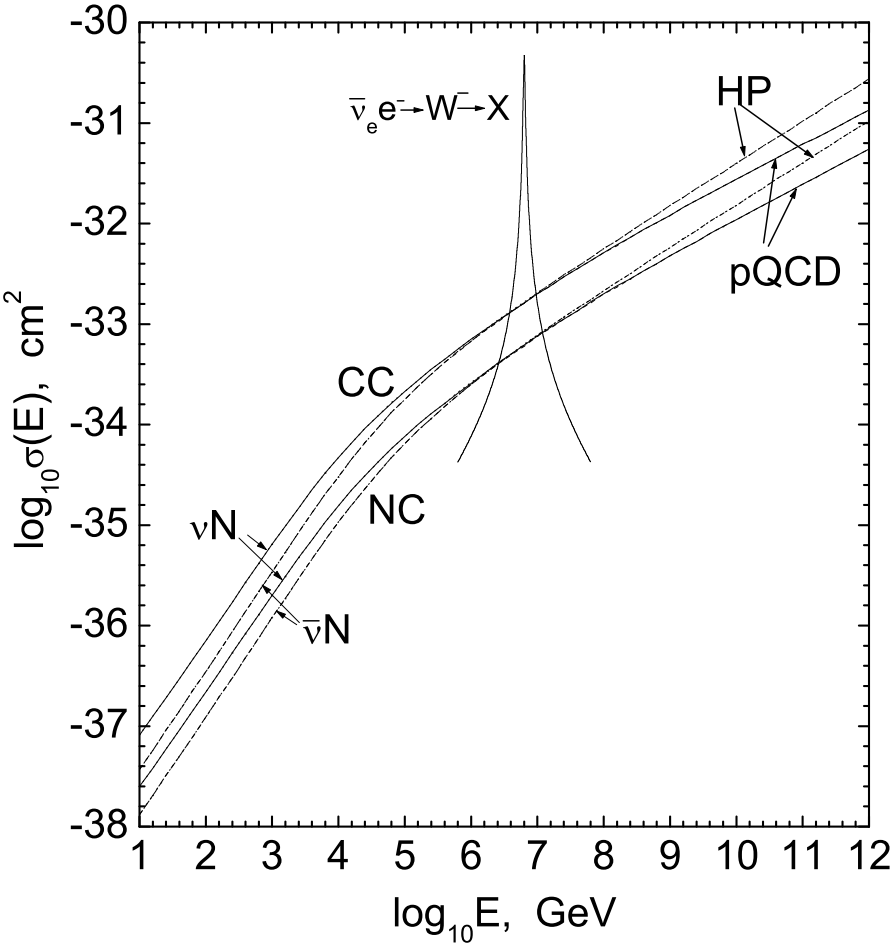

Fig. 2.3.: Neutrino (solid line) and anti-neutrino (dashed) cross-sections at high energies for Charged Current (CC) and Neutral Current (NC) interactions with the matter nuclei according to the pQCD CTEQ5 parameterization. At energies E_ν>1 PeV, different extrapolation techniques as an hard-pomeron [504] enhanced model [505] (HP) or an extrapolation of the pQCD CTEQ5 parameterization is used. The so-called Glashow resonance at $E^{res}_{\bar{\nu}_e}$~6.3 PeV is shown. The figure is taken from [503].

The Eq. 2.5 is proved by the kinematics since $Q^2 = -q^2 = 4E_\nu E_l sin^2(\frac{\theta}{2})$ [501]:

$$cos\theta = 1 - \frac{xy}{1-y}\frac{M_N}{E_\nu} = 1 - \frac{Q^2}{2M_N E_\nu}\frac{E_\nu}{E_l}\frac{M_N}{E_\nu} = 1 - \frac{Q^2}{2E_\nu E_l} = 1 - 2sin^2(\frac{\theta}{2}) \qquad (2.6)$$

Various scattering processes must be taken into account while generating neutrino interactions with matter: deep inelastic scattering (DIS), quasi-elastic nucleon (QE) scattering, several nucleon N and Δ resonance (RES) channels (with mass values below 2 GeV) [500] (QE scattering is predominant in neutrino interactions for neutrino energies less than ~2 GeV [497]). Thus, the QE and RES channels are often neglected since their contribution is only significant at low energies ($E \leq 10$ GeV) [500]. As a result, the DIS channel is dominant for neutrino interactions with matter at the energy range of interest for modern neutrino telescopes, i.e. for ($E \geq 10$ GeV).

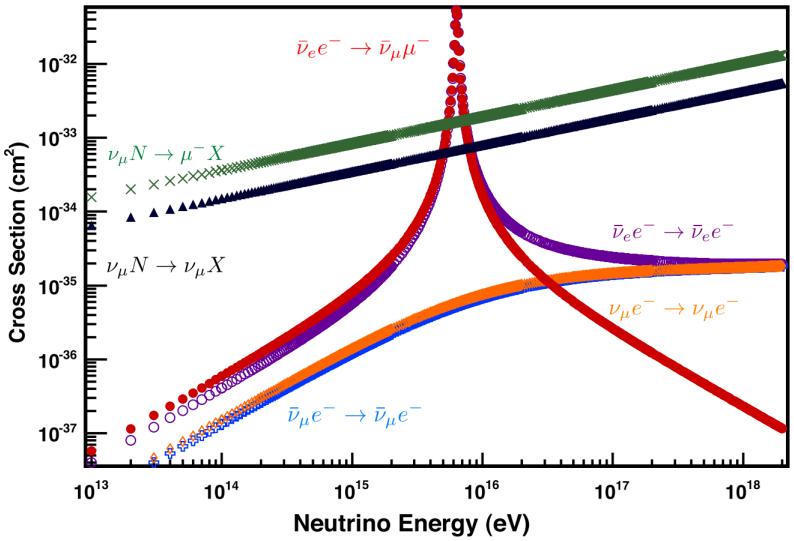

Fig. 2.4.: Neutrino electron and nucleon scattering processes in the UHE regime ($E_\nu \geq 10^4$ GeV). The electron interactions $\bar{\nu}_\mu e^- \to \bar{\nu}_\mu e^-$ (crosses, blue), $\nu_\mu e^- \to \nu_\mu e^-$ (diamonds, orange), $\bar{\nu}_e e^- \to \bar{\nu}_e e^-$ (hollow circles, violet), $\bar{\nu}_e e^- \to \bar{\nu}_\mu e^-$ (filled circles, red), and the nucleon CC (cross markers, green) and NC (filled triangles, black) interactions are shown. The leptonic W resonance channel with decay into an electron (violet) and muon (red) is clearly evident. The figure is taken from [497].

At low neutrino energies such that $E_\nu \ll M_W^2/2M_N \approx 5$ TeV, Q^2 can be neglected in the W propagator and in this case the average DIS νN cross-sections rises linearly (see Fig. 2.3) with the neutrino energy [506]:

$$\begin{aligned} \sigma_{DIS}(\nu N) &\simeq 0.67 \times 10^{-38} E_\nu [\text{GeV}] \text{ cm}^2 \\ \sigma_{DIS}(\bar{\nu} N) &\simeq 0.34 \times 10^{-38} E_\nu [\text{GeV}] \text{ cm}^2 \end{aligned} \tag{2.7}$$

At even lower energies such that $E_\nu < 100$ TeV, QE and RES contributions to CC interactions become significant, Q^2 has to be small enough to allow a coherent interaction with the complete target nucleon and in this case cross-sections are essentially constant with energy [506]:

$$\begin{aligned} \sigma_{QE}(\nu_\mu N) + \sigma_{RES}(\nu_\mu N) &= 1.50 \times 10^{-38} \text{ cm}^2 \\ \sigma_{QE}(\bar{\nu}_\mu N) + \sigma_{RES}(\bar{\nu}_\mu N) &= 1.58 \times 10^{-38} \text{ cm}^2 \end{aligned} \tag{2.8}$$

At high energies such that $E_\nu \gg M_W^2/2M_N \approx 5$ TeV, QE and RES contributions to CC interactions become negligible [506]. On the other hand, the W propagator limits the growth of Q^2 to $\langle Q^2 \rangle \sim M_W^2$ and the cross-section is dominated by the behavior of the distribution functions at small x [506].

At energies $E_\nu \gtrsim 1 \times 10^6$ GeV, the DIS νN-cross-sections can be described in the framework of perturbative Quantum Chromodynamics (QCD), pQCD [503]. The differential neutrino-nucleon cross-sections in the energy range addressed by high-energy neutrino telescopes is

shown in Fig. 2.3 which have been obtained with the CTEQ5 [507] parametrization [508] for the parton distribution functions of the nucleon.

As seen in Fig. 2.3, the neutrino cross-section for NC predicted to be 1/3 of the CC cross-section. At energies above 1 PeV, the $\bar{\nu}N$ cross-section becomes nearly identical to the νN cross-section, for both NC and CC interactions. This is due to the interaction contribution of sea quarks, which exist as equal proportions of q and $\bar{q}$ [509].

The peak observed at energy ~6.3 PeV (see Fig. 2.3) corresponds to the Glashow resonance [510]. The cross-section for this process is generalized in [511]. Since $m_e \ll M_N$, at high energies practically all νe^--cross-sections are negligibly small with the exception of resonant W^- production at $E^{res}_{\bar{\nu}_e}$~6.3 PeV [503]:

$$\bar{\nu}_e + e^- \rightarrow W^- \rightarrow X. \tag{2.9}$$

The resonant effect should exceed by more than one order of magnitude the background due to the nonresonant neutrino events [511]. Figure 2.4 shows more detailed comparison of Glashow resonant and DIS cross-sections. As seen in Fig. 2.4, W^--boson decay peak is about 50 and 100 times higher than CC and NC interactions cross-sections respectively.

As the cross-sections of the interactions are on the weak scale, large detector volumes, such as in multi-km^3-sized KM3NeT neutrino telescope [173, 174, 175] (see Section 2.4.4), are required to allow them to be sensitive to astrophysical neutrino sources.

2.3.2 Neutrino signatures

The different neutrino signatures correspond to diffrent types of interaction (CC, NC or Glashow resonance) and neutrino flavors involved (ν_l, where $l = e, \mu, \tau$) are observed by a neutrino telescope. All possible channels are gathered in Fig. 2.5 and discussed below.

NC interactions of neutrinos of all flavors. Neutrinos of all flavor ν_l interacting through NC produces only a hadronic shower, or cascade, and no charged lepton capable of leaving a detectable track. Only a small fraction of the neutrino energy y is transferred to a hadronic shower; the residual energy is carried away by the outgoing neutrino [512]. As a result, the error on the true energy estimation increases and the total energy of the incoming neutrino can not be determined; the remaining deposited energy is seen as a hadronic shower. In ANTARES, the shower position is reconstructed with a precision of about 1 m, and for the neutrino, direction resolutions of $2^\circ - 3^\circ$ are achieved; a statistical uncertainty for the shower energy of about 5%−10% is obtained [512]. Topologically, the NC event signature indistinguishable from CC ν_e event signature.

CC interactions of electron neutrinos. Electron neutrinos ν_e interacting through CC produces an electromagnetic and a hadronic shower. In CC ν_e, the two initiated showers combine, and their sum energy equals the incoming neutrino energy [513]. In contrast to ν_e

NC interaction, the neutrino in ν_e CC interaction changes to an electron, which initiates a leptonic cascade. The interaction length of the particles produced in the shower is small and the shower looks like a point-like source. Both showers overlap and look like one single shower. The hadronic shower has a complex structure with hadronic or electromagnetic sub-showers, depending on the decay modes of individual particles in the shower [175]. In ANTARES, such events are reconstructed with a median angular resolution of the order of 3° and a relative energy resolution as low as 10% in the case of CC ν_e interactions above some tens of TeV [514, 316]. In KM3NeT [173, 174, 175], the ν_e CC event is the best in a sense of energy estimation since 1σ energy resolution is around 5%, while the median directional resolution is 1.5° [175]. Such energy resolution is close to the limit imposed by variations in the hadronic cascade component, which yields less Čherenkov light (~90% at 100 TeV) than the electromagnetic component [175].

CC interactions of muon neutrinos. Muon neutrinos ν_μ interacting through CC produces a hadronic shower and a muon. The outgoing muon signature generated in ν_μ CC interactions is referred to as a track. Such a muon, traversing the medium at a relativistic speed, polarizes it, producing the so-called Čerenkov radiation (see Section 2.3.5) along its track. The Čherenkov light emitted by muons is then detected. For ν_μ, a median angular resolution as low as 0.4° is achieved [514, 316]. The muon can propagate from a few hundred meters up to several kilometers (as illustrated in Fig. **??**) before decaying into an electron; a muon transit time through the whole ANTARES detector is 2.2 μs (see Section 3.3.3). The hadronic shower produced in ν_μ CC interactions is referred to an *inverted lollipop* signature, which ends up a muon track, while the muon decay produces the *lollipop* signature. Both, a shower and a track can be identified in ANTARES. Muon losses in pure water are mostly dominated by radiative processes at energies above TeV and by ionization at energies less than TeV. The muon propagation is discussed in detail in Section 2.3.4.

CC interactions of tau neutrinos. The tau can decay [515]:

> **Leptonically** In ν_τ/l channel, the electrons (BR: 17.82% [39]) or muons (BR: 17.39% [39]) are produced: $\tau \rightarrow l\nu_l\nu_\tau$, where $l = e, \mu$.
>
> **Hadronically** In ν_τ/h channel, the charged and neutral pions and/or kaons (BR: 64.79% [39]) are produced. The hadronic decay modes have a wide variation with small branching fractions. The most significant decay modes[5] are [39]: $\pi^-\pi^0\nu_\tau$ (BR: 25.49%), $\pi^-2\pi^0\nu_\tau$ (BR: 9.26%), $\pi^-\pi^-\pi^+\nu_\tau$ (BR: 8.99%), $\pi^-\pi^-\pi^+\pi^0\nu_\tau$ (BR: 2.74%), $\pi^-\pi^-\pi^+\nu_\tau$ (BR: 8.99%).

The τ decays into a muon (BR: 17.36% [39]) or another cascade (BR: 82.64% [39]), either be an electromagnetic (BR: 17.82% [39]) or a hadronic (BR: 64.79% [39]).

[5] Those with BR>2% are listed

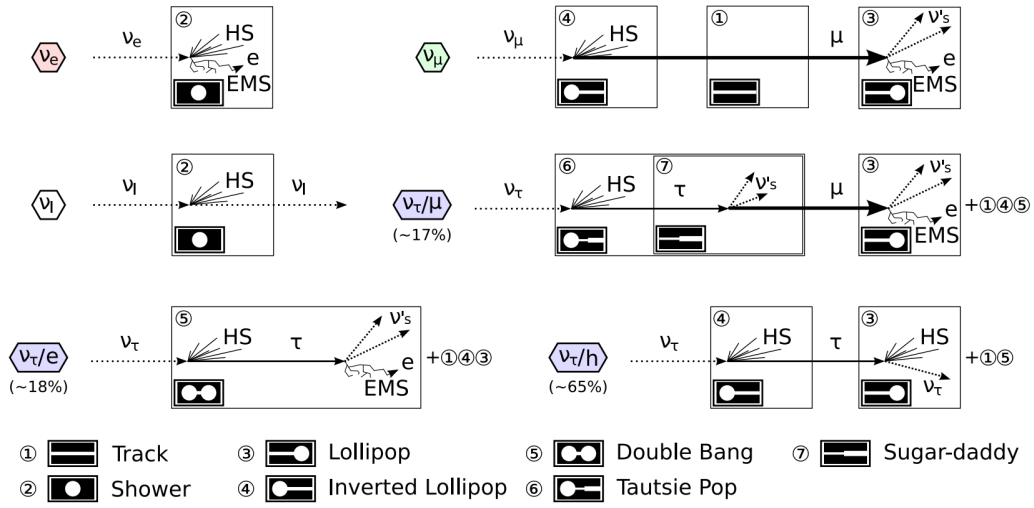

Fig. 2.5.: Different neutrino event signatures in neutrino telescopes. HS and EMS denote hadronic and electromagnetic showers respectively. The figure is taken from [516].

Tau neutrinos ν_τ interacting through CC produces a hadronic shower and traces different event signatures such as *double bang*, *lollipop*, *inverted lollipop*, *sugar daddy* and *tautsie pop*:

Double Bang The signature is a double cascade[6]: a big hadronic shower from the initial ν_τ CC interaction, a muon-like τ track, and then a second big particle cascade (usually 3 times larger), due to the τ decay, where the electromagnetic shower is produced [517] (see Fig. 2.5). The τ which connects the two showers will also emit a Čherenkov light [515]. The charged τ will be hard to resolve from the bright light and not very different times from the cascades, but simply connecting the two cascades will suffice to make an unambiguous association [517]. The two showers are separated by the tau decay length $L_\tau = \gamma c t_\tau \approx 50\ (E_\tau/\text{PeV})$ m (neglecting energy losses along the track) [518]. To be fully contained in the detector volume of ANTARES, a tau with a decay length about 50 m per PeV can have energy up to few PeV; thus, the *double bang* signature is only expected to be detectable for ν_τ with energy at PeV scale[7]. Above ~20 PeV, the τ decay length exceeds 1 km, a scale of modern km^3 neutrino telescopes and both showers are no longer contained within the volume of such detectors [518]; the resulting signature of a τ track and one shower is known as a *lollipop* [320]. In KM3NeT [173, 174, 175], both showers can be resolved when separated by 10 m[8] or more, i.e. for ν_τ at ~250 TeV and above.

Lollipop The signature is a track ending in a shower [515]: the τ created outside of the fiducial volume of the detector enters it and decays to produce a shower (BR:

[6] Can be created only in CC ν_τ interactions

[7] At energies below this scale, the two *double bang* showers are irresolvable but there is an energy range in which nearby DOMs see the double-pulsed waveform [515]. Such a signature is known as a *double pulse*.

[8] It is expected that an even closer separation will be resolvable.

82.64% [39]) inside a volume. In order to detect a *lollipop* event, these conditions must be fulfilled [320]:

- The shower, either an electromagnetic or a hadronic, produced by the τ decay must occur within the fiducial volume of the detector and be of sufficient energy to trigger the detector.
- The τ track must be long enough (within the detector) to be reconstructed and separable from the shower.

Inverted Lollipop The signature is a shower ending in a track [515]: the τ is created inside the fiducial volume of the detector and decays undetectably outside of it. Thus, it resembles a *lollipop* but created in inverse order. The *inverted lollipop* is often be confused with a hadronic shower in which a ~100 GeV muon is produced [320]. A μ can have a CC interaction in the fiducial volume, creating the combination of a shower and a muon, which will be very hard to distinguish on an event-by-event basis from *inverted lollipops* [515].

Sugar Daddy The signature is a muon [515]: the τ created outside of the fiducial volume of the detector enters it and decays to produce a muon rather than a shower (BR: 17.36% [39]) inside a volume. The τ is much heavier than μ and thus suffers much less bremsstrahlung and will emit significantly less light along its length compared to its lighter daughter muon [515]. The moment the τ decays into a muon is also the moment of a sudden increase in brightness by an amount that should be detectable in a neutrino telescope [518].

Tautsie Pop The signature is *inverted lollipop*-like event together with two neutrinos causing the measured shower/track energy ratio, E_{shower}/E_{track}, to be larger by a factor of 2-3 in τ events than in background events [515]: a low-energetic τ decays[9] immediately into a muon (very similar to the *inverted lollipop* event) with the additional two neutrinos that leave the shower carrying a significant amount of energy in turn leading to a larger measured shower/track energy ratio.

The *double bang* and *lollipop* events are signatures unique to τ neutrinos [320]. The detection of τ neutrinos offers an excellent method for detecting astrophysical neutrinos, since there is essentially no atmospheric τ neutrino background and both signatures provide a clear and background-free evidence of ν_τ detection [517, 519, 518].

The Earth is nearly transparent to low-energy neutrinos but opaque to neutrinos above 40 TeV [520] (see Section 2.3.3). Nonetheless, ν_τ well above 100 TeV can produce a signal in ANTARES because unlike the $e^\pm$ and $\mu^\pm$ produced in ν_e and ν_μ interactions, the $\tau^\pm$ produced in ν_τ interactions decay before they are absorbed, producing ν_τ of lower energy which continue along the original ν_τ flight path, but with decreasing interaction

[9] Decay length and is too short to be resolved; the products and vertices are indistinguishable [515].

probability [506]. As soon as ν_τ energy falls to about 40 TeV, it propagates the Earth and produces VHE events in the detector, a signal for ν_τ. In addition, the flux of ν_τ from a given source would be constant during the Earth's rotation, whereas the flux of ν_μ would vary with the sidereal day because of the change in elevation seen from ANTARES[10] [506].

Because of neutrino oscillation, the cosmic neutrino flux measured at Earth should constitute a flavor ratio of around $\Phi_{\nu_e}:\Phi_{\nu_\mu}:\Phi_{\nu_\tau}$ = 1:1:1 [517] (see Section 1.5.2).

2.3.3 Neutrino propagation in the Earth

The majority of neutrinos that reach the Earth can traverse it without being affected and leaving any detectable trace. However, the neutrino-nucleon interaction cross-section increases with increasing neutrino energy (see Fig. 2.4) and the absorption depends on the cross-section. Figure 2.6 shows the predicted zenith angle distribution for different neutrino energies. The Earth attenuation effects become important for neutrinos with energy greater than tens of TeV. The interaction length(see Eq. 2.10) for neutrino $\mathcal{L}_{int}(E_\nu)$ becomes equal to the Earth's diameter when $E_\nu \simeq 40$ TeV [520]. Since the Earth's diameter exceeds the CC interaction length of neutrinos with energy greater than 40 TeV, the Earth becomes opaque to VHE neutrinos [499, 521]. Such neutrinos with energy greater than tens of TeV are expected to be absorbed as they traverse through the Earth but this effect depends on the distance traveled by neutrinos and on their energy. Thus, studying the zenith and energy distributions of TeV atmospheric neutrinos passing through the Earth [522] offers an opportunity to infer the Earth's density profile [523, 524, 525, 526], i.e. performing neutrino tomography of the Earth. The neutrino tomography method deduces the Earth's density structure from the number of neutrino-induced muon events. The idea of the method is straightforward: the Earth becomes opaque to neutrinos whose energy exceeds tens of TeV and the diameter of the Earth represents one absorption length for neutrinos with such energy. The atmospheric neutrinos which are produced in collisions of CRs with nuclei in the Earth's atmosphere have a spectrum with a steeply falling energy spectrum of $E_\nu^{-3.7}$ become rare at these energies; therefore, the

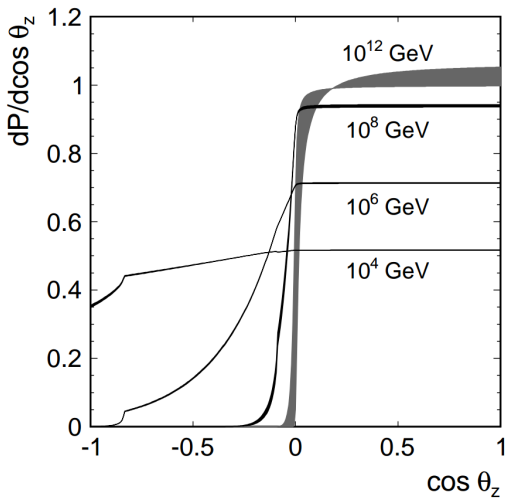

Fig. 2.6.: Predicted zenith angle distribution of neutrinos observed in a detector, after traversing the Earth for different energies for the standard-model cross-sections. The width of each band is due to the cross-section uncertainties. Here, $cos\theta_z = \pm 1$ corresponds to vertically downward- and upward-going neutrinos, respectively. The breaks in the distributions at $cos\theta_z = -0.1$ and $cos\theta_z = -0.8$ are due to the neutrino trajectory intersecting the Earth's mantle and core, respectively [502]. The figure is taken from [502].

[10] Such variation of ν_μ flux could not be observed from IceCube, because it is located at the South Pole.

cosmic neutrinos would perform radiography of the Earth's interior as it moves relative to the cosmic source [523]. The atmospheric muon background is small at such energies, and it is beneficial to look for events induced by the cosmic neutrinos from directions above the horizon [527, 173].

The study of the Earth's internal structure based on neutrino absorption has been performed with IceCube [522] and the potential of the method based on atmospheric neutrino oscillations has been investigated within KM3NeT-ORCA and IceCube-PINGU projects [528, 529, 530, 531]. The studies with KM3NeT-ORCA [530, 531] show that after ten years of operation the Earth's electron density in both the lower mantle and the outer core can be measured with a precision of a few percent.

To quantify the effect of neutrino absorption the Earth density is taken into account. To date, the Preliminary Reference Earth Model (PREM), suggested by Dziewonski & Anderson in 1981 [532], is one of the best known and comprehensive Earth density models. Figure 2.7 illustrates a profile view of the variation in the density of Earth with the depth that comes from the PREM model. This model is based on the analysis of years of seismic waves from earthquakes, volcanic eruptions, etc. It is a reference model since it has only radial variations of density (one-dimensional model) and provides the average Earth properties as a function of radius. It includes the seismic velocities, elastic properties, attenuation, density, and auxiliary parameters such as gravity, pressure, etc. Figure 2.8 shows the amount

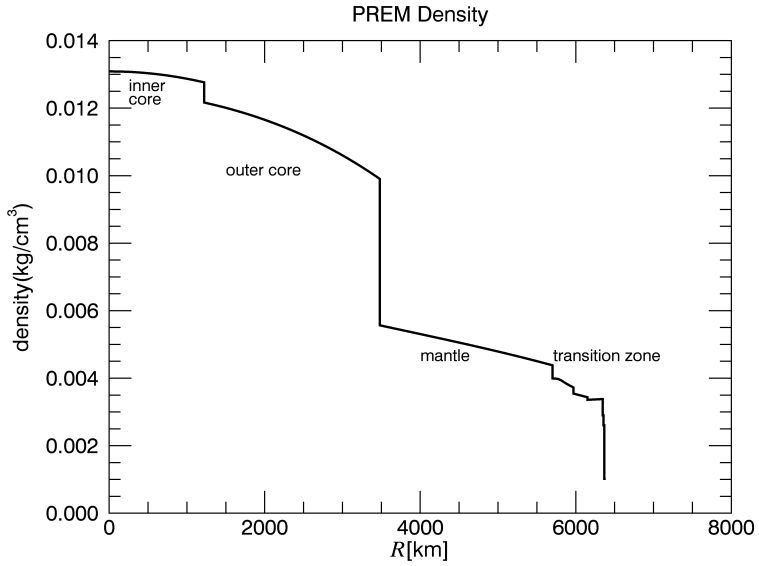

Fig. 2.7.: The density profile of the Earth with respect to radius according to the PREM model. The kink at 1221 km [532] is due to the boundary between the inner core and outer core. The kink at 3480 km [532] is due to the boundary between the core and mantle. The figure is taken from [533].

of matter $z(\theta)$ that the up-going neutrino encounters while propagating through the Earth ($z(\theta) = 0$ for down-going events). The column density enhancement at $\theta > 145°$ is due

to the increased density of the Earth's core. The probability of a neutrino to survive from absorption during propagation through the Earth, $P_{\oplus}$, is given by [499, 521]:

$$P_{\oplus}(E_\nu, \theta_\nu) = e^{-z(\theta)/\mathcal{L}_{int}(E_\nu)}, \tag{2.10}$$

where $\mathcal{L}_{int}(E_\nu) = 1/(\sigma_{\nu N}(E_\nu)N_A)$ is the interaction length that corresponds to the total (CC plus NC) cross-section $\sigma_{\nu N}(E_\nu)$. The N_A stands for Avogadro's number, $N_A = 6.022 \times 10^{23}\text{mol}^{-1} = 6.022 \times 10^{23}\text{cm}^{-1}$ (water equivalent) [39]. As stated in Section 5, this probability is taken into account in the calculation of the expected event rate. The

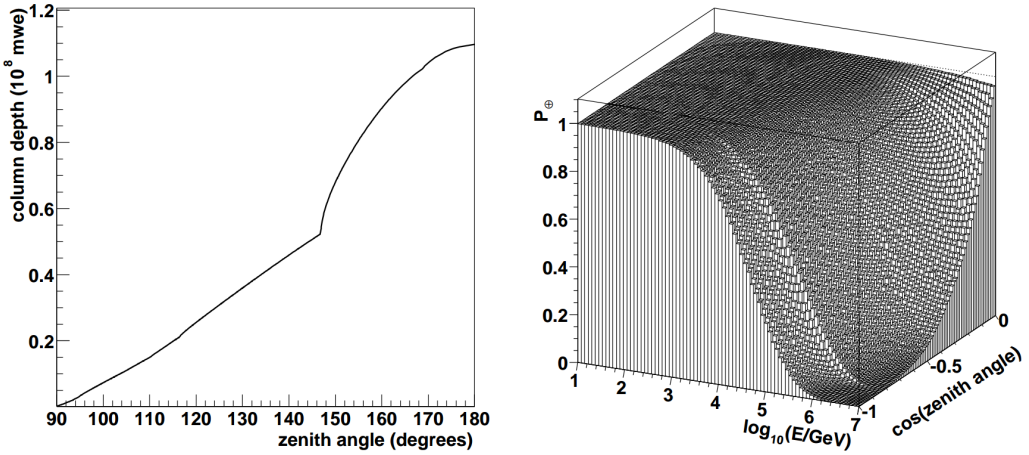

Fig. 2.8.: *Left:* Thickness of the Earth (in meters of water equivalent, mwe) as a function of the neutrino direction. Based upon PREM. The kink at $\theta > 145°$ is caused by the density discontinuity associated with the boundary of the Earth's core. *Right:* The probability of a neutrino to traverse the Earth without undergoing an interaction as a function of the direction (zenith angle) of the neutrino and its energy. The figures areken from [498].

Earth becomes opaque from up-going directions at the high energies (see Fig. 2.8) due to increased neutrino cross-section. The absorption for neutrinos from the near-horizontal direction (equivalent to 90 degrees in Fig. 2.8) is small and the Earth is unable to absorb neutrinos from that direction since the amount of matter crossed is negligible. Thereby, the neutrino telescopes are sensitive to UHE neutrinos with energies above 1 PeV mostly in those directions.

However, one should also take into account that the Earth never becomes opaque to ν_τ since the τ^- produced in a CC ν_τ interaction decays back into new ν_τ before losing too much energy [534, 535, 520]. This effect is called tau regeneration (see Section 2.3.4). Also, such penetration of tau neutrinos through the Earth above 100 TeV provides an experimental signature for neutrino oscillations [534, 535, 520]. The appearance of a ν_τ component would be evident as a flat zenith angle dependence of a source intensity at the highest neutrino energies and the differential attenuation of ν_μ versus ν_τ can be used in existing and future multi-km^3-sized neutrino telescopes such as KM3NeT [173, 174, 175] (see Section 2.4.4)(see Section 2.4.4), IceCube [482, 490, 491] (see Section 2.4.3) and Baikal-GVD [536, 537] (see Section 2.4.2).

2.3.4 Muon propagation

Muon neutrinos are especially interesting in a search for cosmic point sources of neutrinos with energies larger than ~1 TeV [117]. In this energy range, ν_μ interaction can occur outside the detector volume, while in most cases muons are energetic enough to completely traverse the detector [117]. This gives a clean experimental signal which allows for accurate reconstruction of muon direction, closely correlated with the neutrino direction [117]. The relation between neutrino and muon directions is essential for the concept of a neutrino telescope [117]. Since neutrinos are not deflected by (extra-) galactic magnetic fields, it is possible to trace the muon back to the neutrino source which is equivalent to traditional astronomy where photons point back to their source [117].

The mean square root mismatch angle θ between the incident neutrino and the outgoing muon directions is decreasing with the square root of the neutrino energy [538]:

$$\sqrt{\langle\theta^2\rangle} \approx \frac{1.5^\circ}{\sqrt{E_\nu[\mathrm{TeV}]}}. \tag{2.11}$$

The average scattering angle $\theta_{\nu\mu}$ between the incident neutrino and the outgoing muon in the CC channel can be approximated by [506]:

$$\langle\theta_{\nu-\mu}\rangle \approx \frac{0.7^\circ}{(E_\nu[\mathrm{TeV}])^{0.6}}, \tag{2.12}$$

where E_ν is the neutrino energy. As seen in Fig. 2.9, at 1 TeV the average difference between the incident neutrino direction and the outgoing muon is about 0.7°.

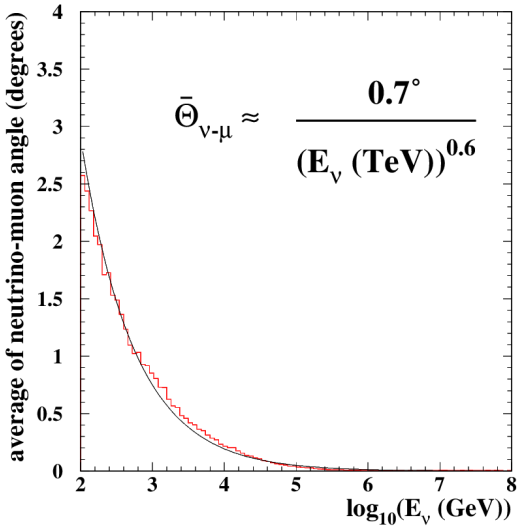

Fig. 2.9.: Angular difference between the direction of the incident neutrino and the muon track at the detector; the functional form shown reproduces the observed energy dependence well (solid curve). The figure is taken from [506].

During the propagation in rock, ice or water, the muon undergoes multiple scattering. The deviation of the muon direction due to the scattering process after traveling a distance X (in units of g/cm2) in the medium is given by [39]:

$$\theta_{ms} = \frac{13.6\mathrm{MeV}}{E_\mu}\sqrt{\frac{X}{X_0}}\left[1 + 0.0038\ln\left(\frac{X}{X_0}\right)\right], \tag{2.13}$$

where X_0 is the radiation length of the medium.

Despite suffering multiple Coulomb scattering while traversing a rock, ice or water, the deviation θ_{ms} described in Eq. 2.13 is an order of magnitude smaller than the scattering angle $\theta_{\nu-\mu}$ described in Eq. 2.12; thus, the effect of multiple Coulomb scattering can be neglected. As a result, the muon direction can be reconstructed with an accurate estimation of the

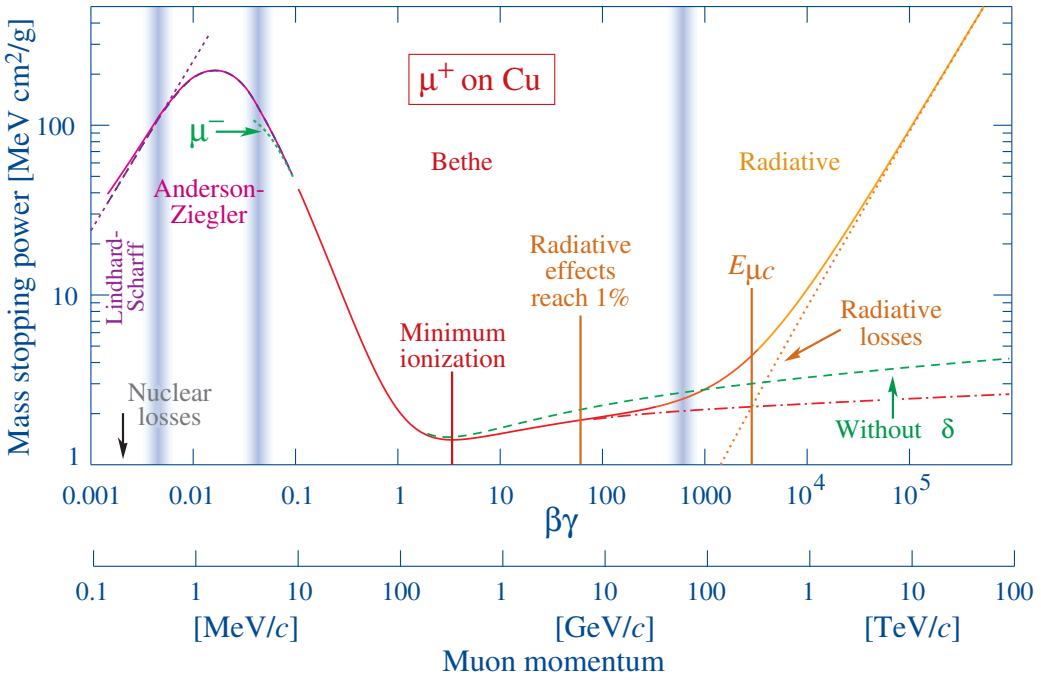

Fig. 2.10.: Mass stopping power (i.e. average energy loss) of muons in copper as a function of muon momentum $\beta\gamma = p/Mc$. Solid curves indicate the total stopping power. Vertical bands indicate boundaries between different approximations discussed in [39]. The muon critical energy $E_{\mu c}$ defined as the energy for which ionization and radiative losses are equal (at ~1 TeV) is shown. The correction to the energy loss due to the production of δ-rays is also marked. The dE/dx in the radiative region is not simply a function of β. The figure is taken from [39].

neutrino direction since the muon retains its original direction to a very good approximation. This, in turn, leads to a precise localization of the neutrino source in the sky, which is essential for neutrino astronomy. The precision obtained in Monte Carlo simulations is of the order of less than 1° in ice, and ~0.2° in water [117]. Muon losses energy due to several processes including ionization, pair production, bremsstrahlung, and photonuclear interactions [539] (see Fig. 2.11):

Ionization Atoms in the medium are ionized by a traverse of a charged particle, e.g., a muon. Ionization becomes dominant over radiative processes (pair production, bremsstrahlung, and photonuclear interactions) at energies less than TeV (see Fig. 2.11) and almost constant at about 0.3 GeV per m.w.e. Rarely but the muons able to lose a non-negligible fraction of energy with the production of high-energy recoil electrons, known as *knock-on electrons* or *δ-rays* (see corrections due to this effect in Fig. 2.10).

Pair production An e^+e^- pair [540, 541, 542] is produced. It becomes dominant over ionization at energies beyond 1 TeV (see Fig. 2.11).

Bremsstrahlung Deceleration of the fast-moving charged particle in the Coulomb field of a nucleus by emitting a fraction of its kinetic energy in the form of real

photons [543, 540]. IT becomes dominant over ionization at energies beyond 1 TeV (see Fig. 2.11).

Photonuclear interactions Inelastic lepton-nucleon or lepton-nucleus scattering process which goes through a virtual photon exchange [544, 545]. IT becomes dominant over ionization at energies beyond 1 TeV (see Fig. 2.11).

As seen in Fig. 2.11, the average loss in pair production dominates the bremsstrahlung which loss, in turn, is about an order of magnitude larger than for the photonuclear interactions.

The total rate of energy loss per unit length can be parameterized as [546, 539]:

$$\frac{dE_\mu}{dX} = \alpha(E_\mu) + \beta(E_\mu)E, \tag{2.14}$$

where $\alpha(E_\mu)$ is almost constant electronic stopping power that accounts for ionization and $\beta(E_\mu)$ is the energy-scaled contribution which accounts the losses due to radiative processes such as bremsstrahlung, pair production, and photonuclear interactions [539]: $b \equiv b_{brems} + b_{pair} + b_{nucl}$. Such a notation is convenient because $\alpha(E)$ and $\beta(E)$ are both weakly dependent on the muon energy E_μ where radiative effects become important while $\beta(E)E$ accounts less than 1% of $\alpha(E)$ for $E \lesssim 100$ GeV (see Fig. 2.10) for most materials [539].

Muons with energies above ~1 TeV can propagate in water large distances such as tens of km making them with such a long range as the most penetrating charged CR particle to which neutrino telescopes are most sensitive to. Notable, that the most penetrating lepton must be the heaviest ones, i.e. the tau leptons since the radiation length grow quadratically with mass at high energies [547]. However, the lifetime of the unstable tau lepton makes its track extremely short (with respect to the muon ones) [547]. At highest energies ($E_\tau \gg 100$ TeV) the huge Lorentz factor boosts the observed short tau lifetime and increase its value linearly with energy (see Fig. 2.11) while the corresponding muon tracks already reached a nearly steady maximum (a logarithmic growth) of a few km long [547] (see Fig. 2.11). Therefore, at highest energies such as above 10^8 GeV, the tau radiation length will be the longest one and the cosmic tau neutrinos will be the dominant source of signals in km^3 detectors over other leptons at the same energies [547]. Thus, be of interest to for the future underwater experiments such as KM3NeT, the next-generation multi-km^3-sized neutrino telescope [173, 174, 175] (see Section 2.4.4).

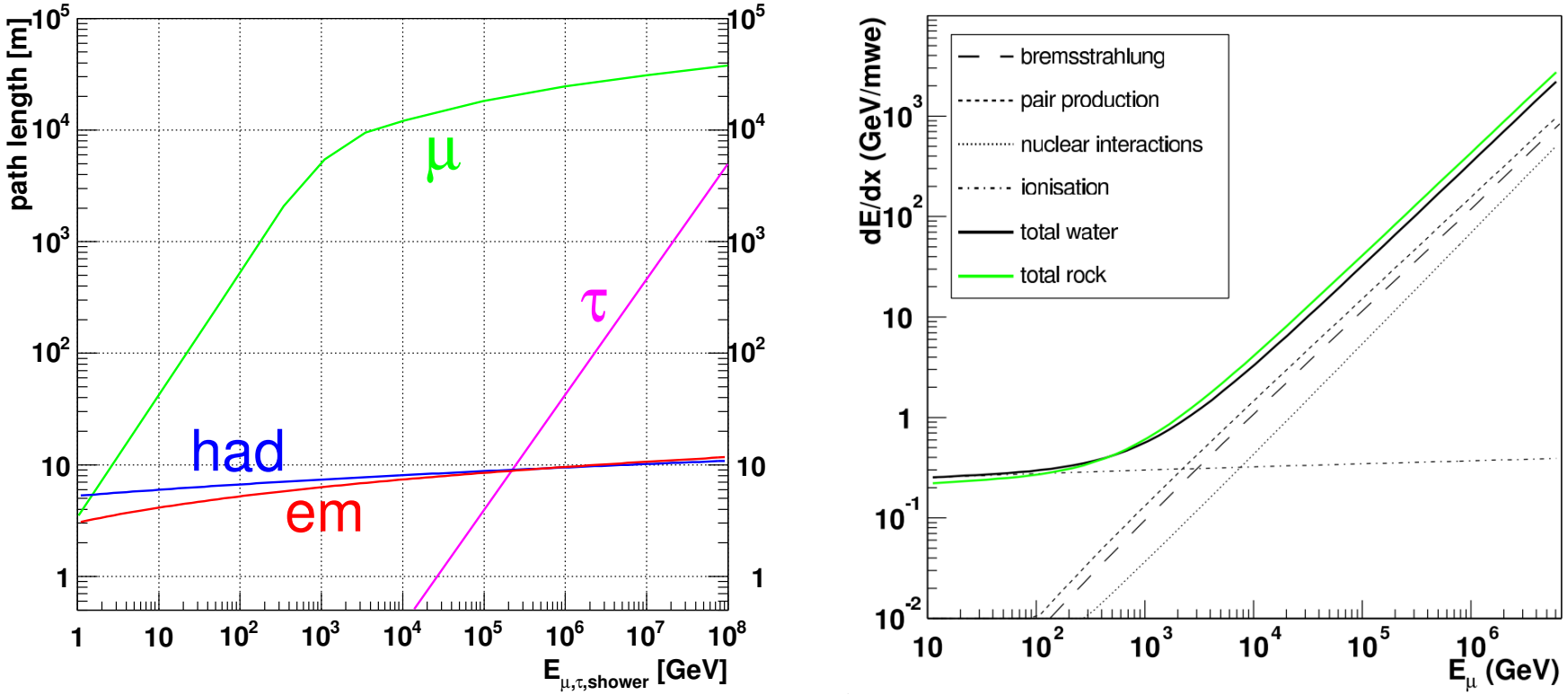

Fig. 2.11.: *Left:* The path length of different neutrino interaction products in water: muons, taus, electromagnetic and hadronic showers as a function of their respective energy. The shower lengths are calculated using a shower profile parameterization as described in [548]. The figure is taken from [548]. *Right:* Average energy loss per meter water equivalent (m.w.e) for muons in rock and seawater as a function of the muon energy. The contributions of the different processes for energy loss in water are detailed. The figure is taken from [498].

Another important parameter is the energy response for muon neutrino interactions. It is determined by [506]:

- the energy fraction transferred to the muon in the neutrino interaction;
- the energy lost by the muon outside the detector;
- the energy resolution of the detector.

The energy determination for muons requires different techniques in different energy ranges such as [506]:

$<$ **100 GeV** The energy of contained events, with start and end points measured inside the detector can be determined accurately from the range since the muons are close to minimum-ionizing. The threshold for this method is about 5-10 GeV for vertical tracks, depending on the vertical distance between groups of OMs, and about 15 GeV for more isotropic events, depending on the horizontal distance between lines [506].

$>$ **100 GeV** The energy for only partially-contained events can be determined due to the limited size of the detector. It is done with the visible range which determines the minimum energy that can be used for the analysis of partially-contained events: starting events in which the vertex point is measured inside the detector and stopping events in which the endpoint is measured [506].

$>$ **1 TeV** The muon energy loss becomes proportional to the energy due to stochastic processes (bremsstrahlung, pair production, $\delta-$rays) (see Fig. 2.11) which are dominant at this energy (above critical energy $E_{\mu c}$). The muon range increases only logarithmically with the muon energy but, in turn, the detection efficiency increases with energy due to additional energy loss [506].

$>$ **1 PeV** The Earth becomes opaque to upward-going vertical neutrinos. The VHE tau neutrinos can be observed due to the production of $\tau^{\pm}$ produced in ν_τ interactions decay before they are absorbed which, in turn, produces ν_τ of lower energy which continues along the original ν_τ flight path but with decreasing interaction probability, resulting in an accumulation of events at the highest detectable energies [506].

It is necessary to state [315] that all energy loss mechanisms producing relativistic charged particles, in particular, $e^{\pm}$ from pair production and conversion of bremsstrahlung photons, also lead to additional Čherenkov light [549, 550, 551] which is discussed in Section 2.3.5.

2.3.5 Čerenkov radiation

Usage of water or ice as a detection medium enable the detection of the neutrino-induced charged particles via the detection of the Čerenkov radiation. The charged particle passing through the polarizable medium excites the molecules and atoms arranging the dipoles (see

Fig. 2.12). As long as the speed of the particle $u<c/n$, the dipoles are symmetrically arranged around the particle path, so that the dipole field integrated over all dipoles vanishes and no radiation occurs [552]. If, however, the particle moves with $u > c/n$, the symmetry is broken resulting in a non-vanishing dipole moment, which leads to the radiation [552]. When the disruption has passed, the molecules rapidly revert to their ground state and re-emit electromagnetic radiation, known as Čherenkov radiation [549, 550, 551]. This radiation can be measured in photon detectors.

Such particle traveling through a transparent medium at speed greater than that at which light propagates in the same medium, $u>c/n$, it emits spherical waves of light along with its trajectory. The emitted waves add up constructively leading to coherent radiation at a so-called Čerenkov angle θ_C with respect to the particle direction [553]. This angle can be determined by the equation:

$$cos\theta_C = \frac{1}{\beta n}, \tag{2.15}$$

where $\beta = u/c$ denotes the Lorentz factor of the particle, c is the speed of light in vacuum, n is the refractive index of the medium ($n = 1.33$ for water) [39]. The Čherenkov angle for a relativistic track ($\beta \approx 1$) is $\theta_C \approx arccos(1/n)$, which gives $\approx 41.2°$. The refractive index of seawater is n=1.35 for a wavelength of 450 nm [506], 400-500 nm is the wavelength at which the PMTs are most effective; therefore, the Čherenkov light is emitted under 42.2° for this wavelength. This easy geometrical pattern of light emission allows a precise reconstruction of tracks from the measurement of only a few hits at different space points. The measurement of the arrival time of the Čerenkov light allows the reconstruction of the particle direction, and the amount of light collected can be used to estimate the particle energy.

Figure 2.12 illustrates the schematic view of the Čherenkov radiation with the typical spherical wavefront and the resultant conical radiation at angle θ_C. The Čerenkov emission occurs only if the speed of the charged particle u exceeds the phase velocity of the light c/n in a given medium, i.e. $u > c/n$. The distance traveled by the particle is βct, at the same time the light propagates the distance equal to ct/n.

The amount of Čerenkov photons emitted per track length x and wavelength λ is generally given by Frank-Tamm equation [554]:

$$\frac{d^2N}{dxd\lambda} = \frac{2\pi\alpha Z^2}{\lambda^2}(1 - \frac{1}{\beta^2 n^2}) = \frac{2\pi\alpha Z^2}{\lambda^2} sin^2\theta_C, \tag{2.16}$$

where Z is the charge of the particle and α is the fine-structure constant[11] [39].

Since the intensity of the Čerenkov radiation (see Eq. 2.16) is proportional to $1/\lambda^2$, the short wavelengths dominate. Its intensities are mostly distributed in the ultra-violet (UV) and blue bands of the spectrum, where the photomultiplier tubes (PMTs) are most sensitive [555].

[11] see Table A.3 in Appendix A.2.2.

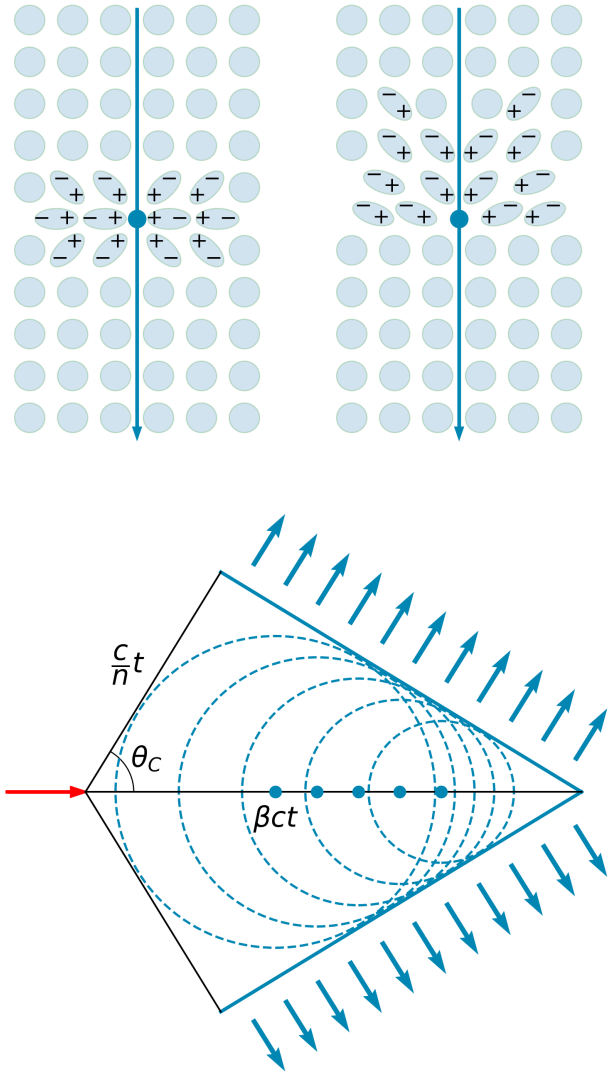

Fig. 2.12.: *Top:* Illustration of the Čerenkov cone. The Čerenkov angle is denoted by θ_C. *Bottom:* Illustration of the Čerenkov cone. The Čerenkov angle is denoted by θ_C.

Therefore, such light detectors are used in neutrino telescopes. The PMTs of ANTARES are sensitive to photons in the wavelength range between 300 nm and 600 nm [556], where about 340 emitted photons per centimeter (see Eq. 2.17) of the track are expected according to Frank-Tamm formula (see Eq. 2.16). If $Z = 1$, with $sin^2\theta_C \approx 0.451$ for :

$$\frac{dN}{dx} = 2\pi\alpha Z^2 sin^2\theta_C \left(\frac{1}{\lambda_1} - \frac{1}{\lambda 2}\right) \tag{2.17}$$

$$\approx 765\, sin^2\theta_C \frac{\text{ph}}{\text{cm}}, \tag{2.18}$$

2.3.6 Neutrino backgrounds

Cosmic rays continuously bombarding the atmosphere inducing the air showers, the product of the collision with the nuclei present in the atmosphere. Amongst a variety of particles produced in the showers (see Fig. 2.13), neutrinos and muons are placed. Both constitute the two main sources of physical background in neutrino telescopes.

Neutrinos should follow the energy spectrum of their parent CRs, $\propto E^{-\Gamma}$ with $\Gamma \sim 2$ [316] according to the diffusive shock acceleration mechanism [91]. Under the assumption that neutrinos are produced in charged meson decays, the intrinsic flux at source assumed to have the $\Phi_{\nu_e}:\Phi_{\nu_\mu}:\Phi_{\nu_\tau} = 1:2:0$ flavor composition. After propagation over cosmic distances, because of oscillation, the flavor composition changes to $\Phi_{\nu_e}:\Phi_{\nu_\mu}:\Phi_{\nu_\tau} = 1:1:1$[12] (see Section 1.5.2).

To provide shielding against secondary particles produced by CRs, the neutrino telescopes are set at large depth in deep water or ice. It remarkably reduces the background from atmospheric muons. Nevertheless, these particles can penetrate the atmosphere reaching up to several kilometers of ice/water. The atmospheric muons can be rejected by requiring an up-going direction (i.e., cut on elevation) for the reconstructed events since only neutrinos can propagate the Earth without interaction. As shown in Fig. 2.14, the flux of down-going atmospheric muons exceed the flux induced by atmospheric neutrino interactions by many orders of magnitude, decreasing with increasing detector depth.

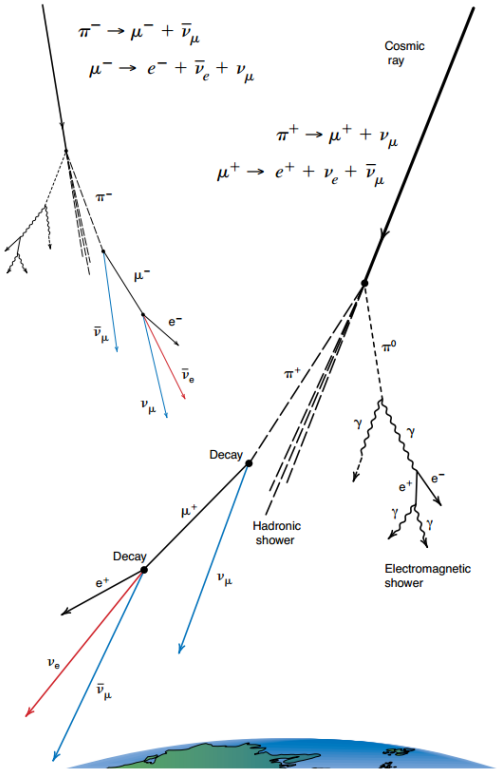

Fig. 2.13.: Schematic diagram of a CR air shower. The incident CRs collide the nuclei in the upper atmosphere and produce high-energy pions which decay into muons, neutrinos, and γ-rays. The collision shown on the right produces a π^+, π^0, and other heavy particles (the hadronic shower). The π^0 decays and produces γ-rays and leptons (the electromagnetic shower) but no neutrinos. The π^+ produces two muon neutrinos (blue) and an electron neutrino (red). The collision shown on the left produces a π^-, leading to the production of two muon neutrinos and an electron antineutrino. CR showers produce a continuous flux of neutrinos with flavor $(1:2:0)_{atm}$. The figure is taken from [557].

The down-going atmospheric muons may be wrongly reconstructed as up-going, and muons produced by CRs can mimic high-energy neutrino interactions. Thus, additional conditions on the reconstruction are needed. Even though above hundreds of TeV ν_e and ν_μ neutrinos become absorbed by the Earth, the ν_τ is regenerated [534, 535, 520] (see Section 2.3.4):

[12] The mixing $\nu_\mu \leftrightarrow \nu_\tau$ is assumed to be maximal.

τ^- produced in a CC ν_τ interaction decays back into new ν_τ of lower energy such as 10^{15} eV [117], where Earth is transparent.

Therefore, the cosmic neutrino search analyses face the presence of an irreducible background of atmospheric ν_e and ν_μ. Thus, in order to find evidence of a cosmic neutrino, one might search for an accumulation of events into clusters (atmospheric neutrinos are distributed isotropically over the sky, and event excess can be a signature of a cosmic neutrinos), differences in spectrum energy (a harder energy spectrum for cosmic neutrinos regarding to atmospheric neutrinos [316, 558, 559]) and in arrival directions (i.e. non-isotropic in contrast to atmospheric neutrinos). In this analysis, to improve the search and reduce the background significantly, time information from γ-ray flares are used [176, 177, 178].

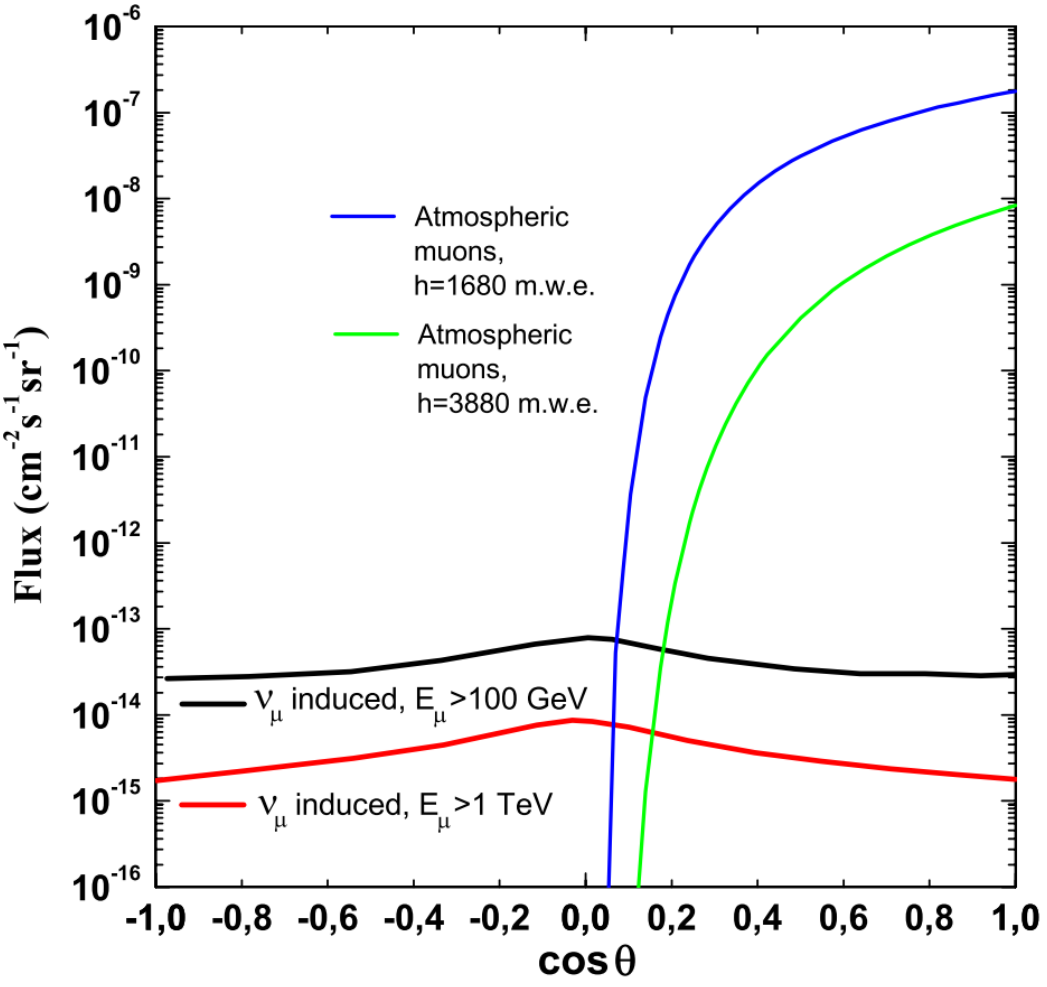

Fig. 2.14.: Muon flux as a function of the elevation due to atmospheric muons (computed according to [560]) for two different depths and atmospheric neutrino-induced muons (from [561]) for two different muon energy thresholds. The figure is taken from [117].

2.4 The neutrino telescopes

Ever since Markov brought the idea of "setting up apparatus in an underground lake or deep in the ocean in order to separate charged particle directions by Čerenkov radiation" in 1960 [486], there have been many attempts to perform such an experiment. The first step from conceptual ideas to large-scale experimental efforts was done by the Deep Underwater Muon and Neutrino Detector (DUMAND)[13] Collaboration [487, 488, 489] (see Section 2.4.1). Even though DUMAND was stopped, its experience led to the successful efforts of the Baikal Neutrino Telescope (Baikal NT)[14] [562, 563] Collaboration to built the first full detector in the deepest freshwater lake on Earth, Lake Baikal. The construction of NT200 and its upgraded version NT200+, a 10-Mton scale detector, were the first step towards a km^3-scale Baikal neutrino telescope, the Baikal the Gigaton Volume Detector (GVD)[15] [536, 537]. The Section 2.4.2 gives an overview of the NT200 and discusses the GVD which is currently in installation into Lake Baikal.

Next, the Neutrino Extended Submarine Telescope with Oceanographic Research Project (NESTOR) [564] and NEutrino Mediterranean Observatory (NEMO) [565] collaborations have performed necessary technical R&D work and deployed prototypes of their detectors for short periods of time. The NESTOR has been targeted to build a neutrino telescope off the coast of Pylos in Greece, while NEMO aimed to investigate the feasibility of a cubic-kilometer-scale deep-sea neutrino detector and to identify a suitable site. Eventually, the activities carried out by NEMO towards the realization of a km^3 neutrino detector resulted in an understanding that technological solutions exist for the realization of an underwater km^3 detector and identification of an optimal place for the installation of such a detector the Ionian Sea at a depth of 3500 m, about 100 km off Capo Passero in Sicily, Italy [565, 566]. As a suitable place for NESTOR detector, the underwater plateau of 3800 m depth and more with the deepest part 5200 m a little further away in the Ionian Sea 30 km off the coast of Pylos in Greece has been identified [564, 567]. The NESTOR detector performed data-taking in 2003 using a test element of the NESTOR detector which was operated successfully for more than one month [568, 569, 567, 570]. The detector functionality has been validated by a thorough test of the electrical supply and distribution systems, the monitoring and control systems, and the full data acquisition and transmission chain from the sea to the shore station [568, 569]. The measured atmospheric muon flux was found to agree with the expectations from previous underwater measurements and with phenomenological predictions [568, 569, 567]. Both NESTOR and NEMO are now part of the ANTARES and KM3NeT collaborations which pursued the efforts of NESTOR and NEMO further.

[13] DUMAND Collaboration, https://www.phys.hawaii.edu/~dumand/
[14] Baikal NT200 Collaboration, https://web.archive.org/web/20100831210755/http://baikalweb.jinr.ru/
[15] Baikal-GVD Collaboration, https://baikalgvd.jinr.ru/

The Astronomy with a Neutrino Telescope and Abyss environmental RESearch (ANTARES)[16] [506, 481] proposal [506] was presented in 1999 and it was the first undersea neutrino telescope and at present the largest operating water Čherenkov detector in the Northern Hemisphere. The first line of ANTARES was deployed in 2006 with the measurements of the atmospheric muon flux performed shortly after [571]. The final 12-line detector configuration was completed in 2008. With the expected decommissioning of ANTARES at the end of 2019, the next-generation multi-km^3-sized Cubic Kilometer Neutrino Telescope (KM3NeT)[17] neutrino telescope [173, 174, 175] (see Section 2.4.4) with a unique design of multi-PMT optical modules will take up with new vigor the challenges faced by ANTARES and will have surpassed it in the sensitivity in few years raising a new era in neutrino astronomy. The ANTARES is discussed in detail in Section 3 and the brief overview of the KM3NeT is given in Section 2.4.4.

In contrast to the deep-sea neutrino detectors, the Antarctic Muon And Neutrino Detector Array (AMANDA)[18] [572] detector even though used the same fundamental detector concepts but was the first-ever detector utilized deep polar ice as a detection medium. Preliminary explorations of the detector site and the drilling technology were performed during the 1991/1992 Antarctic summer [572]. During the 1993/1994 Antarctic summer campaign, a few strings of an exploratory phase of the project, AMANDA-A, not suitable for track reconstruction, were deployed [572]. As a first step towards a large neutrino telescope at the South Pole, the first four strings of a deeper AMANDA-B4 was deployed during the Antarctic summer 1995/1996, and the first neutrino candidates have been identified right after [572]. A ten-string array, AMANDA-B10, has been taking data since 1997 [572]. In subsequent years, additional strings were added forming the larger detector, called AMANDA-II, which consisted of about 700 OMs and had an improved acceptance for muons over a larger angular interval [572, 573]. Due to predicted low fluxes of very high energy neutrinos, it has been concluded that a neutrino detector with an effective area up to 1 km^2 is required and plans for a much larger detector were made [417, 573]. The efforts began by AMANDA [572] has been successfully continued by its successor, the IceCube Neutrino Observatory[19] [482, 490, 491] (see Section 2.4.3), a cubic-kilometer-scale high-energy neutrino detector built into the Antarctic ice at the South Pole.

Table 2.1 provides an overview of the neutrino telescopes and their main parameters.

[16] ANTARES Collaboration, http://antares.in2p3.fr/
[17] KM3NeT Collaboration, https://www.km3net.org/
[18] AMANDA Colaboration, http://amanda.uci.edu/
[19] IceCube Collaboration, https://icecube.wisc.edu/

Tab. 2.1.: Past, present and future neutrino telescope projects and their main parameters* [39]

Experiment	Milestones$^{\alpha}$	Mediam/Location	Size$^{\beta}$	Remarks
DUMAND	1978/–/–/1995	Pacific/Hawaii		Terminated due to technical/funding problems
NT200	1980/1993/1998/2015	Lake Baikal	10^{-4}	First proof of principle
GVD [574]	2012/2015/–/–	Lake Baikal	0.5-1.5	High-energy ν astronomy, first two clusters installed
NESTOR	1991/–/–/–	Mediterranean Sea		2004 data taking with prototype
NEMO	1998/–/–/–	Mediterranean Sea		R&D project, prototype tests
AMANDA	1990/1996/2000/2009	Ice/South Pole	0.015	First deep-ice neutrino telescope
ANTARES	1997/2006/2008/–	Mediterranean Sea	0.010	First deep-sea neutrino telescope
IceCube	2001/2005/2010/–	Ice/South Pole	1.0	First km^3-sized detector
†*IceCube-Gen2* [362]	2014/–/–/–	Ice/South Pole	5-10	Planned extension of IceCube covering low and high energies, a surface array and radio detection
KM3NeT/ARCA [175]	2013/(2015)/–/–	Mediterranean Sea	1-2	First construction phase started
KM3NeT/ORCA [175]	2014/(2017)/–/–	Mediterranean Sea	0.003	Low-energy configuration for neutrino mass hierarchy
†*KM3NeT Phase 3*	2013/–/–/–	Mediterranean Sea	3-6	6 building blocks plus ORCA

* See the text or [315] for references to the different projects where unspecified.
α The milestone years give the times of project start, of first data taking with partial configurations, of detector completion, and of project termination.
† Projects with first data expected past 2020 are indicated in italics.
β The size refers to the largest instrumented volume reached during the project development an given in km^3.

2.4.1 The DUMAND project

The goal of DUMAND was to build the first deep ocean neutrino telescope at 4800 m depth in the Pacific Ocean about 30 km off-shore from Keahole Point on the Big Island of Hawaii [575] for the study of high-energy neutrinos. The Island of Hawaii was selected for a variety of compelling reasons: exceptional water clarity, the proximity of an abyssal plain with appropriate seabed characteristics to a suitable shore site (30 km away), presence of an active particle physics group at the nearby University of Hawaii in Honolulu, and pre-existing laboratory infrastructure at the shore site, due to an ocean thermal energy research project [576]. If the original proposal were followed, the full DUMAND will be a 250 m × 250 m × 500 m array of 756 16-inch PMTs mounted with 25 m spacing on 36 vertical detector strings [577]. In 1987, a series of ocean operations were carried out to test the concept and the design of the components of the DUMAND project and demonstrated the technology with a prototype string controlled from a ship [578, 579, 580, 581] (refers as DUMAND-I). The deployment of a Short Prototype String (SPS) has validated the basic design of the detector [582]. In 1993, a highly complex string deployment procedure had been conducted in one uninterrupted operation together with the deployment of the JB and the 36 km twelve-fiber electro-optical cable which links the junction box (JB) to shore [575] (refers as DUMAND-II). A total of 3 Gb of data, corresponding to about two minutes of real-time, were transmitted from the string and accumulated in a buffer onboard the ship and dumped onto a disk [575]. It also confirmed observations made in the 1987 DUMAND-I experiment. The project was ultimately stopped but left an exceptionally rich legacy of ideas and technical principles and pioneered many of the technologies for neutrino telescopes in use today.

2.4.2 The Baikal telescope

The Baikal Neutrino Telescope [563, 583, 536, 537] is operated in Lake Baikal, Siberia, at a depth of 1100 m. The Baikal Neutrino Telescope NT200 has been taking data since 1998; its first stage telescope NT36 was - back in 1993 - the first constructed underwater Čherenkov neutrino detector [584]. The first stage telescope configuration NT200 [563] consisted of 8 strings, each with 24 pairwise arranged OMs, each contained a 37-cm diameter hybrid photodetector QUASAR-370 [585], developed especially for this project [536]. The upgraded 10-Mton scale Baikal telescope NT200+ [583] was commissioned in April 2005 and is made of a central part (the old, densely instrumented NT200 telescope) and three additional external strings [536], as displayed in Fig. 2.15. The construction of NT200+ was the first step towards a km^3-scale Baikal neutrino telescope [536] with a relatively flexible structure, which allows for a rearrangement of the main building blocks (clusters), to adapt for requirements of new scientific goals, if necessary [537].

The upgraded km^3-scale telescope is called Baikal the Gigaton Volume Detector (GVD) [536, 493, 494], or Baikal-GVD, and currently under construction since 2015. The Baikal-GVD is located in the southern basin of the Lake Baikal close to the NT200+ telescope (51°50′ N

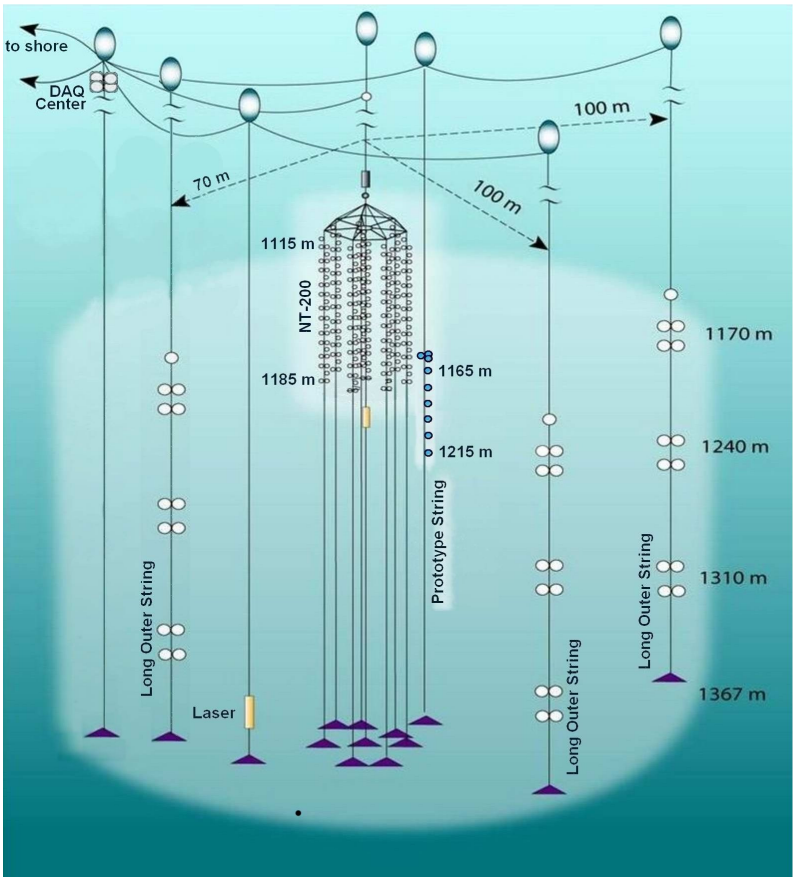

Fig. 2.15.: A sketch of the Baikal Telescope NT200+. The compact NT200 (inner strings), 3 long outer strings and the new technology km^3-prototype string. The figure is taken from [584].

104°20′ E), at a depth of about 1400 m [586]. The R&D program for the GVD was started in 2006 [583] and the important milestones of the Baikal-GVD telescope includes [587] the construction and the installation of prototype strings in 2009-2010 [588, 589] and the engineering GVD cluster [586], comprising 3 strings, in 2011-2012 [590, 588, 589, 591]. The primary goals of the prototype array installation were investigation and *in-situ* test of basic elements of the future detector [587]. The first phase (Phase 1) of the construction of the Baikal-GVD telescope with 8 clusters with 2304 light sensors in total covering 0.4 km^3 of the instrumented volume is expected to be finished in 2021 [592]. In April 2015 the first Baikal-GVD cluster *Dubna* [593] of 192 OMs arranged at eight 345 m long strings, was deployed and started operation. Since April 2018 the telescope had been successfully operated in complex of three functionally independent clusters (see Fig. 2.16) i.e. sub-arrays of OMs hosting 864 OMs on 24 vertical strings‘[592]. A significant amount of work has been accomplished during the 2019 year winter expedition resulting in the operation of two new clusters, altogether 5 clusters with effective volume of 0.25 km^3, starting April 2019 [592].

The configuration of the telescope consists of functionally independent clusters of strings, which are connected to the shore by individual electro-optical cables [592]. Each cluster comprises eight strings of 288 OMs arranged at depths down to 1300 m [592]. Seven peripheral strings are uniformly located at a 60 m distance around a central one with the distances between the central strings of neighboring clusters are about 300 m [592] (see Fig. 2.16). OMs on each string are combined in sections, DUs of the telescope [592]. A basic element of the operation of the Baikal-GVD detector is a section of 12 OMs distributed vertically along the string, spaced by 15 m, and a central electronics module (CEM) [592]. There are 3 sections of 36 OMs per string and 8 strings in a cluster (see Fig. 2.16), each is an independently working subarray of the Baikal-GVD [592]. As the light sensor of OM, a single PMT Hamamatsu R7081-100 with a 10-inch hemispherical photo-cathode and quantum efficiency up to 35% is exploited [592].

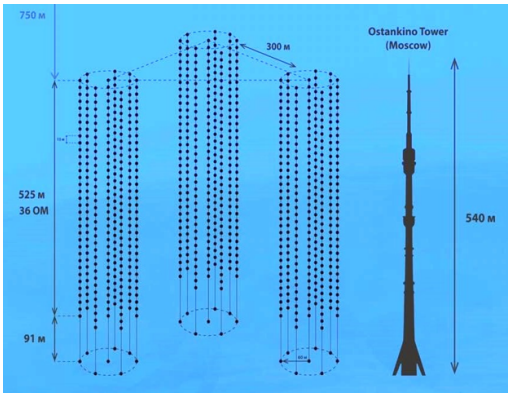

Fig. 2.16.: Schematic drawing of the Baikal-GVD three clusters operated in 2018, compared to the Moscow television tower. The figure is taken from [592].

The main scientific goal of Baikal-GVD is to map the high-energy neutrino sky in the Southern Hemisphere including the region of the galactic center [587]. Other topics include the indirect search for dark matter by searching for neutrinos produced by WIMP annihilation in the Sun or in the center of the Earth [587]. Baikal-GVD will also search for exotic particles like magnetic monopoles, super-symmetric Q-balls or nuclearites [587]. The current effective volume of the Baikal-GVD detector is just one-fourth of the size of the present world leader - the IceCube Neutrino Observatory at the South Pole [592] (see Section 2.4.3). However, important progress has been achieved in the construction of the Baikal-GVD telescope by putting in operation 5 clusters with an effective volume of one-fourth of the km^3. A possible extension of Phase 1 to Phase 2 with the construction of an additional 14 clusters will depend on the performance and physical output of the Baikal GVD detector in 2021 [592]. To reach an optimal performance of the Baikal-GVD detector advanced calibrations and analysis techniques have to be further developed, tested and implemented in data processing [592]. With increasing data records of steadily extending the Baikal-GVD detector the importance of the largest freshwater neutrino telescope for the multimessenger study of astrophysical objects is growing [592]. Without any doubts, the Baikal-GVD telescope is able to offer a unique view on our universe and provide powerful insights into the performance of some of the most energetic and enigmatic objects in the cosmos [592] together with multi-km^3-sized neutrino telescopes such as IceCube [482, 490, 491] and KM3NeT [173, 174, 175] which are discussed in detail in the next two sections.

2.4.3 The IceCube telescope

The IceCube Neutrino Observatory [482, 490, 491] is a cubic-kilometer-scale high-energy neutrino detector built into the Antarctic ice at the South Pole[20] continuing the efforts began by its predecessor AMANDA [572]. Construction of IceCube, the largest neutrino detector built to date, was completed on December 18, 2010, and commissioning was completed in 2011 and enabled the discovery of high-energy astrophysical neutrinos which was achieved in 2013 [496, 11] together with the identification and characterization of their sources which was achieved in 2017 [14, 15]. Figure 2.17 illustrates the IceCube detector. It consists of 5160 PMTs distributed over 86 vertical strings which are deployed between 1450 m and 2450 m below the surface of the ice [491]. Besides a subsurface "in-ice" array of PMTs, the IceCube includes the more densely instrumented sub-array called DeepCore [594] and an extensive air shower array on the surface called IceTop [363], both fully integrated into the IceCube Data Acquisition System (DAQ) [363, 491]. The objective of the DeepCore "in-fill" array is to identify a smaller sample with energies as low as 10 GeV [490] while the IceTop array extends IceCube's capabilities for CR physics allowing the use of the full IceCube Observatory as a 3D array for the study of high-energy CRs [363].

IceTop

The IceTop surface array [363] is a CR air shower array with an area of 1 km^2 which is mainly designed to extend the telescope's capabilities for CR physics and to partially veto the background of down-going muons in order to efficiently enhance the neutrino searches. The IceTop allows a detailed exploration of the mass composition of primary CRs in the energy range from about 100 TeV to 1 EeV by exploiting the correlation between the shower energy measured in IceTop and the energy deposited by muons in the deep-ice. It is located on the surface above the "in-ice" IceCube detector at a height of 2835 m a.s.l. and consists of 162 ice-filled tanks, instrumented with PMTs that detect Čherenkov radiation and arranged in 81 stations and distributed over an area of 1 km^2 on a grid with a mean spacing of 125 m [363, 491]. Figure 2.18 shows a view of the IceTop array. The IceCube Laboratory (ICL) (see Fig. 2.17), located at the surface in the center of the IceTop array (see Fig. 2.18), is the central operations building for the experiment.

The two adjacent tanks at each surface station are separated by 10 m [491] and each contains two standard IceCube DOMs (see Fig. 2.20). Air showers initiated in the atmosphere by CRs are typically spread over a number of stations [363, 491]. The light generated in the tanks by the shower particles (electrons, photons, muons, and hadrons) is a measure of the energy deposit of these particles in the tanks [363, 491]. The information from multiple stations is fitted to a model of the overall shower shape and intensity, called "shower size"

[20] The detector is built near the Amundsen-Scott South Pole Station located at an elevation of 2835 m (9301 ft) above sea level (a.s.l.) and administered by the National Science Foundation (NSF) under the United States Antarctic Program (USAP)

S, and the direction described by the zenith and azimuth angles θ, ϕ [363]. The threshold for efficient reconstruction of air showers that trigger 3 or more stations is approximately 300 TeV in most of the detector and lowered to approximately 100 TeV in a denser "in-fill" region [363]. The geometrical acceptance of the combined surface and "in-ice" detectors are approximately 0.3 km^2 sr which provides a useful rate of showers with energies up to few EeV; thus, the energy range of IceCube as a CR detector fully covers the "*knee*" region of the spectrum and extends to the energies where a transition (see Section 1.1.4) from galactic CRs to a population of extra-galactic particles may occur [363, 491].

DeepCore

The DeepCore "in-fill" array [594] is an array of eight stations in the center of IceTop (see Fig. 2.18) with a denser inter-string spacing and primarily designed to lower the IceCube neutrino energy threshold by over an order of magnitude, to energies as low as about 10 GeV. It is located 2100 m below the surface (see Fig. 2.19) at the bottom center of the existing IceCube array [594]. Using the Čherenkov light emitted by charged particles arising from neutrino interactions in the ice, the DeepCore sub-array achieves improved sensitivity through a combination of increased module density (roughly five times higher than that of the standard IceCube array), the higher quantum efficiency of the PMTs (about 35% better), deployment in the exceptionally clear ice at those depths which allows to use the surrounding IceCube detector as a highly efficient active veto against the principal background of downward-going muons produced in CR air showers [594]. Taken together, these features of DeepCore increases the sensitivity of IceCube to neutrinos from WIMP dark matter annihilation, atmospheric neutrino oscillations, and Galactic SN, and point sources of neutrinos in the Northern and Southern skies [594].

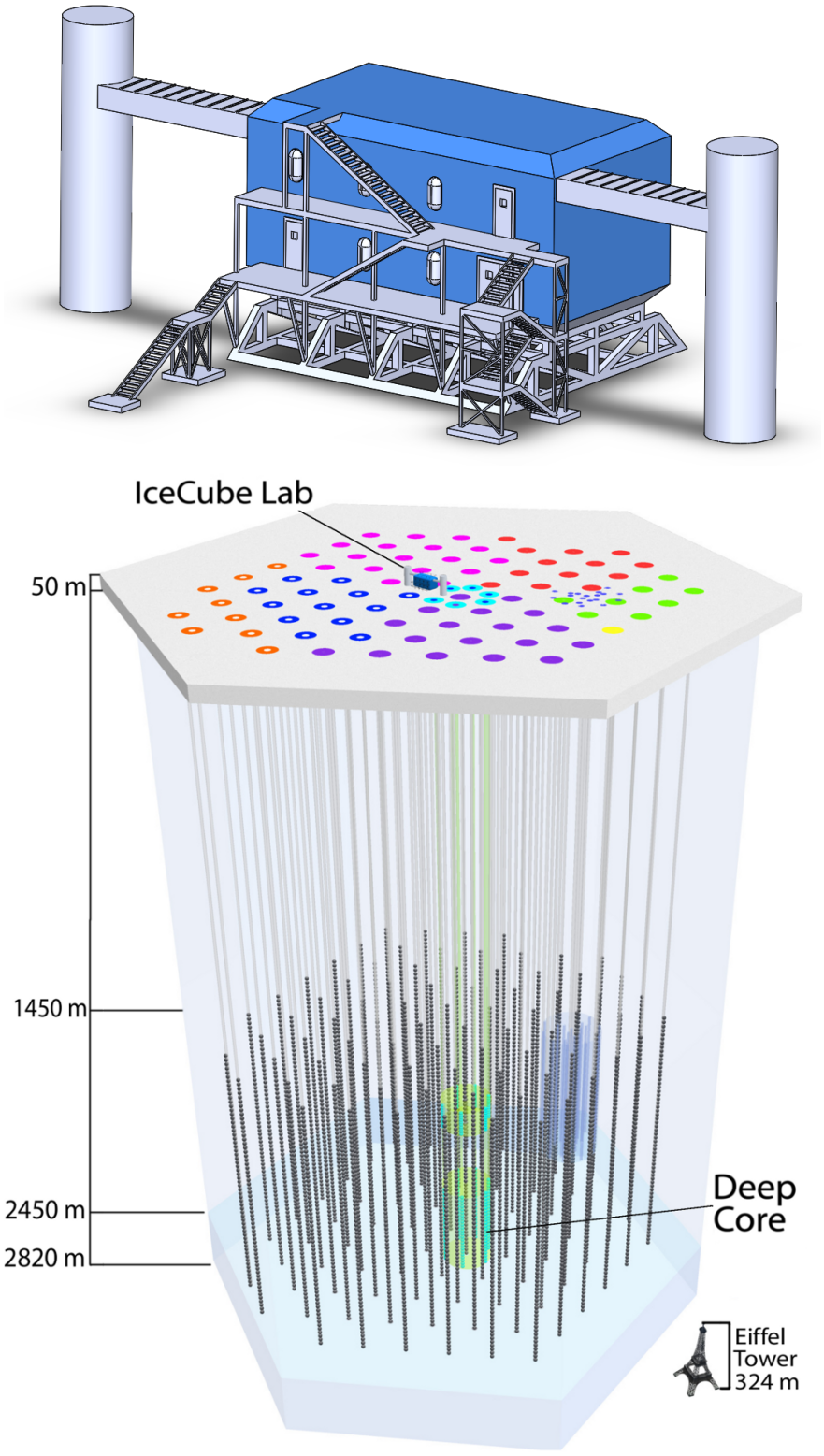

Fig. 2.17.: *Top:* Illustration of the IceCube Laboratory (ICL). The figure is taken from [491]. *Bottom:* The IceCube detector situated at a depth between 1450 and 2450 meters below the surface of the South Pole ice sheet. The dotted lines at the bottom represent the instrumented portion of the ice. Each dot represents a DOM. The circles on the top surface represent IceTop [363], a surface air-shower subdetector with 81 stations covering an area of 1 km^2. The colored part represent the DeepCore sub-array dedicated to lower energies. The IceCube Lab located at the surface in the center of the IceTop array, is the central operations building for the experiment. The Eiffel tower is added for a dimensional reference. The figure is taken from [595].

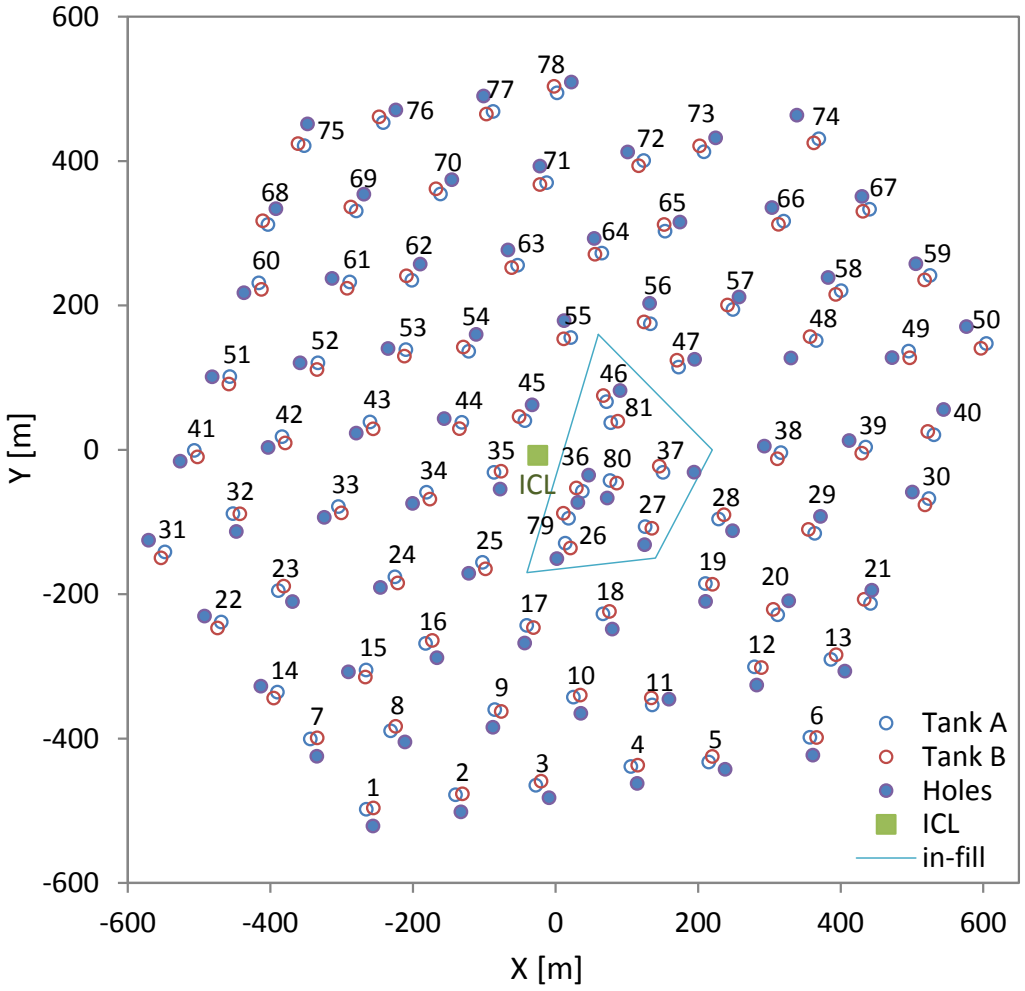

Fig. 2.18.: Locations of IceCube string holes and IceTop tanks with the ICL in the center. The holes 81 to 86, belonging to DeepCore and not related to IceTop tanks, are not shown. IceTop stations are located next to IceCube strings (except for the "in-fill" station 81) and consist of two tanks, A and B. The irregularity of the array arises because tank locations were constrained by surface cabling and IceCube drilling operations. A denser DeepCore "in-fill" array is formed by the 8 stations: 26, 27, 36, 37, 46, 79, 80, 81. The figure is taken from [363].

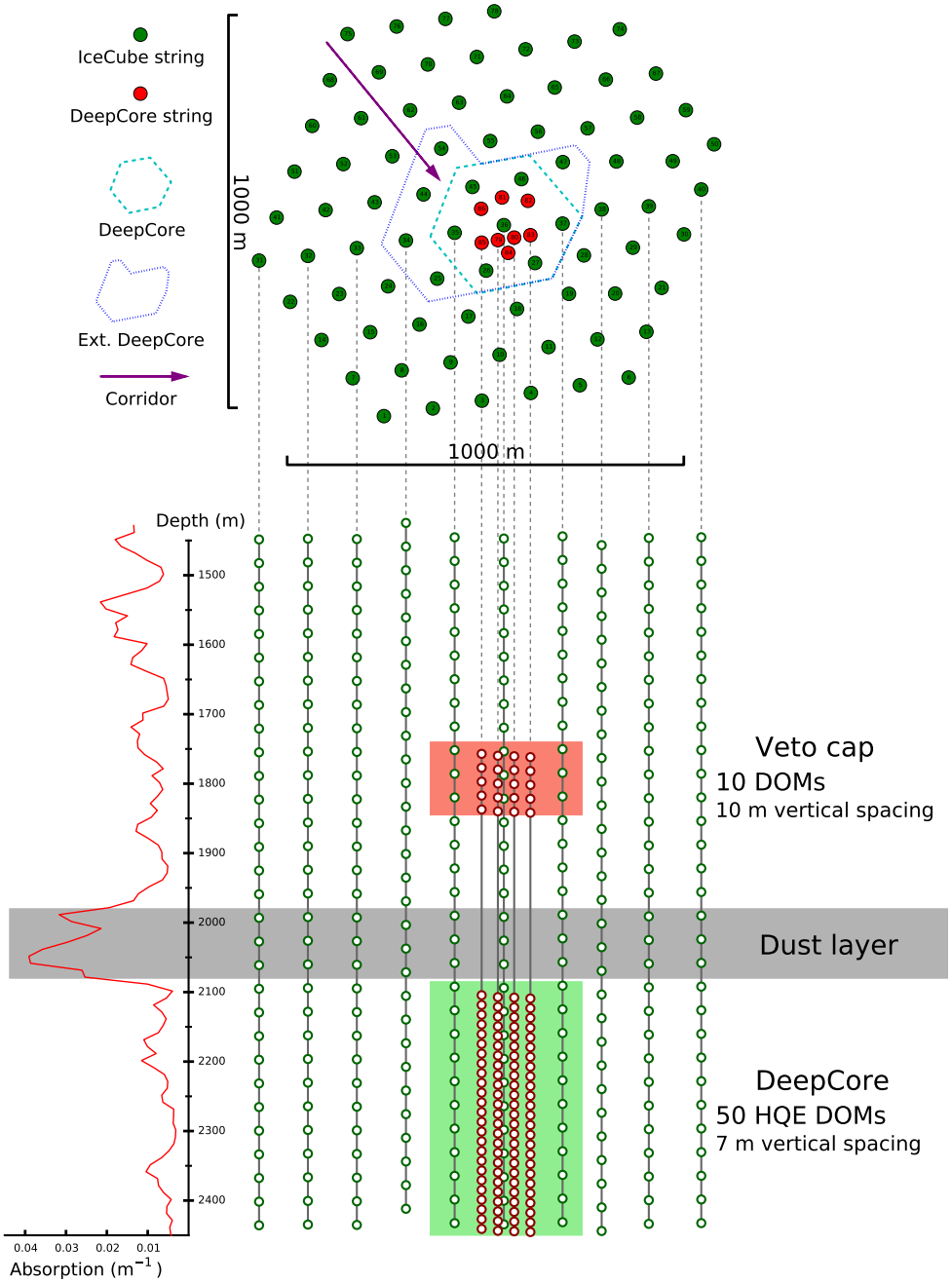

Fig. 2.19.: Top and side views of IceCube indicating the positions of DeepCore (red circles) and surrounding IceCube (green circles) DOMs. The DeepCore fiducial region is shown as a green box at the bottom center. The DeepCore DOMs were deployed mostly 2100 m below the surface (highlighted in green) with some DeepCore DOMs also deployed around 1800 m below the surface (highlighted in red) to aid in rejection of atmospheric muons. The so-called ”dust layer” [596] in a depth band between 2000 and 2100 m is also indicated by a gray band. It has the highest dust concentrations and hence higher scattering and absorption; thus, the DeepCore is not instrumented there. The bottom left of the plot shows the absorption length for Čherenkov light as a function of depth. The purple arrow in the top view shows one example of a ”corridor” path along which atmospheric muons can circumvent the simple veto cuts, as they may not leave a clearly detectable track signature. The figure is taken from [597].

Optical Module

The optical sensor called Digital Optical Module (DOM) [598] is a key component of the IceCube detector. It is composed of a transparent 13-inch diameter pressure-resistant glass sphere housing a 10-inch PMT and all the electronics. Figure 2.20 illustrates a DOM with its components. A 13 mm thick glass sphere withstands the pressure up to 70 MPa [599] and provides convenient housing for IceCube PMTs. A μ-metal protects the PMT against the Earth's magnetic field [598]. A flexible gel provides support and optical coupling from the glass sphere to the PMT's face [598]. The DOM also contains an HV generator with divides the voltage to the PMT while the DOM Mainboard or DOM MB digitizes the signals from the phototube, actives the LEDs on the LED flasher board, and communicates with the surface [598].

The PMT model selected during R&D phase is the R7081-20 Hamamatsu[21], emphasizing the criteria of low dark noise and good time and charge resolution for single photons [599]. It has a quantum efficiency of 25% at 390 nm and sensitive to photons in the wavelength range between 300 nm and 675 nm [599, 491]. The low dark noise rates below 500 Hz (at −40 °C) in the cold and radio-pure Antarctic ice allows IceCube to record all events that satisfy simple multiplicity conditions and is particularly important for the search for MeV neutrinos from galactic core-collapse SNe [599, 600].

Once deployed, the ambient temperature varies between approximately −45 °C to −20 °C [594], becoming warmer with increasing depth [601]. Thus, for each DOM the final acceptance testing (FAT) has been performed before the deployment. The FAT lasts approximately 3 weeks and during this time the DOMs experience "in-ice" conditions with temperature over the range −55 °C to 20 °C and are soaked at −45 °C at least 180 hours for long stability checks [602].

The IceTop uses DOMs identical to those in the deep-ice while for the DeepCore the Hamamatsu R7081-MOD with higher quantum efficiency about 40% at 390 nm is selected [594, 491].

Strings

The 86 IceCube strings are deployed between 1450 m and 2450 m below the surface of the ice with a regularly spaced array of 5160 PMTs (with 60 PMTs per string) [491]. The primary "in-ice" array consists of 78 strings and is deployed within a hexagonal footprint on a triangular grid with 125 m horizontal spacing and 17 m vertical spacing instrumenting a volume of 1 km^3 of ice [491]. Such a design was chosen to meet the primary science requirement of detecting astrophysical neutrinos in the TeV-PeV energy range [491]. The DeepCore sub-array consists of eight specialized and closely-spaced strings of sensors in

[21] Hamamatsu Photonics, Electron tube division, http://www.hamamatsu.com

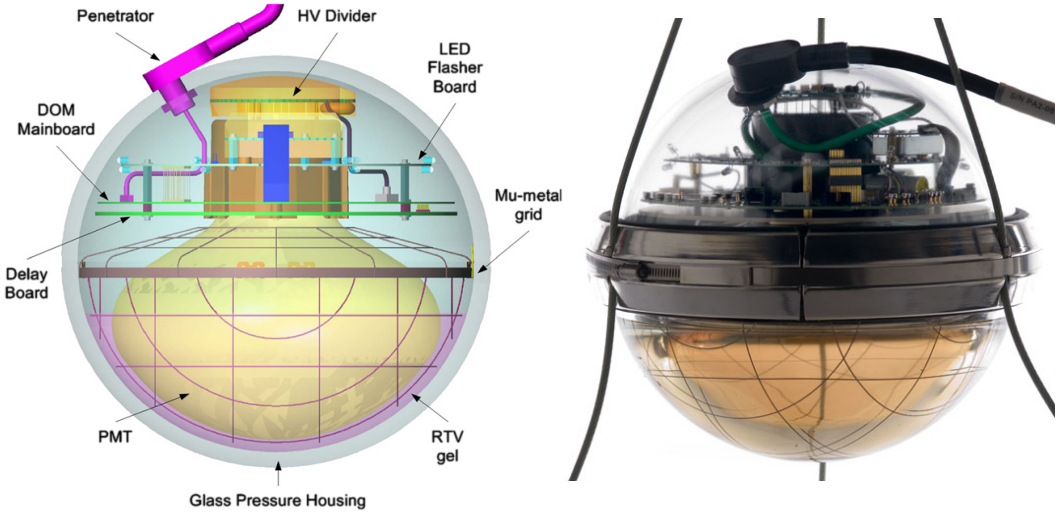

Fig. 2.20.: Schematic 3D view (*Left*) and picture (*Right*) of the IceCube digital optical module and its components. A large 10-inch diameter hemispherical photomultiplier is protected by a pressure-resistant glass sphere. An internal LED system is used for the calibration. The figures are taken from [595] and [603] respectively.

the center of the array, along with the seven central standard IceCube strings [491]. The inter-string spacing in DeepCore varies from 41 m to 105 m, with an average spacing of 72 m [491]. The eight specialized DeepCore strings have a 7 m vertical spacing for the bottom 50 DOMs, deployed in the deepest ice instrumented by IceCube at depths of 2100 m to 2450 m below the surface of the polar ice cap, where the scattering and absorption lengths are substantially longer than at shallower depths [594, 491]. The remaining 10 DOMs are deployed at depths shallower than 2000 m with a spacing of 10 m to form a veto cap (see Fig. 2.19) to further enhance background rejection of down-going atmospheric muons [594, 491]. Due to the significantly increased optical scattering and absorption in the region of the ice from 2000 m to 2100 m (the ”dust layer” [596]), these depths are not instrumented (see Fig. 2.19).

Strings of DOMs are deployed into water columns that have been melted by a hot-water drill and after refreezing, DOMs are optically well coupled to the surrounding glacial ice [599].

Detector site properties

In contrast to other neutrino telescopes, IceCube is the only one uses ice as a detection medium for detection of the neutrino-induced charged particles via the detection of the Čerenkov radiation. Therefore, as in the case of seawater, a precise knowledge of the absorption and scattering lengths of the ice traversed by the Čherenkov photons is crucial for accurate reconstruction of the properties of traversing relativistic particles and to realize the full potential of the detector [604, 605]. In fact, absorption reduces the amplitude of the Čherenkov wavefront, i.e. the total amount of light on PMTs, while the scattering

changes the direction of propagation of the Čherenkov photons and the distribution of their arrival time on the PMTs which degrades the measurement of the direction of the incoming neutrino [117].

It has been found that at depths greater than 1300 m the optical ice properties follow the variations with depth (see Fig. 2.21) which found to closely track the concentrations of mineral dust impurities, which are seen in ice cores from other Antarctic sites and are correlated with climatological history [606, 604]. Dust concentrations are the highest in a depth band between 2000 and 2100 m (the "dust layer" [596]) and corresponds to a stadial about 65 000 years ago, in the last glacial period [594]. As stated in Section 2.4.3, the DeepCore was designed to avoid this highly absorbing and scattering ice.

Figure 2.21 shows the scattering and absorption lengths of ice (averaged in 10 m depth bins) which were obtained from a fit to the *in situ* light source data collected in 2008 [604]. The sum of the statistical and systematic uncertainties in the measured values of the effective scattering and absorption coefficients inside the instrumented volume of the IceCube detector was estimated to be less than 10% [604].

The absorption lengths in ice (which is more transparent) is larger than in water while the effective scattering length is smaller which causes a larger degradation of the angular resolution of the detected neutrino-induced muons in ice with respect to the water [117]. Consequently, this gives the advantage to ANTARES and to the next-generation multi-km^3-sized KM3NeT telescope [173, 174, 175] (see Section 2.4.4 for details) with the excellent angular resolution afforded by seawater.

In IceCube, the angular resolution for muon tracks and hence the incident neutrino direction is typically 0.6° [491] and about 15° [607] for cascades with 15% [607] energy resolution for both track and cascade events.

In ANTARES, the median angular resolution for the tracks is ~0.4° [608] becoming lower than 0.3° for neutrino energies exceeding 10 TeV [609]. For cascade events the 2°-3° angular resolution and 5%-10% energy resolution is achieved in the 1 TeV - 1 PeV energy range [610].

In KM3NeT, a very good angular resolution of about 0.2° is achieved for neutrinos above 10 TeV for track events (to be better than 0.1° for energies above 100 TeV) and about 2° for cascade events (an angular resolution of about 1° may be attainable with improved efficiency) [175].

In Baikal-GVD, the angular resolution for tracks and cascades are about 0.25° and about 3.5°-6.5° respectively. The accuracy of cascade energy reconstruction is about 20%-35% depending on energy [492, 574].

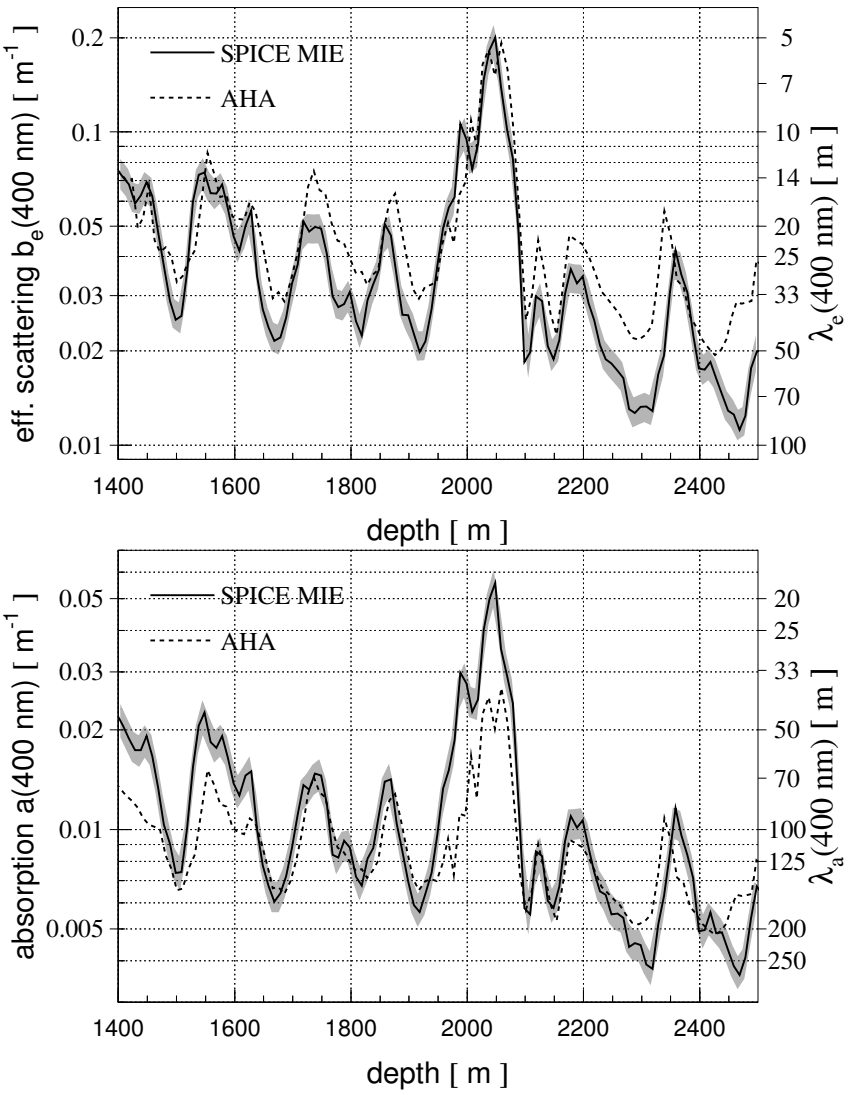

Fig. 2.21.: The effective scattering (*Top*) and absorption (*Bottom*) coefficients as a function of the depth. Two models are compared [604], the South Pole Ice (SPICE Mie) model (solid line) and the Additionally Heterogeneous Absorption (AHA) model (dashed line). The range of values allowed by estimated uncertainties is indicated with a grey band around solid line. The scale and numbers to the right of each plot indicate the corresponding effective scattering λ_e (= $1/b_e$) and absorption λ_a (= $1/a$) lengths in a meter. The figure is taken from [604].

The big advantage of the deep-ice compared to deep-water in lakes and seas is that the ice is almost background-free, e.g., with dark noise rates below 0.5 kHz for IceCube, while in water the optical background from bioluminescence produced by living organisms and from the ^{40}K disintegration is present, together producing a continuous background rate of several tens of kHz from each OM, e.g., ~60 kHz for ANTARES (see Fig. 3.25). Notable, that Baikal-GVD telescope benefits from its location in the clean and transparent water of the deepest freshwater lake on Earth having a moderately low background in the absence of high luminosity bursts from living organisms and ^{40}K disintegration in freshwater. The Section 3.4 provides more details about ANTARES detector site properties such as optical background and light transmission.

2.4.4 The KM3NeT telescope

KM3NeT [173, 174, 175] will be a deep-sea research infrastructure hosting a neutrino telescope, but also providing continuous, long-term access to deep-sea measurements to a variety of science communities, such as marine biologists, oceanographers, geophysicists and environmental scientists [175]. The successful deployment and operation of the ANTARES neutrino telescope [481] has demonstrated the feasibility of performing neutrino studies with large volume detectors in the deep-sea [175]. The same technology can be used for studying neutrinos from GeV (for KM3NeT/ORCA) to PeV energies and above (for KM3NeT/ARCA) [175]. ARCA stands for Astroparticle Research with Cosmics in the Abyss while ORCA stands for Oscillation Research with Cosmics in the Abyss. The goal of the KM3NeT technology is to instrument, at minimal cost and maximal reliability, the largest possible volume of seawater with a 3D spatial grid of ultra-sensitive photo-sensors, while remaining sensitive to neutrino interactions in the target energy range [175]. The KM3NeT design builds upon the ANTARES experience and improves the cost-effectiveness of its design by about a factor four [175]. The ANTARES neutrino telescope design and technology are discussed in detail in Section 3. The KM3NeT components are designed for at least ten years of operation with negligible loss of efficiency [175]. As discussed above, longevity plays a decisive role due to inaccessibility to the detector components in case of problems [117]. The system should provide nanosecond precision on the arrival time of single photons, while the position and orientation of the photo-sensors must be known to a few centimeters and few degrees, respectively [175]. The photo-sensors and the readout electronics are hosted within pressure-resistant glass spheres, DOMs, which are distributed in space along flexible strings, one end of which is fixed to the seafloor and the other end is held close to vertical by a submerged buoy [175]. The concept of strings is modular by design that allows the construction and operation of the research infrastructure for a phased and distributed implementation [175]. The modular design allows the collections of 115 strings, called building blocks, to be constructed with different spacings between lines/DOMs, in order to target different neutrino energies [175].

The full KM3NeT telescope comprises 7 building blocks distributed on 3 sites [175, 611] (see Fig. 2.22):

KM3NeT-France: this site is located at 42°48′ N 6°02′ E at a depth of 2500 m, about 40 km off-shore from Toulon, France (see Fig. 2.22). The site is outside of the French territorial waters and about 10 km west of the site of the ANTARES telescope;

KM3NeT-Italy: this site is located at 36°16′ N 16°06′ E at a depth of 3500 m, about 100 km off-shore from Porto Palo di Capo Passero, Sicily, Italy (see Fig. 2.22). The site is the former NEMO site;

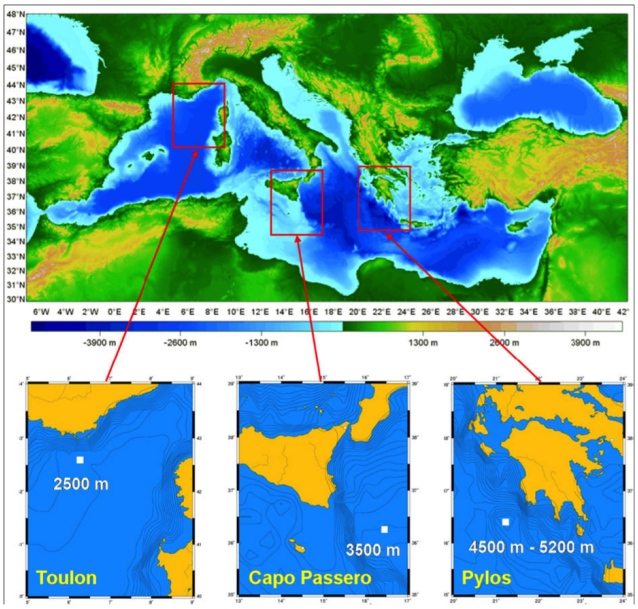

Fig. 2.22.: Location of the three proposed installation sites of the KM3NeT neutrino telescope in the Mediterranean Sea. The figure is taken from [612].

KM3NeT-Greece: this site is located at a depth of 4500-5200 m, about 30 km southwest of Pylos, Greece (see Fig. 2.22). This site is the deepest site of the three proposed locations. The site is the former NESTOR site.

The KM3NeT Research Infrastructure is planned to be built in three steps, called phases [175]:

1 During the first phase (Phase-1), the technical design has been validated through *in situ* prototypes; data analysis tools have been developed; assembly sites for the production of OMs and strings have been set up; deployment and connection of strings in the deep-sea are being optimized for speed and reliability;

2 During the second phase (Phase-2.0), the KM3NeT Collaboration will complete the construction of ARCA and ORCA by 2020. Three building blocks are planned: two KM3NeT/ARCA blocks, with a large spacing to target astrophysical neutrinos at TeV energies and above; and one KM3NeT/ORCA block, to target atmospheric neutrinos in the few-GeV range;

3 During the third phase (Phase-3), the ultimate goal is to fully develop the KM3NeT Research Infrastructure to comprise a distributed installation at the three foreseen sites and operate it for ten years or more.

Two ARCA building blocks will be sparsely configured in order to fully explore the IceCube signal with comparable instrumented volume, different methodology, improved resolution and complementary field of view, including the Galactic plane while one ORCA building block will be densely configured to precisely measure atmospheric neutrino oscillations [175].

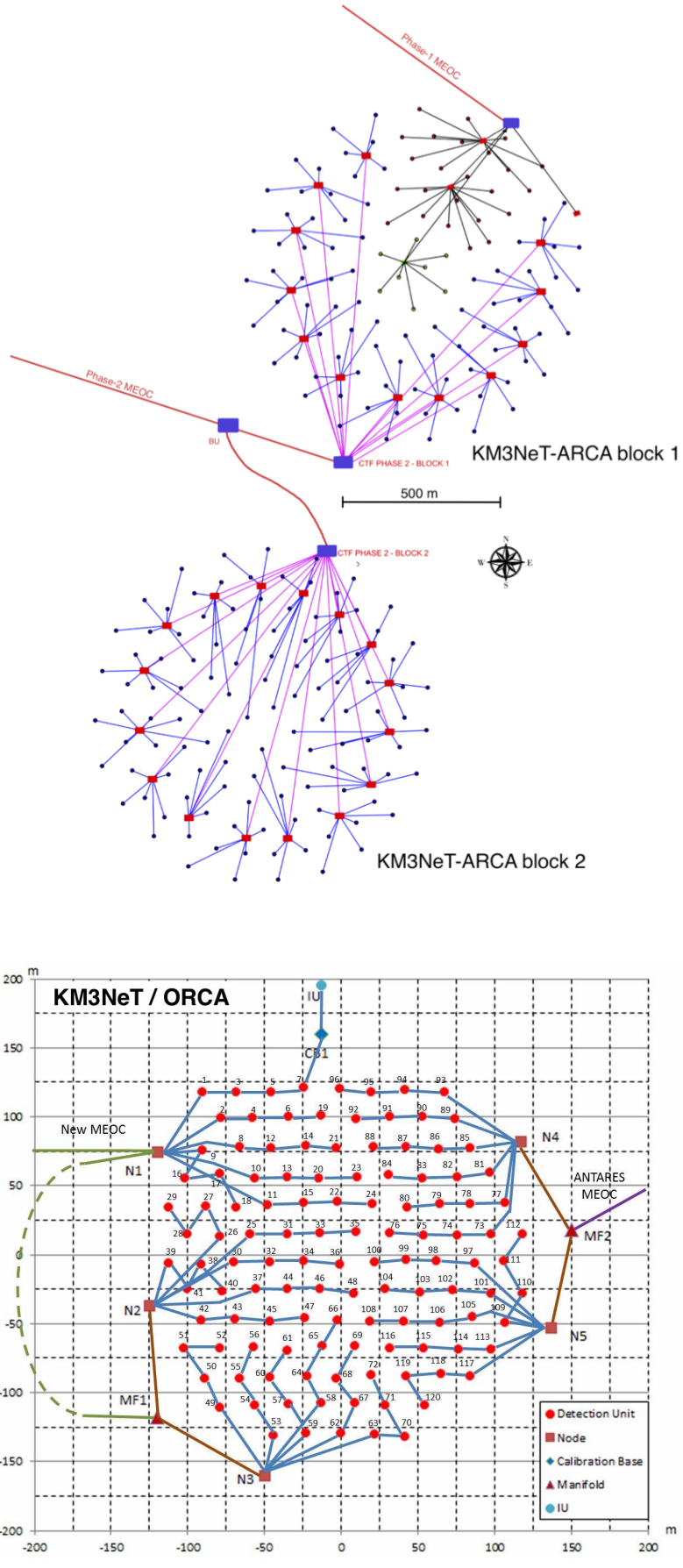

Fig. 2.23.: Layout of the building blocks. *Top:* ARCA (two building blocks). *Bottom:* ORCA (one building block). The figure is taken from [175].

Due to KM3NeT's flexible design, the technical implementation of ARCA and ORCA is almost identical [175]. Figure 2.23 shows the layout of the telescopes at the KM3NeT-Italy (ARCA) and KM3NeT-France (ORCA) installation sites. For ORCA, it depicts the 115 (+5 contingency) DUs, cables and connection devices of the full array [175]. The power/data are transferred to/from the infrastructure via two Main Electro-Optical Cables (MEOCs) [175]. On-shore each MEOC is connected to a power feeding equipment located in the shore station, which also hosts the DAQ electronics and a commodity PC farm used for data filtering [175]. For the ARCA, in addition to the already operating cable serving the Phase-1 detector, a new Phase-2 cable will be installed (see Fig. 2.23) which will comprise 48 optical fibers while for the ORCA it will comprise 36/48 optical fibers and a single power conductor (the return is via the sea) [175]. For the ORCA, the strings are connected to five JBs, located on the periphery of the array [175] (see Fig. 2.23). For the ARCA, close to the underwater installation, the cable is split by means of a Branching Unit (BU) into two branches (see Fig. 2.23), each one terminated with a Cable Termination Frame (CTF) [175]. Each CTF is connected to secondary JBs, 12 for the ARCA block 1 and 16 for the ARCA block 2 [175]. Each secondary JB allows the connection of up to 7 KM3NeT detection strings [175]. For both detectors, the underwater connection of the strings to the JBs is via interlink cables running along the seabed [175]. For the ORCA configuration, the average horizontal spacing between detection strings is about 20 m [175] (see Fig. 2.23). For the ARCA configuration, the average horizontal spacing between detection strings is about 95 m [175] (see Fig. 2.23).

The KM3NeT DOM [613] (see Fig. 2.24) is a transparent 17-inch diameter glass sphere comprising two separate hemispheres, housing 31 PMTs, and their associated readout electronics [175]. The design of the DOM has several advantages over traditional OMs using single large PMTs such as used in ANTARES, as it houses three to four times the photo-cathode area in a single sphere and has an almost uniform angular coverage [175]. As the photo-cathode is segmented, the identification of more than one photon arriving at the DOM can be done with high efficiency and purity [175]. In addition, the directional information provides improved rejection of optical background [175]. The PMTs are arranged in 5 rings of 6 PMTs plus a single PMT at the bottom pointing vertically downwards and are spaced at 60° in azimuth and successive rings are staggered by 30° [175]. There are 19 PMTs in the lower hemisphere and 12 PMTs in the upper hemisphere. The PMTs are held in place by a 3D printed support [175]. The photon collection efficiency is increased by 20-40% by a reflector ring around the face of each PMT [175]. In order to assure optical contact, an optical gel fills the cavity between the support and the glass [175]. The support and the gel are sufficiently flexible to allow for the deformation of the glass sphere under hydrostatic pressure [175]. Due to the small size of the PMT, the influence of the Earth's magnetic field is negligible and a μ-metal shield is not required, unlike ANTARES (see Section 3.2.1). Each DOM in a string has a dedicated wavelength to be later multiplexed with other DOM wavelengths for transfer via a single optical fiber to the shore [175]. The

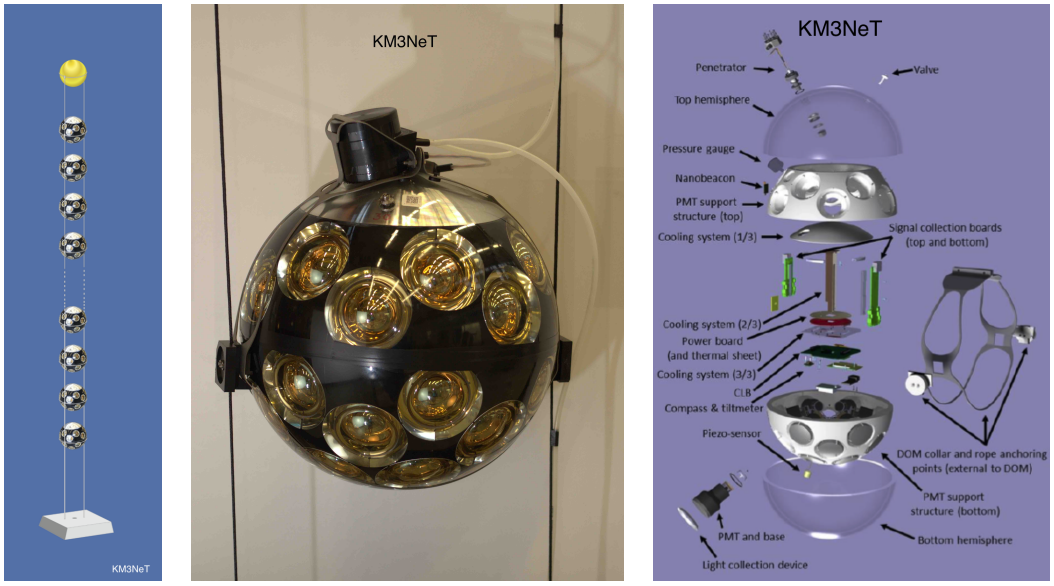

Fig. 2.24.: *Left:* Scheme of a DU. *Middle:* A photograph of a DOM. *Right:* Exploded view of the inside of a DOM. The figure is taken from [175].

broadcast of the onshore clock signal, needed for time stamping in each DOM, is embedded in the Gb Ethernet protocol [175].

The OM also contains three calibration sensors [175]:

1 The LED nano-beacon, which illuminates the OMs vertically above;

2 A compass and tilt-meter for orientation calibration;

3 An acoustic piezo sensor glued to the inner surface of the glass sphere for position calibration.

Each KM3NeT DU [614] (see Fig. 2.24) hosts 18 DOMs. For KM3NeT/ARCA, each is about 700 m in height, with DOMs spaced 36 m apart in the vertical direction, starting about 80 m from the seafloor [175]. For KM3NeT/ORCA, each string is 200 m in height with DOMs spaced 9 m apart in the vertical direction, starting about 40 m from the seafloor. Each string comprises two thin (4 mm diameter) parallel Dyneema® ropes (see Fig. 2.24) to which the DOMs are attached via a titanium collar [175]. Additional spacers are added in between the DOMs to maintain the ropes parallel [175]. Attached to the ropes is the vertical electro-optical cable, a pressure-balanced, oil-filled, plastic tube that contains two copper wires for the power transmission (400 V DC) and 18 optical fibers for the data transmission [175] (see Fig. 2.24). At each storey, two power conductors and a single fiber are branched out via the breakout box (see Fig. 2.24) which also contains a DC/DC converter (400 V to 12 V) [175]. The power conductors and optical fiber enter the glass sphere via a penetrator [175]. Even though the KM3NeT string design minimizes drag and itself is buoyant, additional buoyancy is introduced at the top of the string as shown in Fig. 2.24 to

reduce the horizontal displacement of the top relative to the base for the case of large sea currents [175].

The KM3NeT fiber-optic data transmission system performs the transfers of all the data to shore with the bandwidth per DOM is 1 Gb/s, the timing synchronization with relative time offsets between any pair of DOMs to be stable within 1 ns, the individual controls for each DOM (via setting the HV of a PMT, turn off/on a single PMT, turn on/off nano-beacon, update soft- and firmware) and for each base of a string (via turning string power on/off, control optical amplifiers, monitor AC/DC converter), and also provides slow control for the JBs [175].

The KM3NeT DAQ [615] is based on the "all-data-to-shore" concept, following the experience of the ANTARES detector (see Section 3.3). In this concept, all analog signals from the PMTs that pass a preset threshold (typically 0.3 p.e.) are digitized and all digital data are sent to shore where they are processed in real-time [175]. The physics events are filtered from the background using designated software [175]. To maintain all available information for the offline analyses, each event will contain a snapshot of all the data in the detector during the event [175]. Different filters can be applied to the data simultaneously [175]. For the detection of muons and showers, the time-position correlations that are used to filter the data follow from causality. Similarly to the ANTARES, the KM3NeT has three levels of filters, called L0, L1, and L2 [175] (see Section 3.3.3 for details about the ANTARES triggers). More information about the KM3NeT triggers can be found in [175].

A multiPMT DOM has several advantages if compared to the traditional, large cathode single-PMT OM used in ANTARES, Baikal and IceCube detectors, like, e.g., a larger (three to four times) total photo-cathode area and better discrimination of single vs multi photoelectron [612]. The photon-counting capability and the directionality provided by the photo-cathode, segmentation will enable a single DOM to identify muons and to be sensitive to their arrival directions [616], as demonstrated in Fig. 2.25. Here, the event rate is shown as a function of the coincidence level which is defined as the number of PMTs having a detected hit within a 20 ns time window [616]. Below a coincidence level of six [616], the measured event rate is in good agreement with the event rate given by the simulation of the ^{40}K decays [617]. Above the coincidence level of seven, the signals from atmospheric muons dominate [616]. As a result, simply requiring a coincidence among 6-7 PMTs the bulk of hits due to the decay of ^{40}K dissolved in the seawater can be rejected [611], as shown in Fig. 2.25. A cut applied at a coincidence level larger than seven selects a pure muon sample [616].

From submission of a proposal for the KM3NeT preparatory phase in the European 7th framework program (FP7) on May 2nd, 2007 the KM3NeT has come a long and fruitful way. On January 29th, 2013, 40 institutes formed a collaboration for the implementation of the first phase of the KM3NeT Research Infrastructure.

On May 7th, 2014, an ARCA prototype string comprising three active DOMs was successfully deployed and connected to the KM3NeT-Italy site. On September 22nd, 2017 the first DU of ORCA was successfully deployed and connected to the KM3NeT-France site. At the beginning of 2016, the Letter of Intent [175] which details the science performance, as well as the technical design of the KM3NeT 2.0 infrastructure, was published. Today, the KM3NeT telescopes, ARCA and ORCA, are routinely operating with five DUs: four at the ORCA site, one at the ARCA site. First data results have been reported on international conferences and workshops such as the International Cosmic Ray Conference (ICRC) 2019[22], one of the most important conferences where astroparticle physicists share their latest results. Furthermore, KM3NeT sent out its first GCN circular (GCN #26249 [618]) on November 14th, 2019 performing a follow-up analysis of the GW burst candidate S191110af (GCN #26222 [619]) recently reported by LIGO/Virgo. This event opened multimessenger astronomy for KM3NeT. These all promise a brighter future for neutrino astronomy, where one of the main roles in the forthcoming discoveries will be played by KM3NeT.

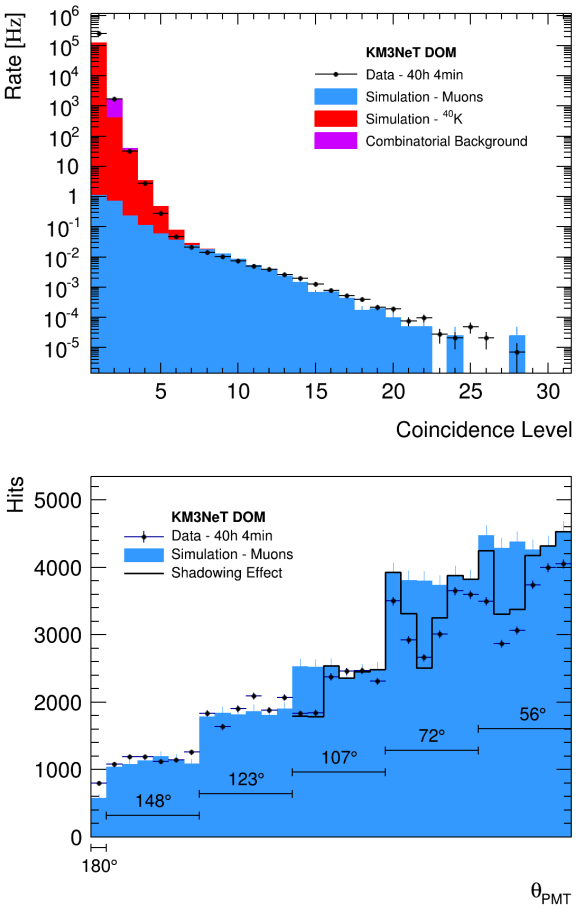

Fig. 2.25.: *Top:* The rate of events as a function of the coincidence level (number of PMTs with a signal in a 20 ns time window). Black dots correspond to data while coloured histograms represent simulations (muons in blue, ^{40}K in red and accidental coincidences in purple). *Bottom:* The number of hits as a function of the zenith position of the center of the PMT for coincidence levels above seven. One PMT is looking downward (180°). The others are grouped by six at five different angles. The black dots are data, the blue histogram is a simulation of atmospheric muons and the black histogram show the calculated effect of the shadowing by the ANTARES electronics cylinder. The figure is taken from [616].

[22] See KM3NeT at ICRC 2019, https://www.km3net.org/km3net-at-icrc2019/ The 36th edition held in Madison, WI, USA. https://www.icrc2019.org/

The ANTARES neutrino telescope

3

ANTARES [506, 481] (Astronomy with a Neutrino Telescope and Abyss environmental RESearch) is the first undersea neutrino telescope and at present the largest operating water Cherenkov detector in the Northern Hemisphere. ANTARES is an international collaboration involving more than 150 physicists, engineers and sea-science experts from 29 institutes of 8 countries (France, Germany, Italy, Morocco, The Netherlands, Romania, Russia, and Spain) (see Fig. 3.1). It is located in the Mediterranean sea, 40 km off the coast of Toulon, France (42°48′ N 6°10′ E), at a depth of 2475 m [620] (see Fig. 3.2). The first line of ANTARES was deployed on February 14th, 2006 and measurements of the atmospheric muon flux were performed shortly after [571]. The detector has been completed on May 30th, 2008 and is expected to continue until at least the end of 2019.

In this section, a general description of the detector design and its operation is given. An overview of the detector layout is given in Section 3.2. The "eyes" of the detector, i.e. the Optical Modules, which actually detect the Čerenkov light from charged secondary particles created in neutrino interactions near or inside the detector, are described in Section 3.2.1. The storeys setups and configuration of lines are discussed in Section 3.2.2 and Section 3.2.3 respectively. The infrastructure to power and control the off-shore detector with its main elements is briefly described in Section 3.2.4. The data acquisition system is discussed in Section 3.3. The overview of ANTARES detector site properties such as light transmission, environmental background, biofouling, and sedimentation is given in Section 3.4. The detector calibration procedure is described in Section 3.5.

3.1 Detector design

The ANTARES detector is mainly designed to search for high-energy neutrinos from astrophysical sources by detecting the Cherenkov light emission of neutrino-induced charged particles in the very deep waters of the Mediterranean Sea and most sensitive for neutrino energies 100 GeV $< E_\nu <$ 100 TeV [177, 178]. The ANTARES observatory as proved to be a highly successful instrument for performing a wide range of physics analyses from atmospheric neutrino oscillations to dark matter annihilation or potential exotics such as nuclearites and magnetic monopoles[621]. As a detector located in the Northern Hemisphere, the ANTARES benefits from its latitude and is able to explore the Southern Sky, providing unprecedented sensitivity to the central region of our Galaxy, where the neutrino source candidates are expected. The search program also includes multi-messenger analyses based on time and/or space coincidences with other cosmic probes such as Active Galactic Nuclei, the brightest sources in our Universe [621].

Fig. 3.1.: Location of institute members of the ANTARES collaboration.

Compared to South Pole experiments, the ANTARES telescope gives the extra possibility to study galactic sources like Binary Stars, Supernova Remnants, or Microquasars and search for Dark Matter accumulation at the center of the Galaxy. However, the view given by Southern and Northern telescopes is complementary both in the potential sky map and the objects that can be studied. They have a common view of the sky of 0.5π steradian at any moment, and 1.5π steradians for a whole day [622, 623].

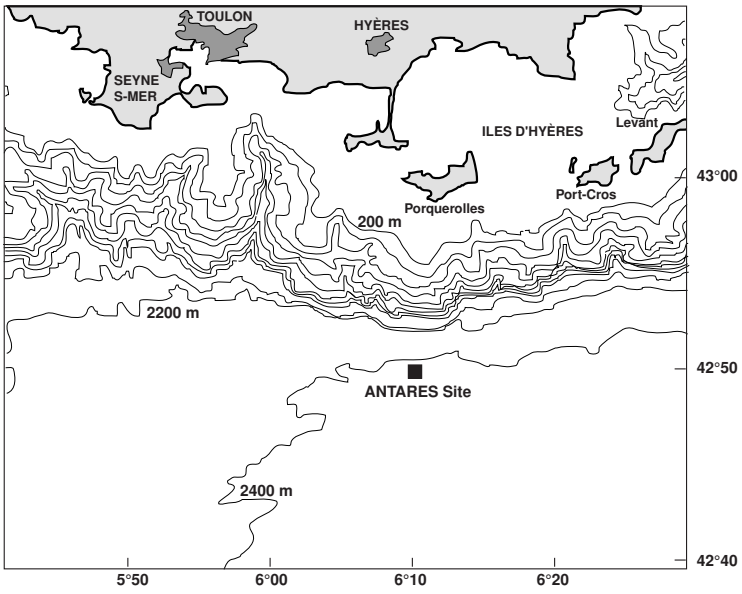

Fig. 3.2.: Location of the ANTARES site, near the Mediterranean French coast. Each profile line corresponds to 200 m depth change. The figure is taken from [506].

3.2 Detector layout

A schematic view of the ANTARES layout is given in Fig. 3.3. The detector consists of an array of 885 PMTs distributed in 12 detection lines (or strings), each one equipped with 25 storeys of 3 OMs, except line 12 with only 20 storeys of OMs completed with a device dedicated to acoustic detection [624, 625]. The lines are arranged in an octagonal configuration, the horizontal spacing among the lines is ~60 m, while the vertical spacing between the storeys is 14.5 m starting 100 m from the seabed [625]. The distances between OMs are optimized with respect to the absorption length in the water, which has a maximum of ~60 m [555]. The line is anchored on the seabed and is held vertical by a submerged buoy. Each OM is a glass sphere which hosts a PMT, the 10-inch tube from Hamamatsu [626], whose axis points 45° downwards (see Fig. 3.6) in order to optimize the detection of light from up-going muons [620]. The OMs are grouped in triplets for the essential reduction of the deep-sea environmental optical background such as radioactive ^{40}K decays or bioluminescence by using coincidences on the same storey in a short time interval [625]. The relative position of each OM in the detector is monitored in real-time by a dedicated positioning system [620]. All signals from the PMTs that pass a threshold of 0.3 Single PhotoElectron (SPE), called hits, are digitized and sent to the shore station [627, 628]. To provide a continuous stream of data to the shore station and to be electrically fed, each line is connected to a JB on the seabed, to which the shore 40 km long electro-optical cable is connected.

3.2.1 Optical Module

The optical sensor, or OM [626], is a key component of the ANTARES detector. It is composed of a transparent 17-inch diameter pressure-resistant glass sphere housing a 10-inch PMT and all the electronics. A schematic view and a picture of the OM is shown in Fig. 3.4. The glass sphere protects the PMT from the pressure of the surrounding seawater while ensuring good light transmission, implying a refractive index close to that of seawater and of the PMT glass. It is made up of borosilicate glass with a refractive index n=1.47. A highly transparent silicone gel SilGel 612 A/B[1] with a refractive index n=1.404 (after polymerization [626]) is used to glue the PMT to the glass sphere. Such a refractive index of a gel comparable to that of glass serves to reduce light reflection on the glass surface. The glass sphere is thick enough (15 mm) and has been designed to resist high hydrostatic pressures in the deep-sea extreme environment. The pressure at the operating depths of the ANTARES requires the PMTs to withstand up to 260 atm. The sphere is fully resistant to corrosion; it is chemically, electrically and magnetically inert. A μ-metal cage with high magnetic permeability protects the PMT against the Earth's magnetic field. These glass spheres, because of their mechanical resistance to a compressive stress and of their transparency, provide a convenient housing for the ANTARES PMTs [481]. Table 3.1

[1] Wacker-Chemie AG, http://www.wacker.com

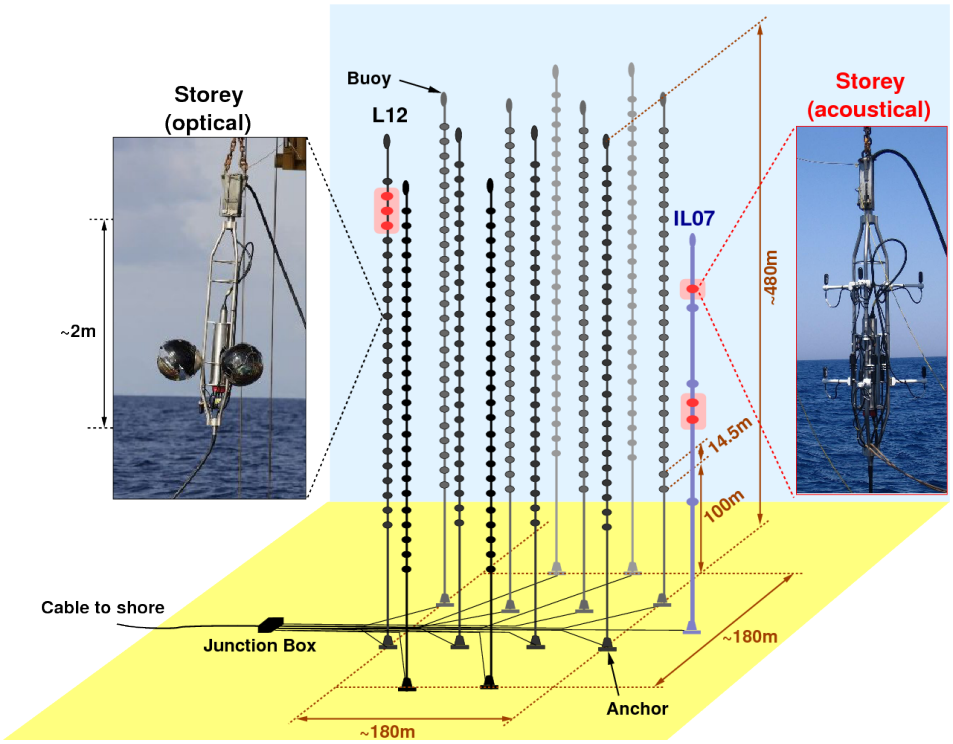

Fig. 3.3.: Schematic view of the ANTARES layout with the main elements outlined. The two types of storeys, optical and acoustic, are shown. Optical and acoustical storeys are drawn in black and red respectively. Line anchors, buoys, interconnection cables and the JB are also indicated. The figure is taken from [624].

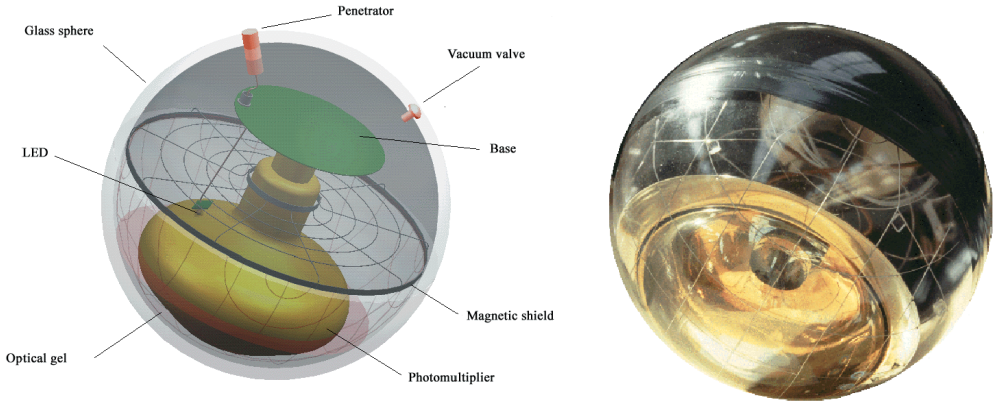

Fig. 3.4.: Schematic 3D view (*Left*) and picture (*Right*) of the ANTARES optical module and its components. A large 10-inch diameter hemispherical photomultiplier is protected by a pressure-resistant glass sphere. An internal LED system is used for the calibration. The figure is taken from [626].

summarizes the main characteristics of the Vitrovex®[2] [481] glass spheres used [481]. Several types of PMTs with various photocathode diameters from different manufacturers have been evaluated during R&D phase and the R7081-20 Hamamatsu[3] PMT model has

[2]Nautilus Marine Service GmbH, http://www.nautilus-gmbh.de
[3]Hamamatsu Photonics, Electron tube division, http://www.hamamatsu.com

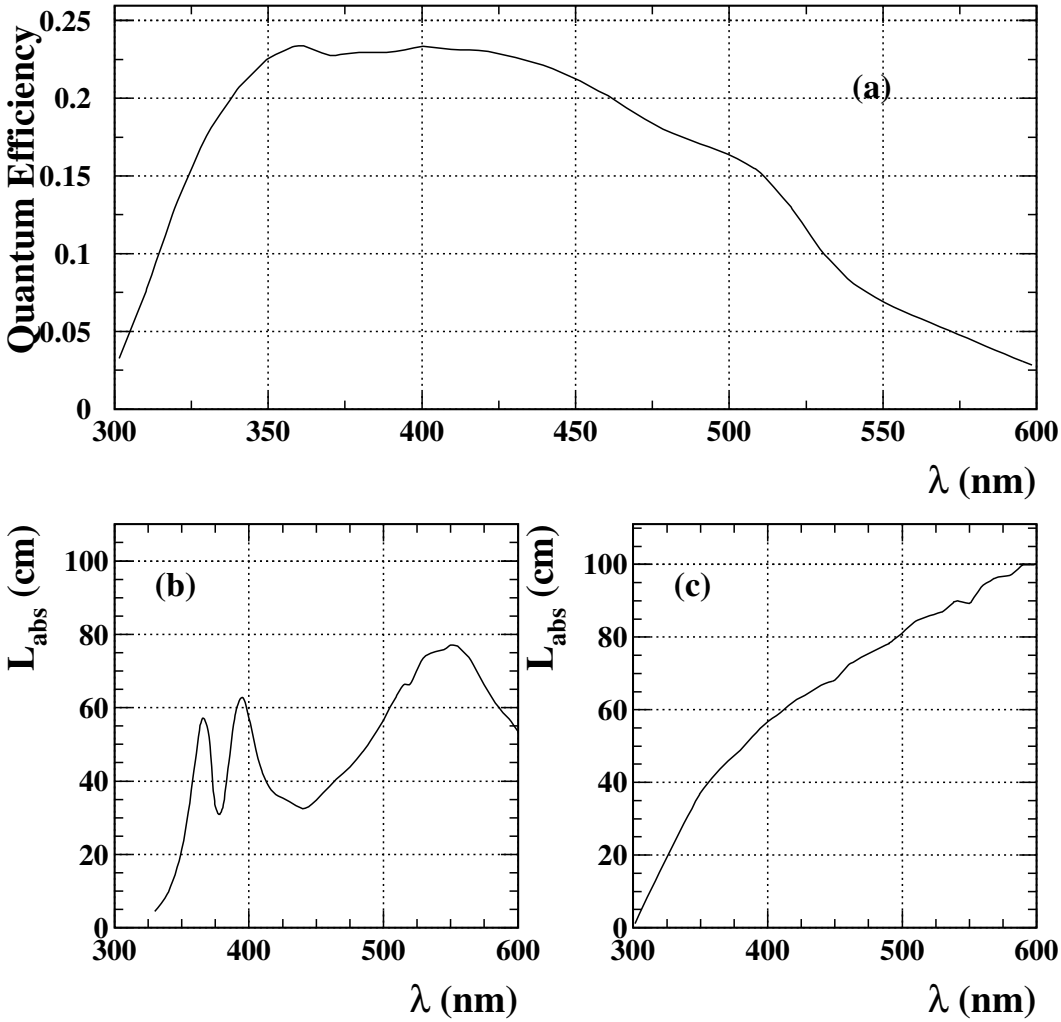

Fig. 3.5.: Characteristics of the R7081-20 Hamamatsu PMT: (a) quantum efficiency, (b) measured absorption length of the glass sphere and (c) of the silicone gel as a function of the incident light wavelength. The figure is taken from [626].

been selected [626]. It is sensitive to photons in the wavelength range between 300 nm and 600 nm with a good light transmission: the attenuation length is greater than 30 cm above 350 nm, which corresponds to a transmission of at least 95% (see Tab. 3.1). The Transit Time Spread (TTS), which characterizes the time response of the PMT (defined as the FWHM of the main peak), is one of the key parameters that determine the angular resolution of the detector. The TTS of R7081-20 is about 2.6 ns (FWHM) which provides a good timing resolution. The maximum quantum efficiency ranges from 350 to 450 nm where it reaches 25% (see Fig. 3.5). An overview of the tests performed by the collaboration and describes in detail the features of the PMT chosen for ANTARES is given in [629].

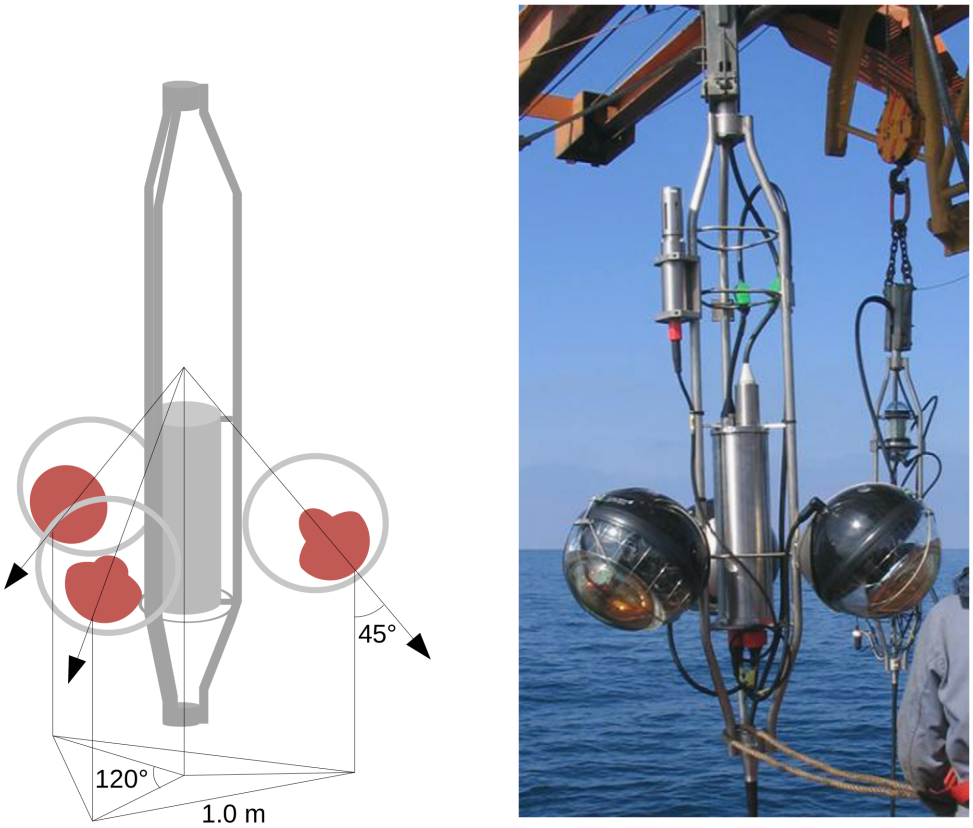

Fig. 3.6.: *Left:* Schematic representation of an ANTARES storey. The spheres stand for the OMs, which contain one PMT each, facing 45° downwards. The figure is taken from [625]. *Right:* View of an OMF showing the mounting of the electronics cylinder together with the electro-mechanical cable penetrators and cable routing. The figure is taken from [630].

3.2.2 Storeys

As stated above, the OMs are grouped in triplets (storeys). Each storey (see Fig. 3.6) is the assembly of a mechanical structure, the Optical Module Frame (OMF), which holds three OMs, and a pressure resistant titanium (Ti) container, the Local Control Module (LCM), housing the off-shore electronics and embedded processors [481]. The container is placed at the center of the structure and it is made of a hollow cylinder (600 mm long, 179 mm outer diameter and 22 mm wall thickness) closed by two end caps 30 mm thick each with the entire volume optimally used for housing the electronics [481]. The LCM contains all the electronics necessary for the data acquisition [628], control of storey devices (OM signal processing, the instrument readout, the acoustic positioning, the power system) and communication with the shore.

A standard LCM elements are [481]:

Local Power Box (LPB) Provides the 48 V for the OMs and several different low voltages for the electronics boards. An embedded microcontroller allows the monitoring of the voltages, the temperatures and the current consumptions as well as the

Tab. 3.1.: Summary of the main properties of the high-pressure glass sphere [626, 481].

Material	Vitrovex 8330
Outer diameter	432 mm (17 in.)
Wall thickness	15 mm
Type of glass	Borosilicate
Refractive index	1.47 ($300 < \lambda < 600$ nm)
Light transmission above 350 nm	>95% (above 350 nm)
Density	2.23 g cm^{-}3
Pressure of qualification test	700 bar (70 MPa)
Diameter shrinking at 250 bar	1.25 mm (0.3%)
Absolute internal air pressure	0.7 bar (70 kPa)
Depth rating	6700 m
Hole diameters (penetrator and vacuum port)	20 mm, 5 mm

remote setting of the 48 V for the OMs. The 400 V DC feeds the LPB from the bottom of the line.

Clock The clock reference signal (see Fig. 3.12) coming from shore reaches the bottom of the line where it is repeated and sent to each sector (each detection line is divided into 5 functional units, called sectors, each one comprising 5 storeys). Within a sector, the clock signal is daisy-chained between LCMs. The role of the clock card is to receive the clock signal from the lower LCM, to distribute it on the backplane and to repeat it toward the upper LCM of the sector. The clock signal generated on-shore is synchronized with a Global Positioning System (GPS) receiver for absolute time reference and delivered to all off-shore electronics by means of a dedicated optical fiber network to establish a common time reference for the complete apparatus.

Analog Ring Sampler (ARS) board Hosts the front-end electronics of the OMs (one board per OM) (see Fig. 3.8). This front-end electronics [628] consists of a custom-built ARS chip [631] (see Fig. 3.7) which digitizes the charge and the time of the analog signal coming from the PMTs. The arrival time is determined from the signal of the clock system in the LCM and from a Time to Voltage Converter (TVC) which provides a sub-nanosecond resolution.

The Data Acquisition/Slow-Control (DAQ/SC) card Host the local processor and memory used to handle the data from the ARS chips and from the SC (see Fig. 3.8), respectively. The processor has a fast 100 Mb/s Ethernet controller that is optically connected to an Ethernet switch in the Master Local Control Module (MLCM) (see Fig. 3.10) of the corresponding sector which acts as the gateway for all communications between its sector and the shore (see Fig. 3.12). The specific hardware for the readout of the ARS chips and data formatting is implemented in a high-density Field-Programmable Gate Array (FPGA)[4] (see Fig. 3.8). The data are temporarily stored

[4] Virtex-EXCV1000E, http://www.xilinx.com

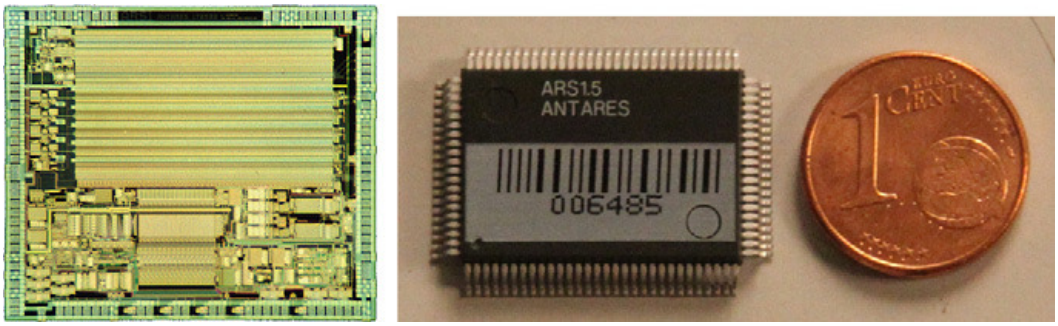

Fig. 3.7.: The ARS chip, bare die (left) and packaged chip (right). The figure is taken from [628].

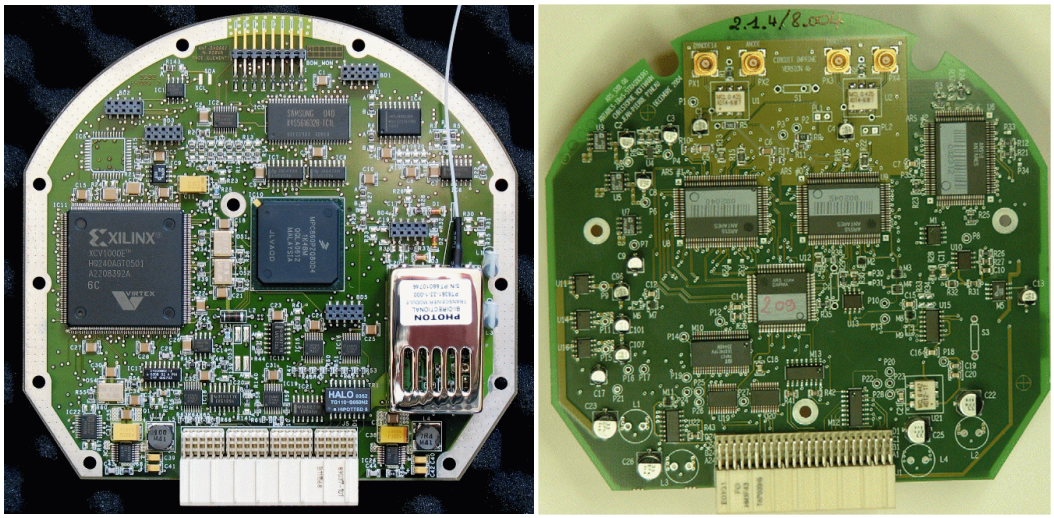

Fig. 3.8.: *Left:* The DAQ/SC board holding the processor (center), the FPGA (left) and the optical link to the MLCM (right). *Right:* The ARS motherboard (⌀~15 cm). The figures are taken from [481] and [628] respectively.

in a high capacity memory with a 64 MB Synchronous Dynamic Random Access Memory (SDRAM) allowing a de-randomization of the data flow (see Fig. 3.12).

Compass board Hosts a TCM[5] sensor which provides heading, pitch and roll of the LCM used for the reconstruction of the line shape and PMT positions (see Fig. 3.10). The heading is measured with an accuracy of 1° over the full cycle and the tilts with an accuracy of 0.2° over a range of ±20°.

Most of the LCMs contain the same set of electronics cards but, as mentioned, due to the segmentation of a line in sectors, a specific LCM located every fifth storey, MLCM, acts as a master for other LCMs of the same sector (see Fig. 3.12) and houses additional boards to gather the data from the local OMs and from the four connected storeys [481]. Other differences between individual LCMs are due to electronics necessary for optional equipment on the storey: LED Optical Beacon (OB) used for time calibration and for monitoring the water optical properties; hydrophone (Rx modules) used to produce the acoustic positioning of the detector; etc.

[5]PNI Sensor Corp., http://www.pnicorp.com

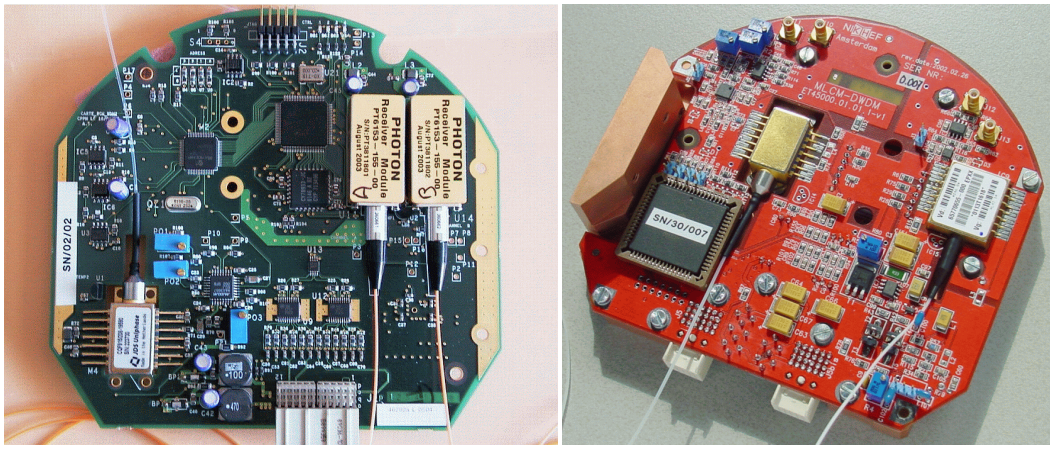

Fig. 3.9.: *Left:* The SCM_WDM board. *Right:* The DWDM board. The figures are taken from [481].

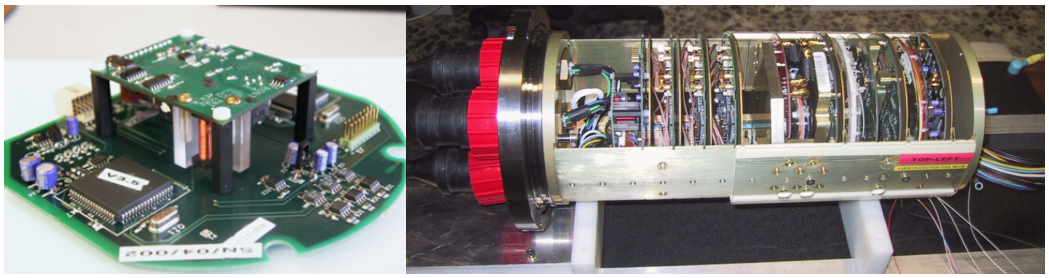

Fig. 3.10.: *Left:* The Compass motherboard equipped with a TCM2 sensor on a daughter card. *Right:* The MLCM's crate equipped with the electronics boards. The figures are taken from [481].

The acoustic neutrino detection is integrated into ANTARES in the form of Acoustic Storeys (AS) [481] which are modified standard storeys with the PMTs replaced by acoustic sensors with custom-designed electronics for signal processing. This system called AMADEUS (Antares Modules for the Acoustic Detection Under the Sea) [632] is a feasibility study for a prospective future large scale acoustic detector. This technique aims to detect neutrinos with energies exceeding 100 PeV [481]. AMADEUS consists of six ASs, three of them located on the Instrumentation Line (IL) 2007, IL07, and three on Line 12 (see Fig. 3.6). Each AS comprises six acoustic sensors that are arranged at distances of roughly 1 m from each other. The maximum distance between two ASs is 340 m.

3.2.3 Lines

ANTARES 12 lines and instrumentation line (see Fig. 3.11) IL07 are arranged in an octagonal configuration covering an area of about 180 m × 180 m on the seabed (see Fig. 3.3). The lines are separated by distances of 60-70 m from each other. The lines, each with a total height of 450 m, are anchored on the seabed with the Bottom String Socket (BSS) [481] and are kept vertical by a buoy on their top. The 11 lines are equipped with the nominal 25 storeys configuration, the twelfth line being equipped with 20 storeys and completed by devices dedicated to acoustic detection. The vertical spacing between the storeys is 14.5 m

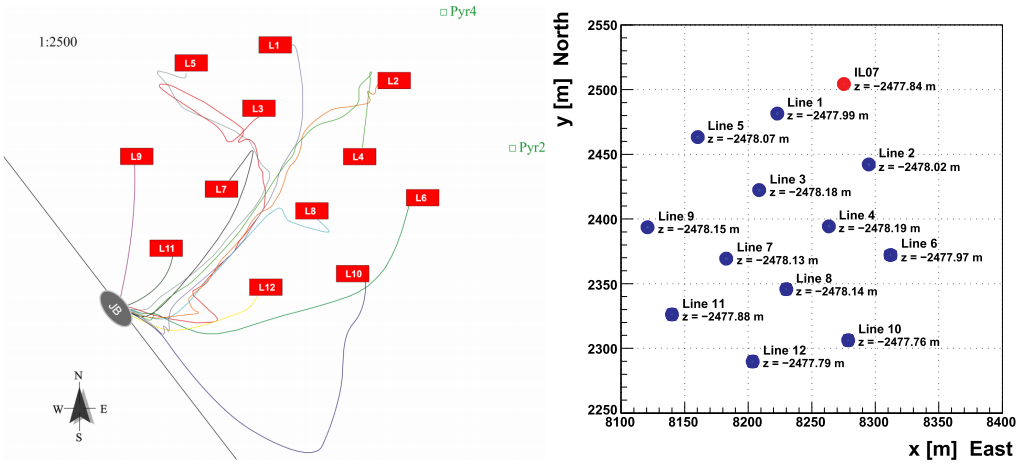

Fig. 3.11.: *Left:* Detector layout at the seabed. The colour lines indicate the position of the interlink cables between the bottom of the lines and where they converge. Acoustic pyramids (Pyr) are located surrounding the lines and used for positioning. The figure is taken from [633]. *Right:* Triangulated anchor positions of the Antares detection strings Line 1-12 (marked by blue points) and the instrumentation line IL07 (indicated in red) on the seafloor end of 2009. The horizontal axis (x) points towards East, the vertical axis (y) towards North. Distances are given in meters. The lines are arranged in an octogonal structure. The depth (z-coordinate) of each anchor is also stated, confirming that the seafloor at the installation site is almost flat. The figure is taken from [516].

starting 100 m from the seabed. Storeys are grouped in sectors with 5 storeys each. The apparatus is designed so as to allow independent communications with each sector from shore [628]. The MLCM controls each unit and acts as the gateway for all communications between its sector and the shore [628].

A String Control Module (SCM) [481], situated on the BSS at the bottom of each line, contains the electronics for the data transfer and provides the connection of MLCM to the JB. The JB, in turn, is connected to the shore station by a standard deep-sea 40 km long electro-optical communication cable (see Fig. 3.12) and provides a continuous stream of data [481].

A String Power Module (SPM) [481], located on the BSS powers each sector. The SPM part, at the top, contains transformers that deliver the five 400 V DC supplies needed for the sectors, starting from the 480 V AC provided by the JB [481]. An embedded microcontroller operates the remote powering of sectors. Voltages, temperatures and current consumptions are monitored [481]. The microcontroller can also detect anomalies and is programmed to turn off the power in case of over-consumption [481]. Like a standard LCM container, the SCM cylinder houses a crate equipped with Compass board, Clock and DAQ cards [481].

In order to perform the distribution of the clock signal to the sectors, the SCM crate houses specific boards receive receive the 20 MHz clock signal via an optical link from the shore and converts it to an electrical signal and distributes it to the sectors. This allows communicating with the shore. The SCM specific board is a Dense Wavelength Division Multiplexing

(DWDM) [481] (together called SCM_WDM (see Fig. 3.9)), similar to the MLCM one but working at 100 Mb/s and using its own DWDM channel. The role of the DWDM transceiver is to perform the electrical↔optical conversion for the full sector and to communicate with the shore via the SCM located at the bottom of the line [481] (see Fig. 3.12). The pair of fibers of the DWDM is connected, as well as the five pairs of fibers coming from the sectors to six channels of a 1-to-8 passive optical mux/demux[6] performing the merging/separation of the six colors [481]. The DWDM system is connected to the JB on the seabed via the interlink cables [481]. In the JB the outputs from up to 16 lines are gathered onto the MEOC and sent to the shore station. This element links the JB to the Power Hut (PH), located on-shore. In the shore station, the data are demultiplexed and treated by a PC farm where they are filtered and then sent via the commercial fiber optic network to be stored remotely at a computer center in Lyon[7] [481] (see Fig. 3.12).

3.2.4 Detector infrastructure

The infrastructure on the seabed [481] powers and controls the off-shore detector and provides data communication and the power distribution to the line. It includes the on-shore buildings to house the electronics required for monitoring and data acquisition, the MEOC providing the electrical power and the data link between the detector and the shore, the JB and the interlink cables to distribute the power and the optical fibers to the twelve data-taking lines and one IL07 instrumentation line.

The infrastructure consists of [481]:

InterLink cables (IL) Connects each line to the JB (see Fig. 3.11). The interlink cables produced by ODI[8]. In order to compensate for failures experienced in some of the 16 outputs of the JB, interlink cables of a special design are used in the seabed infrastructure. Each of these special cables connects two separate lines of the detector with one single JB output.

Junction Box (JB) Provides 16 electro-optical sockets to plug the interlink cables and power supply for each line. The JB is a pressure-resistant titanium container mounted to the JB Frame (JBF). Each JB output has four optical fibers: data uplink to shore (DAQ Tx_n, n=1→16), data downlink from shore (DAQ Rx_n, n=1→16), and the others for duplicated distribution of the central clock pulse train, clock channel A and B. DAQ Tx and Rx are specific to each line and are accommodated using 32 fibers in the undersea cable, which are point-to-point spliced in the JB hub to their respective fibers in the 16 output connectors. The central clock signal, vital for time referencing of PMT data to sub-nanosecond precision, is transmitted with a 4-fold redundancy.

[6] Multi-Channel Mux/Demux Module 400 GHz spacing; JDS Uniphase Corp., http://www.jdsu.com
[7] Centre de Calcul de l'IN2P3, http://cc.in2p3.fr
[8] Ocean Design Inc. (ODI), http://www.odi.com

Pulse trains from two independent, identical clock transmitters at the shore station are split for broadcast into four undersea fibers.

Main Electro-Optical Cable (MEOC) Provides the electrical power link and the optical data link between the shore station and the detector via JB (see Fig. 3.12). The selected cable, a standard telecommunications type, satisfies the electrical and optical transmission specifications as well as the environmental and mechanical criteria such as temperature tolerance, bending radius, and mechanical strength. The MEOC has been deployed from the site to the shore by a specialized cable-laying ship and crew under the responsibility of Alcatel[9]. The cable was tested for optical and power transmission prior to the deployment operation.

The on-shore infrastructure consists of two separate buildings, the Shore Station housing control and data management infrastructure and providing space for onsite personnel, and the PH devoted to power distribution requirements. The shore station is situated at La Seyne-sur-Mer (see Fig. 3.2) and has three rooms dedicated to the operation of the ANTARES experiment [481]: a computer room, a control room, and a service room. The computer room hosts the racks for the clock crate, the 13 on-shore DWDM crates (counterparts of the DWDM boards of the 13 lines) and the PC farm for data filtering and storage [481]. The control room contains various computers for apparatus control and status monitoring [481]. The PH is located near to the MEOC landing point at Les Sablettes and is connected to the latter with a fiber optical link 1.5 km long. The PH is connected to the 60 kVA, 400 V three-phase electrical distribution from Électricité de France. The building has been adapted to house the transformer 400/4000 V, the MEOC to shore link rack as well as the return current electrodes.

3.3 Data Acquisition System

The main purpose of the DAQ [481, 627, 628] is to convert the analog signals from the PMTs into a format suitable for the physics analysis. To achieve this, the DAQ system has the task to prepare the detector for data taking, convert the analog signals from the PMTs into digital data, transport the data to shore, filter the different physics signals from the background, store the filtered data on disk, and archive the run settings. The strategy is chosen for the ANTARES DAQ system is based on the ”all-data-to-shore” concept, which requires the transfer of all raw data above a certain given threshold to shore, where different software triggers are applied for filtering before storage.

3.3.1 Charge and time measurements

Digitization of the analog PMT signals, the total charge of the pulse and the arrival time is performed by a dedicated pair of ARS readout chips in LCMs. The settings of each ARS

[9] Alcatel URC3 Type 4 (unrepeatered); Alcatel-Lucent, http://www.alcatel-lucent.com

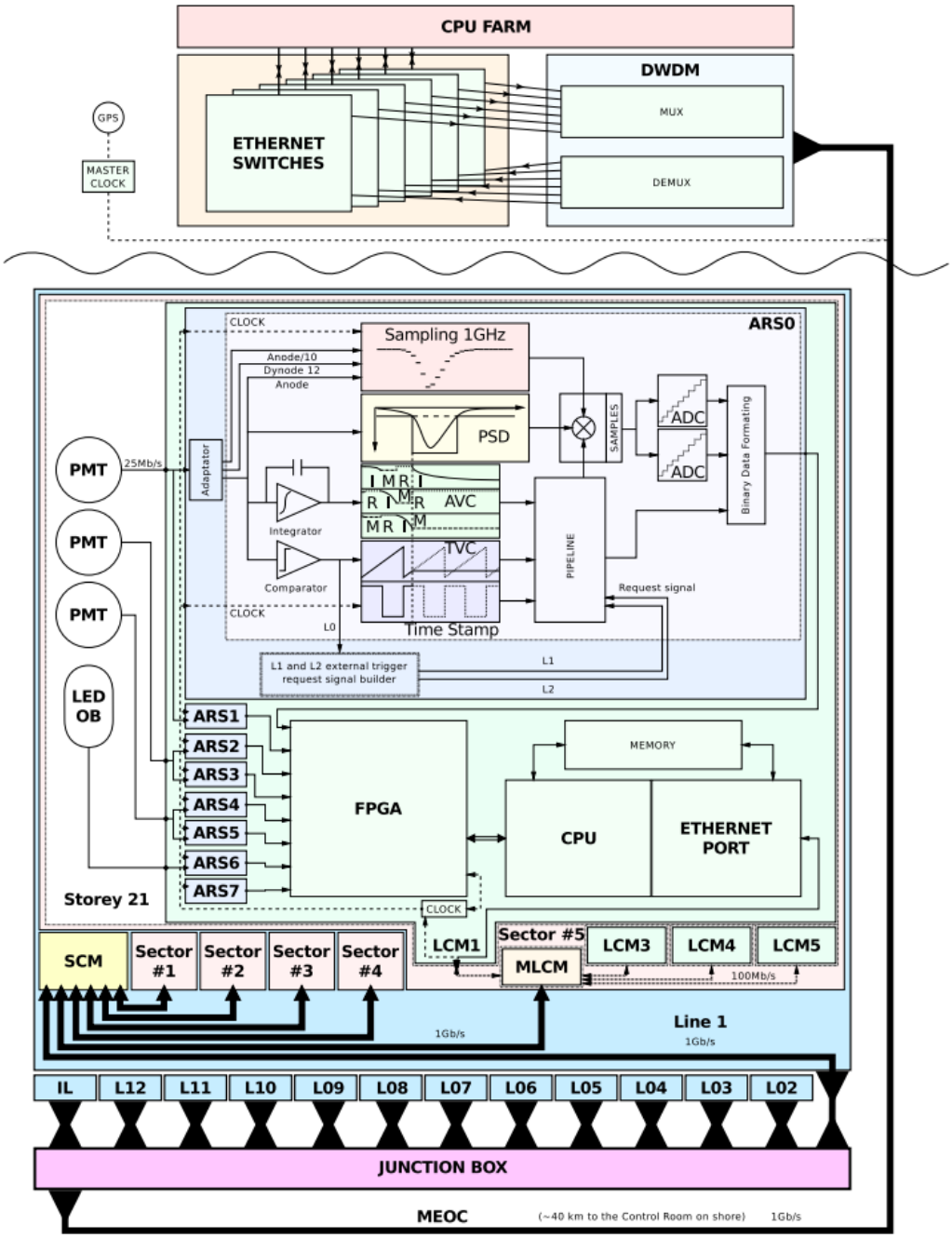

Fig. 3.12.: An example of the ANTARES DAQ for storey 21 in line 1. The PMT signal is transmitted to one of the two ARS chips assigned, where the hit is measured. The FPGA in the LCM in which the readout system of the chips is implemented processes the information and transfers it to MCLM, the LCM that centralizes the traffic on the sector. Transmission is carried out by the Ethernet port. Afterward, the MCLM communicates with the SCM on the BSS using the DWDM transceiver which performs the electrical↔optical conversion for the full sector. The DWDM is connected to the JB on the seabed which distributes the signals and commands to the shore station via MEOC, a 40 km long electro-optical cable. A CPU farm in the shore station filters and stores the data. The figure is taken from [516].

chip can be adjusted are the comparator threshold and the integration gate (see Fig. 3.12). When the signal crosses the threshold, an L0 trigger pulse is sent to the DAQ board. The

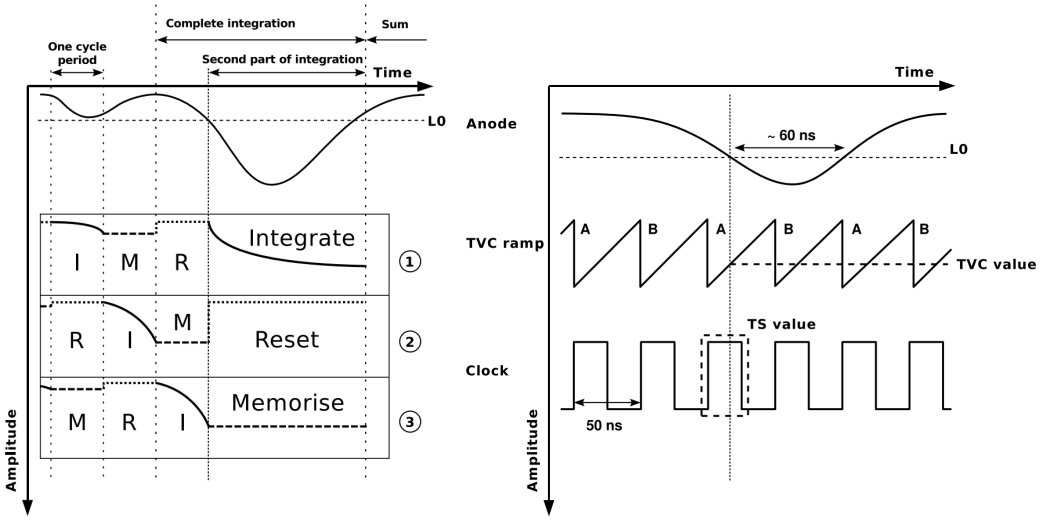

Fig. 3.13.: *Left:* Charge signal integration with 3 capacitors working in different phases. When the L0 is crossed, the ramp voltage is frozen and memorized. *Right:* Time measurement procedure in the ARS. When the L0 is crossed, a TS and a TVC are generated. The TS is given by the number of 50 ns cycles since the last reset (RTS). The TVC gives a refined time within the cycle. Two independent ramps, A and B, are used to avoid dead-time effects. The figure is taken from [516].

level of this charge threshold is tuneable by slow-control commands and corresponds to the 0.3 single p.e (SPE mode). The integration of the analog charge signal is carried out by a 8-bit Amplitude-to-Voltage Converter (AVC) [481] (see Fig. 3.12) and the integration gate is set typically to 35 ns [627] after threshold crossing which allows covering a length of most 1 p.e signals. The charge integration is carried out in three steps in order not to lose any charge by means of three capacitors working in three different phases (see Fig. 3.13):

- the integration phase (I), where the signal from the anode is integrated;
- the memorization phase (M), where the integrated charge is recorded in memory;
- the charge erasing phase (R), where a reset is done.

The combined charge-time information forms a single *hit*. The hit in the pipeline memory is digitized by the Analogue-to-Digital Converters (ADC).

About 99% of the signals are essentially due to optical background from bioluminescence or the disintegration of ^{40}K in seawater, which provides on average a single p.e. (~1 p.e.). The transfer function $n=f(Q)$ infers the number of p.e. from the digitized charge Q. Due to the intrinsic spread of the PMT gain, the p.e. peak is not a narrow spike but rather an extended distribution which is well described by a Gaussian function with mean $\mathrm{AVC}_{1\mathrm{pe}}$. The conversion from AVC units to charge units (p.e.) is computed in the laboratory for each ARS. The two most convenient reference points are the charge pedestal, the offset AVC value corresponding to the null point (0 p.e.) of the ADC, the $\mathrm{AVC}_{0\mathrm{pe}}$, and the p.e peak (1 p.e.), $\mathrm{AVC}_{1\mathrm{pe}}$, corresponding to a single photon hits. Based on these two reference points

and taken into consideration that the 8-bit ADC provides values from 0 to 255, the charge in p.e. can be expressed as:

$$Q_{\mathrm{pe}} = \frac{\mathrm{AVC} - \mathrm{AVC}_{0\mathrm{pe}}}{\mathrm{AVC}_{1\mathrm{pe}} - \mathrm{AVC}_{0\mathrm{pe}}}. \tag{3.1}$$

Besides the digital values for the charge (AVC), the digital values for the time are generated for the selected hits. It includes a Time Stamp (TS) which is assigned to the hit with respect to the master clock at which the L0 threshold is surpassed and a Time-to-Voltage Converter (TVC) which provides a linear voltage ramp to measure the L0 time within the 50 ns interval between two subsequent clock pulses. This voltage is generated and stopped by the L0 signal. The TVC procedure is illustrated in Fig. 3.13. The TVC voltage is digitized with an 8-bit ADC and provides a subdivision of the complete clock cycle (50 ns) in 256 parts leading to the precision of about 200 ps. The first and the last TVC channels exceeding 10% of the average bin occupancy, $\mathrm{TVC}_{\mathrm{min}}$ and $\mathrm{TVC}_{\mathrm{max}}$, can be estimated.

The TVC is considered linear between these two limits. Based on these channel values the time (in ns) is:

$$t(\mathrm{ns}) = 50 \times \frac{\mathrm{TVC} - \mathrm{TVC}_{\mathrm{min}}}{\mathrm{TVC}_{\mathrm{max}} - \mathrm{TVC}_{\mathrm{min}}}. \tag{3.2}$$

After the integration time, the ARS chip is idle for about 200 ns [627]. To limit the dead-time in the data acquisition, two ARSs work in a flip-flop mode.

If the signal has a more complex structure, the ARS chip has also the capability to perform full waveform sampling (WF) of the PMT signal in addition to the charge measurement of the PMT pulse and its arrival time. The pulse shape classification of the signal as single SPE or WF is provided by a Pulse Shape Discriminator (PSD) (see Fig. 3.12). Three criteria are used as illustrated in Fig. 3.14: the pulse height is greater than several p.e., the time over L0 threshold longer than nominal or the L0 threshold crossed more than once during the charge integration time [631]. If any of these conditions are fulfilled, the event is called a WF event, else it is called an SPE event. This discrimination between common SPE events (about 99%) and rare WF events efficiently reduces the data flow and of the dead time of the ARS [631]. As stated above, for a further limit of the dead time, two ARS are connected to each PMT and used in a flip-flop mode.

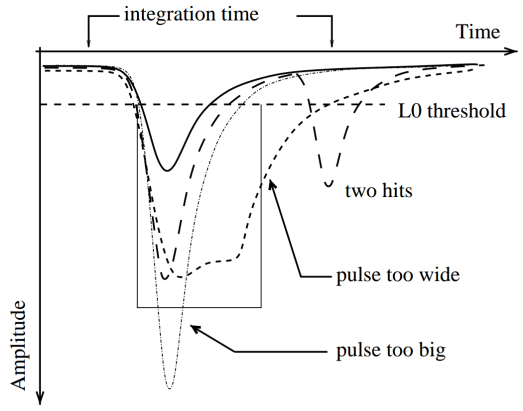

Fig. 3.14.: Pulse shape discrimination using three criteria: time width, pulse height, and multiple hit during integration. The figure is taken from [631].

3.3.2 Data transfer

Transmission Control Protocol and Internet Protocol (TCP/IP) are used for communication and data transport. The `ControlHost` package [634] is used for the data transfer between processes at three different stages in the DAQ: data processing, data storage, and detector operation. `ControlHost` implements the tagged data concept, which means that any program in the system can send data accompanied by a tag to a `ControlHost` server. The server will distribute the data to all processes that subscribed to the specific tag using TCP sockets [627]. In each storey, a Motorola MPC860P processor running the VxWorks Operating System[10] is in charge of the DAQ/SC. The MPC860P features a 100 Mb/s Ethernet port used for external data/SC communications. The data of five storeys (sector) are merged by the Ethernet switch into a single Gb/s Ethernet link. An electro-optical cable links each line with the JB and the MEOC distributes the data from the detector to the shore. Finally, the filtered data (see Section 3.3.3) are written on the disk by `DataWriter` program in `CERN ROOT`[11] [635] Data Analysis Framework format (.root) and copied every night to the computer center in Lyon.

3.3.3 Triggers

All the raw data containing mostly the optical background are delivered to the shore and the amount of data for storage becomes huge. Such a high data flow requires some filtering before the storage which is done by different trigger algorithms. Various different trigger algorithms [636] have been developed in ANTARES depending on the type of physics signal searched. The software in charge of filtering, the DataFilter, is referred to as a trigger [636].

The triggers are designed to filter the data and selecting the signal from particles by the space-time correlation between hits. The randomness in time for the background is what separates it from a muon track signal which should appear as a sequence of hits along its trajectory. The optical activity due to the ^{40}K radioactive isotope decays in the seawater and bioluminescent bacteria can trigger the L0 threshold. The rate of accidental correlations of hits can be limited by some preselection. The causality relationship principle implies that no consecutive hits can take place faster than it takes for the light to travel between these two positions. In order to reduce the random background, the hit coincidences between two neighboring PMTs of the same storey, so-called local coincidences, within a tunable time window (20 ns by default) is required or hit with an amplitude exceeding the certain value (tunable from 3 p.e. to 10 p.e. depending on the period of time) in a single PMT. These hits are tagged as L1 hits and such trigger logic based on the local coincidences is called first level, or L1, trigger.

[10] http://www.windriver.com
[11] http://root.cern.ch

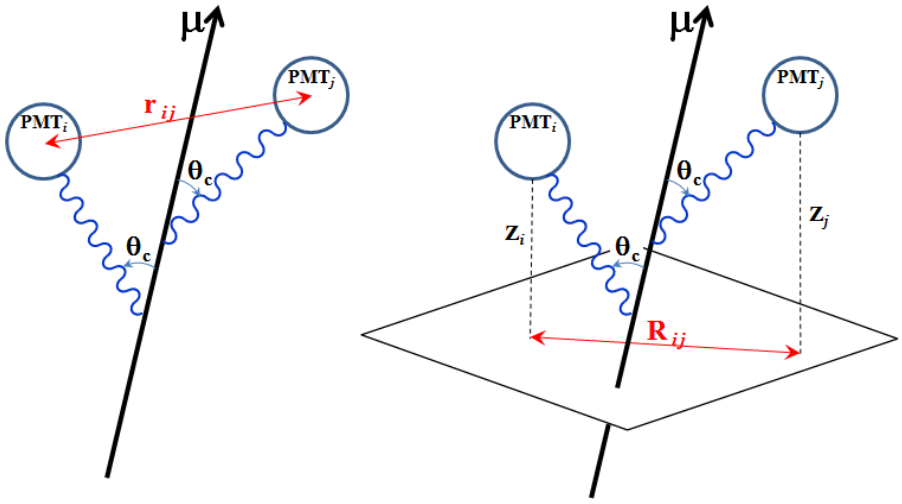

Fig. 3.15.: Definitions of the symbols used in causality relations. *Left:* General for standard trigger (see Eq. 3.3). *Right:* Specific for directional trigger (see Eq. 3.4). The Cherenkov photons are emitted under angle θ_C with respect to the muon trajectory. The figure is taken from [481].

The general purpose, or "standard", muon trigger makes use of the causality relationship between hits [481]:

$$|t_i - t_j| \leq r_{ij}\frac{n}{c}, \tag{3.3}$$

where t_i (t_j) refers to the time of hit i (j), and r_{ij} to the distance between PMTs i and j, c is the speed of light in vacuum and n the index of refraction of the seawater (see Fig. 3.15).

In addition to the standard trigger, a directional trigger has been implemented to maximize the detection efficiency of tracks arriving from the predefined directions, such as e.g., coming from the Galactic center. This trigger makes use of the direction-specific causality relationship between hits [481]:

$$z_i - z_j - R_{ij}\,tan\theta_C \leq c(t_i - t_j) \leq z_i - z_j + R_{ij}\,tan\theta_C, \tag{3.4}$$

where z_i (z_j) refers to the position of hit i (j) along the neutrino direction, and R_{ij} to distance between the positions of hits i and j in the plane perpendicular to the neutrino direction and θ_C is the Čherenkov angle in seawater (see Fig. 3.15).

In contrast with Eq. 3.3, the condition in Eq. 3.4 is more stringent because of the 2D distance R_{ij} is always smaller than the corresponding 3D distance r_{ij}. Moreover, this distance corresponds to the distance traveled by the photon (and not by the muon). As a consequence, it can be restricted to several absorption lengths without loss of detection efficiency. Such limitation reduces the combinatorics significantly. Thus, for the directional trigger, all hits can be considered and not only the preselected hits used for the standard trigger. Furthermore, this is not compromising the purity of physics events.

A group of L1 hits each pair of which satisfies the causal relation as noted in Eq. 3.3 within 20 ns in order to account for (forward) scattered photons and uncertainties due to calibration and contain a minimum number of hits (typically 5 hits, so $N_{L1} \geq 5$) is called a cluster. This set of L1 hits which forms a cluster is considered as a candidate event which is the input for the reconstruction strategies described in section 5.2. If such an event is triggered, all PMT pulses are recorded in a time window ($-2.2\ \mu s$, $2.2\ \mu s$) which corresponds to a muon transit time through the whole detector. For single-PMT background rates of 100 kHz, the clustering algorithm allows for suppressing the background event rate to about 0.1 Hz [636]. All hits which satisfy one or more trigger conditions are selected as L2 [637] hits. Inclusion of hits possibly produced by a physics signal and not previously added in the cluster is done at trigger L3. In order to include all those signals the time window of the triggered hits is extended by adding t_{max} after the first and before the last triggered hit (see Fig. 3.16). The t_{max} is $2.2\ \mu s$ refers to the maximum casual time of an event within the whole detector. All hits within this new time window are called snapshot hits. Moreover, at this level, all overlapping events are merged. Two events are considered being overlap if the cluster of one event falls in time with the snapshot of another event. There is also an L4 trigger where all the hits within the snapshot of every event are saved forming a `PhysicsEvent` following the ANTARES data format [639].

Summary of the categorized hits:

L0 hits A PMT signal crosses the defined threshold (typically 0.3 p.e.);

L1 hits If at least two L0 hits on the same storey within 20 ns or a single hit PMT signal which crosses the defined threshold (typically 3 p.e.);

L2 hits If any trigger conditions are fulfilled.

L3 hits All the hits possibly produced by a physics signal were not included previously in the cluster. Also, all the overlapping events are merged.

L4 hits All the hits within the snapshot of every event are saved in ANTARES data format.

The ANTARES DAQ system runs multiple triggers at the same time (see Fig. 3.18). The main triggers, based on local and directional coincidences, include K40 [641, 642], 3N [636], T3 [643], 2T3 [636, 644, 645], GC, TQ:

K40 Searches the coincidence of 2×L0 hits in the same storey within a time window of 20 ns. This trigger is not directly focused on neutrino events and used for *in situ* calibration purposes (see Section 3.5).

3N Searches the coincidence of 5×L1 hits from a certain direction (see Fig. 3.17) within a time window consistent with a muon track (within $2.2\ \mu s$). The 3N is a well approach for high-energy neutrinos since the produced muon induces a lot of

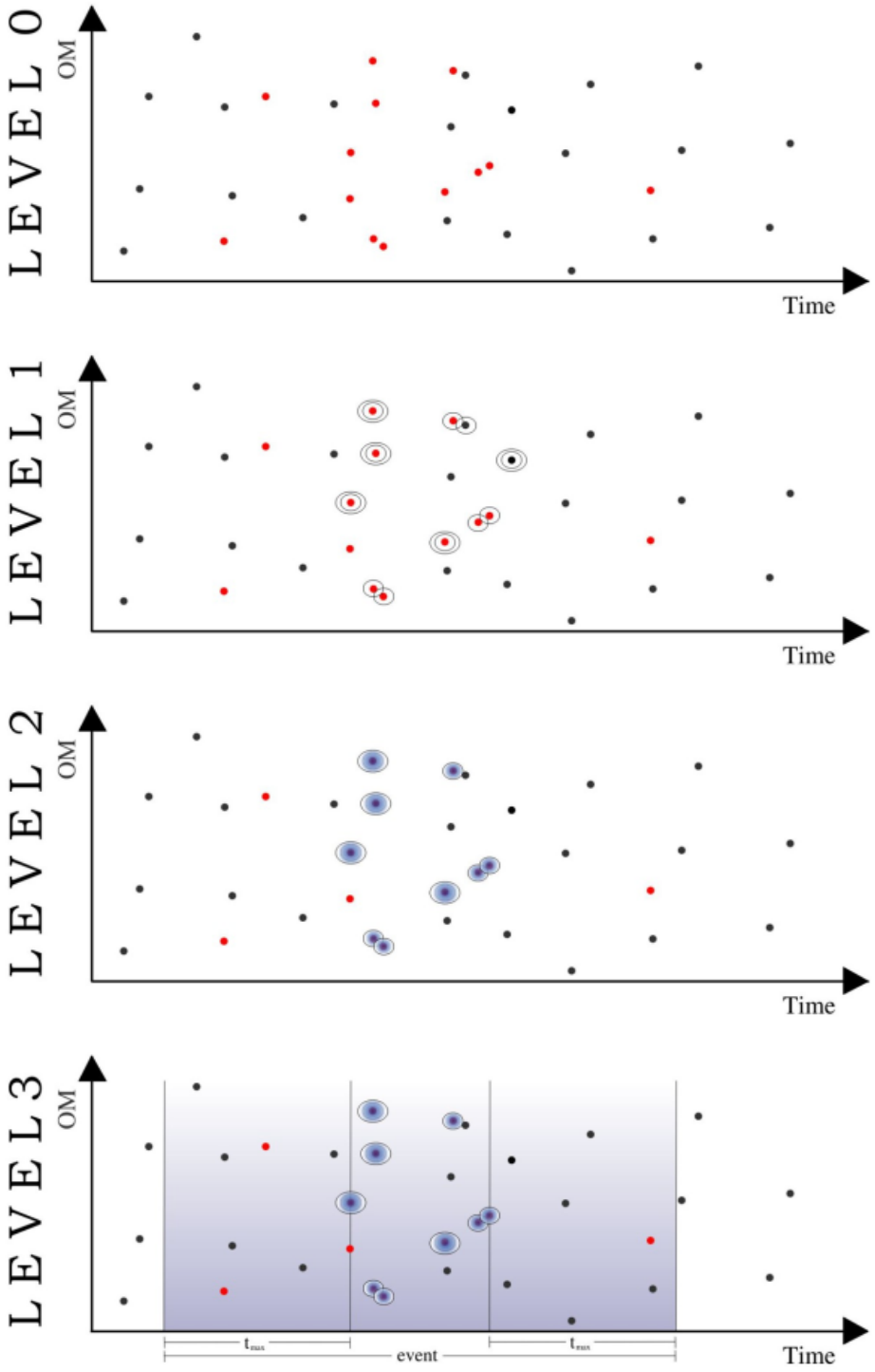

Fig. 3.16.: Schematic description of the ANTARES software trigger stages. Level 0: Illustration of the data stream with hits containing physics hits (red) and background (black). Level 1: Large hits are encircled twice, coincident hits once. Here two background hits are also marked as L1 hits, as one in coincidence with a true hit and the other which has a high charge. Level 2: One or more trigger algorithms look for correlations and causal relationships between the L1 hits to identify the (red) signal hits. The blue colored circles contain the final triggered (L2) hits. Level 3: The event is built by adding twice a time window with a length of 2.2 μs. The figure is taken from [638].

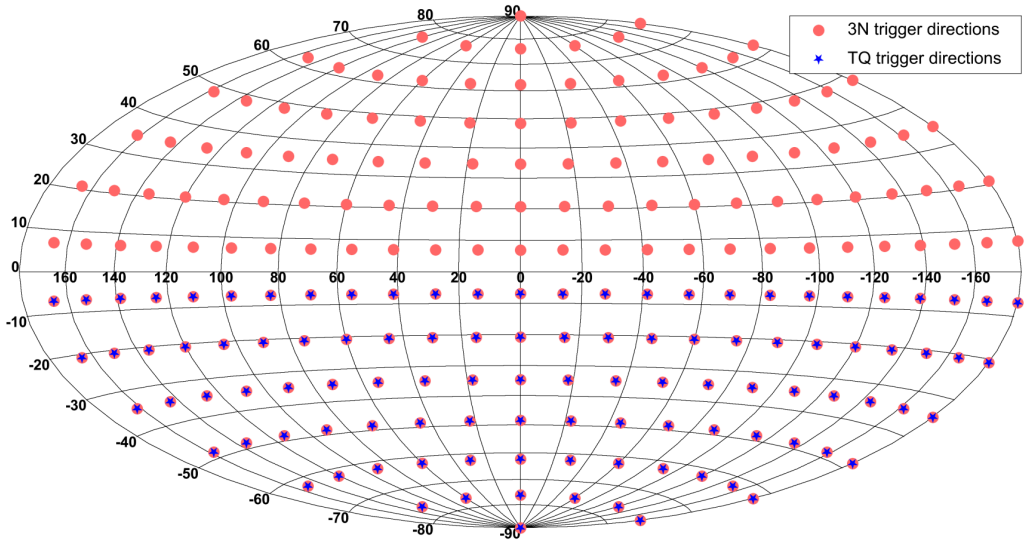

Fig. 3.17.: Skymap with the directions used for the directional causality criterion in the 3N trigger and in the TQ trigger. An isotropic grid of 210 directions defined on the full sky (with an average spacing between directions of about 14°) is shown. The figure is taken from [640].

light, but less so for neutrinos at lower energies. The typical rate of this trigger is 10 Hz. The observed trigger rate is dominated by the background of atmospheric muons and only a small fraction of the events $\ll 1\%$ [481] is found to be due to accidental correlations.

T3 Searches the coincidence of 2×L1 hits in adjacent storeys within a 100 ns or in the next-to-adjacent storeys within a 200 ns. The typical rate of this trigger is 20 Hz.

2T3 Searches the coincidence of 2×T3 hits in a whole detector within within a time window 2.2 μs. In order to increase the sensitivity for the low-energy neutrinos additional conditions are required. The following algorithm has the advantage over 3N trigger algorithm and improves the efficiency for the low-energy region: 2×T3 with 3×L1 in the same line or 4×L1 in the whole detector. At the same time, the 3N trigger is more efficient for astrophysical high-energy neutrinos.

GC Seacrhes the 1×T3 and 4×L0 hits in the direction of the Galactic Center. Apart from the triggers with general purpose that look for neutrinos coming from any direction, this trigger tracks the Galactic center position in the sky which maximizes the efficiency to detect neutrinos coming from that specific direction.

TQ Searches the coincidence not for a given direction but for a set of directions, from 0° to 90° in 14° increments in zenith and azimuth. Hence, this multi-directional trigger scans the 105 upward directions, half of 210 directions involved (see Fig. 3.17).

Also, the minimum bias trigger which continuously takes data (records 10 s of data every hour) is used for monitoring the current detector status and the data quality conditions. The

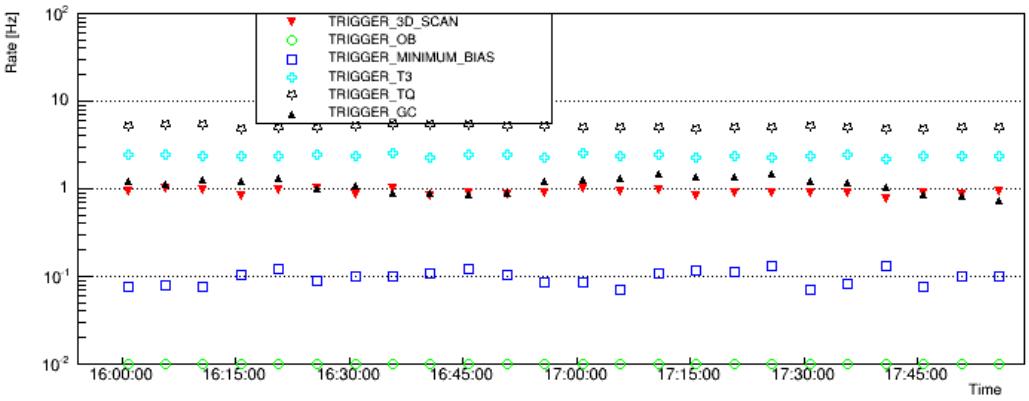

Fig. 3.18.: A screenshot of the actual trigger rates as viewed at a computer at the control station of ANTARES.

3D SCAN is almost identical to the 3N trigger with the only difference in using a simple time correlation instead of checking for correlation with a grid of directions. Besides K40 trigger used for calibration purposes, the OB trigger is elaborated for time calibration using the photons emitted from the LED Optical Beacons (see Section 3.5.1).

3.4 Detector site properties

The deep-sea extreme, uncontrollable and hostile environment demands the extensive and detailed site evaluation studies to ensure the success of the deployment of a large-scale detector and that the detector elements will withstand its harsh conditions. The selection of a suitable site for a neutrino telescope requires sufficient depth in order to provide shielding against atmospheric muons, acceptable meteorological conditions, proximity to the coast and developed infrastructure for on-shore support, ease deployment and substantial reduction of the costs for power and signal connections to shore. Furthermore, the strength of the deep-sea currents, fouling of optical surfaces, the water transparency (e.g. for desirable absorption and scattering lengths), optical background and level of bioluminescence have to be attentively and rigorously considered. The ANTARES location was chosen after carrying out a detailed evaluation of the site candidates during the R&D phase of the project and *in situ* measurements of the optical and environmental properties which are relevant for the detector performance [506, 646]. Some of the most important issues are discussed in this section.

3.4.1 Light transmission

The muon track is reconstructed from the arrival time of detected photons; therefore, the performance of the detector is critically dependent on the optical properties of seawater, in particular on the velocity of light and on the absorption and scattering cross-sections [555]. The scattering length affects the angular resolution and the absorption length affects the optimization of the line separation distances. The scattering processes deviate the direction of the Čerenkov photons while the absorption may reduce the amount of light reaching the PMT. For instance, large absorption lengths result in a better light collection, large scattering lengths in superior angular resolution [39].

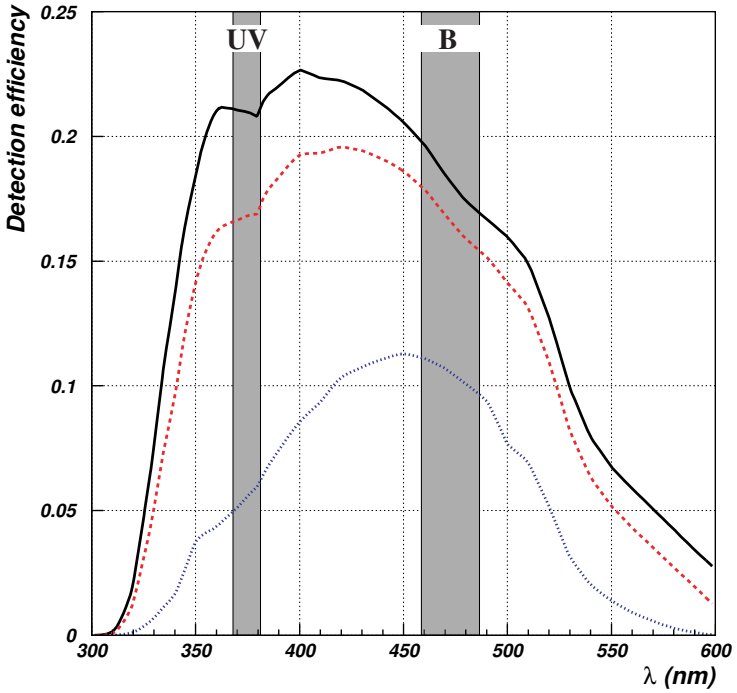

Fig. 3.19.: Detection efficiency as a function of wavelength. The solid curve shows the PMT quantum efficiency and the absorption by the PMT glass, the optical gel and the protective PMT glass sphere [506]. The dashed and dotted curves are calculated with a path length in water of 5 m and 30 m respectively, assuming a characteristic wavelength dependence of the water absorption length as given in [647]. The effect of scattering is not included. The bands labeled "UV" and "B" indicate the wavelengths at which measurements were undertaken at the ANTARES site. The figure is taken from [555].

Both absorption and scattering vary with the photon wavelength and spanning the relevant spectrum from ultraviolet to green (see Fig. 3.19). The region of interest for detection of Čherenkov light is $320 \leq \lambda \leq 620$ nm [648]. As given by Frank-Tamm equation [554] (see Eq. 2.16), the Čherenkov light spectrum varies like $1/\lambda^2$ (see Section 2.3.5); hence, the PMT quantum efficiency becomes too low to probe wavelengths longer than 600 nm, while the glass pressure sphere that surrounds the phototube absorbs the light at wavelengths shorter than 320 nm [555, 648]. Deep-sea sites typically have effective scattering lengths of >100 m and, at their peak transparency around 450 nm, absorption lengths of 50-65 m [39, 555].

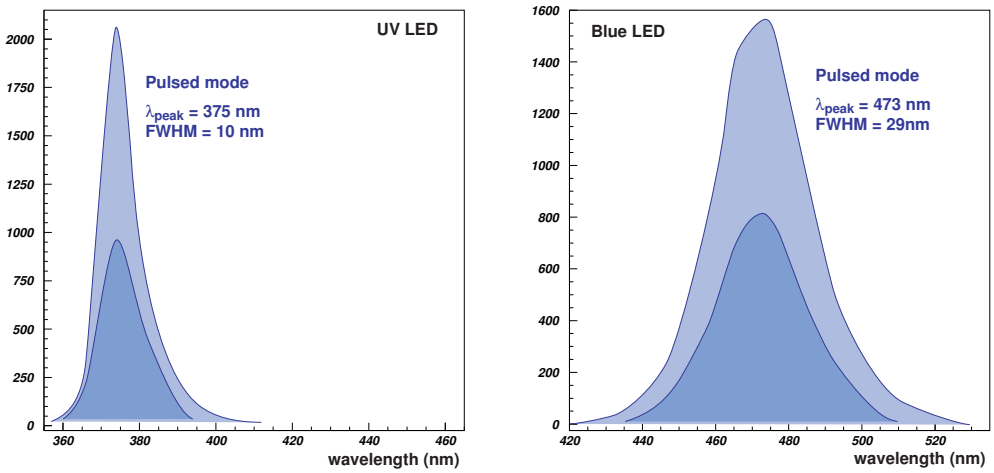

Fig. 3.20.: Spectral emission of the UV and Blue LEDs (smoothed curves, the intensity in arbitrary units). The light and dark areas correspond to the two extreme values of the range of source intensities used for the measurements, with no significant difference in the spectra. The figure is taken from [555].

The photon propagation is governed by the following inherent optical parameters: group velocity of light in the seawater υ_g, absorption length λ_{abs}, scattering length λ_{sct}, and the angular distribution of scattered photons θ. For an isotropic source of photons with the intensity I_0, the intensity I detected at a distance R from the source by a PMT with an active area A is [555]:

$$I = I_0 \frac{A}{4\pi R^2} e^{-R/\lambda_{att}^{eff}}, \tag{3.5}$$

where λ_{att}^{eff} is the effective attenuation length, extracted from the total number of photons (i.e. from the integrated time distributions) recorded for two source-detector (see Fig. 3.21) distances [555]. The effective attenuation length defines the distance where the intensity of the Čerenkov light has dropped by a factor of $1/e$ and indicates the fraction of photons emitted by the source that are actually detected.

Since the attenuation of the Čerenkov photons intensity in seawater is caused by the combination of absorption and scattering, an effective attenuation can be expressed as:

$$\frac{1}{\lambda_{att}^{eff}} = \frac{1}{\lambda_{abs}} + \frac{1}{\lambda_{sct}^{eff}}. \tag{3.6}$$

Here, the effective scattering length λ_{sct}^{eff} which depends on the scattering angle θ, defined as $\lambda_{sct}/(1 - \langle cos\theta \rangle)$, replaces the scattering length λ_{sct} since in ANTARES the scattered photons are not necessarily lost due to a slight delay of the photons that are scattered under a very small angle. The $\langle cos\theta \rangle$ is the average cosine of the total scattering angular distribution. The definition in Eq. 3.6 holds if and only if when $\langle cos\theta \rangle \sim 1$, which is the case for multiple scattering in seawater.

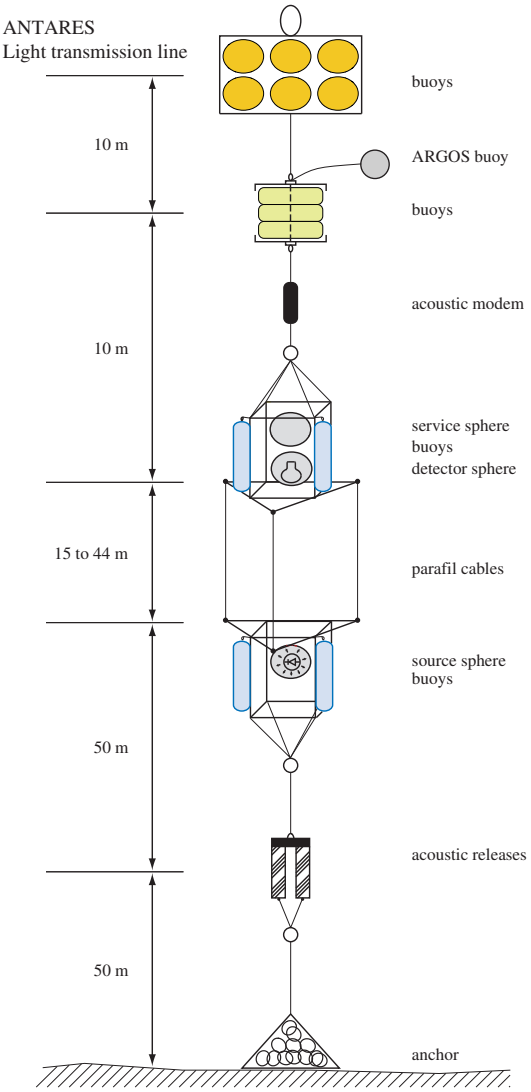

Fig. 3.21.: Sketch of the mooring line used at the ANTARES site for the measurements of the water transmission properties. The line remains vertical through the flotation provided by syntactic buoys and a flexible structure was gradually improved for light propagation studies. The figure is not to scale. The figure is taken from [555].

During several sea campaigns, the light transmission properties measurements were carried out. An autonomous mooring line was deployed at the ANTARES site to study both parameters, scattering, and absorption, in order to confirm that this site satisfies the constraints of the ANTARES physics program. A sketch of the mooring line including information on approximate heights from the seafloor is shown in (see Fig. 3.21). The pulsed isotropic light source (pulsed LEDs) emitting in two wavelengths, UV and Blue, at 375 nm and 473 nm respectively (see Fig. 3.22), were placed at different distances from a 1-inch diameter PMT collecting the light. The results from these measurements [555] can be seen in (see Fig. 3.22). The values for UV (Blue) light are found to be $\lambda_{abs} \simeq 26(60)$ m and $\lambda_{sct}^{eff} \simeq 122(265)$ m with a time variability around ~15%. The effective attenuation length λ_{att}^{eff} measured for Blue (λ = 466 m, collimated) was [555]:

$$\lambda_{att}^{eff} = 41 \pm 1 \text{ (stat.)} \pm 1 \text{ (syst.)} \text{ m}, \quad (3.7)$$

while the distance between the source and the PMT was varied from 6 to 27 m, the intensity of the source was adjusted so as to yield a constant current intensity on the PMT. The emitted and detected intensities in seawater are:

$$I_{\text{PMT}} \propto \frac{\Phi_{LED}}{D^2} \times exp\Big(-\frac{D}{\lambda}\Big) \quad (3.8)$$

where D denotes the distance, varied from 6 to 27 m, Φ_{LED} refers to the source intensity and I_{PMT} is the intensity that is actually detected. Such a dependence of the required LED intensity with the distance makes possible the estimation of the effective attenuation length.

At present, the optical properties of the seawater are measured *in situ* using the LED Optical Beacon system [649].

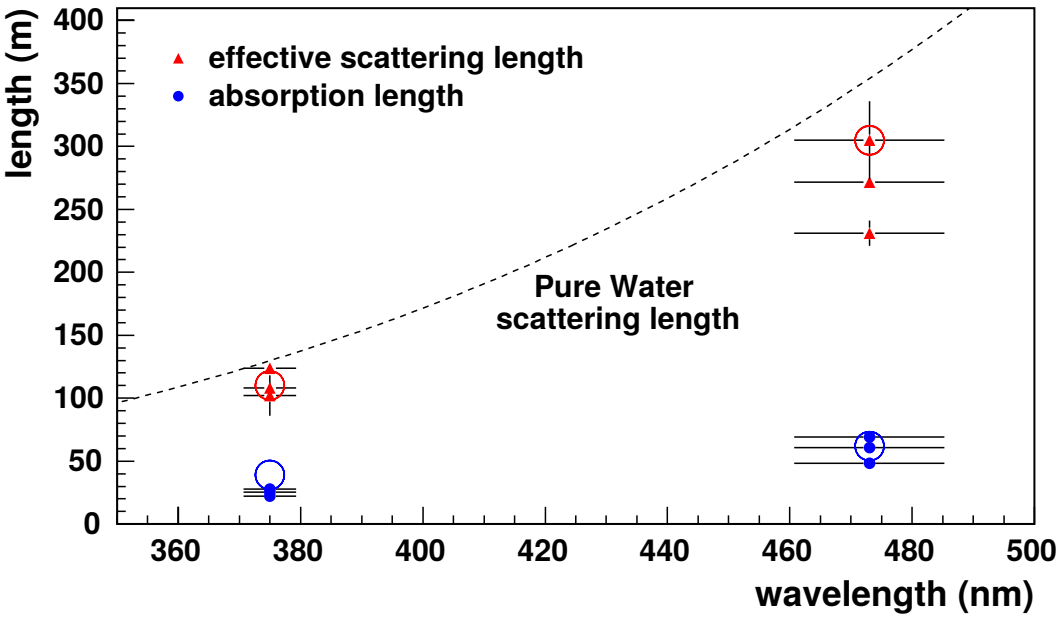

Fig. 3.22.: Absorption (dots) and effective scattering (triangles) lengths measured at the ANTARES site at various epochs for UV and Blue band. Horizontal error bars illustrate the source spectral resolution at the $\pm 1\sigma$ level. The large circles denote the estimation of the absorption and scattering lengths in pure seawater while the dashed curve is the pure water scattering length and corresponds to the upper limit on the effective scattering length in seawater. The figure is taken from [555].

In addition, the group velocity of light in seawater which is essential for the muon track reconstruction has been also measured [555] and the results are summarized in Fig. 3.23. As can be seen from the figure, the wavelength dependence of both models, Quan & Fry [650] and Millar & Seaver [651], are showing excellent compatibility and the experimental values from both models are in good agreement with the values derived analytically. This velocity is defined as:

$$v_g = \frac{d\omega}{dk}, \tag{3.9}$$

where $k = 2\pi/\lambda$ is the wave number and ω is the frequency of wave packet.

Considering that $\omega/k = c/n_p$ where n_p is the phase velocity refractive index, the group velocity can be expressed as:

$$v_g = \frac{c}{n_p} - \frac{ck}{n_p^2}\frac{dn_p}{d\omega} = \frac{c}{n_p}\left(1 + \frac{\lambda}{n_p}\frac{dn_p}{d\lambda}\right). \tag{3.10}$$

The group velocity of light was given by the ratio [555]:

$$v_g = \frac{\Delta d}{\Delta t}, \tag{3.11}$$

where Δd corresponds to the difference between the source-detector distances, i.e. between the light source and the detection unit, for the two immersions, and Δt represents the

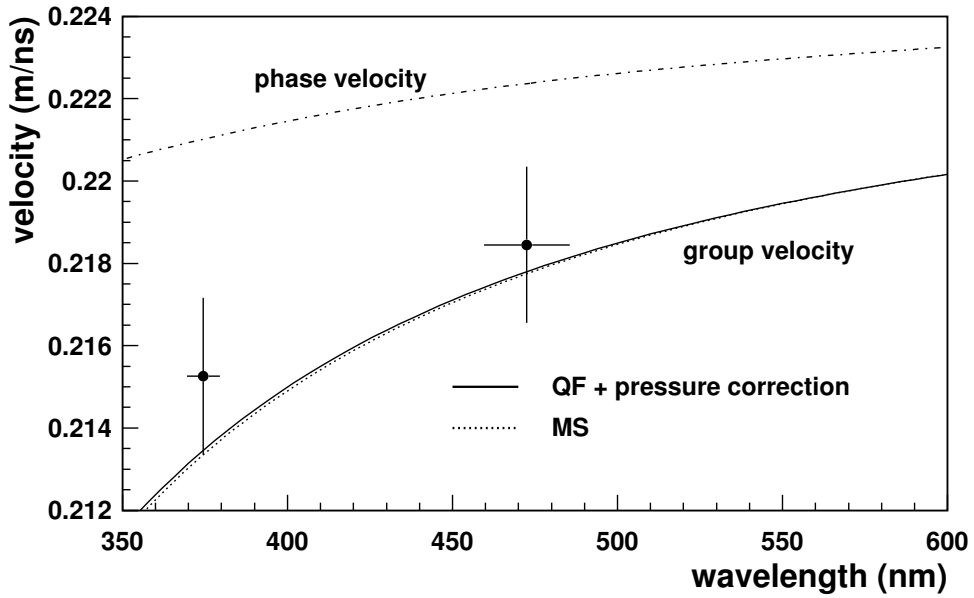

Fig. 3.23.: Comparison of measurements of the group velocity of light with model predictions, Quan & Fry (QF) [650] and Millar & Seaver (MS) [651], for $\lambda = 374.5$ nm (UV) and $\lambda = 472.5$ nm (Blue). The phase velocity as a function of wavelength is also indicated. The figure is taken from [555].

difference between the times at which the non-scattered photons emitted by the source reach the detectors located at the two different distances from the source.

The group velocity of light values obtained in the two source-detector measurements are [555]:

$$v_g = \begin{cases} 0.2153 \pm 0.0015 \text{ m/ns (UV)} \\ 0.2185 \pm 0.0015 \text{ m/ns (Blue)} \end{cases} . \tag{3.12}$$

Another key parameter for the muon track reconstruction is the group velocity refractive index which can be expressed from Eq. 3.10 as:

$$n_g(\lambda) = \frac{c}{v_g} = \frac{n_p(\lambda)}{1 + \frac{\lambda}{n_p(\lambda)} \frac{dn_p(\lambda)}{d\lambda}} . \tag{3.13}$$

As a key parameter for the track reconstruction, the index of refraction corresponding to the group velocity of light as a function of the wavelength has been recently performed at the ANTARES site (pressure $p = 230$ atm, salinity $S = 38.44‰$ and temperature $T = 13.2°$ C) using the LEDs of the multi-wavelength Optical Beacon [556]. The results are summarized in Fig. 3.24. The density of seawater depends on the temperature, the salinity and the pressure of the water [650]; hence, the velocity of light in seawater at a given wavelength is also dependent on these variables. With known variations of temperature, salinity, and pressure, the refractive index for a particular wavelength and at a given depth can be determined with an accuracy of better than 4×10^{-5} [556]. The Quan & Fry [650] proposed the parametrization

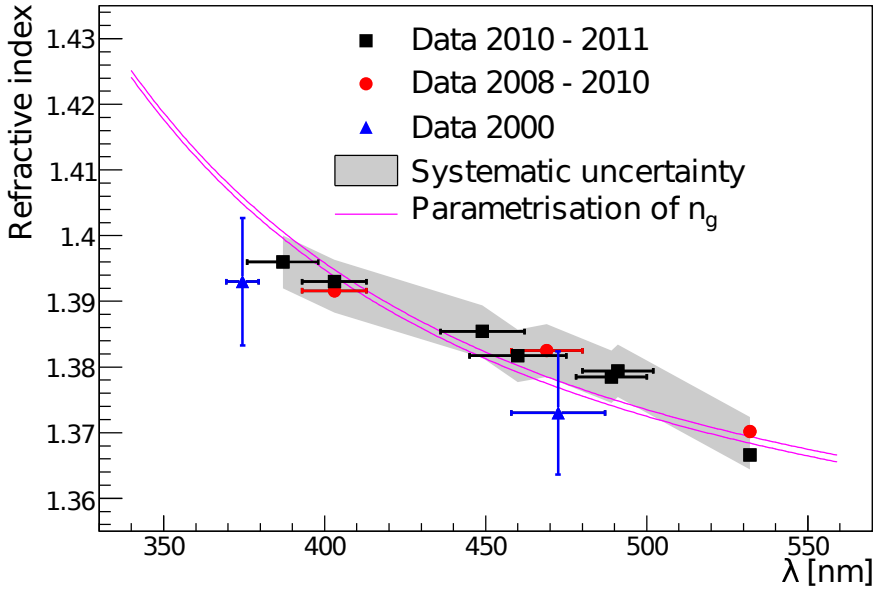

Fig. 3.24.: Measurements of the group refractive index in seawater at the ANTARES site. The grey band shows the systematic uncertainty. The two solid lines correspond to a parametrization of the index of refraction evaluated at a pressure of 200 atm (lower line) and 240 atm (upper line). The figure is taken from [556].

of the light velocity and a simple empirical equation for the index of refraction of seawater, $n = n(S,T,\lambda)$, with the base on experimental data from Austin & Halikas [652]. The measurements are compatible with the Quan & Fry predictions [650] within its systematic uncertainty. Some modifications of the parametrization were made [555] to incorporate a correction for the pressure-dependence which was not included in their equation; this provides better agreement with the measurements.

The shorter absorption length in water rather than in ice and as a result the longer attenuation length because of the longer scattering length leads to a better angular resolution which is essential for neutrino astronomy and gives the advantage to ANTARES telescope.

3.4.2 Environmental background

In addition to the Čerenkov photons produced by a muon passage within the detector, other sources of light are presented in the deep-sea environment. The sewater at the ANTARES detector site is affected by two unavoidable environmental background sources of light [646]: the decay of radioactive potassium-40 (^{40}K) dissolved in seawater and the biological activity of the bioluminescent organisms presented there. These two natural phenomena producing light constitute the optical background puts constraints on the trigger logic and electronics as well as on the mechanical layout of the OMs; hence, a knowledge of the background light behavior on site is of prime importance [646]. The radioactive decays of ^{40}K, presented in salt, produce the background light which is constant in time depending only on the salinity (38.5‰, constant in time) and affect mainly the trigger rates and track reconstruction. While the bioluminescence emission has two components, one is a continuous baseline and the

other one is a random component of spontaneous emission ("bursts") which is responsible for the sudden increase of background counting rates registered in ANTARES up to 1 MHz [646] (see Fig. 3.25). As a result, such bursts from the biological activity can induce dead-time in data acquisition.

The bioluminescence light is a result of a natural chemical reaction (chemiluminescence) which appears to be the most common form of communication in this remote realm of ANTARES deep-sea site [653, 654]. Accordingly, the rate of bioluminescence light is assumed to correlate with the number of luminescent organisms around the detector, and therefore increases with the sea current speed. The observation in [654] demonstrates a consistent and rapid connection between deep open-sea convection and biological activity, as expressed by bioluminescence. The luminescent organisms suffer the high-velocity motion in seawater and in turn produce the bioluminescent light.

The ^{40}K is the most abundant among other long-lived natural radio-nuclides (decays from the ^{238}U/^{232}Th chains can be neglected) [625] and constitutes $\approx 0.0117\%$ [655, 656] of the total 400 [657] part per million (ppm) of potassium presented in the seawater. It decays mainly (see Eq. 3.16) to calcium-40 (^{40}Ca) by emitting an electron (β^-) with a maximum energy of 1.311 MeV and an antineutrino (89.28%) and to argon-40 (^{40}Ar) via electron capture (E.C.) by emitting a neutrino and a γ-ray (10.72%) with the energy 1.461 MeV, and the rest (0.001%) to ^{40}Ar by emitting a positron (β^+) and a neutrino [655, 656, 625]. The β-decay modes the ^{40}K undergo are:

$$\beta^- : \quad {}^{40}\mathrm{K} \longrightarrow {}^{40}\mathrm{Ca} + \overline{\nu}_e + \mathrm{e}^- \qquad (89.28\%) \qquad (3.14)$$

$$\text{E.C.} : \quad {}^{40}\mathrm{K} + e^- \longrightarrow {}^{40}\mathrm{Ar}^* + \nu_e \qquad (10.72\%) \qquad (3.15)$$

$$\hookrightarrow {}^{40}\mathrm{Ar} + \gamma$$

$$\beta^+ : \quad {}^{40}\mathrm{K} \longrightarrow {}^{40}\mathrm{Ar} + \nu_e + e^+ \qquad (0.001\%) \qquad (3.16)$$

The electron produced in the β-decay channel, with an energy up to 1.311 MeV, leads to the production of Čherenkov light when traversing in water while in the E.C. channel, fast electrons with subsequent Čherenkov light emission are produced by Compton scattering of the 1.461 MeV photon, released by the excited argon nuclei (Ar*) [625].

Together 40K decays and bioluminescence produce a continuous background rate (quiescent phase) from each OM ~60 kHz. As stated above, the counting rate can raise occasionally up to several MHz due to the biological activity of living organisms in seawater. Figure 3.25 shows the typical background behavior during data taking. The almost flat mean background rate around 60 kHz and several high bioluminescence bursts due to the biological activity of living organisms crossing the detector can be seen. The baseline (in kHz) for the period from 2007 to 2017 years can be seen in Fig. 3.26. Several high and low optical background rates can be observed. The bioluminescence is not a predictable phenomenon. However, the high rates and high bioluminescence bursts as the indicators for extreme biological activity

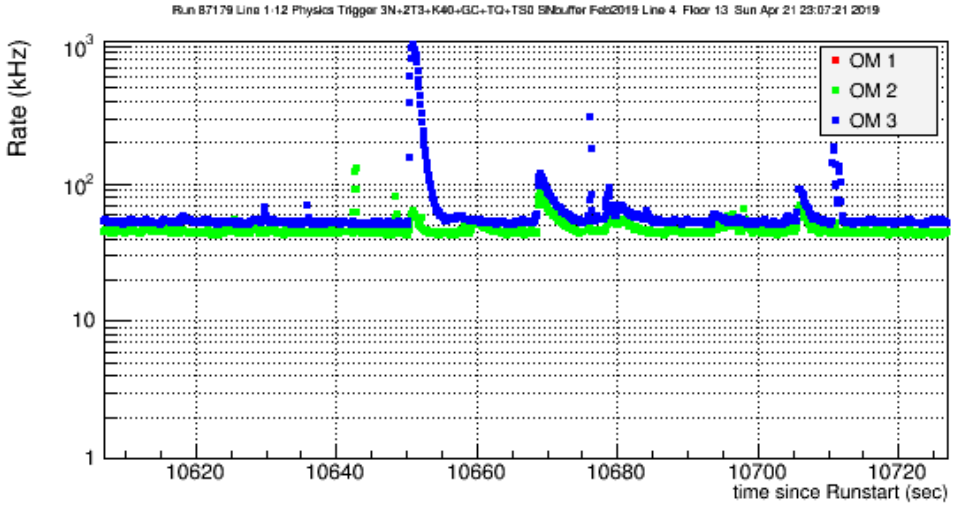

Fig. 3.25.: Optical background rate measured by three PMTs on the same storey of the ANTARES detector, in a time window of two minutes. Measured with Floor 13 of Line 4 on April 21st, 2019.

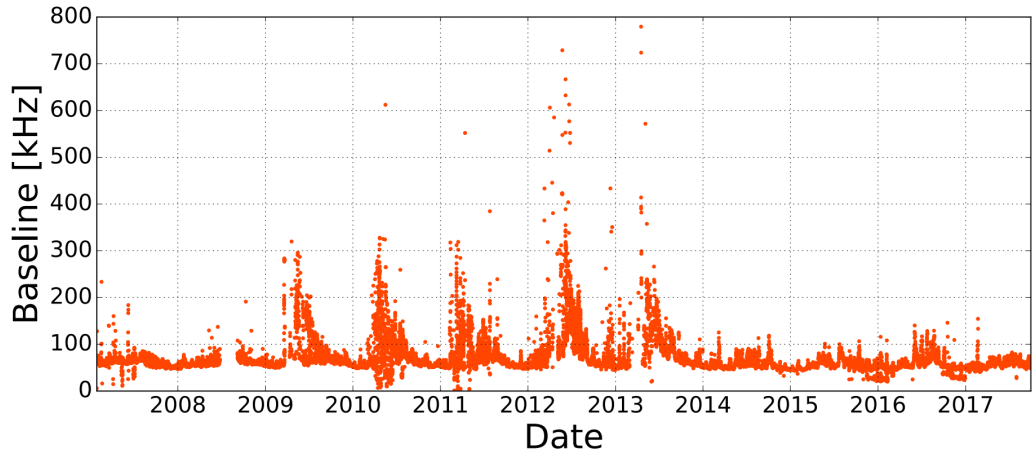

Fig. 3.26.: Optical background rate from 2007 to 2017 years. The figure is taken from [658].

are more frequent in seasons such as spring and the beginning of summer reducing the time of data-taking. Afterward, it goes back to the quiet data-taking period and the mean rates return to nominal baseline 60 kHz rate.

3.4.3 Biofouling and sedimentation

The ANTARES detector sensors are exposed to underwater sedimentation and biofouling processes. They affect the transparency by reducing the efficiency in the light transmission into the PMT. The surfaces of OMs are fouled by the combination of processes: grow of the living organisms, mostly bacteria, on the outer surface, and sediments fall on the upward-looking surfaces. While the bacterial growth is expected to be almost transparent, sediments will adhere to it and make it gradually opaque, thus diminishing the sensitivity of the detector. This phenomenon is site-dependent as the bacterial growth decreases with depth and the sedimentation rate depends on local sources of sediments such as nearby rivers [506].

Biofouling processes play an important role in the loss of light transmission on glass spheres of the PMTs. Given the objective of operating the telescope for several years without maintenance, it is mandatory that the active optical surfaces are not significantly fouled during this period [659]. In order to understand the cause of this effect, an extensive *in situ* complementary measurements of sedimentation and biofouling were performed in [659]. It was shown [659] a decreasing trend of the transparency of the glass spheres with time (see Fig. 3.27). The average loss of light transmission is small, estimated to be only around 2% [659] at the equator of the sphere one year after deployment and decreases with increasing zenith angle θ. The loss of transmissivity due to the fouling is expected to be small even after several years of operation since the OMs are oriented pointing downwards, with the minimum zenith angle of the sensitive area of the PMT photocathode barely reaching the equator. As also seen in Fig. 3.27, it is obvious that the $\theta = 0$ curve corresponding to the top of the sphere has the largest effect of sedimentation. The increase in light transmission after a period of decreasing transmission is correlated with the sea current speed which suggests that sediments are washed off by water high currents [659].

3.5 Calibration

The calibration of the detector is vitally important for the physics goals of ANTARES and to ensure the optimal functionality of the detector. It enables researchers to have confidence in their observations and results. The time, charge and position information of each hit detected by the OMs are essential for the event reconstruction precision. A preliminary on-shore calibration is performed in a dark room in the laboratory before the deployment [609]. Once the detector is deployed in the sea, an *in situ* calibration is crucial due to the movements, variations in temperature, changes in high voltage and other factors. In this section, the three main calibration schemes are described.

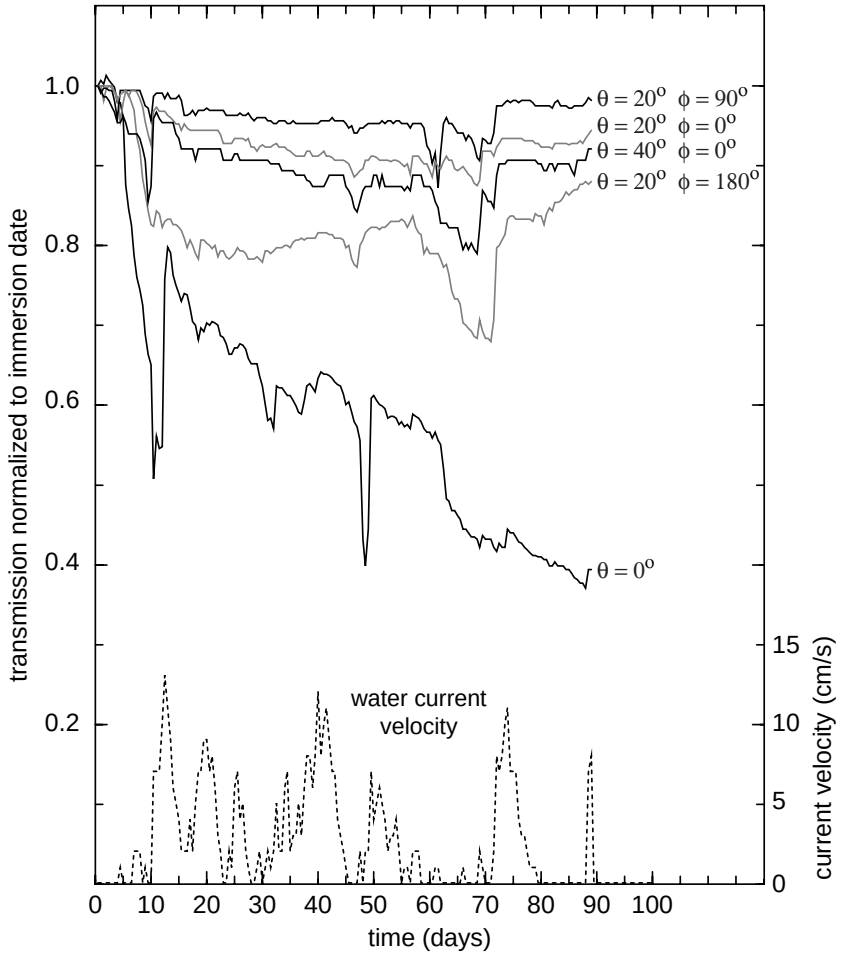

Fig. 3.27.: Light transmission as a function of time since the first immersion for the two spheres mounted vertically. The measurements are normalized to unity on the immersion date. Five different coordinates of photodiodes on the glass sphere surface are used. The curves are labeled according to the zenith angle θ and azimuthal angle ϕ. The current velocity is also indicated. See explanation in the text. The figure is taken from [659].

3.5.1 Time calibration

The time calibration in ANTARES is described in detail in [609]. In ANTARES, the two types of resolution time calibration carried out: absolute time calibration and calibration of the relative time resolution between OMs.

The absolute time resolution is the precision with which the detector can measure the time of an event with respect to the Universal Time Coordianted (UTC). The absolute time stamping of an event is performed by synchronization with a GPS receiver for absolute time reference. The absolute time calibration is less demanding than the relative time resolution calibration since the precision of a few seconds is sufficient to correlate reconstructed neutrino directions with steady point sources and accuracy of the order of milliseconds is sufficient to associate the events with transient astrophysical phenomena such as AGNs, GRBs, etc [609].

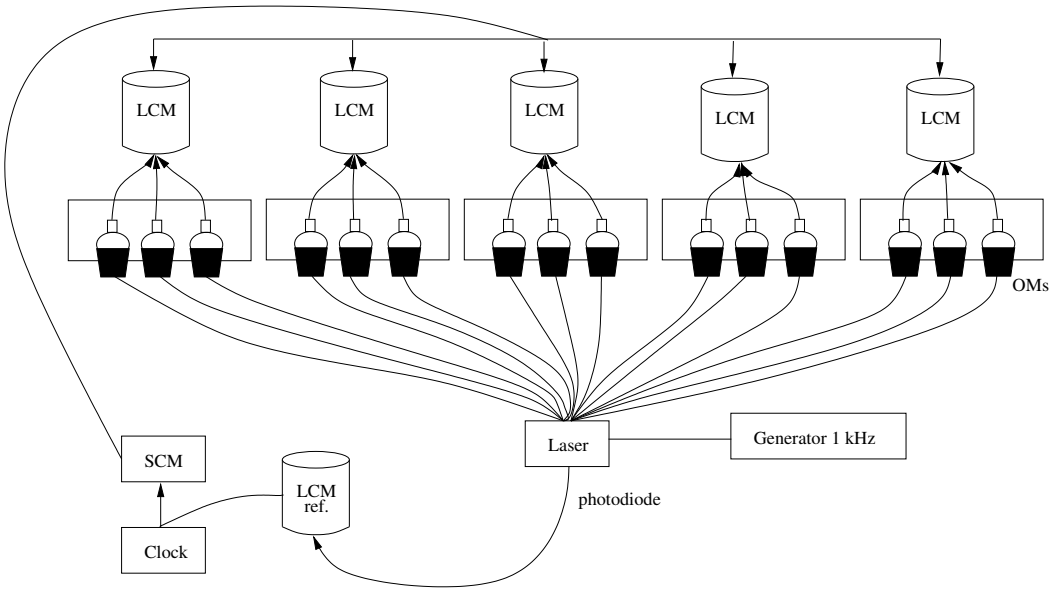

Fig. 3.28.: Schematic view of the set-up for on-shore time calibration. The figure is taken from [609].

On the other hand, the pointing accuracy closely related to the precision in the determination of the arrival time of the Čherenkov photons at the PMTs is crucial for a good angular resolution. As stated, the arrival times at the PMTs is measured based on the clock signals distributed from shore so that a common reference time is used in the whole apparatus. It determines the propagation delays for these signals to reach the different electronics containers off-shore. However, the time measurements have to be corrected by appropriate offsets, which are determined *in situ* by means of calibration with the OB system emitting light flashes at known times. Thus, it is necessary to have ∼1 ns precision [609] with which all such offsets are determined in the relative time calibration so that the resulting systematic error is significantly smaller than the intrinsic event-by-event fluctuations. Therefore, the calibration of the relative time resolution between OMs is of utmost importance. The large scattering length of light in the deep-sea facilitates a very good angular resolution of $< 0.3°$ for neutrino energies exceeding 10 TeV [609].

On-shore *dark-room* calibration

An on-shore calibration performed in a *dark-room* in the integration laboratory prior to the installation of the lines in the deep-sea and provides a preliminary time calibration. In the calibration, the batch of five storeys (a sector) is involved at once (see Fig. 3.28). A group of OMs is simultaneously illuminated by the short laser pulses. Since the propagation times from SCM to LCM are known from the clock system calibration; therefore, the following values can be extracted such as the contribution from the cable that links the LCM to the OM, the PMT transit time (TT) and the front-end electronics delay [609].

The Q-switched, Nd-YAG[12] pulsed laser is used to produce the light. It emits intense (E ∼1 μJ, equivalent to ∼10^{12} photons) and short (FWHM ∼0.8 ns) pulses of green light (λ = 532 nm) at a frequency of 1 kHz [609]. The light is split using a 1-to-16 optical splitter and distributed to the 15 OMs of each sector through optical fibers adjusted so that adds the time delay of fewer than 0.3 ns. The laser light is afterward spread over the full area of the corresponding PMT photocathode by means of the Lambertian diffuser[13] (∼$cos\theta$[14]) coupled with the optical fiber. The first OM of the lowest storey of the line is chosen as a reference for the full line. The time offsets between each OM and this reference OM are computed for each of all ARSs of a sector. Each sector comprises 5 storeys with 3 OMs each equipped by 2 ARS chips; hence, 30 ARS in total.

An example result is shown in Fig. 3.29. The spread of the time offsets corresponds to a few nanoseconds. This is because of the differences in PMT transit times and in internal cabling between OMs and the electronics in a storey. These offsets define the first set of time calibration parameters, usually referred to as the *intra-line* calibration parameters and were stored in the ANTARES database to be used for the prompt data analysis after deployment. They may change after first immersion due to variations in the environmental conditions; thus, they are corrected by *in situ* calibration after the detector deployment.

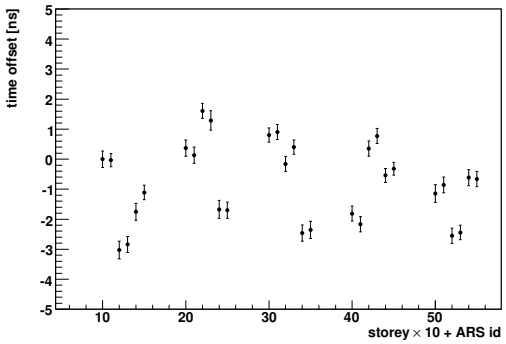

Fig. 3.29.: Time offsets measured for all ARSs of one of the line sectors. The time offsets are relative to the first ARS of the first OM of the lowest storey (reference OM). The ARS id runs from 0 to 5 within each storey. Time offsets are spread within ±3 ns. The figure is taken from [609].

In situ calibration

After the detector deployment, time calibrations are performed *in situ* [609] with an Optical Beacon system [660], a set of external and well-controlled pulsed light sources located throughout the detector. The idea behind this calibration procedure is similar to that in *dark-room*: a pulsed light is used to simultaneously illuminate a group of OM in order to obtain the time offsets. The OB system allows to determine the relative time calibration of different OMs by means of independent and well-controlled pulsed light sources. In addition to calibration, it is used to monitor the optical properties, e.g., the influence of the seawater on the light transmission (see Section 3.4.1).

[12] JDS Uniphase Co., http://www.nanolase.com
[13] Thermo Oriel Co., http://www.oriel.com
[14] The θ denotes the angle between the direction of the incident light and the surface normal.

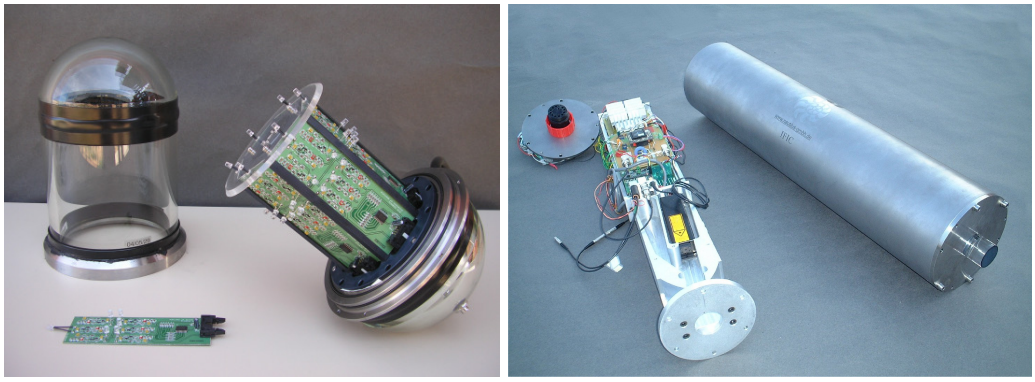

Fig. 3.30.: Picture of an Optical Beacon devices. *Left:* An LED Optical Beacon composed of several LEDs, pulsed by dedicated electronic circuits. *Right:* A Laser Beacon using a solid-state pulsed laser whose light is spread out by a diffuser. The LED beacons are placed uniformly along every detector line so that their light can illuminate all storeys on the neighboring lines while the Laser Beacons are located at the bottom of a few lines on the BSS. The figures are taken from [609].

The OB system comprises two kinds of complementary devices [609]: LED Beacons that emit Blue light ($\lambda = 470$ nm) and Laser Beacons emitting green light ($\lambda = 532$ nm). The description of the response of the OM as a function of the wavelength is described in [626]. Pictures of both OB devices before assembly are shown in Fig. 3.30. The LED beacons are used to monitor the relative time offsets among OMs of the same line (*intra-line* calibration), whereas the Laser Beacons are used for monitoring the relative time offsets among the lines (*inter-line* calibration) and the calibration of the lowest storeys. The *in situ* calibration allows to re-measure the time constants computed on-shore and is particularly important in case of a change in the PMT high-voltage and threshold settings [609].

Along every detector line (in the 2^{nd}, 9^{th}, 15^{th} and 21^{st} storeys, counted from the bottom), four LED Optical Beacons are strategically placed to allow the illumination of almost all the lines (see Fig. 3.31). The LEDs emit blue light with a maximum intensity of ~160 pJ per flash ($\sim 4 \times 10^8$ photons per pulse) and a pulse width of 4 ns (FWHM) [609]. Each of the LED OB is equipped by a special small 8-mm PMT and used to measure the emission time of the LED light [660]. Seven storeys above each OB, excluding the one just above the beacon which receives too much light, can be calibrated [609]. The storeys farther away, which do not receive enough light, are monitored with the next OB along the line. Some disadvantages of the LED OB calibration are that LED Beacons are not efficient for the timing calibration of the lowest storeys of the lines, e.g. the first three storeys of each line since they are below or just above the lowest OB (see Fig. 3.31). Thereby, the LED Beacons are complemented by light sources sitting on the BSS. However, because of the larger distances, the required light intensity demands the use of a laser [481]. The time offsets given by the *dark-room* measurements are used, corrected by the Laser Beacon and ^{40}K measurements as discussed later. Laser Beacons are located at the bottom of Lines 7 and 8 (central lines) and the IL07 and attached to their BSS.

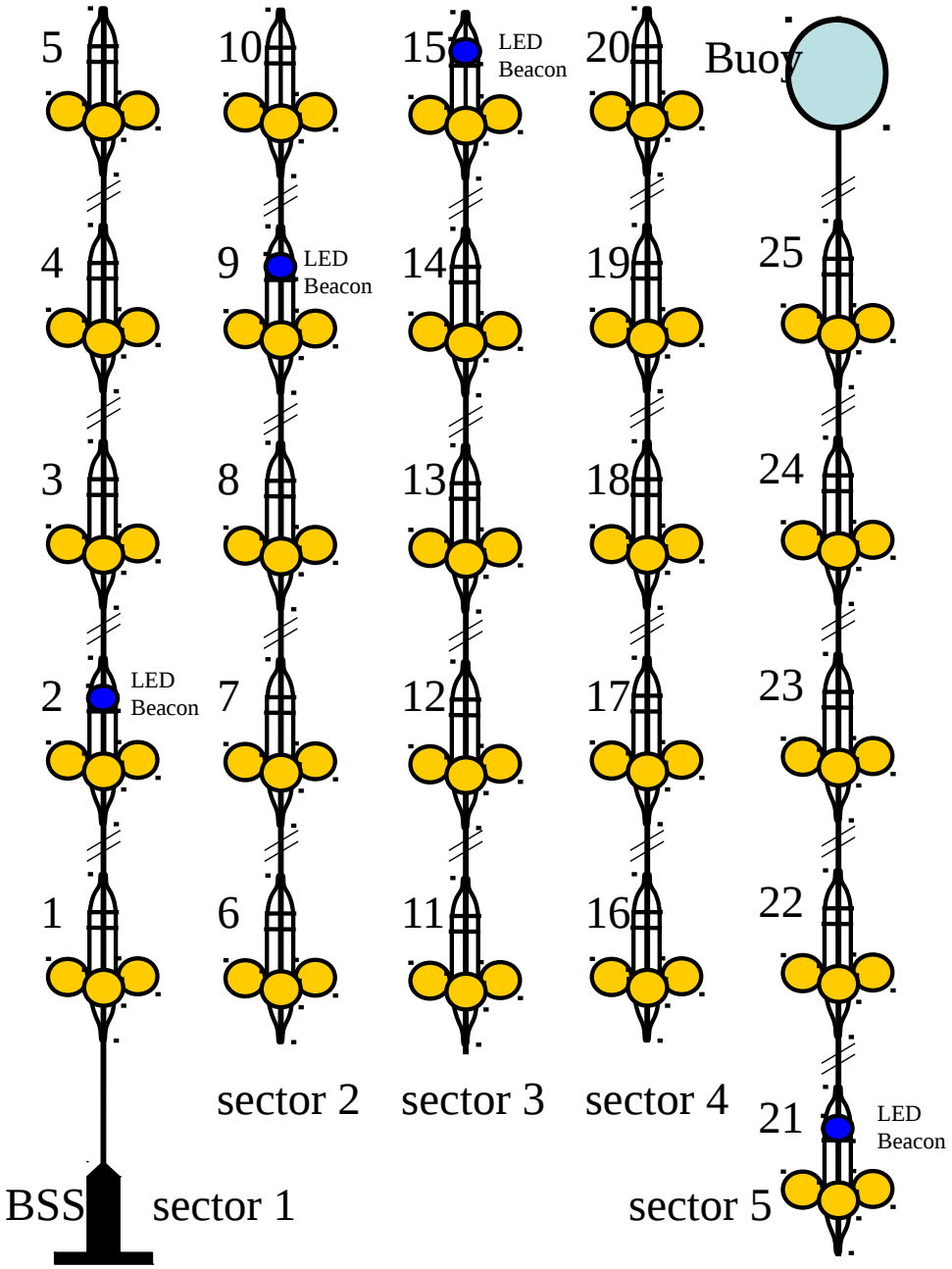

Fig. 3.31.: Schematic view of a standard ANTARES line with 25 storeys. To display in a handy way the LED Optical Beacon positions the line is shown separated in sectors. Each sector comprises a LED Optical Beacon (located in the 2nd, 9th, 15th and 21st storeys, counted from the bottom) except the 4th sector. The figure is taken from [661].

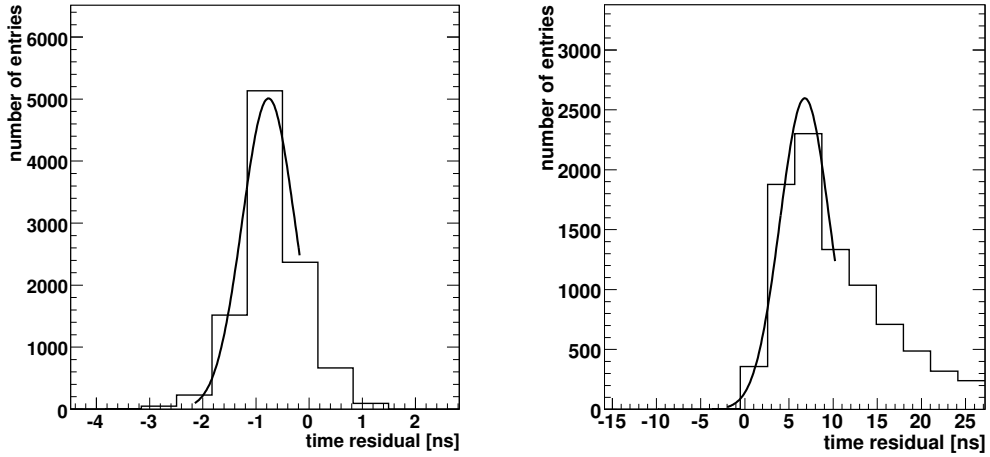

Fig. 3.32.: Time residual distribution in two different OMs located 2 storeys (left) and 7 storeys (right) above the flashing LED Beacon. The solid curve is the Gaussian fit. See explanation in the text. The figure is taken from [609].

The so-called time difference ΔT (or the signal time residuals) is the difference in time between the light signal time recorded in the OMs, t_{OM}, and emission time of the pulse (flash) measured by the photodiode (Laser OB) or PMT (LED OB), t_{OB}, corrected via subtraction of the nominal travel time of the light from the Beacon to the OM, $(d_{OM} - d_{OB})/c_{water}$, and can be expressed as [661]:

$$\Delta T = t_{OM} - t_{OB} - \frac{d_{OM} - d_{OB}}{c_{water}}, \tag{3.17}$$

where $d_{OM} - d_{OB}$ denotes the distance between OB and OM travelled by OB light and c_{water} is the speed of the OB light in water. The t_{OM} and t_{OB} are the *in situ* time values corrected by the corresponding time offsets measured in *dark-room* ($T_{0,OM}$ and $T_{0,OB}$), so that $t_{OM} = T_{OM} - T_{0,OM}$ ($t_{OB} = T_{OB} - T_{0,OB}$).

Figure 3.32 shows the distribution of signal time residuals. The distributions of these ΔT are expected to be centered at zero if the used time calibration is correct and the time offsets are correctly subtracted. If the time residuals are greater than 3 ns (the time offsets are spread within ±3 ns as shown in Fig. 3.29), the correction of the time offsets measured in *dark-room* is required. The left plot distribution corresponds to an OM close to the OB (∼30 m), 2 storeys above the OB, and thus receives a high amount of light, while the right plot distribution is for an OM located 7 storeys above the OB (∼100 m) (see Fig. 3.32) and a tail at positive times due to the light scattering in seawater is observed [609]. The range of the Gaussian fit is restricted in order to use mostly the earliest photons (*"early photon"* effect), whose delay due to light scattering can be neglected.

Figure 3.33 shows the time residual peak position, i.e. the mean value of the Gaussian best-fit curve described above, as a function of the OB-OM distance, i.e. the distance between the optical beacon and the different OMs. As seen, the time residual increases linearly with respect to the distance. This phenomenon originates from an *"early photon"* effect, arising from the duration of the light pulse and the fact that the first photons detected by the PMT determine the recorded time of the pulse [661]. Actually, the *"early photon"* effect is well described by the *order statistics* [662].

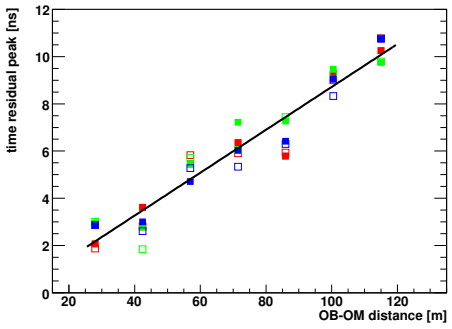

Fig. 3.33.: Time residual peak position as a function of the OB-OM distance for all the ARSs along 7 storeys. The six points at each distance correspond to the six ARSs in each storey (two ARSs per OM). The additional delay with distance is due to the *"early photon"* effect. The figure is taken from [609].

Optical Beacon operates in high intense regimes emitting very intense pulses with a width smaller than the PMTs integration time, but larger than the time resolution for single photoelectron hits. In that case, PMTs are unable to resolve multiple photons arriving in a short period of time, contrary, the time recorded by the PMTs is the arrival time of the earliest photons or pulse [661]. As a result, an approximately linear effect is observed for the time delay versus distance between the source (OB) and the OM (see Fig. 3.33). If a point deviates more than 2 ns [609] from the straight line, the fit is redone excluding it. Such deviations from the fit are later used for the time offset correction. Figure 3.34 shows the distribution of the time offset corrections for all OMs that can be calibrated with the OBs.

In addition to the *"early photon"* effect, the limitations on the ANTARES electronics, e.g. the ARS design features, can produce non-negligible deviations on the time measurement of the hits. The fact that the PMT signals are discriminated by the ARSs using a fixed amplitude threshold (typically 0.3 p.e.) leads to a so-called *walk effect* [609, 628]: a PMT signal with high-amplitude crosses the threshold earlier than a coincident low-amplitude signal leading to its delay as a function of the amplitude. Figure 3.32 shows the scheme of the *walk effect* and the time offset due to effect as a function of the PMT pulse amplitude.

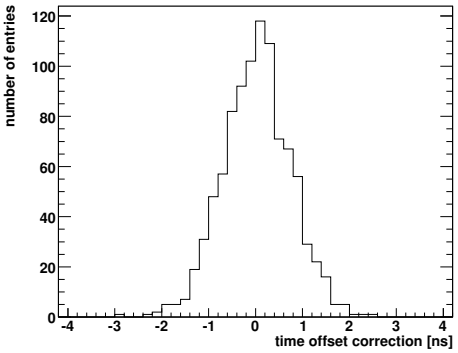

Fig. 3.34.: Distribution of the time offset corrections measured *in situ* with the LED Optical Beacons. Each entry is calculated as the difference between the time residual peak (see Fig. 3.33) and the corresponding value of the fitted line. The figure is taken from [609].

The *walk effect* occurs when two signals coincident in time at their maximum but with different amplitudes exceed the fixed voltage L0 threshold (typically 0.3 p.e.) at different times which gives a photon time delay as a function of the pulse amplitude (charge). Such a correlation between the signal charge and arrival time at the PMT provides a possibility to correct this effect with the known shape of the pulse. The procedure is as follows: the known PhotoElectron Pulse Shape (PPS) [609] is scaled up or down to reproduce the total charge of the hit and the corresponding threshold-crossing time is calculated. The *walk effect* correction as a function of the pulse amplitude is shown in Fig. 3.35. This correction is applied before event reconstruction.

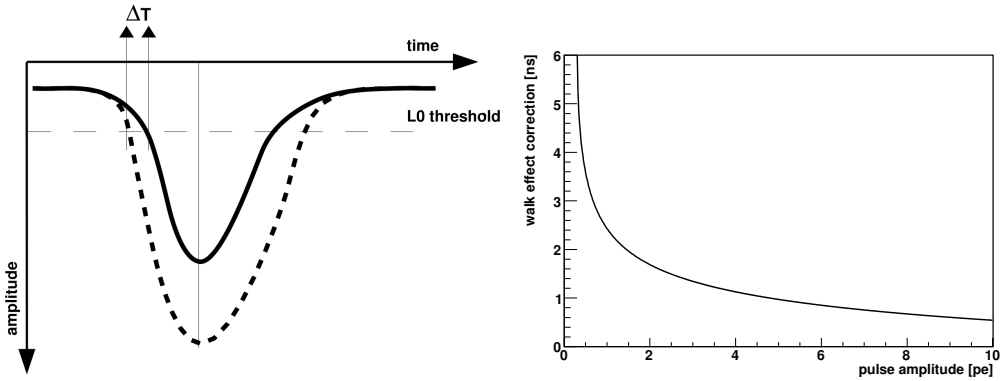

Fig. 3.35.: The *walk effect*. *Left:* A schematic picture of the *walk effect*. The biggest the signal in amplitude the sooner it crosses the L0 threshold (typically 0.3 p.e). *Right:* Time offset due to the *walk effect* as a function of the PMT pulse amplitude in units of p.e. See explanation in the text. The figures are taken from [661] and [609] respectively.

As stated, because of the disadvantages of the calibration of the lowest storeys using LED Beacons, it is complemented by a Laser Beacons sitting on the BSS. The time offsets measured in the *dark-room* are calculated with respect to the so-called reference OM, which is specific to each line; thus, the *inter-line* calibration among lines with Laser Beacons is required. In addition to the *inter-line* calibration, the time offsets of the OMs in the lowest storeys can be obtained using the Laser Beacons.

The main advantages of the Laser Beacons over the LED Beacons are [609]: the laser is much more powerful and can illuminate all detector lines, the laser pulse time width is very narrow (FWHM ~0.8 ns) leading to the fact that the *"early photon"* effect becomes negligible. Hence, the time residuals do not depend on the distance to the source (see Fig. 3.36) as observed for the LED Beacons (see Fig. 3.33). Therefore, the relative time offsets among lines are calculated as the average of the peaks.

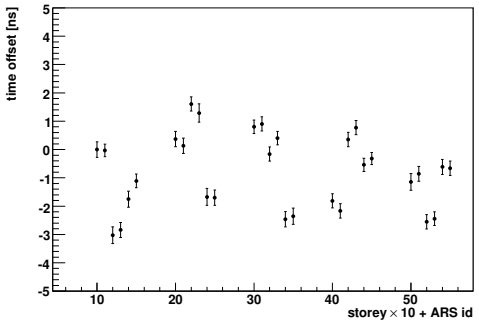

Fig. 3.36.: Time residual peak position as a function of the distance between the Laser Beacon and the OM. Each point is the average over all the OMs in the same storey. The figure is taken from [609].

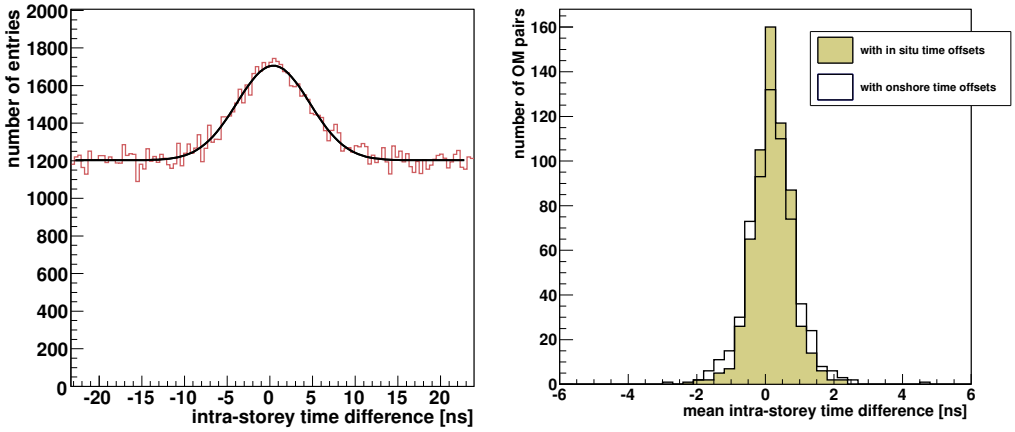

Fig. 3.37.: *Left:* Distribution of the time differences between the background hits for one pair of OMs in the same storey. The peak is due to single ^{40}K coincident decays detected by two OMs. The flat pedestal is caused by random coincidences. The black curve is a fit (sum of a Gaussian and a flat pedestal). *Right:* Comparison of the distributions of mean intra-storey time differences from ^{40}K using the on-shore and *in situ* time offsets. The figures are taken from [609].

Currently, one Laser Beacon run of 5-10 minutes duration is taken every Monday, while the LED OB runs of 5-10 minutes duration are scheduled for every two months.

^{40}K calibration

In order to provide an additional check of the timing calibration accuracy, the radioactive ^{40}K present in seawater can be used for time and efficiency calibration of the detector [646, 609] using the Čherenkov light induced by the electron emitted in the β-decay of potassium (see Eq. 3.16). If such a decay occurs within a distance of a few meters from a storey, coincident signals the associated Čherenkov light can be recorded by two OMs almost simultaneously [609, 625]: this kind of signal is referred to as *genuine* coincidence.

Figure 3.37 shows an example of the distribution of the measured time differences between hits in two OMs of the same storey (within a ±20 ns coincidence time window). A clear peak on top of the flat pedestal (or background, due to random coincidences) is evident which is in good agreement with the expectations from simulations [609]. The data have been fitted to the sum of a Gaussian distribution and a flat pedestal. The distribution width is 9 ns (FWHM) and set by the difference in the distance from the point where the decay occurs to each of the neighboring OMs [609]. The time offsets provided by the on-shore *dark-room* and OB calibrations (see Fig. 3.37) can be cross-checked using the position of the peak obtained with ^{40}K calibration. In case of the non-correct time offsets given by one of the neighboring OMs, the peak will be not centered at zero and small displacement from zero is expected. The RMS of the mean intra-storey time difference distribution determined by the ^{40}K improves from 0.72 ns to 0.57 ns [609] when the time offsets calculated *in situ* is used rather than the time offsets obtained in the *dark-room* calibration. In addition, the ^{40}K calibration can

be performed with physics runs, not requiring dedicated calibration runs that interrupt the data-taking. Recently, the ^{40}K calibration has been performed [625] using data collected by the ANTARES neutrino telescope from mid-2008 to the end of 2017. Furthermore, such a *genuine* coincidences due to ^{40}K decays were used to derive the relative photon detection efficiencies [663]. A modest loss in OM detection efficiency of only 20% for 9 years is observed [625]. Figure 3.38 shows an example of the measured time difference distribution between two neighboring OMs. Here, the Gaussian peak from *genuine* coincidences is also clearly visible and a flat pedestal from uncorrelated coincidences.

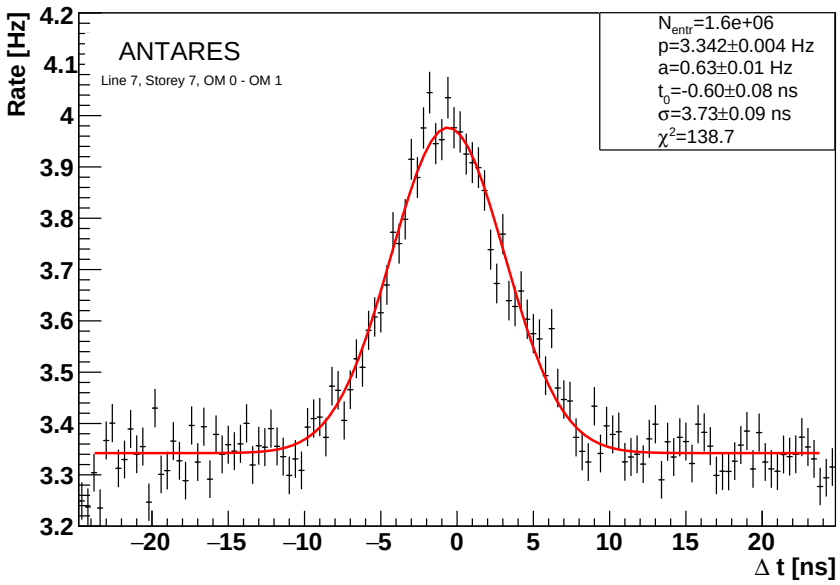

Fig. 3.38.: Example of the detected hit time differences, Δt, between two neighboring OMs. The fitted parameters are listed (see Eq. 3.18 for details). The plot refers to one pair of OMs in the same storey (Line 7, Storey 7, OM0-OM1) for one of the periods considered in the analysis. The figure is taken from [625].

The Gaussian fit for the distribution of the coincidence signals can be expressed as [625]:

$$f(t) = p + a \cdot exp\Big(- \frac{(t - t_0)^2}{2\sigma^2} \Big), \tag{3.18}$$

where p is the baseline, a is the amplitude of the Gaussian peak due to *genuine* coincidences, σ is the width of the peak and t_0 is the residual time offset between the hits recorded by neighboring OMs. A value of $\sigma \sim 4$ ns (see Fig. 3.38) is expected [625], mostly because of the distance between the OMs and the spatial distribution of the detected ^{40}K coincidences around the storey. The loss in OM detection efficiency of only 20% for 9 years shows the stability of a PMT based the detector in the hostile environment of the deep-sea, for the longest period ever recorded [625]; which in turn demonstrates the ability for the future underwater experiments such as KM3NeT, the next-generation multi-km^3-sized neutrino telescope [173, 174, 175], to remain in operation for the timescale of at least a decade without major efficiency degradation. In addition, the ^{40}K calibration procedure

can be used for KM3NeT and the presence of multi-PMT OM with 31×3-inch PMTs in the unique configuration on each storey instead of 3×10-inch PMTs as in ANTARES will allow to collect not only double coincidences from ^{40}K decays but also higher multiplicities, improving the technique to determine the photon detection efficiencies [625]; apart from this, it is possible at the level of 8-fold coincidences (within total 31) to select a virtually background-free sample of atmospheric muons [616, 174], demonstrating the background suppression capabilities of the new OM design (see Section 2.4.4).

Internal calibration

An internal LED [609] is also incorporated in each OM (see Fig. 3.4), the same model as the those used in the LED beacons. The aim of this LED is exclusively to monitor the stability (time offset variations) of the PMT transit time. The LED is glued to the back of every PMT and illuminates the photocathode from behind. The clock signal at a constant rate is used to trigger the LED. Figure 3.39 shows an example of the TVC mean time of the internal LED flashes as recorded by the corresponding PMT as a function of time. The values measured *in situ* vary less than 0.2 ns (RMS) over an eight-month period [609]. Currently, the internal LED calibration is scheduled for every two months.

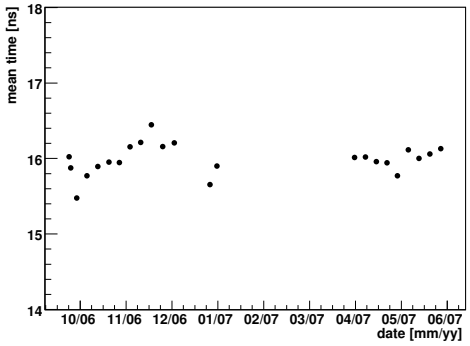

Fig. 3.39.: Example of the TVC mean time distribution measured with the internal LED. The figure is taken from [609].

Contribution of the front-end electronics

During on-shore and *in situ* calibrations, the influence of the front-end electronics on the time resolution can be determined. Three different methods to estimate the front-end electronics contribution are used in ANTARES [609]:

- At low light intensity, the time resolution of an OM measured in the laboratory is dominated by the TTS of the PMT (σ_{TTS}~1.3 ns). At high light intensity, the contribution decreases as the square root of the number of p.e. and therefore the dominant term to the width of this distribution is the constant contribution due to the front-end electronics. In the *dark-room* calibration this irreducible contribution is found to be ~0.5 ns.

- In the *in situ* calibration, the estimation of the time resolution of the electronics is obtained from the time difference distribution measured by an OM close to an OB

with respect to the OB pulse emission time. The sigma of the time distribution of the signal in an OM can be expressed as [609]:

$$\sigma_{OM}^2 = \frac{\sigma_{TTS}^2}{N_{pe}} + \frac{\sigma_{water}^2}{N_\gamma} + \sigma_{OB}^2 + \sigma_{elec}^2, \tag{3.19}$$

where σ_{TTS} is the TTS of the PMT, σ_{water} is the spread due to the scattering and chromatic dispersion of light in water (~1.5 ns for a light path of 40 m), σ_{OB} is the uncertainty of the measured emission time of the pulse and σ_{elec} is the spread due to the electronics. The N_{pe} and N_γ are high for an OM close to an OB (high light regime); thus, their corresponding contributions become negligible. Due to the fast rise time of the internal PMT of the OB, σ_{OB} can also be neglected. Taking into account many measurements at high light regime a time resolution of ~0.5 ns for the electronics is obtained. This is in agreement with the results obtained during the first (on-shore) calibration.

- Comparing the times measured by two OMs in the same storey when illuminated at high intensity, a front-end electronics time resolution of 0.5 ns can be obtained. In this case, the sigma of the distribution is given by $\sigma_{OM\text{-}OM} = \sqrt{2}\sigma_{elec}$ and indicates a front-end electronics resolution of 0.5 ns: $\sigma_{OM\text{-}OM} = 0.7$ ns then $\sigma_{\text{elec}} = 0.7/\sqrt{2}$~0.5 ns.

Based on this, one can conclude that the uncertainty introduced by the readout system is negligible with respect to the irreducible contributions from the chromatic dispersion (~1.5 ns) and TTS (~1.3 ns) [609].

3.5.2 Charge calibration

The charge calibration [664] and threshold tuning of the PMTs and their associated front-end electronics such as ARS chips are of primary importance. The accuracy on the charge calibration is essential for the neutrino energy estimation, therefore, has a strong impact on physics analysis. It enables ANTARES to discriminate the neutrinos of atmospheric origin with the soft energy spectra from neutrinos of astrophysical origin with the hard energy spectra.

The analog charge signal has to be integrated and converted into the number of p.e. that caused the PMT pulse. The charge integration is carried out by an 8-bit AVC [481] (see Section 3.3.1), which enables to convert the analog signal amplitudes (charge Q) into a number of p.e. (see Eq. 3.1) as the relevant information for track and energy reconstruction. In order to estimate the charge over the full dynamical range of the ADC, the knowledge of the p.e. peak and the pedestal is required [664, 665]. The individual measurements are converted into p.e. units using the difference in ADC channels between the 1 p.e. peak and the pedestal (see Eq. 3.1). Charge distributions obtained with minimum bias data (based on

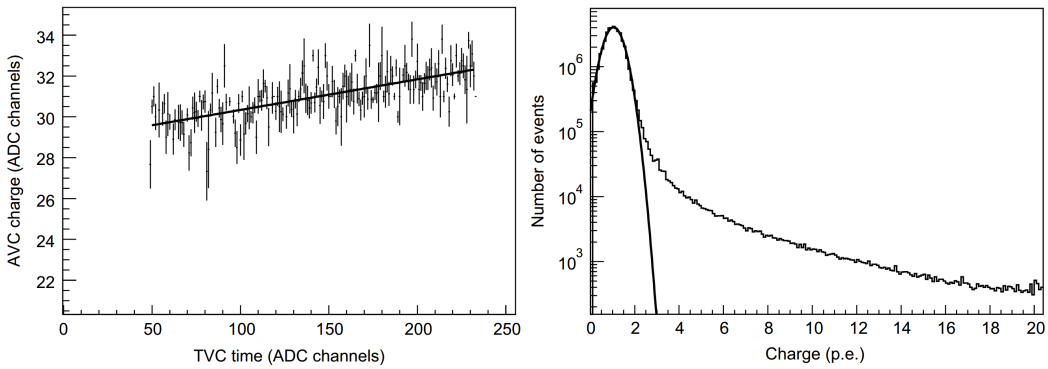

Fig. 3.40.: *Left:* Example of the observed "cross-talk" effect affecting the charge measurement. *Right:* Example of overall charge distribution in p.e. units obtained after calibration. The Gaussian fit of the p.e. peak gives a mean value of 1.05 p.e. with a σ of 0.4. The figures are taken from [628].

a snapshot of the overall OM activity above a given threshold) can be parameterized using the following simple formula [666, 664]:

$$\frac{dN}{dx} = Ae^{-\alpha(x-x_{th})} + Be^{-\frac{(x-x_{pe})^2}{2\sigma^2}}, \tag{3.20}$$

where x, x_{th} and x_{pe} are respectively the charge, the effective thresholds ("offset") and p.e. peak ("center") in AVC units. The first and second term account the dark current of the PMT and the the p.e. distribution itself (follows a Gaussian with mean x_{pe} and standard deviation σ) respectively [664, 628].

The charge measurements, performed inside the ARS (in the AVC channels), are affected by the time measurements in the TVC channel (the inverse effect does not apply) [664, 481]. This effect is supposed to be caused by a so-called "cross-talk effect" of the capacitors inside the ARS pipeline and can be as high as 0.2 p.e. on an event-by-event basis [664, 628]. The effect is linear and does not require correction on high statistics basis since when hits populate the full range of the TVC, the effect washes out [664, 628]. However, a correction to the measured charge of a single event has to be applied. Such a correction can be inferred with *in situ* measurements by plotting the AVC value versus the TVC value [664, 628, 481] as shown in Fig. 3.40. A small slope (~10%) for the AVC channel is arisen as result of "cross-talk" effect. As soon as the "cross-talk" correction is made, the charge calibration is applied in order to perform the reconstruction of the amplitude of the individual signals detected from the OMs. The minimum bias events recorded by the detector are coming predominantly from ^{40}K decay and bioluminescence and dominated by SPE charges [664] as is shown in Fig. 3.40. The distribution is peaked at ~1 p.e. as expected from ^{40}K decay and bioluminescence. The estimated accuracy of the measurement is of the same order as the RMS of the distribution of the PMT response to 1 p.e., which is ~0.3 p.e [628]. In all of the above, the linear response of the system is assumed. Thus, a transfer function inferring the number of p.e. n from the digitized charge Q (see Eq. 3.1) supposed to be also linear. This provides the simple equivalence of ADC counts into p.e.

units as the difference between the 1 p.e. peak and the pedestal value of the AVC as shown in Eq. 3.1. But even if the integral linearity of the ADC used in the ARS chip is satisfactory in a wide range [667, 628], nevertheless small deviations from the linearity caused by local non-linearities are present. The ADCs suffer from differential non-linearities, i.e., inhomogeneous bin sizes (the so-called Differential Non-Linearities (DNL) effect [628]). In the TVC of equal binning and events uniformly distributed in time, the resolution is given by $\sigma = \Delta t/sqrt12$, where Δt is the bin size. But since the DNL effect leads to a different bin occupancy, the theoretical resolution expected with respect to the DNL effect is then $\sigma^2 = \frac{\Delta t^2}{12}\frac{\sum x_i^3}{\sum x_i}$, where $\Delta t \cdot x_i$ is the width of bin i. The main systematic error of the charge measurement is due to the measurements of the pedestal and of the p.e. peak is due to the DNL effect [628]. Some investigation to correct the influence of the DNL effect is performed in [668]. The investigation has shown that a global DNL correction is not feasible. However, the DNL effect of the AVC can be minimized if the integral form is considered instead of the differential form in Eq. 3.20:

$$\int_0^x \frac{dN}{dx}dx = \frac{A}{-a}e^{-\alpha(x-x_{th})} + \frac{B}{\sqrt{\pi}}\Gamma\Big(\frac{1}{2}, \frac{(x-x_{pe})^2}{2\sigma^2}\Big), \tag{3.21}$$

where Γ is the incomplete Gamma function.

In order to determine the SPE peak, the fit on the integrated spectrum is applied and since the contribution of PMT dark current is negligible in the region of the peak, the $A = 0$ can be considered. Also, the pedestal region is identified; then, a fit is applied. The parametrization used for the fit is:

$$\frac{C}{\sqrt{\pi}}\Gamma\Big(\frac{1}{2}, \frac{(x-x_{ped})^2}{2\sigma_{ped}^2}\Big), \tag{3.22}$$

where x_{ped} is the charge pedestal. The transfer function is then calculated with the measurements of the SPE peak and the pedestal values.

3.5.3 Position calibration

The ANTARES detector lines are fixed to the seabed by BSS anchors and are held taut and kept vertical by a buoy on the top of the line. Since the lines are not rigid structures, so deep-sea currents (typically around 5 cm/s) can drift the buoy and cause the lines to be displaced from the vertical and the storeys to rotate around the line axis [620]. It can result in a few meters displacement of the top storeys (see Fig. 3.41). A precise absolute detector alignment is crucial for searches of potential neutrino point sources in the sky; also, the pointing accuracy closely related to the precision in the determination of the arrival time of the Čherenkov photons at the PMTs which in turn highly sensitive to the distances between the OMs and thus crucial for a good angular resolution. In order to ensure optimal track reconstruction accuracy, it is necessary to monitor the relative positions of all OMs with accuracy better than 20 cm, equivalent to the 1 ns precision of the timing measurements [481]. Also, a few degrees precision of the OM orientation is essential for the

muon energy reconstruction [481]. To achieve a suitable precision on the overall positioning accuracy, a two-fold system is used [481, 620]:

A High-Frequency Long Base Line acoustic system (HFLBL)[15] Serves for distance triangulation. Measures the relative positions of the different elements of the ANTARES detector within the local detector frame (relative to BSS) with high accuracy. Gives the 3D spatial position (see Fig. 3.42) of 5 hydrophones (Rx modules) placed along the line (mounted on the 1^{st}, 8^{th}, 14^{th}, 20^{th} and 25^{th} storeys, counted from the bottom) [481, 620]. The positioning method is based on a measurement of travel times of high-frequency acoustic sinusoidal pulses (40-60 kHz) between acoustic transceivers (RxTx modules) fixed at the line anchors and receiving hydrophones on the detector lines [620]. The purpose of RxTx modules are to emit acoustic signals (to be detected by the Rx modules), triggered by an external synchronization signal (Master Clock), to detect the signals of other RxTx modules (operated as receivers and emitters), to stamp the detection time with respect to the Master Clock and to transmit the timestamps and amplitudes to the shore station [620]. The measured acoustic distances are used to triangulate the position of each Rx hydrophone with respect to all emitters anchored in the base of the line (additional autonomous transponders are used). These autonomous transponders installed around the detector are used in order to enlarge the triangulation basis and thus to improve the precision of the positioning [481]. These are autonomous emitter-receiver beacons fixed on pyramidal structures (see Fig. 3.11) anchored on the seabed (at a distance of about 150 meters from the detector) and powered by batteries.

A tiltmeter-compass system Serves for the storeys orientation and inclination measurements in order to provide unambiguous information about the movement of the lines. Gives the local tilt angles (pitch and roll) of each storey with respect to the vertical line as well as its orientation with respect to the Earth Magnetic North (heading) [481]. The TCM2 sensor is used (for measurement range and accuracy details see Section 3.2.2).

Direct measurement of the storey position is only possible for the five storeys containing a hydrophone and for the position evaluation for all storeys of a line a mechanical model was developed and described in [620]. Using the combined information gathered with this two-fold system the shape of each line is reconstructed (every two minutes) by performing a global χ^2-fit based on the model which predicts the mechanical behavior of the line under the influence of the sea current [620]. The relative positions of the OMs are then deducted from the reconstructed line shape and from the known geometry of the storeys with the precision of the order of 10 cm (RMS) even for seawater currents as strong as 15 cm/s [620, 665]. The 10 cm accuracy corresponds to an uncertainty in the travel time of light in the water of 0.5 ns and well matches the requirements for track reconstruction.

[15] Developed and constructed by ECA (formerly GENISEA), http://www.eca.fr

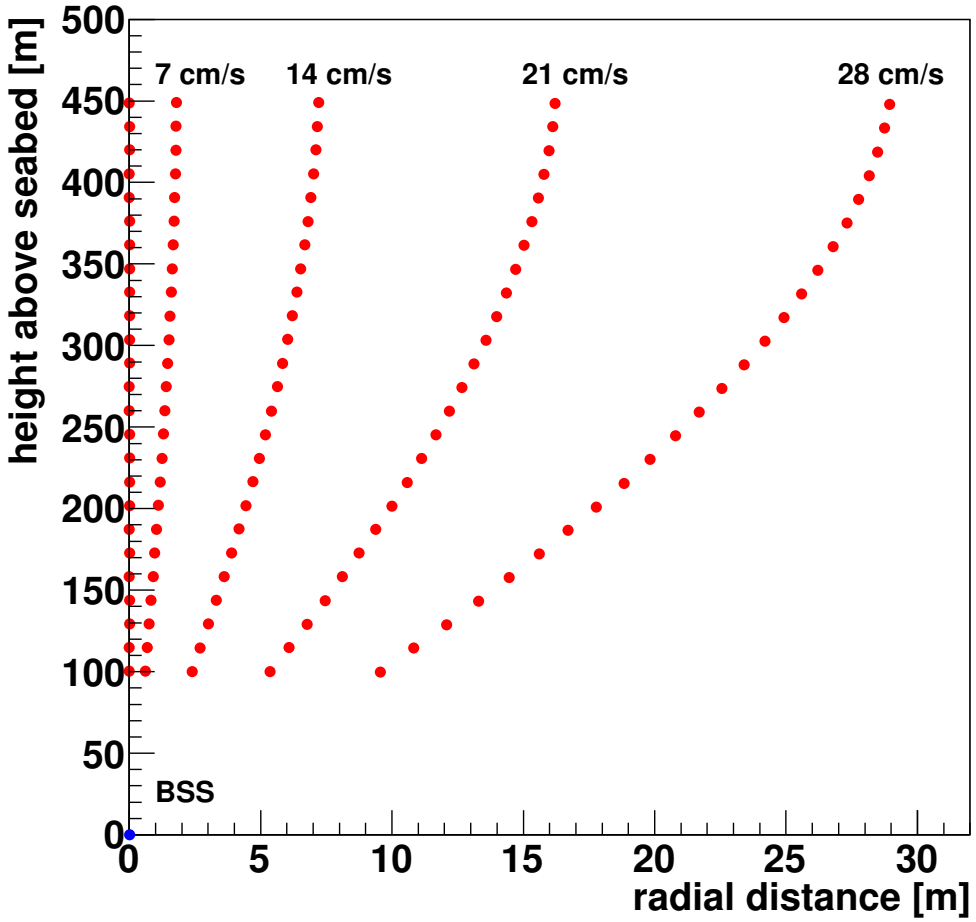

Fig. 3.41.: Calculated positions (height and radial displacement) of the storeys of a line (dots) with respect to the anchor of the line (BSS) for different sea current speeds according to the line shape model in [620]; note the different scales on the axes. See explanation in the text. The figure is taken from [620].

Figure 3.41 shows the calculated positions of the 25 storeys of a line for different sea current speeds. The radial displacement increases quadratically with the sea current speeds [620]. As seen in Fig. 3.41, the radial displacement is < 2 m even for the uppermost storey for typical sea current speeds ~5 cm/s, while the displacement is around 15 m for a speed of ~20 cm/s.

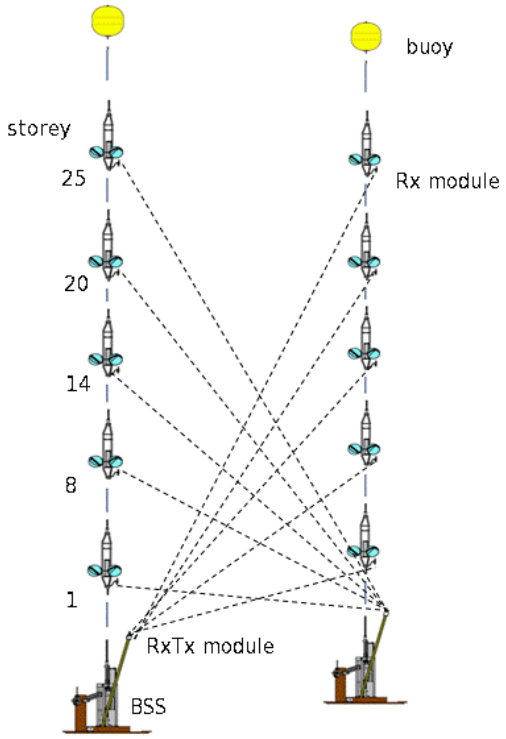

Fig. 3.42.: Schematic demonstrating the principle of the HFLBL positioning system for two lines (for simplicity only storeys with an Rx module are shown). The figure is taken from [620].

The behavior of the positioning system using the first ANTARES data is described in [669, 670]. Figure 3.43 shows the x-y displacement in the horizontal plane of the 5 hydrophones at different heights along a line as a function of time for a period of 6 months (from July to December 2007). As seen, the hydrophone displacements are followed with an accuracy of a few centimeters. As expected, larger displacements are observed for the top storeys and the movement of the line is dominated by the east-west heading of the Ligurian current [669]. This is also well confirmed by the fact that the radial displacement increases quadratically with the sea current speed as can be seen in Fig. 3.41. A detailed analysis of the system performance indicates that the resolution is better than the 20 cm specification [670] at which value it does not degrade the angular resolution [481]. The excellent performance and flexibility of this system and successful operation in ANTARES made it a recommended technique for the design of the detector positioning system of the multi-km^3-sized KM3NeT telescope [173, 174, 175].

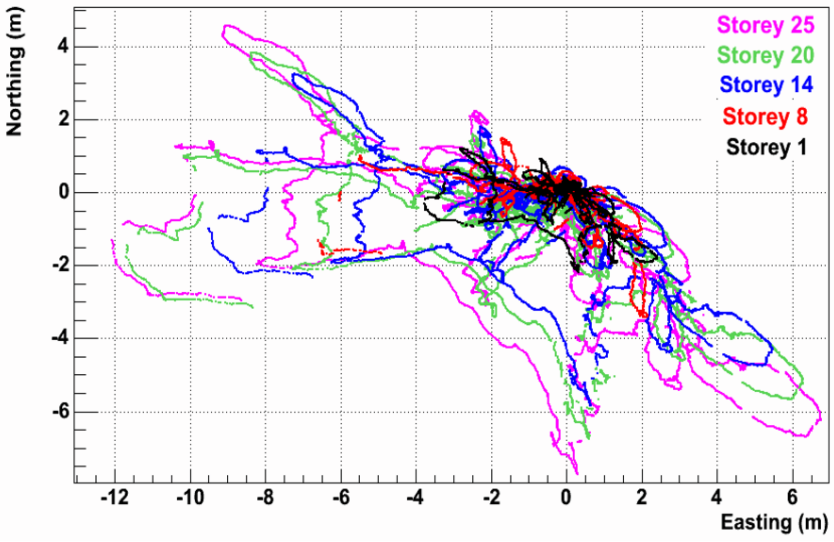

Fig. 3.43.: Displacements in the horizontal plane of the five storeys equipped with positioning hydrophones of a line as determined by the positioning system. See explanation in the text. The figure is taken from [481].

3.6 Construction milestones and status

This section reviews the major construction milestones successfully achieved by the ANTARES collaboration, discusses the current status and the future of the project.

- **1996-1999:** Start of the project in 1996 [506, 671] and an intense R&D program during the next few years [506]. At this stage, the seawater properties were the first studied, in order to choose the best site, and marine technologies which were developed and improved [672]. A visual and bathymetric survey of the seafloor was performed in December 1998, using the "Nautile" submarine of the French IFREMER[16] oceanographic research agency [506]. In the area selected as a potential ANTARES site, the seafloor is flat with no topographic anomalies such as steps and rocks.

- **November 30th, 1999:** Deployment of the so-called "Demonstrator String" (of a different mechanical design to the current design) at an 1100 m depth and connection to shore via a 37-km electro-optical cable in order to prove the feasibility of the foreseen project. The 350 m long string was instrumented with 7 PMTs and allowed to check the acoustic positioning system and measure the first atmospheric muons [671]. The ANTARES relative/absolute positioning acoustic system of range meters, compasses, and tilt miters were tested, the accuracy obtained is of ∼5 cm/∼1 m, respectively [673].

- **October 2001:** The MEOC to carry electrical power and data between the ANTARES site and shore in La Seyne-sur-Mer was successfully deployed [674, 671, 673].

- **December 21st, 2002:** The JB deployment and connection to the shore station [674]. The successful deployment of the first of two final-design prototype lines, a "Prototype Detection String" (or "Pre-production Sector Line" (PSL) [675]), equipped with 15 OMs (5 storeys corresponding to 1/5 version (a sector) of a complete ANTARES line) and final-design acquisition electronics [674, 673, 676]. Apart from 15 OMs, the following devices were instrumented to the line: a Laser and a LED Beacons (for time calibration purposes); an acoustic transceiver and a hydrophone (for triangulation needed for determining the positions of the OMs); a pressure sensor and a sound velocimeter [676].

- **February 12th, 2003:** The successful deployment of the second of two final-design prototype lines, a "Prototype Instrumentation String" (or "Mini-Instrumentation Line" (MIL) [675]), equipped with devices for environmental measurements [674, 676, 673]. The following devices were instrumented to the line: a Laser and a LED Beacons (for time calibration of the OM of the prototype detection line); an acoustic transceiver and a hydrophone (for triangulation); a pressure sensor, a seismometer, a sound velocime-

[16] Institut français de recherche pour l'exploitation de la mer (IFREMER), wwz.ifremer.fr

ter, an acoustic Doppler current profiler, a conductivity-temperature-density meter, a deep-sea light transmissometer (for environmental parameters monitoring) [676].

- **March 16th-17th, 2003:** Connection of both lines, PSL and MIL, to the shore station through the already installed MEOC and JB during the mission with the "Nautile" manned submarine of the French IFREMER oceanographic research agency [676, 673, 674]. The start of data-taking. The PSL successfully took data between the end of 2002 until its recovery in July 2003 [672].

- **March 15th-18th, 2005:** Deployment of two lines: Line 0 [630] and Mini Instrumentation Line with Optical Modules (MILOM) [677]. Line 0 was the first mechanical test of a line composed of 23 storeys, equipped with water leak sensors and instruments for transmission attenuation measurements [678]. The MILOM was a new upgraded version (with an extra storey with 3 OMs) of the MIL and was connected on April 12th, 2005. The main objective of the MILOM operation (and Line 0) was to test all systems and to provide an *in-situ* check of the modified detector elements and validation of the performance of the time calibration and the acoustic positioning devices and to monitor the seawater optical properties [677]. With the MILOM, the required specification for the absolute clock timing (~1 ms), the relative timing of the OMs (~0.5 ns), and the required precision on the 3D position determination of the OMs (~10 cm) has been verified [678]. The MILOM took data for 2 years (April 2005 - March 2007), before the deployment, connection, and operation of the first complete ANTARES line [672]. The results of the MILOM line are presented in detail in [677].

- **March 2nd, 2006:** The first ANTARES detector line (Line 1) came into operation [679, 680] (was deployed in February 2006). The first data were recorded immediately.

- **September 21st 2006:** The second ANTARES detector line (Line 2) came into operation [679] (was deployed in July 2006). The first 2-lines muons were recorded.

- **January 29th, 2007:** The ANTARES was upgraded by three additional lines, forming a real 3D 5-line detector [679]. Line 3, 4, 5 were deployed on November 29th, 2006, January 8th and 16th, 2007, respectively. On January 29th, 2007 The ANTARES collaboration brought into service a 5-line detector marked the beginning of neutrino astronomy in ANTARES. At this stage, ANTARES became the largest neutrino telescope ever built in the Northern Hemisphere. The data-taking with 5 lines has been performed during February-May 2007 (with equivalent livetime 54 days and $\sim 5 \times 10^6$ events have been collected) [672, 681].

- **April 2007** The MILOM was recovered, reequipped and redeployed in July 2007 under the name IL07 [481]. The IL07 contains an ensemble of oceanographic sensors dedicated to the measurement of the environmental parameters [680].

- **December 7th, 2007:** The ANTARES was upgraded to the 10-line detector (lines 6-10 were deployed between March and November) [681, 680] (was doubled in size and significantly enhanced the sensitivity of the detector). Also, IL07 became operational [481].

- **May 30th, 2008:** The ANTARES detector construction was completed with the installation of eleventh and twelfth lines [681, 680], making it the largest neutrino telescope in the Northern Hemisphere and the first to operate in the deep-sea [624]. Figure 3.44 displays an event recorded a few hours only after the 2 new lines were powered on, on May 30th, 2008. The scheme of the ANTARES complete 12-line detector (and the 13th instrumentation line IL07) can be seen in Fig. 3.3.

- **End of 2019:** The scheduled decommissioning of the ANTARES telescope, at which point the KM3NeT neutrino telescope [173, 174, 175] with a unique design of multi-PMT OMs and of a multi-km^3 instrumented volume will have surpassed ANTARES in sensitivity raising a new era in neutrino astronomy.

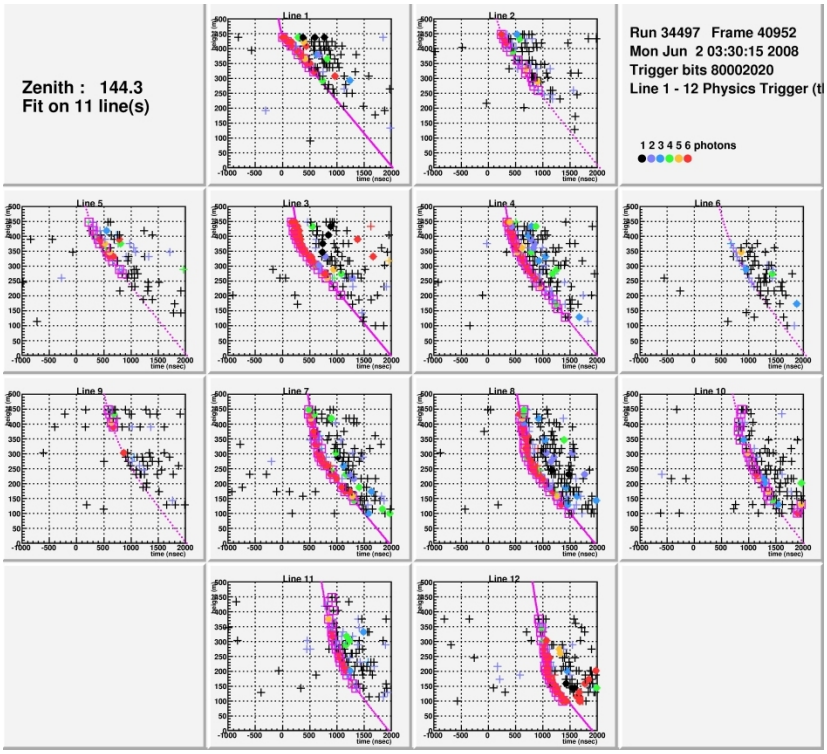

Fig. 3.44.: The ANTARES event display with an event recorded on May 30th, 2008. The OMs that were fired by one downgoing event, for each of the 12 lines are shown. The bright muon bundle is seen. The curves present the result of the reconstruction of this event (a fitted track), once projected on each of the line used for the fit. Each panel shows the arrival time of the hits (x-axis) and the vertical position (y-axis) for each detector line (y=0 is the sea bottom). Crosses are hits in a time window of 3 μs around the trigger, while the full circles are hits passing the trigger condition and open boxes are hits used in the final reconstruction, represented with pink lines.

4 The HAWC Gamma-Ray observatory

HAWC [155, 156] (High Altitude Water Cherenkov) observatory is the second generation of water Čherenkov style detectors for gamma and cosmic rays. It is located at 4100 meters a.s.l. [682, 156] on the flanks of the volcano Sierra Negra (or Tliltepetl) (see Fig. 4.1) in the state of Puebla, Mexico (18°59′41″ N 97°18′30.6″ W). The data-taking started in August 2013 with a partially deployed detector [683]. The complete detector has been inaugurated on March 20th, 2015 [683].

In this section, a general description of the detector design, its operation, and the detected extragalactic sources, the target for this work, are given. Section 4.2 gives an overview of the detector layout. The detector operation and advantage of the HAWC are discussed in Section 4.1 and Section 4.3. The HAWC scientific goals are expounded in Section 4.4. The brief description of the two extragalactic sources detected by HAWC and are the target of this work are given in Section 4.5 together with other sources detected by HAWC. Finally, the future of the HAWC γ-ray observatory and its possible extension are discussed in Section 4.6.

4.1 Detector design

The design of HAWC (see Fig. 4.1) is optimized for the detection of air showers induced by γ-rays between ~0.1 and ~100 TeV with the peak sensitivity being reached at a few TeV, depending on source spectra [154]. The footprint of an air shower is recorded through the collection of PMT signals induced by the passing of the shower front through the array (see Fig. 4.2) and is referred to as an event in the following [154]. The HAWC design builds upon the experience with the Milagro [157, 158] detector, which was the first generation of γ-ray detectors using the water Čherenkov technology [155]. In order to have a much larger active area than Milagro for the same photo-cathode area, in HAWC a single deep layer of PMTs with a wider separation is used in contrast to the double layer of PMTs used in Milagro [155]. In addition, the HAWC uses a large array of Water Čherenkov Detectors (WCDs) in contrast to a big pond used in Milagro [155]. Re-deploying the existing Milagro PMTs and electronics in a different configuration at a higher altitude, with the increased physical area, and the optical isolation of the PMTs [155] led to a sensitivity increase of a factor of ~15 over Milagro [155].

Fig. 4.1.: The view of the HAWC Observatory. Image credit: HAWC.

HAWC is most sensitive to sources between declinations $-26°$ and $+64°$, but due to the rotation of the Earth, any location in this declination range passes over HAWC once every sidereal day [154]. The wide instantaneous FOV of ~2 sr and unprecedentedly high duty cycle of >95% allow HAWC to observe every source that transits over HAWC for up to ~6 hours each sidereal day [154]. HAWC is optimized for the energy range above 300 GeV, with detections above 100 TeV possible [684]. HAWC's sensitivity improves with the γ-ray energy, and above 10 TeV, it is the most sensitive currently-operating γ-ray observatory in the world [684]. The strength of HAWC over the IACT technique is that photon showers may be detected across the entire ~2 sr FOV of the instrument, day or night, regardless of weather conditions with duty cycle of >95% [156, 154]. The IACTs have a few degrees FOV and can only operate on clear nights. All this makes HAWC to be uniquely suited to study the long-duration LC of objects and to search for flaring sources in real-time [156]. Thus, the flare information provided by HAWC is significant. The γ-ray flare timing information from HAWC is able to noticeably improve the efficiency of the search Section 6 for a neutrino counterpart with ANTARES.

4.2 Detector layout

HAWC consists of a large 22 000 m^2 area[1] densely covered with 300 WCDs [156] (see Fig. 4.2), each filled with 190 000 liters of highly purified water [154] and instrumented with 4 PMTs looking up to detect Čherenkov light from charged particles in EAS (see Fig. 1.1). The WCD tanks are 7.5 meters diameter and 5 meters high [682, 156]. At the bottom of each WCD (see Fig. 4.3), three 8-inch Hamamatsu R5912 PMTs (previously used in the Milagro experiment) are anchored in an equilateral triangle of side length 3.2 meters,

[1]The active surface is 12 000 m^2 [682].

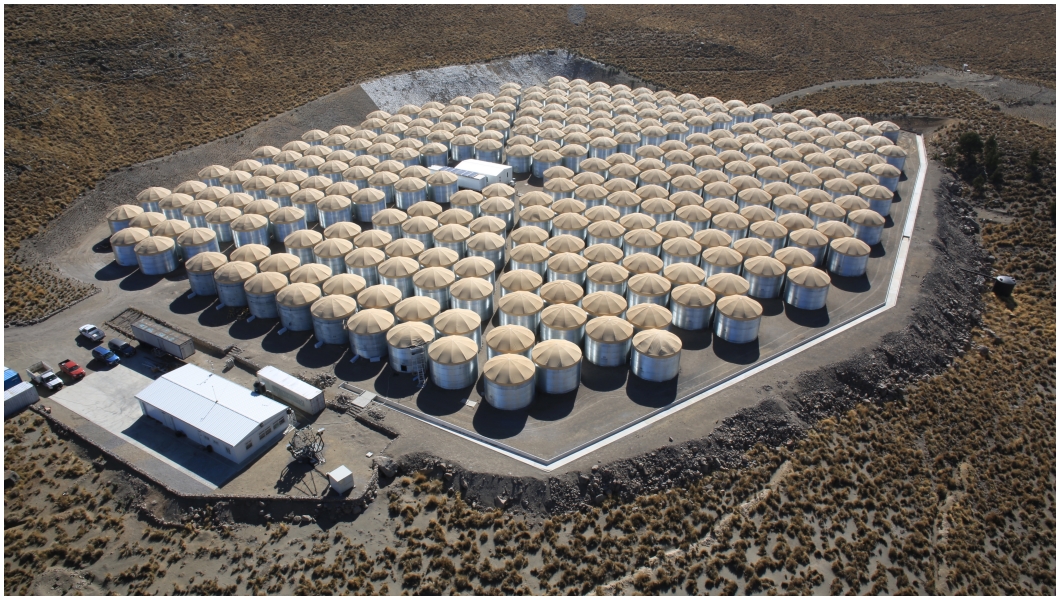

Fig. 4.2.: The view of the HAWC array. The figure is taken from [685].

with one 10-inch High-Quantum Efficiency (HQE) Hamamatsu R7081 PMT[2] anchored at the center [156], designed to increase the efficiency of the observatory to low-energy showers [155]. The water in each WCD is filled to a depth of 4.5 meters with 4.0 meters of water above each PMT [156].

A high-energy photon impinging on the atmosphere above HAWC initiates an electromagnetic EAS with the resulting mix of relativistic electrons, positrons, and γ-rays propagates to the ground at nearly the speed of light [156] (see Fig. 1.1). These energetic particles may reach the instrument and interact in the water and produce Čherenkov radiation that can be detected. The necessity to build the telescope at a high altitude of 4100 meters is driven by the aspiration to be closer to the shower maximum. The location of the HAWC array thereby allows to increase the lower energy response and improve the sensitivity, the angular, and energy resolution and the γ/hadron discrimination [682]. The high altitude of HAWC also sets the scale for the photon energy that can be detected: at HAWC's location, the shower from a 1 TeV photon from directly overhead will have about 7% of the original photon energy left when the shower reaches the ground while rising to about 28% at 100 TeV [156]. The HAWC detector is fully efficient to γ-rays with primary energy above about 1 TeV [156] with a peak sensitivity is reached at a few TeV [154], depending on source spectra.

[2] In ANTARES, the Hamamatsu R7081-20 is used. In Section 4.6, the possible re-use of ANTARES PMTs for HAWC detector extension stage is discussed.

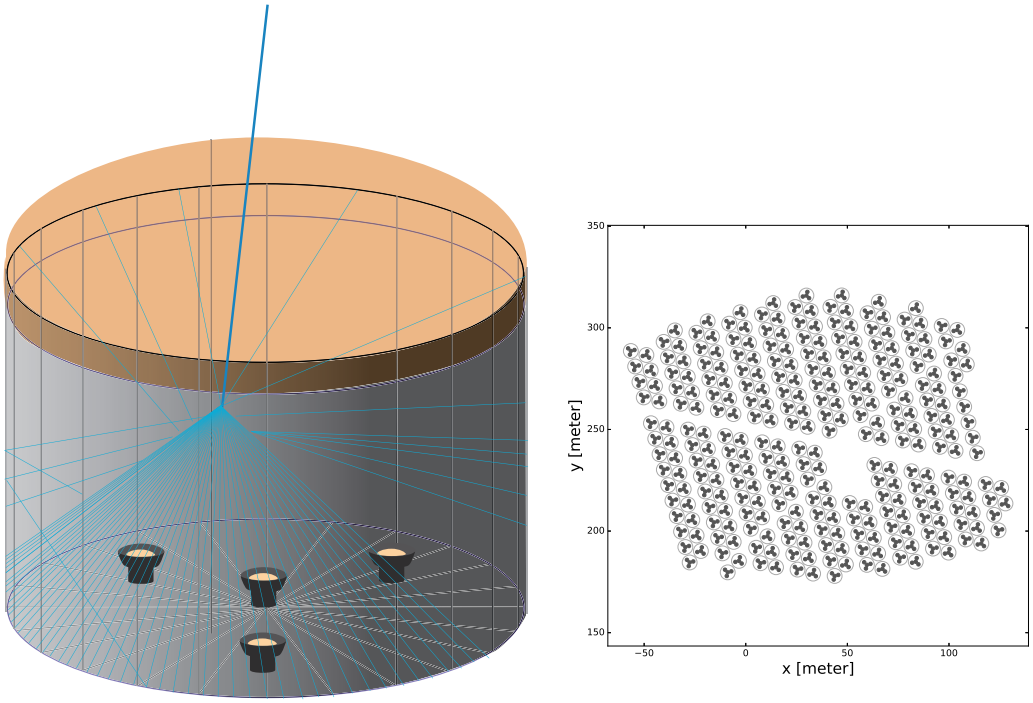

Fig. 4.3.: Schematic view of the HAWC layout and a single WCD. *Left:* Scheme of a single HAWC WCD: the steel tank, the covering roof, and the four PMTs. A sketch of a charged particle passing through a tank and emitting Čherenkov light is shown. *Right:* The completed HAWC instrument, covering 22 000 m^2. The location of each WCD is indicated by a large circle and PMTs are indicated with smaller circles. The gap in the center hosts a building with the data acquisition system. The figure is taken from [156].

4.3 Detector operation

The PMTs detect Čherenkov light inside the WCDs produced by relativistic secondary particles from an EAS [686]. The large depth of water above the PMTs guarantees that the e^-, e^+, and γ-s in the air shower are fully absorbed by the HAWC detector well above the PMT level so that the detector itself acts as an electromagnetic calorimeter providing an accurate measurement of electromagnetic energy deposition [377]. Analog signals from the PMTs are transmitted by 600 feet RG59 coaxial cable to the DAQ in a central counting-house to be processed by custom-made front-end boards [686, 377]. PMT pulses are amplified, shaped, and passed through two discriminators at approximately 1/4 and 4 PEs, low and high voltage thresholds, and digitized [686, 156]. The timestamp of a pulse that crosses at least the lower of the two thresholds is recorded by CAEN VX1190A time-to-digital converters (TDCs) with a precision of 0.1 ns and passed to a farm of computers for real-time triggering and processing [686, 377, 156]. To infer the pulse size and the total amount of charge collected in the PMT, the ToT is used, i.e., the length of time that PMT pulses spend above the threshold [686, 156]. Noise arises from a number of sources including PMT afterpulsing, fragments of sub-threshold air showers, PMT dark noise, and other sources [156]: the 8-inch PMTs have a hit rate of 20-30 kHz while the 10-inch PMTs have a hit rate of 40-50 kHz. High-energy electrons are also detected via the Čherenkov light

they produce in the water and γ-rays are converted to electrons through pair production and Compton scattering [377]. Muons are also detected, and they are more likely to be produced in air showers originating from hadronic CR interactions with the atmosphere and tend to have higher transverse momentum producing large signals in the PMTs far from the air shower axis and thus serve as useful tags for rejecting hadronic backgrounds [377]. Air shower events are preserved by the computer farm if they pass the trigger condition: a simple multiplicity trigger, requiring some sufficient number, N_{thresh}, of PMTs record a hit within a 150 ns time window [686, 156]. Hits 500 ns prior to a trigger and up to 1000 ns after a trigger are also saved for reconstruction [156]. During the operation of HAWC, N_{thresh} varies, and the trigger rate at the time of writing, due primarily to hadronic CR air showers, is ~24 kHz with $N_{thresh} = 28$ [156]. The accurate reconstruction of the air shower event requires precise timing and charge measurements from the PMT signals, thus once an air shower triggers the detector, the charge and timing calibration are applied to each PMT signal [682, 686]. For each triggered event, the direction, the size, and some γ/hadron separation variables of the air shower are extracted from the recorded hit times and amplitudes, using a shower model developed through the study of Monte Carlo simulations [377] and optimized using Crab Nebula observations [156]. A full description of HAWC design, calibration, and operation are given in [682], while HAWC data reconstruction, analysis method, performance, and systematic uncertainties are presented in [156].

4.4 Scientific goals

The scientific goals of HAWC range from γ-ray astronomy and direct studies of CRs in TeV energy band to a variety of topics in astrophysics and particle physics [687]: survey the sky for a point sources such as GRBs [688] and AGNs [689, 154]; measure the galactic diffuse flux in order to find regions of CR acceleration in the Galaxy [690]; probe the EBL via AGNs and the intergalactic magnetic field (IGMF)[3] [691] traversed by γ-rays in their propagation, both are of considerable importance for cosmology; inspection of the Lorentz invariance [691, 692, 693]; measure the CR anisotropy [694, 695, 696], a small deviations from isotropy in the CR flux; hunt the Primordial Black Holes (PBHs) [691, 697, 698] and exotic signals such as massive relic particles (SUSY[4] Q-Balls[5] [701, 691, 702], WIMP[6] dark matter [691, 704, 705], KK[7] dark matter [704]).

[3] The IGMF is presumed to exist in the void regions between galaxy clusters [691].
[4] An acronym for SUperSYmmetry [699].
[5] An exotic form of matter predicted by SUSY theory [691]. These objects rely on the existence of a conserved charge, Q, associated with an ungauged unbroken continuous internal symmetry. They are spherically symmetric, and for a large Q, their energies and volumes grow linearly with Q; thus they act like homogeneous balls of ordinary matter, with Q playing the role of particle number, thus these systems are called "Q-balls" [700].
[6] An acronym for Weakly Interacting Massive Particle. It is thought that most dark matter is cold (CDM) and is made up of WIMPs [703].
[7] An acronym for Kaluza-Klein [706].

HAWC aims to [687]:

- Provide an unbiased map of the TeV sky with daily coverage of 2π sr in order to search for transient phenomena like GRBs and flares in AGN.
- Provide TeV alerts for other instruments [707], e.g., to IACTs that can follow up with detailed observations of any flare region discovered by HAWC, or to neutrino telescopes such as KM3NeT, the next-generation multi-km^3-sized neutrino telescope [173, 174, 175];
- Provide a significant contribution to multiwavelength campaigns that study a selected object at various wavelengths, from radio to TeV γ-rays. Also, to contribute for a follow-up searches;
- Provide important clues on the origin of Galactic CRs.

In recent years, HAWC sent several alerts in AT informing about an enhanced activity of Mrk 421 and Mrk 501: ATel #8922 [708], ATel #9137 [709], #9936 [710], #9946 [711], #12683 [712]. In addition, the discoveries of the new TeV γ-ray sources HAWC J0543+233 (ATel #10941 [713]), HAWC J0635+070 (ATel #12013 [714]) have been announced by AT. Furthermore, several follow-up searchs have been performed by HAWC, including search for a γ-ray enhanced activity (ATel #10802 [715]) correlated with IceCube-170922A neutrino event [14] (see Section 1.7.1), follow-up [716] regarding a bright transient spatially coincident with galaxy CGCG 137-068 (60 Mpc) named ATLAS18qqn (AT2018cow[8]) reported on ATel #11727 [717], and study (ATel #7868 [718]) of HAWC archival data in the sky region corresponding to the multi-PeV neutrino-induced event from the Northern sky reported by IceCube (ATel #7856 [719])

4.5 HAWC sources

In the 2HWC catalog [377], the result of the first source search realized with 507 days of data of the complete HAWC-300 detector, the 39 sources have been found, of which 19 were new. The only sources that have confirmed extragalactic associations in 2HWC catalog [377] are Mrk 421 (2HWC J1104+381) and Mrk 501 (2HWC J1653+397) (see Fig. 4.5). These two blazars are the two closest and brightest extragalactic sources in the TeV as well as the X-ray band [377]. The results of the 17-month long daily monitoring of the blazars are presented in [154]. In [177], it is presented the ANTARES search for high-energy neutrino emission, in coincidence with TeV γ-ray flares from Mrk 421 and Mrk 501 obtained during HAWC long-term TeV light curve studies. The full results based on the ANTARES dataset covering same period (see Section 7.3.1) as 17-month HAWC analysis (1017 days) is discussed in Section 7.4.1. The γ-ray LCs for each source, shown in Fig. 4.4,

[8] Available on Transient Name Server (TNS), https://wis-tns.weizmann.ac.il/object/2018cow

were used (see Section 7.1.1) to search for temporally correlated neutrinos, that would be produced in pp or $p\gamma$ interactions [177]. In [154], the Bayesian blocks algorithm is used to identify the distinct flux states (see Fig. 4.4) for Mrk 421 and Mrk 501, which were released in tabular form and used in part of this work (see Section 7.3.1).

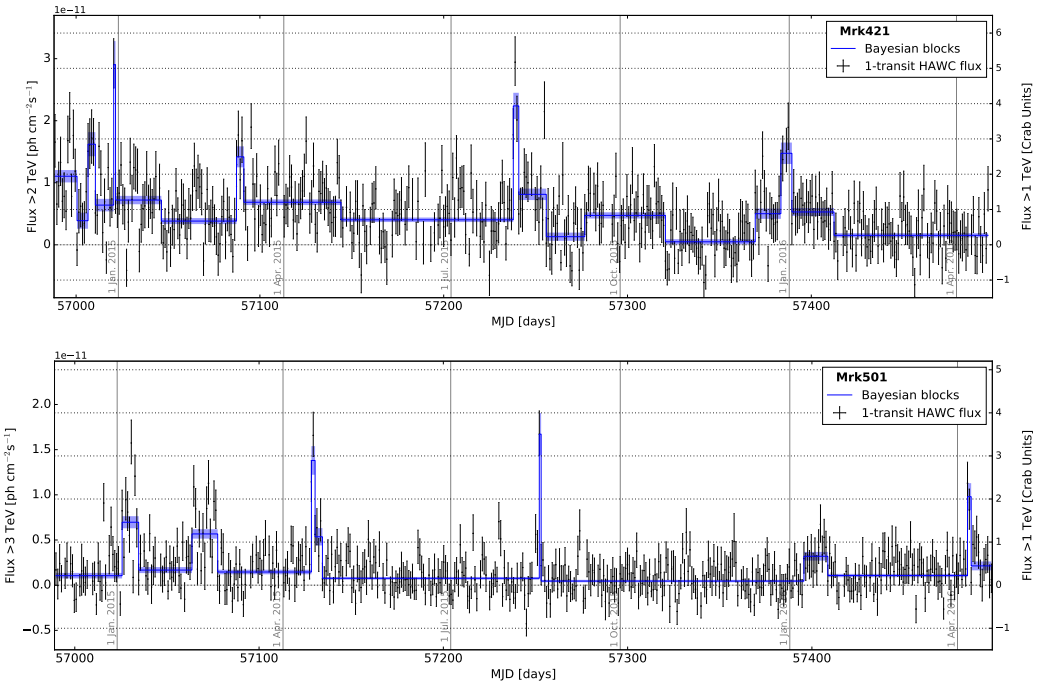

Fig. 4.4.: Flux light curves for Mrk 421 (*Top*) and Mrk 501 (*Bottom*) with sidereal-day sampling for respectively 471 and 479 transits between November 26, 2014, and April 20, 2016. The integrated fluxes are derived from fitting and converted to Crab Units by dividing by the HAWC measurement of the average Crab Nebula γ-ray flux. The blue lines show the distinct flux states between change points identified via the Bayesian blocks analysis with a 5% false-positive probability. The figure is taken from [154].

The Crab Nebula, the brightest steady TeV γ-ray source in the sky, has been also observed (the nearest TeVCat source is 2HWC J0534+220) [156, 377] (see Fig. 4.5). The Crab Nebula has been used for the past decades as a reference source in TeV astronomy, for calibration and verification of new TeV instruments [156]. For example, the pointing of the HAWC detector is verified using data from the Crab Nebula since it is relatively isolated in the sky and does not suffer overlap with additional sources [686]. The PSF describes how accurately the directions of γ-ray events are reconstructed [156]. In HAWC, the PSF of the reconstructed events depends on the event size: large events have a better PSF, a better hadronic background rejection, and correspond to higher energy primary particles [377]. Therefore, to measure the PSF, HAWC uses the Crab Nebula [686]. The error in the measured PSF from the Crab Nebula corresponds to 15% – 20% uncertainty in the flux estimate [686]. Figure 1.14 shows the multiwavelength observation of the Crab Nebula and also discussed in Section 1.1.4.

Figure 4.6 (*Top*) shows the Crab spectrum measured with HAWC between 1 and 37 TeV compared to the spectrum reported by other experiments and is consistent with prior measurements within the systematic errors of the HAWC measurement [156]. The observation of the Crab validates the HAWC's analysis presented in [156] for subsequent application to the sources across the rest of the sky. As seen, the HAWC measures the Crab Nebula up to 30 TeV. In recent analysis [720], the new HAWC reconstruction is used with a significant improvement over the original energy estimation technique used in HAWC [156], shown in Fig. 4.6 (*Top*), and allows HAWC to measure the spectrum of sources to 100 TeV and beyond. Consequently, the photons above 200 TeV at 95% CL [720] have been observed from the Crab Nebula with that new performance. The measurement with the new performance is shown in Fig. 4.6 (*Bottom*). It is based on the two energy estimators, the Ground Parameter (GP) and the Neural Network (NN). The GP energy estimator is based on the fit of measured events to a lateral distribution shape, evaluated at an optimal radius, and corrected for zenith angle, while the NN energy estimator combines various measures of event size, the zenith angle, the location of the shower on the array, and the lateral distribution of the shower represented in fractional charge deposited in rings about the shower location [720]. The resulting spectrum is in agreement within 20% in flux of measurements from IACTs, where there are overlapping measurements [720].

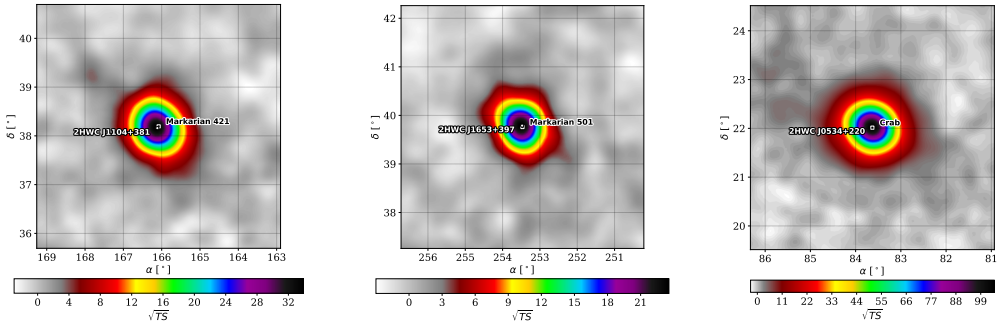

Fig. 4.5.: Equatorial TS maps of HAWC sources, for a point source hypothesis with a spectral index of −2.7. *Left:* Mrk 421 *Middle:* Mrk 501. *Right:* Crab. The 2HWC sources are represented by white circles and labels below the circle; whereas the source listed in TeVCat are represented with black squares and labels above the square symbol. The figure is taken from [377].

In this work, the Crab is excluded from the analysis because in daily monitoring of TeV γ-ray emission of Crab Nebula with HAWC [154] no variability has been found. In contrast to that, the fluxes observed from Mrk 501 and Mrk 421 exceed the Crab Nebula flux by a factor of approximately three and five respectively [154].

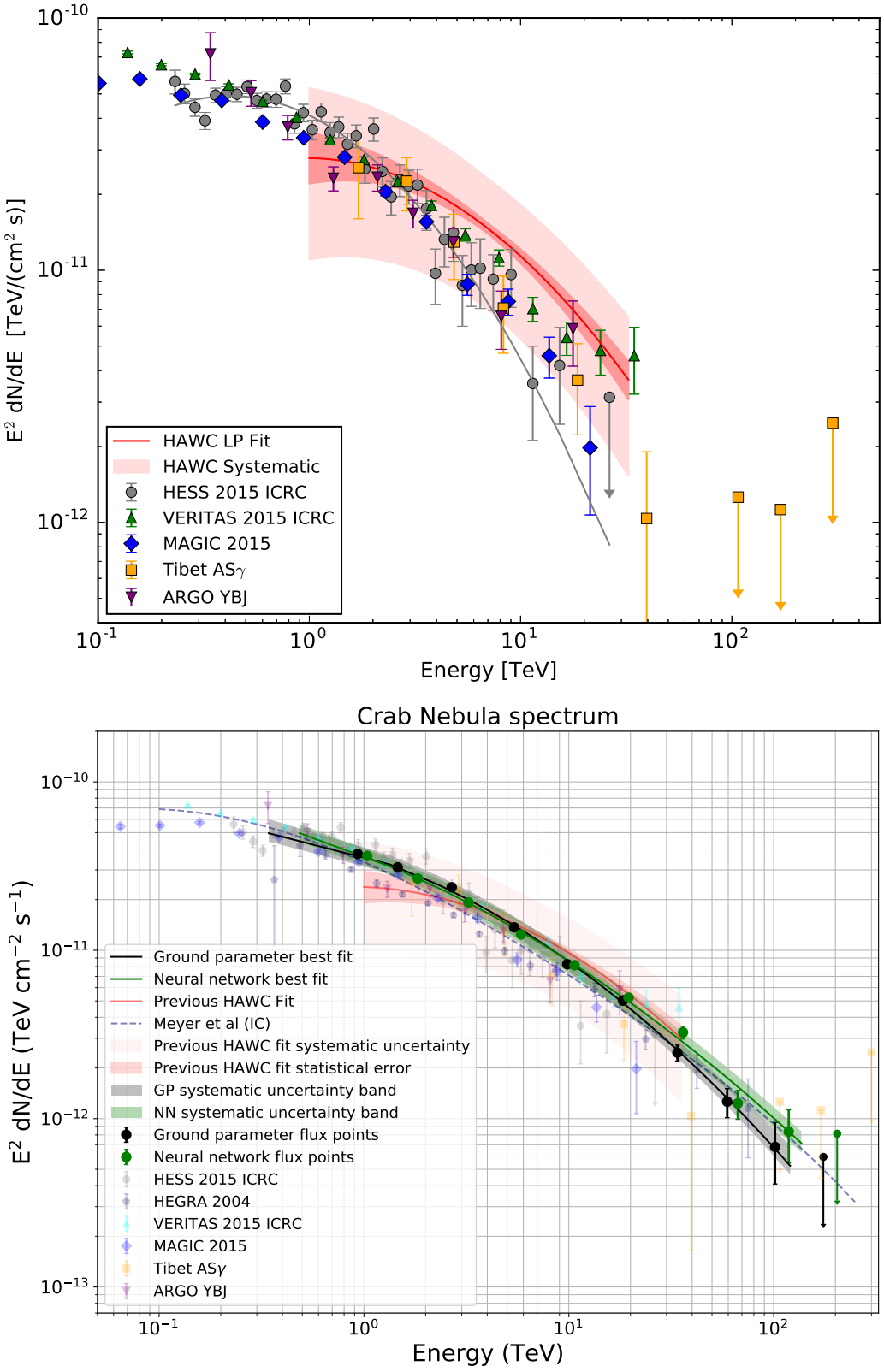

Fig. 4.6.: The Crab photon energy spectrum. *Top:* Spectrum measured with HAWC and compared to other measurements using other instruments. See [156] for references to the different instruments involved. The red band shown for HAWC is the ensemble of fluxes allowed at 1σ, and the best-fit is indicated with a dark red line. The light-red band indicates the systematic extremes of the HAWC flux. *Bottom:* Spectrum measured with HAWC new method. The figures are taken from [156] and [720] respectively.

Among HAWC's many successes are [721]: the detection of TeV jets from SS 433 [397] and discovery of a new class of halos, named TeV-Halos, such as Geminga [722]. SS 433 microquasar is a binary system containing a supergiant star that is overflowing its Roche lobe with matter accreting onto a compact object (either a black hole or neutron star) [397]. Two jets of ionized matter with a bulk velocity of $\sim 0.26c$ extend from the binary, perpendicular to the line of sight, and terminate inside W50 (about 40 pc from the central source), an SNR that is being distorted by the jets [397]. In 1017 days of measurements with HAWC, an excess of γ-rays with a post-trials significance of 5.4σ has been observed in a joint fit of the eastern and western interaction regions of the jets of SS 433 [397]. The emission is plotted in galactic coordinates in Fig. 4.7, which includes an overlay of the X-ray observations of the jets and the central binary [397]. In the SS 433/W50 complex shown in Fig. 4.7, several regions located west of the central binary (w1 and w2) and east (e1, e2, e3) are observed to emit hard X-rays [397]. The γ-ray emission is spatially coincident with the X-ray hotspots w1 and e1 (see Fig. 4.7); no significant emission is observed at the location of the central binary where the jets are produced [397]. As also seen, the lobes in the SS 433/W50 system are spatially resolved. Geminga[9] is a neutron star approximately 250 pc from the Earth [722]. The TeV γ-ray emissions from the pulsars Geminga and PSR B0656+14 were found in a search for extended sources that was performed for the HAWC catalog, in which these two pulsars have the designations 2HWC J0635+180 and 2HWC J0700+143 [722] (see Fig. 4.8). By fitting to a diffusion model, the two sources were detected with a significance at the pulsar location of 13.1σ and 8.1σ, respectively [722] (see Fig. 4.8). The TeV emission region is several degrees across which is attributed to electrons and positrons diffusing away from the pulsar (see Fig. 4.8) and upscattering the CMB photons. Geminga was previously detected at TeV energies by the Milagro [724], the predecessor of HAWC, with flux and angular extent consistent with that observed by HAWC but with lower statistical significance [722].

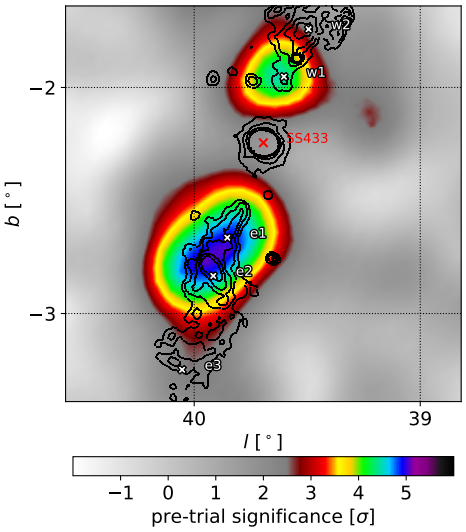

Fig. 4.7.: VHE γ-ray image of the SS 433/W50 region. The color scale indicates the statistical significance of the excess counts above the background of nearly isotropic CRs before accounting for statistical trials. The figure shows the γ-ray excess measured after the fitting and subtraction of γ-rays from the spatially extended source MGRO J1908+06. The jet termination regions e1, e2, e3, w1, and w2 observed in the X-ray data are indicated, as well as the location of the central binary. The solid contours show the X-ray emission observed from this system.. The figure is adapted from [397].

[9] The name *Geminga* is a contraction of *Gemini*, due to its location in the Gemini constellation, and of *ga*mma-ray source. Also, it is the pronunciation of the word gh'è minga in the Milanese dialect of Lombard, which means "does not exist" or "it is not there" [723].

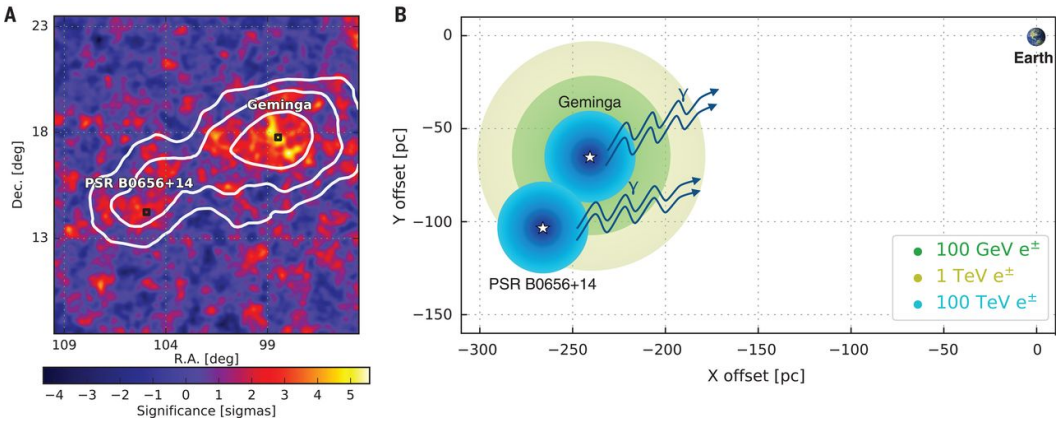

Fig. 4.8.: Spatial morphology of Geminga and PSR B0656+14. *Left:* HAWC significance map (between 1 and 50 TeV) for the region around both sources, convolved with the HAWC point spread function and with contours of 5σ, 7σ, and 10σ for a fit to the diffusion model. *Right:* Schematic illustration of the observed region and Earth, shown projected onto the Galactic plane. The colored circles correspond to the diffusion distance of leptons with three different energies from Geminga; for clarity, only the highest energy (blue) is shown for PSR B0656+14. The balance between diffusion rate and cooling effects means that TeV particles diffuse the farthest (for details see [722]). The figure is taken from [722].

Figure 4.9 shows HAWC an equatorial skymap of statistical significance above background. The three outstanding point sources, Crab, Mrk 421, Mrk 501, are clearly visible and also Geminga, but with lower significance. The bright arc on the left in Fig. 4.9 is the emission band at the first quadrant of the Milky Way Galaxy, the sources of which are resolved in the zoomed-in view in Fig. 4.10. The SS 433 microquasar is spatially coincident with MGRO J1908+06, which is the nearest TevCat source to 2HWC J1908+063 [377] detected by HAWC. Both, 2HWC J1908+063 and MGRO J1908+06, are shown in Fig. 4.10, the zoomed-in view of the Galactic Plance showing sources of TeV γ-rays observed by HAWC.

Most of the sources detected by HAWC are plausible neutrino sources and are in the visibility of ANTARES telescope. For example, 16 sources in 2HWC catalog are in ANTARES candidate list [393]. In recent ANTARES searches for point-like sources of cosmic neutrinos with 11 years of data [393], all these 16 sources have been included together with Crab, Geminga, SS 433 and Mrk 421. Generally, the Mrk 501 is not included in ANTARES neutrino point sources search (and not presented in 11 years search [393]) but included in this work since it is located in a similar region of the edge of ANTARES visibility (see Fig. 7.9 and Fig. 7.10) as Mrk 421 and its LCs show clear variability [154] as for Mrk 421 (see Section 7.1).

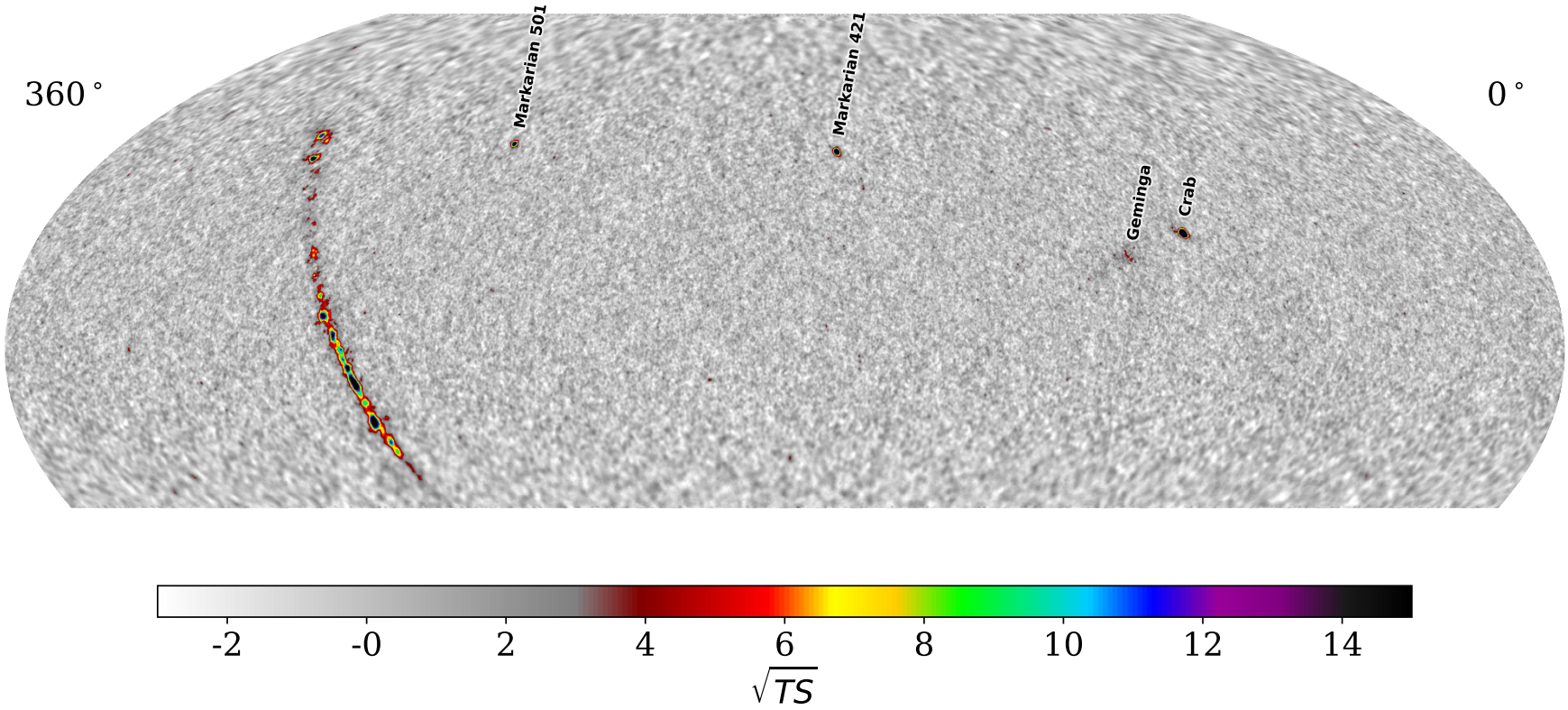

Fig. 4.9.: Equatorial full-sky TS map, for a point source hypothesis with a spectral index of −2.7. The figure is taken from [377].

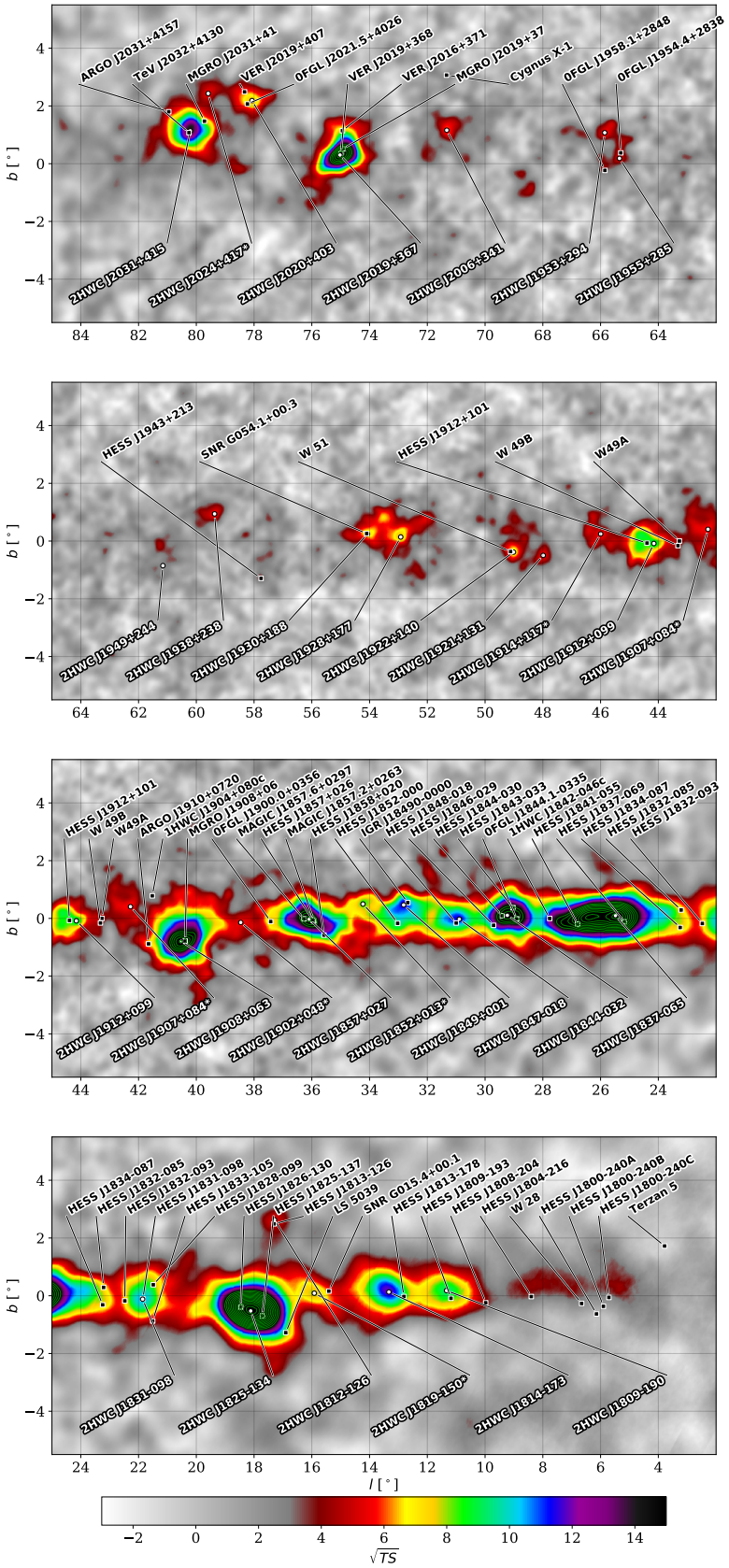

Fig. 4.10.: The 2HWC catalog sources along the inner Galactic Plane region, in Galactic coordinates. The TS map corresponds to a point source hypothesis with a spectral index of −2.7. The green contour lines indicate values of TS of 15, 16, 17, etc. The 2HWC sources are represented by white crosses and labels below; whereas the source listed in TeVCat are represented with black circles and labels above them. The figure is adapted from [377].

4.6 HAWC extension

After the success of the HAWC, the issue of its extension has become long overdue. It was known that the sensitivity of a HAWC-like array grows, to first order linearly with the area of the array [682]. Increasing the footprint of the detector would naturally improve the shower detection sensitivity and the available event statistics [726]. The air shower footprint on the ground is inherently dependent on the primary particle energy and on the altitude of the detector plane [727], and above 10 TeV the shower footprint on the ground becomes comparable to the size of the HAWC array [728]. Therefore, most of the air showers above 10 TeV are not contained in the HAWC array [728, 727]. Although the HAWC main array still has enough information in order to do γ/hadron separation, direction reconstruction, and shower size estimation there is ambiguity present because of large uncertainty in the core location and the misinterpretation of high-energy γ-ray showers reduce HAWC performance at these energies [727, 728]. To tackle this was the main motivation for HAWC to propose the deployment of additional small tanks, called outriggers, sparsely around the main array [729]. The outriggers are of diameter 1.55 m and height 1.65 m [727], smaller than WCDs in the HAWC main array, and will be mutually separated by a distance of 12 to 18 m with Hamamatsu R5912 8-inch PMT anchored at the bottom of each tank [728, 727]. The full outrigger array will consist of 350 cylindrical tanks [727, 728]. The outrigger array will allow HAWC to accurately determine the core position, and therefore the direction and the energy of the shower, so that the ambiguities in the shower reconstruction can be resolved, hence improving the sensitivity of HAWC at higher energies [728, 727]. Also, the increase of the effective area above 10 TeV by a factor of 3-4 will enhance the sensitivity above this energy [729, 728].

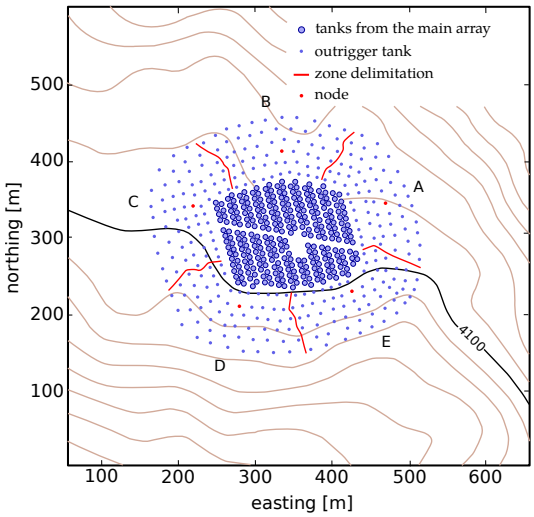

Fig. 4.11.: The high energy extension of the HAWC observatory: the extended layout including the additional outrigger WCDs. The 5 sections of the outrigger array are delimited by red lines and named by letters from A to E. The red dots show the node locations hosting the trigger, readout electronics, and power supply for each tanks. The figure is taken from [725].

It is worth noting, that with HAWC is located on the Northern Hemisphere, a next-generation, large FOV γ-ray observatory should be located in the south to allow for an all-sky coverage, which in addition will allow to fully exploit the synergies with modern CTA telescope, provide an access to the central region of Galaxy with its wealth of known high-energy γ-ray sources [726]. This new γ-ray observatory will have significant synergies with another major high-energy astroparticle observatory, KM3NeT [173, 174, 175], due to its advantage over IceCube in that region of the sky. KM3NeT will be particularly sensitive

to multi-TeV neutrino sources within our Galaxy and thus be able to monitor the Southern Sky with unprecedented sensitivity and would be a perfect partner for a Southern TeV γ-ray observatory [726]. In addition, after more than 11 years of successful operation, the ANTARES neutrino telescope, predecessor of KM3NeT, will be decommissioned. In this regard, the Antares Modules In a Gamma-ray Observatory project (AMIGO) project [726] proposes to re-use the OM of the ANTARES for the analog of the HAWC detector in the Southern Hemisphere. Thereby, to deliver the OMs "from the bottom of the sea to the top of the mountain" [726], bringing such different telescopes as ANTARES neutrino telescope and new γ-ray observatory in the Southern Hemisphere closer.

5 Simulation and reconstruction of muon tracks in ANTARES

> *Users do not care about what is inside the box, as long as the box does what they need done.*
>
> — **Jef Raskin**
> about Human Computer Interfaces

In this chapter, the ANTARES simulation chain and event reconstruction are described. The simulations are necessary to understand the detector response to physics events and to validate analysis techniques such as optimization of selection cuts to ensure proper background events rejection. The simulation chain can be divided into different steps but can be summarized into two as a physics simulation and detector response simulation Section 5.1. The physics simulation includes simulation of neutrinos Section 5.1.1, atmospheric muons Section 5.1.2, and light Section 5.1.3 that induced by the charged particles via the Čerenkov effect in their propagation through the water. After that, the detector response is simulated Section 5.1.4. A variety of event reconstruction algorithms have been developed in ANTARES for attaining the most relevant information about the event signatures produced in the neutrino or the atmospheric muon interactions. The ANTARES event reconstruction algorithms with an emphasis on those that have been used in this work are described in Section 5.2.

5.1 Monte Carlo simulation

The MC simulation strategy used for ANTARES is called run-by-run (rbr). For each physics run, a MC file is produced extracting information concerning the data acquisition conditions directly from the data, which allows accounting for the variability of the environmental conditions and the status of the ANTARES detector [730].

The simulation chain, developed in ANTARES, can be divided into two main steps and summarized as following [731, 730]:

- **Physics simulation**: neutrinos and atmospheric muons are generated in the proximity of the detector. Particles are propagated through the detector and the light coming from the Čerenkov effect is simulated and propagated to the PMTs.

- **DAQ simulation**: the behavior of the PMTs and data acquisition electronics (see Section 3.3) are simulated. Filtering and triggering algorithms are applied using the `TriggerEfficiency` program, which takes care of the addition of the optical background to the hits generated by the physical events and of the triggering of events. The optical background due to environmental light (mainly bioluminescent organisms and ^{40}K radioactive salt decay) (see Section 3.4.2) is added to the PMTs according to the counting rates actually observed in data on each PMT. Non-working PMTs are switched off and the time-dependent loss of efficiency of the PMTs can be also considered.

The simulation of neutrinos is described in Section 5.1.1. The simulation of atmospheric muons is described in Section 5.1.2. And lastly, the simulation of the light transmission is described in Section 5.1.2. The detector simulation is summarized in Section 5.1.4.

5.1.1 Neutrinos generation

For the purposes of neutrino interactions generation, the instrumented volume of the detector is treated as a cylinder which contains all the PMTs and surrounded by a larger cylinder, called *can* [732]. Figure 5.1 shows the schematic view of the ANTARES detector geometry used in simulations. For any given simulation, it is required for the *can* to be sufficiently large to contain the volume within which the vast majority of the Čerenkov light is generated [732], i.e., the *can* defines the volume which is necessary for Čerenkov light to reach the instrumented volume where it can be detected. In ANTARES, the *can* has been selected so that its surface is at a distance of $\sim$ 200 m around the instrumented volume (see Fig. 5.1), which is roughly three times the longest light absorption length in water ($3\times\lambda_{abs}$) at the ANTARES site [732]. The light absorption at the ANTARES site (see Section 3.4.1) has a maximum of about 60 m [555] (see Fig. 3.22).

The *can* is the base for the *generation volume*, which is an energy-dependent extension of the *can*, within which neutrino interactions are generated [733]. It is defined to ensure the generation of all the possible interactions which could yield a muon that may cross the detector [516]. Its size is determined from the maximal muon range associated with the highest neutrino energy that is generated, typically $E_{max} = 10^8$ GeV, and corresponds to a cylinder of 25 km in radius and height around the detector [516]. Outside this volume, only particle energy losses in propagation are considered [733].

In ANTARES, the high-energy neutrino interactions are generated using the MC event generator `GENHEN` (GENerator of High Energy Neutrinos) [734, 735, 736] developed by ANTARES. The `GENHEN` code is written in `FORTRAN` and makes use of several libraries and modules from the `CERN` Program Library[1]; in particular [737]: `FFREAD` [738], part of the `PACKLIB`[2], for the processing of Free Format *data cards* to enable the input of user

[1] `CERNlib`, http://cernlib.web.cern.ch/cernlib/
[2] `PACKLIB`, http://cernlib.web.cern.ch/cernlib/packlib.html

settings; LEPTO [739], part of the Monte Carlo libraries[3], for the simulation of DIS (deep inelastic lepton-nucleon scattering is discussed in Section 2.3.1). LEPTO requires [737] a set of parton distribution functions to be specified by the user via *data cards* and that ones used in GENHEN are from the CTEQ family[4] (see discussion in Section 2.3.1). Information is collected in the form of tables and the CTEQ6 [508] data table of parton distribution functions is used [737].

The basic documentation on GENHEN, written for release v5r1, is given in [736] and contains an overview of the simulation method, describes the code structure, provides a user manual with a list of user inputs and file outputs. After release v5r1, the GENHEN has undergone several upgrades [740, 741, 737] such as that :

Release v6 [740] implementation of the option to propagate neutrinos of all flavors through the Earth;

Release v6r3 [741] implementation of the Glashow resonance[5] and the inclusion of a new code, MUSIC (MUon SImulation Code) [742], for muon propagation. In case the neutrino is generated outside the *can*, the resulting muons are propagated using MUSIC until its surface [516].

Release v7r1 [737] implementation of the cross-section parametrization; inclusion of a new feature for a point-like mode, enabling to specify the position of the source in local coordinates, useful for the simulation of transient sources; inclusion of a wide number of bug-fixes; inclusion of a new feature to make GENHEN free from GEASIM [743], which allows running GENHEN with no specification of a detector file (.det) and with ability to set the geometry parameters, useful for testing purposes of new geometries (e.g., such as KM3NeT geometry); inclusion of a new tool genhenROOT, a program developed to convert the ASCII .evt output of GENHEN into a ROOT format (.root), so that information can be smoothly accessed and visualized through the CERN ROOT Data Analysis Framework [635]. The genhenROOT program is written in C++ and creates a simple root format TTree ("neutrino") in which the information on the interacting neutrinos are stored [737]. GEASIM is the ANTARES software package to simulate the detector response (hits) to particle showers and based on GEANT (GEometry ANd Tracking) [744] version 3.21. It computes and propagates the Čherenkov light produced at the passage of particle tracks in the water.

[3] Monte Carlo libraries, http://cernlib.web.cern.ch/cernlib/mc.html
[4] CTEQ, http://www.phys.psu.edu/~cteq/
[5] The GENHEN versions [734, 735, 736, 740] prior to v6r3 could not simulate neutrino interactions with electrons, but only neutrino-nucleon scattering; however, the cross-section for interactions overcome the cross-section for in the PeV energy range (see Section 2.3.1).

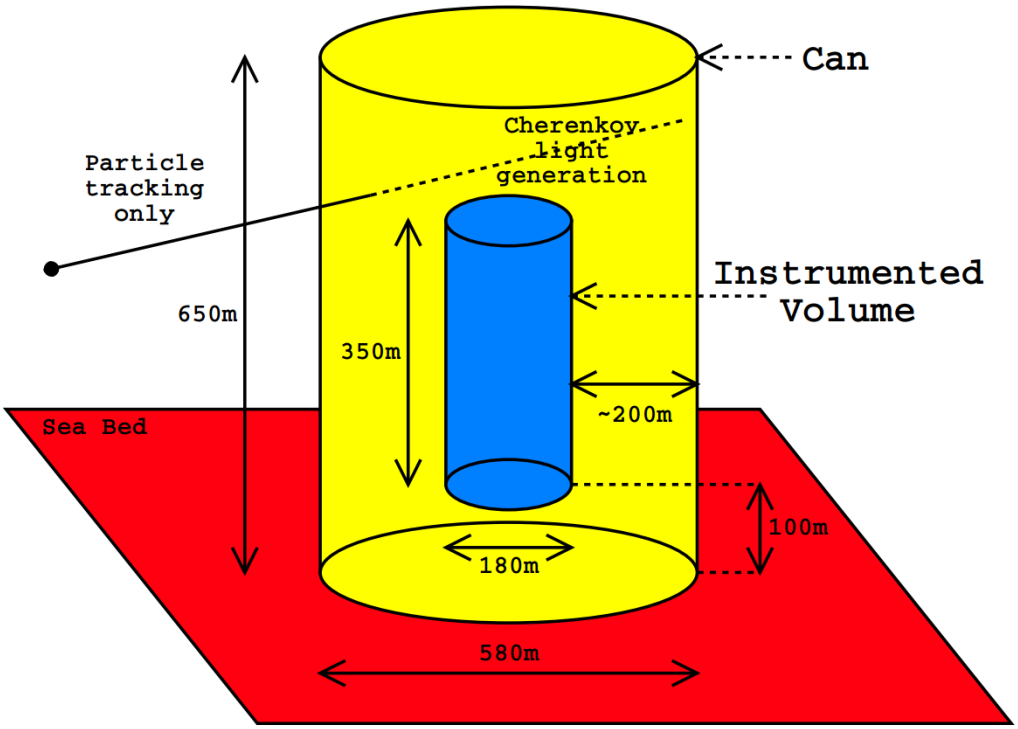

Fig. 5.1.: Schematic view of the ANTARES detector geometry for the event generation stage of the simulation. The size of the can (shown in yellow) exceeds the instrumented volume (shown in blue) by ~200 m except from below where it is bounded by seabed from which no Čerenkov light can emerge. The figure is taken from [732].

The neutrino flux arriving at the Earth that is simulated is given per units of energy dE_ν, solid angle $d\Omega$, area dS and time dt by the relation [732]:

$$\frac{d\Phi_\nu^{gen}}{dE_\nu d\Omega dS dt} = \frac{N_{total}}{I_\theta I_E E^\gamma V_{gen} t_{gen}} \times \frac{1}{\sigma(E_\nu)\rho N_A} \times \frac{1}{P_\oplus(E_\nu, \theta_\nu)}, \tag{5.1}$$

where

- N_{total} is the total number of generated events specified by the user in the simulation inputs;
- I_θ [sr] is the angular phase space factor, which depends on the range of the zenith angles, θ_{min} to θ_{max}, specified by the user in the simulation inputs. $I_\theta = 2\pi \cdot [cos(\theta_{max}) - cos(\theta_{min})]$ [732], so that it is the integral of the solid angle between $cos(\theta_{max})$ and $cos(\theta_{min})$;
- I_E is the energy phase factor, which depends on the spectral index, γ, specified by the user in the simulation inputs. $I_E = \frac{E_{max}^{1-\gamma} - E_{min}^{1-\gamma}}{1-\gamma}$ if $\gamma \neq 1$ or $I_E = ln(\frac{E_{max}}{E_{min}})$ for $\gamma = 1$ [745], so that it is the integral of the generation spectrum between the minimum and maximum energies, E_{min} to E_{max}, specified by the user in the simulation inputs [732];

- γ is the generation spectral index;
- V_{gen} $[m^3]$ is the total generation volume of the Čerenkov light (in water equivalent units in this case);
- t_{gen} $[s]$ is the (arbitrary) time represented by the simulation;
- $\sigma(E_\nu)$ $[m^2]$ is the CC neutrino interaction cross-section for neutrino energy E_ν (see Section 2.3.1);
- ρN_A $[m^{-3}]$ is the number of target nucleons per unit volume (e.g., m^3);
- $P_\oplus(E_\nu, \theta_\nu)$ is the probability for the neutrino to survive while penetrating the Earth (see Section 2.3.3) and it depends on energy E_ν and zenith angle θ_ν (see Eq. 2.10) [745]. The $P_\oplus$ is shown in Fig. 2.8.

For a given flux model, the events in each interval $dE_\nu d\theta_\nu$ are reweighted by the ratio of the two fluxes, the model neutrino flux and the generated neutrino flux, at the point (E_ν, θ_ν) [732]. Thus, the event weight w_{event} is defined as follows [732]:

$$w_{event} = w_{generation} \times \frac{d\Phi_\nu^{model}}{dE_\nu d\Omega dS dt} = \left(\frac{d\Phi_\nu^{gen}}{dE_\nu d\Omega dS dt}\right)^{-1} \times \frac{d\Phi_\nu^{model}}{dE_\nu d\Omega dS dt}, \tag{5.2}$$

where w_{gen} is a flux independent part of the event weight w_{event} associated with each individual neutrino event for a particular flux model [745]. The generation weight w_{gen} is adopted for simulations in both experiments, ANTARES and KM3NeT.

The w_{event} is used to reweight the neutrino events to a power-law E_ν^{-2} or any user-specified spectrum from initially generated following a $E_\nu^{-1.4}$ spectrum. In the ANTARES convention of MC simulations, three weighting parameters are introduced [745]:

- $w1$ contains the *can* volume (in $[m^3]$ units) for volume drawing or the angular dependent effective *can* surface (in $[m^2]$ units) for surface drawing [745];
- $w2$ contains the generation weight and is defined as follows [745]:

$$w2 = \frac{N_{total}}{t_{gen}} \times \left(\frac{d\Phi_\nu^{gen}}{dE_\nu d\Omega dS dt}\right)^{-1} \times F = I_\theta I_E E^\gamma V_{gen} t_{gen} \sigma(E_\nu) \rho N_A P_\oplus(E_\nu, \theta_\nu) F, \tag{5.3}$$

  where F is the number of seconds per year, i.e., in $[s/\text{year}]$ units. Consequently, $w2$ has the unit GeV m^2 s^1 sr^{1}year^{-1} [745];
- $w3$ is the global weight and is defined as follows [745]:

$$w3 = w2 \times \frac{d\Phi_\nu^{model}}{dE_\nu d\Omega dS dt}, \tag{5.4}$$

where $\frac{d\Phi_\nu^{model}}{dE_\nu d\Omega dS dt}$ is the differential flux of neutrinos before penetrating the Earth or muons at the detector and has units GeV m^{-2} s^{-1} sr^{-1}. Consequently, $w3$ has the simple unit year^{-1} which can be understood as "rate per year" [745].

All three neutrino flavors and both interaction channels, CC and NC, are supported in GENHEN [746], but at a time only one ν or $\bar{\nu}$ flavor and one type of interaction are simulated [733]. In this analysis (see Section 7), the search relies on track-like event signatures (see Section 7.3), so only CC interactions of muon neutrinos are considered. The simulation of neutrinos is performed using GENHEN v7r6[6]. Neutrinos are generated uniformly in the zenith angle $\theta_\nu \in [0,\pi]$ and in the azimuth angle $\phi \in [0,2\pi]$, so that a uniform neutrino flux is generated. At the generation level, for CC interactions of muon neutrinos two energy ranges are defined, low energies with $E_\nu \in [5, 2\times10^4]$ GeV and high energies with $E_\nu \in [2\times10^4, 10^8]$ GeV, with arbitrary user input spectral indices $\gamma = 1.7$ and $\gamma = 1.2$ respectively. The separation into two energy ranges is to ensure high statistics of events in each energy bin.

5.1.2 Atmospheric muons simulation

Apart from neutrinos, the atmospheric muons, as the main background for neutrinos (see Section 2.3.6), are also simulated. In ANTARES, atmospheric muons are generated using the MUPAGE[7] [747] software with the muon flux parameterization based on CORSIKA[8] [748, 749] in order to reduce significantly the CPU time. MUPAGE is capable to simulate muon bundles[9] from the single shower and relies on parametric formulas that describe the flux of a single and multiple underwater or in-ice muon events, their angular distribution and their energy spectrum [560]. The muon energy depends on vertical depths h (from 1.5 to 5 km w.e.), on the zenith angle θ and, for muon in bundles, on bundle multiplicity m and on the distance R of each muon with respect to the shower axis [560]. These parameterizations are taken from complete simulations and data collected with the MACRO[10] experiment at Gran Sasso, which is located at a depth comparable to that of neutrino telescopes [731, 747]. To optimize the full MC simulation, the MUPAGE is restricted to follow secondary particles with energies above 500 GeV, so that muons reaching the sea level with such energies are propagated through the water down to 5 km using the MUSIC program [747]. The so-called *prompt muons*, which are originated from the decay of charmed mesons and other short-lived particles, are not included since they are expected to give a non-negligible contribution for muon energies from ~10 TeV to ~10^3 TeV, depending on the charm production model[11] [747]. The range of validity of the MUPAGE event generator is

[6] In MC production for analysis with Dataset 2014-2016 (see Section 7.3.1), the GENHEN v7r1 is used for period ≤2015 year.
[7] MUPAGE: Atmospheric MUons from PArametric formulas: a fast GEnerator for neutrino telescopes.
[8] CORSIKA: COsmic Ray SImulation for KAscade.
[9] Muons that are produced in the same CR interaction
[10] MACRO: Monopole, Astrophysics and Cosmic Rays Observatory.
[11] See [750] for details about *prompt muon* contribution to the muon flux at the depths of the locations of the underwater neutrino telescopes.

from 0° to 85° for the zenith angle [747]. In this work, `MUPAGE v3r5` is used for analysis with both datasets.

The usage of parametric formulas is required for the production of an extremely large number of events with a reasonable CPU time consumption, the main limitation being the primary CR flux that cannot be modified [731]. Thus, `MUPAGE` as a fast generator of the kinematics of atmospheric muon bundles, represents a useful tool for underwater or ice neutrino telescopes to produce a large amount of simulated data [747]. As an example, the generation rate of atmospheric muon bundles on a cylinder with an area of 1.4 km^2 laying at the ANTARES depth of 2475 m and with total energy larger than 3 TeV is 27 Hz. The $8.5{\times}10^8$ events corresponding to one year of data were produced with 232 hours of CPU on a 2.33 GHz processor [747].

The output of `MUPAGE` is an `ASCII` table containing the kinematics of events at the surface of a *can*, which can be used as input in the following steps of a detector-dependent MC simulation, which includes the production of light in water or ice and simulation of the signal in the detection devices [747] that are described next.

5.1.3 Light simulation

The Čherenkov light emission can arise by the propagation of charged muons and electrons through the water. The `ASCII` output of `GENHEN` is processed with `KM3` [751] (`GEANT`-based package) and with `GEASIM` [743] software packages, to simulate the Čherenkov light production and propagation to the detector PMTs, where the hits are generated [737]. A model of the seawater, that contains information on the composition, density, and attenuation length, at the ANTARES site is given as input to `KM3` [730]. Since a full simulation where every Čherenkov photon is generated and propagated individually is computationally unfeasible, `KM3` works with photon tables that store the distributions of the numbers and arrival times of PMT hits at different distances, positions, and orientations with respect to a given muon track [733].

The `KM3` software package consists of three programs designed to be run in a step-by-step manner, with the output of one program being used as an input to the next [751]:

`GEN`: Generates photon fields at various radii from a muon track segment or an electromagnetic shower;

`HIT`: Transforms the photon fields from `GEN` into hit probability distributions in a PMT;

`KM3MC`: A detector simulation program which uses the hit probability distributions generated in `HIT` along with a geometrical description of the detector to simulate events in the ANTARES detector.

Both programs, `GEN` and `HIT`, are run only once to generate the relevant tables of the hit probabilities in the PMTs, while `KM3MC` reads the user inputs from the cards file, the description files and the tables containing the information with the hit distributions for muons and electrons [733]. In this work, `KM3 v5r3` is used[12].

5.1.4 Detector simulation

The output of KM3 is forwarded to the `TriggerEfficiency` program [752]. It is used to process the MC data through the ANTARES software trigger and different triggers can be processed simultaneously [752]. It is also possible to specify the ARS settings and PMT characteristics so that the main features of the PMT and the ARSs are taking into account in the simulation [752]. The simulated charge of the analog pulses is generated according to a Gaussian distribution with a specified width and (relative) gain [752]. A relative QE is applied that makes it possible to simulate the effect of a reduced QE on-the-fly (with the value between 0 and 1) [752]. The simulated hit times are generated according to a Gaussian distribution with a specified width, TTS, which characterizes the time response of the PMT [752] (see Section 3.5.1). The background is generated based on the specified singles rate of each PMT [752].

5.2 Event reconstruction

A variety of event reconstruction algorithms have been developed in ANTARES for attaining the information about the event direction, position, and energy using the hits arrival times and amplitudes.

The pointing accuracy of the ANTARES detector is determined by the precision in the determination of the arrival time of the Čherenkov photons at the PMTs, making the accuracy of the reconstruction of the muon, direction to be crucial for a good angular resolution[13]. Thus, it plays a decisive role in the searches for neutrinos from point-like sources, i.e., such as that performed in this work. The searches performed in this work relies on track-like event signatures[14], so only CC interactions of muon neutrinos are considered.

The original neutrino energy can be determined by the energy reconstruction of muons produced in the CC interactions of neutrinos, making the accuracy of the reconstruction of the muon energy to be crucial for the cosmic and atmospheric[15] neutrinos separation which have different spectra and therefore differently dependent on energy.

All these make rigorous, accurate and careful event track (see Section 5.2.1) and energy (see Section 5.2.2) reconstruction to be essential for effective searches in ANTARES.

[12] In MC production for analysis with Dataset 2014-2016 (see Section 7.3.1), the `KM3 v5r1` is used for period ≤2015 year.
[13] See discussion in Section 3.5.1
[14] See discussion in Section 7.3
[15] See discussion about irreducible background in Section 2.3.6

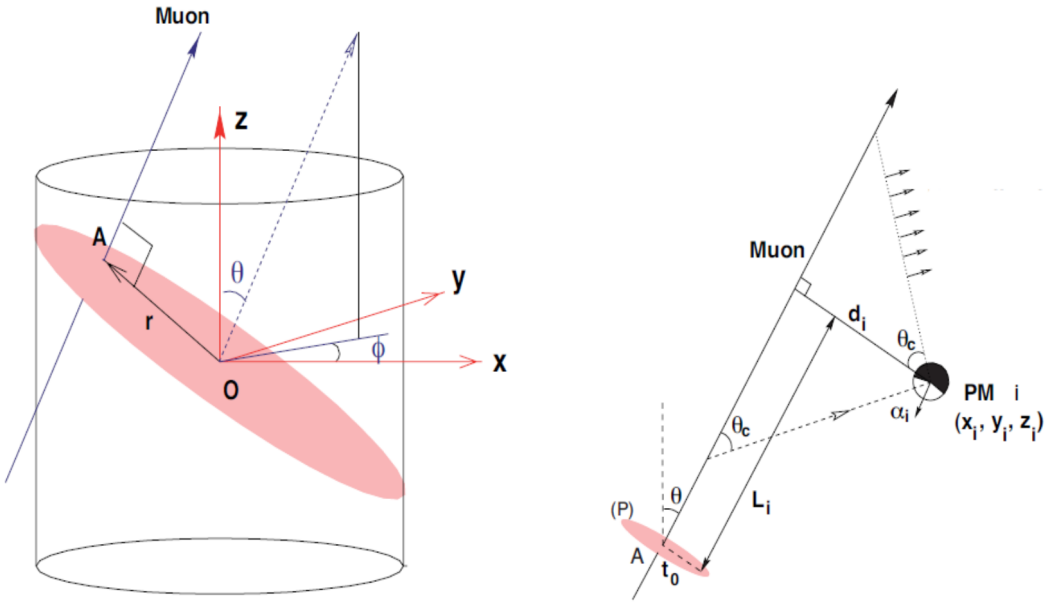

Fig. 5.2.: Schematic view of the reconstruction strategy. *Left:* The geometrical description of the *can* and the coordinates used for the reconstruction. *Right:* The geometrical structure of the muon track induced by a muon neutrino: definition of variables. The figure is taken from [753].

5.2.1 Track reconstruction

In general, the track reconstruction consists of finding values for the free parameters in the assumed model which most likely caused the outcome of the measurement [753]. In the case of muon track reconstruction, the basic model is a straight line passing through the detector along which a muon moves with the speed of light[16] producing a Čherenkov light on its way [753] as shown in Fig. 5.2. The muon trajectory can be characterized by the position $\vec{p} \equiv (p_x; p_y; p_z)$ and the direction $\vec{d} \equiv (d_x; d_y; d_z)$ of the muon at some fixed time t_0 [498]. The direction can be parameterized in terms of the azimuth and zenith angles θ and ϕ: $\vec{d} = (sin\theta cos\phi; sin\theta sin\phi; cos\theta)$ [498]. By convention, the time t_0 is defined as the time when the muon passes through the plane perpendicular to its direction and containing the center of gravity of the detector [753] as shown in Fig. 5.2. The reconstruction algorithm thus gives five independent parameters that characterize the muon trajectory [498]. The expected (*th*eoretical) arrival time of the photon t_i^{th} can be expressed as a sum as follows [753, 498]:

$$t_i^{th} = t_0 + t^{transition} + t^{travel}, \tag{5.5}$$

where $t^{transition}$ is the time it takes for the muon to reach the point where the detected light is emitted and t^{travel} is the time it takes for the photon to travel from that point to the PMT [498, 753]. The length of the Čerenkov photon path is given by [498]:

$$\frac{d_i}{sin\theta_C}. \tag{5.6}$$

[16] At energies above the detection threshold (10 GeV or so), the muon is relativistic; hence, the speed of the muon is taken to be equal to the speed of light in vacuum [498].

Using the geometry in Fig. 5.2, one can get the $t^{transition}$ and t^{travel} [753]:

$$t^{transition} = \frac{L_i}{c} - \frac{d_i}{ctan\theta_C} \tag{5.7}$$

$$t^{travel} = \frac{d_i}{\upsilon_g sin\theta_C}, \tag{5.8}$$

where c is the velocity of light in vacuum and υ_g is the group velocity of light in the water (see Eq. 3.10), θ_C is the Čerenkov angle (see Section 2.3.5).

Summarizing the information from Eq. 5.5, Eq. 5.7 and Eq. 5.8, one can obtain the arrival time of the light to the PMT [754, 498]:

$$t_i^{th} = t_0 + \frac{1}{c}\Big(L_i - \frac{d_i}{tan\theta_C}\Big) + \frac{1}{\upsilon_g}\Big(\frac{d_i}{sin\theta_C}\Big). \tag{5.9}$$

Online reconstruction algorithm

A fast and robust reconstruction algorithm, called `BBfit` [755], has been developed by ANTARES for muon tracks which can reliably distinguish up-going neutrinos from the overwhelming background of down-going muons. It is very fast and therefore well-qualified for real-time applications such as an online event display (see Fig. 5.3), a neutrino monitor and a program sending an alert to trigger optical follow-up observations of selected neutrino events [755]. This makes `BBfit` be well-suited for multi-messenger studies [755].

To qualify for real-time applications `BBfit` uses only time-independent geometrical information; therefore, few approximations are made [755]. Firstly, the detector lines are considered to be perfectly vertical and line distortions due to sea currents are ignored [755]. Secondly, the detailed geometry of the storey is ignored and each storey is considered as a single PMT, which is located directly on the detector line with an axis-symmetric field of view, and signals of the three PMTs within one storey are merged [755].

In `BBfit`, a χ^2 function is used to fit the hits into a muon track and an M-estimator[17] is used to improve the fit [757]. Eventually, the `BBfit` algorithm consists of a hit merging and hit selection procedure followed by fitting steps for a track hypothesis and a point-like light source [755]. Figure 5.3 displays an example of the result of the hit selection on some bright neutrino candidate events from the 2008 data-taking period [755].

Offline reconstruction algorithm

Another reconstruction method, called `AAfit` [498], more advantageous and precise than `BBfit` has been developed by ANTARES for data analysis purposes. The `AAfit` algorithm

[17] A so-called M-estimator is a variant of a χ^2-fit in which hits with large residuals are given less importance compared to a regular χ^2 [756].

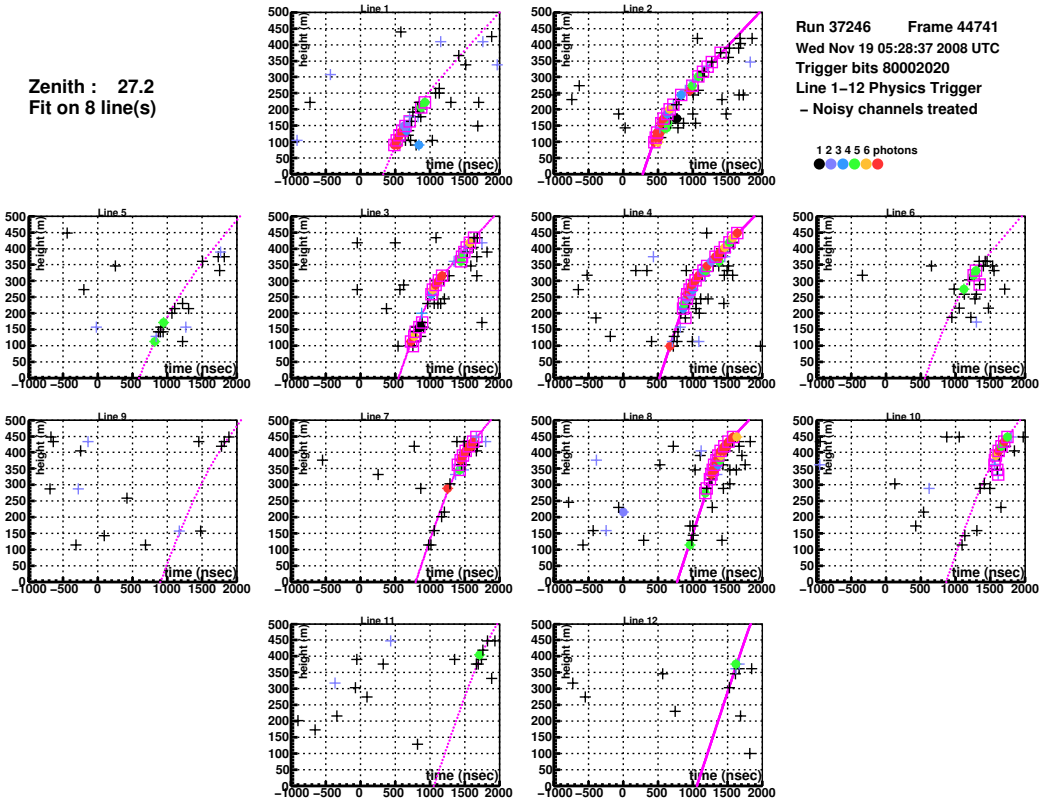

Fig. 5.3.: Online display showing a fitted track of a bright event recorded on November 19th, 2008. The 12 lines of the ANTARES octagonal layout is shown. Each panel shows the arrival time of the hits (x-axis) and the vertical position (y-axis) for each detector line (y=0 is the sea bottom). Crosses are hits in a time window of 3 μs around the trigger. t=0 corresponds to the time of the first hit which participated in the trigger and a window of −1000/+2000 ns is shown with respect to this time. The full circles are hits passing the trigger condition and open boxes are hits used in the final reconstruction, represented with pink lines. Colors refer to the hit charge. The line width and style of the fitted track illustrates the minimal distance between the track and detector line; thick and solid lines stand for closer distances than thin or dotted lines. The figure is taken from [755].

has better detection efficiency[18] and angular resolution [757, 658]. It can achieve an angular resolution of 0.3° at E_ν=1 TeV and a better effective area for high-energy events (above 200 GeV) [757]. This makes `AAfit` advantageous in the searches of the point-like sources neutrinos, especially with its excellent angular resolution, and is used in this work.

In contrast to `BBfit`, the offline `AAfit` algorithm fully uses the dynamic geometry of the detector with information about the real detector alignment and the simulation of the detector electronics [757].

The `AAfit` track reconstruction algorithm consists of four consecutive fitting procedures [498]. It includes a linear prefit utilizing a χ^2, an M-estimator, a maximum likelihood fit (without

[18] The `BBfit` algorithm is being known to have a better efficiency at low energy than `AAFit`.

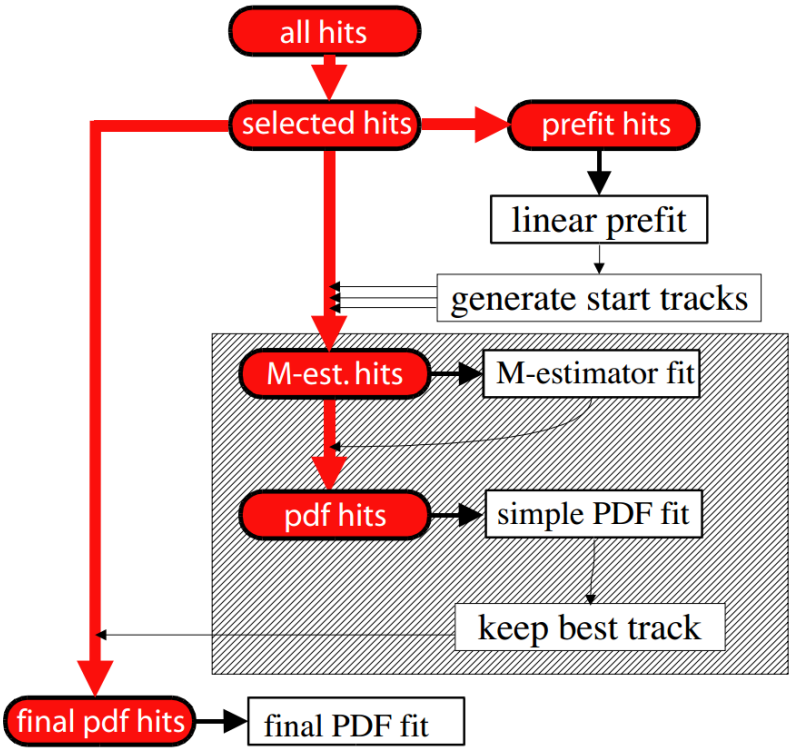

Fig. 5.4.: Schematic depiction of the reconstruction algorithm. The figure is taken from [754].

and with background hits[19]) when fitting the hits into a muon track [757, 756, 498]. The combination of the fitting algorithms into one reconstruction algorithm is schematically shown in Fig. 5.4.

The full description of the `AAit` reconstruction algorithm is given in [498] and may be summarised as follows:

1 **Linear prefit**: The first stage in the track reconstruction procedure. The "linear prefit" is performed through the positions of the hits, with the hit time as an independent variable [498]. It is not very accurate, it has the advantage that it requires no starting point and therefore suited as a first step [498]. In the simulated events, background hits are generated in an arbitrary time window around the event; thus, in order to make the algorithm insensitive to the amount of background simulated, a rough, first selection is made [498]. All hits are selected for which [498]:

$$|\Delta t_{ij}| \leq \frac{d_{ij}}{v_g} + 100 \text{ ns}, \tag{5.10}$$

where Δt_{ii} is the time difference between a hit i and the hit j with the largest amplitude in the sample and d_{ij} is the distance between the PMTs of the two hits [498]. Hits

[19] Non-inclusion of background hits, especially those with negative residuals, in the original likelihood fit can degrade the performance of the track reconstruction; thus, using an improved Probability Density Function (PDF) in which background hits are taken into account, a large improvement can be observed [498].

with larger time differences cannot be related to the same muon, unless they have a residual larger than the "safety factor" of 100 ns [498]. The linear prefit is made with a sub-sample of the hits and only hits in local coincidences and hits with amplitudes larger than 3 p.e. are used[20] [498], which provides a robust starting point for the further fitting procedure [753]. The position associated with the ith hit is denoted by (x_i, y_i, z_i) [498]. In order to obtain a linear relation between the hit positions and the track parameters, it is assumed that the hits occur on points that are located on the muon track, which is expected to be a reasonable approximation if the length of the muon track in the detector is much larger than the attenuation length of the light [498]. This allows deriving analytically a starting point from the minimization of the χ^2, although with poor precision [753].

2 **M-estimator fit**: The second stage in the track reconstruction procedure. The insensitivity to the quality of the starting point of the M-estimator fit makes it a natural choice for the next step [498]. M-estimator is used to prevent the influence of large residuals, called "outliers", in the fit. As a robust estimator, the M-estimator fit allows a better estimate of a set of track parameters, using the residual Δt_i, and reduces the effect of outlier hits [753]. The hits used for this fit are selected on the basis of the result of the prefit [498]. In order to be selected, a ith hit must have a time residual w.r.t. the t_i^{th} calculated from the parameters obtained with the linear prefit between -150 and 150 ns and a distance from the fitted track of less than 100 m [498]. Hits with an amplitude larger than 2.3 p.e. are always selected [498]. By choosing an M-estimator that behaves suitably for large residuals, it can be expected that a reasonable track estimate can be obtained without the requirement of an accurate starting point [498]. A χ^2 estimator of the form $g(r) = -r^2$, on the other hand, is not suitable[21] since it does not take into account background hits [759]. For the residual r_i of the ith datum (i.e. the difference between the ith observation and its fitted value), the standard least-squares method tries to minimize $\sum_i r_i^2$, which is unstable if there are outliers present in the data since the outlying data give an effect so strong in the minimization that the parameters thus estimated are distorted [758]. The M-estimators try to reduce the effect of outliers by replacing the squared residuals r_i^2 by another function of the residuals [758]. It has been found that the following function gives good results [754, 498]:

$$g(r) = -2\sqrt{1 + \frac{r^2}{2}} + 2, \tag{5.11}$$

where r stands for residuals, so that $r_i = t_i - t_i^{th}$. For large values of r, this M-estimator, called "L1-L2", is a linear function of r, while for small r it is quadratic [754, 498] (see Fig. 5.5). The performance of the M-estimator was found to improve when the hit amplitude A of the hits is used as a weighting factor for the time residuals [498], so that A_i stands for ith hit with r_i. Furthermore, a term was added, which contains the

[20] Such hits are called L1 hits, more details in Section 3.3.3.
[21] The least-squares estimators are not robust because their influence function is not bounded [758].

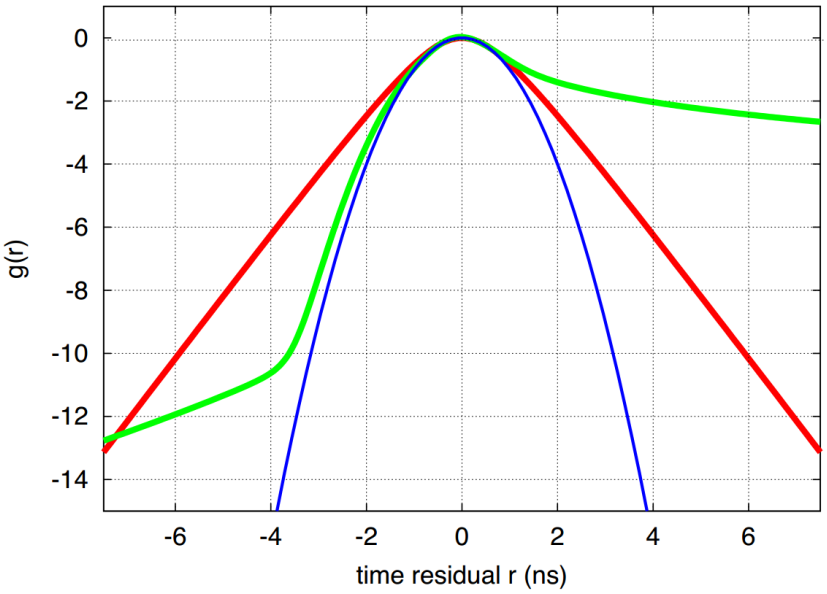

Fig. 5.5.: Comparison of the fitting functions: $-r^2$ (blue), $-2\sqrt{1+\frac{r^2}{2}}+2$ (red), and the logarithm of the likelihood $ln\mathcal{L}(r)$ (green). The figure is taken from [754].

angular response function $f_{ang}(\alpha)$ of the PMT [754, 498] which is a function of the incident angle of the photon (with respect to the PMT axis) α_i [753]. The function that is finally maximised to obtain a track estimate is given by [754, 498]:

$$M = G(r) = \sum_i k\left(-2\sqrt{1+A_i\frac{r_i^2}{2}}\right) - (1-k)f_{ang}(\alpha_i), \tag{5.12}$$

where k is the parameter that determines the relative weights of the two terms and is optimized using MC events [498]. The k value is set to 0.05; nevertheless, the small value of k does not mean that the second term is dominant in the fit since the influence of the two terms depends on their derivatives w.r.t. the track parameters [498].

3 **Maximum likelihood fit (with "original" PDF)**: The third stage in the track reconstruction procedure. This fit uses the principle of the Maximum Likelihood (ML) and is performed with hits that are selected based on the result of the M-estimator fit. For each possible set of track parameters, the probability to obtain the observed events can be calculated, which is called the likelihood of the event [498]. The likelihoods that are used take into account only the probability of the time of the hits [498]. In the case of uncorrelated hits, the likelihood of the event can be written as the product of the likelihood of the individual hits as follows [754, 498]:

$$P(\text{event}|\text{track}) \equiv P(\text{hits}|\vec{p},\vec{d}) = \prod_i (t_i|t_i^{th}, a_i, b_i, A_i), \tag{5.13}$$

where i is the time of hit i, A_i the hit amplitude introduced in Eq. 5.12, t_i^{th} is the expected arrival time of the photon introduced in Eq. 5.5, a_i and b_i are the length of the photon path (see Eq. 5.6) and the cosine of the angle of incidence of the photon on the PMT[22] respectively [498]. Here, $\prod_i (t_i|t_i^{th}, a_i, b_i, A_i)$ is the statistical probability of observing t_i with the expectation of t_i^{th}, a_i, b_i, and A_i. The maximum likelihood estimate of the track is defined by this set of track parameters for which the value of the likelihood function is maximal[23] [498]. In the simplest case, the a, A and b dependence in Eq. 5.14 are neglected and the likelihood is expressed solely in terms of the probability density of the residuals r [498]:

$$\mathcal{L} = \prod_i (t_i|t_i^{th}), \tag{5.14}$$

The probability of a hit with a certain residual Δt_i is described by a PDF which is a combination of a signal PDF and a background PDF [498]. At this stage, the "original" PDF is used, in which the background hits are not taken into account [498]. At this stage, hits are selected with residuals within $[-0.5 \times \text{RMS}; \text{RMS}]$ range, where RMS is the Root Mean Square of the residuals used for the M-estimator fit [498]. Also, hits that are part of a local coincidence, or that have an amplitude larger than 2.5 p.e. are selected [498]. The asymmetry in the selection interval reflects the fact that the original PDF is asymmetric [498]. It was found that the efficiency of the algorithm is improved by repeating stage 2 with M-estimator and this one with ML fit with a number of starting points that differ from the pre-fit in stage 1 [498]. The result with the best likelihood per degree of freedom (DOF), as obtained in this stage, is kept [498]. The two stages are repeated 9 times with some additional information inferred from the pre-fit [498]. Four of the additional starting points are obtained by rotating the pre-fit track by an angle of 25°[24] [498]. Four more starting points are obtained by translating the track ±50 m in the direction $\vec{d} \times \vec{z}$ (where $\vec{d}$ is the track direction) and ±50 m in the $\vec{z}$ (i.e. upward) direction [498]. The number of starting points that result in track estimates which are compatible with the preferred result (i.e. which gives the same track direction to within 1°), called N_{comp}, is used in the event selection [498].

4 **Maximum likelihood fit (with "improved" PDF)**: The fourth and last stage in the track reconstruction procedure. The preferred result obtained in stage 3 is used as a starting point for the ML fit with the "improved" PDF, in which background hits are taken into account [498]. The background hits, especially those with negative residuals can degrade the performance of the track reconstruction [498]. The background hits are uniformly distributed in time; as a consequence, the PDF of the hit residuals $P(r)$ can only be normalized if the duration of the event is specified [498]. It is assumed

[22] For a head-on collision of a photon with the photocathode $a = -1$, whereas $a = 1$ means the photon hits the insensitive rear of the PMT [498].
[23] In practice, the maximum of $\mathcal{L}$ is found by minimising $-log\mathcal{L}$ as in this work.
[24] The origin of the rotation is the point on the track that is closest to the center of gravity of the hits.

that an event consists of all hits with residuals within $[-T/2; T/2]$ range [498]. The PDF has contributions from background hits and from signal hits and the relative contributions of the two are independent of the event duration T [498]. However, if the value of T is incorrect (i.e. if the fit is performed with hits from a larger time window than what is assumed), the normalization of the PDF will depend on the track parameters, which is undesirable [498]. Thus, the knowledge of T is needed in the reconstruction [498]. The hits are selected with residuals within $[-250; 250]$ ns (in order to add background hits) and with amplitudes larger than 2.5 p.e. or in local coincidences [498]. Since the background is taken into account in the PDF, the presence of background hits in the sample does not jeopardize the reconstruction accuracy [498]. This is reflected in the large time window used for the hit selection, so that the event duration as an input parameter for the final fit is set to $T = 500$ ns [498].

The philosophy adopted in the reconstruction algorithm is to reconstruct as many events as possible without trying to reduce the number of badly reconstructed events by intermediate selection criteria [498]. Rather, selection criteria can be applied afterwards, depending on the demands of the various physics analyses [498] such as performed in this work. As a consequence, many events are reconstructed with large errors [498]. Nevertheless, two variables are introduced which can be used to reject badly reconstructed events [498], e.g. atmospheric muons mis-reconstructed as up-going. This is crucial for time-dependent analyses as such one performed in this work. The first parameter that can be obtained is Λ quality parameter and is given by a combination of the variable $log\mathcal{L}/N_{DOF}$ used to select the well-reconstructed events and the number of compatible solutions, N_{comp}, found by the reconstruction algorithm [498]:

$$\Lambda = \frac{log\mathcal{L}}{N_{DOF}} + 0.1(N_{comp} - 1), \tag{5.15}$$

where $N_{DOF} = N_{hits} - 5$ is the number of degrees of freedom (DOF) in the fit and is equal to the number of hits used minus the number of free parameters, which is five [498]. The Λ parameter characterizes the quality of the fit. The second parameter is the angular error estimate on the direction of the reconstructed muon track, β, which is obtained from the error estimates of the track's zenith σ_θ and azimuth angles σ_ϕ as follows [498]:

$$\beta = \sqrt{\sigma_\theta^2 + sin^2\theta\sigma_\phi^2}. \tag{5.16}$$

These two variables, Λ and β, can be used to select well-reconstructed muons from badly reconstructed up-going muons [498]. The same parameters are used to reject the background of wrongly reconstructed atmospheric muons, which form a more dangerous background than up-going muons [498]. This allows the background suppression and enhances the signal-to-noisy ratio which are essential in this work. Examples of Λ and β distributions are shown in Fig. 7.17 and Fig. 7.18.

5.2.2 Energy reconstruction

The methods used to reconstruct the muon energy are based on the amount of detected light on the PMTs [760]. The muon estimated energy was determined for each event; the parent neutrino distribution was derived with unfolding procedures that have to be used in order to draw the actual energy spectrum from the distribution of the measured event-by-event measured[25] [760]. The expected number of p.e. on each PMT, $\langle n_{pe} \rangle$, is a function of the muon energy, water properties, of the detector configuration and PMT distance and orientation from the light source [760]. This number is calculated considering the amount of light emitted while a muon traverses the detector, taking into account contributions from direct and scattered light [760]. Direct photons are those originating along with the muon trajectory and arriving on PMTs in the Čherenkov wavefront without being scattered while scattered photons are delayed by the increased optical path from the emission point to the PMT [760]. Above ~500 GeV most of the Čherenkov light emitted along the muon path comes from the secondary particles produced in radiation losses [760]. The total amount of light emitted from the muon and collected by the PMTs is directly correlated to its energy [760].

Two independent methods are used to estimate the muon energy. The first one - denoted in the following as *energy likelihood method* [759] - maximizes the agreement of the expected amount of light in the PMTs with the amount of light that is actually observed [760]. Starting from the direction information of the track reconstruction procedure and keeping the energy of the muon E_μ as a free parameter, an ML function is constructed as follows [760, 761]:

$$\mathcal{L}(E_\mu) = \frac{1}{N_{PMT}} \prod_{i}^{N_{PMT}} \mathcal{L}_\rangle(E_\mu). \tag{5.17}$$

This product is taken over all the N_{PMT} PMTs positioned up to 300 m from the reconstructed track, regardless of whether a hit was recorded or not [760]. The PMTs with unusually high or low counting rates in a particular run, as well as those that are not operational, are excluded [760]. $\mathcal{L}_\rangle(E_\mu)$ depends on the probability of observing a pulse of measured amplitude A_i given a certain number of p.e. produced on the ith PMT. These individual likelihood functions $\mathcal{L}_\rangle(E_\mu)$ are constructed as follows [760, 761]:

$$\mathcal{L}_\rangle(E_\mu) \equiv P(A_i; \langle n_{pe} \rangle) = \prod_{n_{pe}=1}^{n_{pe}^{max}} P(n_{pe}; \langle n_{pe} \rangle) \cdot G(A_i; n_{pe}), \tag{5.18}$$

when a hit is recorded and

$$\mathcal{L}_\rangle(E_\mu) \equiv P(0; \langle n_{pe} \rangle) = e^{-\langle n_{pe} \rangle} + P_{th}(\langle n_{pe} \rangle), \tag{5.19}$$

[25] This procedure has to take into account the stochastic nature of the muon energy losses, the large uncertainty in the reconstructed energy, the detection inefficiencies and the fact that only the daughter muon energy is measured.

when there is no hit on the optical module [760, 761]. The Eq. 5.18 consists of two terms, the Poisson probability $P(n_{pe}; \langle n_{pe} \rangle)$ of having n_{pe} p.e. given an expectation of $\langle n_{pe} \rangle$, and a Gaussian term $G(A_i; n_{pe})$ which expresses the probability that n_{pe} p.e. on the photocathode will yield the measured amplitude A_i [760, 761]. The Eq. 5.19 consists of a term describing the Poisson probability of observing zero p.e. when the expected value is $\langle n_{pe} \rangle$, and a term, $P_{th}(\langle n_{pe} \rangle)$, describing the probability that a photon conversion in the PMT will give an amplitude below the threshold level of 0.3 p.e. [760, 761].

The second muon energy estimation method - denoted in the following as *energy loss method* [762] - relies on the muon energy losses along its trajectory (see Eq. 2.14). The muon energy deposit per unit path length is approximated by an estimator ρ which can be derived from measurable quantities[762, 760]:

$$\frac{dE}{dX} \propto \rho = \frac{\sum_{i=1}^{N_{hit}} A_i}{\epsilon} \cdot \frac{1}{L_\mu}, \tag{5.20}$$

where L_μ represents the length of the reconstructed muon path starting from the entry point on the surface of the cylinder surrounding the instrumented volume of the detector. Due to the light transmission properties of the water, this volume is defined extending the radius and height of the cylinder by twice the light attenuation length; thus, L_μ is longer than the effective visible track in the detector [760, 761]. To remove the contribution from background light, a causality criterion embedded in the reconstruction algorithm, is used [760, 761]. Only hits used in the last part of the `AAFit` reconstruction mechanisms are used to compute the ρ parameter [658]. Finally, the quantity ϵ represents the overall ANTARES light detection capability. This quantity depends on the geometrical position and direction of the muon track. It is derived on an event-by-event basis as [760, 761]:

$$\epsilon \sum_{i=1}^{N_{PMT}} exp\left(- \frac{r_i}{\lambda_{abs}} \right) \cdot \frac{\eta_i(\theta_i)}{r_i}. \tag{5.21}$$

Here the sum runs over all the active PMTs, N_{PMT} [762, 760]. The distance from the muon track, r_i, and the photon angle of incidence, θ_i, are calculated for each PMT; θ_i is used to obtain the corresponding angular acceptance $\eta_i(\theta_i)$ [626] of the involved PMT [760, 761]. The distance r_i is used to correct for the light absorption in water (with characteristic absorption length $\lambda_{abs} = 55$ m) taking into account the light distribution within the Čherenkov cone (by a factor of $1/r$) [760, 761, 762].

Neutrinos generated in the atmosphere have a much softer energy spectrum ($\propto E^{-3.7}$) than neutrinos from the expected astrophysical flux (for example, $\propto E^{-2.0}$). Hence, the energy estimator information is used in the likelihood to further distinguish between cosmic signal and atmospheric background. Various energy estimators have been developed in ANTARES: *nhit*, *dE/dX* [763, 764], *ANNr* [765]. The simplest one is *nhit*, which is the total number of hits in the PMTs selected by the track reconstruction, which is expected to be proportional

to the incident particle energy[26]. Surely, this number is highly dependent on the geometry of the detector and the localization of the neutrino event within it. Nonetheless, *nhit* estimator so far served in many analyses as an energy proxy [766] as well as a selection criterion for well-reconstructible neutrino events so that it is adopted for this work. Examples of *nhit* distributions are shown in Fig. 7.17 and Fig. 7.18. The more sophisticated energy estimators, *dE/dX* and *ANNr*, have not been used. The *dE/dX* energy estimator is based on the energy loss per unit length of a charged particles while crossing the fiducial volume of the ANTARES detector [763, 762, 764]. The *ANNr* energy estimator is based on Artificial Neural Networks (ANNs) with over 50 different input parameters which range from parameters describing the distribution of hits in the detector by their time, location and charge, to track-related parameters like average time residuals [766].

[26] See the total muon energy loss parametrization in Eq. 2.14 in Section 2.3.4.

Time-dependent search method

6

> *The time will come when diligent research over long periods will bring to light things which now lie hidden. A single lifetime, even though entirely devoted to the sky, would not be enough for the investigation of so vast a subject... And so this knowledge will be unfolded only through long successive ages. There will come a time when our descendants will be amazed that we did not know things that are so plain to them... Many discoveries are reserved for ages still to come when the memory of us will have been effaced.*
>
> **— Lucius Annaeus Seneca**
> Natural Questions, 65 AD

This chapter focuses on the time-dependent point-source search method. The advantage of this method over the standard point source search method is discussed at the beginning of the chapter. Section 6.1 introduces to unbinned extended maximum likelihood method, while in Section 6.2 the likelihood ingredients are discussed: direction, energy, and time. The background time probability distribution function is discussed in Section 6.2.3, while the discussion of the signal time probability distribution function is postponed to the analysis section (see Section 7). The pseudo-experiments simulation and possible systematics are discussed in Section 6.3. The test statistic is explained briefly in Section 6.4. The optimization strategy is described in Section 6.5 where the model discovery potential is also discussed (see Section 6.5.1). Finally, the way how the upper limits are set is given in Section 6.5.2.

The advantage of the time-dependent analysis over the standard point source search is that the additional time information from the flares improves the analysis restricting the data to a period of interest and hence reducing the atmospheric neutrino and muon backgrounds; hence, requires a lower number of signal events for a discovery. The light curves from the flares can be used as a time probability distribution function in the likelihood. The flaring sources are interesting from a physics point of view since processes required for flare production might involve the hadronic processes in which the neutrinos can also be produced. The good angular resolution in ANTARES, less than 1^0 [608, 609], allows the search for spatial correlations with known astrophysical sources.

In this work, the two targeted sources for the time-dependent search are blazars, Mrk 421 and Mrk 501 (see Section 7.1). The blazars are the first identified sources of the high-energy astrophysical neutrinos [15, 16] (see Section 1.7.2), which motivates to chase for high-energy neutrinos from the two of the closest and brightest blazars, Mrk 421 and Mrk 501. As the first [375] and the second [376] extragalactic objects discovered in the TeV energy band, Mrk 421 and Mrk 501 are of a high good candidate for a neutrino counterpart [178]. Remarkable, that the Mrk 421 is respectively the strongest in the IceCube error circle of event #9 [369]. In addition, both blazars have confirmed extragalactic associations in the 2HWC catalog [377] and are subject to long-term monitoring campaigns [154] by the HAWC TeV γ-ray observatory located in Mexico. The HAWC detector operates nearly continuously and it is currently the most sensitive wide FOV γ-ray telescope in the very promising high-energy band from 100 GeV to 100 TeV, to which the ANTARES neutrino detector is also most sensitive for. This advantage of HAWC opens prospects to study such energetic astrophysical phenomena in the Universe as blazars, together to shed light on the mechanisms that power them and endeavor to break the mystery of their origin. Thereby, the γ-ray flare timing information provided by HAWC and involved in the search method discussed in this chapter, able to improve the efficiency of the search for a neutrino counterpart with ANTARES.

6.1 Unbinned Extended Maximum Likelihood method

An unbinned method based on an Extended Maximum Likelihood (EML) [767] ratio is employed in this analysis. This method has been already successfully used in several time-dependent searches in ANTARES [768, 769, 177, 178]. In contrast to the standard Maximum Likelihood (ML) with the total probability distribution normalized to unity, the normalisation of the PDF in EML is allowed to vary [767]. Thus, such method is applicable to problems in which the number of samples obtained is itself a relevant measurement [767], i.e., with a-priori known expected number of background events in the sample. In ANTARES, the signal is expected to be small compared to the full data sample can be used can be treated as background [768]. Consequently, the EML has real advantages over the standard ML in the measurement of the properties of a signal in the presence of a known but random background.

6.1.1 Extended Maximum Likelihood

A set of m unknown parameters $\{a_1 \cdots a_m\}$ is estimated by maximazing the likelihood (or, equivalently, its logarithm) for the particular set of N data values $\vec{x} = \{x_1 \cdots x_N\}$ observed [767]:

$$\mathcal{L} = \prod_{i=1}^{N} p(x_i; a_1 \cdots a_m). \tag{6.1}$$

Here $p(x_i; a_1 \cdots a_m)$ is the probability density for the sampling variable x. As the measurement is certain to give some result, the integral of $p(x)$ over the entire range of x (or, if x is a discrete variable, the summation), is normalized to unity [767]:

$$\int p(x_i; a_1 \cdots a_m)\, \mathrm{d}x = 1 \tag{6.2}$$

It is the relaxation of this requirement that leads to the method of extended maximum likelihood [767]. The function $p(x_i; a_1 \cdots a_m)$, normalized according to Eq. 6.2, is replaced by a function $P(x_i; a_1 \cdots a_m)$, the normalisation of which is not constrained [767]:

$$\int P(x_i; a_1 \cdots a_m)\, \mathrm{d}x = \mathcal{N}(a_1 \cdots a_m). \tag{6.3}$$

The Eq. 6.3 is interpreted so that the $P(x_i; a_1 \cdots a_m)$ function describes not only the *shape* of the expected distribution in x, but also its *size* [767]. Events occur at random in the range of x, governed by Poisson statistics, and $P(x)\delta x$ gives the number of events expected in the interval x to $x + \delta x$. $\mathcal{N}$ is thus the total number of events expected over the whole range of observation. The observed number N will in general be different from this due to the fluctuations of Poisson statistics [767].

However, it is obvious that simply replacing the normalized $p(x)$ by the unnormalized $P(x)$ in the likelihood to be maximised (see Eq. 6.1) is not a correct procedure, as the maximisation process will tend to make the normalisation large [767]. To fix this, the likelihood for a particular set of data $\{x_1, x_2, \cdots x_N\}$ must incorporate not only the information that events were observed at $x_1, x_2, \cdots x_N$, but also the information from the total number N - i.e. that events were not observed anywhere else [767].

Division of the range of x into narrow bins of width Δx, so small that the probability of a bin containing more than one event is negligible, makes plain of the effect [767]. The probabilities for 0, P_0, and 1,P_1, events in a bins are given by Poisson statistics [767]:

$$\begin{aligned} P_0(x) &= e^{-\Delta x\, P(x)}. \\ P_1(x) &= \Delta x\, P(x)\, e^{-\Delta x\, P(x)}. \end{aligned} \tag{6.4}$$

The extended likelihood $\mathcal{L}$ is thus combined probability for a complete data sample [767]:

$$\mathcal{L} = \prod_i \Delta x\, P(x_i) \prod_j e^{-\Delta x\, P(x_j)}, \tag{6.5}$$

where the first product is over all bins containing an event, and the second is over all bins.

In this limit $\Delta x \to \mathrm{d}x$, the first term becomes $\prod_i P(x_i)\, \mathrm{d}^N x$ analogously to Eq. 6.1 - the $\mathrm{d}^N x$ merely expresses the fact that the functions are probability densities, not probabilities. The second is [767]:

$$e^{-\sum_j \Delta x\, P(x_j)} \to e^{-\int P(x_j)\, \mathrm{d}x} = e^{-\mathcal{N}}. \tag{6.6}$$

Thus, the extended likelihood is given by [767]:

$$\mathcal{L} = \left[\prod_{i=1}^{N} P(x_i)\right] e^{-\mathcal{N}}. \tag{6.7}$$

Then, the logarithm of $\mathcal{L}$ is [767]:

$$\ln \mathcal{L} = \sum_{i=1}^{N} \ln P(x_i) - \mathcal{N}. \tag{6.8}$$

Increasing the normalisation will increase $\mathcal{L}$ through the first term, but will decrease it through the second, and maximising $\mathcal{L}$ will involve finding the appropriate balance [767].

To perform the analysis, the ANTARES data sample is parametrized as two-component mixture of "signal" (S) and "background" (B) [178]. Since the signal is expected to be small, the total number of events $\mathcal{N}$ in the considered data sample can be treated as background. The expected number of signal events, $\mathcal{N}_S$, is uknown, while the background rate, $\mathcal{N}_B$, is a priori known when building the likelihood $\mathcal{L}$ [177]. The corresponding PDFs are $P_S(x)$ and $P_B(x)$. Thus, the probability distribution $P(x_i)$ in Eq. 6.8 can be expressed as $P(x_i) = \mathcal{N}_S P_S(x_i) + \mathcal{N}_B P_B(x_i)$. Hence, the likelihood $\mathcal{L}$ is:

$$\ln \mathcal{L} = \sum_{i=1}^{N} \ln \left[\mathcal{N}_S P_S(x_i) + \mathcal{N}_B P_B(x_i)\right] - \left[\mathcal{N}_S + \mathcal{N}_B\right] \tag{6.9}$$

The N_S is fitted by maximizing the likelihood $\mathcal{L}$ [178]. The goal of the method is to determine in a given direction in the sky and at a given time the relative contribution of signal and background [768]. The $P_S(x_i)$ and $P_B(x_i)$ are defined as the PDFs for an event i, at time t_i, energy E_i, declination δ_i; hence, the final likelihood with all terms [178]:

$$\ln \mathcal{L} = \sum_{i=1}^{N} \ln \left[\mathcal{N}_S P_S(\alpha_i) P_S(E_i) P_S(t_i) + \mathcal{N}_B P_B(\delta_i) P_B(E_i) P_B(E_i)\right] - \left[\mathcal{N}_S + \mathcal{N}_B\right]. \tag{6.10}$$

Here [177],

- Directional PDFs: $P_S(\alpha_i)$ for signal and $P_B(\delta_i)$ for background, the parameter α_i represents the angular distance between the direction of the event i and direction to the source δ_i;

- Energy PDFs: $P_S(E_i)$ and $P_B(E_i)$; Various energy estimators have been developed in ANTARES (see Section 5.2.2): *nhit* [770], *dE/dX* [763, 764], *ANNr* [765]. The simplest one is the total number of hits in the PMTs selected by the track reconstruction, which is expected to be proportional to the incident particle energy. Neutrinos generated in the atmosphere have a much softer energy spectrum ($\propto E^{-3.7}$) than neutrinos from the expected astrophysical flux (for example, $\propto E^{-2.0}$). Hence, the energy estimator information is used in the likelihood to further distinguish between cosmic

signal and atmospheric background. In this work, the *nhit* energy estimator is selected since so far served in many analyses as an energy proxy as well as a selection criterion for well-reconstructible neutrino events [766].

- Time PDFs: $P_S(t_i)$ for signal and $P_B(t_i)$ for background. The LCs for each source derived from HAWC show the periods of interest for the coincident neutrino search and used as a time PDFs. The background time PDF $P_B(t_i)$ is the probability to have a background event at a given time t_i. It is built using the distribution in time of ANTARES events with following criteria: the cut on quality parameter Λ>−5.6, the number of hits in PMTs *nhit*>5 in more than one line *nline*>1, and an estimated angular uncertainty on the fitted muon track direction β<1.0° (see Section 6.2.3).

These ingredients are determined using the ANTARES Monte Carlo simulations (MC) and data (see Section **??**); the background PDFs are all computed using data only [176].

6.2 Likelihood ingredients

6.2.1 Directional: Point Spread Function

One of the most important parameter in point source search is the angular distance to the source, characterized by the Point Spread Function (PSF) - $P_S(\alpha_i)$ (see Fig. 6.1), which is defined as the probability density of α per unit solid angle, Ω [178]:

$$P_S(\alpha_i) = \frac{dP}{d\Omega} = \frac{d\alpha_i}{d\Omega}\frac{dP}{d\alpha_i} = \frac{1}{2\pi sin\alpha_i}\frac{dP}{d\alpha_i}, \tag{6.11}$$

where $\alpha_i = |\alpha_i^{true} - \alpha_i^{rec}|$ is the difference between simulated neutrino direction α_i^{true} and reconstructed muon direction α_i^{rec}. The $Log_{10}\alpha$ distribution (see Fig. 6.1) is characterized

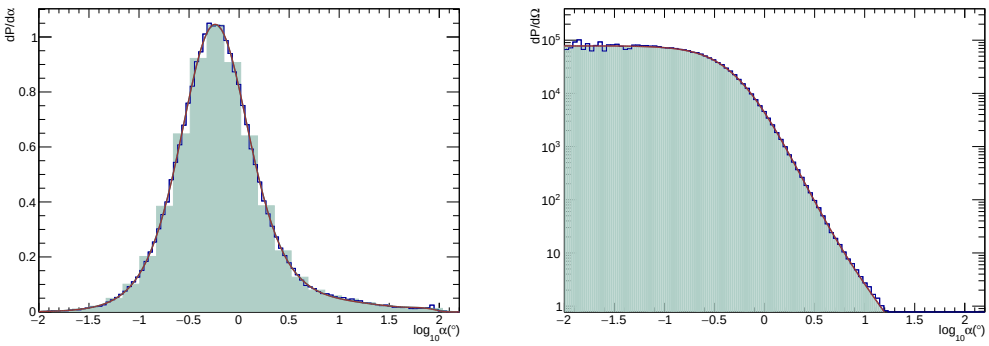

Fig. 6.1.: Sample of PSF parametrization for Mrk 421 with Λ>−5.2 cut and E^{-2} energy spectrum. *Left:* $Log_{10}\alpha$ distribution (green filled histogram) with the parametrized PSF before normalization with the solid angle deconvolved (red line) (see Eq. 6.11). *Right:* PSF parameterization before normalization (red line) with the $Log_{10}\alpha$ distribution convolved with the solid angle (green filled histogram).

with a `TSpline3` - an interpolator object - and converted into a `TF1` - a function object

- both ROOT [635] objects [516]. Its correct normalization is obtained normalizing the α distribution to unity.

The PSF depends on the cut on the quality parameter of the reconstructed track Λ and also on the energy. Thus, it is computed for each Λ and each energy spectrum. As seen from Fig. 6.1, the contribution of the events farther than 30° from the source are negligible; thus, it is enough to simulate the events only within a 30° cone around the source. Such conditions allow reducing the computation time and simulate a sufficient number of PEXs.

6.2.2 Energy

The energy PDF for the signal event is produced according to the studied energy spectrum [178]. The presence of the energy estimator in the likelihood, such as *nhit*, aid to a separation of expected cosmic signal from the atmospheric background with a softer energy spectrum. From various energy estimators developed in ANTARES, the *nhit* energy estimator has been selected in this work. The *nhit* is the simplest one and represent the total number of hits in the PMTs selected by the track reconstruction, which is expected to be proportional to the incident particle energy. Several energy spectra are used in this work, such as $E^{-1.0}\exp(-E/1\,\mathrm{PeV})$, $E^{-2.0}$, $E^{-2.5}$, $E^{-2.25}$ (for Mrk 501 only, as suggested by [771]) neutrino energy spectra.

6.2.3 Time

Background time PDF

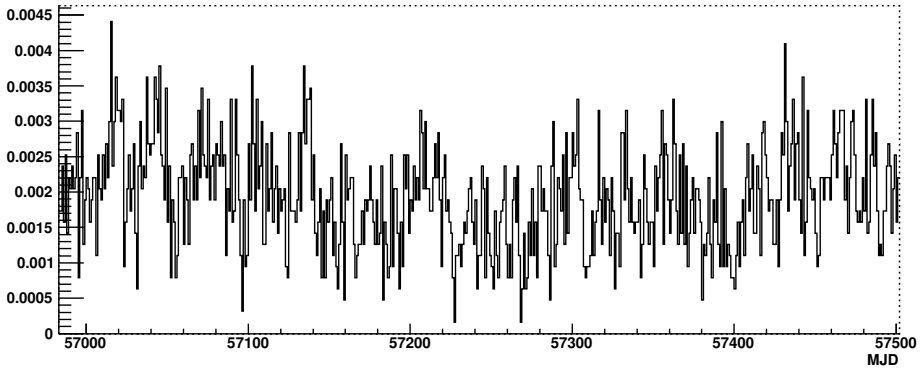

Fig. 6.2.: The normalized to unity ANTARES background time distribution of selected period made for quality parameter Λ>−5.6, reconstructed zenith $\cos(\theta)$>−0.1, and an estimated angular uncertainty on the fitted muon track direction β<1.0° with number of hits in PMTs $nhit > 5$ in more than one line $nline > 1$. The size of the bin is 1 day.

The background time PDF $P_B(t)$ is the probability to have a background event at a given time. It is built using the distribution in time of ANTARES events with the following criteria applied: the number of hits in PMTs $nhit > 5$ in more than one line $nline > 1$, the reconstructed zenith $\cos(\theta)$>−0.1, and an estimated angular uncertainty on the fitted muon track direction β<1.0°. Cuts on both, θ and β, allow the background suppression and

enhance the signal-to-noisy ratio (see Section 5.2.1) which are essential in this work. The cuts $\cos(\theta)>-0.1$ and $\beta<1.0^\circ$ are selected to provide good DATA/MC agreement as shown in Fig. 7.17 and Fig. 7.18.

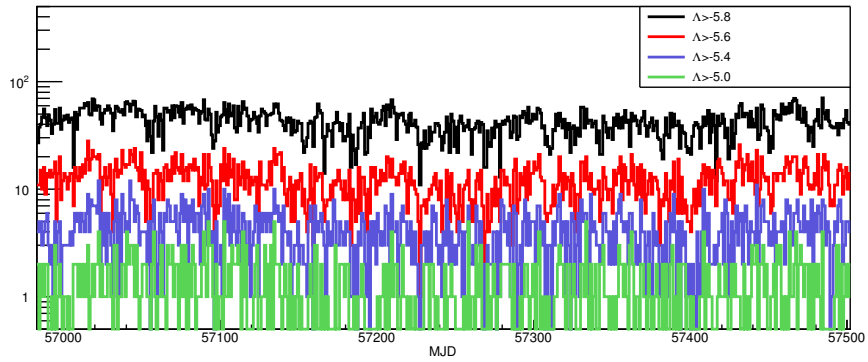

Fig. 6.3.: Background time PDF of selected period for several Λ values with $\cos(\theta)>-0.1$, $\beta<1.0^\circ$, $nhit > 5$, $nline > 1$ conditions applied.

In contrast to other ingredients, the background time PDF is built once for the whole analysis with one Λ>−5.6 cut (see Fig. 6.2). Therefore, it requires an additional check[1] of the stability for different Λ cuts. Background time PDFs for different Λ cuts are presented in Fig. 6.3. As seen in Fig. 6.4, background time PDF shows good stability, especially for in Λ∈[−5.8; −5.0] range.

[1] The check has been performed at the early stage of this work using the 2014-2016 dataset (see Section 7.3.1).

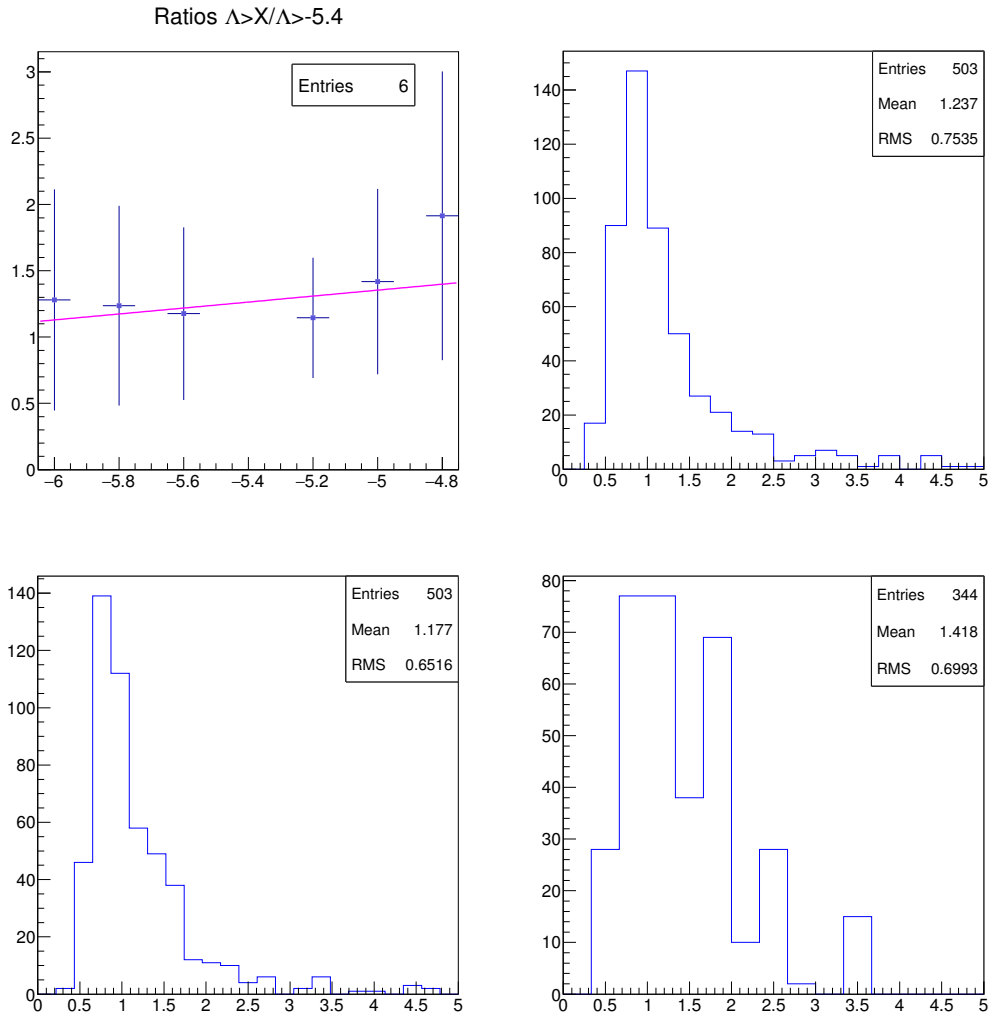

Fig. 6.4.: *Top Left:* The mean value and the errors of distributions of the background time PDF ratios of $\Lambda{>}X_i/\Lambda{>}X_{ref}$ for $X_i = -6.0, -5.8, -5.6, -5.2, -5.0, -4.8$ with the reference to $\Lambda_{ref} > -5.4$. The pink color line represent the linear fit. *Bottom* and *Top Right*: Example of the distributions of the normalized background time PDF ratios $\Lambda{>}X_i/\Lambda{>}X_{ref}$ for $X_i = -5.8$ (*Top Right*), -5.6 (*Bottom Left*), -5.0 (*Bottom Right*) with the reference to $\Lambda_{ref} > -5.4$.

Signal time PDF

Taking advantage of γ-ray flux time variation information from potential neutrino emitters, the neutrino background can be significantly reduced and signal-to-noise discrimination improved. The γ-ray LC can be used to determine the periods of interest for the coincident neutrino search. The precise shape of the signal time PDF is directly extracted from the γ-ray LC assuming proportionality between the γ-ray and the neutrino fluxes and is supposed to have a square shape. The signal time PDF is discussed in details in Section 7.

6.2.4 Possible other ingredients

The neutrinos produced by a given flare may not reach the Earth at the same time as the associated γ-rays. It can be considered to introduce in the likelihood a possible lag between γ-ray and the neutrino in order to take into account a possible arrival time difference of γ-ray and the neutrino signals. In this work, no possible lag between γ-ray and the neutrino is considered. For example, the ±5 days lag considered in [768, 769], is much larger than the theoretical estimation given in [772] and has been introduced to only not miss a neutrino signal for the shortest flares if the assumption of the simultaneous arrival of the γ-ray and the neutrino signals is off by one day. In that case it allowed a small lags in the proportionality which corresponds to a possible shift of the entire time PDF.

A neutrino with a mass m_ν (in eV) and energy E_ν (in MeV) will experience an energy-dependent delay Δt (in s) relative to a massless neutrino in traveling over a distance D (in 10 kpc[2]) of [772]:

$$\Delta t = 0.515 \frac{m_\nu}{E_\nu} D, \tag{6.12}$$

where only the lowest order in the small mass has been kept. For example, taken the extreme values such as $z \approx 11$ ($D \approx$ 13 Gpc)[3], $m_\nu \approx 1$ eV[4], and an $E_\nu \approx 1$ GeV[5], one can obtain:

$$\Delta t \approx 0.515 \frac{1}{10^9} 13 \cdot 10^9 \approx 1 \ s. \tag{6.13}$$

Due to the fact, that the durations of the flares used in this work are much longer than one day, and the theoretical estimation [772] (see Eq. 6.12) gives the arrival time difference between γ-ray and the neutrino of order of seconds (see Eq. 6.13), much less than one day, it is considered for the lag to be set to zero.

[2] Approximately the distance to the Galactic center
[3] Given by a remarkably bright galaxy candidate, GN-z11, measured at $z \approx 11$ by HST/WFC3 [773].
[4] As of order of magnitude given by upper limits in [774, 775].
[5] If considered that the ANTARES is the most sensitivity to neutrino energies 100 GeV $< E_\nu <$ 100 TeV and that for typical E^{-2} spectrum the 5% energy detection s at ≈10 TeV as seen in Fig. 7.29 in Section 7.4.1.

6.3 Pseudo experiments

In the discussed time-dependent search method, the significance of the discovery is determined by means of Pseudo-Experiments (PEXs) performed on blinded data. The PEX is a simulated event distribution generated from a background including a given number of fake signal events. The unknown parameter N_S in Eq. 6.9 is fitted by maximizing the likelihood in order to evaluate the Test Statistic (TS) (see Section 6.4) as shown in Eq. 6.14, which is used to estimate the significance of the result.

The pseudo-experiments (PEXs) are generated using the known background distributions for declination, $P_B(\delta)$, energy, $P_B(E)$, and time, $P_B(t)$, and injecting signal events, N_S, in a 30° cone around the considered source. For each background event, a random value following the background distributions is assigned. For the right ascension, the events are uniformly simulated in the $-\pi, \pi$ range. The total quantity of simulated background events in each PEX, $\mathcal{N}_B$, is given by a random number that follows a Poisson distribution with mean equal to the number of events of the full ANTARES data sample that are selected by the corresponding quality cut, while for the signal PEXs, a fixed and known amount of signal events, $\mathcal{N}_B$, is simulated [516]. The coordinates for the signal events are computed from the direction of the studied source adding a randomly-drawn angle, α (30° cone is considered). The time is computed randomly from the time PDF, $P_S(t)$, which is one-day binned. The total 3×10^5 PEXs are produced for background and 3×10^4 PEXs for a signal with injection from 1 up to 20 possible signals. Later, the signal distribution $\mathrm{H}_1(\mathrm{Q})$ is derived and test statistics values for each hypothesis are evaluated.

The discovery potentials for 3σ and 5σ discoveries as the average number of signal events required to achieve a p-value lower than $2.7 \cdot 10^{-3}$ and $5.7 \cdot 10^{-7}$ respectively are also computed.

6.3.1 Systematics

The possible systematics intrinsically inherent to the detector are considered. The systematics on the absolute pointing accuracy, angular resolution, and the energy resolution are applied as a correction over the simulated parameter that is obtained from a Gaussian distribution with that uncertainty as a standard deviation. Since the events are simulated in equatorial coordinates (δ,RA), the systematic uncertainty in local coordinates (θ,ϕ) is considered in the PEX by determining an elevation θ and azimuth ϕ for that source in the moment of the day at which the event was simulated. In addition, the uncertainty on detector acceptance is taken into account.

- Absolute pointing accuracy uncertainty in the local coordinates established in [620]: uncertainty of 0.13° and 0.06° on the horizontal (ϕ) and vertical (θ) directions, respectively. This corresponds to 0.0023 and 0.0011 in radians and set in the PEX simulation.

- Angular resolution uncertainty: 15% degradation on the angular resolution in the track channel is considered as in [769]. The accuracy of the detected hit times can directly impact on the angular resolution of the track reconstruction algorithm; thus a 15% degradation on the angular resolution in the track channel is assumed. The smearing of the hit times was performed in simulations by varying the hit time resolution leading to a 15% degradation on the angular resolution in the track channel [776]. The PSF is highly dependent on the angular resolution of the event sample [514]. Many possible effects can contribute to this resolution, including the PMT transit time spread, mis-calibrations of the timing system and possible spatial misalignments of the detector [776].

- Energy resolution uncertainty: 10% on the number of hits (*nhit*). This is accounted for by smearing the simulated signal values by a Gaussian function with this RMS value. The same systematic uncertainty but for another *dE/dX* energy estimator is used in [768, 769].

- Detector acceptance uncertainty: 15% uncertainty is considered as in [769]. It is not included in the PEX simulations but used when the ULs are derived. This is accounted for by convolving the TS distribution of each discrete signal event case with the convolution of its Poisson probability with a Gaussian distribution with $\sigma = \mathcal{N}_S \cdot 0.15$ around $\mathcal{N}_S$.

Occasionally, the systematics simulations can produce a meaningless value for an event parameter: an undetectable declination due to the elevation cut or an energy estimator with null probability in some of the PDFs used in the likelihood. In that case, it is rejected and the event is simulated again.

6.4 Test Statistic

The maximum likelihood method takes as best-fit values of the unknown parameter $\mathcal{N}_S$ the values that maximize the likelihood function. The maximization of the likelihood function $\mathcal{L}$ is performed with `MINUIT` minimization software [777] (`ROOT` class `TMinuit` [635]) via search of a minimum in $-2\ln\mathcal{L}$ using `MIGRAD` algorithm. The goal of the unbinned search is to determine, for a given direction in the sky and at a given time, the relative contribution of background and signal components, and to calculate the probability to have a signal H_1 above a given background model H_0. Finally, to calculate goodness of fit between two models, H_0 and H_1, and to differentiate hypotheses, we build a TS equivalent to a likelihood ratio:

$$TS = 2(\ln \mathcal{L}_{S+B}^{max} - \ln \mathcal{L}_B). \tag{6.14}$$

Test statistic represents the logarithm of the ratio between the source-model likelihood $\mathcal{L}_{S+B}^{max}$ maximized w.r.t. $\mathcal{N}_S$ over the likelihood $\mathcal{L}_B$ calculated in the background-only hypothesis assuming $\mathcal{N}_S = 0$. Test statistic TS is a ratio of the probability for background plus signal

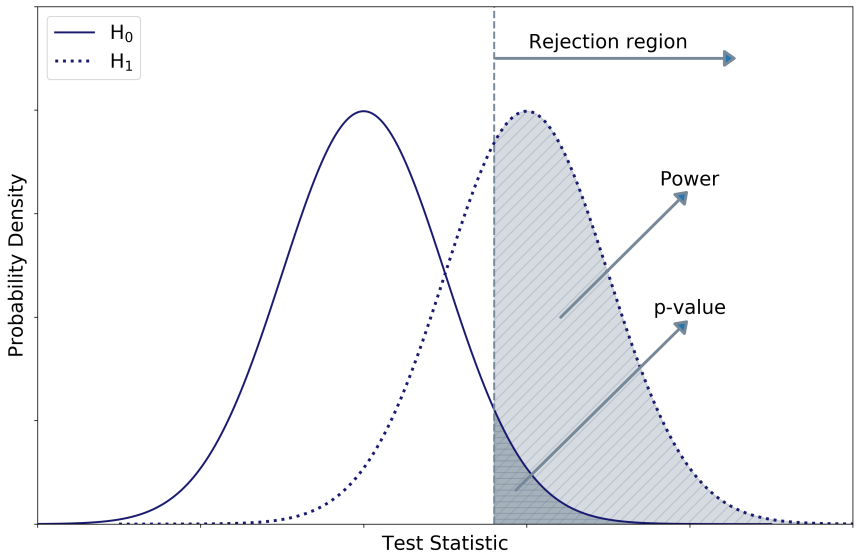

Fig. 6.5.: Definition of the power and *p*-value significance of the Test Statistic. The distributions of the test statistic, TS, for the background-only (H_0) and signal plus background (H_1) hypotheses are shown. The test statistic required for H_0 rejection is shown as a dotted line. Corresponding p-value significance and the power to discriminate H_0 from H_1 are shown as a dark-shaded and light-shaded areas respectively.

hypothesis H_1 over the probability of background-only hypothesis H_0 (see Fig. 6.5). The significance of a measurement is determined by its *p*-value, which is given by the probability to yield TS equal or higher than TS observed if the background-only hypothesis were true. The *p*-value determines how ”likely” or ”unlikely” the data with the true background-only H_0 hypothesis.

6.5 Optimization

The analysis is optimized with respect to different cuts and spectra in order to maximize the chances for the discovery of a particular signal model. In addition, to avoid biasing the analysis, it has been performed according to strict ”blinding” policy defined by the ANTARES Collaboration [178]. The data have been blinded by scrambling of the event right ascension (RA): the true RA of an event is hidden during the optimization steps of the analysis [178]. This procedure avoids the selection procedure becoming inadvertently tuned toward a discovery. The ”blinding” policy requires the simulation of a large number of PEXs, with the generation of both signal and background events. As stated above, in this study 3×10^5 and 3×10^4 PEXs are generated for background and signal (from 1 up to 20 signal events are injected in a 30° cone around the considered source) respectively. The $TS_{3\sigma}$ threshold can be established from the TS distributions by simple counting from the PEXs, while the $TS_{5\sigma}$ threshold (see Fig. 6.6) is not typically reachable with PEX

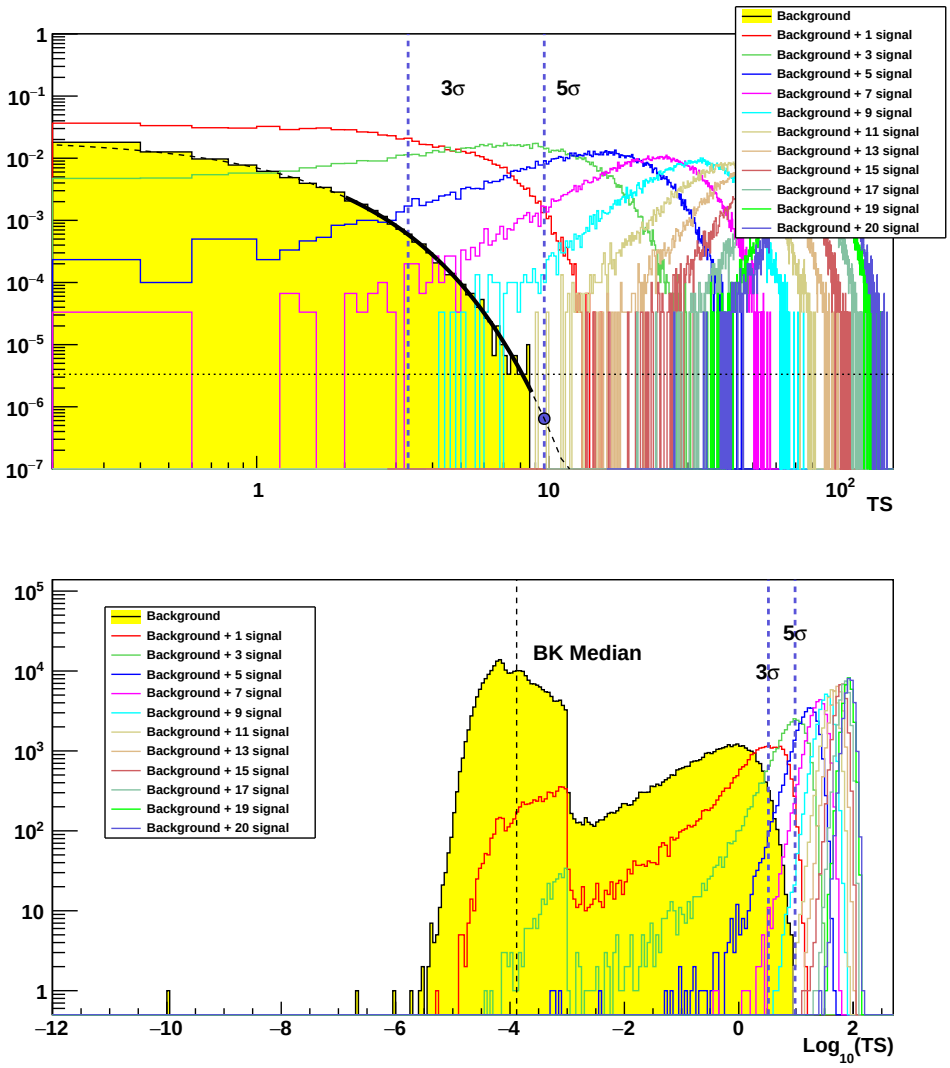

Fig. 6.6.: Sample TS distribution for Mrk 421 with $\Lambda > -5.2$ cut and E^{-2} energy spectrum. Also, the $\cos(\theta) > -0.1$ and $\beta < 1.0°$ cuts have been applied. *Top:* Probability distribution (normalized to unity) of the TS variable issued from PEXs for background-only H_0 (yellow area) and by adding from 1 up to 20 signal neutrinos $\mathcal{N}_S$ around the source (red, green, blue, ... etc colors represent $\mathcal{N}_S$ = 1, 3, 5, ... injected signal events). Dotted vertical lines indicate the threshold values for the 3σ and 5σ significances for the rejection of the background-only hypothesis. The dotted horizontal line marks the point below which the lack of statistics (one over the total amount of PEXs simulated) and implies an extrapolation by an exponential fit (broad black line) to estimate $TS_{5\sigma}$. The mean background events $\mu_B = 1.3 \cdot 10^{-4}$. *Bottom:* Probability distribution of the TS in Log_{10} horizontal scale. The minimum TS is 10^{-10}. Dotted vertical lines indicate the threshold values for the Median, 3σ, 5σ significances.

simulation due to lack of statistics. Thus, it requires extrapolation from an exponential fit performed on the tail of the TS distributions as shown in Fig. 6.6. As seen, due to lack of statistics for background distribution (yellow area in Fig. 6.6), the fit curve does not reach the $TS_{5\sigma}$ threshold, and an extrapolation gives $TS_{5\sigma} = 9.65$, while $TS_{3\sigma} = 3.30$ is obtained simply by count. The background mean is $\mu_B = 1.3 \cdot 10^{-4}$.

The capability of the TS to be higher than a certain significance X over the background-only hypothesis in the presence of a signal, called *discovery power*, can be established. The discovery power of the test, $DP_X^{50\%}$, for a certain TS_X, and is defined as the amount of signal required to have a test statistic TS over TS_X, 50% of the time. For example, discovery powers at 3σ and 5σ level are the amounts of signal required to have a TS over $TS_{3\sigma}$ or $TS_{5\sigma}$ respectively, 50% of the time (see Fig. 6.7). As seen in Fig. 6.6, the percentage of signals above $TS_{3\sigma}$ or $TS_{5\sigma}$ are almost 100% for more than 10-12 injected signals. Indeed, for 11 injected signal events, the distribution is barely intersected with $TS_{5\sigma}$ threshold as shown in Fig. 6.6.

The number of signal events for discovery can be converted into the equivalent source flux, called *discovery flux*, through the acceptance of the detector. Hence, the discovery fluxes for a certain significance, 3σ or 5σ, defines the minimum flux that could give a 3σ or 5σ evidence with 50% probability. Similarly to $DF_{3\sigma}^{50\%}$ and $DF_{5\sigma}^{50\%}$ discovery fluxes, the discovery flux level $DF_{\text{Median}}^{90\%\text{CL}}$ is defined as the sensitivity flux required to have a test statistic TS over the median of the background distribution TS_{Median} in 90% of the trials. The sensitivity flux places the upper limit on fluxes at 90% Confidence Level (CL). In the absence of a signal, it is used for 90% CL sensitivity calculations.

Cuts on the track-fit quality parameter, Λ, the estimated angular uncertainty on the fitted muon track direction, β, and the track elevation parameter, $\cos(\theta)$, are used to improve the signal-to-noise ratio. The analysis is performed for the one cut on the fitted muon track direction β and the reconstructed zenith $\cos(\theta)$. Hence, $\cos(\theta) > -0.1$ is used, which accepts a bit down-going events as it gives an increase of visibility for each source. The $\cos(\theta) > -0.2$ cut is not selected due to non-stability of the ratio between `DATA` and `MC` for this cut. Furthermore, the $\cos(\theta) > -0.1$ cut is traditionally used in ANTARES point-source analyses. The selection of $\beta < 1.0°$ ensures a rather good directional reconstruction of the selected neutrino candidates and enough statistics for the analysis. In the analysis, the Λ cut is optimized source by source for each spectra considered. For the Dataset 2014-2016 (see Section 7.3.1), the 9 Λ parameters in the range [-5.8;-5.0] with step=0.1 have been considered. This range is sufficient out of the full range of 13 Λ [-6.0;-4.8] which could be taken into account due to the vast decrease of the discovery fluxes outside of defined 9 Λ range and evidence of more stability of background time PDF (see Section 6.2.3) in this range. For the Dataset 2014-2017 (see Section 7.3.2), the 7 Λ parameters in the range [-5.6;-5.0] are considered to be sufficient according to the results with Dataset 2014-2016.

The spectra used in the analysis: a generic power-law $E^{-\gamma}$ with $\gamma = -2.0$ and $\gamma = -2.5$ covering most astrophysical models as well as power-law $E^{-\gamma}$ with $\gamma = -1.0$ and exponential cutoff at 1 PeV. In addition, the γ-ray derived neutrino spectrum $E^{-\gamma}$ with $\gamma = -2.25$ is considered for Mrk 501 (as suggested in [771]). In [771], for Mrk 421 the power-law spectrum with $\gamma = -2.0$ has been derived with the additional cutoff at ~5 TeV. Thus, since the ratio between cutoff for γ-ray and neutrino fluxes is not well known, such a spectrum is not considered for this analysis.

Consequently, the final set of spectra used in the analysis is:

- $E^{-\gamma} \cdot \exp(-E/E_{cut})$ with $\gamma = 1.0$ and cutoff at 1 PeV for both sources;
- $E^{-\gamma}$ with $\gamma = 2.0$ for both sources;
- $E^{-\gamma}$ with $\gamma = 2.5$ for both sources;
- $E^{-\gamma}$ with $\gamma = 2.25$ for Mrk 501 only.

6.5.1 Model Discovery Potential

The track quality parameter Λ has been optimized on the basis of maximizing the so-called Model Discovery Potential (MDP) for a 3σ evidence, $\text{MDP}^{3\sigma}$, or 5σ discovery, $\text{MDP}^{5\sigma}$, for each source and energy spectrum. The MDP is based on the evaluation of the probability at a certain significance level, e.g. 3σ, to make a discovery and is the Poisson convolution, $\mathcal{P}$, of the events expected from the model, μ_S, with the discovery power DP:

$$\text{MDP} = \sum_{s=0}^{\infty} \mathcal{P}(s|\mu_S) \times DP_S^{3\sigma}. \tag{6.15}$$

The value of μ_S can be computed via the detector acceptance, so that $\mu_S = \text{A}_{\text{cc}} \times \Phi$. It depends on the normalization (does not depend on the optimization) Φ_0 considered in the simulated flux, e.g. $\Phi = \Phi_0 E^{-2}$, $\Phi' = \Phi_0 E^{-2.5}$, etc.

The discovery power $DP^s_{3\sigma}$ (see Eq. 6.15) is obtained from the PEX simulation, and the only $N_S \leq 20$ are injected due to computation time limit. Such restrictions impose the use of an approximation in the MDP calculation [516]:

$$\text{MDP}(N_S \leq 20) \simeq \sum_{s=0}^{20} \mathcal{P}(s|\mu_S) \times DP_S^{3\sigma} + (1 - \sum_{s=0}^{20} \mathcal{P}(s|\mu_S)). \tag{6.16}$$

Figure 6.8 shows the MDP for different Λ cut as a function of μ_S. The contribution of the main sum and the approximated part is displayed. As seen, the contribution of the approximated part becomes significant only for $\mu_S \geq 10$, which are typically not reached. Nonetheless, the difference between the ideal MDP in Eq. 6.15 and the approximated one in Eq. 6.16 is negligible and the approximation is rather accurate. The difference is not shown in Fig. 6.8 because it is not distinguishable on a given scale. This difference becomes significant at $\mu_S \geq 10$ reaching only a few percent as discussed in [516] and in such case MDP$\rightarrow$1 regardless of the DP values. Figure 6.9 shows the MDP samples for both sources at 3σ level for the case of all flares selected for the analysis (see details in Section 7).

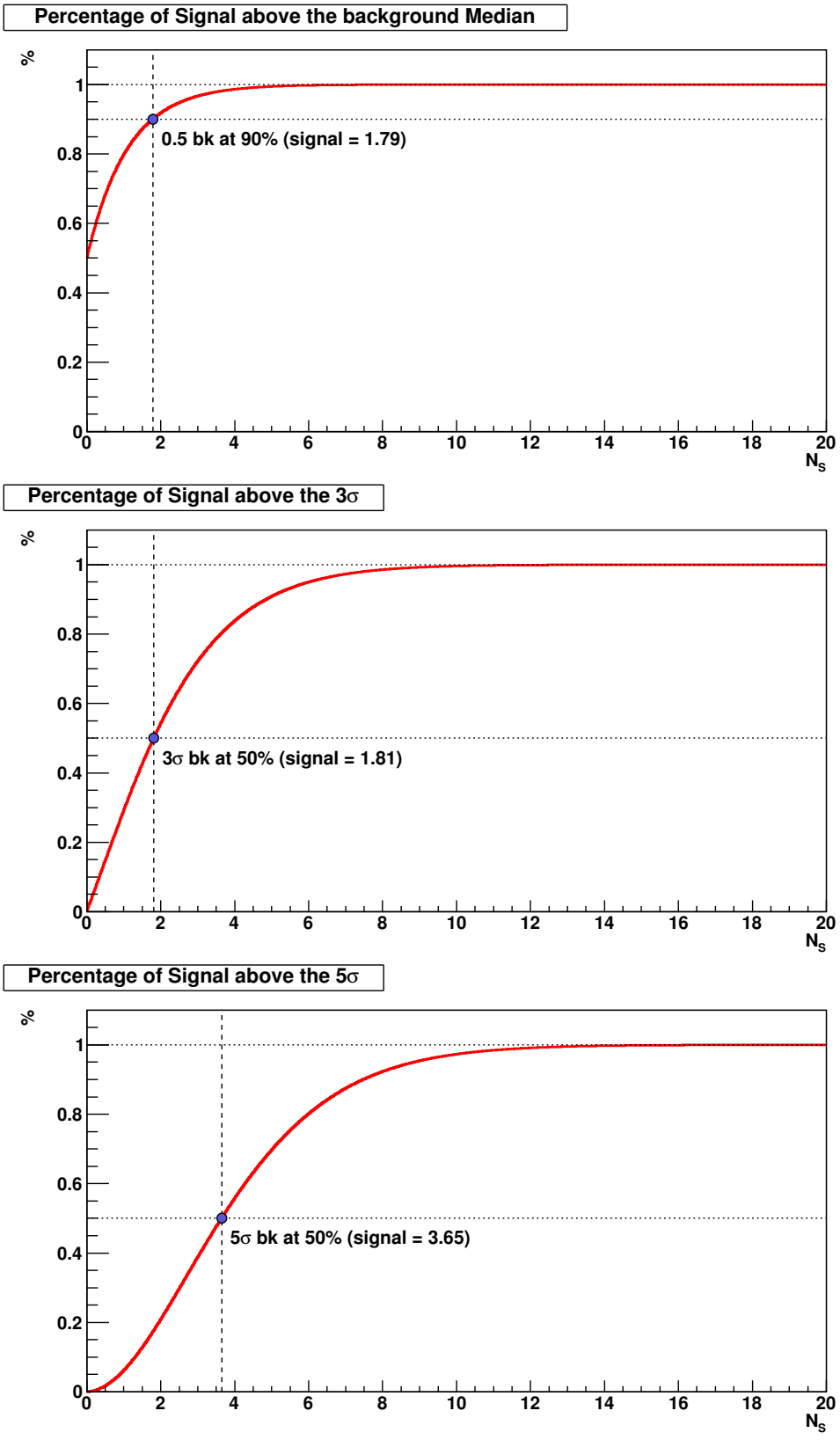

Fig. 6.7.: Samples of discovery powers $DP^{90\%}_{Median}$, $DP^{50\%}_{3\sigma}$, $DP^{50\%}_{5\sigma}$ as a function of the injected number of signal events for Mrk 421 with $\Lambda > -5.2$ cut and E^{-2} energy spectrum. Blue circles represent signals selected at $Median$, 3σ, 5σ levels.

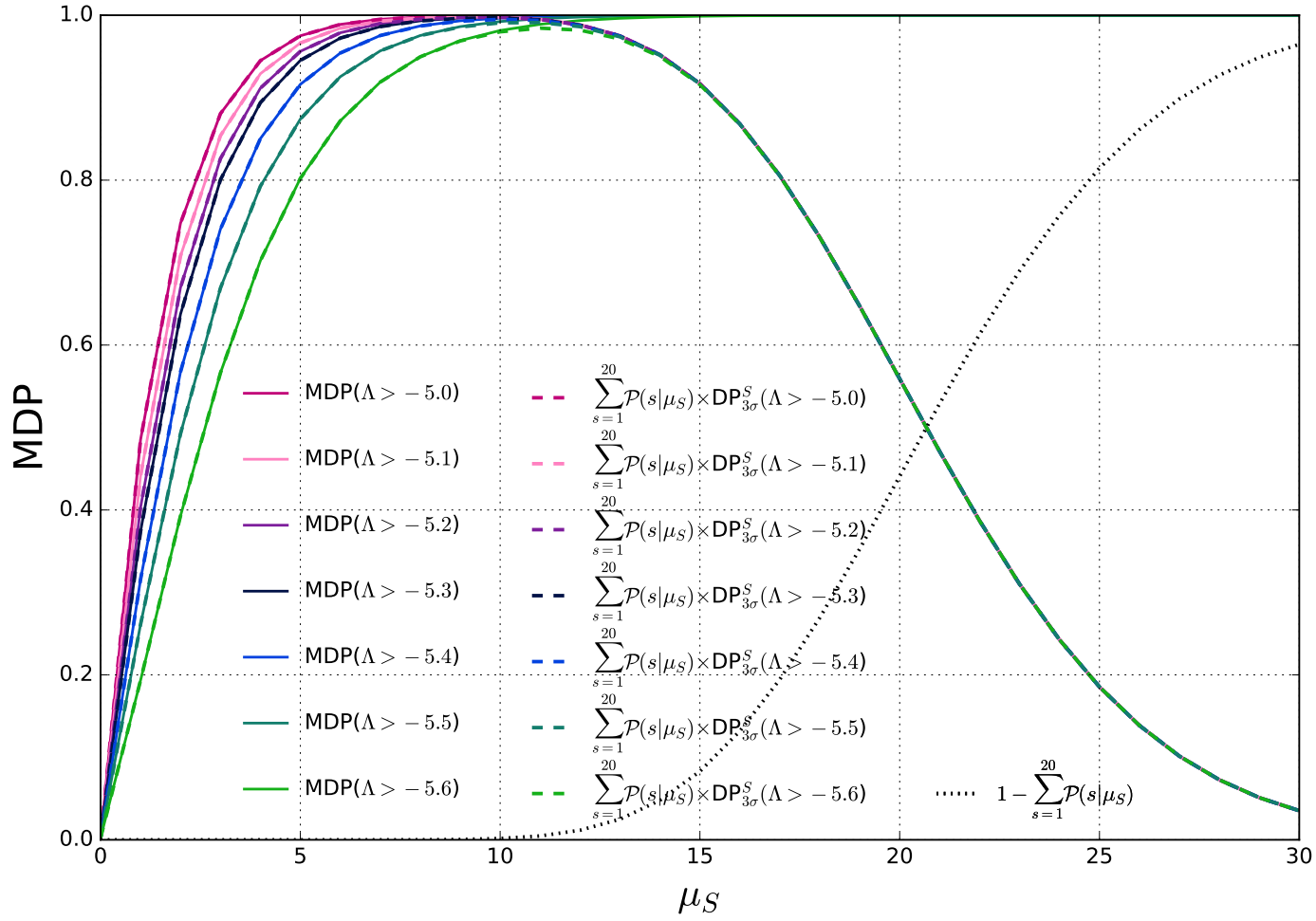

Fig. 6.8.: Sample of MDP values (solid) for DP distributions for $\Lambda > -5.0, -5.1, \cdots -5.6$ (in different colors) as a function of the expected events μ_S. The approximation for the MDP (solid line) is a sum of the $\sum_{s=0}^{20}\mathcal{P}(s|\mu_S) \times DP_S^{3\sigma}$ term (dashed line) and $(1 - \sum_{s=0}^{20}\mathcal{P}(s|\mu_S))$ term (dotted line).

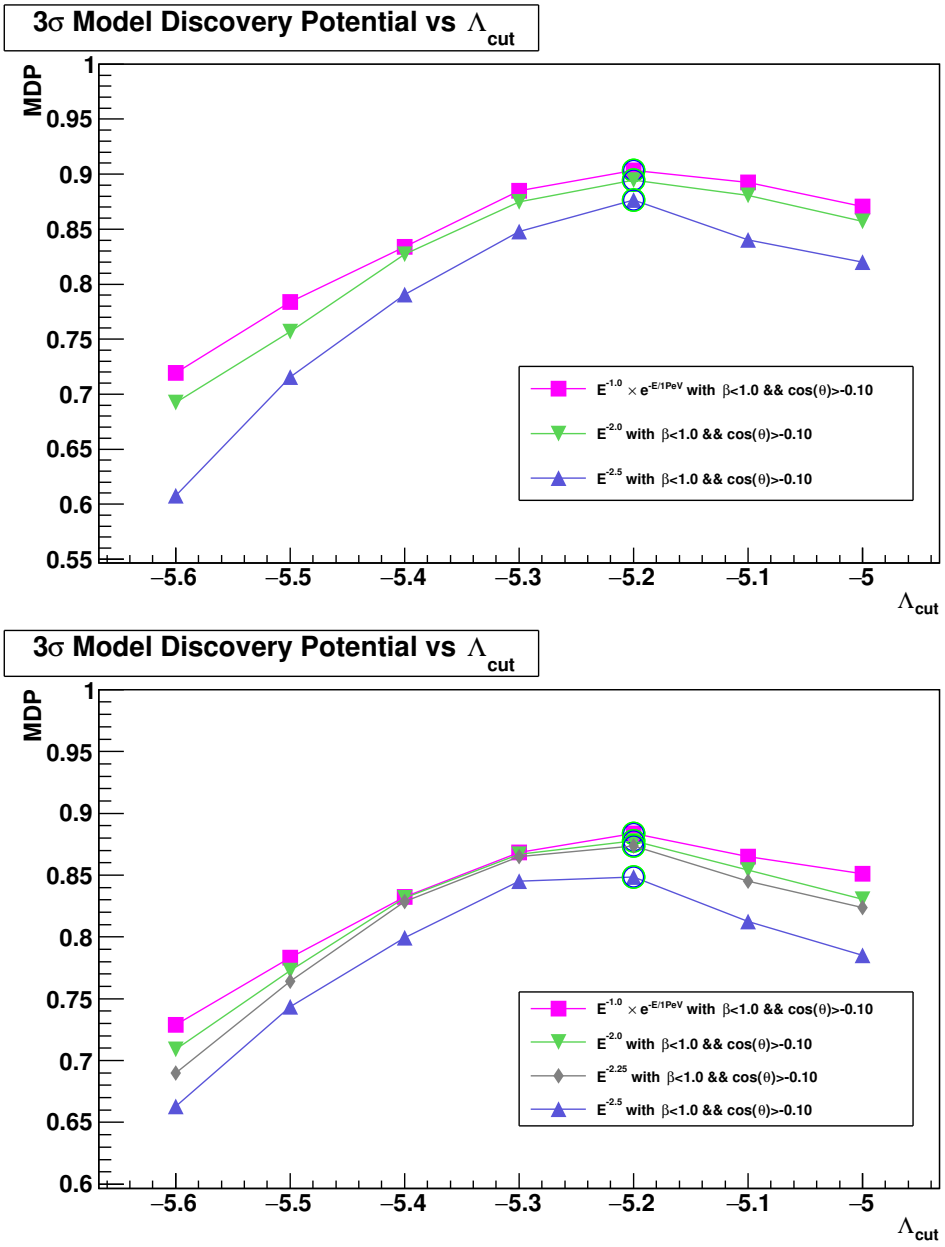

Fig. 6.9.: Sample of the Λ optimization by an MDP on Mrk 421 (*Top*) and Mrk 501 (*Bottom*) for the studied spectra. Light green color circles represent the Λ cuts that maximize the MDP.

6.5.2 Upper limits

If no discovery is made, the upper limits (ULs) on the neutrino energy flux, F, and fluence[6], $\mathcal{F}$, at 90% CL according the classical (frequentist) approach, Neyman's method [778], are established using 5-95% energy bounds, E_{min} and E_{max}[7], defined to contain 90% of neutrino signal events [178]:

$$F^{90\%CL} = \int E\,\Phi_E\,dE = \int E\,\Phi_0\,S(E)\,dE = \Phi_0^{90\%CL}\int E\,S(E)\,dE. \tag{6.17}$$

$$\mathcal{F}^{90\%CL} = \int F dt = F\Delta T = \Delta T\cdot\Phi_0^{90\%CL}\int_{E_{min}}^{E_{max}} E\,S(E)\,dE. \tag{6.18}$$

Here:

- ΔT is the livetime of the search $[s]$;
- $\Phi_0^{90\%CL} = \mathrm{DF}^{90\%CL}$ is the upper limit on the neutrino flux normalization $[\mathrm{GeV}^{-1}\,\mathrm{cm}^{-2}\,\mathrm{s}^{-1}]$;
- $S(E)$ is the dimensionless neutrino spectra $\left(\frac{\mathrm{E}}{\mathrm{GeV}}\right)^{-\gamma}$, and $\mathrm{dN/dE} = \Phi_0\cdot S(E)$;

[6] Fluence is the energy per unit area $[\mathrm{GeV\,cm}^{-2}]$

[7] The E_{min} and E_{max} are the energy range at which ANTARES is sensible for each spectrum $S(E)$ and source, and computed from the MC neutrino simulation used to calculate the PSF. The MC neutrino simulation extends up to 10^8 GeV.

7 Search for neutrinos from Mrk 421 and Mrk 501

> *It does not make any difference how beautiful your guess is. It does not make any difference how smart you are, who made the guess, or what his name is – if it disagrees with experiment it is wrong.*
>
> **— Richard Phillips Feynman**
> The Feynman Lectures on Physics

This chapter focuses on the search for neutrinos from Mrk 421 and Mrk 501, the two brightest and closest extragalactic sources in the TeV band. The Section 7.1 describes the sources and preparation of the signal time PDF applying the Bayesian block algorithm (see Section 7.1.2) to the γ-ray light curve data (see Section 7.1.1). The Section 7.2 discusses the visibility of the two markarians by the ANTARES detector. The overview of the ANTARES dataset used in this work is given in Section 7.3 and the DATA/MC agreement is discussed in Section 7.3.3. In the latter, the results (see Section 7.4) and its discussion (see Section 7.4.3) is given.

7.1 Sources: Mrk 421 and Mrk 501

Mrk 421 and Mrk 501 are two of the brightest and closest extragalactic sources in the TeV band. In contrast to other types of AGNs, BL Lacs are characterized by rapid and large-amplitude flux variability. Such radio-loud AGNs are candidate sources of the observed high-energy CRs [178]. Because their jet is collimated to our line of sight (see Fig. 7.1), the hadronic interactions with the surrounding medium can produce an accompanying neutrino and γ-ray flux. The recent detection of high-energy neutrinos from the direction of TXS 0506+056 (see Section 1.7.2) motivates a search for high-energy neutrinos from blazars with enhanced γ-ray activity [178]. Mrk 421 is known to exhibit a high degree of variability in its emission and yearly average fluxes are known to vary between a few tenths and ~ 1.9 times the flux of the Crab Nebula. Variability of Mrk 421 has been observed down to time scales of hours or less and its spectral shape known to vary with its brightness. Various studies of Mrk 501 at TeV energies have shown different features of low flux state emission and extreme outbursts [154].

These two targeted blazars are subject of long-term monitoring campaigns by the HAWC TeV γ-ray observatory located in Mexico.

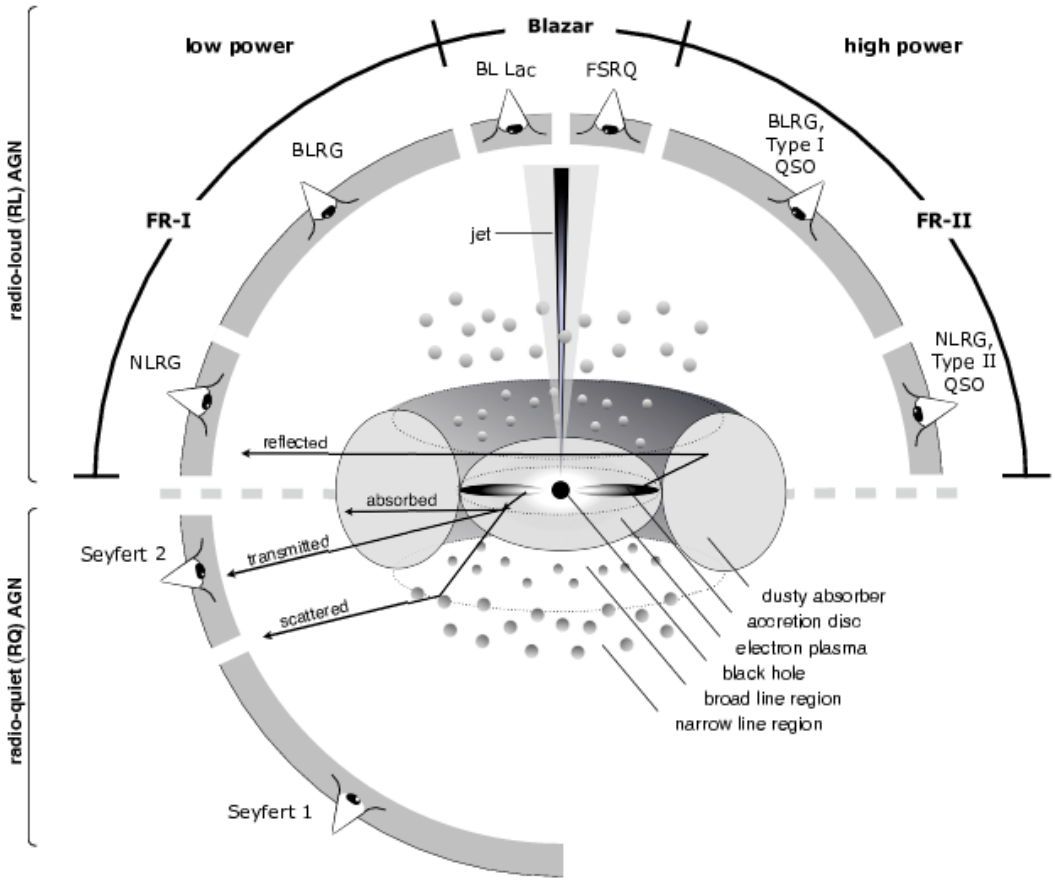

Fig. 7.1.: Schematic representation of our understanding of the AGN phenomenon in the unified scheme. The type of object we see depends on the viewing angle, whether or not the AGN produces a significant jet emission, and how powerful the central engine is. Note that radio loud objects are generally thought to display symmetric jet emission. The figure is taken from [410].

7.1.1 Light Curves

Taking advantage of γ-ray flux time variation information from potential neutrino emitters, the neutrino background can be significantly reduced and signal-to-noise discrimination improved [178]. HAWC has made clear detections of Mrk 421 and Mrk 501 and the last HAWC 1017 day light curves (LCs) of these blazars (see Fig. 7.2) are used to determine the periods of interest for the coincident neutrino search with Dataset 2014-2017 (see Section 7.3.2). The signal time PDF is assumed to have a square shape. The precise shape of the signal time PDF can be extracted directly for the γ-ray LC assuming the proportionality between the γ-ray and the neutrino fluxes [178].

7.1.2 Bayesian Blocks algorithm

The Bayesian blocks algorithm [779] can be applied to detect and characterize signals in noisy time series such as LCs. If an LC is variable, the Bayesian blocks algorithm can be used to find optimal data segmentation into regions that are well represented by constant flux,

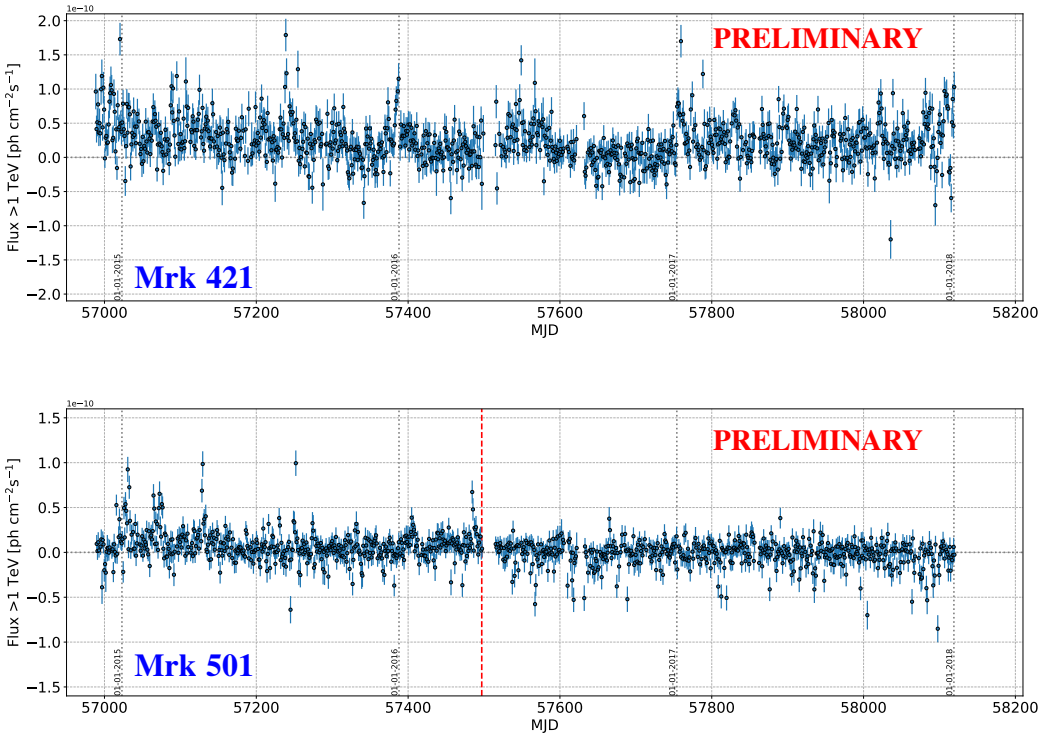

Fig. 7.2.: The LCs of both blazars credited by HAWC. The red dashed line represent the date outside of which there is no activity found (flat long block has been identified), hence the data is not used.

within the statistical uncertainties [154]. It identifies the changes between flux states via finding points at the transition from one flux state to another one and as a result distinguishes distinct flux states [154]. Both Mrk 421 and Mrk 501 show clear variability on time scales of one day [154].

In the HAWC 17-months analysis [154] the Bayesian blocks algorithm is used to identify the distinct flux states for Mrk 421 and Mrk 501 and the resulting distinct fluxes have been released in tabular form. In order to properly use such flare states information in the analysis, the 1-day binning was additionally applied. With the updated analysis using Dataset 2014-2017, the HAWC raw-data LCs are available, but not flare states blocks. Thus, the Bayesian Blocks algorithm has been applied. In order to find the change points at the transition from one flux state to the next, in [154] the so-called point measurements fitness function for the Bayesian blocks algorithm (Section 3.3 in [779]) has been adopted and later applied to the daily flux data points. In this work, the Bayesian blocks algorithm has been implemented according to the procedure in [154]. In addition, some functions have been adopted from the HAWC Public Datasets dedicated to the HAWC 17-months analysis [154].

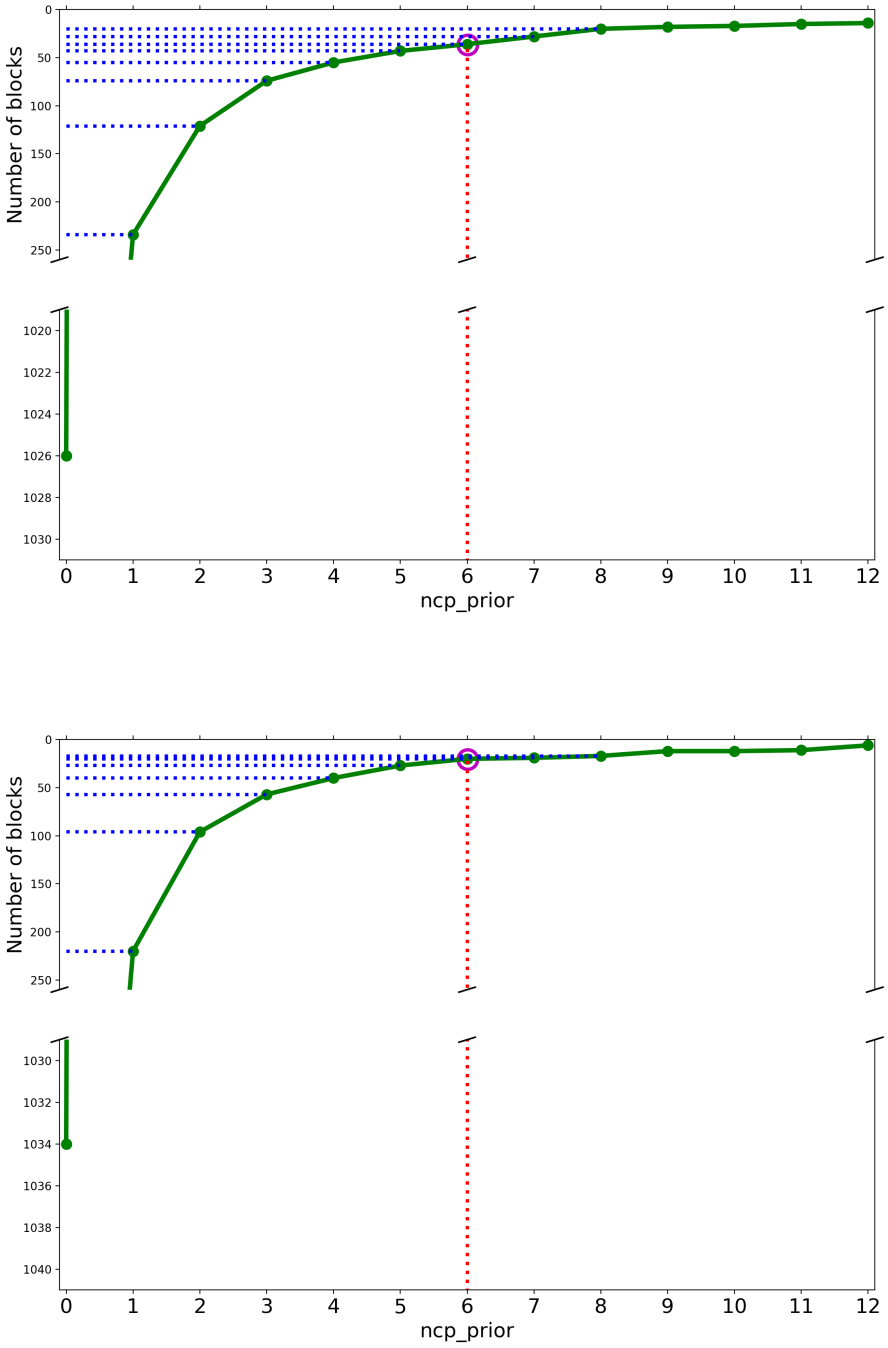

Fig. 7.3.: Bayesian blocks vs ncp_{prior}. *Top:* Mrk 421. *Bottom:* Mrk 501. The 1026 and 1034 blocks for $ncp_{prior} = 0$ are the total number of data points (or days of search) available for Mrk 421 and Mrk 501 respectively.

The Bayesian blocks algorithm requires the initial choice of a Bayesian prior, called $\mathrm{ncp}_{\mathrm{prior}}$, for the probability of finding a new change of flux states, where $\gamma = \exp(-\mathrm{ncp}_{\mathrm{prior}})$ is the constant factor defining a priori how much less likely it is to find $k+1$ change points instead of k points [154]. In the HAWC 17-months analysis [154] the predetermined 5% false positive probability is used. This value results in a relative frequency of 5% for identifying a change point that is not a true flux state change for each light curve [154]. To fulfill the 5% false positive probability for finding one change point, in [154] the $\mathrm{ncp}_{\mathrm{prior}} = 6$ has been adopted from simulations. Same $\mathrm{ncp}_{\mathrm{prior}} = 6$ value is used in this analysis. In addition, different $\mathrm{ncp}_{\mathrm{prior}}$ values have been tested, and $\mathrm{ncp}_{\mathrm{prior}} = 6$ seems to be reasonable (see Fig. 7.3). As axample, for Mrk 421 it has given almost the same block profile for the first 17 months as from the paper [154].

The Bayesian blocks algorithm with $\mathrm{ncp}_{\mathrm{prior}} = 6$ corresponding to a false positive probability of 5% identifies 36 and 30 change points in the LCs shown in Fig. 7.4 for both sources.

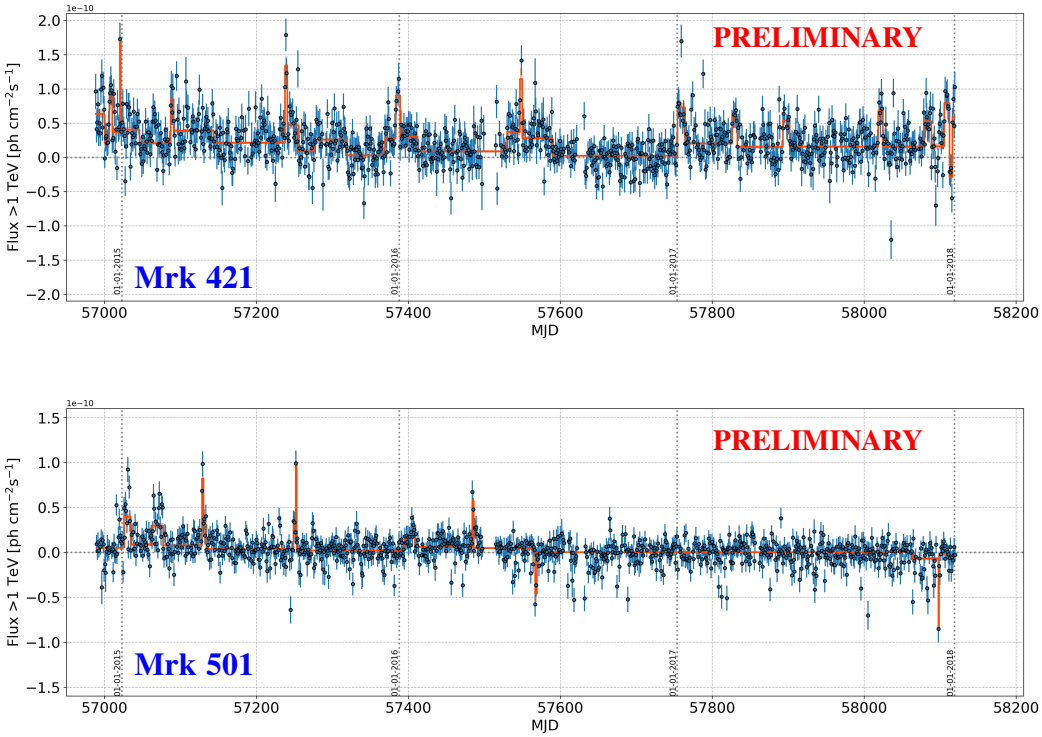

Fig. 7.4.: The HAWC daily flux LCs for Mrk 421 (*Top:*) with 1026 transits between November 27$^{\mathrm{th}}$, 2014 and January 1$^{\mathrm{st}}$, 2018 and for Mrk 501 (BF) with 1034 transits between November 28$^{\mathrm{th}}$, 2014 and January 1$^{\mathrm{st}}$, 2018. The orange lines show the distinct flux states between change points identified via the Bayesian blocks analysis with a 5% false positive probability and $\mathrm{ncp}_{\mathrm{prior}} = 6$. The orange shaded regions represent the statistical uncertainty of 1σ of the flux amplitudes for the periods between two change points.

7.1.3 Flare selection

In addition, several flare selection conditions are considered: all flare states are taken as they are (long case); only those flare states are taken which pass the defined thresholds (short case): *average flux*, *average flux+1*σ, *average flux+2*σ. Due to the shorter lengths of the flaring period that rejects more efficiently the background. Investigations done with Dataset 2014-2016 [177] show that *average flux+2*σ threshold is sufficient from a variety of thresholds have been tested for short case.

7.1.4 Final time PDFs

For the analysis, the 1-day binning is applied to the final distinct fluxes and used as a signal time PDF. Figure 7.5 and Figure 7.6 show the flare states versus threshold for Mr k 421 and Mrk 501 respectively. These time PDFs have been used for the analysis with Dataset 2014-2016.

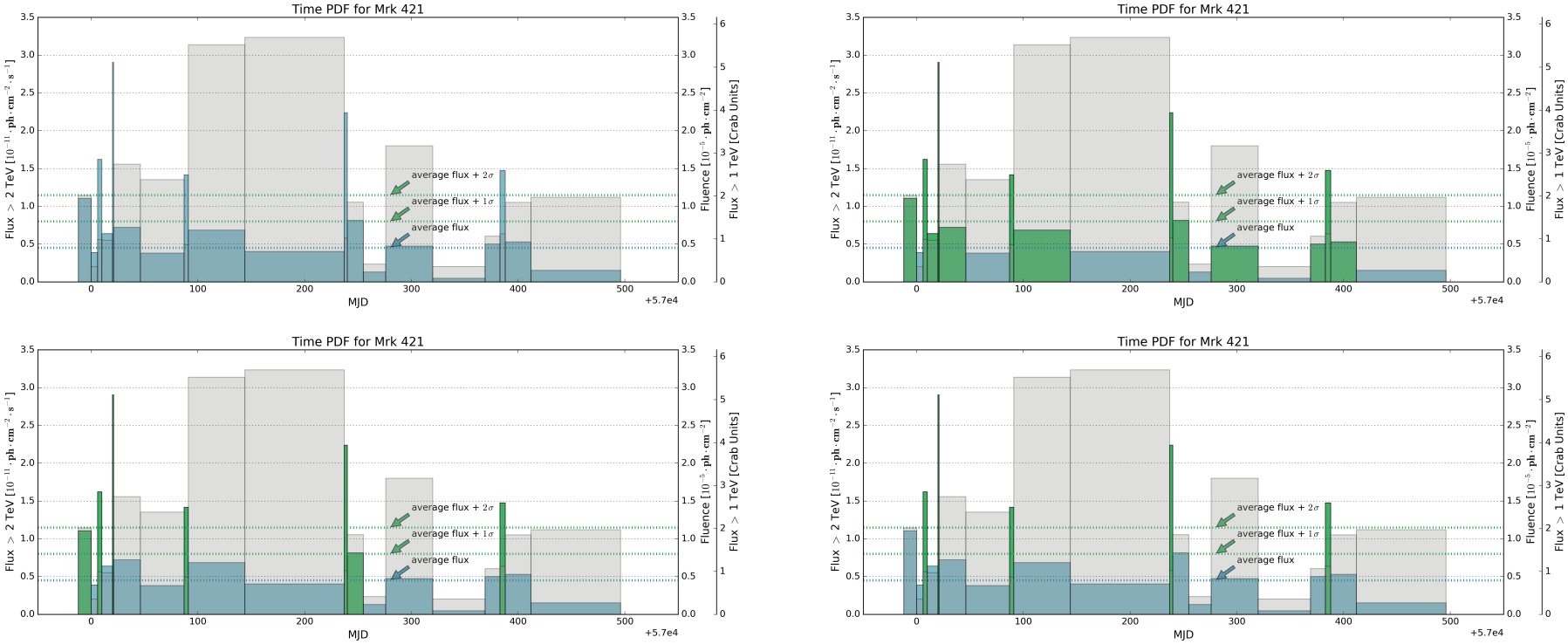

Fig. 7.5.: The time PDF for Mrk 421 vs threshold. The blue dotted line represent the average fluxes ~ 0.8 CU; the green dotted lines represent the peak selection thresholds: *average flux*, *average flux* + 1σ, *average flux* + 2σ. *Top Left: all flares*, *Top Right: average flux*, *Bottom Left: average flux* + 1σ, *Bottom Right: average flux* + 2σ. The left axes represent the units of the fluxes, the right-right axis represent the fluxes in corresponding Crab Units (CU). The right-left axes represent the units of fluences shown as shaded grey areas.

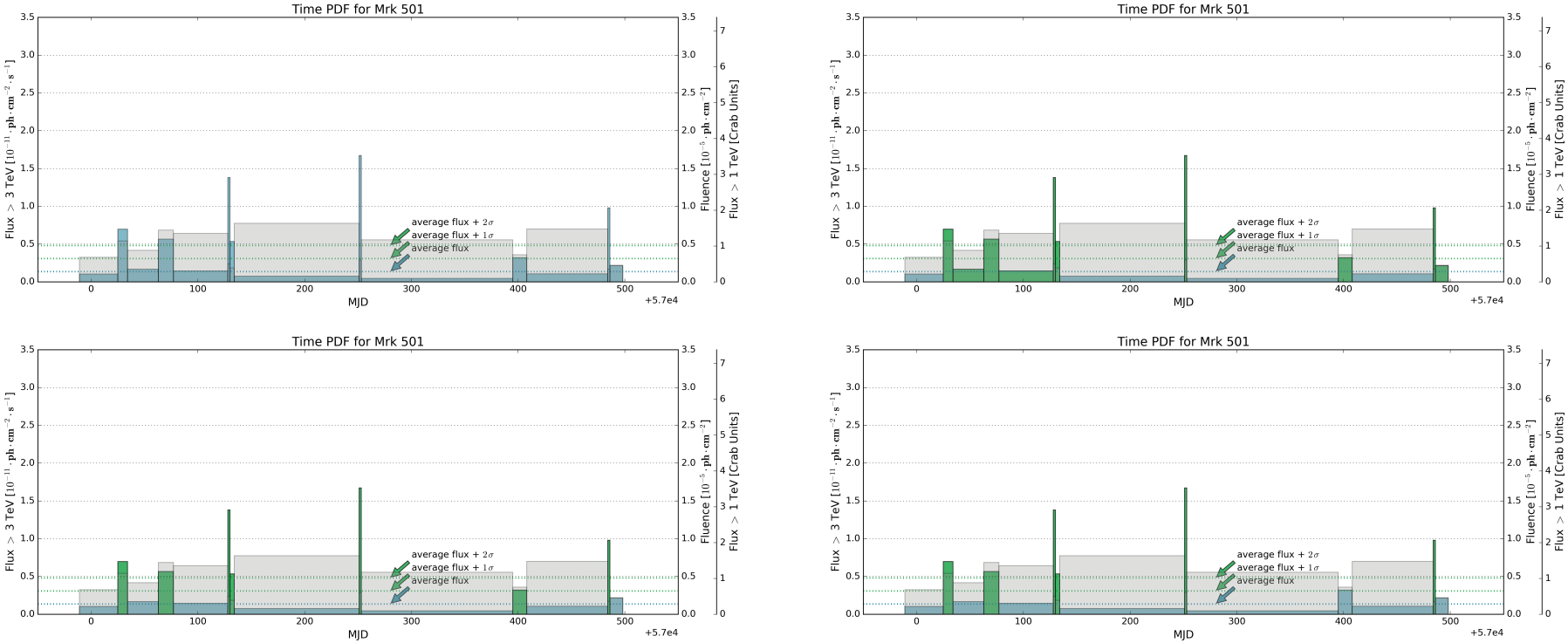

Fig. 7.6.: The time PDF for Mrk 501 vs threshold. The blue dotted line represent the average fluxes ~ 0.3 CU; the green dotted lines represent the peak selection thresholds: *average flux*, *average flux* + 1σ, *average flux* + 2σ. *Top Left: all flares*, *Top Right: average flux*, *Bottom Left: average flux* + 1σ, *Bottom Right: average flux* + 2σ. The left axes represent the units of the fluxes, the right-right axis represent the fluxes in corresponding Crab Units (CU). The right-left axes represent the units of fluences shown as shaded grey areas.

The Bayesian blocks analysis (see Section 7.1.2) for Mrk 501 returns the negative flux amplitude values for the period of approximately during the last 2 months of the 2017 year (see Fig. 7.4) just after MJD=58063 and for the short period around MJD=57568. Moreover, it gives one single block between those two periods with roughly 500 days of duration and positive flux amplitude but very low w.r.t. any other positive distinct flare state fluxes (around one order of magnitude less) obtained for this source. Such a low value can be treated as zero, and the corresponding block with surrounding blocks having negative values have been together excluded from the analysis. In that case, the Bayesian blocks have been recalculated for Mrk 501, but for a new shorter period from the November 28$^{\text{th}}$, 2014 to June 28$^{\text{th}}$, 2016 (MJD: 56989-57567). The final time PDFs for Mrk 421 and Mrk 501 are shown in Fig. 7.7 and in Fig. 7.8 respectively.

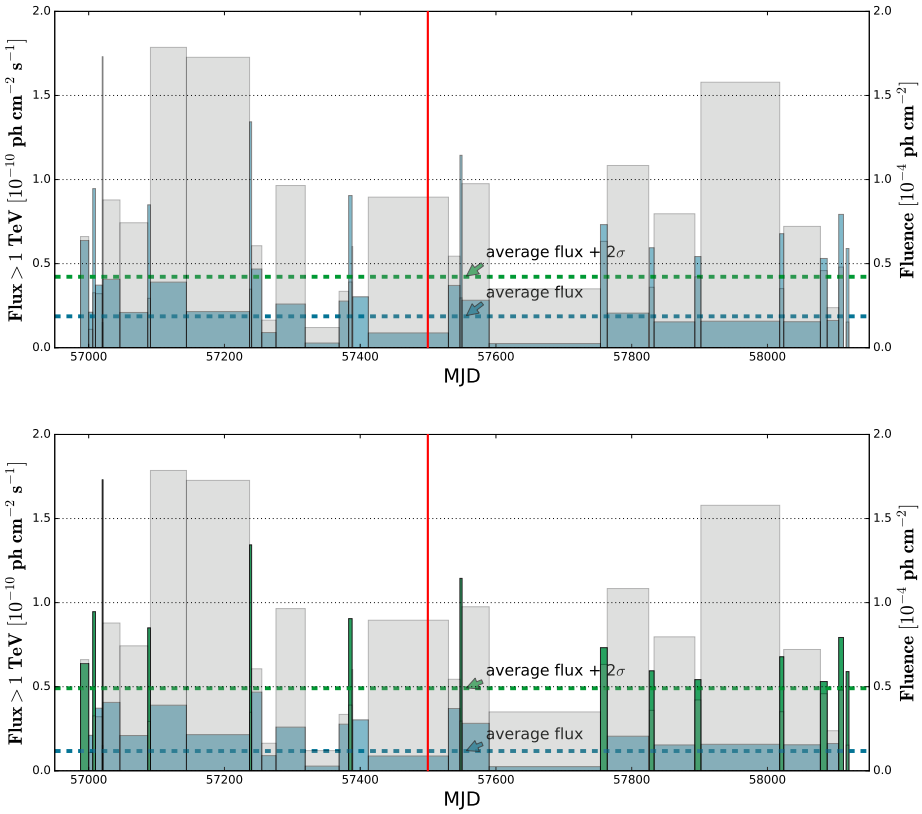

Fig. 7.7.: The time PDF for Mrk 421 vs threshold. *Upper plot* The long case. *Lower plot* The short case for *average flux* + 2σ. The blue dotted line represents the average flux; the green dotted line represents the *average flux* + 2σ peak selection threshold. The left axis represents the units of the flux, the right axis represents the units of the fluences shown as shaded grey areas. The red line represents the edge of the period of interests in the analysis based on HAWC 17 months search [154].

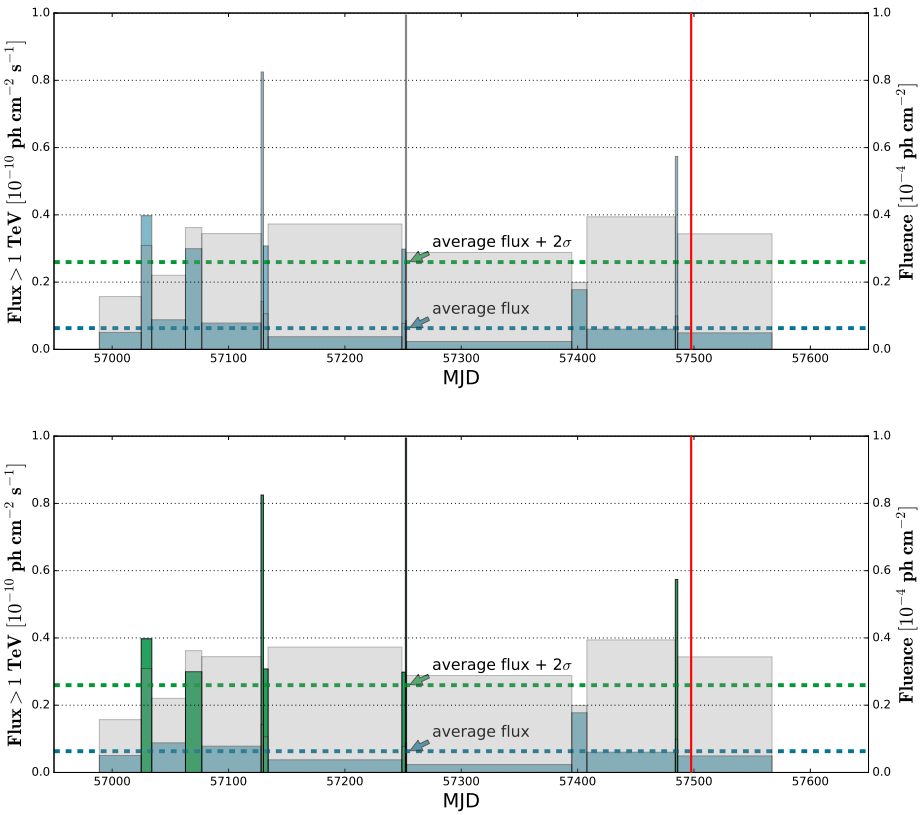

Fig. 7.8.: The time PDF for Mrk 501 vs threshold. *Top:* The long case. *Bottom:* The short case for *average flux* + 2σ. The blue dotted line represents the average flux; the green dotted line represents the *average flux* + 2σ peak selection threshold. The left axis represents the units of the flux, the right axis represents the units of the fluences shown as shaded grey areas. The red line represents the edge of the period of interests in the analysis based on HAWC 17 months search [154].

7.2 The ANTARES visibility of the Markarians

The ANTARES neutrino telescope is located at a latitude of 42°48N latitude and can monitor with only up-going events a wide range of the sky, $\delta \in [-90°, +42.8°]$. Due to the fact that Mrk 421 and Mrk 501 are located at the edge of ANTARES visibility (see Fig. 7.9 and Fig. 7.10), a small amount of down-going events close to the horizon can be accepted to gain $\sim 15\%$ in visibility (see Table 7.1). The ANTARES visibility is a fraction of time that the source is visible by ANTARES due to its declination δ and selected event cuts. In this analysis events with maximum $\cos(\theta) > -0.1$ are selected and the optimization will be done with this cut on the reconstructed zenith. Because of expectation that gain in discovery flux is commensurate with increase of visibility w.r.t. $\cos(\theta)$, the possible extension up to $\cos(\theta) > -0.5$ (see Fig. 7.10) added to estimate the capacity of gain in discovery flux whether $\cos(\theta) > -0.3$ (grey dotted line), $\cos(\theta) > -0.4$ (grey dashed line), or $\cos(\theta) > -0.5$ (grey solid line) applied. A proper cut on zenith angle is essential to limit the contribution from mis-reconstructed atmospheric muons. But due to observed improvement in discovery flux w.r.t. increase in visibility (with the maximum cut on zenith angle $\cos(\theta) > -0.1$ currently applied and giving better discovery flux), it can be assumed a chance to enhance the discovery flux via application of cut on zenith angle above $\cos(\theta) > -0.1$.

Tab. 7.1.: Visibility and Ratio

	(δ, RA)	$\mathrm{V.}^{\mathrm{up}}$	> -0.1	> -0.2	> -0.3	> -0.4	> -0.5
Mrk 421	(38.2,166.1)	24.0	31.5(1.31)	37.7(1.57)	43.6(1.81)	49.0(2.05)	54.5(2.28)
Mrk 501	(39.8,253.5)	21.9	29.7(1.36)	36.2(1.65)	42.2(1.93)	48.2(2.20)	53.8(2.46)

* Visibility in %.

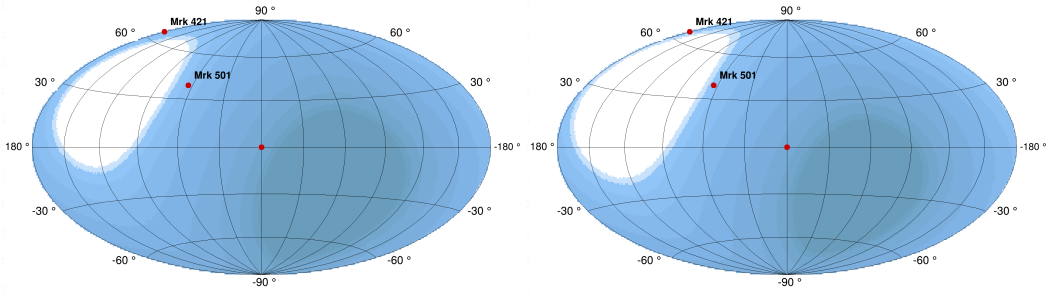

Fig. 7.9.: ANTARES visibility of the sky ranging from 0 (white) to 100% (dark blue) with 10% step. *Left:* Up-going with slightly down-going (angle above the horizon below 5.74°) for $\cos(\theta) > -0.1$; *Right:* Only Up-going $\cos(\theta) > 0$.

The elevation for the sources is shown in Fig. 7.11. As seen from the Fig. 7.11, e.g., the Mrk 421 is below the horizon for only $\sim$ 6 hours per day ($\sim 24\%$ as from the $\mathrm{V.}^{\mathrm{up}}$ in Table. 7.1). For $\cos(\theta) > -0.1$ and $\cos(\theta) > -0.2$ it gives roughly $\sim$ 2h and $\sim$ 3.5h gain respectively in addition to $\sim$ 6h ($\sim 31\%$ and $\sim 57\%$ respectively as from the ratios in Table. 7.1).

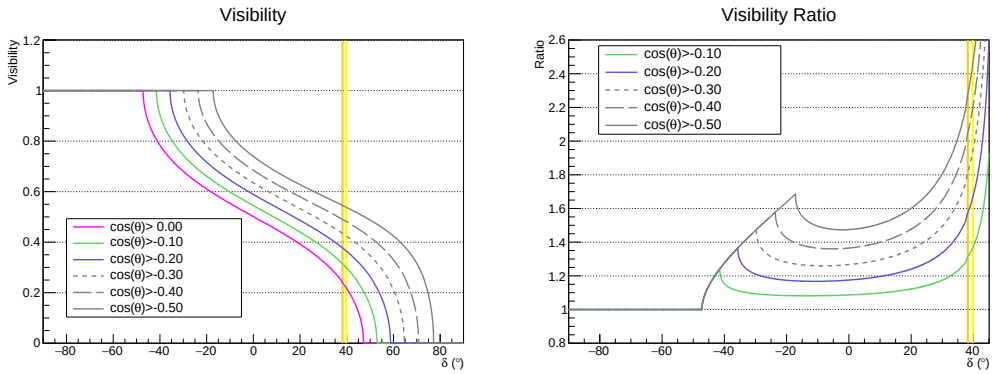

Fig. 7.10.: *Left:* Visibility curves as a function of the declination for cuts on zenith angle used in the analysis $\cos(\theta) > 0.0$, $\cos(\theta) > -0.1$, $\cos(\theta) > -0.2$ (colored solid lines) and for possible extension up to $\cos(\theta) > -0.5$ (grey color dotted, dashed and solid lines respectively). *Right:* Visibility ratio curves as a function of the declination with respect to $\cos(\theta) > 0.0$. The vertical color lines represent the declination of Mrk 421 (orange) and Mrk 501 (yellow).

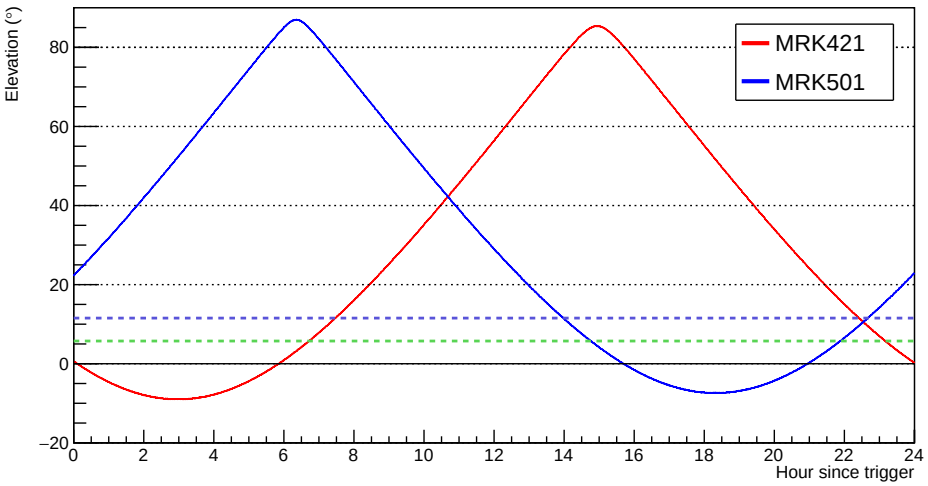

Fig. 7.11.: Elevation of the sources (in degrees). The green and blue dotted lines represent the improvement in the visibility for the $\cos(\theta) > -0.1$ and $\cos(\theta) > -0.2$ cuts and corresponds to 5.74° and 11.54° elevation levels respectively.

7.3 The ANTARES dataset

For the analysis, the only runs are selected that fulfilles the quality conditions below:

- `QualityBasic` >= 1. This flag warranties the quality of the run.
- `SCAN` =! 1. The flag used for runsetup not present the ”SCAN” word in its name, which ensures that the run was taken with the fixed setup parameters stored in the data base.
- No sparking. Sparking runs have an extraordinary rate of events with a remarkable amount of hits, generally above 300, and are associated to unusual bioluminescence activity or sparking OMs. Addition sparking runs observed in the dataset were removed.

The search relies on track-like event signatures, so only CC interactions of muon neutrinos are considered.

7.3.1 Dataset 2014-2016

The selected dataset covers the same period of observation as HAWC, so that the period from the November 26th, 2014 and April 20th, 2016 (MJD: 56988-57497) leading to effective detector livetime of 503.7 days (1.379 years).

The MC production is selected to be complete, i.e. `MUPAGE` and all track-like (a)numu files were available. Besides, since not all DATA runs have a corresponding MC runs and MC complete runs give livetime of 332.8 days (0.911 years), rescaling of incomplete MC is required. Thus, rescale of available MC livetime up to livetime in DATA is applied. It is considered as an additional weight on the MC in order to take into account the livetime difference and done on a year-to-year basis $LT^{DATA}_{year}/LT^{MC}_{year}$. The importance of the MC rescale can be seen in Fig. 7.12, where shaded red area represent fully OFF days in the case if only DATA-MC complete runs to be considered (the list of fully OFF days in such case is collected in Table A.5 in Appendix A.3.1). Obviously, significant amount of time would be excluded from the analysis and some substantial high peaks would be not considered due to OFF days. Such situation leads to null probability in the time distribution of DATA events $P_B(t)$ used in the PEXs to simulate time of the events. This, in turn, able to decrease neutrino discovery potential vastly.

In addition, the part of the Dataset 2014-2016 inherently has a pre-selection cuts, such as $\Lambda > -6.0$ and $\beta < 1.5$ and $\cos(\theta) > -0.2$, thus in order to unify the different parts of the data, these cuts are applied on the whole period as the global cuts.

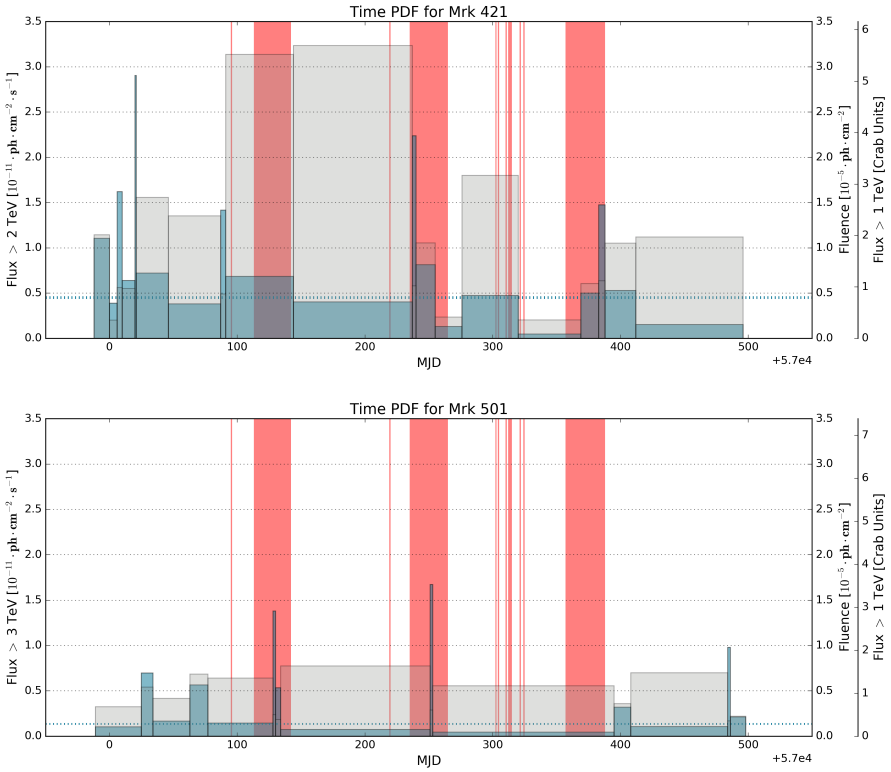

Fig. 7.12.: The flare states of the sources (in blue) and the incomplete MC period (in red). *Top:* Mrk 421. *Bottom:* Mrk 501. The blue dotted lines represent the average fluxes of the sources, $\sim$ 0.8 CU (Mrk 421) and $\sim$ 0.3 CU (Mrk 501). The left axes represent the units of the fluxes, the right-right axis represent the fluxes in corresponding Crab Units (CU). The right-left axes represent the units of fluences shown as shaded grey areas.

7.3.2 Dataset 2014-2017

The selected dataset covers the same period of observation as HAWC. The dataset selected for the Mrk 421 covers the period from the November 27$^{\text{th}}$, 2014 to January 1$^{\text{st}}$, 2018 (MJD: 56988-58119) leading to effective detector livetime of 1099.93 days (3.009 years), which doubles the previous search period of 503.7 days (1.379 y) (see Section 7.3.1). As shown in Section 7.1.2, the period has been cutted for Mrk 501 due to some period not possible to be defined as having distinct flare states. Thus, the data set selected for the Mrk 501 covers the period from the November 28$^{\text{th}}$, 2014 to June 28$^{\text{th}}$, 2016 (MJD: 56989-57567) leading to effective detector livetime of 561.55 days (1.537 years), which increases search period by $\sim$ 10% w.r.t. the previous 503.7 days (1.379 y) (see Section 7.3.1). As for the Dataset 2014-2016, not all DATA runs have a corresponding MC runs and MC complete runs give smaller value as shown in Table 7.2: Thus, as for Dataset 2014-2016, the rescale of available MC livetime up to livetime in DATA is applied. It is considered as an additional weight on the MC in order to take into account the livetime difference and done on a year-to-year basis $\text{LT}^{\text{DATA}}_{\text{year}}/\text{LT}^{\text{MC}}_{\text{year}}$. Since in the Dataset 2014-2017 no pre-selection are inherited, thus no global cuts applied on the whole period as it has been forcedly done with the Dataset 2014-2016 (see Section 7.3.1). So, no preliminary cuts on Λ, β and $\cos(\theta)$ applied.

Tab. 7.2.: Effective livetime vs MC complete period

Source	Effective LT	MC complete
Dataset 2014-2017 [Mrk 421]	1099.93 d (3.009 y)	993.83 d (2.721 y)
Dataset 2014-2017 [Mrk 501]	561.55 d (1.537 y)	462.13 d (1.265 y)
Dataset 2014-2016 [both]	503.70 d (1.379 y)	332.80 d (0.911 y)

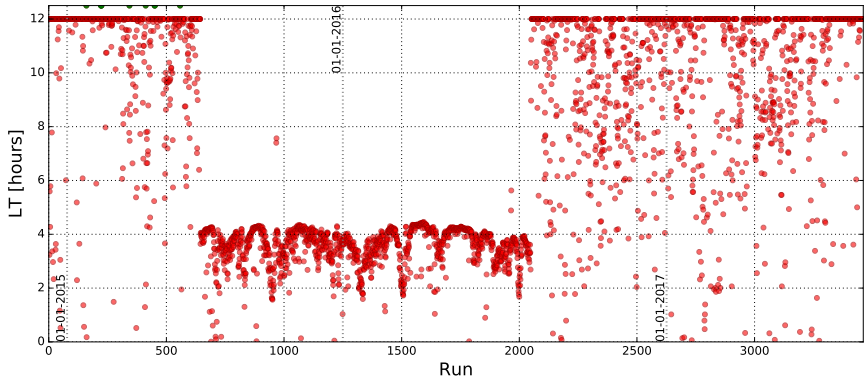

Fig. 7.13.: Livetime of 3461 runs selected for Dataset 2014-2017 (ranked from 1 to 3461). ANTARES is taking data with runs whether 12 hours or 4 hours in duration. Some special runs with much longer runs (not to scale) are marked by green color.

A variety of checks underlie of runs selection. In addition to the selection procedure w.r.t. to quality conditions (see Section 7.3), the runs are checked to not contain zero events or an extraordinarily high number of events (= sparking runs). As shown in Fig. 7.13, ANTARES is taking data with a run duration of 12 hours except for some periods where the average run duration was 4 hours. Figure 7.14 shows the runs with the number of events normalized to the run duration. As seen, no run contains zero events and each run has almost the same event rate of ~5 events per hour whether the data is taken 12 hours or 4 hours. As can be seen, some runs show drops in the events rates which correlates with the duration of data-taking (see Fig. 7.14, *Bottom*, which is a zoom of *Top* around 2100th run in the dataset). In addition, in Fig. 7.15 runs with different ranges of a number of events are shown in different colors, where it is clearly seen that drops in events rate are associated with the shortest runs which happened during the time when ANTARES was taking data with runs 12 hours in duration as standard. One might conclude that such correlations in Fig. 7.14 and Fig. 7.15 are due to manual interventions due to some run conditions itself, e.g., early stops during shifts or due to problems with some storeys and lines, etc.

Figure 7.16 displays a skymap with the events selected after $\Lambda > -5.2$ cut has been applied. In Appendix A.4, all skymaps of the track-like events passing different selection cuts on Λ used for Dataset 2014-2017, are presented.

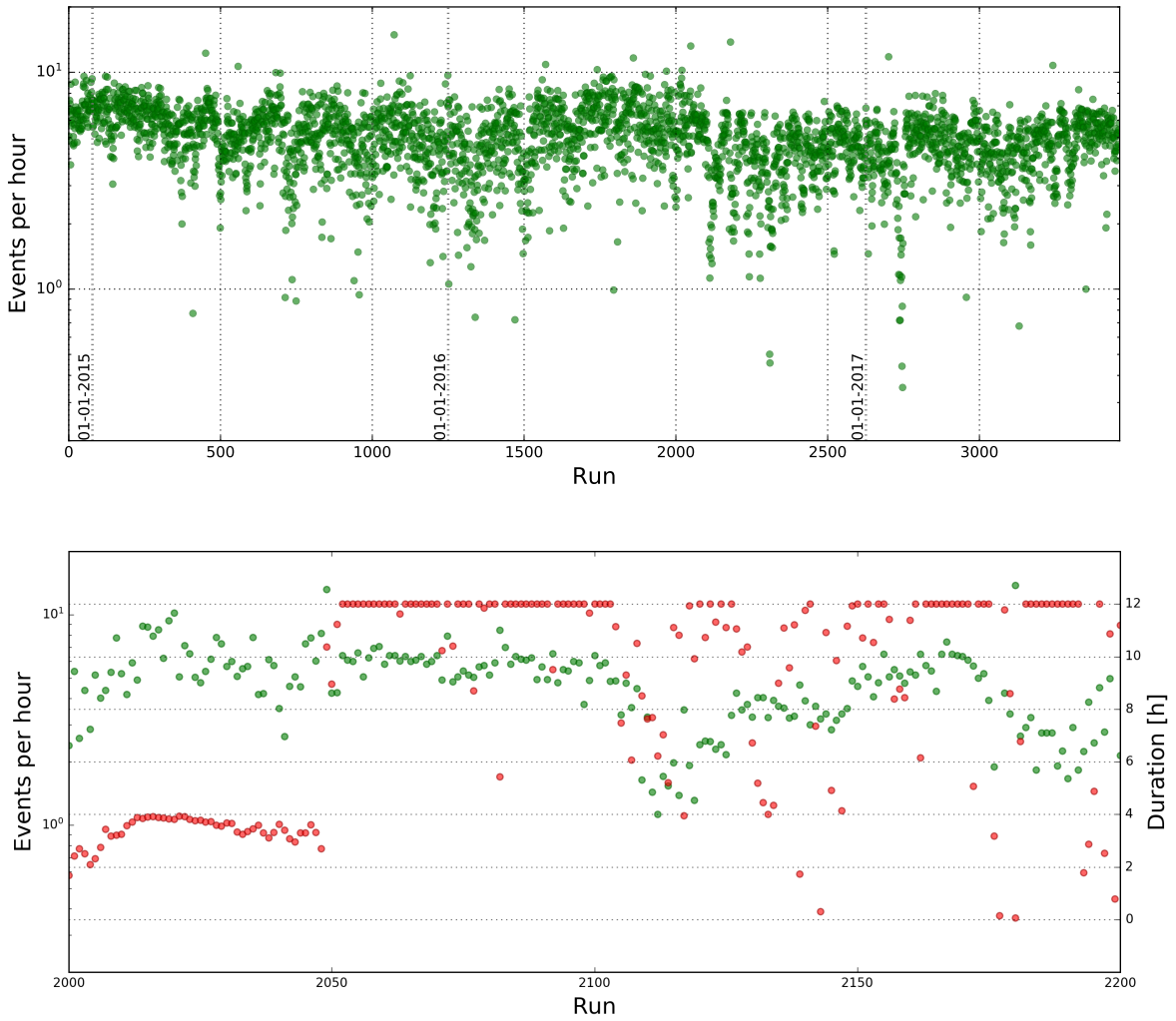

Fig. 7.14.: Events rate for each run (*Top*) with zoom around 2100th run (*Bottom*). The left axis shows the events rate (green circles) in each run, while the right axis shows the duration (red circles) of the runs.

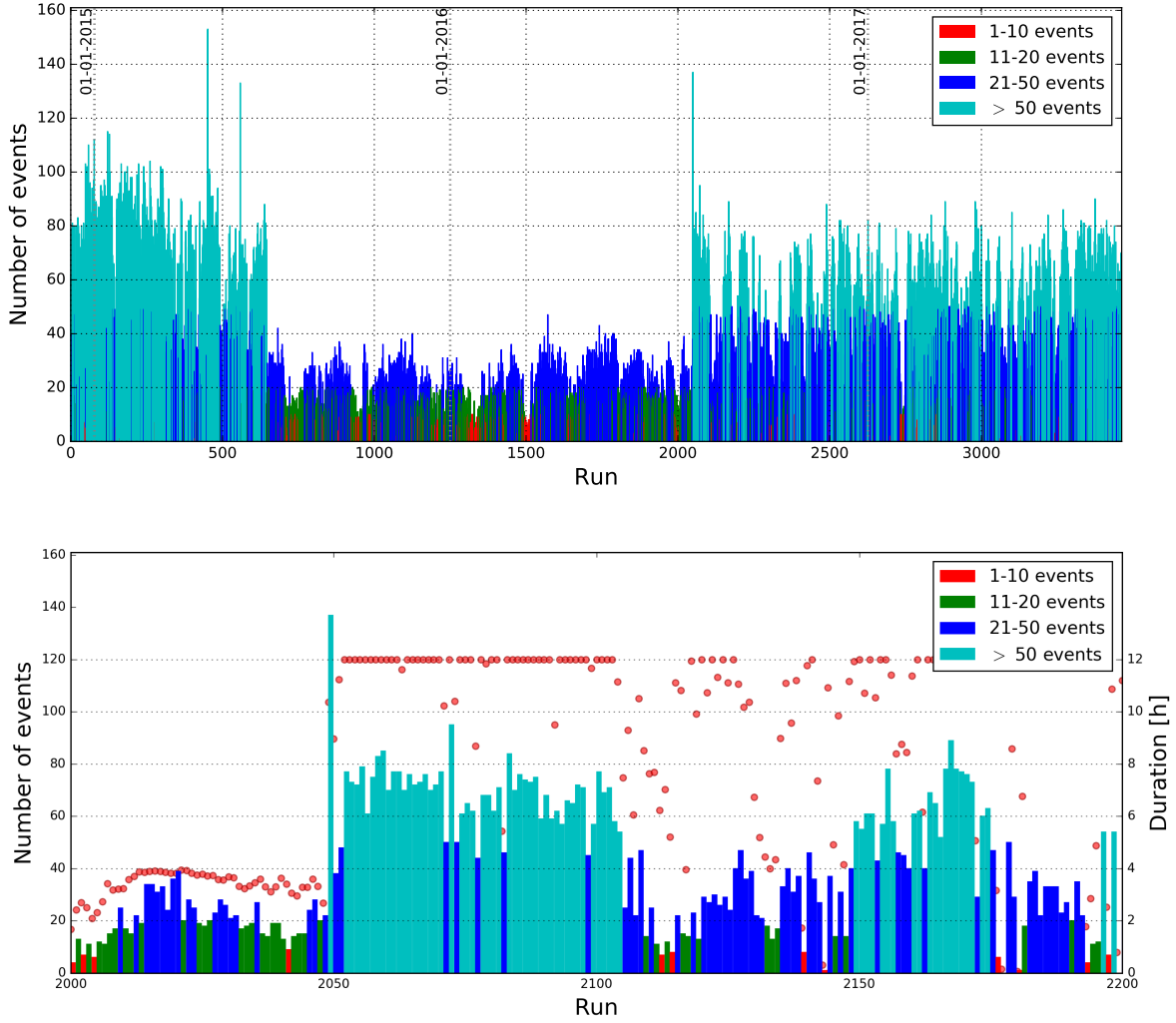

Fig. 7.15.: Number of events for each run (*Top*) with zoom around 2100th run (*Bottom*). The left axis shows the total number of events (green circles) in each run, while the right axis shows the duration (red circles) of the runs.

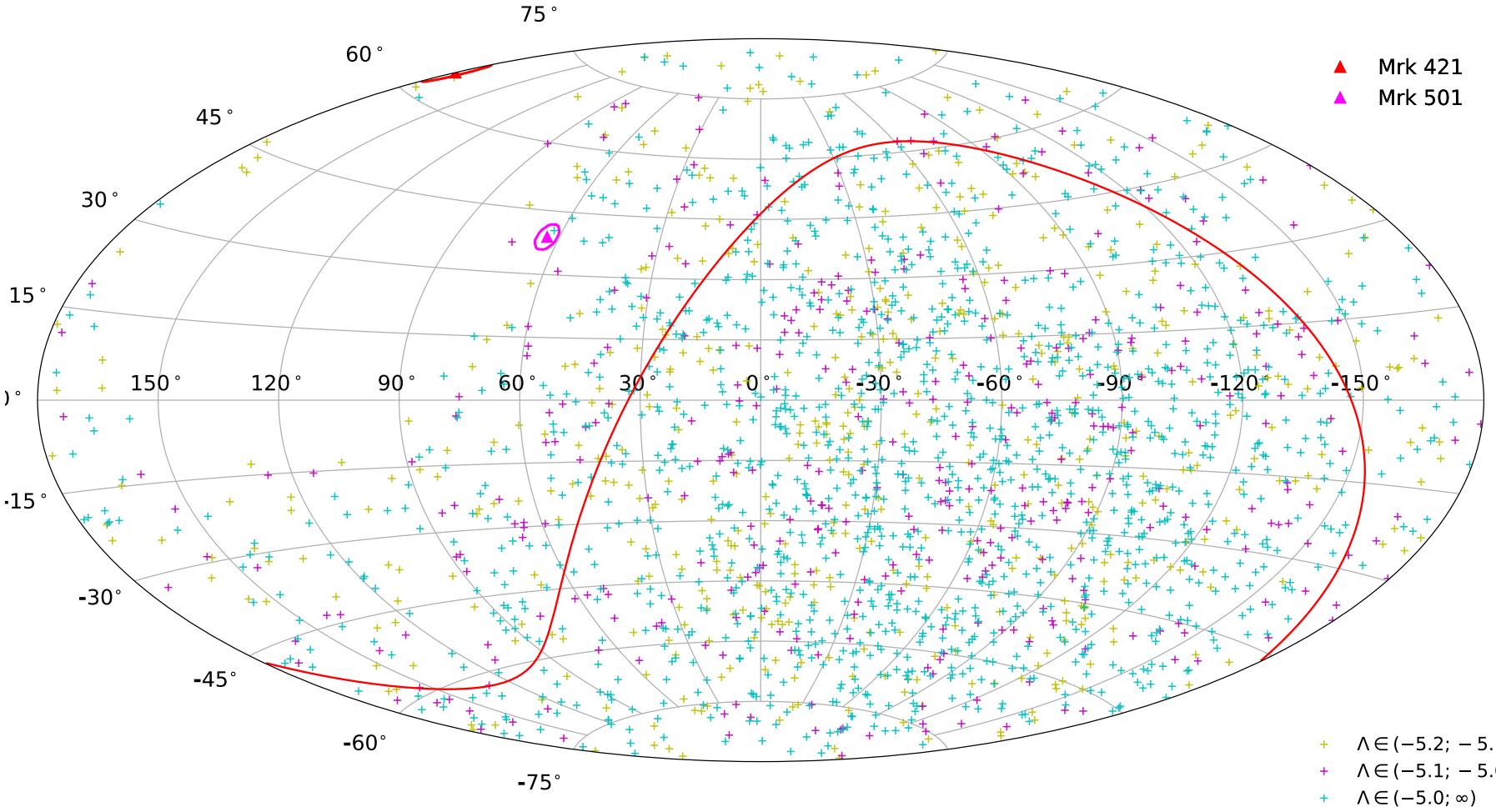

Fig. 7.16.: Skymap of the track-like events passing the selection cuts (total 2286 events selected with $\Lambda > -5.2$) for Dataset 2014-2017. In galactic coordinates using Aitoff projection. The red solid curve denotes the equatorial plane. The red circles denote the 3° radius region around the sources.

7.3.3 DATA/MC agreement

In order to test the goodness of the ANTARES MC production for the period of the analysis, it is compared with measured data. The DATA/MC agreement plots for the energy estimator nhit and for Λ, $\cos(\theta)$, β cuts with non-normalized distributions and with indicated MC contributions (up-going atmospheric neutrinos and mis-reconstructed atmospheric muons) are displayed in Fig. 7.17 (for Dataset 2014-2016) and in Fig. 7.18 (for Dataset 2014-2017).

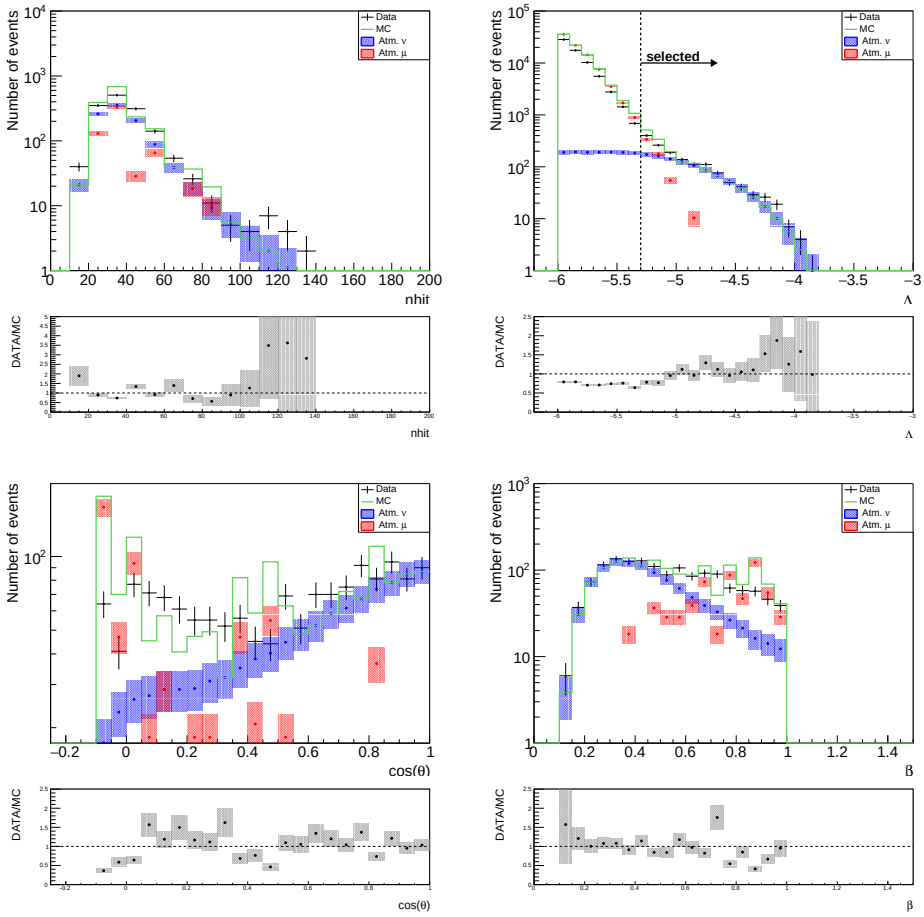

Fig. 7.17.: Comparison of the data with MC simulations as a function of the number of hits nhit (*Top Left*), the quality parameter of the reconstruction of muon track Λ (*Top Right*), the reconstructed cosine of the zenith angle $\cos(\theta)$ (*Bottom Left*), the estimated error on the direction of the reconstructed muon track β (*Bottom Right*). The blue dots show the simulated up-going atmospheric neutrinos with the errors as a dashed area, the red dots show the mis-reconstructed atmospheric muons with the errors as a dashed are, the green line is the sum of both contributions, and the black crosses show the data. The bottom plot shows the data to MC ratio, where the number of MC events is the sum of neutrinos and atmospheric muons. *Top Left:* The energy PDF distribution after applying the cut on the quality parameter $\Lambda > -5.3$ (the global cuts on $\beta < 1.0°$, and $\cos(\theta) > -0.1$ applied). *Top Right:* The event distribution after applying the global cuts on $\beta < 1.0°$, $\cos(\theta) > -0.1$, and $\Lambda > -6.0$. The vertical dotted line with the arrow shows where the optimized selection cuts stand for the various tested spectra of both sources. *Bottom Left:* The event distribution after applying a cut on the quality parameter $\Lambda > -5.3$ (the global cuts on $\beta < 1.0°$, and $\cos(\theta) > -0.1$ applied). *Bottom Right:* The event distribution after applying the cut on zenith angle $\cos(\theta) > -0.1$ and the cut on the quality parameter $\Lambda > -5.3$ (the global cut on $\beta < 1.0°$ applied).

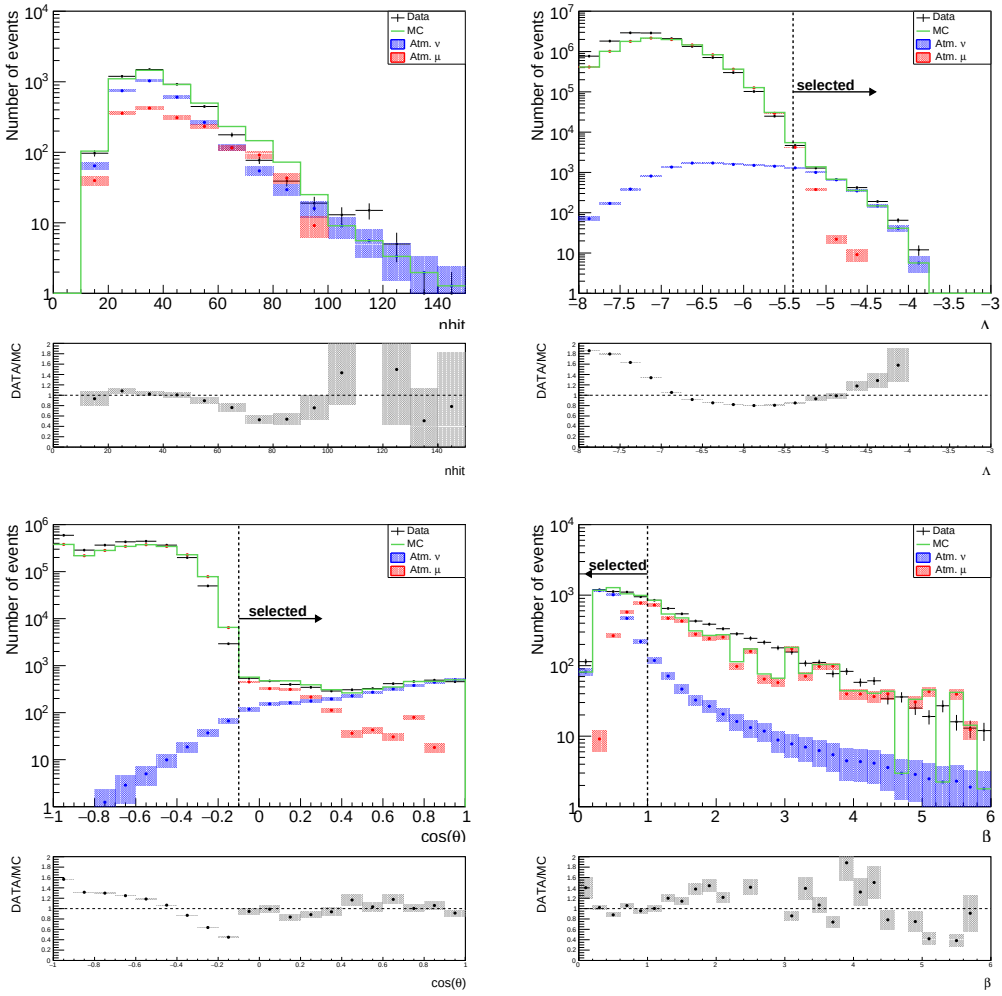

Fig. 7.18.: Comparison of the data with MC simulations as a function of the number of hits nhit (*Top Left*), the quality parameter of the reconstruction of muon track Λ (*Top Right*), the reconstructed cosine of the zenith angle $\cos(\theta)$ (*Bottom Left*), the estimated error on the direction of the reconstructed muon track β (*Bottom Right*). The blue dots show the simulated up-going atmospheric neutrinos with the errors as a dashed area, the red dots show the mis-reconstructed atmospheric muons with the errors as a dashed are, the green line is the sum of both contributions, and the black crosses show the data. The bottom plot shows the data to MC ratio, where the number of MC events is the sum of neutrinos and atmospheric muons. *Top Left:* The figure corresponds to the energy PDF distribution after applying the cut on the quality parameter $\Lambda > -5.4$. *Top Right:* The figure corresponds to the event distribution after applying the cut on the reconstructed cosine of the zenith angle $\cos(\theta) > -0.1$ and the cut on the error on the direction of the reconstructed muon track $\beta < 1.0°$. The vertical dotted line with the arrow shows where the optimized selection cuts stand for the various tested spectra of both sources. *Bottom Left:* The figure corresponds to the event distribution after applying the cut on the quality parameter $\Lambda > -5.4$ and the cut on the error on the direction of the reconstructed muon track $\beta < 1.0°$. The vertical dotted line with the arrow shows the selected $\cos(\theta) > -0.1$ cut. *Bottom Right:* The figure corresponds to the event distribution after applying the cut on zenith angle $\cos(\theta) > -0.1$ and the cut on the quality parameter $\Lambda > -5.4$. The vertical dotted line with the arrow shows the selected $\beta < 1.0°$ cut.

7.4 Results

7.4.1 Search on Dataset 2014-2016

Discovery signal

The number of signal events $N_S^{3\sigma}$, $N_S^{5\sigma}$ required for 3σ evidence or 5σ discovery give the minimum flux that could give an evidence at 3σ level or 5σ discovery in 50% of the trials. The Fig. 7.19 represent $N_S^{5\sigma}$ versus Λ for the long and the short cases.

Acceptance

The declination-dependent acceptance A_{cc} is defined as the proportionality constant between a given flux normalization $\Phi_0 = E^2 d\Phi/dE$ and the expected number of signal events N_{ev} to be detected within the telescope for this particular flux:

$$A_{cc} = \frac{N_{ev}}{\Phi_0} \tag{7.1}$$

It can be expressed in terms of the effective area $A_{eff}(E_\nu)$:

$$A_{cc} = \Phi_0^{-1} \int dt \int dE_\nu \frac{d\Phi}{dE_\nu} A_{eff}(E_\nu) \tag{7.2}$$

The effective area of a detector, A_{eff}, is the equivalent surface, perpendicular to a given flux that would detect with a 100% efficiency the flux that crosses it [516]. The neutrino effective area at a given energy, $A_{eff}(E)$, is defined as the ratio between the neutrino event rate in a detector (units: s^{-1}) and the neutrino flux (units: $cm^{-2}\ s^{-1}$) at that energy [780].

ANTARES has an effective area that ranges from 8 mm^2 at 100 GeV up to 10 m^2 at 3.5 PeV [516]. For a E^{-2} neutrino flux, half of the neutrinos detected are above ~60 TeV energies, where effective are is $\gtrsim$1 m^2 [516]. For E^{-2} spectrum, the average 5%-95% energy range at which ANTARES is sensitive is 2.3 TeV-2.6 PeV, where effective area varies from 90 cm^2 to 9 m^2 [516].

The comparison of acceptances for Mrk 421 and Mrk 501 can be seen in Fig. 7.20 and Fig. 7.21 respectively.

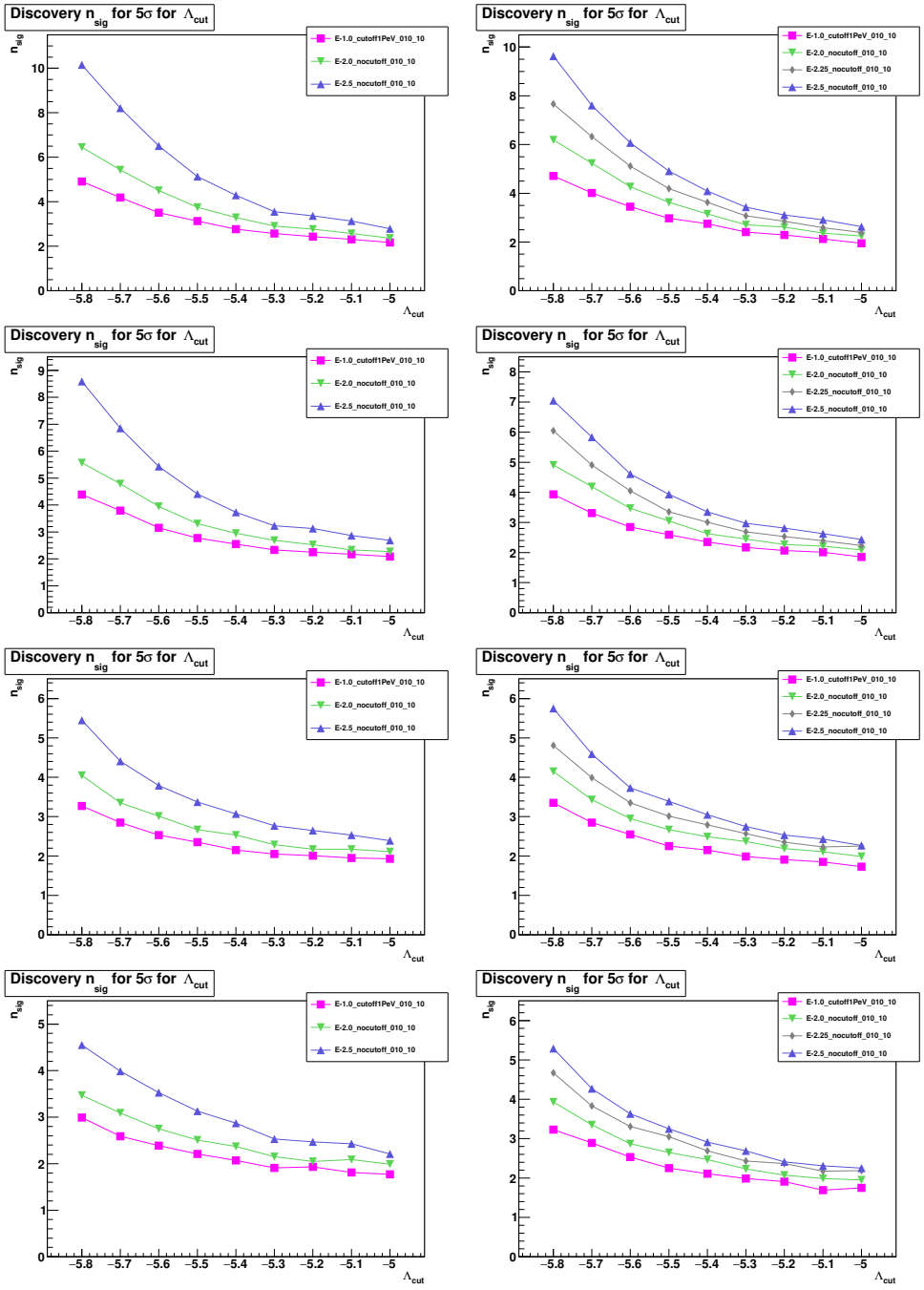

Fig. 7.19.: Discovery power at 5σ level. *Left:* Mrk 421 *Right:* Mrk 501. From upper to bottom: all flares, short flares with *average flux*, *average flux* + 1σ, *average flux* + 2σ thresholds.

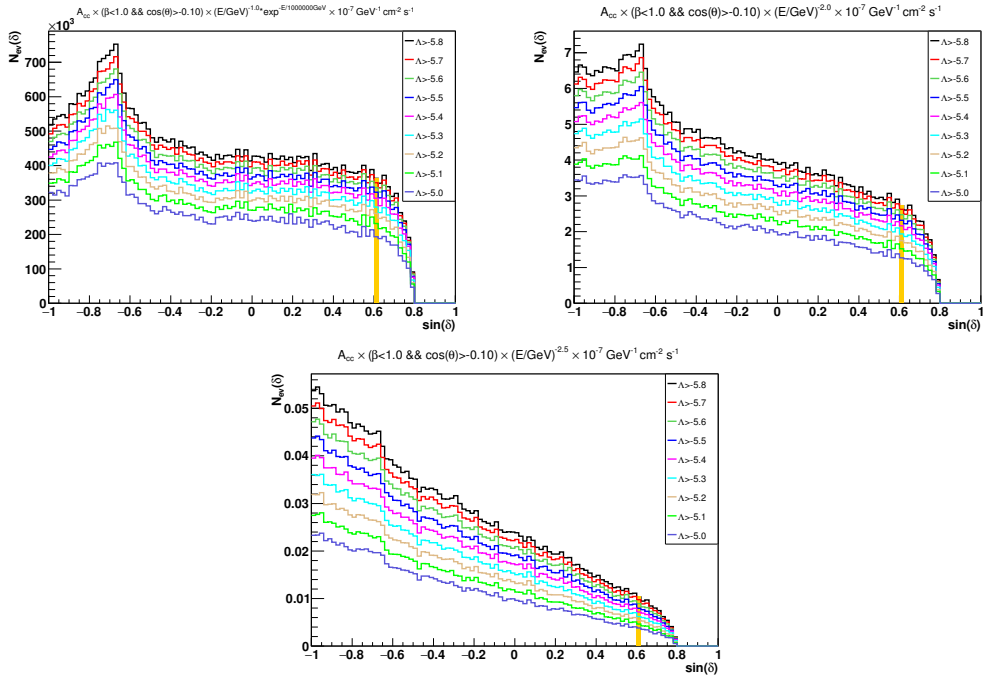

Fig. 7.20.: Examples of acceptance for Mrk 421 as a function of the source declination for the several Λ cuts [with $\beta < 1.0$ and $\cos(\theta) > -0.1$] with a flux normalization factor of $\Phi_0 = 10^{-7}$ GeV^{-1} cm^{-2} s^{-1} in $N_{ev} = A_{cc} \times \Phi_0$ magnitudes. The period used: November 26$^{\text{th}}$, 2014 - April 20$^{\text{th}}$, 2016. *Top Left:* $E^{-1.0} \exp(-E/1\,\text{PeV})$. *Top Right:* $E^{-2.0}$. *Bottom:* $E^{-2.5}$. Orange color represents the bins of the source declination.

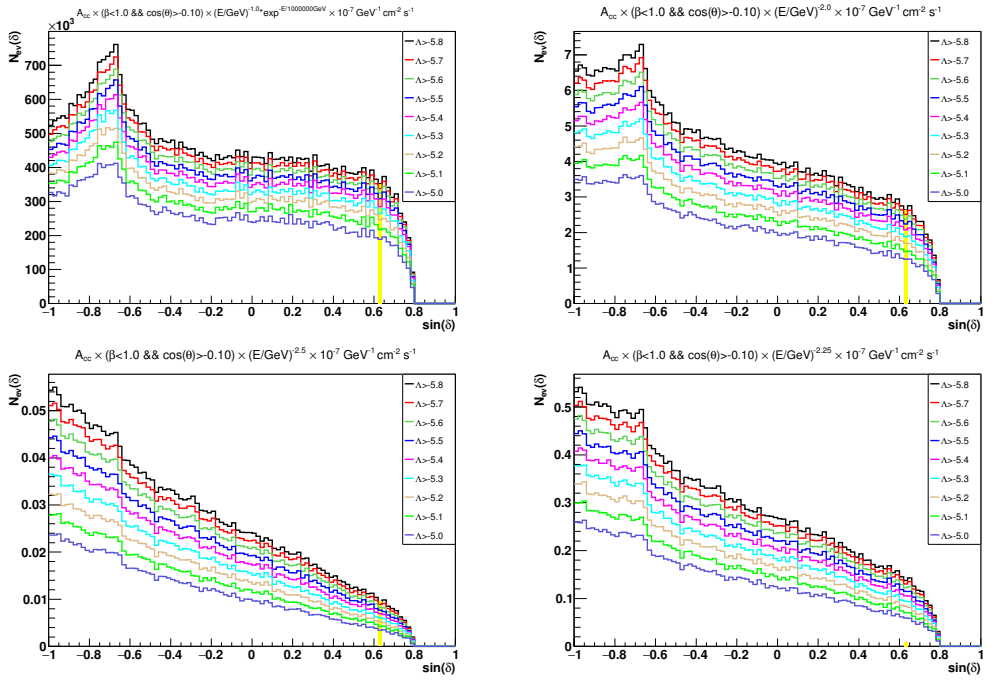

Fig. 7.21.: Examples of acceptance for Mrk 501 as a function of the source declination for the several Λ cuts [with $\beta < 1.0$ and $\cos(\theta) > -0.1$] with a flux normalization factor of $\Phi_0 = 10^{-7}$ GeV^{-1} cm^{-2} s^{-1} in $N_{ev} = A_{cc} \times \Phi_0$ magnitudes. The period used: November 26$^{\text{th}}$, 2014 - April 20$^{\text{th}}$, 2016. *Top Left:* $E^{-1.0} \exp(-E/1\,\text{PeV})$. *Top Right:* $E^{-2.0}$. *Bottom Left:* $E^{-2.5}$. *Bottom Right:* $E^{-2.25}$. Yellow color represents the bins of the source declination.

Discovery fluxes

In this section the discovery fluxes obtained in analysis for all spectra with all flare states selected (long case) and with only flare states above *average flux*, *average flux* + 1σ, *average flux* + 2σ threshold selected (short case) are discussed.

Discovery flux level $\mathrm{DF}_{5\sigma}^{50\%\mathrm{CL}}$is the flux required to have a test statistic TS over $\mathrm{TS}_{5\sigma}$ in 50% of trials. Discovery fluxes $\mathrm{DF}_{5\sigma}^{50\%\mathrm{CL}}$ versus Λ for cut on the reconstructed zenith $\cos(\theta) > -0.1$ and cases of all flares and only peaks are shown in Fig. 7.22 and Fig. 7.23. The plots for discovery fluxes at 3σ level can be seen in Fig. 7.24 and Fig. 7.25.

As far as HAWC detector operates nearly continuously and provide data for almost each day and longer periods have better acceptance, the usage of all available flares (long case) is obviously preferable (see comparison plots in Fig. 7.22, Fig. 7.23 and Fig. 7.24, Fig. 7.25). Taking into account such long duration flare timing information given by HAWC γ-ray observations, it significantly improves the efficiency of the search for a neutrino counterpart with ANTARES telescope.

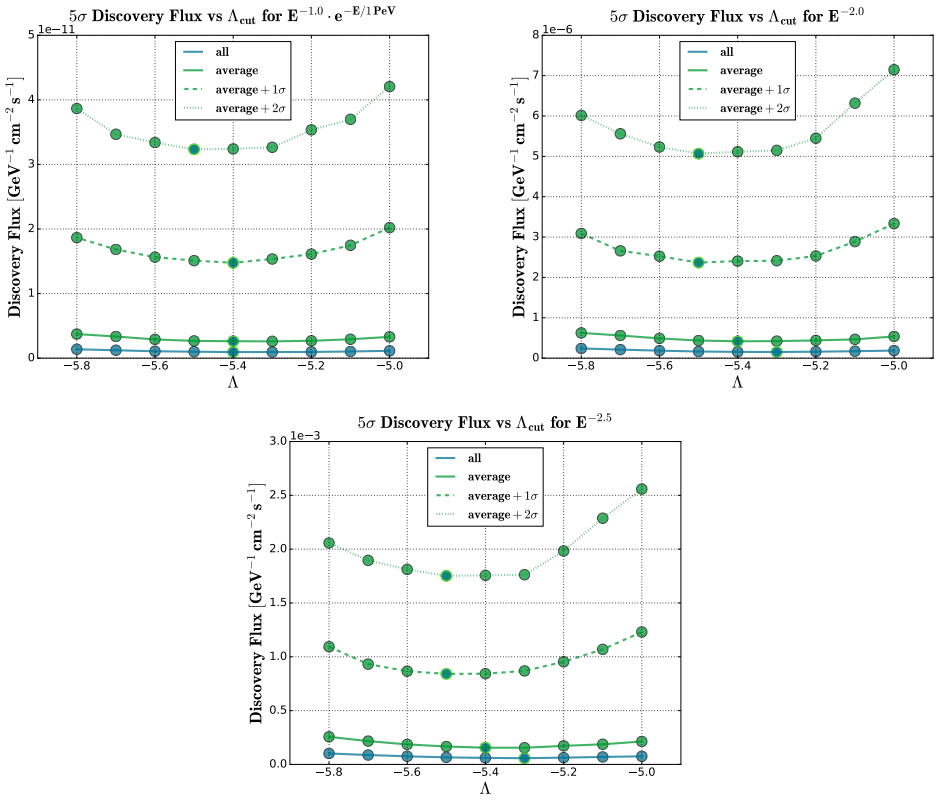

Fig. 7.22.: Discovery fluxes comparison at 5σ level for Mrk 421 for several thresholds. *Top Left:* $\mathrm{E}^{-1.0}\exp(-\mathrm{E}/1\,\mathrm{PeV})$. *Top Right:* $\mathrm{E}^{-2.0}$. *Bottom:* $\mathrm{E}^{-2.5}$. Light green color circles represent the values with Λ that maximizes $\mathrm{MDP}^{5\sigma}$.

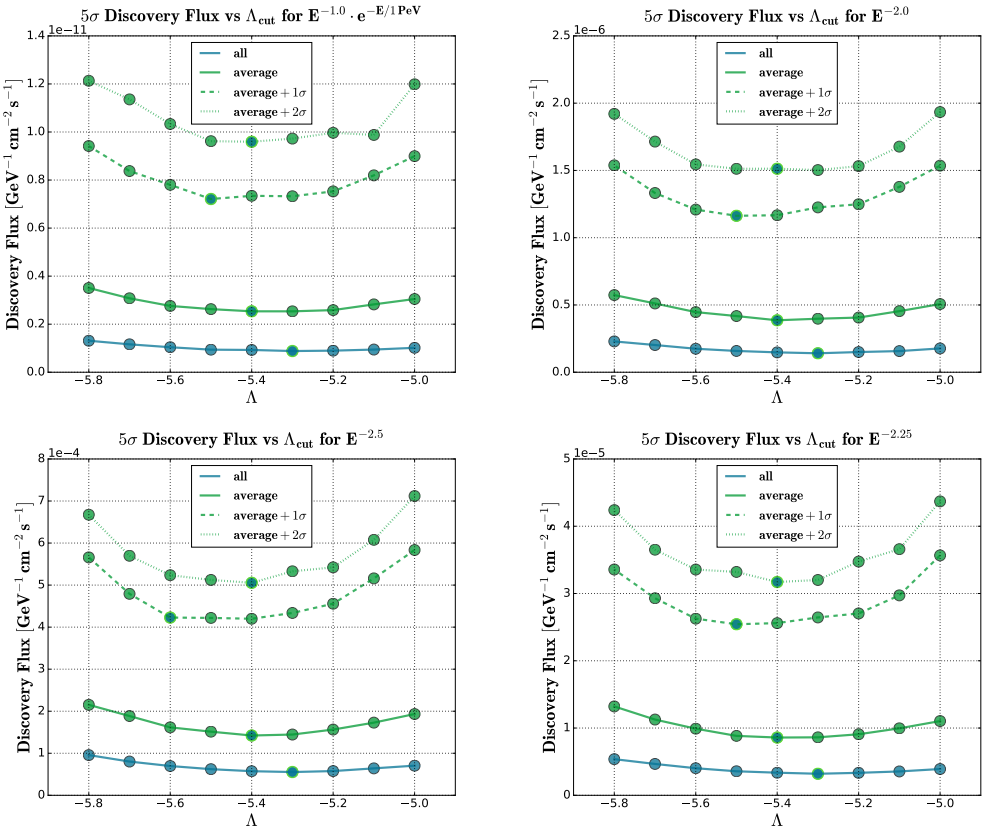

Fig. 7.23.: Discovery fluxes comparison at 5σ level for Mrk 501 for several thresholds. *Top Left:* $E^{-1.0}\exp(-E/1\,\text{PeV})$. *Top Right:* $E^{-2.0}$. *Bottom Left:* $E^{-2.5}$. *Bottom Right:* $E^{-2.25}$. Light green color circles represent the values with Λ that maximizes $MDP^{5\sigma}$.

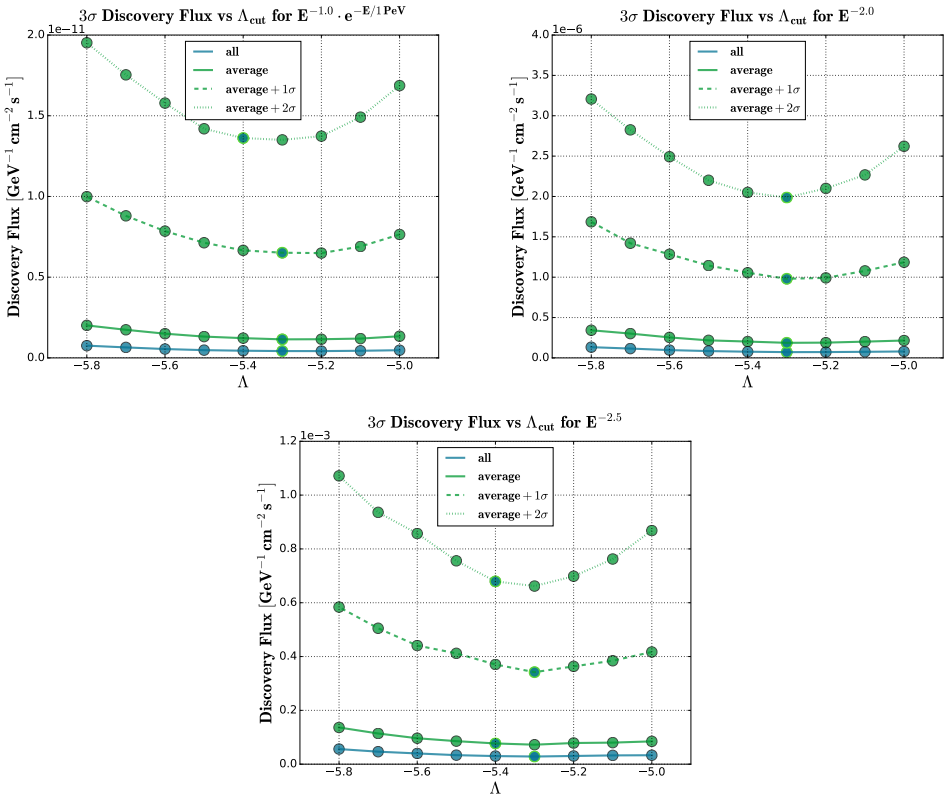

Fig. 7.24.: Discovery fluxes comparison at 3σ level for Mrk 421 for several thresholds. *Top Left:* $E^{-1.0}\exp(-E/1\,\text{PeV})$. *Top Right:* $E^{-2.0}$. *Bottom:* $E^{-2.5}$. Light green color circles represent the values with Λ that maximizes $\text{MDP}^{3\sigma}$.

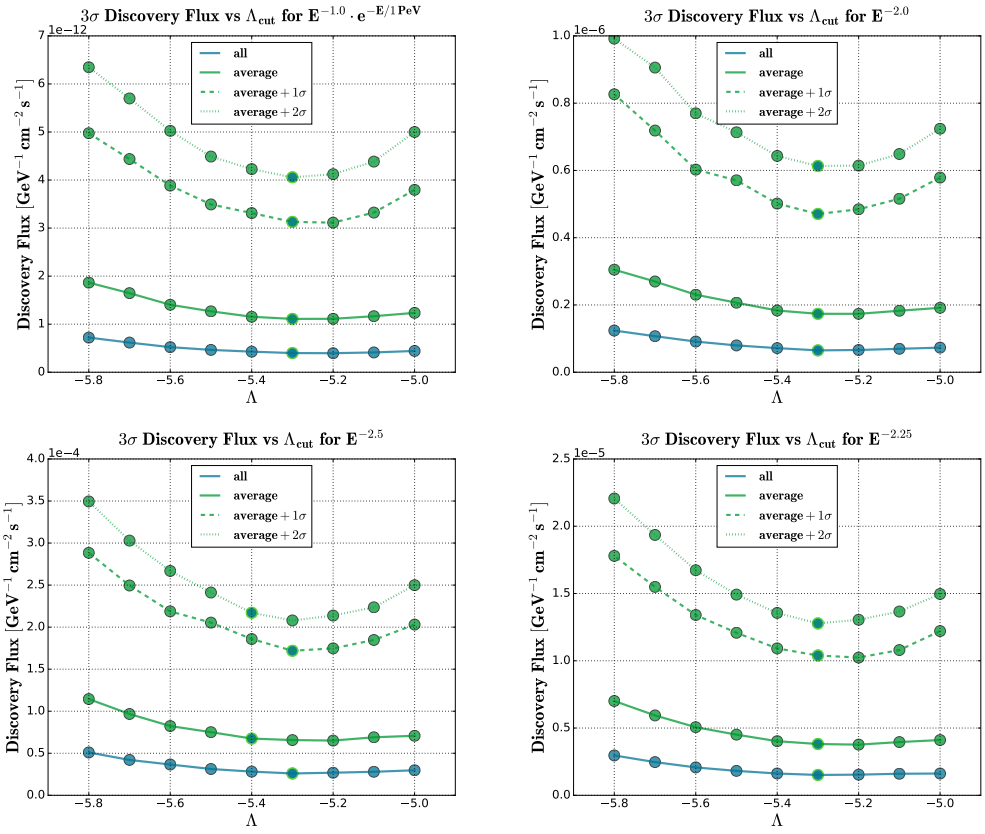

Fig. 7.25.: Discovery fluxes comparison at 3σ level for Mrk 501 for several thresholds. *Top Left:* $E^{-1.0}\exp(-E/1\,\mathrm{PeV})$. *Top Right:* $E^{-2.0}$. *Bottom Left:* $E^{-2.5}$. *Bottom Right:* $E^{-2.25}$. Light green color circles represent the values with Λ that maximizes $\mathrm{MDP}^{3\sigma}$.

Tab. 7.3.: Results on optimization for Mrk 421

	T_{flare}	LT	Λ	$N_S^{3\sigma}$	Λ	$N_S^{5\sigma}$	$DF_{3\sigma}^{50\%CL}$	$DF_{5\sigma}^{50\%CL}$
				$E^{-1.0}\exp(-E/1\,PeV)$				
L	508	491.66	-5.3	1.15	-5.4	2.77	0.42	0.94
S: *av.*	213	210.52	-5.3	1.03	-5.4	2.55	1.15	2.62
S: *av.* + 1σ	44	43.509	-5.3	0.87	-5.4	2.15	6.51	14.8
S: *av.* + 2σ	17	16.149	-5.4	0.87	-5.5	2.21	13.6	32.3
							$\times 10^{-12} \cdot GeV^{-1}\,cm^{-2}\,s^{-1}$	
				$E^{-2.0}$				
L	508	491.66	-5.3	1.37	-5.3	2.91	0.72	1.52
S: *av.*	213	210.52	-5.3	1.19	-5.4	2.95	1.87	4.18
S: *av.* + 1σ	44	43.509	-5.3	0.93	-5.5	2.67	9.80	23.7
S: *av.* + 2σ	17	16.149	-5.3	0.83	-5.5	2.51	19.9	50.7
							$\times 10^{-7} \cdot GeV^{-1}\,cm^{-2}\,s^{-1}$	
				$E^{-2.5}$				
L	508	491.66	-5.3	1.75	-5.3	3.55	0.28	0.58
S: *av.*	213	210.52	-5.4	1.85	-5.4	3.73	0.77	1.55
S: *av.* + 1σ	44	43.509	-5.3	1.09	-5.5	3.37	3.42	8.41
S: *av.* + 2σ	17	16.149	-5.4	1.11	-5.5	3.13	6.79	17.5
							$\times 10^{-4} \cdot GeV^{-1}\,cm^{-2}\,s^{-1}$	

Tab. 7.4.: Results on optimization for Mrk 501

	T_{flare}	LT	Λ	$N_S^{3\sigma}$	Λ	$N_S^{5\sigma}$	$DF_{3\sigma}^{50\%CL}$	$DF_{5\sigma}^{50\%CL}$
				$E^{-1.0}\exp(-E/1\,PeV)$				
L	509	492.88	-5.3	1.09	-5.3	2.41	0.40	0.60
S: *av.*	138	136.55	-5.3	0.95	-5.4	2.35	1.11	2.54
S: *av.* + 1σ	46	45.928	-5.3	0.85	-5.5	2.25	3.13	7.21
S: *av.* + 2σ	33	33.100	-5.3	0.83	-5.4	2.11	4.06	9.59
							$\times 10^{-12} \cdot GeV^{-1}\,cm^{-2}\,s^{-1}$	
				$E^{-2.0}$				
L	509	492.88	-5.3	1.25	-5.3	2.71	0.65	1.41
S: *av.*	138	136.55	-5.3	1.07	-5.4	2.63	1.74	3.86
S: *av.* + 1σ	46	45.928	-5.3	0.91	-5.5	2.67	4.71	11.6
S: *av.* + 2σ	33	33.100	-5.3	0.91	-5.4	2.47	1.37	15.1
							$\times 10^{-7} \cdot GeV^{-1}\,cm^{-2}\,s^{-1}$	
				$E^{-2.25}$				
L	509	492.88	-5.3	1.45	-5.3	3.07	1.51	3.20
S: *av.*	138	136.55	-5.3	1.19	-5.4	3.01	3.81	8.59
S: *av.* + 1σ	46	45.928	-5.3	1.01	-5.5	3.01	10.4	25.4
S: *av.* + 2σ	33	33.100	-5.3	0.97	-5.4	2.69	12.8	31.7
							$\times 10^{-6} \cdot GeV^{-1}\,cm^{-2}\,s^{-1}$	
				$E^{-2.5}$				
L	509	492.88	-5.3	1.61	-5.3	3.43	0.26	0.55
S: *av.*	138	136.55	-5.4	1.59	-5.4	3.35	0.68	1.42
S: *av.* + 1σ	46	45.928	-5.3	1.09	-5.6	3.73	1.72	4.23
S: *av.* + 2σ	33	33.100	-5.4	1.25	-5.4	2.91	2.17	5.05
							$\times 10^{-4} \cdot GeV^{-1}\,cm^{-2}\,s^{-1}$	

MDP

The value of the cut on Λ is optimised for each source on the basis of maximizing a model discovery potential (MDP) [407] for the 3σ or 5σ significance levels for each neutrino spectrum. MDP sets best limits in case of the no-discovery. Figure 7.26 represent the MDP values versus Λ for both sources at 5σ level.

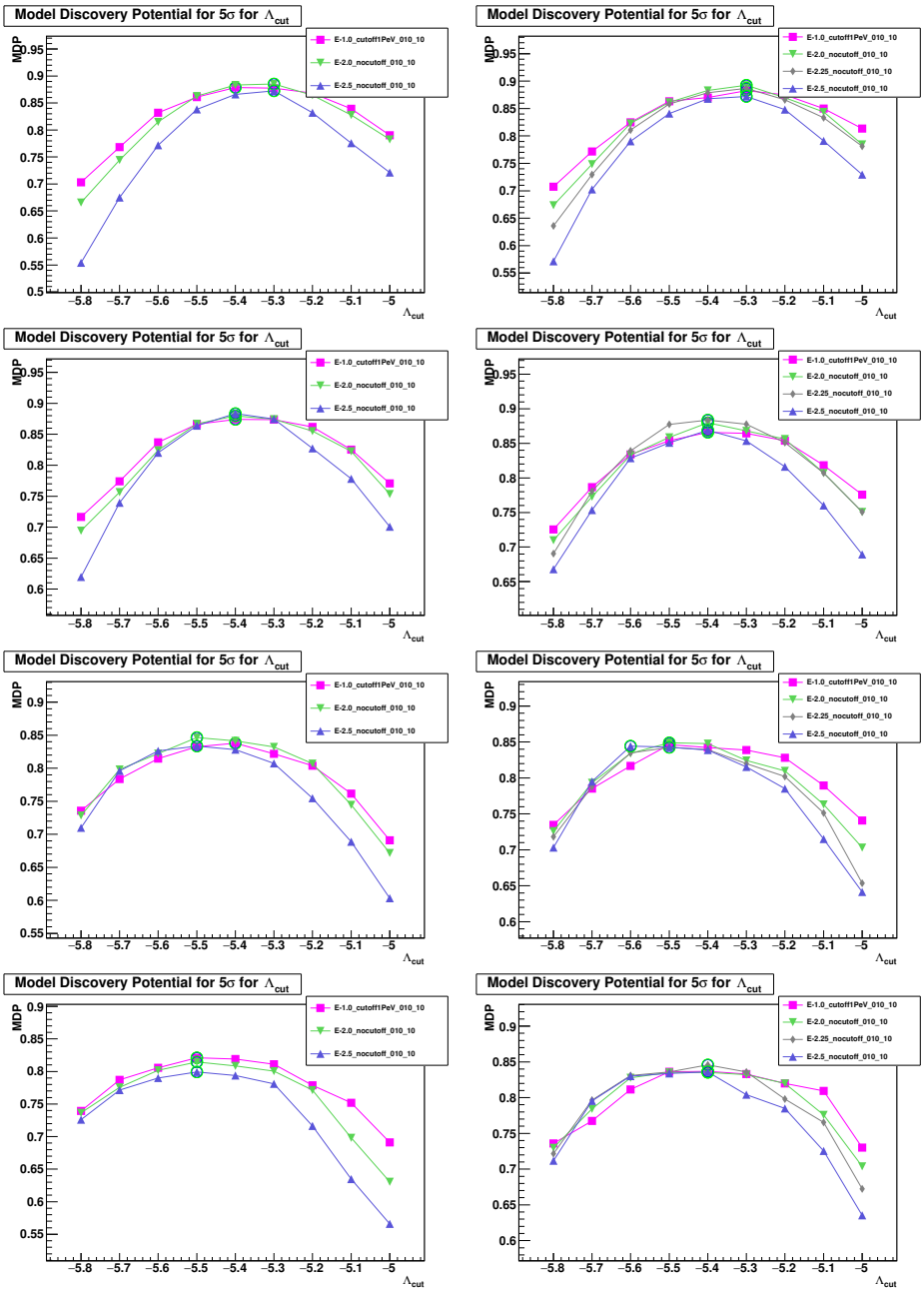

Fig. 7.26.: MDP for 5σ discovery. *Left:* Mrk 421. *Right:* Mrk 501. From upper to bottom: all flares, short flares with *average flux*, *average flux* + 1σ, *average flux* + 2σ thresholds. Light green color circles represent the maximum MDP values.

Sensitivity fluxes

Similarly to 5σ discovery fluxes, the discovery flux level $\mathrm{DF}^{90\%\mathrm{CL}}_{\mathrm{Median}}$ (see Fig. 7.27, 7.28) is defined as the sensitivity flux required to have a test statistic TS over the median of the background distribution $\mathrm{TS}_{\mathrm{Median}}$ in 90% of the trials. The sensitivity flux places the upper limit on fluxes at 90% CL. In the absence of a signal, it is used for 90% C.L. sensitivity calculations.

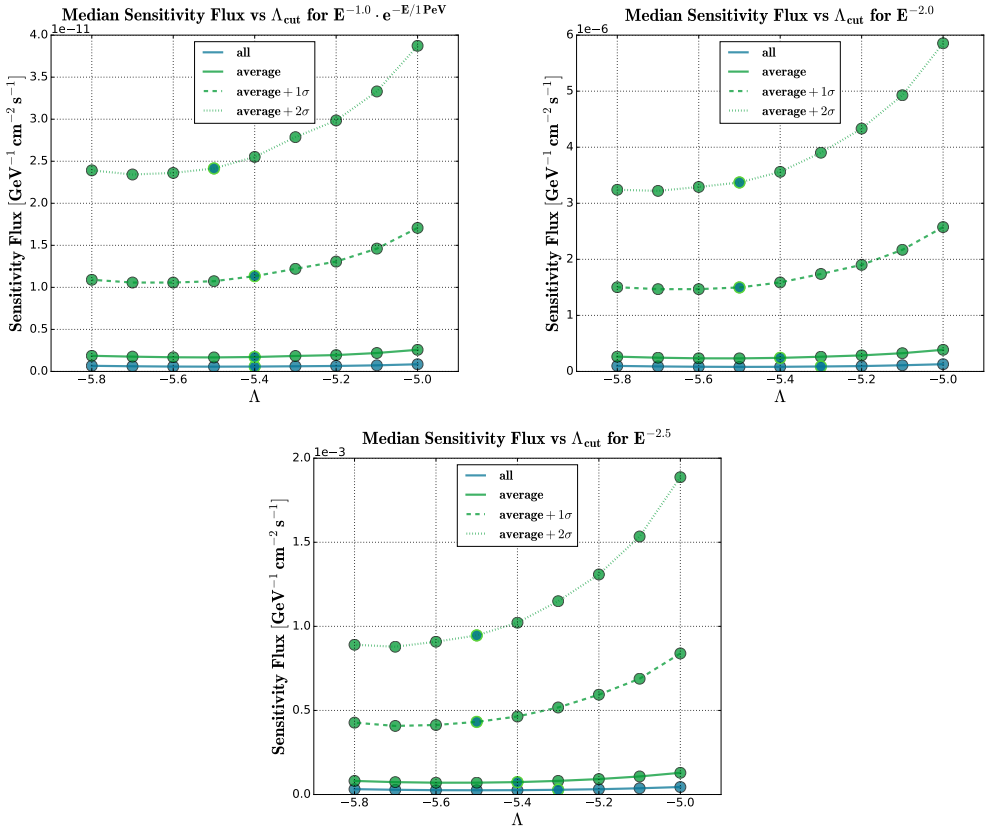

Fig. 7.27.: Sensitivity fluxes comparison for Mrk 421 for several thresholds. *Top Left:* $E^{-1.0}\exp(-E/1\,\mathrm{PeV})$. *Top Right:* $E^{-2.0}$. *Bottom:* $E^{-2.5}$. Light green color circles represent the values with Λ that maximizes $\mathrm{MDP}^{5\sigma}$.

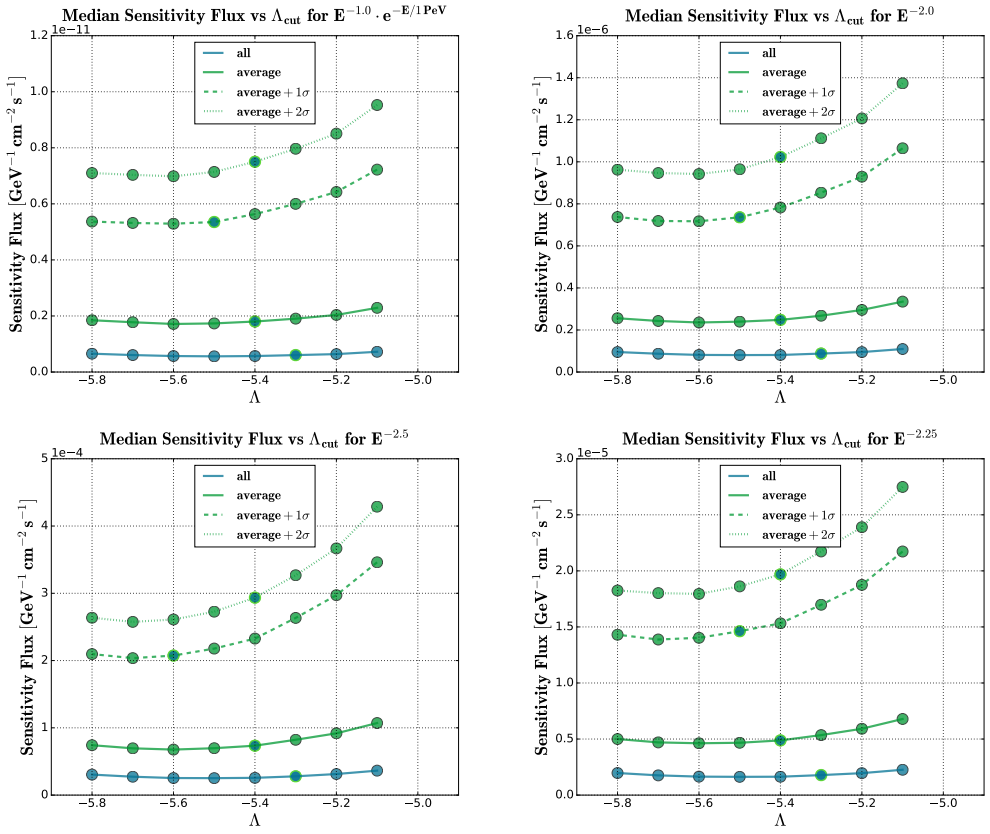

Fig. 7.28.: Sensitivity fluxes comparison for Mrk 501 for several thresholds. *Top Left:* $E^{-1.0}\exp(-E/1\,\text{PeV})$. *Top Right:* $E^{-2.0}$. *Bottom Left:* $E^{-2.5}$. *Bottom Right:* $E^{-2.25}$. Light green color circles represent the values with Λ that maximizes $\text{MDP}^{5\sigma}$.

Sensitivities

If no discovery is made, the upper limits will be calculated according to the classical (frequentist) approach [778] using 5-95% energy bounds, E_{min} and E_{max}. The 5% and 95% energy limits for each spectrum $S(E)$ and source are shown in Fig. 7.29. The sensitivities at 90% C.L. on neutrino fluxes and fluences for each source and spectrum for corresponding limits are listed in Table 7.5. Additionally, Figure 7.30 and Figure 7.31 summarize the sensitivities on the neutrino fluxes and fluences. Fluence 90% C.L. sensitivities vs Λ for different peak selection thresholds are gathered in Fig. 7.32 and Fig. 7.33. The tendencies for fluence in the short case for Mrk 421 and Mrk 501 are different. For Mrk 421 the fluence values are worsening with respect to increase of the threshold except for the *average flux* + 2σ which gives the sensitivities even better than *average flux* + 1σ. For Mrk 501 the fluence values are getting lower with respect to increase of the threshold except for the *average flux* + 1σ which gives some worsening w.r.t. the *average flux* case.

As a result, the better sensitivities on the neutrino fluxes can be obtained with the long case for both sources, but the better sensitivities on the neutrino fluences can be obtained with long case for Mrk 421 and in contrary to that with short case and the *average flux* + 2σ threshold for Mrk 501 (see Fig. 7.32 and Fig. 7.33). Consequently, these two cases can be saved for the future searches, e.g., with Dataset 2014-2017.

Tab. 7.5.: Sensitivities at 90% C.L.

	$S(E)$	T_{flare}	LT	Λ	E_{min}	E_{max}	$\Phi_0^{90\%CL}$	$\mathcal{F}^{90\%CL}$
Mrk 421	$E^{-1.0} \cdot e^{-E/1\,\mathrm{PeV}}$	508	491.659	-5.4	4.792	6.392	5.808^{*1}	21.0
	$E^{-2.0}$			-5.3	3.960	7.080	8.846^{*2}	27.0
	$E^{-2.5}$			-5.3	3.064	5.912	2.812^{*3}	67.8
Mrk 501	$E^{-1.0} \cdot e^{-E/1\,\mathrm{PeV}}$	509	492.878	-5.3	4.808	6.400	6.038^{*1}	22.0
	$E^{-2.0}$			-5.3	3.968	7.096	8.783^{*2}	26.9
	$E^{-2.25}$			-5.3	3.544	6.496	0.178^{*3}	32.3
	$E^{-2.5}$			-5.3	3.088	5.936	2.792^{*3}	65.5
							$\cdot\,\mathrm{GeV}^{-1}\,\mathrm{cm}^{-2}\,\mathrm{s}^{-1}$	$\cdot\,\mathrm{GeV}\,\mathrm{cm}^{-2}$

Note: E_{min} and E_{max} in log.
^{*1} $\times 10^{-13}$
^{*2} $\times 10^{-8}$
^{*3} $\times 10^{-5}$
[LT] = [T_{flare}] = days.

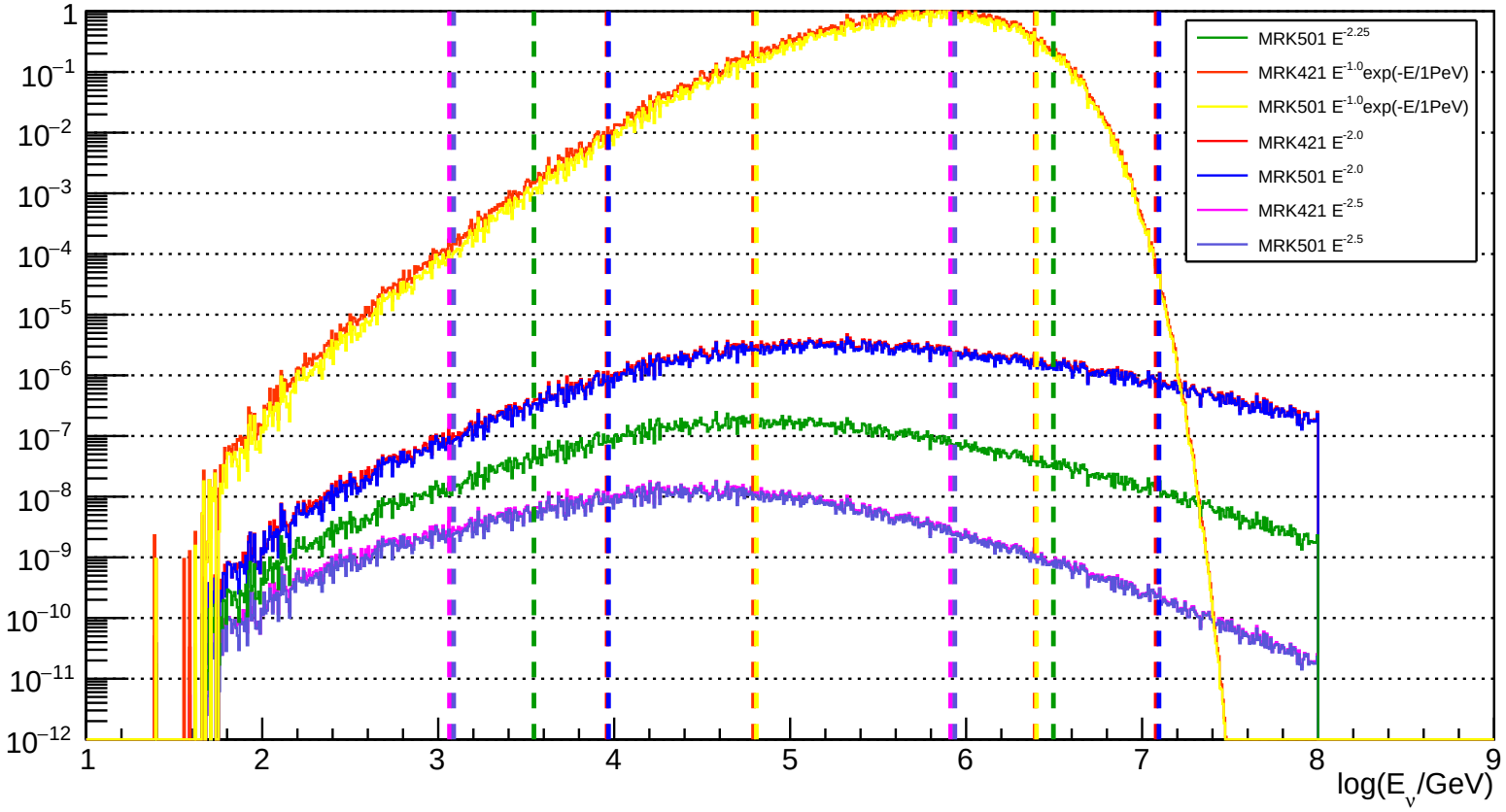

Fig. 7.29.: Distribution of the MC neutrinos $\nu_\mu + \bar{\nu}_\mu$ for each spectrum and source for the optimum Λ cuts (with the optimum $\cos(\theta) > -0.1$ and $\beta < 1.0$ considered) obtained for the long case. The dotted vertical lines represent the corresponding 5% and 95% energy limits.

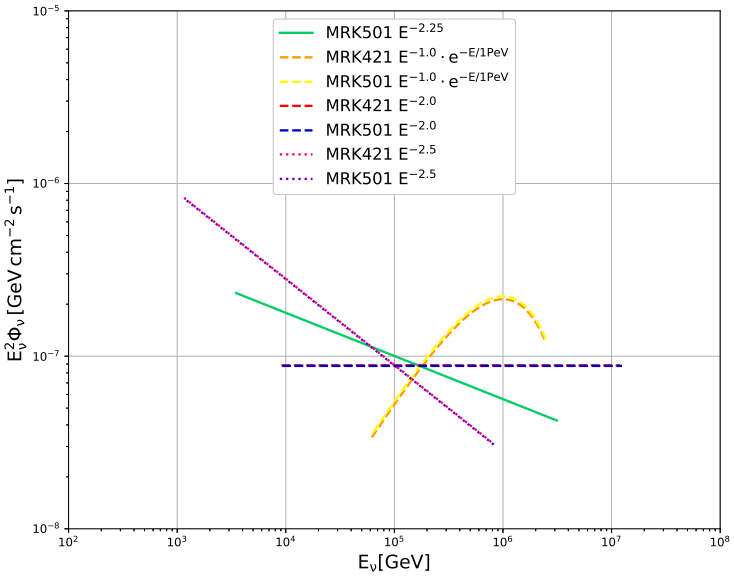

Fig. 7.30.: Neutrino energy flux sensitivities at 90% C.L. obtained in the analysis with $E^{-1.0}$ exp(−E/1 PeV), $E^{-2.0}$, $E^{-2.5}$, $E^{-2.25}$ (this for Mrk 501 only) neutrino energy spectra. Obtained for the long case with sensitivity fluxes for optimum Λ values for each spectrum.

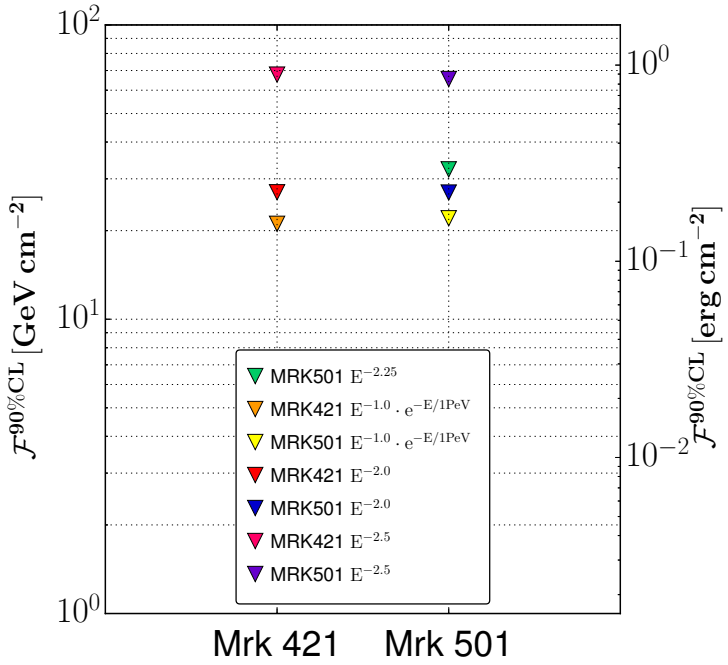

Fig. 7.31.: Neutrino fluence sensitivities for long case at 90% C.L. obtained in the analysis with $E^{-1.0}$ exp(−E/1 PeV), $E^{-2.0}$, $E^{-2.5}$, $E^{-2.25}$ (this for Mrk 501 only) neutrino energy spectra. Obtained for the long case with sensitivity fluxes for optimum Λ values for each spectrum.

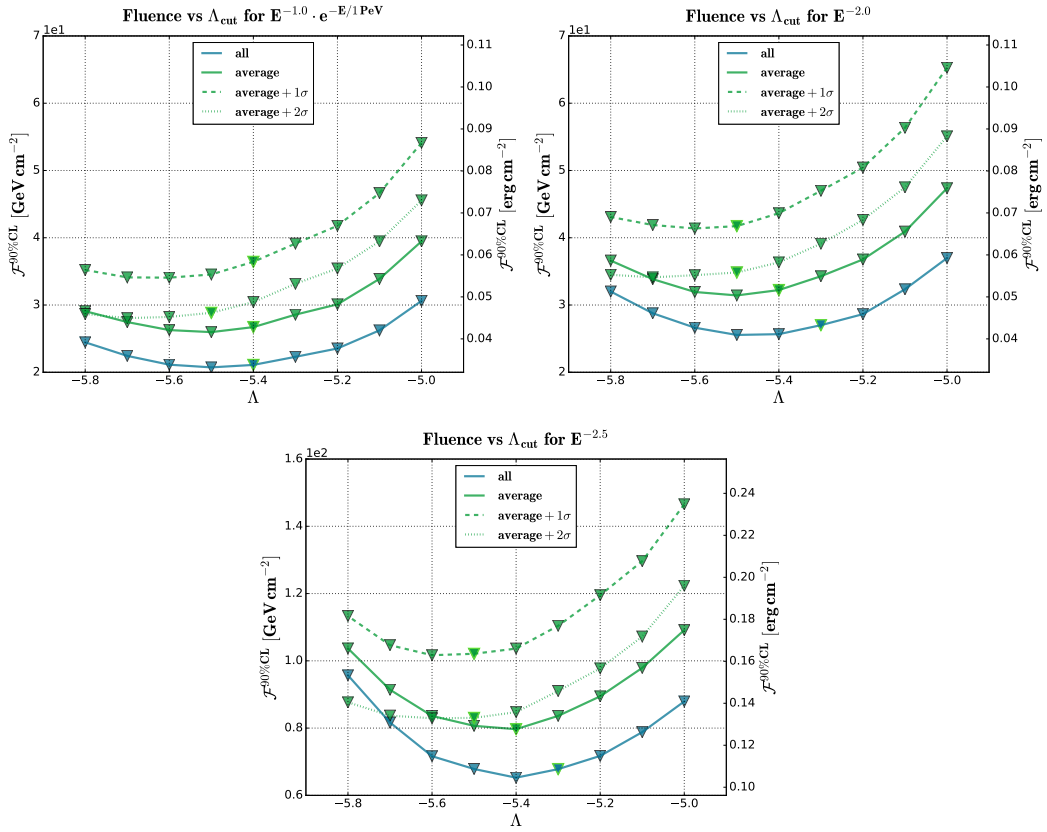

Fig. 7.32.: Neutrino fluence sensitivities at 90% C.L. vs Λ for Mrk 421 for different peak selection thresholds. *Upper left panel:* $E^{-1.0}\exp(-E/1\,\mathrm{PeV})$. *Upper right panel:* $E^{-2.0}$. *Lower panel:* $E^{-2.5}$. Light green color circles represent the sensitivities derived with $DF^{90\%CL}$ of optimum Λ values.

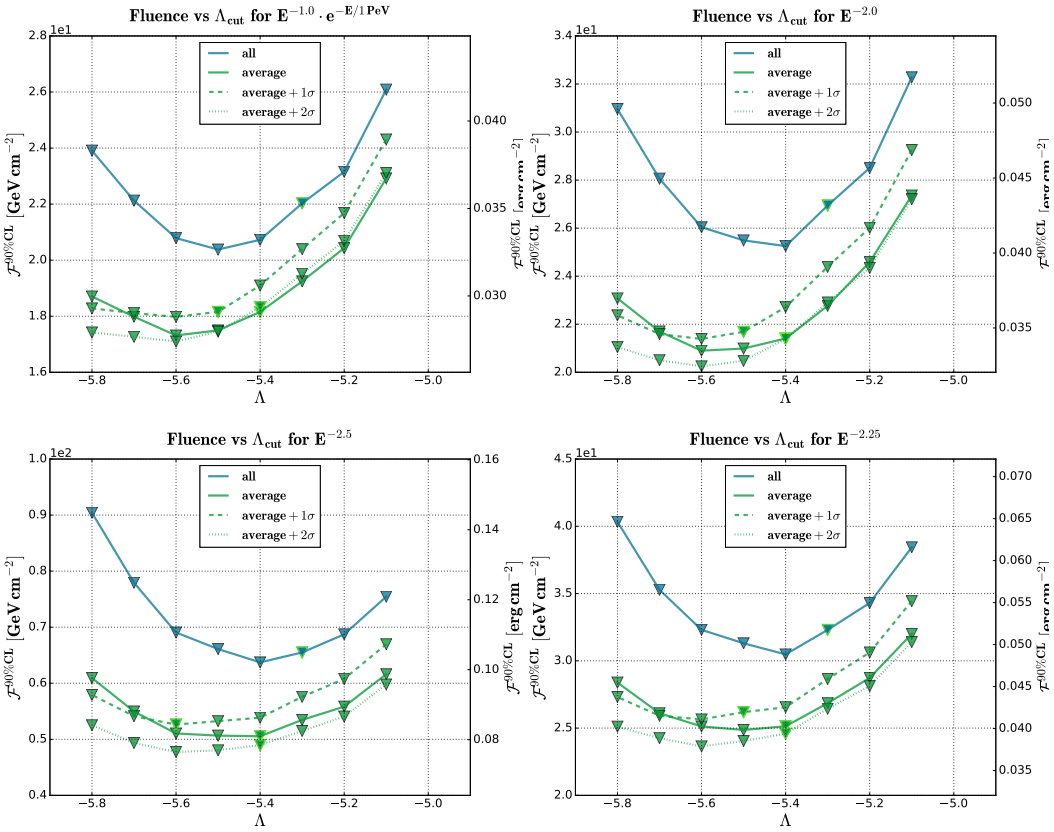

Fig. 7.33.: Neutrino fluence sensitivities at 90% C.L. vs Λ for Mrk 501 for different peak selection thresholds. *Upper left panel:* $E^{-1.0}\exp(-E/1\,\mathrm{PeV})$. *Upper right panel:* $E^{-2.0}$. *Lower left panel:* $E^{-2.5}$. *Lower right panel:* $E^{-2.25}$. Light green color circles represent the sensitivities derived with $DF^{90\%CL}$ of optimum Λ values.

7.4.2 Search on Dataset 2014-2017

No significant excess is found in this updated search. Figure 7.34 gathers the 90% CL ULs on neutrino flux and fluence. The best 90% CL flux ULs (see Fig. 7.34, *Left*) is obtained with the case of all flare states selected, while the best 90% CL fluence ULs (see Fig. 7.34, *Right*) is obtained with *average flux+2*σ threshold. The most significant p-values are fro Mrk 421 for the short case with *average flux+2*σ:

- p=0.40, post-trial 0.59 for $E^{-1} \cdot e^{-E/1PeV}$ spectrum and with $\Lambda > -5.2$;
- p=0.43, post-trial 0.63 for E^{-2} spectrum and with $\Lambda > -5.2$.

In recent search 8 years of data performed by IceCube [559], no significant excess was found and the p-values for the markarians (for E^{-2}) are:

- Mrk 421: p-value 34.6%, best-fit $\hat{n}_s = 0.00$ [UL: $5.79 \cdot 10^{-13}$ TeV cm^{-2} s^{-1}
- Mrk 501: p-value 72.1%, best-fit $\hat{n}_s = 0.00$ [UL: $4.58 \cdot 10^{-13}$ TeV cm^{-2} s^{-1}

Compared to what obtained in this work with ANTARES (for E^{-2}):

- Mrk 421: p-value 43.4%, best-fit $\hat{n}_s = 0.00$ [UL: $4.96 \cdot 10^{-11}$ TeV cm^{-2} s^{-1}
- Mrk 501: p-value 68.2%, best-fit $\hat{n}_s = 0.00$ [UL: $9.79 \cdot 10^{-11}$ TeV cm^{-2} s^{-1}

As seen, the ULs set by IceCube are two orders of magnitude better (with the usage of ≈3 times longer period of searches), which shows the importance of the visibility, especially for the targeted blazars located at the edge of the ANTARES visibility, the search for neutrinos of which suffers a lack of statistics. Nevertheless, in terms of the discovery potential, ANTARES is also able to be competitive.

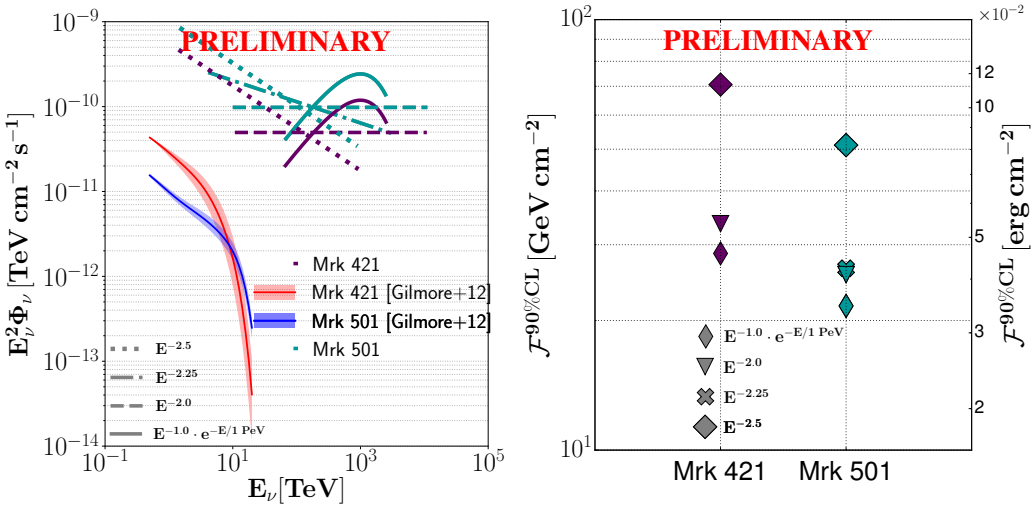

Fig. 7.34.: Upper limits on the flux F (left) and fluence $\mathcal{F}$ (right) for different spectra for both blazars. The attenuated fluxes for blazars with the intrinsic spectra obtained in HAWC [781] are shown.

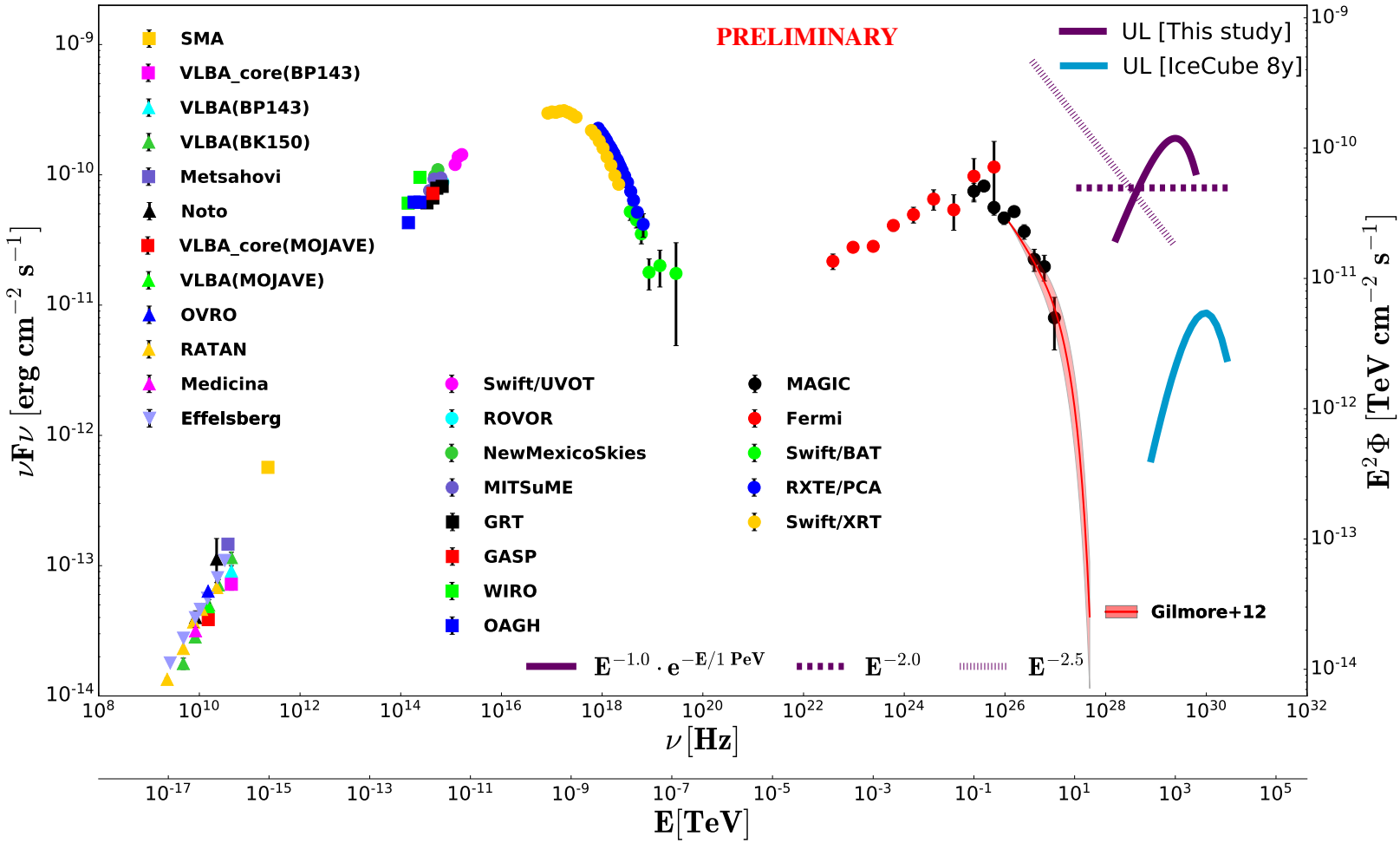

Fig. 7.35.: Neutrino flux ULs vs γ-ray SED of Mrk 421. The SED of Mrk 421 averaged over all the observations taken during the multifrequency campaign in 2009. See [782] for references to the different instruments involved in the campaign. Adapted from [782], credit by David Paneque. The violet lines indicate the ν ULs for different spectra obtained in this study. The ULs for IceCube search [559] with the default spectrum for non-flaring (quiescence) period obtained from [783] is shown (solid blue) for comparison, credit by René Reimann. The attenuated flux for Mrk 421 with the intrinsic spectrum obtained in HAWC [781] is shown.

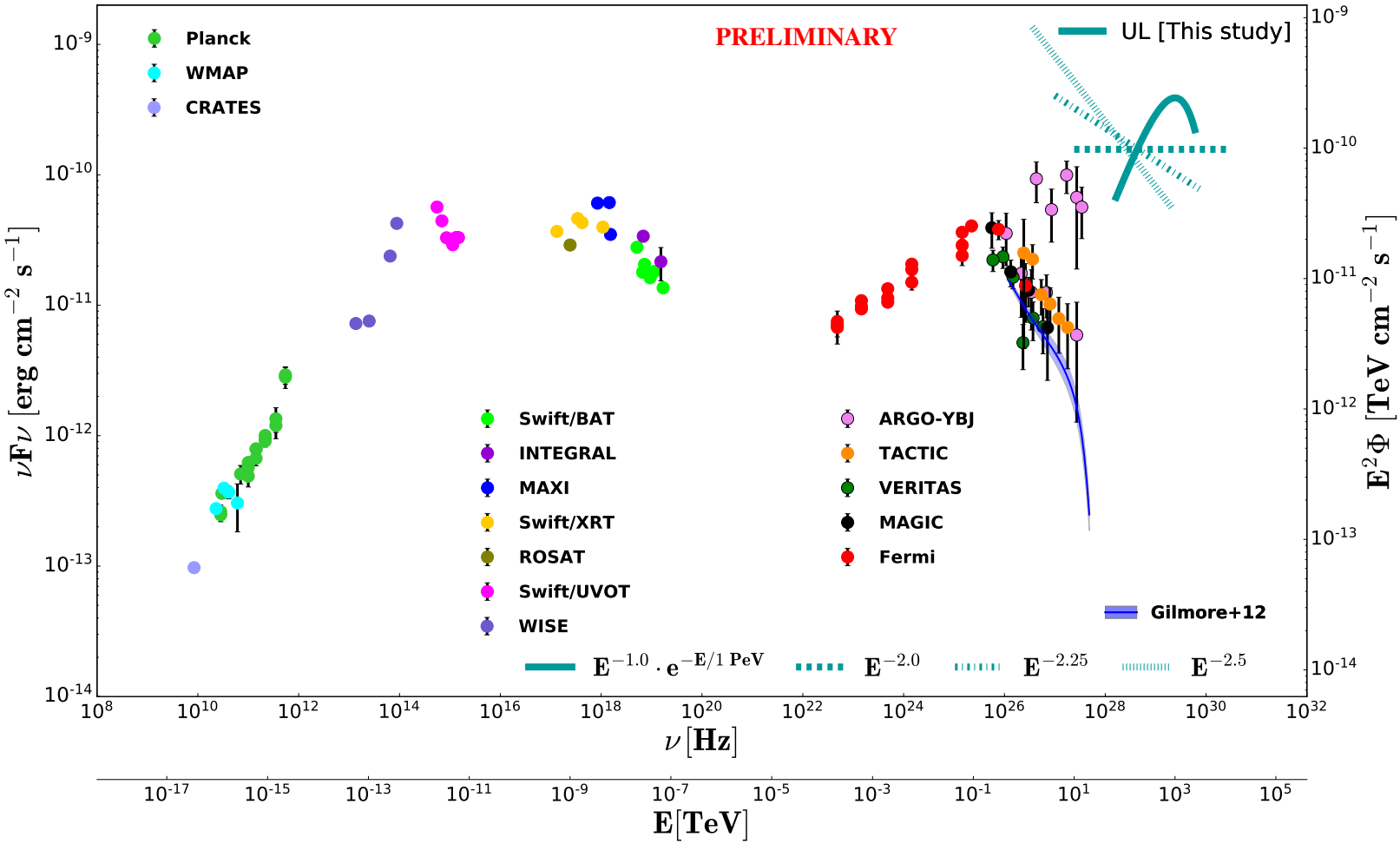

Fig. 7.36.: Neutrino flux ULs vs γ-ray SED of Mrk 501. The data for multi-frequency SED is gathered from the historical observations available in the SED Builder Tool of the ASI Space Science Data Center (SSDC)[1], which combines radio to γ-ray band data from several missions and experiments together. See [178] for references to the different experiments which data were used. The light sea green lines indicate the ν ULs for different spectra obtained in this study. The attenuated flux for Mrk 501 with the intrinsic spectrum obtained in HAWC [781] is shown.

7.4.3 Comparison of two result

The neutrino energy flux sensitivities (see Fig. 7.37) for Mrk 421 in the analysis with Dataset 2014-2017 is getting better by factor ∼1.8 compared to the analysis with Dataset 2014-2016, while for Mrk 501 is getting worse by factor ∼1.1. One can expect much better sensitivities with Dataset 2014-2017 where longer period is analysed, e.g., ∼ 120% for Mrk 421 and ∼ 10% for Mrk 501. The results can be influenced by several parameters such as:

- Different DATA/MC set;
- Different flare states amplitudes used;
  - the analysis with Dataset 2014-2017 involves the raw-data LCs with 1 TeV as a threshold, and flare blocks obtained according to that; the spectral fit parameters are also not similar;
  - the analysis with Dataset 2014-2016 is presumed the Bayesian blocks have already been done, but for that the initial LCs had other thresholds than 1 TeV, e.g., 2 TeV and 3 TeV for Mrk 421 and Mrk 501 respectively.
- Different optimized Λ cuts have impact on sensitivity fluxes $S^{90\%CL}_{Median}$;
  - For Mrk 501, ∼ 18% difference in used fluxes give roughly worsening by factor proportional to ratio 1.1 (longer time) / 1.18 (worse flux) ≈0.9, which is exact ∼1.1 worsening that we observe.
  - For Mrk 421, we use ∼2.2 longer duration, but sensitivities better by factor ∼1.8. Hence, using same idea, if assume e.g. ∼ 20% differences, we obtain 2.2/1.2 ≈1.8, exactly what we observe.

Also, neutrino fluence sensitivities (see Fig. 7.38) are affected by difference in $S^{90\%CL}_{Median}$:

- For Mrk 421 is getting worse compared to the analysis with Dataset 2014-2016 (∼10%).
- For Mrk 501 is getting worse compared to the analysis with Dataset 2014-2016 (∼10%).

These discrepancies have been thoroughly studied. Figure 7.39 shows the comparison of flare blocks amplitudes for Mrk 501. As seen, the discrapancy effect due to this is supposed to be small. Unlike that, the median sensitivity fluxes have remarkable impact comparable with the discrapancy values discussed above (see Fig. 7.40).

[1] https://tools.ssdc.asi.it/SED/

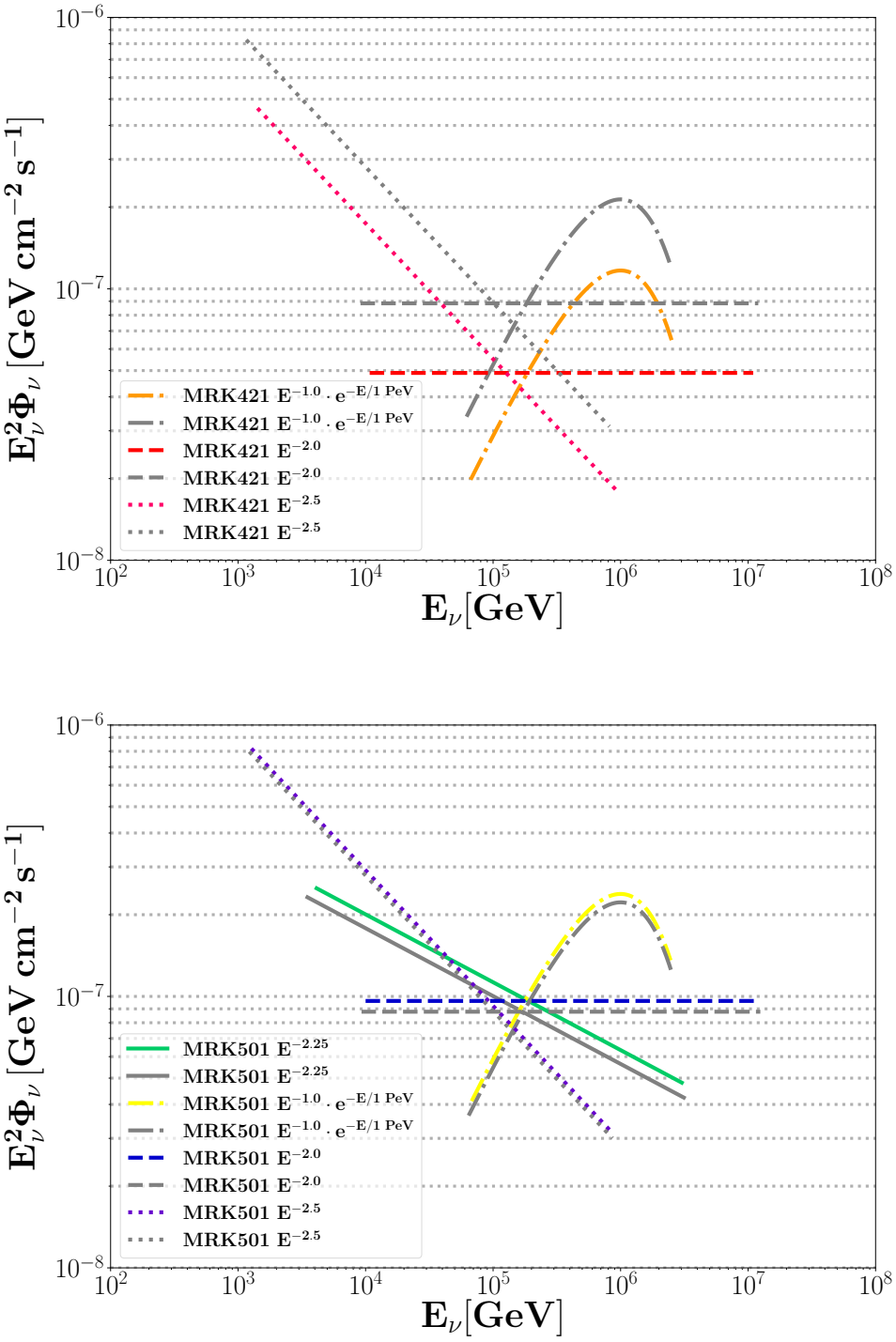

Fig. 7.37.: Neutrino energy flux sensitivities obtained with two datasets, Dataset 2014-2016 (grey color) and Dataset 2014-2017 (colored). *Left:* Mrk 421. *Right:* Mrk 501.

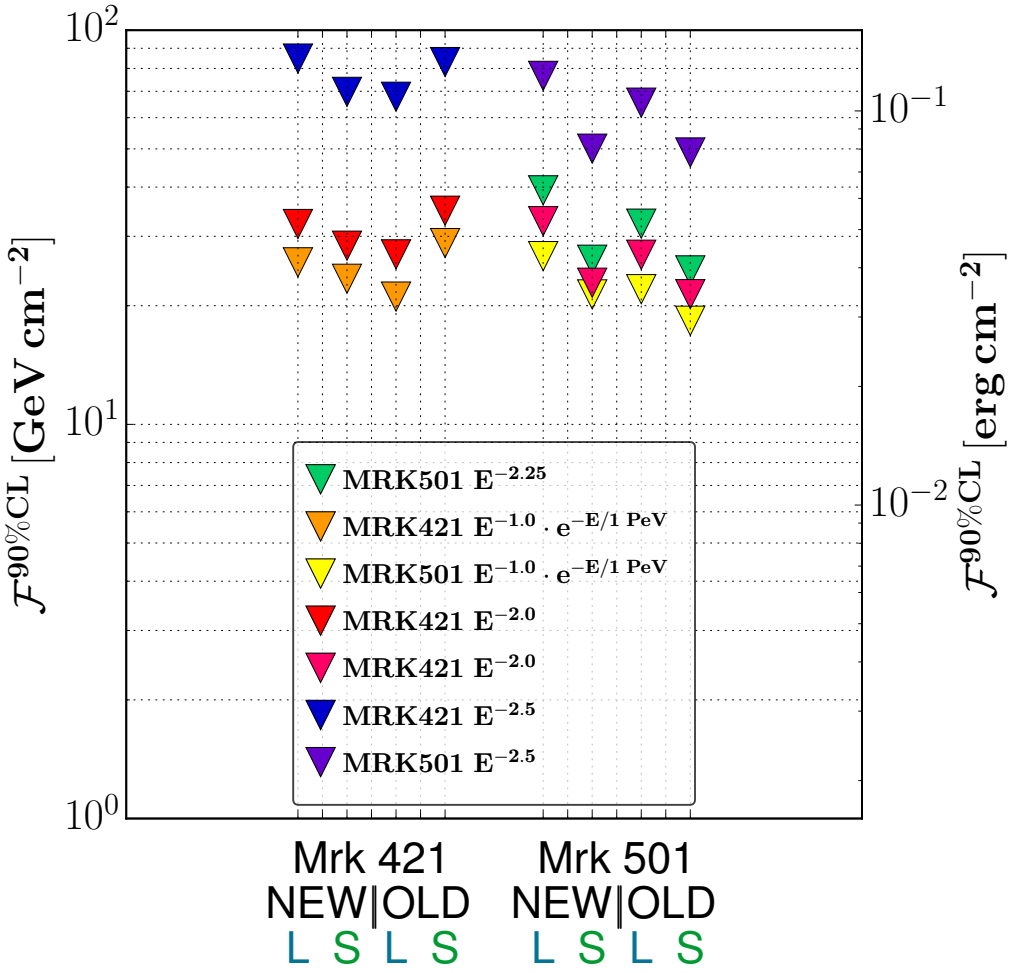

Fig. 7.38.: Neutrino fluence sensitivities obtained with two datasets, Dataset 2014-2016 (old) and Dataset 2014-2017 (new). The ”L” denotes long case when all flares are selected, while ”S” denotes the short case where only flares fulfill the threshold condition to be above *average flux*+2σ are selected.

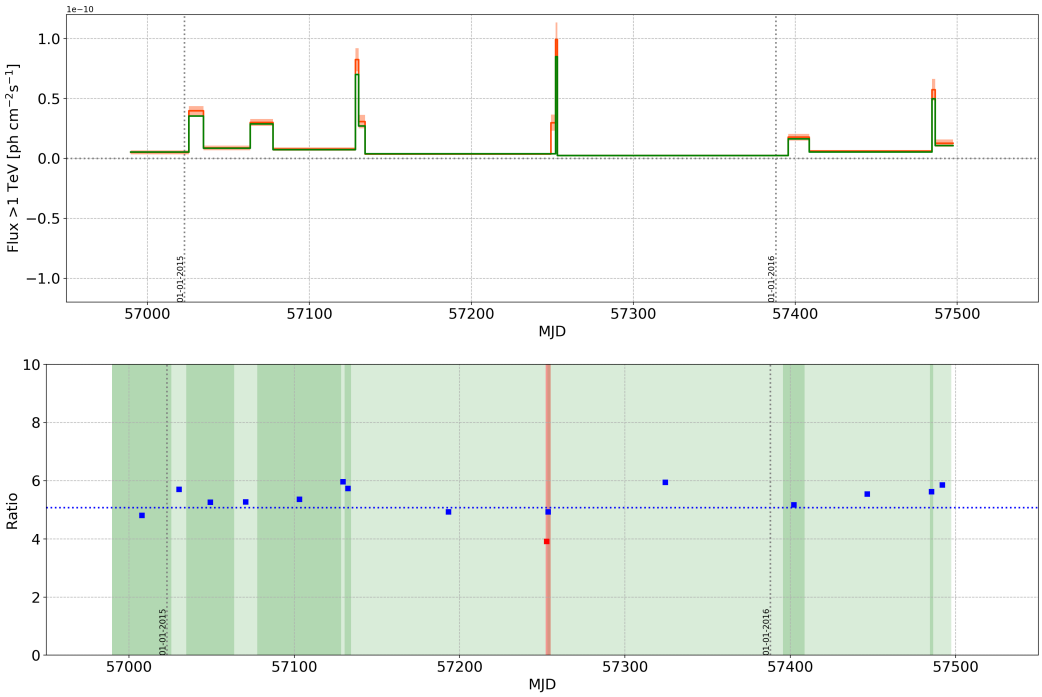

Fig. 7.39.: Comparison of the flare blocks amplitudes for Mrk 501. *Top:* The flare blocks for the analyses with with Dataset 2014-2016 (green) and with Dataset 2014-2017 (orange) are shown. Due to similar shape but different amplitudes, in order to have comparison in one scale, the flare block amplitudes for the analysis with Dataset 2014-2016 have been multiplied by factor of 5. *Bottom:* The amplitudes ratios (blue points) between two are shown. The blue dotted line is the average (obtained without red). The green color repesents the width (duration) of the flares. The ratio for the block exist in the analysis with Dataset 2014-2017 but not in the analysis with Dataset 2014-2016 is colored by red and divided by factor 10 for better visibility.

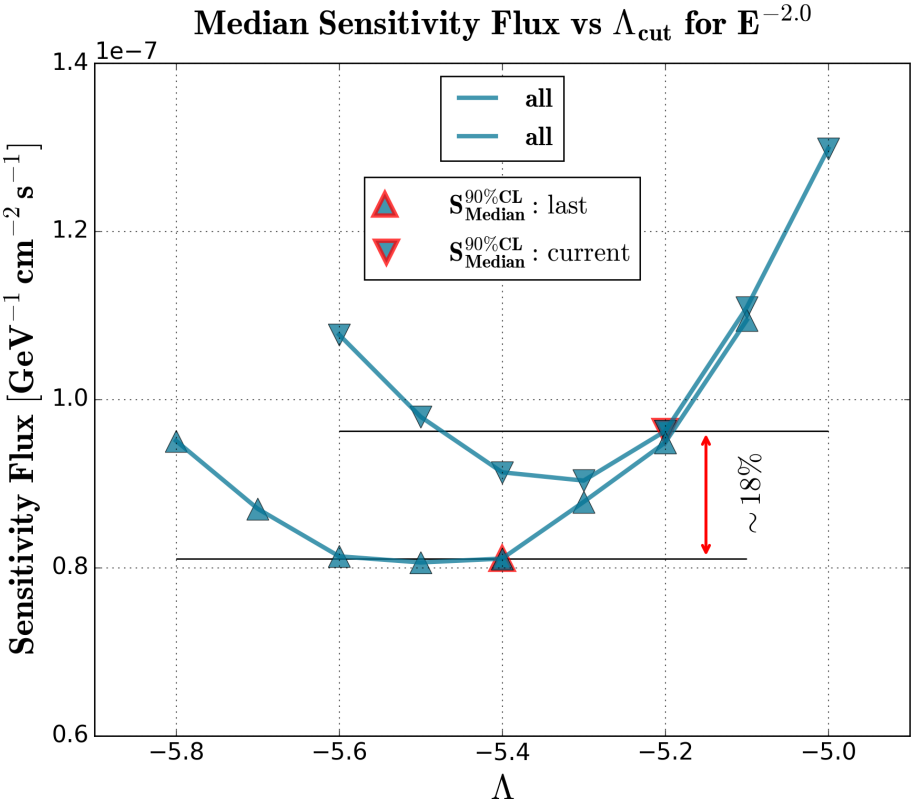

Fig. 7.40.: Comparison of the median sensitivity fluxes for Mrk 501 obtained with two datasets, Dataset 2014-2016 (last) and Dataset 2014-2017 (current).

8 Conclusion

Significant efforts have been made in recent years to unveil the mystery of the origin of neutrinos. The last decades were fruitful for neutrino astronomy and resulted in many revolutionary discoveries. This includes the first detection of an extragalactic diffuse high-energy neutrino flux by IceCube in 2013, the detection of a high-energy neutrino by IceCube associated with observations in γ-rays of different wavelengths, being for the first-ever detection of such correlation between the neutrino and γ-ray skies, leading blazars to be the first identifiable sources of the high-energy astrophysical neutrino flux. Neutrino astronomy has never been so exciting and close to unveiling the processes behind extreme astrophysical phenomena in the Universe, especially after a giant leap is made with the detection of the first extragalactic neutrino source. As more facilities commissioned in the coming years, that would encourage new researchers to develop new techniques and methods and perform a continuous search for neutrinos to finally reveal the sources of the elusive neutrino particles. The work presented in this manuscript supposes a tiny contribution to this goal.

The HAWC detector operates nearly continuously and it is currently the most sensitive wide FOV γ-ray telescope in the very promising high-energy band from 100 GeV to 100 TeV. Therefore, it opens prospects to study the most energetic astrophysical phenomena in the Universe as well as to understand the mechanisms that power them and endeavor to break the mystery of their origin [178]. Taking into account the flare timing information given by γ-ray observations should improve the efficiency of the search for a neutrino counterpart with ANTARES. With the expected decommissioning of ANTARES at the end of 2019, the next-generation multi-km^3-sized KM3NeT [173, 174, 175] neutrino telescope with a unique design of multi-PMT optical modules will take up with new vigor the challenges faced by ANTARES and will have surpassed it in the sensitivity in few years raising a new era in neutrino astronomy. The KM3NeT will provide more than an order of magnitude improvement in sensitivity; therefore, such sources are promising candidates as high-energy neutrino emitters for an improved future time-dependent search. As shown in [784] for Mrk 421, the muon neutrino event rate during a short flaring period is comparable to the one expected from a longer but non-flaring period, i.e. during quiescence; thereby, a collection of flares over a several years is essential to produce a meaningful signal in modern multi-km^3-sized neutrino telescopes [178]. The experience acquired with ANTARES is important since different methods for neutrino search have been developed, which can be successfully employed and improved in KM3NeT with its better sensitivity and angular resolution. In turn, this made possible to detect the neutrinos from Mrk 421 and Mrk 501, the two brightest and closest extragalactic sources in TeV sky. The results in this work have been presented in multiple conferences.

Appendix

A

A.1 Units and definitions

A.1.1 Definitions

MJD: The Modified Julian Day (MJD) is defined as MJD≡JD−2400000.5, where JD is the Julian Day. JD 0 is defined as Greenwich 12:00:00 (noon) on January 1, in the year -4712, which is 4713 BC. The half-day shift makes the day start at midnight. MJD 0 is defined as 00:00:00 (midnight) on November 17, 1858 AD. This date corresponds to 2400000.5 days after day 0 of the Julian calendar. The Julian Date is the Julian Day number followed by the fraction of the day elapsed since the preceding noon.

A.1.2 Prefixes

Tab. A.1.: SI prefixes [39]

10^{21}	Zetta	(Z)
10^{18}	Exa	(E)
10^{15}	Peta	(P)
10^{12}	Tera	(T)
10^{9}	Giga	(G)
10^{6}	Mega	(M)
10^{3}	kilo	(k)
10^{2}	hecto	(h)
10^{1}	deca	(da)
10^{-1}	deci	(d)
10^{-2}	centi	(c)
10^{-3}	milli	(m)
10^{-6}	micro	(μ)
10^{-9}	nano	(n)
10^{-12}	pico	(p)
10^{-15}	femto	(f)
10^{-18}	attp	(a)
10^{-21}	zepto	(z)

A.2 Constants

A.2.1 Mathematical Constants

Tab. A.2.: Mathematical Constants [39]

$\pi = 3.141\ 592\ 653\ 589\ 793\ 238$
$e = 2.718\ 281\ 828\ 459\ 045\ 235$

A.2.2 Physical Constants

Tab. A.3.: Physical Constants [39]

Quantity	Symbol, equation	Value
speed of light in vacuum	c	299 792 458 m s^{-1}
Planck constant	h	$6.626\ 070\ 040(81)\times10^{-34}$ J s
Planck constant, reduce	$\hbar \equiv h/2\pi$	$1.054\ 571\ 800(13)\times10^{-34}$ J s
		$= 6.582\ 119\ 514(40)\times10^{-22}$ MeV s
electron charge		$1.602\ 176\ 6208(98)\times10^{-19}$ C
conversion constant		197.326 9788(12) MeV fm
Fermi coupling constant	$G_F^0 = G_F/(\hbar c)^3$	$1.1663787(6)\times10^{-5}$ GeV^{-2}
strong coupling constant	$\alpha(m_Z)$	0.1181(11)
fine-structure constant	$\alpha = e^2/4\pi\epsilon_0\hbar c$	1/137.035 999 139(31)*
electron mass	m_e	0.510 998 9461(31) MeV/c^2 = $9.109\ 383\ 56(11)\times10^{-31}$ kg
proton mass	m_p	938.272 0813(58) MeV/c^2 = $1.672\ 621\ 898(21)\times10^{-27}$ kg
		$= 1836.152\ 673\ 89(17)\ m_e$
neutron	m_n	
neutral pion	m_{π^0}	
charged pion	$m_{\pi^\pm}$	
$W^\pm$ boson mass	m_W	80.379(12) GeV/c^2
Z^0 boson mass	m_Z	91.1876(21) GeV/c^2

* At $Q^2 = 0$. At $Q^2 \approx m_W^2$ the value is ~ 1/128.

A.2.3 Astrpophysical Constants

Tab. A.4.: Astrophysical Constants and Parameters [39]

Quantity	Symbol, equation	Value
astronomical unit	au	149 597 870 700 m
parsec (1 au/1 arc sec)	pc	$3.085\,677\,581\,49\times10^{16}$ m = 3.262...ly
light year	ly	0.306 6...pc = 0.946 053...$\times10^{16}$ m
Solar mass	$M_\odot$	$1.988\,48(9)\times10^{30}$ kg
jansky (flux density)	Jy	10^{26} W m^{-2} Hz^{-1}
present day CMB temperature	T_0	2.7255(6) K
number density of CMB photons	n_γ	410.7(3) $(T/2.7255)^3$ cm^{-3}
density of CMB photons	p_γ	$4.645(4)\ (T/2.7255)^4\times10^{-34}$ g cm^{-3} ≈ 0.260 eV cm^{-3}
scale factor for Hubble expansion rate	h	0.678(9)
present day Hubble expansion rate	H_0	100 h km s^{-1} Mpc^{-1} = $= h\times(9.777\,752\,\text{Gyr})^{-1}$

A.3 ANTARES datasets

A.3.1 Dataset 2014-2016

The list of possible OFF days in case if only `DATA-MC` complete runs are selected in Dataset 2014-2016 is shown below:

Tab. A.5.: List of possible OFF days

57095	57122	57132	57219	57244	57254	57264	57358	57368	57378
57113	57123	57133	57235	57245	57255	57302	57359	57369	57379
57114	57124	57134	57236	57246	57256	57304	57360	57370	57380
57115	57125	57135	57237	57247	57257	57310	57361	57371	57381
57116	57126	57136	57238	57248	57258	57312	57362	57372	57382
57117	57127	57137	57239	57249	57259	57313	57363	57373	57383
57118	57128	57138	57240	57250	57260	57314	57364	57374	57384
57119	57129	57139	57241	57251	57261	57321	57365	57375	57385
57120	57130	57140	57242	57252	57262	57324	57366	57376	57386
57121	57131	57141	57243	57253	57263	57357	57367	57377	57387

Number of days off: 100.

Total ANTARES OFF period belongs to 2015 (57023-57387) year only.

A.4 Skymap plots with selected events

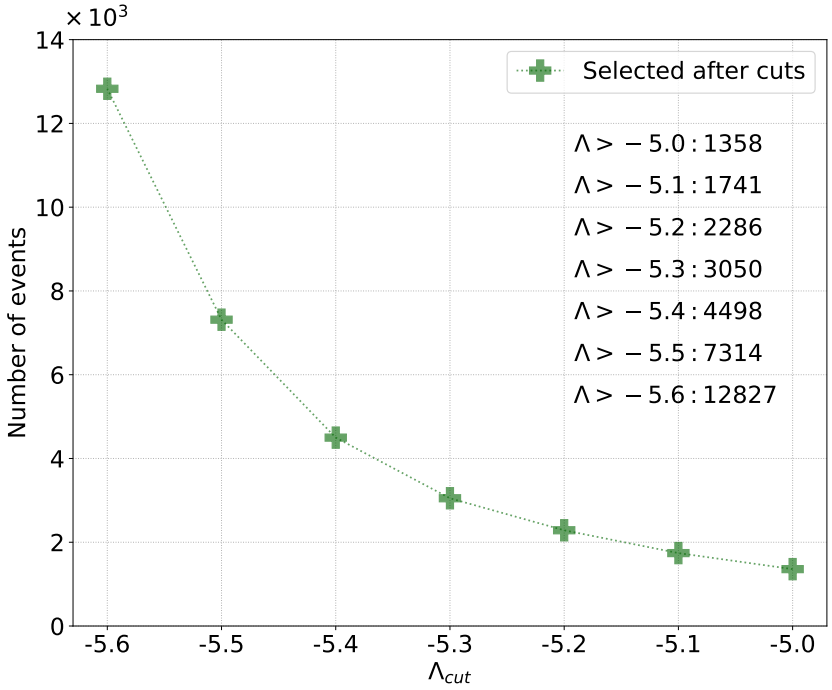

Fig. A.1.: The track-like events passing the selection cuts for Dataset 2014-2017.

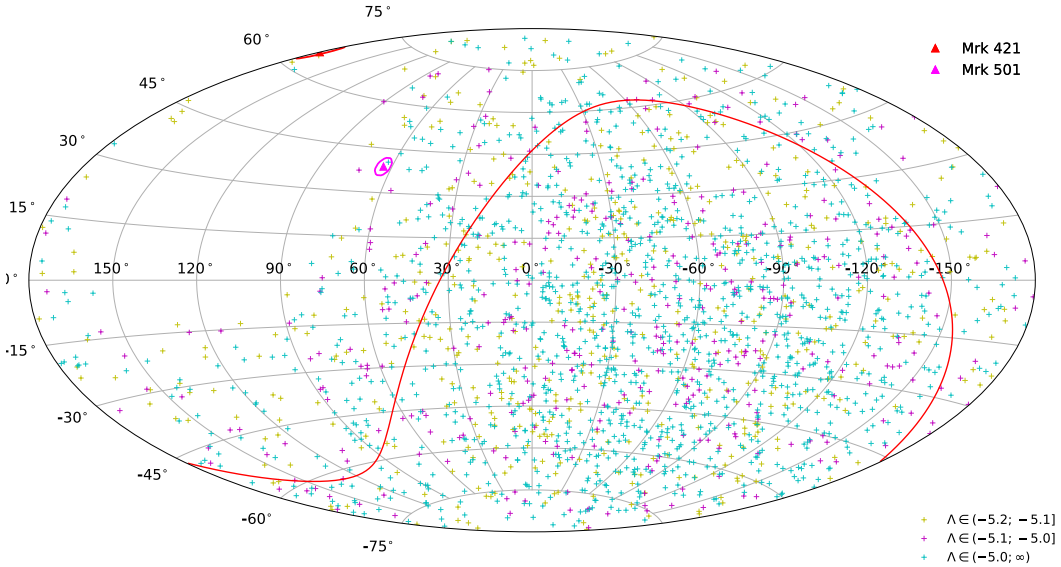

Fig. A.2.: Skymap of the track-like events passing the selection cuts (total 2286 events selected with $\Lambda > -5.2$) for Dataset 2014-2017. In galactic coordinates using Aitoff projection. The red solid curve denotes the equatorial plane. The red circles denote the 3° radius region around the sources. Redrawn here to have full set of 7 skymaps for 7 Λ cuts in Appendix, see the original size in Fig. 7.16.

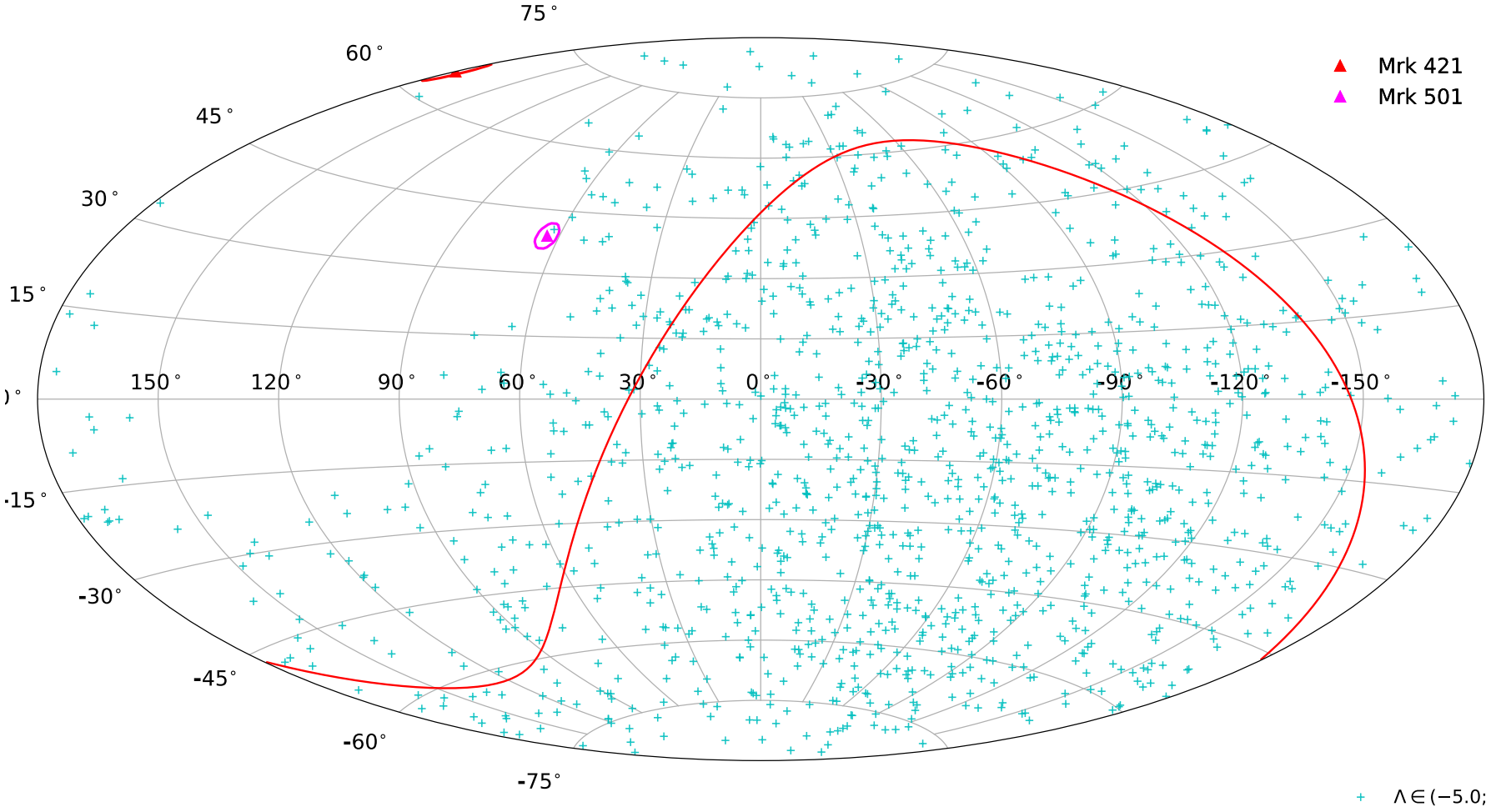

Fig. A.3.: Skymap of the track-like events passing the selection cuts (total 1358 events selected with $\Lambda > -5.0$) for Dataset 2014-2017. In galactic coordinates using Aitoff projection. The red solid curve denotes the equatorial plane. The red circles denote the 3° radius region around the sources.

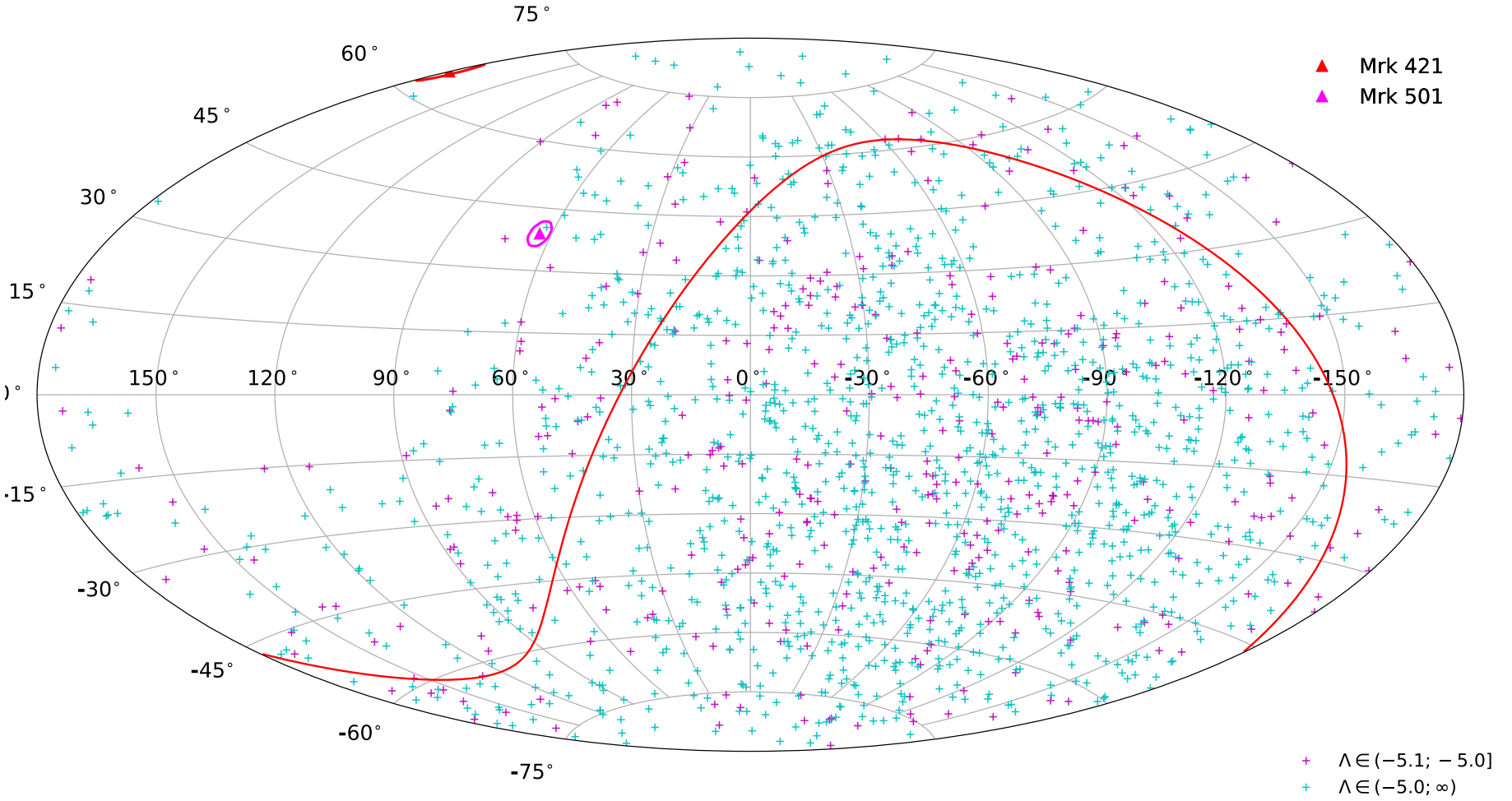

Fig. A.4.: Skymap of the track-like events passing the selection cuts (total 1741 events selected with $\Lambda > -5.1$) for Dataset 2014-2017. In galactic coordinates using Aitoff projection. The red solid curve denotes the equatorial plane. The red circles denote the 3 degree radius region around the sources.

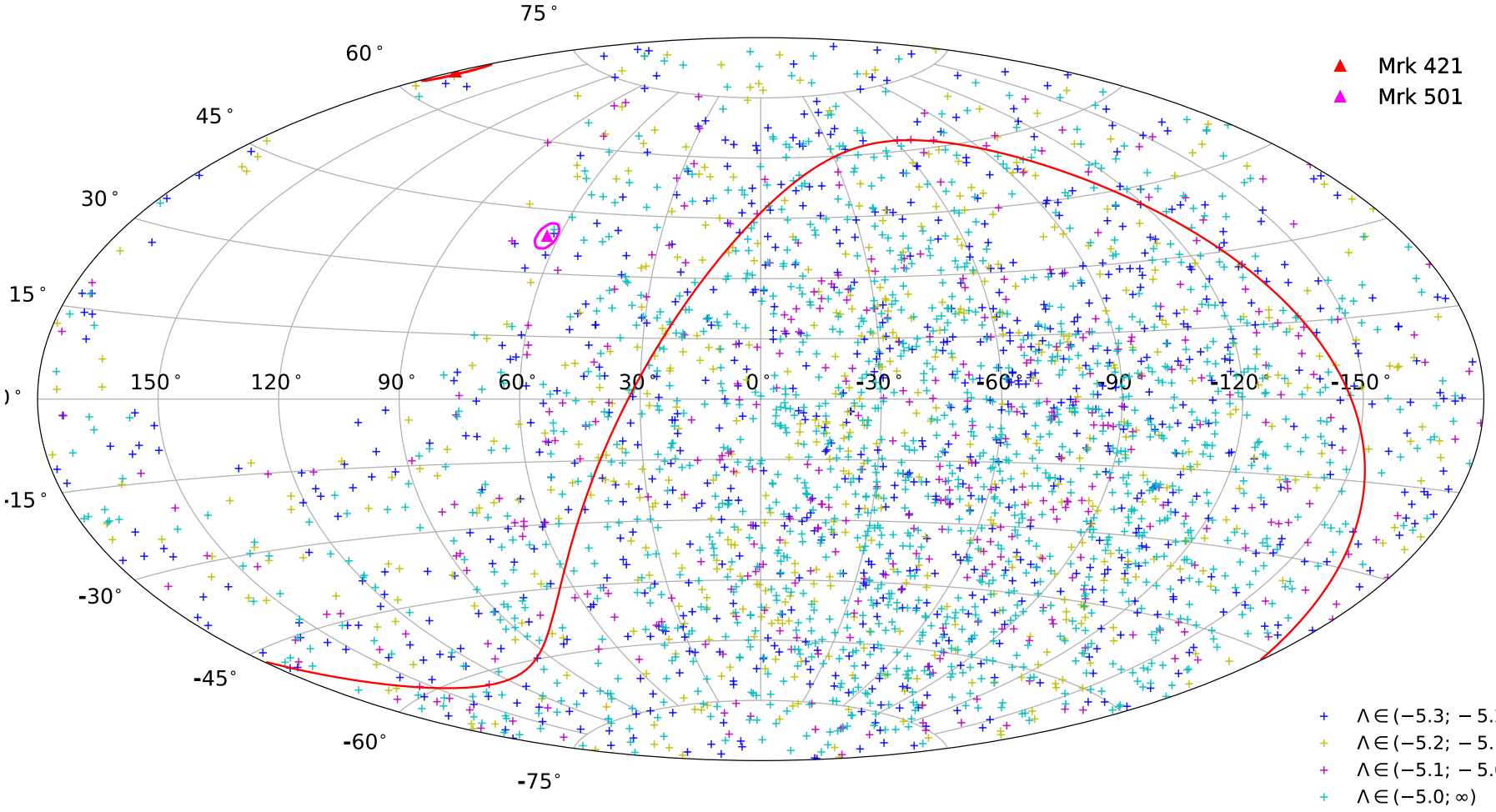

Fig. A.5.: Skymap of the track-like events passing the selection cuts (total 3050 events selected with $\Lambda > -5.3$) for Dataset 2014-2017. In galactic coordinates using Aitoff projection. The red solid curve denotes the equatorial plane. The red circles denote the 3° radius region around the sources.

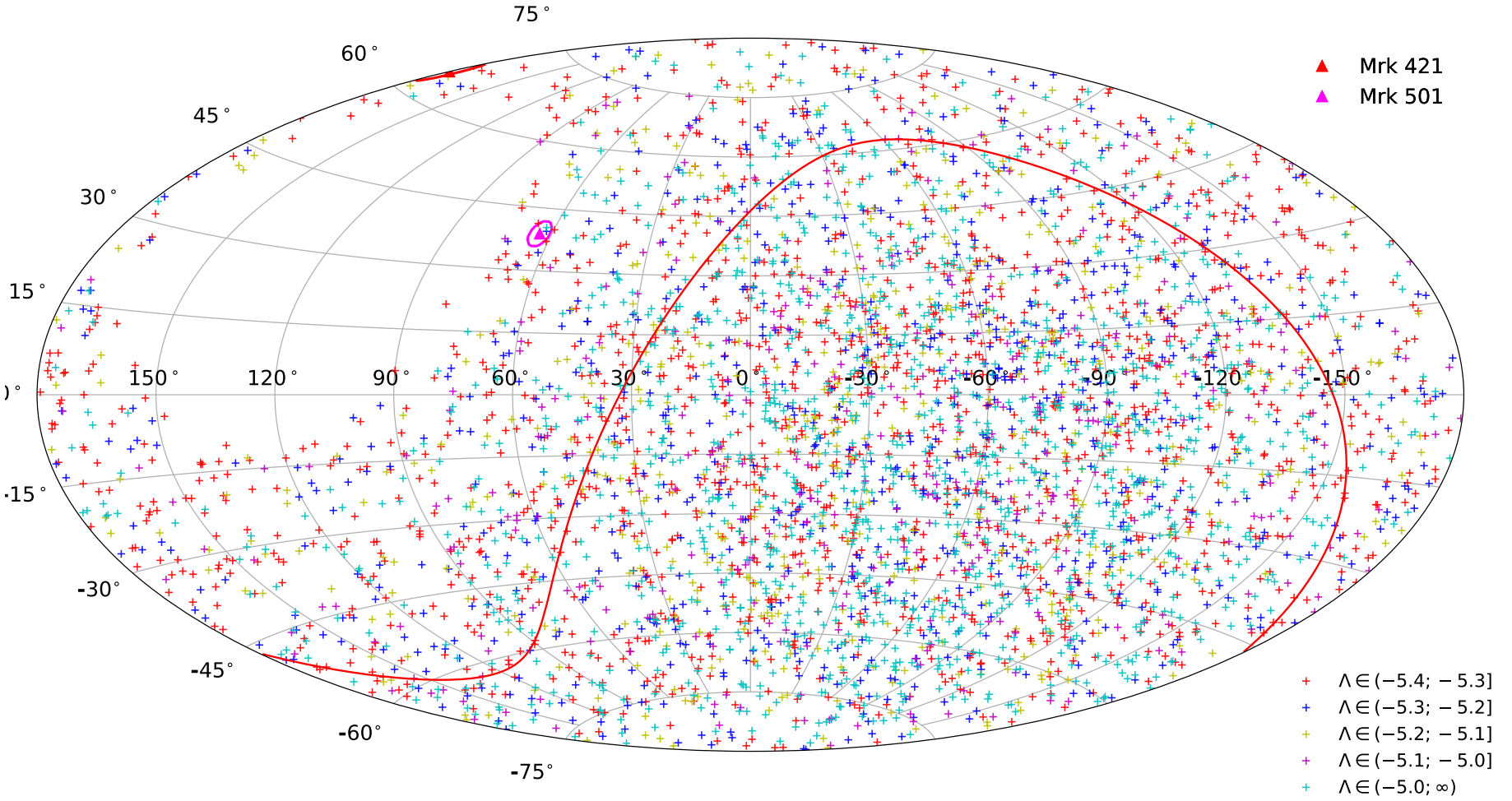

Fig. A.6.: Skymap of the track-like events passing the selection cuts (total 4498 events selected with $\Lambda > -5.4$) for Dataset 2014-2017. In galactic coordinates using Aitoff projection. The red solid curve denotes the equatorial plane. The red circles denote the 3° radius region around the sources.

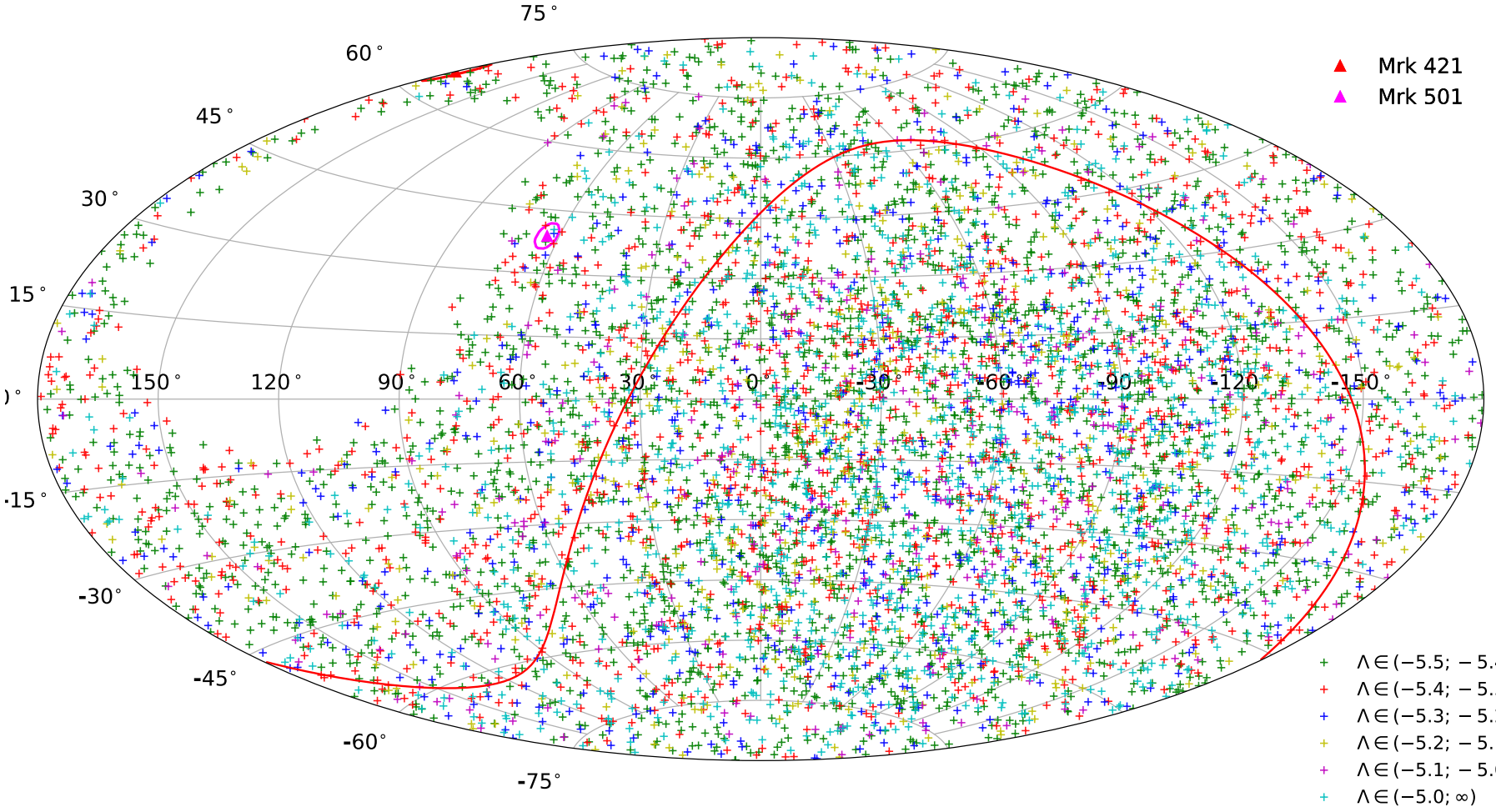

Fig. A.7.: Skymap of the track-like events passing the selection cuts (total 7314 events selected with $\Lambda > -5.5$) for Dataset 2014-2017. In galactic coordinates using Aitoff projection. The red solid curve denotes the equatorial plane. The red circles denote the 3° radius region around the sources.

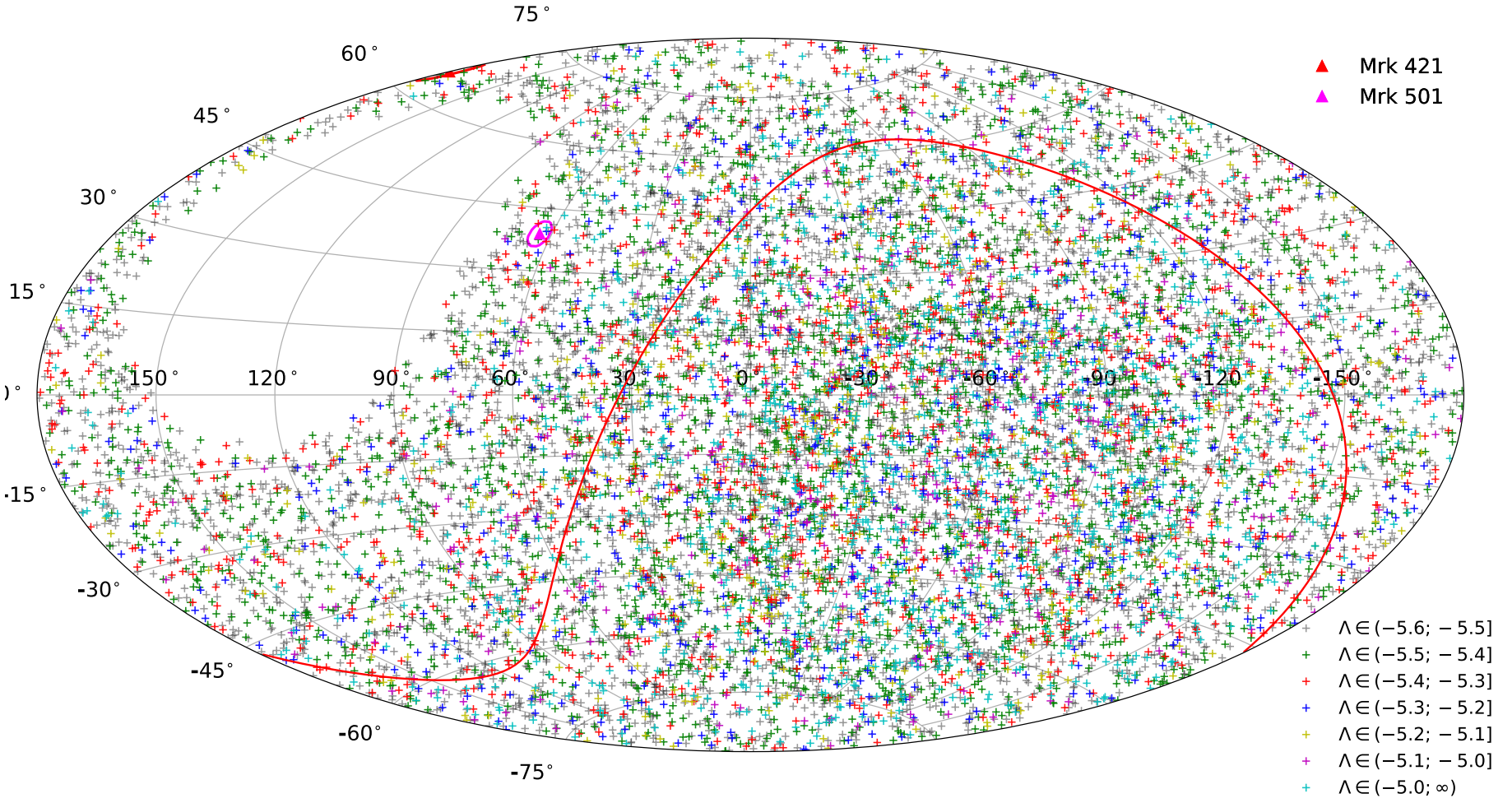

Fig. A.8.: Skymap of the track-like events passing the selection cuts (total 12827 events selected with $\Lambda > -5.6$) for Dataset 2014-2017. In galactic coordinates using Aitoff projection. The red solid curve denotes the equatorial plane. The red circles denote the 3° radius region around the sources.

Bibliography

[1]V. F. Hess. „Über Beobachtungen der durchdringenden Strahlung bei sieben Freiballonfahrten“. In: *Physikalische Zeitschrift* 13 (1912), pp. 1084–1091. URL: https://cds.cern.ch/record/262750 (cit. on pp. 21, 23, 38).

[2]Carl D. Anderson. „The Positive Electron“. In: *Physical Review* 43.6 (1933), pp. 491–494. DOI: 10.1103/PhysRev.43.491 (cit. on p. 21).

[3]Seth H. Neddermeyer and Carl D. Anderson. „Note on the Nature of Cosmic-Ray Particles“. In: *Physical Review* 51.10 (1937), pp. 884–886. DOI: 10.1103/PhysRev.51.884 (cit. on p. 21).

[4]G. D. Rochester and C. C. Butler. „Evidence for the Existence of New Unstable Elementary Particles“. In: Nature 160 (Dec. 1947), pp. 855–857. DOI: 10.1038/160855a0 (cit. on p. 21).

[5]E. Hubble. „A Relation between Distance and Radial Velocity among Extra-Galactic Nebulae“. In: *Proceedings of the National Academy of Science* 15 (Mar. 1929), pp. 168–173. DOI: 10.1073/pnas.15.3.168 (cit. on p. 21).

[6]M. Schmidt. „3C 273 : A Star-Like Object with Large Red-Shift“. In: Nature 197 (Mar. 1963), p. 1040. DOI: 10.1038/1971040a0 (cit. on p. 21).

[7]A. A. Penzias and R. W. Wilson. „A Measurement of Excess Antenna Temperature at 4080 Mc/s.“ In: ApJ 142 (July 1965), pp. 419–421. DOI: 10.1086/148307 (cit. on pp. 21, 29).

[8]A. Hewish, S. J. Bell, J. D. H. Pilkington, P. F. Scott, and R. A. Collins. „Observation of a Rapidly Pulsating Radio Source“. In: Nature 217 (Feb. 1968), pp. 709–713. DOI: 10.1038/217709a0 (cit. on p. 21).

[9]Ray W. Klebesadel, Ian B. Strong, and Roy A. Olson. „Observations of Gamma-Ray Bursts of Cosmic Origin“. In: *The Astrophysical Journal* 182 (1973), p. L85. DOI: 10.1086/181225 (cit. on pp. 21, 47).

[10]M. Mayor and D. Queloz. „A Jupiter-mass companion to a solar-type star“. In: Nature 378 (Nov. 1995), pp. 355–359. DOI: 10.1038/378355a0 (cit. on p. 21).

[11]IceCube Collaboration. „Evidence for High-Energy Extraterrestrial Neutrinos at the IceCube Detector“. In: *Science* 342.6161, 1242856 (2013), p. 1242856. DOI: 10.1126/science.1242856. arXiv: 1311.5238 [astro-ph.HE] (cit. on pp. 21, 86, 91, 94, 102, 103, 118, 146).

[12]B. P. Abbott, R. Abbott, T. D. Abbott, et al. „Observation of Gravitational Waves from a Binary Black Hole Merger“. In: Phys. Rev. Lett. 116.6, 061102 (2016), p. 061102. DOI: 10.1103/PhysRevLett.116.061102. arXiv: 1602.03837 [gr-qc] (cit. on pp. 22, 54, 55, 58–63, 67).

[13]B. P. Abbott, R. Abbott, T. D. Abbott, et al. „GW170817: Observation of Gravitational Waves from a Binary Neutron Star Inspiral“. In: Phys. Rev. Lett. 119.16, 161101 (2017), p. 161101. DOI: 10.1103/PhysRevLett.119.161101. arXiv: 1710.05832 [gr-qc] (cit. on pp. 22, 56, 66, 112, 113).

[14]C. Kopper and E. Blaufuss. „IceCube-170922A - IceCube observation of a high-energy neutrino candidate event.“ In: *GRB Coordinates Network, Circular Service, No. 21916, #1 (2017)* 21916 (2017) (cit. on pp. 22, 81, 94, 102, 104, 105, 110, 118, 146, 218).

[15]IceCube Collaboration, M. G. Aartsen, M. Ackermann, et al. „Neutrino emission from the direction of the blazar TXS 0506+056 prior to the IceCube-170922A alert“. In: *Science* 361.6398 (2018), pp. 147–151. DOI: 10.1126/science.aat2890. arXiv: 1807.08794 [astro-ph.HE] (cit. on pp. 22, 38, 102, 104–106, 111, 118, 146, 250).

[16]IceCube Collaboration, M. G. Aartsen, M. Ackermann, et al. „Multimessenger observations of a flaring blazar coincident with high-energy neutrino IceCube-170922A“. In: *Science* 361.6398, eaat1378 (2018), eaat1378. DOI: 10.1126/science.aat1378. arXiv: 1807.08816 [astro-ph.HE] (cit. on pp. 22, 38, 52, 102, 104–107, 110, 111, 118, 250).

[17]Robert Marcus Wagner. „Measurement of very high energy gamma-ray emission from four blazars using the MAGIC telescope and a comparative blazar study“. PhD thesis. Max-Planck-Institut für Physik, Föhringer Ring 6, 80805 München, Germany, 2006 (cit. on pp. 23, 46).

[18]B. Rossi. „On the Magnetic Deflection of Cosmic Rays“. In: *Physical Review* 36 (Aug. 1930), pp. 606–606. DOI: 10.1103/PhysRev.36.606 (cit. on p. 23).

[19]Thomas H. Johnson and J. C. Street. „The Variation of the Cosmic-Ray Intensity with Azimuth“. In: *Physical Review* 41.5 (1932), pp. 690–690. DOI: 10.1103/PhysRev.41.690 (cit. on p. 23).

[20]Thomas H. Johnson. „Progress of the Directional Survey of Cosmic-Ray Intensities and Its Application to the Analysis of the Primary Cosmic Radiation“. In: *Physical Review* 48.4 (1935), pp. 287–299. DOI: 10.1103/PhysRev.48.287 (cit. on p. 23).

[21]Luis Alvarez and Arthur H. Compton. „A Positively Charged Component of Cosmic Rays“. In: *Physical Review* 43.10 (1933), pp. 835–836. DOI: 10.1103/PhysRev.43.835 (cit. on p. 23).

[22]Bruno Rossi. „Directional Measurements on the Cosmic Rays Near the Geomagnetic Equator“. In: *Physical Review* 45.3 (1934), pp. 212–214. DOI: 10.1103/PhysRev.45.212 (cit. on p. 23).

[23]B. Rossi. „Misure della distribuzione angolare di intensità della radiazione penetrante all'Asmara“. In: *La ricerca scientifica supplemento* (1934) (cit. on pp. 23, 26).

[24]P.C. Bhattacharya. „East-West asymmetry of cosmic rays at Calcutta and Darjeeling“. In: *Proceedings of the National Academy of Sciences of India* (1942) (cit. on p. 23).

[25]Thomas H. Johnson. „The Azimuthal Asymmetry of the Cosmic Radiation“. In: *Physical Review* 43.10 (1933), pp. 834–835. DOI: 10.1103/PhysRev.43.834 (cit. on p. 23).

[26]P. Auger and L. L. Ringuet. „Variation du Rayonnement cosmique suivant la Latitude“. In: Nature 133 (Jan. 1934), pp. 138–139. DOI: 10.1038/133138b0 (cit. on p. 23).

[27]Martin V. Zombeck. *Handbook of Space Astronomy and Astrophysics*. 3rd ed. Cambridge University Press, 2006. DOI: 10.1017/CBO9780511536359 (cit. on p. 24).

[28]J. J. Engelmann, P. Ferrando, A. Soutoul, et al. „Charge composition and energy spectra of cosmic-ray nuclei for elements from Be to NI - Results from HEAO-3-C2“. In: A&A 233 (July 1990), pp. 96–111 (cit. on p. 24).

[29]J. Alcaraz, B. Alpat, G. Ambrosi, et al. „Cosmic protons“. In: *Physics Letters B* 490.1-2 (2000), pp. 27–35. DOI: 10.1016/S0370-2693(00)00970-9 (cit. on p. 24).

[30]AMS Collaboration, J. Alcaraz, B. Alpat, et al. „Helium in near Earth orbit“. In: *Physics Letters B* 494.3-4 (2000), pp. 193–202. DOI: 10.1016/S0370-2693(00)01193-X (cit. on p. 24).

[31]T. Sanuki, M. Motoki, H. Matsumoto, et al. „Precise Measurement of Cosmic-Ray Proton and Helium Spectra with the BESS Spectrometer“. In: ApJ 545 (Dec. 2000), pp. 1135–1142. DOI: 10.1086/317873. eprint: astro-ph/0002481 (cit. on p. 24).

[32]Thomas K. Gaisser and Todor Stanev. „High-energy cosmic rays“. In: Nucl. Phys. A 777 (2006), pp. 98–110. DOI: 10.1016/j.nuclphysa.2005.01.024. arXiv: astro-ph/0510321 [astro-ph] (cit. on pp. 24, 43).

[33]Phyllis Freier, E. J. Lofgren, E. P. Ney, et al. „Evidence for Heavy Nuclei in the Primary Cosmic Radiation“. In: *Physical Review* 74.2 (1948), pp. 213–217. DOI: 10.1103/PhysRev.74.213 (cit. on p. 23).

[34]H. L. Bradt and B. Peters. „Investigation of the Primary Cosmic Radiation with Nuclear Photographic Emulsions“. In: *Physical Review* 74.12 (1948), pp. 1828–1837. DOI: 10.1103/PhysRev.74.1828 (cit. on p. 24).

[35]D. Filges and F. Goldenbaum. *Handbook of Spallation Research: Theory, Experiments and Applications*. 2010 (cit. on p. 24).

[36]Peter Biermann and Gunter Sigl. „Introduction to cosmic rays“. In: *Lect. Notes Phys.* 576 (2001). [,1(2002)], pp. 1–26. arXiv: astro-ph/0202425 [astro-ph] (cit. on p. 24).

[37]Malcolm S. Longair. *High Energy Astrophysics*. 3rd ed. Cambridge University Press, 2011. DOI: 10.1017/CBO9780511778346 (cit. on p. 24).

[38]Hans Peter Dembinski, Ralph Engel, Anatoli Fedynitch, et al. „Data-driven model of the cosmic-ray flux and mass composition from 10 GeV to 10^{11} GeV“. In: *PoS* ICRC2017 (2018). [35,533(2017)], p. 533. DOI: 10.22323/1.301.0533. arXiv: 1711.11432 [astro-ph.HE] (cit. on pp. 25, 26).

[39]M. Tanabashi, K. Hagiwara, K. Hikasa, et al. „Review of Particle Physics*“. In: Phys. Rev. D 98.3, 030001 (2018), p. 030001. DOI: 10.1103/PhysRevD.98.030001 (cit. on pp. 25, 27, 29, 39, 70, 72–75, 77, 78, 90, 101, 119, 120, 125, 127, 130–132, 136, 142, 184, 317–319).

[40]P. Auger, R. Maze, and A.F. Robley. „Extension et pouvoir pénétrant des grandes gerbes de rayons cosmiques“. In: *Comptes Rendus* 208 (1939), pp. 1641–1643 (cit. on p. 26).

[41]P. Auger, P. Ehrenfest, R. Maze, J. Daudin, and R. A. Fréon. „Extensive Cosmic-Ray Showers“. In: *Reviews of Modern Physics* 11 (July 1939), pp. 288–291. DOI: 10.1103/RevModPhys.11.288 (cit. on p. 26).

[42]Anthony M. Hillas. „Cosmic Rays: Recent Progress and some Current Questions“. In: *Conference on Cosmology, Galaxy Formation and Astro-Particle Physics on the Pathway to the SKA Oxford, England, April 10-12, 2006*. 2006. arXiv: astro-ph/0607109 [astro-ph] (cit. on pp. 27, 45).

[43]Johannes Blümer, Ralph Engel, and Jörg R. Hörandel. „Cosmic rays from the knee to the highest energies“. In: *Progress in Particle and Nuclear Physics* 63.2 (2009), pp. 293–338. DOI: 10.1016/j.ppnp.2009.05.002. arXiv: 0904.0725 [astro-ph.HE] (cit. on pp. 26–28, 43).

[44]Jörg R. Hörandel. „Cosmic Rays from the Knee to the Second Knee:. 10^{14} to 10^{18} eV“. In: *Modern Physics Letters A* 22.21 (2007), pp. 1533–1551. DOI: 10.1142/S0217732307024139. arXiv: astro-ph/0611387 [astro-ph] (cit. on pp. 26, 27).

[45]E. G. Zweibel. „The microphysics and macrophysics of cosmic rays“. In: *Physics of Plasmas* 20.5, 055501 (May 2013), p. 055501. DOI: 10.1063/1.4807033 (cit. on pp. 26, 27).

[46]Diego F. Torres and Luis A. Anchordoqui. „Astrophysical origins of ultrahigh energy cosmic rays“. In: *Reports on Progress in Physics* 67.9 (2004), pp. 1663–1730. DOI: 10.1088/0034-4885/67/9/R03. arXiv: astro-ph/0402371 [astro-ph] (cit. on pp. 26, 27).

[47]T. Abu-Zayyad, R. Aida, M. Allen, et al. „The Cosmic-Ray Energy Spectrum Observed with the Surface Detector of the Telescope Array Experiment“. In: ApJ 768.1, L1 (2013), p. L1. DOI: 10.1088/2041-8205/768/1/L1. arXiv: 1205.5067 [astro-ph.HE] (cit. on pp. 26, 27, 31, 32).

[48]R. U. Abbasi, T. Abu-Zayyad, M. Allen, et al. „First Observation of the Greisen-Zatsepin-Kuzmin Suppression“. In: Phys. Rev. Lett. 100.10, 101101 (2008), p. 101101. DOI: 10.1103/PhysRevLett.100.101101. arXiv: astro-ph/0703099 [astro-ph] (cit. on pp. 26, 31, 32).

[49]J. Abraham, P. Abreu, M. Aglietta, et al. „Measurement of the energy spectrum of cosmic rays above 10^{18} eV using the Pierre Auger Observatory“. In: *Physics Letters B* 685.4-5 (2010), pp. 239–246. DOI: 10.1016/j.physletb.2010.02.013. arXiv: 1002.1975 [astro-ph.HE] (cit. on pp. 26, 27).

[50]J. Linsley. „Primary cosmic rays of energy 10^{17} to 10^{20} ev, the energy spectrum and arrival directions“. In: *International Cosmic Ray Conference*. Vol. 4. International Cosmic Ray Conference. 1963, p. 77 (cit. on p. 28).

[51]D. J. Bird, S. C. Corbató, H. Y. Dai, et al. „Evidence for correlated changes in the spectrum and composition of cosmic rays at extremely high energies“. In: Phys. Rev. Lett. 71.21 (1993), pp. 3401–3404. DOI: 10.1103/PhysRevLett.71.3401 (cit. on pp. 28, 44).

[52]M. Nagano, M. Teshima, Y. Matsubara, et al. „Energy spectrum of primary cosmic rays above $10^{17.0}$ eV determined from extensive air shower experiments at Akeno“. In: *Journal of Physics G Nuclear Physics* 18.2 (1992), pp. 423–442. DOI: 10.1088/0954-3899/18/2/022 (cit. on p. 28).

[53]R. M. Baltrusaitis, R. Cady, G. L. Cassiday, et al. „The Utah Fly's Eye detector“. In: *Nuclear Instruments and Methods in Physics Research A* 240.2 (1985), pp. 410–428. DOI: 10.1016/0168-9002(85)90658-8 (cit. on p. 28).

[54]G. L. Cassiday. „Observatory for ultra high-energy processes: the Fly's Eye.“ In: *Annual Review of Nuclear and Particle Science* 35 (1985), pp. 321–349. DOI: 10.1146/annurev.ns.35.120185.001541 (cit. on p. 28).

[55]T. Abu-Zayyad, M. Al-Seady, K. Belov, et al. „The prototype high-resolution Fly's Eye cosmic ray detector“. In: *Nuclear Instruments and Methods in Physics Research A* 450.2-3 (2000), pp. 253–269. DOI: 10.1016/S0168-9002(00)00307-7 (cit. on p. 28).

[56]John H. Boyer, Bruce C. Knapp, Eric J. Mannel, and Michal Seman. „FADC-based DAQ for HiRes Fly's Eye“. In: *Nuclear Instruments and Methods in Physics Research A* 482.1-2 (2002), pp. 457–474. DOI: 10.1016/S0168-9002(01)01517-0 (cit. on p. 28).

[57]T. Hara et al. „THE AKENO AIR SHOWER PROJECT.“ In: *16th International Cosmic Ray Conference. Vol. 8. Conference Papers. EA Session I. Proceedings, Kyoto, Japan, August 6-18, 1979*. 1979, pp. 135–140 (cit. on p. 28).

[58]N. Chiba, K. Hashimoto, N. Hayashida, et al. „Akeno Giant Air Shower Array (AGASA) covering 100 km ^{2} area“. In: *Nuclear Instruments and Methods in Physics Research A* 311.1-2 (1992), pp. 338–349. DOI: 10.1016/0168-9002(92)90882-5 (cit. on p. 28).

[59]D. J. Bird, S. C. Corbato, H. Y. Dai, et al. „Detection of a Cosmic Ray with Measured Energy Well beyond the Expected Spectral Cutoff due to Cosmic Microwave Radiation“. In: ApJ 441 (1995), p. 144. DOI: 10.1086/175344. arXiv: astro-ph/9410067 [astro-ph] (cit. on p. 28).

[60]Kenneth Greisen. „End to the Cosmic-Ray Spectrum?“ In: Phys. Rev. Lett. 16.17 (1966), pp. 748–750. DOI: 10.1103/PhysRevLett.16.748 (cit. on pp. 29, 32).

[61]G. T. Zatsepin and V. A. Kuzmin. „Upper limit of the spectrum of cosmic rays“. In: *JETP Lett.* 4 (1966). [Pisma Zh. Eksp. Teor. Fiz.4,114(1966)], pp. 78–80 (cit. on pp. 29, 32).

[62]R. A. Alpher and R. Herman. „Evolution of the Universe“. In: Nature 162 (Nov. 1948), pp. 774–775. DOI: 10.1038/162774b0 (cit. on p. 29).

[63]R. A. Alpher and R. C. Herman. „Remarks on the Evolution of the Expanding Universe“. In: *Physical Review* 75 (Apr. 1949), pp. 1089–1095. DOI: 10.1103/PhysRev.75.1089 (cit. on p. 29).

[64]C. D. Dermer and A. Atoyan. „Ultra-high energy cosmic rays, cascade gamma rays, and high-energy neutrinos from gamma-ray bursts“. In: *New Journal of Physics* 8.7 (2006), p. 122. DOI: 10.1088/1367-2630/8/7/122. arXiv: astro-ph/0606629 [astro-ph] (cit. on pp. 30, 31).

[65]James W. Cronin. „The highest-energy cosmic rays“. In: *Nuclear Physics B Proceedings Supplements* 138 (2005), pp. 465–491. DOI: 10.1016/j.nuclphysbps.2004.11.107. arXiv: astro-ph/0402487 [astro-ph] (cit. on p. 30).

[66]V. S. Beresinsky and G. T. Zatsepin. „Cosmic rays at ultra high energies (neutrino?)“ In: *Physics Letters B* 28 (Jan. 1969), pp. 423–424. DOI: 10.1016/0370-2693(69)90341-4 (cit. on pp. 30, 90).

[67]G. B. Gelmini, O. E. Kalashev, and D. V. Semikoz. „GZK photons as ultra-high-energy cosmic rays“. In: *Soviet Journal of Experimental and Theoretical Physics* 106.6 (2008), pp. 1061–1082. DOI: 10.1134/S106377610806006X. arXiv: astro-ph/0506128 [astro-ph] (cit. on p. 30).

[68]A. A. Watson. „High-energy cosmic rays and the Greisen-Zatsepin-Kuz'min effect“. In: *Reports on Progress in Physics* 77.3, 036901 (2014), p. 036901. DOI: 10.1088/0034-4885/77/3/036901. arXiv: 1310.0325 [astro-ph.HE] (cit. on pp. 30, 31, 42).

[69]Eli Waxman. „Cosmological Origin for Cosmic Rays above 10 19 eV“. In: ApJ 452 (1995), p. L1. DOI: 10.1086/309715. arXiv: astro-ph/9508037 [astro-ph] (cit. on pp. 30, 91).

[70]R. Ruffini, G. V. Vereshchagin, and S. S. Xue. „Cosmic absorption of ultra high energy particles“. In: Ap&SS 361, 82 (2016), p. 82. DOI: 10.1007/s10509-016-2668-5. arXiv: 1503.07749 [astro-ph.HE] (cit. on pp. 30, 31).

[71]Xavier Bertou, Murat Boratav, and Antoine Letessier-Selvon. „Physics of Extremely High Energy Cosmic Rays“. In: *International Journal of Modern Physics A* 15 (2000), pp. 2181–2224. DOI: 10.1142/S0217751X00000902. arXiv: astro-ph/0001516 [astro-ph] (cit. on pp. 30, 31).

[72]J. Abraham, M. Aglietta, I. C. Aguirre, et al. „Properties and performance of the prototype instrument for the Pierre Auger Observatory“. In: *Nuclear Instruments and Methods in Physics Research A* 523 (May 2004), pp. 50–95. DOI: 10.1016/j.nima.2003.12.012 (cit. on pp. 31, 32).

[73]The Pierre Auger Collaboration. „The Pierre Auger Cosmic Ray Observatory“. In: *arXiv e-prints*, arXiv:1502.01323 (2015), arXiv:1502.01323. arXiv: 1502.01323 [astro-ph.IM] (cit. on pp. 31, 32).

[74]J. Abraham, P. Abreu, M. Aglietta, et al. „Observation of the Suppression of the Flux of Cosmic Rays above 4×10^{19}eV“. In: Phys. Rev. Lett. 101.6, 061101 (2008), p. 061101. DOI: 10.1103/PhysRevLett.101.061101. arXiv: 0806.4302 [astro-ph] (cit. on p. 31).

[75]Valerio Verzi, Dmitri Ivanov, and Yoshiki Tsunesada. „Measurement of energy spectrum of ultra-high energy cosmic rays“. In: *Progress of Theoretical and Experimental Physics* 2017.12 (Nov. 2017). 12A103. ISSN: 2050-3911. DOI: 10.1093/ptep/ptx082. eprint: http://oup.prod.sis.lan/ptep/article-pdf/2017/12/12A103/22075708/ptx082.pdf. URL: https://doi.org/10.1093/ptep/ptx082 (cit. on pp. 31, 32).

[76]H. Kawai, S. Yoshida, H. Yoshii, et al. „Telescope Array Experiment“. In: *Nuclear Physics B Proceedings Supplements* 175 (2008), pp. 221–226. DOI: 10.1016/j.nuclphysbps.2007.11.002 (cit. on p. 31).

[77]T. Abu-Zayyad, R. Aida, M. Allen, et al. „The surface detector array of the Telescope Array experiment“. In: *Nuclear Instruments and Methods in Physics Research A* 689 (2012), pp. 87–97. DOI: 10.1016/j.nima.2012.05.079. arXiv: 1201.4964 [astro-ph.IM] (cit. on pp. 31, 32).

[78]H. Tokuno, Y. Tameda, M. Takeda, et al. „New air fluorescence detectors employed in the Telescope Array experiment“. In: *Nuclear Instruments and Methods in Physics Research A* 676 (2012), pp. 54–65. DOI: 10.1016/j.nima.2012.02.044. arXiv: 1201.0002 [astro-ph.IM] (cit. on pp. 31, 32).

[79]M. Takeda, N. Hayashida, K. Honda, et al. „Extension of the Cosmic-Ray Energy Spectrum beyond the Predicted Greisen-Zatsepin-Kuz'min Cutoff“. In: Phys. Rev. Lett. 81.6 (1998), pp. 1163–1166. DOI: 10.1103/PhysRevLett.81.1163. arXiv: astro-ph/9807193 [astro-ph] (cit. on p. 31).

[80]M. Takeda, N. Sakaki, K. Honda, et al. „Energy determination in the Akeno Giant Air Shower Array experiment“. In: *Astroparticle Physics* 19.4 (2003), pp. 447–462. DOI: 10.1016/S0927-6505(02)00243-8. arXiv: astro-ph/0209422 [astro-ph] (cit. on p. 31).

[81]Y. Uchihori, M. Nagano, M. Takeda, et al. „Cluster analysis of extremely high energy cosmic rays in the northern sky“. In: *Astroparticle Physics* 13.2-3 (2000), pp. 151–160. DOI: 10.1016/S0927-6505(99)00119-X. arXiv: astro-ph/9908193 [astro-ph] (cit. on p. 31).

[82]E. Kido, O. E. Kalashev, and for the Telescope Array Collaboration. „Constraining UHECR source models by the TA SD energy spectrum“. In: *arXiv e-prints*, arXiv:1310.6093 (2013), arXiv:1310.6093. arXiv: 1310.6093 [astro-ph.HE] (cit. on p. 33).

[83]Antoine Letessier-Selvon. „Highlights from the Pierre Auger Observatory“. In: *Brazilian Journal of Physics* 44.5 (2014), pp. 560–570. DOI: 10.1007/s13538-014-0218-6. arXiv: 1310.4620 [astro-ph.HE] (cit. on p. 33).

[84]R. Aloisio, V. Berezinsky, and P. Blasi. „Ultra high energy cosmic rays: implications of Auger data for source spectra and chemical composition“. In: J. Cosmology Astropart. Phys. 2014.10, 020 (2014), p. 020. DOI: 10.1088/1475-7516/2014/10/020. arXiv: 1312.7459 [astro-ph.HE] (cit. on p. 33).

[85]Karl-Heinz Kampert and Peter Tinyakov. „Cosmic rays from the ankle to the cutoff“. In: *Comptes Rendus Physique* 15.4 (2014), pp. 318–328. DOI: 10.1016/j.crhy.2014.04.006. arXiv: 1405.0575 [astro-ph.HE] (cit. on pp. 32–34).

[86]Arjen René van Vliet. „Propagation of ultra-high-energy cosmic rays and their secondaries with CRPropa“. PhD thesis. U. Hamburg, Dept. Phys., 2014. DOI: 10.3204/DESY-THESIS-2015-014. URL: http://bib-pubdb1.desy.de/search?of=hd&p=id:%22DESY-THESIS-2015-014%22 (cit. on p. 32).

[87]R. Aloisio, V. Berezinsky, and A. Gazizov. „Ultra high energy cosmic rays: The disappointing model“. In: *Astroparticle Physics* 34.8 (2011), pp. 620–626. DOI: 10.1016/j.astropartphys.2010.12.008. arXiv: 0907.5194 [astro-ph.HE] (cit. on pp. 33, 90).

[88]Karl-Heinz Kampert and Michael Unger. „Measurements of the cosmic ray composition with air shower experiments“. In: *Astroparticle Physics* 35.10 (2012), pp. 660–678. DOI: 10.1016/j.astropartphys.2012.02.004. arXiv: 1201.0018 [astro-ph.HE] (cit. on p. 34).

[89]Enrico Fermi. „On the Origin of the Cosmic Radiation“. In: *Physical Review* 75.8 (1949), pp. 1169–1174. DOI: 10.1103/PhysRev.75.1169 (cit. on pp. 34, 87).

[90]Giovanni Morlino. „High-Energy Cosmic Rays from Supernovae“. In: *Handbook of Supernovae, ISBN 978-3-319-21845-8. Springer International Publishing AG, 2017, p. 1711*. Ed. by Athem W. Alsabti and Paul Murdin. 2017, p. 1711. DOI: 10.1007/978-3-319-21846-5_11 (cit. on pp. 34–37, 39).

[91]A. R. Bell. „The acceleration of cosmic rays in shock fronts. I“. In: MNRAS 182 (Jan. 1978), pp. 147–156. DOI: 10.1093/mnras/182.2.147 (cit. on pp. 36, 38, 42, 81, 138).

[92]A. R. Bell. „The acceleration of cosmic rays in shock fronts. II“. In: MNRAS 182 (Feb. 1978), pp. 443–455. DOI: 10.1093/mnras/182.3.443 (cit. on pp. 36, 42, 81).

[93]R. D. Blandford and J. P. Ostriker. „Particle acceleration by astrophysical shocks“. In: ApJ 221 (Apr. 1978), pp. L29–L32. DOI: 10.1086/182658 (cit. on pp. 36, 38, 39, 81).

[94]J. Skilling. „Cosmic ray streaming. I - Effect of Alfven waves on particles“. In: MNRAS 172 (Sept. 1975), pp. 557–566. DOI: 10.1093/mnras/172.3.557 (cit. on pp. 36, 42, 81).

[95]J. Skilling. „Cosmic ray streaming. II - Effect of particles on Alfven waves“. In: MNRAS 173 (Nov. 1975), pp. 245–254. DOI: 10.1093/mnras/173.2.245 (cit. on pp. 36, 42, 81).

[96]W. I. Axford, E. Leer, and G. Skadron. „The acceleration of cosmic rays by shock waves“. In: *International Cosmic Ray Conference*. Vol. 11. International Cosmic Ray Conference. 1977, pp. 132–137 (cit. on pp. 36, 81).

[97]G. F. Krymskii. „A regular mechanism for the acceleration of charged particles on the front of a shock wave“. In: *Akademiia Nauk SSSR Doklady* 234 (June 1977), pp. 1306–1308 (cit. on pp. 36, 38, 81).

[98]W. B. Atwood, A. A. Abdo, M. Ackermann, et al. „The Large Area Telescope on the Fermi Gamma-Ray Space Telescope Mission“. In: ApJ 697.2 (2009), pp. 1071–1102. DOI: 10.1088/0004-637X/697/2/1071. arXiv: 0902.1089 [astro-ph.IM] (cit. on pp. 38, 48).

[99]A. A. Abdo, M. Ackermann, M. Ajello, et al. „The on-orbit calibration of the Fermi Large Area Telescope“. In: *Astroparticle Physics* 32.3-4 (2009), pp. 193–219. DOI: 10.1016/j.astropartphys.2009.08.002. arXiv: 0904.2226 [astro-ph.IM] (cit. on pp. 38, 48).

[100]M. Ackermann, M. Ajello, A. Albert, et al. „The Fermi Large Area Telescope on Orbit: Event Classification, Instrument Response Functions, and Calibration“. In: ApJS 203.1, 4 (2012), p. 4. DOI: 10.1088/0067-0049/203/1/4. arXiv: 1206.1896 [astro-ph.IM] (cit. on pp. 38, 48).

[101]M. Ackermann, M. Ajello, A. Allafort, et al. „Detection of the Characteristic Pion-Decay Signature in Supernova Remnants“. In: *Science* 339.6121 (2013), pp. 807–811. DOI: 10.1126/science.1231160. arXiv: 1302.3307 [astro-ph.HE] (cit. on p. 38).

[102]W. Baade and F. Zwicky. „Cosmic Rays from Super-novae“. In: *Proceedings of the National Academy of Science* 20.5 (1934), pp. 259–263. DOI: 10.1073/pnas.20.5.259 (cit. on p. 38).

[103]V. L. Ginzburg. „Proiskhozhdenie kosmicheskikh luchei“. In: *Usp. Fiz. Nauk* 62.6 (1957), pp. 37–98. DOI: 10.3367/UFNr.0062.195706b.0037. URL: https://ufn.ru/ru/articles/1957/6/b/ (cit. on p. 38).

[104]V. L. Ginzburg and S. I. Syrovatskii. „Present status of the question of the origin of cosmic rays“. In: *Phys. Usp.* 3.4 (1961), pp. 504–541. DOI: 10.1070/PU1961v003n04ABEH003303. URL: https://ufn.ru/en/articles/1961/4/b/ (cit. on p. 38).

[105]S.I. Syrovatskii. „On the spectrum of the Galactic and Solar Cosmic Rays“. In: *Zhur. Eksptl'. i Teoret. Fiz.* V.40 (June 1961). URL: http://jetp.ac.ru/cgi-bin/dn/e_013_06_1257.pdf (cit. on p. 38).

[106]V. L. Ginzburg. „Cosmic rays on Earth and in the Universe“. In: *Phys. Usp.* 4.4 (1962), pp. 553–575. DOI: 10.1070/PU1962v004n04ABEH003347. URL: https://ufn.ru/en/articles/1962/4/b/ (cit. on p. 38).

[107]V. L. Ginzburg and S. I. Syrovatskii. *The Origin of Cosmic Rays*. 1964 (cit. on p. 38).

[108]V. L. Ginzburg and S. I. Syrovatsky. „Origin of cosmic rays“. In: *International Cosmic Ray Conference* 1 (1965), p. 53 (cit. on p. 38).

[109]V. L. Ginzburg and S. I. Syrovatskii. „Origin of cosmic rays“. In: *Usp. Fiz. Nauk* 88.3 (1966), pp. 485–504. DOI: 10.3367/UFNr.0088.196603e.0485. URL: https://ufn.ru/ru/articles/1966/3/e/ (cit. on p. 38).

[110]E. G. Berezhko and L. T. Ksenofontov. „Composition of cosmic rays accelerated in supernova remnants“. In: *J. Exp. Theor. Phys.* 89 (1999). [Zh. Eksp. Teor. Fiz.116,737(1999)], pp. 391–403. DOI: 10.1134/1.558996 (cit. on pp. 38, 39).

[111]V. L. Ginzburg, I. M. Khazan, and V. S. Ptuskin. „Origin of cosmic rays - Galactic models with halo. I - Proton nucleon component“. In: Ap&SS 68 (Apr. 1980), pp. 295–314. DOI: 10.1007/BF00639701 (cit. on p. 39).

[112]S. P. Wakely and D. Horan. „TeVCat: An online catalog for Very High Energy Gamma-Ray Astronomy“. In: *International Cosmic Ray Conference* 3 (2008), pp. 1341–1344 (cit. on p. 41).

[113]F. A. Aharonian. „Gamma rays from supernova remnants“. In: *Astroparticle Physics* 43 (Mar. 2013), pp. 71–80. DOI: 10.1016/j.astropartphys.2012.08.007 (cit. on p. 41).

[114]G. Dubner, G. Castelletti, O. Kargaltsev, et al. „Morphological Properties of the Crab Nebula: A Detailed Multiwavelength Study Based on New VLA, HST, Chandra, and XMM-Newton Images“. In: *The Astrophysical Journal* 840.2, 82 (2017), p. 82. DOI: 10.3847/1538-4357/aa6983. arXiv: 1704.02968 [astro-ph.HE] (cit. on p. 41).

[115]V. Trimble. „The Distance to the Crab Nebula and NP 0532“. In: PASP 85 (Oct. 1973), p. 579. DOI: 10.1086/129507 (cit. on p. 41).

[116]A. M. Hillas. „The Origin of Ultra-High-Energy Cosmic Rays“. In: ARA&A 22 (1984), pp. 425–444. DOI: 10.1146/annurev.aa.22.090184.002233 (cit. on pp. 41–44, 93).

[117]T. Chiarusi and M. Spurio. „High-energy astrophysics with neutrino telescopes“. In: *European Physical Journal C* 65.3-4 (2010), pp. 649–701. DOI: 10.1140/epjc/s10052-009-1230-9. arXiv: 0906.2634 [astro-ph.HE] (cit. on pp. 41, 43, 53, 83, 85, 87, 89, 94–100, 118, 131, 132, 139, 153, 155).

[118]P. O. Lagage and C. J. Cesarsky. „The maximum energy of cosmic rays accelerated by supernova shocks“. In: A&A 125 (Sept. 1983), pp. 249–257 (cit. on p. 42).

[119]E. G. Berezhko. „Maximum energy of cosmic rays accelerated by supernova shocks“. In: *Astroparticle Physics* 5 (1996), pp. 367–378. DOI: 10.1016/0927-6505(96)00037-0 (cit. on p. 42).

[120]S. G. Lucek and A. R. Bell. „Non-linear amplification of a magnetic field driven by cosmic ray streaming“. In: MNRAS 314.1 (2000), pp. 65–74. DOI: 10.1046/j.1365-8711.2000.03363.x (cit. on p. 42).

[121]A. M. Hillas. „Can diffusive shock acceleration in supernova remnants account for high-energy galactic cosmic rays?“ In: *Journal of Physics G Nuclear Physics* G31 (2005), R95–R131. DOI: 10.1088/0954-3899/31/5/R02 (cit. on pp. 42, 44, 45).

[122]Tadeusz Wibig and Arnold W. Wolfendale. „At what particle energy do extragalactic cosmic rays start to predominate?“ In: *Journal of Physics G Nuclear Physics* G31 (2005), pp. 255–264. DOI: 10.1088/0954-3899/31/3/005. arXiv: astro-ph/0410624 [astro-ph] (cit. on pp. 42, 45).

[123]R. Aloisio, V. Berezinsky, and A. Gazizov. „Transition from galactic to extragalactic cosmic rays“. In: *Astroparticle Physics* 39 (2012), pp. 129–143. DOI: 10.1016/j.astropartphys.2012.09.007. arXiv: 1211.0494 [astro-ph.HE] (cit. on p. 43).

[124]V. Berezinsky. „UHECR: Signatures and models“. In: *European Physical Journal Web of Conferences*. Vol. 53. European Physical Journal Web of Conferences. 2013, p. 01003. DOI: 10.1051/epjconf/20135301003. arXiv: 1307.4043 [astro-ph.HE] (cit. on pp. 43, 45).

[125]T. K. Gaisser, Todor Stanev, Serap Tilav, et al. „Cosmic-ray composition around 10^{18} eV“. In: Phys. Rev. D 47.5 (1993), pp. 1919–1932. DOI: 10.1103/PhysRevD.47.1919 (cit. on p. 44).

[126]D. J. Bird, S. C. Corbato, H. Y. Dai, et al. „The cosmic-ray energy spectrum observed by the Fly's Eye“. In: ApJ 424 (Mar. 1994), pp. 491–502. DOI: 10.1086/173906 (cit. on p. 44).

[127]Daniel de Marco and Todor Stanev. „On the shape of the ultrahigh energy cosmic ray spectrum“. In: Phys. Rev. D 72.8, 081301 (2005), p. 081301. DOI: 10.1103/PhysRevD.72.081301. arXiv: astro-ph/0506318 [astro-ph] (cit. on p. 45).

[128]D. Allard, E. Parizot, A. V. Olinto, E. Khan, and S. Goriely. „UHE nuclei propagation and the interpretation of the ankle in the cosmic-ray spectrum“. In: A&A 443.3 (2005), pp. L29–L32. DOI: 10.1051/0004-6361:200500199. arXiv: astro-ph/0505566 [astro-ph] (cit. on p. 45).

[129]D. Allard, E. Parizot, and A. V. Olinto. „On the transition from galactic to extragalactic cosmic-rays: Spectral and composition features from two opposite scenarios“. In: *Astroparticle Physics* 27.1 (2007), pp. 61–75. DOI: 10.1016/j.astropartphys.2006.09.006. arXiv: astro-ph/0512345 [astro-ph] (cit. on p. 45).

[130]N. Globus, D. Allard, and E. Parizot. „Propagation of high-energy cosmic rays in extragalactic turbulent magnetic fields: resulting energy spectrum and composition“. In: A&A 479.1 (2008), pp. 97–110. DOI: 10.1051/0004-6361:20078653. arXiv: 0709.1541 [astro-ph] (cit. on p. 45).

[131]C. De Donato and G. A. Medina-Tanco. „Experimental constraints on the astrophysical interpretation of the cosmic ray Galactic-extragalactic transition region“. In: *Astroparticle Physics* 32.5 (2009), pp. 253–268. DOI: 10.1016/j.astropartphys.2009.09.004. arXiv: 0807.4510 [astro-ph] (cit. on p. 45).

[132]V. Berezinsky, A. Z. Gazizov, and S. I. Grigorieva. „Dip in UHECR spectrum as signature of proton interaction with CMB [rapid communication]“. In: *Physics Letters B* 612.3-4 (2005), pp. 147–153. DOI: 10.1016/j.physletb.2005.02.058. arXiv: astro-ph/0502550 [astro-ph] (cit. on p. 45).

[133]Roberto Aloisio, Veniamin Berezinsky, Pasquale Blasi, et al. „A dip in the UHECR spectrum and the transition from galactic to extragalactic cosmic rays“. In: *Astroparticle Physics* 27.1 (2007), pp. 76–91. DOI: 10.1016/j.astropartphys.2006.09.004. arXiv: astro-ph/0608219 [astro-ph] (cit. on p. 45).

[134]Stefan Funk. „Ground- and Space-Based Gamma-Ray Astronomy“. In: *Annual Review of Nuclear and Particle Science* 65 (2015), pp. 245–277. DOI: 10.1146/annurev-nucl-102014-022036. arXiv: 1508.05190 [astro-ph.HE] (cit. on pp. 46, 47).

[135]F. Aharonian, A. G. Akhperjanian, A. R. Bazer-Bachi, et al. „Primary particle acceleration above 100 TeV in the shell-type supernova remnant <ASTROBJ>RX J1713.7-3946</ASTROBJ> with deep HESS observations“. In: *Astronomy and Astrophysics* 464.1 (2007), pp. 235–243. DOI: 10.1051/0004-6361:20066381. arXiv: astro-ph/0611813 [astro-ph] (cit. on p. 46).

[136]K. Pinkau. „History of gamma-ray telescopes and astronomy“. In: *Experimental Astronomy* 25 (Aug. 2009), pp. 157–171. DOI: 10.1007/s10686-009-9143-z (cit. on p. 47).

[137]Bernard Degrange and Gérard Fontaine. „Introduction to high-energy gamma-ray astronomy“. In: *Comptes Rendus Physique* 16.6-7 (2015), pp. 587–599. DOI: 10.1016/j.crhy.2015.07.003. arXiv: 1604.05488 [astro-ph.HE] (cit. on pp. 47, 50, 84).

[138]W. L. Kraushaar, G. W. Clark, and G. Garmire. „Preliminary results of gamma-ray observations from OSO-3“. In: *Canadian Journal of Physics Supplement* 46 (1968), p. 414. DOI: 10.1139/p68-260 (cit. on p. 47).

[139]W. L. Kraushaar, G. W. Clark, and G. Garmire. „OSO-III High-Energy Gamma-Ray Experiment“. In: *Solar Physics* 6.2 (1969), pp. 228–234. DOI: 10.1007/BF00150947 (cit. on p. 47).

[140]W. L. Kraushaar, G. W. Clark, G. P. Garmire, et al. „High-Energy Cosmic Gamma-Ray Observations from the OSO-3 Satellite“. In: *The Astrophysical Journal* 177 (1972), p. 341. DOI: 10.1086/151713 (cit. on p. 47).

[141]G. F. Bignami, G. Boella, J. J. Burger, et al. „The COS-B experiment for gamma-ray astronomy.“ In: *Space Science Instrumentation* 1 (1975), pp. 245–268 (cit. on p. 47).

[142]C. E. Fichtel, D. L. Bertsch, J. Chiang, et al. „The first energetic gamma-ray experiment telescope (EGRET) source catalog“. In: ApJS 94 (Oct. 1994), pp. 551–581. DOI: 10.1086/192082 (cit. on p. 47).

[143]R. C. Hartman, D. L. Bertsch, S. D. Bloom, et al. „The Third EGRET Catalog of High-Energy Gamma-Ray Sources“. In: ApJS 123 (July 1999), pp. 79–202. DOI: 10.1086/313231 (cit. on pp. 47, 48).

[144]D. J. Thompson, D. L. Bertsch, B. L. Dingus, et al. „The Second EGRET Catalog of High-Energy Gamma-Ray Sources“. In: ApJS 101 (Dec. 1995), p. 259. DOI: 10.1086/192240 (cit. on p. 47).

[145]R. C. Hartman, D. L. Bertsch, C. E. Fichtel, et al. „The EGRET High Energy Gamma Ray Telescope.“ In: *NASA Conference Publication*. Vol. 3137. 1992, pp. 116–125 (cit. on p. 47).

[146]The Fermi-LAT collaboration. „Fermi Large Area Telescope Fourth Source Catalog“. In: *arXiv e-prints*, arXiv:1902.10045 (2019), arXiv:1902.10045. arXiv: 1902.10045 [astro-ph.HE] (cit. on pp. 48, 49, 102).

[147]R. D. Blandford. „Present and Future Blazar Variability“. In: *Blazar Continuum Variability*. Ed. by H. Richard Miller, James R. Webb, and John C. Noble. Vol. 110. Astronomical Society of the Pacific Conference Series. 1996, p. 475 (cit. on p. 48).

[148]J. R. P. Angel and H. S. Stockman. „Optical and infrared polarization of active extragalactic objects“. In: ARA&A 18 (1980), pp. 321–361. DOI: 10.1146/annurev.aa.18.090180.001541 (cit. on p. 48).

[149]F. Acero, M. Ackermann, M. Ajello, et al. „Fermi Large Area Telescope Third Source Catalog“. In: ApJS 218.2, 23 (2015), p. 23. DOI: 10.1088/0067-0049/218/2/23. arXiv: 1501.02003 [astro-ph.HE] (cit. on pp. 48, 110, 111).

[150]J. A. Hinton and W. Hofmann. „Teraelectronvolt Astronomy“. In: *Annual Review of Astronomy and Astrophysics* 47.1 (2009), pp. 523–565. DOI: 10.1146/annurev-astro-082708-101816. arXiv: 1006.5210 [astro-ph.HE] (cit. on pp. 48, 49).

[151]T. C. Weekes, M. F. Cawley, D. J. Fegan, et al. „Observation of TeV gamma rays from the Crab nebula using the atmospheric Cerenkov imaging technique“. In: ApJ 342 (July 1989), pp. 379–395. DOI: 10.1086/167599 (cit. on p. 49).

[152]M. F. Cawley, D. J. Fegan, K. Harris, et al. „A high resolution imaging detector for TeV gamma-ray astronomy“. In: *Experimental Astronomy* 1 (May 1990), pp. 173–193. DOI: 10.1007/BF00462039 (cit. on p. 49).

[153]J. P. Finley, I. H. Bond, S. M. Bradbury, et al. „The status of the Whipple 10m GRANITE III upgrade program“. In: *American Institute of Physics Conference Series*. Ed. by Brenda L. Dingus, Michael H. Salamon, and David B. Kieda. Vol. 515. American Institute of Physics Conference Series. 2000, pp. 301–307. DOI: 10.1063/1.1291383 (cit. on p. 49).

[154]A. U. Abeysekara, A. Albert, R. Alfaro, et al. „Daily Monitoring of TeV Gamma-Ray Emission from Mrk 421, Mrk 501, and the Crab Nebula with HAWC“. In: *The Astrophysical Journal* 841.2, 100 (2017), p. 100. DOI: 10.3847/1538-4357/aa729e. arXiv: 1703.06968 [astro-ph.HE] (cit. on pp. 50, 96, 213–215, 217–220, 223, 250, 269, 271, 273, 277, 278).

[155]M. A. Mostafá. „The High-Altitude Water Cherenkov Observatory“. In: *Brazilian Journal of Physics* 44 (Oct. 2014), pp. 571–580. DOI: 10.1007/s13538-014-0225-7. arXiv: 1310.7237 [astro-ph.HE] (cit. on pp. 50, 213, 215).

[156]A. U. Abeysekara, A. Albert, R. Alfaro, et al. „Observation of the Crab Nebula with the HAWC Gamma-Ray Observatory“. In: *The Astrophysical Journal* 843.1, 39 (2017), p. 39. DOI: 10.3847/1538-4357/aa7555. arXiv: 1701.01778 [astro-ph.HE] (cit. on pp. 50, 213–217, 219–221).

[157]R. Atkins, W. Benbow, D. Berley, et al. „Milagrito, a TeV air-shower array“. In: *Nuclear Instruments and Methods in Physics Research A* 449.3 (2000), pp. 478–499. DOI: 10.1016/S0168-9002(00)00146-7. arXiv: astro-ph/9912456 [astro-ph] (cit. on pp. 50, 213).

[158]R. Atkins, W. Benbow, D. Berley, et al. „Observation of TeV Gamma Rays from the Crab Nebula with Milagro Using a New Background Rejection Technique“. In: *The Astrophysical Journal* 595.2 (2003), pp. 803–811. DOI: 10.1086/377498. arXiv: astro-ph/0305308 [astro-ph] (cit. on pp. 50, 213).

[159]W. Hofmann and H. E. S. S. Collaboration. „The high energy stereoscopic system (HESS) project“. In: *American Institute of Physics Conference Series*. Ed. by Brenda L. Dingus, Michael H. Salamon, and David B. Kieda. Vol. 515. American Institute of Physics Conference Series. 2000, pp. 500–509. DOI: 10.1063/1.1291416 (cit. on p. 50).

[160]S. Funk, G. Hermann, J. Hinton, et al. „The trigger system of the H.E.S.S. telescope array“. In: *Astroparticle Physics* 22.3-4 (2004), pp. 285–296. DOI: 10.1016/j.astropartphys.2004.08.001. arXiv: astro-ph/0408375 [astro-ph] (cit. on p. 50).

[161]C. Deil, C. van Eldik, A. Förster, et al. „H.E.S.S. II-Telescope Structure, Reflector and Drive System“. In: *American Institute of Physics Conference Series*. Ed. by Felix A. Aharonian, Werner Hofmann, and Frank Rieger. Vol. 1085. American Institute of Physics Conference Series. 2008, pp. 693–695. DOI: 10.1063/1.3076770 (cit. on p. 50).

[162]Barrio J. et al. *The MAGIC Telescope Design report*. Technical report. MPI Institute Report MPI-PhE/98-5, 1998. URL: https://cds.cern.ch/record/390619 (cit. on p. 50).

[163]C. Baixeras, D. Bastieri, C. Bigongiari, et al. „Commissioning and first tests of the MAGIC telescope“. In: *Nuclear Instruments and Methods in Physics Research A* 518.1-2 (2004), pp. 188–192. DOI: 10.1016/j.nima.2003.10.057 (cit. on p. 50).

[164]D. B. Tridon, T. Schweizer, F. Goebel, et al. „The MAGIC-II gamma-ray stereoscopic telescope system“. In: *Nuclear Instruments and Methods in Physics Research A* 623 (Nov. 2010), pp. 437–439. DOI: 10.1016/j.nima.2010.03.028 (cit. on p. 50).

[165]T. C. Weekes, H. Badran, S. D. Biller, et al. „VERITAS: the Very Energetic Radiation Imaging Telescope Array System“. In: *Astroparticle Physics* 17.2 (2002), pp. 221–243. DOI: 10.1016/S0927-6505(01)00152-9. arXiv: astro-ph/0108478 [astro-ph] (cit. on p. 50).

[166]J. Holder, R. W. Atkins, H. M. Badran, et al. „The first VERITAS telescope“. In: *Astroparticle Physics* 25.6 (2006), pp. 391–401. DOI: 10.1016/j.astropartphys.2006.04.002. arXiv: astro-ph/0604119 [astro-ph] (cit. on p. 50).

[167]Jeremy S. Perkins, Gernot Maier, and The VERITAS Collaboration. „VERITAS Telescope 1 Relocation: Details and Improvements“. In: *arXiv e-prints*, arXiv:0912.3841 (2009), arXiv:0912.3841. arXiv: 0912.3841 [astro-ph.IM] (cit. on p. 50).

[168]Michele Doro and CTA Consortium. „CTA—A project for a new generation of Cherenkov telescopes“. In: *Nuclear Instruments and Methods in Physics Research A* 630.1 (2011), pp. 285–290. DOI: 10.1016/j.nima.2010.06.085. arXiv: 0908.1410 [astro-ph.IM] (cit. on p. 50).

[169]M. Actis, G. Agnetta, F. Aharonian, et al. „Design concepts for the Cherenkov Telescope Array CTA: an advanced facility for ground-based high-energy gamma-ray astronomy“. In: *Experimental Astronomy* 32.3 (2011), pp. 193–316. DOI: 10.1007/s10686-011-9247-0. arXiv: 1008.3703 [astro-ph.IM] (cit. on p. 50).

[170]E. Bernardini. „γ-rays and neutrinos“. In: *Journal of Physics Conference Series*. Vol. 110. Journal of Physics Conference Series. 2008, p. 012007. DOI: 10.1088/1742-6596/110/1/012007 (cit. on pp. 50, 81, 82).

[171]K. D. Hoffman. „High energy neutrino telescopes“. In: *New Journal of Physics* 11.5, 055006 (2009), p. 055006. DOI: 10.1088/1367-2630/11/5/055006. arXiv: 0812.3809 [astro-ph] (cit. on pp. 50, 81).

[172]Marcos Santander. „The Dawn of Multi-Messenger Astronomy“. In: *Neutrino Astronomy: Current Status, Future Prospects. Edited by Thomas Gaisser Albrecht Karle. Published by World Scientific Publishing Co. Pte. Ltd., 2017. ISBN #9789814759410, pp. 125-140*. 2017, pp. 125–140. DOI: 10.1142/9789814759410_0009 (cit. on pp. 52, 104, 105).

[173]P. Kooijman et al., eds. *KM3NeT: Technical Design Report for a Deep-Sea Research Infrastructure in the Mediterranean Sea Incorporating a Very Large Volume Neutrino Telescope*. Available on http://www.km3net.org, 2010. ISBN: 978-90-6488-033-9 (cit. on pp. 53, 98, 99, 104, 105, 115, 118, 124–126, 129, 130, 133, 141, 145, 153, 155, 202, 209, 212, 218, 226, 315).

[174]S. Adrián-Martínez, M. Ageron, F. Aharonian, et al. „The prototype detection unit of the KM3NeT detector“. In: *European Physical Journal C* 76, 54 (2016), p. 54. DOI: 10.1140/epjc/s10052-015-3868-9. arXiv: 1510.01561 [astro-ph.IM] (cit. on pp. 53, 104, 105, 115, 118, 124–126, 130, 133, 141, 145, 153, 155, 202, 203, 209, 212, 218, 226, 315).

[175]S. Adrián-Martínez, M. Ageron, F. Aharonian, et al. „Letter of intent for KM3NeT 2.0“. In: *Journal of Physics G Nuclear Physics* 43.8, 084001 (2016), p. 084001. DOI: 10.1088/0954-3899/43/8/084001. arXiv: 1601.07459 [astro-ph.IM] (cit. on pp. 53, 99, 100, 104, 105, 115, 117, 118, 124–126, 130, 133, 141, 142, 145, 153, 155–161, 202, 209, 212, 218, 226, 315).

[176]Mukharbek Organokov, Thierry Pradier, and Agustin Sanchez Losa. „Time-dependent search for neutrino emission from Mrk 421 and Mrk 501 observed by the HAWC gamma-ray observatory“. In: *PoS* ICRC2017 (2018), p. 946. DOI: 10.22323/1.301.0946 (cit. on pp. 53, 93, 102, 139, 253).

[177]Mukharbek Organokov and Thierry Pradier. „Search for high-energy neutrino emission from Mrk 421 and Mrk 501 with the ANTARES neutrino telescope“. In: *28th International Conference on Neutrino Physics and Astrophysics (Neutrino 2018) Heidelberg, Germany, June 4-9, 2018*. 2018. DOI: 10.5281/zenodo.1300943. arXiv: 1809.05777 [astro-ph.HE] (cit. on pp. 53, 93, 139, 163, 218, 219, 250, 252, 274).

[178]Mukharbek Organokov and Thierry Pradier. „ANTARES search for high-energy neutrinos from TeV-emitting blazars, Markarian 421 and 501, in coincidence with HAWC gamma-ray flares“. In: *HAWC Contributions to the 36th International Cosmic Ray Conference (ICRC2019)*. 2019. arXiv: 1911.04963 [astro-ph.HE] (cit. on pp. 53, 93, 139, 163, 250, 252–254, 260, 267, 269, 270, 309, 315).

[179]C. Stegmann, A. Kappes, J. Hinton, and F. Aharonian. „Potential neutrino signals in a northern hemisphere neutrino telescope from galactic gamma-ray sources“. In: Ap&SS 309 (June 2007), pp. 429–433. DOI: 10.1007/s10509-007-9464-1 (cit. on p. 53).

[180]B. C. Barish and R. Weiss. „LIGO and the detection of gravitational waves.“ In: *Physics Today* 52.10 (1999), pp. 44–50. DOI: 10.1063/1.882861 (cit. on p. 54).

[181]Albert Einstein. „Näherungsweise Integration der Feldgleichungen der Gravitation“. In: *Sitzungsberichte der Königlich Preußischen Akademie der Wissenschaften (Berlin* (1916), pp. 688–696 (cit. on p. 54).

[182]Albert Einstein. „Über Gravitationswellen“. In: *Sitzungsberichte der Königlich Preußischen Akademie der Wissenschaften (Berlin* (1918), pp. 154–167 (cit. on p. 54).

[183]Peter R. Saulson. „Josh Goldberg and the physical reality of gravitational waves“. In: *General Relativity and Gravitation* 43.12 (2011), pp. 3289–3299. DOI: 10.1007/s10714-011-1237-z (cit. on p. 54).

[184]Joshua N. Goldberg. „Gravitational Radiation“. In: *Physical Review* 99.6 (1955), pp. 1873–1883. DOI: 10.1103/PhysRev.99.1873 (cit. on p. 54).

[185]Albert Einstein, L. Infeld, and B. Hoffmann. „The Gravitational Equations and the Problem of Motion“. In: *Annals of Mathematics* 39.1 (1938), pp. 65–100 (cit. on p. 54).

[186]Alex Abramovici, William E. Althouse, Ronald W. P. Drever, et al. „LIGO: The Laser Interferometer Gravitational-Wave Observatory“. In: *Science* 256.5055 (1992), pp. 325–333. DOI: 10.1126/science.256.5055.325 (cit. on p. 54).

[187]LIGO Scientific Collaboration, J. Aasi, B. P. Abbott, et al. „Advanced LIGO“. In: *Classical and Quantum Gravity* 32.7, 074001 (2015), p. 074001. DOI: 10.1088/0264-9381/32/7/074001. arXiv: 1411.4547 [gr-qc] (cit. on pp. 54, 55, 58, 59, 67).

[188]B. Caron, A. Dominjon, C. Drezen, et al. „The VIRGO Interferometer For Gravitational Wave Detection“. In: *Nuclear Physics B Proceedings Supplements* 54 (1997), pp. 167–175. DOI: 10.1016/S0920-5632(97)00109-6 (cit. on p. 54).

[189]F. Acernese, P. Amico, N. Arnaud, et al. „The present status of the VIRGO Central Interferometer*The present status of the VIRGO Central Interferometer“. In: *Classical and Quantum Gravity* 19.7 (2002), pp. 1421–1428. DOI: 10.1088/0264-9381/19/7/325 (cit. on p. 54).

[190]F. Acernese, M. Agathos, K. Agatsuma, et al. „Advanced Virgo: a second-generation interferometric gravitational wave detector“. In: *Classical and Quantum Gravity* 32.2, 024001 (2015), p. 024001. DOI: 10.1088/0264-9381/32/2/024001. arXiv: 1408.3978 [gr-qc] (cit. on pp. 54–56).

[191]R. A. Hulse and J. H. Taylor. „Discovery of a pulsar in a binary system.“ In: ApJ 195 (1975), pp. L51–L53. DOI: 10.1086/181708 (cit. on pp. 54, 66).

[192]J. H. Taylor and J. M. Weisberg. „A new test of general relativity - Gravitational radiation and the binary pulsar PSR 1913+16“. In: ApJ 253 (1982), pp. 908–920. DOI: 10.1086/159690 (cit. on p. 54).

[193]J. Weber. „Detection and Generation of Gravitational Waves“. In: *Physical Review* 117.1 (1960), pp. 306–313. DOI: 10.1103/PhysRev.117.306 (cit. on p. 54).

[194]P. Astone, L. Baggio, M. Bassan, et al. „IGEC2: A 17-month search for gravitational wave bursts in 2005-2007“. In: Phys. Rev. D 82.2, 022003 (2010), p. 022003. DOI: 10.1103/PhysRevD.82.022003. arXiv: 1002.3515 [gr-qc] (cit. on p. 54).

[195]M. E. Gertsenshteĭn and V. I. Pustovoĭt. „On the Detection of Low-Frequency Gravitational Waves“. In: *Soviet Journal of Experimental and Theoretical Physics* 16 (1963), p. 433 (cit. on p. 54).

[196]G. E. Moss, L. R. Miller, and R. L. Forward. „Photon-noise-limited laser transducer for gravitational antenna.“ In: Appl. Opt. 10 (1971), pp. 2495–2498. DOI: 10.1364/AO.10.002495 (cit. on p. 54).

[197]Masaki Ando and TAMA Collaboration. „Current status of TAMA“. In: *Classical and Quantum Gravity* 19.7 (2002), pp. 1409–1419. DOI: 10.1088/0264-9381/19/7/324 (cit. on p. 54).

[198]B. Willke, P. Aufmuth, C. Aulbert, et al. „The GEO 600 gravitational wave detector“. In: *Classical and Quantum Gravity* 19.7 (2002), pp. 1377–1387. DOI: 10.1088/0264-9381/19/7/321 (cit. on p. 54).

[199]Yoichi Aso, Yuta Michimura, Kentaro Somiya, et al. „Interferometer design of the KAGRA gravitational wave detector“. In: Phys. Rev. D 88.4, 043007 (2013), p. 043007. DOI: 10.1103/PhysRevD.88.043007. arXiv: 1306.6747 [gr-qc] (cit. on p. 55).

[200]C. Affeldt, K. Danzmann, K. L. Dooley, et al. „Advanced techniques in GEO 600“. In: *Classical and Quantum Gravity* 31.22, 224002 (2014), p. 224002. DOI: 10.1088/0264-9381/31/22/224002 (cit. on p. 55).

[201]Bala Iyer. „LIGO-India Technical Report No. LIGOM1100296“. In: (2011). URL: https://dcc.ligo.org/LIGO-M1100296/public/main (cit. on pp. 55, 68).

[202]B. P. Abbott, R. Abbott, T. D. Abbott, et al. „GW151226: Observation of Gravitational Waves from a 22-Solar-Mass Binary Black Hole Coalescence“. In: Phys. Rev. Lett. 116.24, 241103 (2016), p. 241103. DOI: 10.1103/PhysRevLett.116.241103. arXiv: 1606.04855 [gr-qc] (cit. on p. 56).

[203]B. P. Abbott, R. Abbott, T. D. Abbott, et al. „GW150914: First results from the search for binary black hole coalescence with Advanced LIGO“. In: Phys. Rev. D 93.12, 122003 (2016), p. 122003. DOI: 10.1103/PhysRevD.93.122003. arXiv: 1602.03839 [gr-qc] (cit. on pp. 56, 60).

[204]B. P. Abbott, R. Abbott, T. D. Abbott, et al. „Binary Black Hole Mergers in the First Advanced LIGO Observing Run“. In: *Physical Review X* 6.4, 041015 (2016), p. 041015. DOI: 10.1103/PhysRevX.6.041015. arXiv: 1606.04856 [gr-qc] (cit. on p. 56).

[205]Alexander H. Nitz, Collin Capano, Alex B. Nielsen, et al. „1-OGC: The First Open Gravitational-wave Catalog of Binary Mergers from Analysis of Public Advanced LIGO Data“. In: ApJ 872.2, 195 (2019), p. 195. DOI: 10.3847/1538-4357/ab0108. arXiv: 1811.01921 [gr-qc] (cit. on p. 56).

[206]B. P. Abbott, R. Abbott, T. D. Abbott, et al. „GW170608: Observation of a 19 Solar-mass Binary Black Hole Coalescence“. In: ApJ 851.2, L35 (2017), p. L35. DOI: 10.3847/2041-8213/aa9f0c. arXiv: 1711.05578 [astro-ph.HE] (cit. on p. 56).

[207]B. P. Abbott, R. Abbott, T. D. Abbott, et al. „GW170104: Observation of a 50-Solar-Mass Binary Black Hole Coalescence at Redshift 0.2“. In: Phys. Rev. Lett. 118.22, 221101 (2017), p. 221101. DOI: 10.1103/PhysRevLett.118.221101. arXiv: 1706.01812 [gr-qc] (cit. on p. 56).

[208]B. P. Abbott, R. Abbott, T. D. Abbott, et al. „GW170814: A Three-Detector Observation of Gravitational Waves from a Binary Black Hole Coalescence“. In: Phys. Rev. Lett. 119.14, 141101 (2017), p. 141101. DOI: 10.1103/PhysRevLett.119.141101. arXiv: 1709.09660 [gr-qc] (cit. on pp. 56, 64, 65).

[209]B. P. Abbott, R. Abbott, T. D. Abbott, et al. „Prospects for observing and localizing gravitational-wave transients with Advanced LIGO, Advanced Virgo and KAGRA“. In: *Living Reviews in Relativity* 21.1, 3 (2018), p. 3. DOI: 10.1007/s41114-018-0012-9. arXiv: 1304.0670 [gr-qc] (cit. on pp. 57, 64, 67, 68).

[210]B. P. Abbott, R. Abbott, T. D. Abbott, et al. „GWTC-1: A Gravitational-Wave Transient Catalog of Compact Binary Mergers Observed by LIGO and Virgo during the First and Second Observing Runs“. In: *Physical Review X* 9.3, 031040 (2019), p. 031040. DOI: 10.1103/PhysRevX.9.031040. arXiv: 1811.12907 [astro-ph.HE] (cit. on pp. 57, 67).

[211]B. P. Abbott, R. Abbott, T. D. Abbott, et al. „Low-latency Gravitational-wave Alerts for Multimessenger Astronomy during the Second Advanced LIGO and Virgo Observing Run“. In: ApJ 875.2, 161 (2019), p. 161. DOI: 10.3847/1538-4357/ab0e8f. arXiv: 1901.03310 [astro-ph.HE] (cit. on p. 57).

[212]B. P. Abbott, R. Abbott, T. D. Abbott, et al. „Localization and Broadband Follow-up of the Gravitational-wave Transient GW150914“. In: ApJ 826.1, L13 (2016), p. L13. DOI: 10.3847/2041-8205/826/1/L13. arXiv: 1602.08492 [astro-ph.HE] (cit. on pp. 57, 112).

[213]Ligoi/VIRGO Scientific Collaboration. „LIGO/Virgo G211117: Identification of a GW CBC Candidate.“ In: *GRB Coordinates Network* 18728 (2015), p. 1 (cit. on p. 57).

[214]A. Effler, R. M. S. Schofield, V. V. Frolov, et al. „Environmental influences on the LIGO gravitational wave detectors during the 6th science run“. In: *Classical and Quantum Gravity* 32.3, 035017 (2015), p. 035017. DOI: 10.1088/0264-9381/32/3/035017. arXiv: 1409.5160 [astro-ph.IM] (cit. on p. 59).

[215]B. P. Abbott, R. Abbott, T. D. Abbott, et al. „Observing gravitational-wave transient GW150914 with minimal assumptions“. In: Phys. Rev. D 93.12, 122004 (2016), p. 122004. DOI: 10.1103/PhysRevD.93.122004. arXiv: 1602.03843 [gr-qc] (cit. on pp. 60, 62).

[216]Luc Blanchet, Thibault Damour, Bala R. Iyer, Clifford M. Will, and Alan G. Wiseman. „Gravitational-Radiation Damping of Compact Binary Systems to Second Post-Newtonian Order“. In: Phys. Rev. Lett. 74.18 (1995), pp. 3515–3518. DOI: 10.1103/PhysRevLett.74.3515. arXiv: gr-qc/9501027 [gr-qc] (cit. on p. 61).

[217]Abdul H. Mroué, Mark A. Scheel, Béla Szilágyi, et al. „Catalog of 174 Binary Black Hole Simulations for Gravitational Wave Astronomy“. In: Phys. Rev. Lett. 111.24, 241104 (2013), p. 241104. DOI: 10.1103/PhysRevLett.111.241104. arXiv: 1304.6077 [gr-qc] (cit. on p. 62).

[218]M. Campanelli, C. O. Lousto, P. Marronetti, and Y. Zlochower. „Accurate Evolutions of Orbiting Black-Hole Binaries without Excision“. In: Phys. Rev. Lett. 96.11, 111101 (2006), p. 111101. DOI: 10.1103/PhysRevLett.96.111101. arXiv: gr-qc/0511048 [gr-qc] (cit. on p. 62).

[219]B. P. Abbott, R. Abbott, T. D. Abbott, et al. „Properties of the Binary Black Hole Merger GW150914“. In: Phys. Rev. Lett. 116.24, 241102 (2016), p. 241102. DOI: 10.1103/PhysRevLett.116.241102. arXiv: 1602.03840 [gr-qc] (cit. on p. 62).

[220]Neil J. Cornish and Tyson B. Littenberg. „Bayeswave: Bayesian inference for gravitational wave bursts and instrument glitches“. In: *Classical and Quantum Gravity* 32.13, 135012 (2015), p. 135012. DOI: 10.1088/0264-9381/32/13/135012. arXiv: 1410.3835 [gr-qc] (cit. on pp. 62, 65).

[221]S. Chatterji, L. Blackburn, G. Martin, and E. Katsavounidis. „Multiresolution techniques for the detection of gravitational-wave bursts“. In: *Classical and Quantum Gravity* 21.20 (2004), S1809–S1818. DOI: 10.1088/0264-9381/21/20/024. arXiv: gr-qc/0412119 [gr-qc] (cit. on p. 62).

[222]B. P. Abbott, R. Abbott, T. D. Abbott, et al. „Tests of General Relativity with GW150914“. In: Phys. Rev. Lett. 116.22, 221101 (2016), p. 221101. DOI: 10.1103/PhysRevLett.116.221101. arXiv: 1602.03841 [gr-qc] (cit. on p. 63).

[223]James Healy, Carlos O. Lousto, and Yosef Zlochower. „Remnant mass, spin, and recoil from spin aligned black-hole binaries“. In: Phys. Rev. D 90.10, 104004 (2014), p. 104004. DOI: 10.1103/PhysRevD.90.104004. arXiv: 1406.7295 [gr-qc] (cit. on p. 63).

[224]Douglas M. Eardley, David L. Lee, Alan P. Lightman, Robert V. Wagoner, and Clifford M. Will. „Gravitational-Wave Observations as a Tool for Testing Relativistic Gravity“. In: Phys. Rev. Lett. 30.18 (1973), pp. 884–886. DOI: 10.1103/PhysRevLett.30.884 (cit. on p. 64).

[225]Douglas M. Eardley, David L. Lee, and Alan P. Lightman. „Gravitational-Wave Observations as a Tool for Testing Relativistic Gravity“. In: Phys. Rev. D 8.10 (1973), pp. 3308–3321. DOI: 10.1103/PhysRevD.8.3308 (cit. on p. 64).

[226]A. von Kienlin, C. Meegan, and A. Goldstein. „GRB 170817A: Fermi GBM detection.“ In: *GRB Coordinates Network* 21520 (2017), p. 1 (cit. on pp. 66, 112, 113).

[227]B. P. Abbott, R. Abbott, T. D. Abbott, et al. „Gravitational Waves and Gamma-Rays from a Binary Neutron Star Merger: GW170817 and GRB 170817A“. In: ApJ 848.2, L13 (2017), p. L13. DOI: 10.3847/2041-8213/aa920c. arXiv: 1710.05834 [astro-ph.HE] (cit. on pp. 66, 67, 112, 115).

[228]B. P. Abbott, R. Abbott, T. D. Abbott, et al. „Multi-messenger Observations of a Binary Neutron Star Merger“. In: ApJ 848.2, L12 (2017), p. L12. DOI: 10.3847/2041-8213/aa91c9. arXiv: 1710.05833 [astro-ph.HE] (cit. on pp. 66, 67, 112–114).

[229]The LIGO Scientific collaboration. „Gravitational wave astronomy with LIGO and similar detectors in the next decade“. In: *arXiv e-prints*, arXiv:1904.03187 (2019), arXiv:1904.03187. arXiv: 1904.03187 [gr-qc] (cit. on pp. 67, 68).

[230]B. P. Abbott, R. Abbott, T. D. Abbott, et al. „Characterization of transient noise in Advanced LIGO relevant to gravitational wave signal GW150914“. In: *Classical and Quantum Gravity* 33.13, 134001 (2016), p. 134001. DOI: 10.1088/0264-9381/33/13/134001. arXiv: 1602.03844 [gr-qc] (cit. on p. 67).

[231]W. Pauli. „Dear radioactive ladies and gentlemen“. In: *Phys. Today* 31N9 (1978), p. 27 (cit. on p. 69).

[232]J. Chadwick. „The Existence of a Neutron“. In: *Proceedings of the Royal Society of London Series A* 136.830 (1932), pp. 692–708. DOI: 10.1098/rspa.1932.0112 (cit. on p. 69).

[233]E. Fermi. „Versuch einer Theorie der β-Strahlen. I“. In: *Zeitschrift fur Physik* 88 (Mar. 1934), pp. 161–177. DOI: 10.1007/BF01351864 (cit. on p. 69).

[234]F. Reines and C. L. Cowan. „Detection of the Free Neutrino“. In: *Physical Review* 92.3 (1953), pp. 830–831. DOI: 10.1103/PhysRev.92.830 (cit. on p. 69).

[235]Jr. Cowan C. L., F. Reines, F. B. Harrison, H. W. Kruse, and A. D. McGuire. „Detection of the Free Neutrino: A Confirmation“. In: *Science* 124.3212 (1956), pp. 103–104. DOI: 10.1126/science.124.3212.103 (cit. on p. 69).

[236]J. N. Bahcall. „How the Sun Shines“. In: JRASC 94 (Dec. 2000), p. 219. eprint: astro-ph/0009259 (cit. on p. 69).

[237]A. S. Eddington. „The internal constitution of the stars“. In: *The Observatory* 43 (Oct. 1920), pp. 341–358 (cit. on p. 70).

[238]F. W. Aston. „Isotopes and Atomic Weights“. In: Nature 105 (July 1920), pp. 617–619. DOI: 10.1038/105617a0 (cit. on p. 70).

[239]John N. Bahcall and Jr. Davis Raymond. „Solar Neutrinos: A Scientific Puzzle“. In: *Science* 191.4224 (1976), pp. 264–267. DOI: 10.1126/science.191.4224.264 (cit. on p. 70).

[240]H. A. Bethe. „Energy Production in Stars“. In: *Physical Review* 55 (Mar. 1939), pp. 434–456. DOI: 10.1103/PhysRev.55.434 (cit. on p. 70).

[241]C.F. von Weizsäcker. „Über Elementumwandlungen im Innern der Sterne. I (On transformations of elements in the interiors of stars. I)“. In: *Physikalische Zeitschrift* 38 (1937), pp. 176–191 (cit. on p. 70).

[242]C.F. von Weizsäcker. „Über Elementumwandlungen im Innern der Sterne. II (On transformations of elements in the interiors of stars. II)“. In: *Physikalische Zeitschrift* 39 (1938), pp. 633–646 (cit. on p. 70).

[243]H. A. Bethe. „Energy Production in Stars“. In: *Physical Review* 55 (Jan. 1939), pp. 103–103. DOI: 10.1103/PhysRev.55.103 (cit. on p. 70).

[244]John N. Bahcall. „Solar Neutrinos. I. Theoretical“. In: Phys. Rev. Lett. 12.11 (1964), pp. 300–302. DOI: 10.1103/PhysRevLett.12.300 (cit. on p. 70).

[245]J. N. Bahcall, W. A. Fowler, I. Iben Jr., and R. L. Sears. „Solar Neutrino Flux.“ In: ApJ 137 (Jan. 1963), pp. 344–346. DOI: 10.1086/147513 (cit. on p. 70).

[246]Raymond Davis. „Solar Neutrinos. II. Experimental“. In: Phys. Rev. Lett. 12.11 (1964), pp. 303–305. DOI: 10.1103/PhysRevLett.12.303 (cit. on pp. 70, 72, 73).

[247]Borexino Collaboration, M. Agostini, K. Altenmüller, et al. „Comprehensive measurement of pp-chain solar neutrinos“. In: Nature 562 (Oct. 2018), pp. 505–510. DOI: 10.1038/s41586-018-0624-y (cit. on pp. 70, 71, 74, 76, 77).

[248]L. C. Stonehill, J. A. Formaggio, and R. G. Robertson. „Solar neutrinos from CNO electron capture“. In: Phys. Rev. C 69.1, 015801 (2004), p. 015801. DOI: 10.1103/PhysRevC.69.015801. arXiv: hep-ph/0309266 [hep-ph] (cit. on p. 70).

[249]F. L. Villante. „ecCNO solar neutrinos: A challenge for gigantic ultra-pure liquid scintillator detectors“. In: *Physics Letters B* 742 (2015), pp. 279–284. DOI: 10.1016/j.physletb.2015.01.043. arXiv: 1410.2796 [hep-ph] (cit. on p. 70).

[250]K. S. Hirata, T. Kajita, T. Kifune, et al. „Observation of ^{8}B solar neutrinos in the Kamiokande-II detector“. In: Phys. Rev. Lett. 63.1 (1989), pp. 16–19. DOI: 10.1103/PhysRevLett.63.16 (cit. on pp. 72, 77).

[251]Q. R. Ahmad, R. C. Allen, T. C. Andersen, et al. „Direct Evidence for Neutrino Flavor Transformation from Neutral-Current Interactions in the Sudbury Neutrino Observatory“. In: Phys. Rev. Lett. 89.1, 011301 (2002), p. 011301. DOI: 10.1103/PhysRevLett.89.011301. arXiv: nucl-ex/0204008 [nucl-ex] (cit. on pp. 72, 74, 77).

[252]S. Fukuda, Y. Fukuda, T. Hayakawa, et al. „The Super-Kamiokande detector“. In: *Nuclear Instruments and Methods in Physics Research A* 501.2 (2003), pp. 418–462. DOI: 10.1016/S0168-9002(03)00425-X (cit. on pp. 72, 74, 79).

[253]J. Boger, R. L. Hahn, J. K. Rowley, et al. „The Sudbury Neutrino Observatory“. In: *Nuclear Instruments and Methods in Physics Research A* 449.1-2 (2000), pp. 172–207. DOI: 10.1016/S0168-9002(99)01469-2. arXiv: nucl-ex/9910016 [nucl-ex] (cit. on pp. 72, 74, 76).

[254]B. Pontecorvo. „Mesonium and anti-mesonium“. In: *Sov. Phys. JETP* 6 (1957). [Zh. Eksp. Teor. Fiz.33,549(1957)], p. 429 (cit. on p. 72).

[255]M. Gell-Mann and A. Pais. „Behavior of Neutral Particles under Charge Conjugation“. In: *Physical Review* 97.5 (1955), pp. 1387–1389. DOI: 10.1103/PhysRev.97.1387 (cit. on p. 72).

[256]S. M. Bilenky. „The History of Neutrino Oscillations“. In: *Physica Scripta Volume T* 121 (2005), pp. 17–22. DOI: 10.1088/0031-8949/2005/T121/001. arXiv: hep-ph/0410090 [hep-ph] (cit. on p. 72).

[257]L. Landau. „On the conservation laws for weak interactions“. In: *Nuclear Physics* 3.1 (1957), pp. 127–131. DOI: 10.1016/0029-5582(57)90061-5 (cit. on p. 72).

[258]T. D. Lee and C. N. Yang. „Parity Nonconservation and a Two-Component Theory of the Neutrino“. In: *Physical Review* 105.5 (1957), pp. 1671–1675. DOI: 10.1103/PhysRev.105.1671 (cit. on p. 72).

[259]A. Salam. „On parity conservation and neutrino mass“. In: *Il Nuovo Cimento* 5 (Jan. 1957), pp. 299–301. DOI: 10.1007/BF02812841 (cit. on p. 72).

[260]G. Danby, J. M. Gaillard, K. Goulianos, et al. „Observation of High-Energy Neutrino Reactions and the Existence of Two Kinds of Neutrinos“. In: Phys. Rev. Lett. 9.1 (1962), pp. 36–44. DOI: 10.1103/PhysRevLett.9.36 (cit. on p. 72).

[261]B. Pontecorvo. „Neutrino Experiments and the Problem of Conservation of Leptonic Charge“. In: *Sov. Phys. JETP* 26 (1968). [Zh. Eksp. Teor. Fiz.53,1717(1967)], pp. 984–988 (cit. on pp. 72, 73).

[262]Z. Maki, M. Nakagawa, and S. Sakata. „Remarks on the Unified Model of Elementary Particles“. In: *Progress of Theoretical Physics* 28.5 (1962), pp. 870–880. DOI: 10.1143/PTP.28.870 (cit. on p. 72).

[263]S. M. Bilenky. „Prehistory of Neutrino Oscillations“. In: *arXiv e-prints*, arXiv:1902.10052 (2019), arXiv:1902.10052. arXiv: 1902.10052 [physics.hist-ph] (cit. on p. 72).

[264]S. M. Bilenky. „Neutrino in standard model and beyond“. In: *Physics of Particles and Nuclei* 46.4 (2015), pp. 475–496. DOI: 10.1134/S1063779615040024. arXiv: 1501.00232 [hep-ph] (cit. on pp. 72, 73).

[265]Mattias Blennow and Alexei Yu. Smirnov. „Neutrino Propagation in Matter“. In: *arXiv e-prints*, arXiv:1306.2903 (2013), arXiv:1306.2903. arXiv: 1306.2903 [hep-ph] (cit. on p. 73).

[266]B. Pontecorvo. *Inverse β Decay*. Technical report. Chalk River Laboratory, Report PD-205, 1946 (cit. on pp. 73, 74).

[267]J. N. Abdurashitov, V. N. Gavrin, S. V. Girin, et al. „Measurement of the solar neutrino capture rate with gallium metal“. In: Phys. Rev. C 60.5, 055801 (1999), p. 055801. DOI: 10.1103/PhysRevC.60.055801. arXiv: astro-ph/9907113 [astro-ph] (cit. on p. 74).

[268]J. N. Abdurashitov, V. N. Gavrin, S. V. Girin, et al. „Measurement of the response of a Ga solar neutrino experiment to neutrinos from a Ar37 source“. In: Phys. Rev. C 73.4, 045805 (2006), p. 045805. DOI: 10.1103/PhysRevC.73.045805. arXiv: nucl-ex/0512041 [nucl-ex] (cit. on p. 74).

[269]P. Anselmann, W. Hampel, G. Heusser, et al. „Solar neutrinos observed by GALLEX at Gran Sasso“. In: *Physics Letters B* 285.4 (1992), pp. 376–389. DOI: 10.1016/0370-2693(92)91521-A (cit. on p. 74).

[270]F. Kaether, W. Hampel, G. Heusser, J. Kiko, and T. Kirsten. „Reanalysis of the GALLEX solar neutrino flux and source experiments“. In: *Physics Letters B* 685.1 (2010), pp. 47–54. DOI: 10.1016/j.physletb.2010.01.030. arXiv: 1001.2731 [hep-ex] (cit. on p. 74).

[271]V. Gavrin, B. Cleveland, S. Danshin, et al. „Current status of new SAGE project with ^{51}Cr neutrino source“. In: *Physics of Particles and Nuclei* 46 (Mar. 2015), pp. 131–137. DOI: 10.1134/S1063779615020100 (cit. on pp. 74, 77, 78).

[272]V. N. Gavrin, V. V. Gorbachev, T. V. Ibragimova, et al. „On the gallium experiment BEST-2 with a ^{65}Zn source to search for neutrino oscillations on a short baseline“. In: *arXiv e-prints*, arXiv:1807.02977 (2018), arXiv:1807.02977. arXiv: 1807.02977 [physics.ins-det] (cit. on p. 74).

[273]V. N. Gavrin, V. V. Gorbachev, E. P. Veretenkin, and B. T. Cleveland. „Gallium experiments with artificial neutrino sources as a tool for investigation of transition to sterile states“. In: *arXiv e-prints*, arXiv:1006.2103 (2010), arXiv:1006.2103. arXiv: 1006.2103 [nucl-ex] (cit. on pp. 74, 77, 78).

[274]S. Fukuda, Y. Fukuda, M. Ishitsuka, et al. „Solar ^{8}B and hep Neutrino Measurements from 1258 Days of Super-Kamiokande Data“. In: *Physical Review Letters* 86 (June 2001), pp. 5651–5655. DOI: 10.1103/PhysRevLett.86.5651. eprint: hep-ex/0103032 (cit. on p. 74).

[275]Q. R. Ahmad, R. C. Allen, T. C. Andersen, et al. „Measurement of the Rate of ν_e + d –> p + p + e$^-$ Interactions Produced by ^{8}B Solar Neutrinos at the Sudbury Neutrino Observatory“. In: Phys. Rev. Lett. 87.7, 071301 (2001), p. 071301. DOI: 10.1103/PhysRevLett.87.071301. arXiv: nucl-ex/0106015 [nucl-ex] (cit. on p. 74).

[276]Carlos Pena-Garay and Aldo Serenelli. „Solar neutrinos and the solar composition problem“. In: *arXiv e-prints*, arXiv:0811.2424 (2008), arXiv:0811.2424. arXiv: 0811.2424 [astro-ph] (cit. on p. 75).

[277]Bruce T. Cleveland, Timothy Daily, Jr. Davis Raymond, et al. „Measurement of the Solar Electron Neutrino Flux with the Homestake Chlorine Detector“. In: ApJ 496.1 (1998), pp. 505–526. DOI: 10.1086/305343 (cit. on p. 75).

[278]GALLEX Collaboration, W. Hampel, J. Handt, et al. „GALLEX solar neutrino observations: results for GALLEX IV“. In: *Physics Letters B* 447.1-2 (1999), pp. 127–133. DOI: 10.1016/S0370-2693(98)01579-2 (cit. on p. 75).

[279]Gno Collaboration, M. Altmann, M. Balata, et al. „Complete results for five years of GNO solar neutrino observations“. In: *Physics Letters B* 616.3-4 (2005), pp. 174–190. DOI: 10.1016/j.physletb.2005.04.068. arXiv: hep-ex/0504037 [hep-ex] (cit. on p. 75).

[280]J. N. Abdurashitov, V. N. Gavrin, V. V. Gorbachev, et al. „Measurement of the solar neutrino capture rate with gallium metal. III. Results for the 2002-2007 data-taking period“. In: Phys. Rev. C 80.1, 015807 (2009), p. 015807. DOI: 10.1103/PhysRevC.80.015807. arXiv: 0901.2200 [nucl-ex] (cit. on p. 75).

[281]B. Aharmim, S. N. Ahmed, A. E. Anthony, et al. „Electron energy spectra, fluxes, and day-night asymmetries of ^{8}B solar neutrinos from measurements with NaCl dissolved in the heavy-water detector at the Sudbury Neutrino Observatory“. In: Phys. Rev. C 72.5, 055502 (2005), p. 055502. DOI: 10.1103/PhysRevC.72.055502. arXiv: nucl-ex/0502021 [nucl-ex] (cit. on p. 75).

[282]S. Fukuda, Y. Fukuda, M. Ishitsuka, et al. „Determination of solar neutrino oscillation parameters using 1496 days of Super-Kamiokande-I data“. In: *Physics Letters B* 539.3 (2002), pp. 179–187. DOI: 10.1016/S0370-2693(02)02090-7. arXiv: hep-ex/0205075 [hep-ex] (cit. on p. 75).

[283]John N. Bahcall, Aldo M. Serenelli, and Sarbani Basu. „New Solar Opacities, Abundances, Helioseismology, and Neutrino Fluxes“. In: ApJ 621.1 (2005), pp. L85–L88. DOI: 10.1086/428929. arXiv: astro-ph/0412440 [astro-ph] (cit. on p. 75).

[284]Ivan Esteban, M. C. Gonzalez-Garcia, Michele Maltoni, Ivan Martinez-Soler, and Thomas Schwetz. „Updated fit to three neutrino mixing: exploring the accelerator-reactor complementarity“. In: *Journal of High Energy Physics* 2017.1, 87 (2017), p. 87. DOI: 10.1007/JHEP01(2017)087. arXiv: 1611.01514 [hep-ph] (cit. on pp. 76, 77).

[285]L. Wolfenstein. „Neutrino oscillations in matter“. In: Phys. Rev. D 17 (May 1978), pp. 2369–2374. DOI: 10.1103/PhysRevD.17.2369 (cit. on p. 76).

[286]S. P. Mikheyev and A. Yu. Smirnov. „Resonance Amplification of Oscillations in Matter and Spectroscopy of Solar Neutrinos“. In: *Sov. J. Nucl. Phys.* 42 (1985). [,305(1986)], pp. 913–917 (cit. on p. 76).

[287]P. C. de Holanda and A. Yu. Smirnov. „LMA MSW solution of the solar neutrino problem and first KamLAND results“. In: *arXiv e-prints*, hep-ph/0212270 (2002), hep–ph/0212270. arXiv: hep-ph/0212270 [hep-ph] (cit. on p. 76).

[288]M. Maris and S. T. Petcov. „The Super - Kamiokande Day - Night Effect Data and the MSW Solutions of the Solar Neutrino Problem“. In: *arXiv e-prints*, hep-ph/0004151 (2000), hep–ph/0004151. arXiv: hep-ph/0004151 [hep-ph] (cit. on p. 76).

[289]S. Fukuda, Y. Fukuda, M. Ishitsuka, et al. „Constraints on Neutrino Oscillations Using 1258 Days of Super-Kamiokande Solar Neutrino Data“. In: Phys. Rev. Lett. 86.25 (2001), pp. 5656–5660. DOI: 10.1103/PhysRevLett.86.5656. arXiv: hep-ex/0103033 [hep-ex] (cit. on p. 76).

[290]A. Yu. Smirnov. „The MSW effect and Solar Neutrinos“. In: *arXiv e-prints*, hep-ph/0305106 (2003), hep–ph/0305106. arXiv: hep-ph/0305106 [hep-ph] (cit. on p. 76).

[291]S. T. Petcov and M. Piai. „The LMA MSW solution of the solar neutrino problem, inverted neutrino mass hierarchy and reactor neutrino experiments“. In: *Physics Letters B* 533.1-2 (2002), pp. 94–106. DOI: 10.1016/S0370-2693(02)01591-5. arXiv: hep-ph/0112074 [hep-ph] (cit. on p. 76).

[292]BOREXINO Collaboration, G. Alimonti, C. Arpesella, et al. „The Borexino detector at the Laboratori Nazionali del Gran Sasso“. In: *Nuclear Instruments and Methods in Physics Research A* 600.3 (2009), pp. 568–593. DOI: 10.1016/j.nima.2008.11.076. arXiv: 0806.2400 [physics.ins-det] (cit. on p. 76).

[293]Super-Kamiokande Collaboration, : K. Abe, et al. „Solar Neutrino Measurements in Super-Kamiokande-IV“. In: *arXiv e-prints*, arXiv:1606.07538 (2016), arXiv:1606.07538. arXiv: 1606.07538 [hep-ex] (cit. on p. 77).

[294]B. Aharmim, S. N. Ahmed, A. E. Anthony, et al. „Combined analysis of all three phases of solar neutrino data from the Sudbury Neutrino Observatory“. In: Phys. Rev. C 88.2, 025501 (2013), p. 025501. DOI: 10.1103/PhysRevC.88.025501. arXiv: 1109.0763 [nucl-ex] (cit. on p. 77).

[295]S. Schael et al. „Precision electroweak measurements on the Z resonance“. In: *Physics Reports* 427 (2006), pp. 257–454. DOI: 10.1016/j.physrep.2005.12.006. arXiv: hep-ex/0509008 [hep-ex] (cit. on p. 77).

[296]W. D. Arnett, J. N. Bahcall, R. P. Kirshner, and S. E. Woosley. „Supernova 1987A“. In: ARA&A 27 (1989), pp. 629–700. DOI: 10.1146/annurev.aa.27.090189.003213 (cit. on p. 79).

[297]Genevieve J. M. Graves, Peter M. Challis, Roger A. Chevalier, et al. „Limits from the Hubble Space Telescope on a Point Source in SN 1987A“. In: ApJ 629.2 (2005), pp. 944–959. DOI: 10.1086/431422. arXiv: astro-ph/0505066 [astro-ph] (cit. on p. 79).

[298]R. M. Bionta, G. Blewitt, C. B. Bratton, et al. „Observation of a neutrino burst in coincidence with supernova 1987A in the Large Magellanic Cloud“. In: *Physical Review Letters* 58 (Apr. 1987), pp. 1494–1496. DOI: 10.1103/PhysRevLett.58.1494 (cit. on pp. 79, 81, 103).

[299]K. Hirata, T. Kajita, M. Koshiba, et al. „Observation of a neutrino burst from the supernova SN1987A“. In: *Physical Review Letters* 58 (Apr. 1987), pp. 1490–1493. DOI: 10.1103/PhysRevLett.58.1490 (cit. on pp. 79, 81, 103).

[300]D. J. McCarthy and T. A. Facey. „Design and fabrication of the NASA 2.4-meter space telescope“. In: *Optical Systems Engineering II*. Ed. by P. R. Yoder Jr. Vol. 330. Proc. SPIE. Jan. 1982, pp. 139–143. DOI: 10.1117/12.934268 (cit. on p. 79).

[301]C. R. O'dell. „The Space Telescope Observatory“. In: *NASA Conference Publication*. Ed. by D. N. B. Hall. Vol. 2244. NASA Conference Publication. Aug. 1982 (cit. on p. 79).

[302]D. N. B. Hall, ed. *The Space Telescope Observatory. Special session of Commission 44, IAU 18th General Assembly*. Vol. 2244. NASA Conference Publication. 1982 (cit. on p. 79).

[303]M. Aglietta, G. Badino, G. Bologna, et al. „On the event observed in the Mont Blanc Underground Neutrino Observatory during the occurrence of supernova 1987a.“ In: *EPL (Europhysics Letters)* 3 (1987), pp. 1315–1320. DOI: 10.1209/0295-5075/3/12/011 (cit. on p. 79).

[304]G. Badino, G. Bologna, C. Castagnoli, et al. „The 90 ton liquid scintillation detector in the Mont Blanc Laboratory“. In: *Nuovo Cimento C Geophysics Space Physics C* 7 (Dec. 1984), pp. 573–590. DOI: 10.1007/BF02573783 (cit. on p. 79).

[305]R. Becker-Szendy, R. M. Bionta, C. B. Bratton, et al. „IMB-3: a large water Cherenkov detector for nucleon decay and neutrino interactions“. In: *Nuclear Instruments and Methods in Physics Research A* 324.1-2 (1993), pp. 363–382. DOI: 10.1016/0168-9002(93)90998-W (cit. on p. 79).

[306]E. N. Alekseev, L. N. Alekseeva, V. I. Volchenko, and I. V. Krivosheina. „Possible Detection of a Neutrino Signal on 23 February 1987 at the Baksan Underground Scintillation Telescope of the Institute of Nuclear Research“. In: *JETP Lett.* 45 (1987). [,739(1987)], pp. 589–592 (cit. on p. 80).

[307]M. Aglietta, G. Badino, G. Bologna, et al. „Comments on the two events observed in neutrino detectors during the supernova 1987A outburst.“ In: *EPL (Europhysics Letters)* 3 (1987), pp. 1321–1324. DOI: 10.1209/0295-5075/3/12/012 (cit. on p. 80).

[308]Vladimir Kulikovskiy. „ANTARES and KM3NeT programs for the supernova neutrino detection“. In: *Supernova 1987A:30 years later - Cosmic Rays and Nuclei from Supernovae and their Aftermaths*. Ed. by A. Marcowith, M. Renaud, G. Dubner, A. Ray, and A. Bykov. Vol. 331. IAU Symposium. 2017, pp. 339–344. DOI: 10.1017/S1743921317004495 (cit. on pp. 80, 95).

[309]A. Trovato, P. Kooijman, R. Coniglione, and P. Sapienza. „Sensitivity of the KM3NeT detector to neutrino fluxes from Galactic point-like sources“. In: *AIP Conference Proceedings* 1630.1 (2014), pp. 62–65. DOI: 10.1063/1.4902772. URL: https://aip.scitation.org/doi/abs/10.1063/1.4902772 (cit. on pp. 80, 95).

[310]A. Trovato. „KM3NeT/ARCA sensitivity and discovery potential for neutrino point-like sources“. In: *European Physical Journal Web of Conferences*. Vol. 116. European Physical Journal Web of Conferences. 2016, p. 04006. DOI: 10.1051/epjconf/201611604006 (cit. on pp. 80, 95).

[311]A. Trovato, R. Coniglione, P. Sapienza, J. Barrios-Martí, and KM3NeT Collaboration. „Expectations for detection of neutrinos from point-like sources with KM3NeT/ARCA“. In: *35th International Cosmic Ray Conference (ICRC2017)*. Vol. 301. International Cosmic Ray Conference. 2017, p. 999 (cit. on pp. 80, 95).

[312]S. Aiello, S. E. Akrame, F. Ameli, et al. „Sensitivity of the KM3NeT/ARCA neutrino telescope to point-like neutrino sources“. In: *Astroparticle Physics* 111 (2019), pp. 100–110. DOI: 10.1016/j.astropartphys.2019.04.002 (cit. on pp. 80, 95).

[313]G. Illuminati. „ANTARES and IceCube combined search for neutrino point-like and extended sources in the Southern Sky“. In: *36th International Cosmic Ray Conference (ICRC2019)*. Vol. 36. International Cosmic Ray Conference. 2019, p. 919. arXiv: 1908.07439 [astro-ph.HE] (cit. on pp. 80, 95).

[314]Alexander Aab et al. „Multi-Messenger Physics with the Pierre Auger Observatory“. In: *Front. Astron. Space Sci.* 6 (2019), p. 24. DOI: 10.3389/fspas.2019.00024. arXiv: 1904.11918 [astro-ph.HE] (cit. on p. 81).

[315]U. F. Katz and Ch. Spiering. „High-energy neutrino astrophysics: Status and perspectives“. In: *Progress in Particle and Nuclear Physics* 67.3 (2012), pp. 651–704. DOI: 10.1016/j.ppnp.2011.12.001. arXiv: 1111.0507 [astro-ph.HE] (cit. on pp. 82–84, 87, 88, 135, 142).

[316]A. Albert, M. André, M. Anghinolfi, et al. „All-flavor Search for a Diffuse Flux of Cosmic Neutrinos with Nine Years of ANTARES Data“. In: ApJ 853.1, L7 (2018), p. L7. DOI: 10.3847/2041-8213/aaa4f6. arXiv: 1711.07212 [astro-ph.HE] (cit. on pp. 81, 125, 138, 139).

[317]F. Reines. „Neutrino Interactions“. In: *Annual Review of Nuclear and Particle Science* 10 (1960), pp. 1–26. DOI: 10.1146/annurev.ns.10.120160.000245 (cit. on p. 83).

[318]K. Greisen. „Cosmic Ray Showers“. In: *Annual Review of Nuclear and Particle Science* 10 (1960), pp. 63–108. DOI: 10.1146/annurev.ns.10.120160.000431 (cit. on p. 83).

[319]H. Athar, C. S. Kim, and Jake Lee. „Intrinsic and Oscillated Astrophysical Neutrino Flavor Ratios Revisited“. In: *Modern Physics Letters A* 21.13 (2006), pp. 1049–1065. DOI: 10.1142/S021773230602038X. arXiv: hep-ph/0505017 [hep-ph] (cit. on pp. 83, 85, 86).

[320]John F. Beacom, Nicole F. Bell, Dan Hooper, Sandip Pakvasa, and Thomas J. Weiler. „Measuring flavor ratios of high-energy astrophysical neutrinos“. In: Phys. Rev. D 68.9, 093005 (2003), p. 093005. DOI: 10.1103/PhysRevD.68.093005. arXiv: hep-ph/0307025 [hep-ph] (cit. on pp. 83, 85, 126, 127).

[321]S. R. Kelner and F. A. Aharonian. „Energy spectra of gamma rays, electrons, and neutrinos produced at interactions of relativistic protons with low energy radiation“. In: Phys. Rev. D 78.3, 034013 (2008), p. 034013. DOI: 10.1103/PhysRevD.78.034013. arXiv: 0803.0688 [astro-ph] (cit. on p. 83).

[322]Maurizio Spurio. *Probes of Multimessenger Astrophysics*. Springer, 2018. DOI: 10.1007/978-3-319-96854-4 (cit. on pp. 83–85).

[323]M. Cardillo, M. Tavani, A. Giuliani, et al. „The supernova remnant W44: Confirmations and challenges for cosmic-ray acceleration“. In: A&A 565, A74 (2014), A74. DOI: 10.1051/0004-6361/201322685. arXiv: 1403.1250 [astro-ph.HE] (cit. on p. 85).

[324]A. Giuliani, M. Cardillo, M. Tavani, et al. „Neutral Pion Emission from Accelerated Protons in the Supernova Remnant W44“. In: ApJ 742.2, L30 (2011), p. L30. DOI: 10.1088/2041-8205/742/2/L30. arXiv: 1111.4868 [astro-ph.HE] (cit. on p. 85).

[325]M. Ackermann, M. Ajello, A. Allafort, et al. „Detection of the Characteristic Pion-Decay Signature in Supernova Remnants“. In: *Science* 339.6121 (2013), pp. 807–811. DOI: 10.1126/science.1231160. arXiv: 1302.3307 [astro-ph.HE] (cit. on p. 85).

[326]M. G. Aartsen, M. Ackermann, J. Adams, et al. „Flavor Ratio of Astrophysical Neutrinos above 35 TeV in IceCube“. In: Phys. Rev. Lett. 114.17, 171102 (2015), p. 171102. DOI: 10.1103/PhysRevLett.114.171102. arXiv: 1502.03376 [astro-ph.HE] (cit. on pp. 85, 86).

[327]Jörg P. Rachen and P. Mészáros. „Photohadronic neutrinos from transients in astrophysical sources“. In: Phys. Rev. D 58.12, 123005 (1998), p. 123005. DOI: 10.1103/PhysRevD.58.123005. arXiv: astro-ph/9802280 [astro-ph] (cit. on p. 85).

[328]T. Kashti and E. Waxman. „Astrophysical Neutrinos: Flavor Ratios Depend on Energy“. In: *Physical Review Letters* 95.18, 181101 (Oct. 2005), p. 181101. DOI: 10.1103/PhysRevLett.95.181101. eprint: astro-ph/0507599 (cit. on p. 85).

[329]M. Kachelrieß and R. Tomàs. „High-energy neutrino yields from astrophysical sources: Weakly magnetized sources“. In: Phys. Rev. D 74.6, 063009 (2006), p. 063009. DOI: 10.1103/PhysRevD.74.063009. arXiv: astro-ph/0606406 [astro-ph] (cit. on p. 85).

[330]Paolo Lipari, Maurizio Lusignoli, and Davide Meloni. „Flavor composition and energy spectrum of astrophysical neutrinos“. In: Phys. Rev. D 75.12, 123005 (2007), p. 123005. DOI: 10.1103/PhysRevD.75.123005. arXiv: 0704.0718 [astro-ph] (cit. on p. 85).

[331]S. R. Klein, R. E. Mikkelsen, and J. Becker Tjus. „Muon Acceleration in Cosmic-Ray Sources“. In: ApJ 779, 106 (Dec. 2013), p. 106. DOI: 10.1088/0004-637X/779/2/106. arXiv: 1208.2056 [astro-ph.HE] (cit. on p. 85).

[332]Luis A. Anchordoqui, Haim Goldberg, Francis Halzen, and Thomas J. Weiler. „Neutrinos as a diagnostic of high energy astrophysical processes [rapid communication]“. In: *Physics Letters B* 621.1-2 (2005), pp. 18–21. DOI: 10.1016/j.physletb.2005.06.056. arXiv: hep-ph/0410003 [hep-ph] (cit. on p. 85).

[333]M. C. Gonzalez-Garcia, Michele Maltoni, and Thomas Schwetz. „Updated fit to three neutrino mixing: status of leptonic CP violation“. In: *Journal of High Energy Physics* 2014, 52 (2014), p. 52. DOI: 10.1007/JHEP11(2014)052. arXiv: 1409.5439 [hep-ph] (cit. on p. 85).

[334]John F. Beacom, Nicole F. Bell, Dan Hooper, Sandip Pakvasa, and Thomas J. Weiler. „Decay of High-Energy Astrophysical Neutrinos“. In: Phys. Rev. Lett. 90.18, 181301 (2003), p. 181301. DOI: 10.1103/PhysRevLett.90.181301. arXiv: hep-ph/0211305 [hep-ph] (cit. on p. 86).

[335]Philipp Baerwald, Mauricio Bustamante, and Walter Winter. „Neutrino decays over cosmological distances and the implications for neutrino telescopes“. In: J. Cosmology Astropart. Phys. 2012.10, 020 (2012), p. 020. DOI: 10.1088/1475-7516/2012/10/020. arXiv: 1208.4600 [astro-ph.CO] (cit. on p. 86).

[336]H. Athar. „Mixed High Energy Neutrinos from the Cosmos“. In: *Chinese Journal of Physics* 42.1 (2004), p. 1. arXiv: hep-ph/0308188 [hep-ph] (cit. on p. 86).

[337]John F. Beacom, Nicole F. Bell, Dan Hooper, et al. „Pseudo-Dirac Neutrinos: A Challenge for Neutrino Telescopes“. In: Phys. Rev. Lett. 92.1, 011101 (2004), p. 011101. DOI: 10.1103/PhysRevLett.92.011101. arXiv: hep-ph/0307151 [hep-ph] (cit. on p. 86).

[338]Dan Hooper, Dean Morgan, and Elizabeth Winstanley. „Lorentz and CPT invariance violation in high-energy neutrinos“. In: Phys. Rev. D 72.6, 065009 (2005), p. 065009. DOI: 10.1103/PhysRevD.72.065009. arXiv: hep-ph/0506091 [astro-ph] (cit. on p. 86).

[339]L. A. Anchordoqui, H. Goldberg, M. C. Gonzalez-Garcia, et al. „Probing Planck scale physics with IceCube“. In: Phys. Rev. D 72.6, 065019 (Sept. 2005), p. 065019. DOI: 10.1103/PhysRevD.72.065019. eprint: hep-ph/0506168 (cit. on p. 86).

[340]Eli Waxman and John Bahcall. „High energy neutrinos from astrophysical sources: An upper bound“. In: Phys. Rev. D 59.2, 023002 (1999), p. 023002. DOI: 10.1103/PhysRevD.59.023002. arXiv: hep-ph/9807282 [hep-ph] (cit. on pp. 87–91).

[341]John Bahcall and Eli Waxman. „High energy astrophysical neutrinos: The upper bound is robust“. In: Phys. Rev. D 64.2, 023002 (2001), p. 023002. DOI: 10.1103/PhysRevD.64.023002. arXiv: hep-ph/9902383 [hep-ph] (cit. on pp. 87, 90, 91, 93).

[342]Frejus Collaboration, W. Rhode, K. Daum, et al. „Limits on the flux of very high energy neutrinos with the Frejus detector“. In: *Astroparticle Physics* 4.3 (1996), pp. 217–225. DOI: 10.1016/0927-6505(95)00038-0 (cit. on pp. 87, 89).

[343]R. Abbasi, Y. Abdou, T. Abu-Zayyad, et al. „Search for a diffuse flux of astrophysical muon neutrinos with the IceCube 40-string detector“. In: Phys. Rev. D 84.8, 082001 (2011), p. 082001. DOI: 10.1103/PhysRevD.84.082001. arXiv: 1104.5187 [astro-ph.HE] (cit. on p. 87).

[344]J. A. Aguilar, I. Al Samarai, A. Albert, et al. „Search for a diffuse flux of high-energy ν with the ANTARES neutrino telescope“. In: *Physics Letters B* 696.1-2 (2011), pp. 16–22. DOI: 10.1016/j.physletb.2010.11.070. arXiv: 1011.3772 [astro-ph.HE] (cit. on p. 87).

[345]M. G. Aartsen, M. Ackermann, J. Adams, et al. „Observation of High-Energy Astrophysical Neutrinos in Three Years of IceCube Data“. In: Phys. Rev. Lett. 113.10, 101101 (2014), p. 101101. DOI: 10.1103/PhysRevLett.113.101101. arXiv: 1405.5303 [astro-ph.HE] (cit. on pp. 87, 91, 92).

[346]F. W. Stecker. „Note on high-energy neutrinos from active galactic nuclei cores“. In: Phys. Rev. D 72.10, 107301 (2005), p. 107301. DOI: 10.1103/PhysRevD.72.107301. arXiv: astro-ph/0510537 [astro-ph] (cit. on p. 87).

[347]K. Mannheim. „High-energy neutrinos from extragalactic jets“. In: *Astroparticle Physics* 3 (May 1995), pp. 295–302. DOI: 10.1016/0927-6505(94)00044-4 (cit. on pp. 87, 89, 93).

[348]Julia K. Becker, Peter L. Biermann, and Wolfgang Rhode. „The diffuse neutrino flux from FR-II radio galaxies and blazars: A source property based estimate“. In: *Astroparticle Physics* 23.4 (2005), pp. 355–368. DOI: 10.1016/j.astropartphys.2005.02.003. arXiv: astro-ph/0502089 [astro-ph] (cit. on p. 87).

[349]J. P. Rachen, R. J. Protheroe, and K. Mannheim. „The relation of extragalactic cosmic ray and neutrino fluxes: the logic of the upper bound debate“. In: *Nuclear Physics B Proceedings Supplements* 80 (2000), p. 240. arXiv: astro-ph/9908031 [astro-ph] (cit. on p. 89).

[350]Karl Mannheim, R. J. Protheroe, and Jörg P. Rachen. „Cosmic ray bound for models of extragalactic neutrino production“. In: Phys. Rev. D 63.2, 023003 (2001), p. 023003. DOI: 10.1103/PhysRevD.63.023003. arXiv: astro-ph/9812398 [astro-ph] (cit. on p. 89).

[351]Eli Waxman and John Bahcall. „High Energy Neutrinos from Cosmological Gamma-Ray Burst Fireballs“. In: Phys. Rev. Lett. 78.12 (1997), pp. 2292–2295. DOI: 10.1103/PhysRevLett.78.2292. arXiv: astro-ph/9701231 [astro-ph] (cit. on pp. 89, 99, 100).

[352]P. Lipari. „Lepton spectra in the earth's atmosphere“. In: *Astroparticle Physics* 1 (Mar. 1993), pp. 195–227. DOI: 10.1016/0927-6505(93)90022-6 (cit. on p. 89).

[353]M. G. Aartsen, K. Abraham, M. Ackermann, et al. „Constraints on Ultrahigh-Energy Cosmic-Ray Sources from a Search for Neutrinos above 10 PeV with IceCube“. In: Phys. Rev. Lett. 117.24, 241101 (2016), p. 241101. DOI: 10.1103/PhysRevLett.117.241101. arXiv: 1607.05886 [astro-ph.HE] (cit. on p. 90).

[354]M. G. Aartsen, R. Abbasi, M. Ackermann, et al. „Probing the origin of cosmic rays with extremely high energy neutrinos using the IceCube Observatory“. In: Phys. Rev. D 88.11, 112008 (2013), p. 112008. DOI: 10.1103/PhysRevD.88.112008. arXiv: 1310.5477 [astro-ph.HE] (cit. on p. 90).

[355]M. G. Aartsen, K. Abraham, M. Ackermann, et al. „A Combined Maximum-likelihood Analysis of the High-energy Astrophysical Neutrino Flux Measured with IceCube“. In: ApJ 809.1, 98 (2015), p. 98. DOI: 10.1088/0004-637X/809/1/98. arXiv: 1507.03991 [astro-ph.HE] (cit. on p. 90).

[356]Ralph Engel, David Seckel, and Todor Stanev. „Neutrinos from propagation of ultrahigh energy protons“. In: Phys. Rev. D 64.9 (2001), p. 093010. DOI: 10.1103/PhysRevD.64.093010. arXiv: astro-ph/0101216 [astro-ph] (cit. on p. 90).

[357]A. Aab, P. Abreu, M. Aglietta, et al. „Improved limit to the diffuse flux of ultrahigh energy neutrinos from the Pierre Auger Observatory“. In: Phys. Rev. D 91.9, 092008 (2015), p. 092008. DOI: 10.1103/PhysRevD.91.092008. arXiv: 1504.05397 [astro-ph.HE] (cit. on p. 90).

[358]I. Kravchenko, C. Cooley, S. Hussain, et al. „RICE limits on the diffuse ultrahigh energy neutrino flux“. In: Phys. Rev. D 73.8, 082002 (2006), p. 082002. DOI: 10.1103/PhysRevD.73.082002. arXiv: astro-ph/0601148 [astro-ph] (cit. on p. 90).

[359]I. Kravchenko, S. Hussain, D. Seckel, et al. „Updated results from the RICE experiment and future prospects for ultra-high energy neutrino detection at the south pole“. In: Phys. Rev. D 85.6, 062004 (2012), p. 062004. DOI: 10.1103/PhysRevD.85.062004. arXiv: 1106.1164 [astro-ph.HE] (cit. on p. 90).

[360]P. W. Gorham, P. Allison, B. M. Baughman, et al. „Observational constraints on the ultrahigh energy cosmic neutrino flux from the second flight of the ANITA experiment“. In: Phys. Rev. D 82.2, 022004 (2010), p. 022004. DOI: 10.1103/PhysRevD.82.022004. arXiv: 1003.2961 [astro-ph.HE] (cit. on p. 90).

[361]P. W. Gorham, P. Allison, B. M. Baughman, et al. „Erratum: Observational constraints on the ultrahigh energy cosmic neutrino flux from the second flight of the ANITA experiment [Phys. Rev. D 82 022004 (2010)]“. In: Phys. Rev. D 85.4, 049901 (2012), p. 049901. DOI: 10.1103/PhysRevD.85.049901 (cit. on p. 90).

[362]IceCube-Gen2 Collaboration, : M. G. Aartsen, et al. „IceCube-Gen2: A Vision for the Future of Neutrino Astronomy in Antarctica“. In: *arXiv e-prints*, arXiv:1412.5106 (2014), arXiv:1412.5106. arXiv: 1412.5106 [astro-ph.HE] (cit. on pp. 91, 92, 100, 142).

[363]R. Abbasi, Y. Abdou, M. Ackermann, et al. „IceTop: The surface component of IceCube. The IceCube Collaboration“. In: *Nuclear Instruments and Methods in Physics Research A* 700 (2013), pp. 188–220. DOI: 10.1016/j.nima.2012.10.067. arXiv: 1207.6326 [astro-ph.IM] (cit. on pp. 91, 146–149).

[364]The IceCube Collaboration, M. G. Aartsen, R. Abbasi, et al. „Search for a diffuse flux of astrophysical muon neutrinos with the IceCube 59-string configuration“. In: *arXiv e-prints*, arXiv:1311.7048 (2013), arXiv:1311.7048. arXiv: 1311.7048 [astro-ph.HE] (cit. on p. 91).

[365]ANTARES Collaboration, S. Adrián-Martínez, A. Albert, et al. „ANTARES constrains a blazar origin of two IceCube PeV neutrino events“. In: A&A 576, L8 (2015), p. L8. DOI: 10.1051/0004-6361/201525670. arXiv: 1501.07843 [astro-ph.HE] (cit. on p. 93).

[366]F. Krauß, M. Kadler, K. Mannheim, et al. „TANAMI blazars in the IceCube PeV-neutrino fields“. In: A&A 566, L7 (2014), p. L7. DOI: 10.1051/0004-6361/201424219. arXiv: 1406.0645 [astro-ph.HE] (cit. on p. 93).

[367]V. S. Berezinskii and A. Iu. Smirnov. „Cosmic Neutrinos of Ultra High Energies and Detection Possibility“. In: Ap&SS 32.2 (1975), pp. 461–482. DOI: 10.1007/BF00643157 (cit. on p. 93).

[368]F. W. Stecker and M. H. Salamon. „High Energy Neutrinos from Quasars“. In: Space Sci. Rev. 75.1-2 (1996), pp. 341–355. DOI: 10.1007/BF00195044. arXiv: astro-ph/9501064 [astro-ph] (cit. on p. 93).

[369]P. Padovani and E. Resconi. „Are both BL Lacs and pulsar wind nebulae the astrophysical counterparts of IceCube neutrino events?“ In: MNRAS 443 (Sept. 2014), pp. 474–484. DOI: 10.1093/mnras/stu1166. arXiv: 1406.0376 [astro-ph.HE] (cit. on pp. 93, 250).

[370]A. P. Szabo and R. J. Protheroe. „Implications of particle acceleration in active galactic nuclei for cosmic rays and high energy neutrino astronomy“. In: *Astroparticle Physics* 2 (Oct. 1994), pp. 375–392. DOI: 10.1016/0927-6505(94)90027-2. eprint: astro-ph/9405020 (cit. on p. 93).

[371]Armen Atoyan and Charles D. Dermer. „High-Energy Neutrinos from Photomeson Processes in Blazars“. In: Phys. Rev. Lett. 87.22, 221102 (2001), p. 221102. DOI: 10.1103/PhysRevLett.87.221102. arXiv: astro-ph/0108053 [astro-ph] (cit. on p. 93).

[372]S. R. Kelner, F. A. Aharonian, and V. V. Bugayov. „Energy spectra of gamma rays, electrons, and neutrinos produced at proton-proton interactions in the very high energy regime“. In: Phys. Rev. D 74.3, 034018 (2006), p. 034018. DOI: 10.1103/PhysRevD.74.034018. arXiv: astro-ph/0606058 [astro-ph] (cit. on p. 93).

[373]J. Becker Tjus, B. Eichmann, F. Halzen, A. Kheirandish, and S. M. Saba. „High-energy neutrinos from radio galaxies“. In: Phys. Rev. D 89.12, 123005 (June 2014), p. 123005. DOI: 10.1103/PhysRevD.89.123005. arXiv: 1406.0506 [astro-ph.HE] (cit. on p. 93).

[374]Charles D. Dermer, Kohta Murase, and Yoshiyuki Inoue. „Photopion production in black-hole jets and flat-spectrum radio quasars as PeV neutrino sources“. In: *Journal of High Energy Astrophysics* 3 (2014), pp. 29–40. DOI: 10.1016/j.jheap.2014.09.001. arXiv: 1406.2633 [astro-ph.HE] (cit. on p. 93).

[375]M. Punch, C. W. Akerlof, M. F. Cawley, et al. „Detection of TeV photons from the active galaxy Markarian 421“. In: Nature 358 (Aug. 1992), p. 477. DOI: 10.1038/358477a0 (cit. on pp. 93, 250).

[376]J. Quinn, C. W. Akerlof, S. Biller, et al. „Detection of Gamma Rays with E > 300 GeV from Markarian 501“. In: ApJ 456 (Jan. 1996), p. L83. DOI: 10.1086/309878 (cit. on pp. 93, 250).

[377]A. U. Abeysekara, A. Albert, R. Alfaro, et al. „The 2HWC HAWC Observatory Gamma-Ray Catalog“. In: ApJ 843.1, 40 (2017), p. 40. DOI: 10.3847/1538-4357/aa7556. arXiv: 1702.02992 [astro-ph.HE] (cit. on pp. 93, 216–220, 223–225, 250).

[378]B. E. Markarian. „Galaxies with an Ultraviolet Continuum“. In: *Astrofizika* 3 (1967) (cit. on p. 93).

[379]B. E. Markarian. „Galaxies with the ultraviolet continuum“. In: *Non-stable Phenomena in Galaxies*. Vol. 29. IAU Symposium. 1968, p. 99 (cit. on p. 93).

[380]B. E. Markarian. „Galaxies with Ultraviolet Continuum I“. In: *Astrofizika* 5 (1969) (cit. on p. 93).

[381]B. E. Markarian, V. A. Lipovetsky, J. A. Stepanian, L. K. Erastova, and A. I. Shapovalova. „The First Byurakan Survey - a Catalogue of Galaxies with Ultraviolet Continuum“. In: *Soobshcheniya Spetsial'noj Astrofizicheskoj Observatorii* 62 (1989), p. 5 (cit. on p. 93).

[382]Ke Fang, Toshihiro Fujii, Tim Linden, and Angela V. Olinto. „Is the Ultra-high Energy Cosmic-Ray Excess Observed by the Telescope Array Correlated with IceCube Neutrinos?“ In: ApJ 794.2, 126 (2014), p. 126. DOI: 10.1088/0004-637X/794/2/126. arXiv: 1404.6237 [astro-ph.HE] (cit. on p. 93).

[383]Stavros Dimitrakoudis, Maria Petropoulou, and Apostolos Mastichiadis. „Self-consistent neutrino and UHE cosmic ray spectra from Mrk 421“. In: *Astroparticle Physics* 54 (2014), pp. 61–66. DOI: 10.1016/j.astropartphys.2013.10.005. arXiv: 1310.7923 [astro-ph.HE] (cit. on p. 93).

[384]J. Albert, E. Aliu, H. Anderhub, et al. „Discovery of Very High Energy γ-Rays from 1ES 1011+496 at z = 0.212“. In: ApJ 667.1 (2007), pp. L21–L24. DOI: 10.1086/521982. arXiv: 0706.4435 [astro-ph] (cit. on p. 93).

[385]M. Kadler, F. Krauß, K. Mannheim, et al. „Coincidence of a high-fluence blazar outburst with a PeV-energy neutrino event“. In: *Nature Physics* 12 (Aug. 2016), pp. 807–814. DOI: 10.1038/nphys3715. arXiv: 1602.02012 [astro-ph.HE] (cit. on p. 93).

[386]M. G. Aartsen, M. Ackermann, J. Adams, et al. „The IceCube realtime alert system“. In: *Astroparticle Physics* 92 (2017), pp. 30–41. DOI: 10.1016/j.astropartphys.2017.05.002. arXiv: 1612.06028 [astro-ph.HE] (cit. on pp. 94, 102, 103, 105).

[387]U. F. Katz. „Neutrino telescopy in the Mediterranean Sea“. In: *Progress in Particle and Nuclear Physics* 57.1 (2006), pp. 273–282. DOI: 10.1016/j.ppnp.2006.01.006. arXiv: astro-ph/0601012 [astro-ph] (cit. on p. 94).

[388]F. Aharonian, A. G. Akhperjanian, A. R. Bazer-Bachi, et al. „A detailed spectral and morphological study of the gamma-ray supernova remnant <ASTROBJ>RX J1713.7-3946</ASTROBJ> with HESS“. In: A&A 449.1 (2006), pp. 223–242. DOI: 10.1051/0004-6361:20054279. arXiv: astro-ph/0511678 [astro-ph] (cit. on p. 94).

[389]F. Aharonian, A. G. Akhperjanian, A. R. Bazer-Bachi, et al. „Detection of TeV γ-ray emission from the shell-type supernova remnant RX J0852.0-4622 with HESS“. In: A&A 437.1 (2005), pp. L7–L10. DOI: 10.1051/0004-6361:200500130. arXiv: astro-ph/0505380 [astro-ph] (cit. on p. 94).

[390]Francesco Vissani. „Neutrinos from galactic sources of cosmic rays with known γ-ray spectra“. In: *Astroparticle Physics* 26.4-5 (2006), pp. 310–313. DOI: 10.1016/j.astropartphys.2006.07.005. arXiv: astro-ph/0607249 [astro-ph] (cit. on p. 95).

[391]Alexander Kappes, Jim Hinton, Christian Stegmann, and Felix A. Aharonian. „Potential Neutrino Signals from Galactic γ-Ray Sources“. In: ApJ 656.2 (2007), pp. 870–878. DOI: 10.1086/508936. arXiv: astro-ph/0607286 [astro-ph] (cit. on p. 95).

[392]G. Morlino, E. Amato, and P. Blasi. „Gamma-ray emission from SNR RX J1713.7-3946 and the origin of galactic cosmic rays“. In: MNRAS 392.1 (2009), pp. 240–250. DOI: 10.1111/j.1365-2966.2008.14033.x. arXiv: 0810.0094 [astro-ph] (cit. on p. 95).

[393]Julien Aublin, Giulia Illuminati, and Sergio Navas. „Searches for point-like sources of cosmic neutrinos with 11 years of ANTARES data“. In: *arXiv e-prints*, arXiv:1908.08248 (2019), arXiv:1908.08248. arXiv: 1908.08248 [astro-ph.HE] (cit. on pp. 95, 96, 98, 223).

[394]Elena Amato. „Particle acceleration and radiation in Pulsar Wind Nebulae“. In: *arXiv e-prints*, arXiv:1503.02402 (2015), arXiv:1503.02402. arXiv: 1503.02402 [astro-ph.HE] (cit. on p. 96).

[395]D. Horns, F. Aharonian, A. Santangelo, A. I. D. Hoffmann, and C. Masterson. „Nucleonic gamma-ray production in <ASTROBJ>Vela X</ASTROBJ>“. In: A&A 451.3 (2006), pp. L51–L54. DOI: 10.1051/0004-6361:20065116 (cit. on p. 96).

[396]Sylvain Chaty. „Microquasars and Jets“. In: *arXiv e-prints*, astro-ph/0506008 (2005), astro–ph/0506008. arXiv: astro-ph/0506008 [astro-ph] (cit. on p. 97).

[397]HAWC Collaboration, A. U. Abeysekara, A. Albert, et al. „Very high energy particle acceleration powered by the jets of the microquasar SS 433“. In: *arXiv e-prints*, arXiv:1810.01892 (2018), arXiv:1810.01892. arXiv: 1810.01892 [astro-ph.HE] (cit. on pp. 97, 222).

[398]S. Gillessen, F. Eisenhauer, S. Trippe, et al. „Monitoring Stellar Orbits Around the Massive Black Hole in the Galactic Center“. In: ApJ 692.2 (2009), pp. 1075–1109. DOI: 10.1088/0004-637X/692/2/1075. arXiv: 0810.4674 [astro-ph] (cit. on p. 98).

[399]H. E. S. S. Collaboration, : and F. Aharonian. „Very high energy gamma rays from the direction of Sagittarius A*“. In: *arXiv e-prints*, astro-ph/0408145 (2004), astro–ph/0408145. arXiv: astro-ph/0408145 [astro-ph] (cit. on p. 98).

[400]F. Aharonian, A. G. Akhperjanian, A. R. Bazer-Bachi, et al. „Discovery of very-high-energy γ-rays from the Galactic Centre ridge“. In: Nature 439.7077 (2006), pp. 695–698. DOI: 10.1038/nature04467. arXiv: astro-ph/0603021 [astro-ph] (cit. on p. 99).

[401]M. Ackermann, M. Ajello, W. B. Atwood, et al. „Fermi-LAT Observations of the Diffuse γ-Ray Emission: Implications for Cosmic Rays and the Interstellar Medium“. In: ApJ 750.1, 3 (2012), p. 3. DOI: 10.1088/0004-637X/750/1/3. arXiv: 1202.4039 [astro-ph.HE] (cit. on p. 99).

[402]A. Albert, M. André, M. Anghinolfi, et al. „New constraints on all flavor Galactic diffuse neutrino emission with the ANTARES telescope“. In: Phys. Rev. D 96.6, 062001 (2017), p. 062001. DOI: 10.1103/PhysRevD.96.062001. arXiv: 1705.00497 [astro-ph.HE] (cit. on p. 99).

[403]M. G. Aartsen, K. Abraham, M. Ackermann, et al. „Observation and Characterization of a Cosmic Muon Neutrino Flux from the Northern Hemisphere Using Six Years of IceCube Data“. In: ApJ 833.1, 3 (2016), p. 3. DOI: 10.3847/0004-637X/833/1/3. arXiv: 1607.08006 [astro-ph.HE] (cit. on p. 99).

[404]Kohta Murase. „High energy neutrino early afterglows from gamma-ray bursts revisited“. In: Phys. Rev. D 76.12, 123001 (2007), p. 123001. DOI: 10.1103/PhysRevD.76.123001. arXiv: 0707.1140 [astro-ph] (cit. on pp. 99, 100).

[405]A. Albert, M. André, M. Anghinolfi, et al. „Search for high-energy neutrinos from bright GRBs with ANTARES“. In: MNRAS 469.1 (2017), pp. 906–915. DOI: 10.1093/mnras/stx902. arXiv: 1612.08589 [astro-ph.HE] (cit. on p. 100).

[406]Pasquale Blasi. „Origin of very high- and ultra-high-energy cosmic rays“. In: *Comptes Rendus Physique* 15.4 (2014), pp. 329–338. DOI: 10.1016/j.crhy.2014.02.008. arXiv: 1403.2967 [astro-ph.HE] (cit. on p. 100).

[407]S. Adrián-Martínez, A. Albert, I. Al Samarai, et al. „Search for muon neutrinos from gamma-ray bursts with the ANTARES neutrino telescope using 2008 to 2011 data“. In: A&A 559, A9 (2013), A9. DOI: 10.1051/0004-6361/201322169. arXiv: 1307.0304 [astro-ph.HE] (cit. on pp. 100, 298).

[408]Hagai Netzer. „Revisiting the Unified Model of Active Galactic Nuclei“. In: ARA&A 53 (2015), pp. 365–408. DOI: 10.1146/annurev-astro-082214-122302. arXiv: 1505.00811 [astro-ph.GA] (cit. on p. 101).

[409]P. N. Best and T. M. Heckman. „On the fundamental dichotomy in the local radio-AGN population: accretion, evolution and host galaxy properties“. In: MNRAS 421.2 (2012), pp. 1569–1582. DOI: 10.1111/j.1365-2966.2012.20414.x. arXiv: 1201.2397 [astro-ph.CO] (cit. on p. 101).

[410]V. Beckmann and C. Shrader. „The AGN phenomenon: open issues“. In: *Proceedings of “An INTEGRAL view of the high-energy sky (the first 10 years)” - 9th INTEGRAL Workshop and celebration of the 10th anniversary of the launch (INTEGRAL 2012). 15-19 October 2012. Bibliotheque Nationale de France*. 2012, p. 69. arXiv: 1302.1397 [astro-ph.HE] (cit. on pp. 101, 270).

[411]C. Megan Urry and Paolo Padovani. „Unified Schemes for Radio-Loud Active Galactic Nuclei“. In: PASP 107 (1995), p. 803. DOI: 10.1086/133630. arXiv: astro-ph/9506063 [astro-ph] (cit. on p. 101).

[412]M. Cerruti, M. Böttcher, N. Chakraborty, et al. „Target of opportunity observations of blazars with H.E.S.S.“ In: *6th International Symposium on High Energy Gamma-Ray Astronomy*. Vol. 1792. American Institute of Physics Conference Series. 2017, p. 050029. DOI: 10.1063/1.4968975. arXiv: 1610.05523 [astro-ph.HE] (cit. on p. 102).

[413]A. Konigl. „Relativistic jets as X-ray and gamma-ray sources.“ In: ApJ 243 (1981), pp. 700–709. DOI: 10.1086/158638 (cit. on p. 102).

[414]Marek Sikora, Mitchell C. Begelman, and Martin J. Rees. „Comptonization of Diffuse Ambient Radiation by a Relativistic Jet: The Source of Gamma Rays from Blazars?“ In: ApJ 421 (1994), p. 153. DOI: 10.1086/173633 (cit. on p. 102).

[415]A. Zech, M. Cerruti, and D. Mazin. „Expected signatures from hadronic emission processes in the TeV spectra of BL Lacertae objects“. In: A&A 602, A25 (2017), A25. DOI: 10.1051/0004-6361/201629997. arXiv: 1703.05937 [astro-ph.HE] (cit. on p. 102).

[416]T. K. Gaisser, F. Halzen, and T. Stanev. „Particle astrophysics with high energy neutrinos“. In: Phys. Rep. 258 (1995), pp. 173–236. DOI: 10.1016/0370-1573(95)00003-Y. arXiv: hep-ph/9410384 [hep-ph] (cit. on p. 102).

[417]John G. Learned and Karl Mannheim. „High-Energy Neutrino Astrophysics“. In: *Annual Review of Nuclear and Particle Science* 50 (2000), pp. 679–749. DOI: 10.1146/annurev.nucl.50.1.679 (cit. on pp. 102, 141).

[418]Antonio Marinelli, Barbara Patricelli, and Nissim Fraija. „Hadronic flares and associated neutrinos for Markarian 421“. In: *Extragalactic Jets from Every Angle*. Ed. by F. Massaro, C. C. Cheung, E. Lopez, and A. Siemiginowska. Vol. 313. IAU Symposium. 2015, pp. 177–178. DOI: 10.1017/S174392131500215X. arXiv: 1505.03165 [astro-ph.HE] (cit. on p. 102).

[419]Anna Franckowiak. „Detection of a flaring blazar coincident with an IceCube high-energy neutrino“. In: *European Physical Journal Web of Conferences*. Vol. 207. European Physical Journal Web of Conferences. 2019, p. 02001. DOI: 10.1051/epjconf/201920702001 (cit. on p. 103).

[420]M. W. E. Smith, D. B. Fox, D. F. Cowen, et al. „The Astrophysical Multimessenger Observatory Network (AMON)“. In: *Astroparticle Physics* 45 (May 2013), pp. 56–70. DOI: 10.1016/j.astropartphys.2013.03.003. arXiv: 1211.5602 [astro-ph.HE] (cit. on p. 103).

[421]Hugo A. Ayala Solares, Stephane Coutu, D. F. Cowen, et al. „The Astrophysical Multimessenger Observatory Network (AMON): Performance and science program“. In: *Astroparticle Physics* 114 (2020), pp. 68–76. DOI: 10.1016/j.astropartphys.2019.06.007. arXiv: 1903.08714 [astro-ph.IM] (cit. on p. 103).

[422]Joshua Wood, Jordan Goodman, and Joshua Randall Wood. „An All-Sky Search for Bursts of Very High Energy Gamma Rays with HAWC“. PhD thesis. Maryland U., 2016. DOI: 10.13016/M2B24Z. arXiv: 1801.01550 [astro-ph.HE]. URL: https://drum.lib.umd.edu/handle/1903/18949 (cit. on p. 103).

[423]Hugo Alberto Ayala Solares. „AMON Multimessenger Alerts: Past and Future“. In: *Galaxies* 7.1 (2019). ISSN: 2075-4434. DOI: 10.3390/galaxies7010019. URL: https://www.mdpi.com/2075-4434/7/1/19 (cit. on pp. 103, 104).

[424]H. A. Ayala Solares, D. F. Cowen, J. J. DeLaunay, et al. „A Search for Cosmic Neutrino and Gamma-Ray Emitting Transients in 7.3 Years of ANTARES and Fermi LAT Data“. In: *arXiv e-prints*, arXiv:1904.06420 (2019), arXiv:1904.06420. arXiv: 1904.06420 [astro-ph.HE] (cit. on p. 104).

[425]Y. T. Tanaka, S. Buson, and D. Kocevski. „Fermi-LAT detection of increased gamma-ray activity of TXS 0506+056, located inside the IceCube-170922A error region.“ In: *The Astronomer's Telegram* 10791 (Sept. 2017) (cit. on pp. 104, 107, 108, 118).

[426]R. E. Rutledge. „The Astronomer's Telegram: A Web-based Short-Notice Publication System for the Professional Astronomical Community“. In: PASP 110 (June 1998), pp. 754–756. DOI: 10.1086/316184. eprint: astro-ph/9802256 (cit. on p. 107).

[427]D. Dornic and A. Coleiro. „Search for counterpart to IceCube-170922A with ANTARES“. In: *The Astronomer's Telegram* 10773 (Sept. 2017) (cit. on p. 107).

[428]M. de Naurois and H.E.S.S. Collaboration. „H.E.S.S. follow-up of IceCube-170922A“. In: *The Astronomer's Telegram* 10787 (Sept. 2017) (cit. on p. 107).

[429]P. A. E. A. Keivani, J. A. Kennea, D. B. Fox, et al. „Further Swift-XRT observations of IceCube 170922A“. In: *The Astronomer's Telegram* 10792 (Sept. 2017) (cit. on p. 108).

[430]B. J. Shappee, J. L. Prieto, D. Grupe, et al. „The Man behind the Curtain: X-Rays Drive the UV through NIR Variability in the 2013 Active Galactic Nucleus Outburst in NGC 2617“. In: ApJ 788, 48 (June 2014), p. 48. DOI: 10.1088/0004-637X/788/1/48. arXiv: 1310.2241 [astro-ph.HE] (cit. on p. 108).

[431]A. Franckowiak, K. Z. Stanek, C. S. Kochanek, et al. „ASAS-SN optical light-curve of blazar TXS 0506+056, located inside the IceCube-170922A error region, shows increased optical activity“. In: *The Astronomer's Telegram* 10794 (Sept. 2017) (cit. on p. 108).

[432]A. S. Piascik, I. A. Steele, S. D. Bates, et al. „SPRAT: Spectrograph for the Rapid Acquisition of Transients“. In: *Ground-based and Airborne Instrumentation for Astronomy V*. Vol. 9147. Proc. SPIE. July 2014, 91478H. DOI: 10.1117/12.2055117 (cit. on p. 108).

[433]I. A. Steele. „Optical Spectrum of TXS 0506+056 (possible counterpart to IceCube-170922A)“. In: *The Astronomer's Telegram* 10799 (Sept. 2017) (cit. on p. 108).

[434]M. Tavani, G. Barbiellini, A. Argan, et al. „The AGILE Mission“. In: A&A 502.3 (2009), pp. 995–1013. DOI: 10.1051/0004-6361/200810527. arXiv: 0807.4254 [astro-ph] (cit. on p. 108).

[435]F. Lucarelli, G. Piano, C. Pittori, et al. „AGILE confirmation of gamma-ray activity from the IceCube-170922A error region“. In: *The Astronomer's Telegram* 10801 (Sept. 2017) (cit. on p. 108).

[436]I. Martinez, I. Taboada, M. Hui, and R. Lauer. „HAWC gamma ray data prior to IceCube-170922A“. In: *The Astronomer's Telegram* 10802 (Sept. 2017) (cit. on p. 108).

[437]R. Mirzoyan. „First-time detection of VHE gamma rays by MAGIC from a direction consistent with the recent EHE neutrino event IceCube-170922A“. In: *The Astronomer's Telegram* 10817 (Oct. 2017) (cit. on p. 108).

[438]Lisa A. Crause, Ray M. Sharples, David G. Bramall, et al. „Performance of the Southern African Large Telescope (SALT) High Resolution Spectrograph (HRS)“. In: Proc. SPIE. Vol. 9147. Society of Photo-Optical Instrumentation Engineers (SPIE) Conference Series. 2014, 91476T. DOI: 10.1117/12.2055635 (cit. on p. 109).

[439]B. van Soelen, D. A. H. Buckley, and M. Boettcher. „SALT-HRS observation of the blazar TXS 0506+056 associated with IceCube-170922A“. In: *The Astronomer's Telegram* 10830 (Oct. 2017) (cit. on p. 109).

[440]R. Mukherjee. „VERITAS follow-up observations of IceCube neutrino event 170922A“. In: *The Astronomer's Telegram* 10833 (Oct. 2017) (cit. on p. 109).

[441]Masaru Matsuoka, Kazuyoshi Kawasaki, Shiro Ueno, et al. „The MAXI Mission on the ISS: Science and Instruments for Monitoring All-Sky X-Ray Images“. In: PASJ 61 (2009), p. 999. DOI: 10.1093/pasj/61.5.999. arXiv: 0906.0631 [astro-ph.IM] (cit. on p. 109).

[442]H. Negoro, S. Ueno, H. Tomida, et al. „MAXI/GSC observations of IceCube-170922A and TXS 0506+056“. In: *The Astronomer's Telegram* 10838 (Oct. 2017) (cit. on p. 109).

[443]J. Vernet, H. Dekker, S. D'Odorico, et al. „X-shooter, the new wide band intermediate resolution spectrograph at the ESO Very Large Telescope“. In: A&A 536, A105 (Dec. 2011), A105. DOI: 10.1051/0004-6361/201117752. arXiv: 1110.1944 [astro-ph.IM] (cit. on p. 109).

[444]A. Coleiro and S. Chaty. „VLT/X-Shooter spectrum of the blazar TXS 0506+056 (located inside the IceCube-170922A error box)“. In: *The Astronomer's Telegram* 10840 (Oct. 2017) (cit. on p. 109).

[445]Hiroshi Akitaya, Yuki Moritani, Takahiro Ui, et al. „HONIR: an optical and near-infrared simultaneous imager, spectrograph, and polarimeter for the 1.5-m Kanata telescope“. In: Proc. SPIE. Vol. 9147. Society of Photo-Optical Instrumentation Engineers (SPIE) Conference Series. 2014, 91474O. DOI: 10.1117/12.2054577 (cit. on p. 109).

[446]M. Yamanaka, Y. T. Tanaka, H. Mori, et al. „Kanata optical imaging and polarimetric follow-ups for possible IceCube counterpart TXS 0506+056“. In: *The Astronomer's Telegram* 10844 (Oct. 2017) (cit. on p. 109).

[447]F. A. Harrison, W. W. Craig, F. E. Christensen, et al. „The Nuclear Spectroscopic Telescope Array (NuSTAR) High-energy X-Ray Mission“. In: ApJ 770, 103 (June 2013), p. 103. DOI: 10.1088/0004-637X/770/2/103. arXiv: 1301.7307 [astro-ph.IM] (cit. on p. 109).

[448]D. B. Fox, J. J. DeLaunay, A. Keivani, et al. „Joint Swift XRT and NuSTAR Observations of TXS 0506+056“. In: *The Astronomer's Telegram* 10845 (Oct. 2017) (cit. on p. 109).

[449]A. R. Thompson, B. G. Clark, C. M. Wade, and P. J. Napier. „The Very Large Array“. In: ApJS 44 (Oct. 1980), pp. 151–167. DOI: 10.1086/190688 (cit. on p. 109).

[450]R. A. Perley, C. J. Chandler, B. J. Butler, and J. M. Wrobel. „The Expanded Very Large Array: A New Telescope for New Science“. In: ApJ 739, L1 (Sept. 2011), p. L1. DOI: 10.1088/2041-8205/739/1/L1. arXiv: 1106.0532 [astro-ph.IM] (cit. on p. 109).

[451]A. J. Tetarenko, G. R. Sivakoff, A. E. Kimball, and J. C. A. Miller-Jones. „VLA Radio Observations of the blazar TXS 0506+056 associated with the IceCube-170922A neutrino event“. In: *The Astronomer's Telegram* 10861 (Oct. 2017) (cit. on p. 109).

[452]Nobunari Kashikawa, Kentaro Aoki, Ryo Asai, et al. „FOCAS: The Faint Object Camera and Spectrograph for the Subaru Telescope“. In: PASJ 54.6 (2002), pp. 819–832. DOI: 10.1093/pasj/54.6.819 (cit. on p. 109).

[453]T. Morokuma, Y. T. Tanaka, K. Ohta, et al. „Subaru/FOCAS Optical Spectroscopy for a possible IceCube-170922A counterpart TXS 0506+056“. In: *The Astronomer's Telegram* 10890 (Oct. 2017) (cit. on p. 109).

[454]G. Stratta, M. Capalbi, P. Giommi, et al. „The ASDC SED Builder Tool description and Tutorial“. In: *arXiv e-prints*, arXiv:1103.0749 (2011), arXiv:1103.0749. arXiv: 1103.0749 [astro-ph.IM] (cit. on p. 111).

[455]Elisabetta Bissaldi. „Multi-Messenger Observations of GRBs: The GW connection“. In: *arXiv e-prints*, arXiv:1909.05960 (2019), arXiv:1909.05960. arXiv: 1909.05960 [astro-ph.HE] (cit. on p. 112).

[456]S. Adrián-Martínez, A. Albert, M. André, et al. „High-energy neutrino follow-up search of gravitational wave event GW150914 with ANTARES and IceCube“. In: Phys. Rev. D 93.12, 122010 (2016), p. 122010. DOI: 10.1103/PhysRevD.93.122010. arXiv: 1602.05411 [astro-ph.HE] (cit. on p. 112).

[457]Joan Centrella, John G. Baker, Bernard J. Kelly, and James R. van Meter. „Black-hole binaries, gravitational waves, and numerical relativity“. In: *Reviews of Modern Physics* 82.4 (2010), pp. 3069–3119. DOI: 10.1103/RevModPhys.82.3069. arXiv: 1010.5260 [gr-qc] (cit. on p. 112).

[458]Rosalba Perna, Davide Lazzati, and Bruno Giacomazzo. „Short Gamma-Ray Bursts from the Merger of Two Black Holes“. In: ApJ 821.1, L18 (2016), p. L18. DOI: 10.3847/2041-8205/821/1/L18. arXiv: 1602.05140 [astro-ph.HE] (cit. on p. 112).

[459]D. et al. Coulter. „LIGO/Virgo G298048: Potential optical counterpart discovered by Swope telescope.“ In: *GRB Coordinates Network* 21529 (2017), p. 1 (cit. on pp. 112, 113).

[460]B. J. Teegarden and S. J. Sturner. „INTEGRAL Observations of Gamma-Ray Bursts“. In: *AAS/High Energy Astrophysics Division #4*. AAS/High Energy Astrophysics Division. 1999, p. 17.01 (cit. on p. 113).

[461]C. Winkler, T. J. L. Courvoisier, G. Di Cocco, et al. „The INTEGRAL mission“. In: A&A 411 (2003), pp. L1–L6. DOI: 10.1051/0004-6361:20031288 (cit. on p. 113).

[462]G. Vedrenne, J. P. Roques, V. Schönfelder, et al. „SPI: The spectrometer aboard INTEGRAL“. In: A&A 411 (2003), pp. L63–L70. DOI: 10.1051/0004-6361:20031482 (cit. on p. 113).

[463]A. von Kienlin, V. Beckmann, A. Rau, et al. „INTEGRAL Spectrometer SPI's GRB detection capabilities. GRBs detected inside SPI's FoV and with the anticoincidence system ACS“. In: A&A 411 (2003), pp. L299–L305. DOI: 10.1051/0004-6361:20031231. arXiv: astro-ph/0308346 [astro-ph] (cit. on p. 113).

[464]Connaughton V. et al. „LIGO/Virgo G298048: Fermi GBM trigger 170817.529 and LIGO single IFO trigger.“ In: *GRB Coordinates Network* 21506 (2017), p. 1 (cit. on p. 113).

[465]Savchenko V. et al. „LIGO/Virgo G298048: INTEGRAL detection of a prompt gamma-ray counterpart.“ In: *GRB Coordinates Network* 21507 (2017), p. 1 (cit. on pp. 113, 114).

[466]K. et al. Alexander. „LIGO/Virgo G298048: VLA Detection.“ In: *GRB Coordinates Network* 21545 (2017), p. 1 (cit. on p. 113).

[467]K. et al. Alexander. „LIGO/Virgo G298048: VLA Refined Analysis.“ In: *GRB Coordinates Network* 21548 (2017), p. 1 (cit. on p. 113).

[468]K. et al. Bannister. „LIGO/Virgo G298048: ATCA detection of a radio source coincident with NGC 4993.“ In: *GRB Coordinates Network* 21559 (2017), p. 1 (cit. on p. 113).

[469]B. et al. Cenko. „LIGO/Virgo G298048: Continued Swift UV and X-ray Monitoring of SSS17a.“ In: *GRB Coordinates Network* 21572 (2017), p. 1 (cit. on p. 113).

[470]D. et al. Malesani. „LIGO/Virgo G298048: optical spectral energy distribution of SSS17a.“ In: *GRB Coordinates Network* 21577 (2017), p. 1 (cit. on p. 113).

[471]P. et al. Evans. „LIGO/Virgo G298048: Possible X-ray detection with Swift.“ In: *GRB Coordinates Network* 21612 (2017), p. 1 (cit. on p. 113).

[472]E. Margaret Burbidge, G. R. Burbidge, William A. Fowler, and F. Hoyle. „Synthesis of the Elements in Stars“. In: *Reviews of Modern Physics* 29.4 (1957), pp. 547–650. DOI: 10.1103/RevModPhys.29.547 (cit. on p. 113).

[473]I. Martinez-Castellanos and Smith A. „LIGO/Virgo G298048: HAWC follow-up.“ In: *GRB Coordinates Network* 21683 (2017), p. 1 (cit. on p. 113).

[474]M. et al. Ageron. „LIGO/Virgo G298048 ANTARES search.“ In: *GRB Coordinates Network* 21522 (2017), p. 1 (cit. on p. 114).

[475]M. et al. Ageron. „LIGO/Virgo G298048 ANTARES search (2).“ In: *GRB Coordinates Network* 21631 (2017), p. 1 (cit. on p. 114).

[476]I. et al. Bartos. „LIGO/Virgo G298048: Found coincident IceCube neutrino observation.“ In: *GRB Coordinates Network* 21508 (2017), p. 1 (cit. on p. 114).

[477]I. et al. Bartos. „LIGO/Virgo G298048: UPDATE on IceCube neutrino candidates - no coincidence with newest GW skymap.“ In: *GRB Coordinates Network* 21568 (2017), p. 1 (cit. on p. 114).

[478]J. et al. Alvarez-Muniz. „LIGO/Virgo G298048: Pierre Auger Observatory neutrino follow-up.“ In: *GRB Coordinates Network* 21686 (2017), p. 1 (cit. on p. 114).

[479]A. Albert, M. André, M. Anghinolfi, et al. „Search for High-energy Neutrinos from Binary Neutron Star Merger GW170817 with ANTARES, IceCube, and the Pierre Auger Observatory“. In: ApJ 850.2, L35 (2017), p. L35. DOI: 10.3847/2041-8213/aa9aed. arXiv: 1710.05839 [astro-ph.HE] (cit. on pp. 114, 115).

[480]D. A. Coulter, R. J. Foley, C. D. Kilpatrick, et al. „Swope Supernova Survey 2017a (SSS17a), the optical counterpart to a gravitational wave source“. In: *Science* 358.6370 (2017), pp. 1556–1558. DOI: 10.1126/science.aap9811. arXiv: 1710.05452 [astro-ph.HE] (cit. on p. 115).

[481]M. Ageron, J. A. Aguilar, I. Al Samarai, et al. „ANTARES: The first undersea neutrino telescope“. In: *Nuclear Instruments and Methods in Physics Research A* 656.1 (2011), pp. 11–38. DOI: 10.1016/j.nima.2011.06.103. arXiv: 1104.1607 [astro-ph.IM] (cit. on pp. 117, 141, 155, 163, 165, 166, 168–174, 176, 179, 182, 196, 204–207, 209, 211, 212).

[482]IceCube Collaboration, A. Achterberg, M. Ackermann, et al. „First year performance of the IceCube neutrino telescope“. In: *Astroparticle Physics* 26.3 (2006), pp. 155–173. DOI: 10.1016/j.astropartphys.2006.06.007. arXiv: astro-ph/0604450 [astro-ph] (cit. on pp. 117, 118, 130, 141, 145, 146).

[483]I.M. Zheleznykh. „On interactions of high-energy neutrinos in cosmic rays with substance“. Diploma paper. Dep. of Phys., Moscow St. Univ., 1958 (cit. on p. 117).

[484]I. M. Zheleznykh and M. A. Markov. „On high energy neutrino physics in cosmic rays“. In: *High-Energy Neutrino Physics* D-577 (1960) (cit. on p. 117).

[485]M. A. Markov and I. M. Zheleznykh. „On high energy neutrino physics in cosmic rays“. In: *Nuclear Physics* 27.3 (1961), pp. 385–394. DOI: 10.1016/0029-5582(61)90331-5 (cit. on p. 117).

[486]M. A. Markov. „On high energy neutrino physics“. In: *Proceedings, 10th International Conference on High-Energy Physics (ICHEP 60): Rochester, NY, USA, 25 Aug - 1 Sep 1960*. 1960, pp. 578–581. URL: http://inspirehep.net/record/1341439/files/C60-08-25-p578.pdf (cit. on pp. 117, 140).

[487]A. Roberts, H. Blood, J. Learned, and F. Reines. „Dumand: The Ocean as a Neutrino Detector“. In: *Proceedings of the International Neutrino Conference Aachen 1976: Held at Rheinisch-Westfälische Technische Hochschule Aachen June 8–12, 1976*. Ed. by H. Faissner, H. Reithler, and P. Zerwas. Wiesbaden: Vieweg+Teubner Verlag, 1977, pp. 688–702. ISBN: 978-3-322-90614-4. DOI: 10.1007/978-3-322-90614-4_68. URL: https://doi.org/10.1007/978-3-322-90614-4_68 (cit. on pp. 117, 140).

[488]A. Roberts. „DUMAND summer workshop“. In: *Proceedings of the 1978 DUMAND Summer Study (DUMAND 1978): University of California, La Jolla, CA, July 24 - September 2*. 1978 (cit. on pp. 117, 140).

[489]P. Bosetti et al. „DUMAND-II: Proposal to construct a deep-ocean laboratory for the study of high energy neutrino astrophysics and particle physics“. In: (1988) (cit. on pp. 117, 140).

[490]Francis Halzen and Spencer R. Klein. „Invited Review Article: IceCube: An instrument for neutrino astronomy“. In: *Review of Scientific Instruments* 81.8 (2010), pp. 081101–081101. DOI: 10.1063/1.3480478. arXiv: 1007.1247 [astro-ph.HE] (cit. on pp. 118, 130, 141, 145, 146).

[491]M. G. Aartsen, M. Ackermann, J. Adams, et al. „The IceCube Neutrino Observatory: instrumentation and online systems“. In: *Journal of Instrumentation* 12.3 (2017), P03012. DOI: 10.1088/1748-0221/12/03/P03012. arXiv: 1612.05093 [astro-ph.IM] (cit. on pp. 118, 130, 141, 145–148, 151–153).

[492]A. D. Avrorin, A. V. Avrorin, V. M. Aynutdinov, et al. „The prototyping/early construction phase of the BAIKAL-GVD project“. In: *Nuclear Instruments and Methods in Physics Research A* 742 (2014), pp. 82–88. DOI: 10.1016/j.nima.2013.10.064. arXiv: 1308.1833 [astro-ph.IM] (cit. on pp. 118, 153).

[493]A. D. Avrorin, A. V. Avrorin, V. M. Aynutdinov, et al. „Status of the Baikal-Gvd Project“. In: *Particle Physics at the Year of Centenary of Bruno Pontecorvo - Proceedings of the sixteenth Lomonosov conference on elementary particle physics. Edited by Studenikin Alexander I. Published by World Scientific Publishing Co. Pte. Ltd.* 2015, pp. 98–101. DOI: 10.1142/9789814663618_0019 (cit. on pp. 118, 143).

[494]Vladimir Aynutdinov et al. „Status of the Baikal-GVD experiment - 2017“. In: *PoS* ICRC2017 (2018), p. 1034. DOI: 10.22323/1.301.1034 (cit. on pp. 118, 143).

[495]R. Abbasi, Y. Abdou, T. Abu-Zayyad, et al. „Measurement of the atmospheric neutrino energy spectrum from 100 GeV to 400 TeV with IceCube“. In: Phys. Rev. D 83.1, 012001 (2011), p. 012001. DOI: 10.1103/PhysRevD.83.012001. arXiv: 1010.3980 [astro-ph.HE] (cit. on p. 118).

[496]M. G. Aartsen, R. Abbasi, Y. Abdou, et al. „First Observation of PeV-Energy Neutrinos with IceCube“. In: Phys. Rev. Lett. 111.2, 021103 (2013), p. 021103. DOI: 10.1103/PhysRevLett.111.021103. arXiv: 1304.5356 [astro-ph.HE] (cit. on pp. 118, 146).

[497]J. A. Formaggio and G. P. Zeller. „From eV to EeV: Neutrino cross sections across energy scales“. In: *Reviews of Modern Physics* 84.3 (2012), pp. 1307–1341. DOI: 10.1103/RevModPhys.84.1307. arXiv: 1305.7513 [hep-ex] (cit. on pp. 118, 122, 123).

[498]Aart Heijboer. „Track reconstruction and point source searches with ANTARES“. PhD thesis. Amsterdam U., 2004. URL: https://antares.in2p3.fr/Publications/thesis/2004/Aart-Heijboer-phd.pdf (cit. on pp. 119, 130, 134, 237–244).

[499]Raj Gandhi, Chris Quigg, Mary Hall Reno, and Ina Sarcevic. „Ultrahigh-energy neutrino interactions“. In: *Astroparticle Physics* 5.2 (1996), pp. 81–110. DOI: 10.1016/0927-6505(96)00008-4. arXiv: hep-ph/9512364 [hep-ph] (cit. on pp. 120, 121, 128, 130).

[500]Claudine Marie Marguerite Colnard. „Ultra-High Energy Neutrino Simulations“. PhD thesis. Amsterdam U., 2009. URL: http://cdsweb.cern.ch/record/1170507 (cit. on pp. 120, 122).

[501]J. D. Bjorken and E. A. Paschos. „High-Energy Inelastic Neutrino-Nucleon Interactions“. In: Phys. Rev. D 1.11 (1970), pp. 3151–3160. DOI: 10.1103/PhysRevD.1.3151 (cit. on pp. 121, 122).

[502]Amy Connolly, Robert S. Thorne, and David Waters. „Calculation of high energy neutrino-nucleon cross sections and uncertainties using the Martin-Stirling-Thorne-Watt parton distribution functions and implications for future experiments“. In: Phys. Rev. D 83.11, 113009 (2011), p. 113009. DOI: 10.1103/PhysRevD.83.113009. arXiv: 1102.0691 [hep-ph] (cit. on pp. 121, 128).

[503]A. Gazizov and M. Kowalski. „ANIS: High energy neutrino generator for neutrino telescopes“. In: *Computer Physics Communications* 172.3 (2005), pp. 203–213. DOI: 10.1016/j.cpc.2005.03.113. arXiv: astro-ph/0406439 [astro-ph] (cit. on pp. 121–124).

[504]A. Donnachie and P. V. Landshoff. „Small x: two pomerons!“ In: *Physics Letters B* 437.3-4 (1998), pp. 408–416. DOI: 10.1016/S0370-2693(98)00899-5. arXiv: hep-ph/9806344 [hep-ph] (cit. on p. 122).

[505]A. Z. Gazizov and S. I. Yanush. „Hard Pomeron Enhanced Cascade Production and Flux Shadowing in High-Energy Neutrino Astrophysics“. In: *arXiv e-prints*, astro-ph/0201528 (2002), astro–ph/0201528. arXiv: astro-ph/0201528 [astro-ph] (cit. on p. 122).

[506]ANTARES Collaboration. „A Deep Sea Telescope for High Energy Neutrinos“. In: *arXiv e-prints*, astro-ph/9907432 (1999), astro–ph/9907432. arXiv: astro-ph/9907432 [astro-ph] (cit. on pp. 123, 128, 131, 135, 136, 141, 163, 164, 183, 184, 192, 210).

[507]H. L. Lai, J. Huston, S. Kuhlmann, et al. „Global QCD analysis of parton structure of the nucleon: CTEQ5 parton distributions“. In: *European Physical Journal C* 12.3 (2000), pp. 375–392. DOI: 10.1007/s100529900196. arXiv: hep-ph/9903282 [hep-ph] (cit. on p. 124).

[508]Jonathan Pumplin, Daniel Robert Stump, Joey Huston, et al. „New Generation of Parton Distributions with Uncertainties from Global QCD Analysis“. In: *Journal of High Energy Physics* 2002.7, 012 (2002), p. 012. DOI: 10.1088/1126-6708/2002/07/012. arXiv: hep-ph/0201195 [hep-ph] (cit. on pp. 124, 231).

[509]Sandra Christine Miarecki. „Earth versus Neutrinos: Measuring the total muon-neutrino-to-nucleon cross section at ultra-high energies through differential Earth absorption of muon neutrinos from cosmic rays using the IceCube Detector“. PhD thesis. UC, Berkeley, 2016-01-01. URL: https://escholarship.org/uc/item/7q09d51t (cit. on p. 124).

[510]Sheldon L. Glashow. „Resonant Scattering of Antineutrinos“. In: *Physical Review* 118.1 (1960), pp. 316–317. DOI: 10.1103/PhysRev.118.316 (cit. on p. 124).

[511]V. S. Berezinsky and A. Z. Gazizov. „Cosmic neutrino and the possibility of Searching for W bosons with masses 30-100 GeV in underwater experiments“. In: *JETP Lett.* 25 (1977). [Pisma Zh. Eksp. Teor. Fiz.25,276(1977)], pp. 254–256 (cit. on p. 124).

[512]A. Albert et al. „An algorithm for the reconstruction of neutrino-induced showers in the ANTARES neutrino telescope“. In: *Astron. J.* 154.6 (2017), p. 275. DOI: 10.3847/1538-3881/aa9709. arXiv: 1708.03649 [astro-ph.IM] (cit. on p. 124).

[513]Shirley Weishi Li, Mauricio Bustamante, and John F. Beacom. „Echo Technique to Distinguish Flavors of Astrophysical Neutrinos“. In: Phys. Rev. Lett. 122.15, 151101 (2019), p. 151101. DOI: 10.1103/PhysRevLett.122.151101. arXiv: 1606.06290 [astro-ph.HE] (cit. on p. 124).

[514]A. Albert, M. André, M. Anghinolfi, et al. „First all-flavor neutrino pointlike source search with the ANTARES neutrino telescope“. In: Phys. Rev. D 96.8, 082001 (2017), p. 082001. DOI: 10.1103/PhysRevD.96.082001. arXiv: 1706.01857 [astro-ph.HE] (cit. on pp. 125, 259).

[515]D. F. Cowen and Ice Cube Collaboration. „Tau Neutrinos in IceCube“. In: *Journal of Physics Conference Series*. Vol. 60. Journal of Physics Conference Series. 2007, pp. 227–230. DOI: 10.1088/1742-6596/60/1/048 (cit. on pp. 125–127).

[516]A. Sánchez-Losa. „Search for high energy cosmic muon neutrinos from variable gamma-ray sources and time calibration of the optical modules of the ANTARES telescope“. PhD thesis. Universitat de València, Valencia, Spain, 2015. URL: http://digital.csic.es/handle/10261/140636 (cit. on pp. 126, 172, 175, 176, 230, 231, 254, 258, 263, 289).

[517]John G. Learned and Sandip Pakvasa. „Detecting ν_τ oscillations at PeV energies“. In: *Astroparticle Physics* 3.3 (1995), pp. 267–274. DOI: 10.1016/0927-6505(94)00043-3. arXiv: hep-ph/9405296 [hep-ph] (cit. on pp. 126–128).

[518]T. De Young, S. Razzaque, and D. F. Cowen. „Astrophysical tau neutrino detection in kilometer-scale Cherenkov detectors via muonic tau decay“. In: *Astroparticle Physics* 27.4 (2007), pp. 238–243. DOI: 10.1016/j.astropartphys.2006.11.003. arXiv: astro-ph/0608486 [astro-ph] (cit. on pp. 126, 127).

[519]Edgar Bugaev, Teresa Montaruli, Yuri Shlepin, and Igor Sokalski. „Propagation of τ-neutrinos and τ-leptons through the Earth and their detection in underwater/ice neutrino telescopes“. In: *Astroparticle Physics* 21.5 (2004), pp. 491–509. DOI: 10.1016/j.astropartphys.2004.03.002. arXiv: hep-ph/0312295 [hep-ph] (cit. on p. 127).

[520]Sharada Iyer Dutta, Mary Hall Reno, and Ina Sarcevic. „Secondary neutrinos from tau neutrino interactions in Earth“. In: Phys. Rev. D 66.7, 077302 (2002), p. 077302. DOI: 10.1103/PhysRevD.66.077302. arXiv: hep-ph/0207344 [hep-ph] (cit. on pp. 127, 128, 130, 138).

[521]Raj Gandhi, Chris Quigg, Mary Hall Reno, and Ina Sarcevic. „Neutrino interactions at ultrahigh energies“. In: Phys. Rev. D 58.9, 093009 (1998), p. 093009. DOI: 10.1103/PhysRevD.58.093009. arXiv: hep-ph/9807264 [hep-ph] (cit. on pp. 128, 130).

[522]Andrea Donini, Sergio Palomares-Ruiz, and Jordi Salvado. „Neutrino tomography of Earth“. In: *Nature Physics* 15.1 (2019), pp. 37–40. DOI: 10.1038/s41567-018-0319-1. arXiv: 1803.05901 [hep-ph] (cit. on pp. 128, 129).

[523]M. C. Gonzalez-Garcia, Francis Halzen, Michele Maltoni, and Hiroyuki K. M. Tanaka. „Radiography of Earth's Core and Mantle with Atmospheric Neutrinos“. In: Phys. Rev. Lett. 100.6, 061802 (2008), p. 061802. DOI: 10.1103/PhysRevLett.100.061802. arXiv: 0711.0745 [hep-ph] (cit. on pp. 128, 129).

[524]E. Borriello, G. Mangano, A. Marotta, et al. „Sensitivity on earth core and mantle densities using atmospheric neutrinos“. In: J. Cosmology Astropart. Phys. 2009.6, 030 (2009), p. 030. DOI: 10.1088/1475-7516/2009/06/030. arXiv: 0904.0796 [astro-ph.EP] (cit. on p. 128).

[525]N. Takeuchi. „Simulation of heterogeneity sections obtained by neutrino radiography“. In: *Earth, Planets, and Space* 62.2 (2010), pp. 215–221. DOI: 10.5047/eps.2009.05.004 (cit. on p. 128).

[526]I. Romero and O. A. Sampayo. „About the Earth density and the neutrino interaction“. In: *European Physical Journal C* 71, 1696 (July 2011), p. 1696. DOI: 10.1140/epjc/s10052-011-1696-0 (cit. on p. 128).

[527]Joshua R. Klein and Alfred K. Mann. „Prototype detector for ultrahigh energy neutrino detection“. In: *Astroparticle Physics* 10.4 (1999), pp. 321–329. DOI: 10.1016/S0927-6505(98)00067-X. arXiv: astro-ph/9806152 [astro-ph] (cit. on p. 129).

[528]C. Rott, A. Taketa, and D. Bose. „Spectrometry of the Earth using Neutrino Oscillations“. In: *Scientific Reports* 5, 15225 (2015), p. 15225. DOI: 10.1038/srep15225. arXiv: 1502.04930 [physics.geo-ph] (cit. on p. 129).

[529]Walter Winter. „Atmospheric neutrino oscillations for Earth tomography“. In: *Nuclear Physics B* 908 (2016), pp. 250–267. DOI: 10.1016/j.nuclphysb.2016.03.033. arXiv: 1511.05154 [hep-ph] (cit. on p. 129).

[530]Simon Bourret, João A. B. Coelho, Véronique Van Elewyck, and KM3NeT Collaboration. „Neutrino oscillation tomography of the Earth with KM3NeT-ORCA“. In: *Journal of Physics Conference Series*. Vol. 888. Journal of Physics Conference Series. 2017, p. 012114. DOI: 10.1088/1742-6596/888/1/012114. arXiv: 1702.03723 [physics.ins-det] (cit. on p. 129).

[531]Simon Bourret and Véronique Van Elewyck. „Earth tomography with neutrinos in KM3NeT-ORCA“. In: *European Physical Journal Web of Conferences*. Vol. 207. European Physical Journal Web of Conferences. 2019, p. 04008. DOI: 10.1051/epjconf/201920704008 (cit. on p. 129).

[532]Adam M. Dziewonski and Don L. Anderson. „Preliminary reference Earth model“. In: *Physics of the Earth and Planetary Interiors* 25.4 (1981), pp. 297–356. DOI: 10.1016/0031-9201(81)90046-7 (cit. on p. 129).

[533]G. Prézeau. „Dense Dark Matter Hairs Spreading Out from Earth, Jupiter, and Other Compact Bodies“. In: ApJ 814.2, 122 (2015), p. 122. DOI: 10.1088/0004-637X/814/2/122. arXiv: 1507.07009 [astro-ph.CO] (cit. on p. 129).

[534]F. Halzen and D. Saltzberg. „Tau Neutrino Appearance with a 1000 Megaparsec Baseline“. In: Phys. Rev. Lett. 81.20 (1998), pp. 4305–4308. DOI: 10.1103/PhysRevLett.81.4305. arXiv: hep-ph/9804354 [hep-ph] (cit. on pp. 130, 138).

[535]Sharada Iyer Dutta, Mary Hall Reno, and Ina Sarcevic. „Tau neutrinos underground: Signals of ν_μ–>ν_τ oscillations with extragalactic neutrinos“. In: Phys. Rev. D 62.12, 123001 (2000), p. 123001. DOI: 10.1103/PhysRevD.62.123001. arXiv: hep-ph/0005310 [hep-ph] (cit. on pp. 130, 138).

[536]V. Aynutdinov, A. Avrorin, V. Balkanov, et al. „The prototype string for the km^3-scale Baikal neutrino telescope“. In: *Nuclear Instruments and Methods in Physics Research A* 602.1 (2009), pp. 227–234. DOI: 10.1016/j.nima.2008.12.149. arXiv: 0811.1110 [astro-ph] (cit. on pp. 130, 140, 143).

[537]A. Avrorin, V. Aynutdinov, V. Balkanov, et al. „The Baikal Experiment - from Megaton to Gigaton“. In: *Journal of Physics Conference Series*. Vol. 203. Journal of Physics Conference Series. 2010, p. 012123. DOI: 10.1088/1742-6596/203/1/012123 (cit. on pp. 130, 140, 143).

[538]T. K. Gaisser. *Cosmic rays and particle physics*. 1990. ISBN: 9780521339315. URL: http://www.cambridge.org/uk/catalogue/catalogue.asp?isbn=0521326672 (cit. on p. 131).

[539]Donald E. Groom, Nikolai V. Mokhov, and Sergei I. Striganov. „Muon Stopping Power and Range Tables 10 MeV-100 TeV“. In: *Atomic Data and Nuclear Data Tables* 78.2 (2001), pp. 183–356. DOI: 10.1006/adnd.2001.0861 (cit. on pp. 132, 133).

[540]H. Bethe and W. Heitler. „On the Stopping of Fast Particles and on the Creation of Positive Electrons“. In: *Proceedings of the Royal Society of London Series A* 146 (Aug. 1934), pp. 83–112. DOI: 10.1098/rspa.1934.0140 (cit. on pp. 132, 133).

[541]Giulio Racah. „Sulla Nascita di Coppie per Urti di Particelle Elettrizzate“. In: *Il Nuovo Cimento* 14.3 (1937), pp. 93–113. DOI: 10.1007/BF02960616 (cit. on p. 132).

[542]R. P. Kokoulin and A. A. Petrukhin. „Analysis of the cross-section of direct pair production by fast muons“. In: *International Cosmic Ray Conference* 4 (1970), p. 277 (cit. on p. 132).

[543]H. A. Kramers. „XCIII. On the theory of X-ray absorption and of the continuous X-ray spectrum“. In: *The London, Edinburgh, and Dublin Philosophical Magazine and Journal of Science* 46.275 (1923), pp. 836–871. DOI: 10.1080/14786442308565244 (cit. on p. 133).

[544]Leonid B. Bezrukov and E. V. Bugaev. „Nucleon Shadowing Effects in Photon Nucleus Interaction. (In Russian)“. In: *Yad. Fiz.* 33 (1981). [Sov. J. Nucl. Phys.33,635(1981)], pp. 1195–1207 (cit. on p. 133).

[545]E. V. Bugaev and Y. V. Shlepin. „Photonuclear interaction of high energy muons and tau leptons“. In: Phys. Rev. D 67.3, 034027 (Feb. 2003), p. 034027. DOI: 10.1103/PhysRevD.67.034027. eprint: hep-ph/0203096 (cit. on p. 133).

[546]Paul H. Barrett, Lowell M. Bollinger, Giuseppe Cocconi, Yehuda Eisenberg, and Kenneth Greisen. „Interpretation of Cosmic-Ray Measurements Far Underground“. In: *Reviews of Modern Physics* 24.3 (1952), pp. 133–178. DOI: 10.1103/RevModPhys.24.133 (cit. on p. 133).

[547]D. Fargion. „The role of ν_τ ultrahigh energy astrophysics in Km$\hat{3}$ detectors“. In: *arXiv e-prints*, astro-ph/9704205 (1997), astro–ph/9704205. arXiv: astro-ph/9704205 [astro-ph] (cit. on p. 133).

[548]Bettina Diane Hartmann. „Reconstruction of Neutrino-Induced Hadronic and Electromagnetic Showers with the ANTARES Experiment“. PhD thesis. Erlangen - Nuremberg U., 2006. arXiv: astro-ph/0606697 [astro-ph]. URL: http://arxiv.org/pdf/astro-ph/0606697v1.pdf (cit. on p. 134).

[549]P. A. Čerenkov. „Visible emission of clean liquids by action of γ radiation“. In: *Doklady Akademii Nauk SSSR* 2 (1934), p. 451. URL: http://ufn.ru/en/articles/2007/4/g/ (cit. on pp. 135, 136).

[550]P. A. Čerenkov. „Visible Radiation Produced by Electrons Moving in a Medium with Velocities Exceeding that of Light“. In: *Physical Review* 52.4 (1937), pp. 378–379. DOI: 10.1103/PhysRev.52.378 (cit. on pp. 135, 136).

[551]S. I. Vavilov. „About possible reasons of blue γ-radiation of liquids“. In: *Doklady Akademii Nauk SSSR* 2 (1934), p. 457 (cit. on pp. 135, 136).

[552]Claus Grupen and Boris Shwartz. *Particle Detectors*. 2nd ed. Cambridge Monographs on Particle Physics, Nuclear Physics and Cosmology. Cambridge University Press, 2008. DOI: 10.1017/CBO9780511534966 (cit. on p. 136).

[553]I. M. Frank and I. E. Tamm. „Coherent visible radiation of fast electrons passing through matter“. In: *Compt. Rend. Acad. Sci. URSS* 14.3 (1937). [Usp. Fiz. Nauk93,no.2,388(1967)], pp. 109–114. DOI: 10.1007/978-3-642-74626-0_2, 10.3367/UFNr.0093.196710o.0388 (cit. on p. 136).

[554]I. E. Tamm. „Radiation emitted by uniformly moving electrons“. In: *J. Phys. USSR* 1 (1939), pp. 439–454. URL: https://ci.nii.ac.jp/naid/10000089092/en/ (cit. on pp. 136, 184).

[555]ANTARES Collaboration, J. A. Aguilar, A. Albert, et al. „Transmission of light in deep sea water at the site of the ANTARES neutrino telescope“. In: *Astroparticle Physics* 23.1 (2005), pp. 131–155. DOI: 10.1016/j.astropartphys.2004.11.006. arXiv: astro-ph/0412126 [astro-ph] (cit. on pp. 136, 165, 184–189, 230).

[556]S. Adrián-Martínez, I. Al Samarai, A. Albert, et al. „Measurement of the group velocity of light in sea water at the ANTARES site“. In: *Astroparticle Physics* 35.9 (2012), pp. 552–557. DOI: 10.1016/j.astropartphys.2011.12.003. arXiv: 1110.5184 [hep-ex] (cit. on pp. 137, 188, 189).

[557]B. Louis, V. Sandberg, G. Garvey, H. White, and R. Tayloe. „The Evidence for Oscillations“. In: *Los Alamos Science* 25 (1997). URL: http://library.lanl.gov/cgi-bin/getfile?25-09.pdf. DOI: 10.2172/569122 (cit. on p. 138).

[558]Christian Haack and Christopher Wiebusch. „A measurement of the diffuse astrophysical muon neutrino flux using eight years of IceCube data.“ In: *PoS* ICRC2017 (2018), p. 1005. DOI: 10.22323/1.301.1005 (cit. on p. 139).

[559]M. G. Aartsen et al. „Search for steady point-like sources in the astrophysical muon neutrino flux with 8 years of IceCube data“. In: *Eur. Phys. J.* C79.3 (2019), p. 234. DOI: 10.1140/epjc/s10052-019-6680-0. arXiv: 1811.07979 [hep-ph] (cit. on pp. 139, 306, 308).

[560]Y. Becherini, A. Margiotta, M. Sioli, and M. Spurio. „A parameterisation of single and multiple muons in the deep water or ice“. In: *Astroparticle Physics* 25.1 (2006), pp. 1–13. DOI: 10.1016/j.astropartphys.2005.10.005. arXiv: hep-ph/0507228 [hep-ph] (cit. on pp. 139, 234).

[561]Vivek Agrawal, T. K. Gaisser, Paolo Lipari, and Todor Stanev. „Atmospheric neutrino flux above 1 GeV“. In: Phys. Rev. D 53.3 (1996), pp. 1314–1323. DOI: 10.1103/PhysRevD.53.1314. arXiv: hep-ph/9509423 [hep-ph] (cit. on p. 139).

[562]L.B. Bezrukov et al. (Baikal Coll.) „Progress report on Lake Baikal neutrino experiment: Site studies and stationary string“. In: *Proceedings of the International Conference "Neutrino84"*. World Sci. Publ., Singapore, 1984, p. 550. URL: http://adsabs.harvard.edu/abs/1984npa..conf..550B (cit. on p. 140).

[563]I. A. Belolaptikov, L. B. Bezrukov, B. A. Borisovets, et al. „The Baikal underwater neutrino telescope: Design, performance, and first results“. In: *Astroparticle Physics* 7.3 (1997), pp. 263–282. DOI: 10.1016/S0927-6505(97)00022-4 (cit. on pp. 140, 143).

[564]E. Anassontzis, M. Barone, G. Contopoulos, et al. „NESTOR: A neutrino particle astrophysics underwater laboratory for the Mediterranean“. In: *Nuclear Physics B Proceedings Supplements* 35 (1994), pp. 294–300. DOI: 10.1016/0920-5632(94)90267-4 (cit. on p. 140).

[565]E. Migneco, S. Aiello, E. Amato, et al. „NEMO: Status of the Project“. In: *Nuclear Physics B Proceedings Supplements* 136 (2004), pp. 61–68. DOI: 10.1016/j.nuclphysbps.2004.10.062 (cit. on p. 140).

[566]E. Migneco, S. Aiello, M. Ambriola, et al. „Status of NEMO“. In: *Nuclear Instruments and Methods in Physics Research A* 567.2 (2006), pp. 444–451. DOI: 10.1016/j.nima.2006.05.257 (cit. on p. 140).

[567]S. E. Tzamarias. „Operation and performance of the NESTOR test detector: A measurement of the atmospheric muon flux“. In: *Nuclear Physics B Proceedings Supplements* 143 (2005), pp. 355–358. DOI: 10.1016/j.nuclphysbps.2005.01.129 (cit. on p. 140).

[568]G. Aggouras, E. G. Anassontzis, A. E. Ball, et al. „Operation and performance of the NESTOR test detector“. In: *Nuclear Instruments and Methods in Physics Research A* 552.3 (2005), pp. 420–439. DOI: 10.1016/j.nima.2005.06.083 (cit. on p. 140).

[569]Nestor Collaboration, G. Aggouras, E. G. Anassontzis, et al. „A measurement of the cosmic-ray muon flux with a module of the NESTOR neutrino telescope“. In: *Astroparticle Physics* 23 (May 2005), pp. 377–392. DOI: 10.1016/j.astropartphys.2005.02.001 (cit. on p. 140).

[570]G. Aggouras, E. G. Anassontzis, A. E. Ball, et al. „Recent results from NESTOR“. In: *Nuclear Instruments and Methods in Physics Research A* 567 (Nov. 2006), pp. 452–456. DOI: 10.1016/j.nima.2006.05.256 (cit. on p. 140).

[571]M. Ageron, J. A. Aguilar, A. Albert, et al. „Performance of the first ANTARES detector line“. In: *Astroparticle Physics* 31.4 (2009), pp. 277–283. DOI: 10.1016/j.astropartphys.2009.02.008. arXiv: 0812.2095 [astro-ph] (cit. on pp. 141, 163).

[572]E. Andres, P. Askebjer, S. W. Barwick, et al. „The AMANDA neutrino telescope: principle of operation and first results“. In: *Astroparticle Physics* 13.1 (2000), pp. 1–20. DOI: 10.1016/S0927-6505(99)00092-4. arXiv: astro-ph/9906203 [astro-ph] (cit. on pp. 141, 146).

[573]E. Andrés, P. Askebjer, X. Bai, et al. „Observation of high-energy neutrinos using Čerenkov detectors embedded deep in Antarctic ice“. In: Nature 410 (Mar. 2001), pp. 441–443 (cit. on p. 141).

[574]A. D. Avrorin et al. „Status and recent results of the BAIKAL-GVD project“. In: *Phys. Part. Nucl.* 46.2 (2015), pp. 211–221. DOI: 10.1134/S1063779615020033 (cit. on pp. 142, 153).

[575]P. K. F. Grieder and Dumand Collaboration. „DUMAND II: String 1 deployment, initial operation, results and system retrieval“. In: *Nuclear Physics B Proceedings Supplements* 43 (June 1995), pp. 145–148. DOI: 10.1016/0920-5632(95)00466-M (cit. on p. 143).

[576]R. Jeffrey Wilkes. „DUMAND and AMANDA: High Energy Neutrino Astrophysics“. In: *arXiv e-prints*, astro-ph/9412019 (1994), astro–ph/9412019. arXiv: astro-ph/9412019 [astro-ph] (cit. on p. 143).

[577]C. Pryor, C. E. Roos, and M. S. Webster. „Detecting thermal neutrinos from supernovae with DUMAND“. In: ApJ 329 (June 1988), pp. 335–338. DOI: 10.1086/166381 (cit. on p. 143).

[578]H. Bradner, M. Bartlett, G. Blackinton, et al. „Bioluminescence profile in the deep Pacific Ocean“. In: *Deep Sea Research Part A. Oceanographic Research Papers* 34.11 (1987), pp. 1831–1840. ISSN: 0198-0149. DOI: https://doi.org/10.1016/0198-0149(87)90057-4. URL: http://www.sciencedirect.com/science/article/pii/0198014987900574 (cit. on p. 143).

[579]International Dumand Collaboration. „DUMAND and its First Stage: the Short Prototype String“. In: *International Cosmic Ray Conference* 2 (1987), p. 462 (cit. on p. 143).

[580]J. Babson, B. Barish, R. Becker-Szendy, et al. „Cosmic-ray muons in the deep ocean“. In: Phys. Rev. D 42.11 (1990), pp. 3613–3620. DOI: 10.1103/PhysRevD.42.3613 (cit. on p. 143).

[581]P. C. Bosetti and Dumand Collaboration. „DUMAND Status Report“. In: *Nuclear Physics B Proceedings Supplements* 48 (May 1996), pp. 466–468. DOI: 10.1016/0920-5632(96)00292-7 (cit. on p. 143).

[582]T. Aoki, R. Becker-Szendy, P. Bosetti, et al. „DUMAND II status report“. In: *High Energy Gamma Ray Astronomy*. Ed. by J. Matthews. Vol. 220. American Institute of Physics Conference Series. Apr. 1991, pp. 285–289. DOI: 10.1063/1.40310 (cit. on p. 143).

[583]V. Aynutdinov, V. Balkanov, I. Belolaptikov, et al. „The BAIKAL neutrino experiment: From NT200 to NT200+“. In: *Nuclear Instruments and Methods in Physics Research A* 567.2 (2006), pp. 433–437. DOI: 10.1016/j.nima.2006.05.259. arXiv: astro-ph/0507709 [astro-ph] (cit. on pp. 143, 144).

[584]V. Aynutdinov, A. Avrorin, V. Balkanov, et al. „The BAIKAL neutrino experiment—Physics results and perspectives“. In: *Nuclear Instruments and Methods in Physics Research A* 602.1 (2009), pp. 14–20. DOI: 10.1016/j.nima.2008.12.012. arXiv: 0811.1109 [astro-ph] (cit. on pp. 143, 144).

[585]R. I. Bagduev, V. Balkanov, I. A. Belolaptikov, et al. „The optical module of the Baikal deep underwater neutrino telescope“. In: *Nuclear Instruments and Methods in Physics Research A* 420.1-2 (1999), pp. 138–154. DOI: 10.1016/S0168-9002(98)01156-5. arXiv: astro-ph/9903347 [astro-ph] (cit. on p. 143).

[586]A. V. Avrorin, V. M. Aynutdinov, I. A. Belolaptikov, et al. „Current status of the BAIKAL-GVD project“. In: *Nuclear Instruments and Methods in Physics Research A* 725 (2013), pp. 23–26. DOI: 10.1016/j.nima.2012.11.151 (cit. on p. 144).

[587]A. Avrorin, V. Aynutdinov, R. Bannasch, et al. „Present status of the BAIKAL-GVD project development“. In: *Journal of Physics Conference Series*. Vol. 409. Journal of Physics Conference Series. 2013, p. 012141. DOI: 10.1088/1742-6596/409/1/012141 (cit. on pp. 144, 145).

[588]A. Avrorin, V. Aynutdinov, I. Belolaptikov, et al. „The Gigaton Volume Detector in Lake Baikal“. In: *Nuclear Instruments and Methods in Physics Research A* 639.1 (2011), pp. 30–32. DOI: 10.1016/j.nima.2010.09.137 (cit. on p. 144).

[589]A. Avrorin, V. Aynutdinov, V. Balkanov, et al. „The Baikal neutrino experiment“. In: *Nuclear Instruments and Methods in Physics Research A* 626 (2011), S13–S18. DOI: 10.1016/j.nima.2010.06.209 (cit. on p. 144).

[590]V. Aynutdinov, A. Avrorin, V. Balkanov, et al. „The Baikal neutrino experiment: Status, selected physics results, and perspectives“. In: *Nuclear Instruments and Methods in Physics Research A* 588.1-2 (2008), pp. 99–106. DOI: 10.1016/j.nima.2008.01.011 (cit. on p. 144).

[591]A. V. Avrorin, V. M. Aynutdinov, R. Bannasch, et al. „Status of the Baikal-GVD project“. In: *Nuclear Instruments and Methods in Physics Research A* 692 (2012), pp. 46–52. DOI: 10.1016/j.nima.2011.12.106 (cit. on p. 144).

[592]Baikal-GVD Collaboration, : A. D. Avrorin, et al. „Neutrino Telescope in Lake Baikal: Present and Future“. In: *arXiv e-prints*, arXiv:1908.05427 (2019), arXiv:1908.05427. arXiv: 1908.05427 [astro-ph.HE] (cit. on pp. 144, 145).

[593]A. D. Avrorin, A. V. Avrorin, V. M. Aynutdinov, et al. „Baikal-GVD: first cluster Dubna“. In: *arXiv e-prints*, arXiv:1511.02324 (2015), arXiv:1511.02324. arXiv: 1511.02324 [physics.ins-det] (cit. on p. 144).

[594]R. Abbasi, Y. Abdou, T. Abu-Zayyad, et al. „The design and performance of IceCube DeepCore“. In: *Astroparticle Physics* 35.10 (2012), pp. 615–624. DOI: 10.1016/j.astropartphys.2012.01.004. arXiv: 1109.6096 [astro-ph.IM] (cit. on pp. 146, 147, 151–153).

[595]Klas Hultqvist and IceCube Collaboration. „IceCube: Physics, status, and future“. In: *Nuclear Instruments and Methods in Physics Research A* 626 (2011), S6–S12. DOI: 10.1016/j.nima.2010.05.014. arXiv: 1003.2300 [astro-ph.HE] (cit. on pp. 148, 152).

[596]M. G. Aartsen, R. Abbasi, Y. Abdou, et al. „Measurement of South Pole ice transparency with the IceCube LED calibration system“. In: *Nuclear Instruments and Methods in Physics Research A* 711 (2013), pp. 73–89. DOI: 10.1016/j.nima.2013.01.054. arXiv: 1301.5361 [astro-ph.IM] (cit. on pp. 150, 152, 153).

[597]M. G. Aartsen, M. Ackermann, J. Adams, et al. „Measurement of atmospheric tau neutrino appearance with IceCube DeepCore“. In: Phys. Rev. D 99.3, 032007 (2019), p. 032007. DOI: 10.1103/PhysRevD.99.032007. arXiv: 1901.05366 [hep-ex] (cit. on p. 150).

[598]R. Abbasi, M. Ackermann, J. Adams, et al. „The IceCube data acquisition system: Signal capture, digitization, and timestamping“. In: *Nuclear Instruments and Methods in Physics Research A* 601.3 (2009), pp. 294–316. DOI: 10.1016/j.nima.2009.01.001. arXiv: 0810.4930 [physics.ins-det] (cit. on p. 151).

[599]R. Abbasi, Y. Abdou, T. Abu-Zayyad, et al. „Calibration and characterization of the IceCube photomultiplier tube“. In: *Nuclear Instruments and Methods in Physics Research A* 618.1-3 (2010), pp. 139–152. DOI: 10.1016/j.nima.2010.03.102. arXiv: 1002.2442 [astro-ph.IM] (cit. on pp. 151, 152).

[600]Volker Baum and IceCube Collaboration. „The IceCube data acquisition system for galactic core collapse supernova searches“. In: *AIP Conference Proceedings* 1630.1 (2014), pp. 150–153. DOI: 10.1063/1.4902794. URL: https://aip.scitation.org/doi/abs/10.1063/1.4902794 (cit. on p. 151).

[601]P. Buford Price, Oleg V. Nagornov, Ryan Bay, et al. „Temperature profile for glacial ice at the South Pole: Implications for life in a nearby subglacial lake“. In: *Proceedings of the National Academy of Sciences* 99.12 (2002), pp. 7844–7847. ISSN: 0027-8424. DOI: 10.1073/pnas.082238999. URL: https://www.pnas.org/content/99/12/7844 (cit. on p. 151).

[602]K. Hanson and O. Tarasova. „Design and production of the IceCube digital optical module“. In: *Nuclear Instruments and Methods in Physics Research A* 567 (Nov. 2006), pp. 214–217. DOI: 10.1016/j.nima.2006.05.091 (cit. on p. 151).

[603]Benedikt Riedel. „Modeling and Understanding Supernova Signals in the IceCube Neutrino Observatory.“ PhD thesis. University of Wisconsin - Madison., 2014, p. 193. URL: https://docushare.icecube.wisc.edu/dsweb/Get/Document-72537/thesis.pdf (cit. on p. 152).

[604]M. G. Aartsen, R. Abbasi, Y. Abdou, et al. „Measurement of South Pole ice transparency with the IceCube LED calibration system“. In: *Nuclear Instruments and Methods in Physics Research A* 711 (2013), pp. 73–89. DOI: 10.1016/j.nima.2013.01.054. arXiv: 1301.5361 [astro-ph.IM] (cit. on pp. 152–154).

[605]Martin Rongen. „Measuring the optical properties of IceCube drill holes“. In: *European Physical Journal Web of Conferences*. Vol. 116. European Physical Journal Web of Conferences. 2016, p. 06011. DOI: 10.1051/epjconf/201611606011 (cit. on p. 152).

[606]M. Ackermann, J. Ahrens, X. Bai, et al. „Optical properties of deep glacial ice at the South Pole“. In: *Journal of Geophysical Research (Atmospheres)* 111.D13, D13203 (2006), p. D13203. DOI: 10.1029/2005JD006687 (cit. on p. 153).

[607]M. G. Aartsen, R. Abbasi, M. Ackermann, et al. „Energy reconstruction methods in the IceCube neutrino telescope“. In: *Journal of Instrumentation* 9.3, P03009 (2014), P03009. DOI: 10.1088/1748-0221/9/03/P03009. arXiv: 1311.4767 [physics.ins-det] (cit. on p. 153).

[608]S. Adrián-Martínez, A. Albert, M. André, et al. „Searches for Point-like and Extended Neutrino Sources Close to the Galactic Center Using the ANTARES Neutrino Telescope“. In: ApJ 786.1, L5 (2014), p. L5. DOI: 10.1088/2041-8205/786/1/L5. arXiv: 1402.6182 [hep-ex] (cit. on pp. 153, 249).

[609]ANTARES Collaboration, J. A. Aguilar, I. Al Samarai, et al. „Time calibration of the ANTARES neutrino telescope“. In: *Astroparticle Physics* 34.7 (2011), pp. 539–549. DOI: 10.1016/j.astropartphys.2010.12.004. arXiv: 1012.2204 [astro-ph.IM] (cit. on pp. 153, 192–196, 198–201, 203, 204, 249).

[610]A. Albert, M. André, M. Anghinolfi, et al. „An algorithm for the reconstruction of high-energy neutrino-induced particle showers and its application to the ANTARES neutrino telescope“. In: *European Physical Journal C* 77.6, 419 (2017), p. 419. DOI: 10.1140/epjc/s10052-017-4979-2. arXiv: 1708.03649 [astro-ph.IM] (cit. on p. 153).

[611]Annarita Margiotta. „The KM3NeT deep-sea neutrino telescope“. In: *Nuclear Instruments and Methods in Physics Research A* 766 (2014), pp. 83–87. DOI: 10.1016/j.nima.2014.05.090. arXiv: 1408.1392 [astro-ph.IM] (cit. on pp. 155, 160).

[612]A. Margiotta. „Status of the KM3NeT project“. In: *Journal of Instrumentation* 9.4, C04020 (2014), p. C04020. DOI: 10.1088/1748-0221/9/04/C04020. arXiv: 1408.1132 [astro-ph.IM] (cit. on pp. 156, 160).

[613]R. Bruijn and D. van Eijk. „The KM3NeT Multi-PMT Digital Optical Module“. In: *34th International Cosmic Ray Conference (ICRC2015)*. Vol. 34. International Cosmic Ray Conference. 2015, p. 1157 (cit. on p. 158).

[614]P. Kooijman and KM3NeT Collaboration. „The Mechanical structure and deployment procedure of the KM3NeT detection unit.“ In: *34th International Cosmic Ray Conference (ICRC2015)*. Vol. 34. International Cosmic Ray Conference. 2015, p. 1173 (cit. on p. 159).

[615]S. Biagi, T. Chiarusi, P. Piattelli, and D. Real. „The data acquisition system of the KM3NeT detector“. In: *34th International Cosmic Ray Conference (ICRC2015)*. Vol. 34. International Cosmic Ray Conference. 2015, p. 1172 (cit. on p. 160).

[616]S. Adrián-Martínez, M. Ageron, F. Aharonian, et al. „Deep sea tests of a prototype of the KM3NeT digital optical module“. In: *European Physical Journal C* 74, 3056 (2014), p. 3056. DOI: 10.1140/epjc/s10052-014-3056-3. arXiv: 1405.0839 [astro-ph.IM] (cit. on pp. 160, 161, 203).

[617]Bjoern Herold and KM3NeT Consortium. „Study of ^{40}K-induced rates for a KM3NeT design option with multi-PMT optical modules“. In: *Nuclear Instruments and Methods in Physics Research A* 626 (2011), S234–S236. DOI: 10.1016/j.nima.2010.04.137 (cit. on p. 160).

[618]A. Coleiro, M. Colomer, D. Dornic, V. Kulikovskiy, and M. Lincetto. „LIGO/Virgo S191110af: Upper limits from KM3NeT MeV neutrino search.“ In: *GRB Coordinates Network* 26249 (2019), p. 1 (cit. on p. 161).

[619]Ligo Scientific Collaboration and VIRGO Collaboration. „LIGO/Virgo S191110af: Identification of a GW unmodeled transient candidate“. In: *GRB Coordinates Network* 26222 (2019), p. 1 (cit. on p. 161).

[620]S. Adrián-Martínez, M. Ageron, J. A. Aguilar, et al. „The positioning system of the ANTARES Neutrino Telescope“. In: *Journal of Instrumentation* 7.8 (2012), T08002. DOI: 10.1088/1748-0221/7/08/T08002. arXiv: 1202.3894 [astro-ph.IM] (cit. on pp. 163, 165, 206–209, 258).

[621]A. Kouchner. „High Energy Neutrino Astronomy and Neutrino Telescopes“. In: *Journal of Physics Conference Series*. Vol. 593. Journal of Physics Conference Series. 2015, p. 012008. DOI: 10.1088/1742-6596/593/1/012008 (cit. on p. 163).

[622]Maurizio Spurio. „Status report (2006) of the ANTARES project“. In: *Proceedings, 20th European Cosmic Ray Symposium (ECRS 2006): Lisbon, Portugal, September 5-8, 2006*. 2006, S5–127. arXiv: hep-ph/0611032 [hep-ph]. URL: http://www.lip.pt/events/2006/ecrs/proc/ecrs06-s5-127.pdf (cit. on p. 164).

[623]Th. Stolarczyk. „Neutrinos in the northern hemisphere“. In: *Proceedings, 20th Rencontres de Blois on Challenges in Particle Astrophysics: Blois, France, May 18-23, 2008*. 2008, pp. 235–244 (cit. on p. 164).

[624]Paschal Coyle and Clancy W. James. „Recent Results from the ANTARES Neutrino Telescope“. In: *Neutrino Astronomy: Current Status, Future Prospects*. Ed. by Thomas Gaisser and Albrecht Karle. 2017, pp. 97–113. DOI: 10.1142/9789814759410_0007 (cit. on pp. 165, 166, 212).

[625]ANTARES collaboration, A. Albert, M. André, et al. „Long-term monitoring of the ANTARES optical module efficiencies using ^{40}K decays in sea water“. In: *arXiv e-prints*, arXiv:1805.08675 (2018), arXiv:1805.08675. arXiv: 1805.08675 [astro-ph.IM] (cit. on pp. 165, 168, 190, 201–203).

[626]ANTARES Collaboration, P. Amram, M. Anghinolfi, et al. „The ANTARES optical module“. In: *Nuclear Instruments and Methods in Physics Research A* 484.1-3 (2002), pp. 369–383. DOI: 10.1016/S0168-9002(01)02026-5. arXiv: astro-ph/0112172 [astro-ph] (cit. on pp. 165–167, 169, 196, 246).

[627]J. A. Aguilar, A. Albert, F. Ameli, et al. „The data acquisition system for the ANTARES neutrino telescope“. In: *Nuclear Instruments and Methods in Physics Research A* 570.1 (2007), pp. 107–116. DOI: 10.1016/j.nima.2006.09.098. arXiv: astro-ph/0610029 [astro-ph] (cit. on pp. 165, 174, 176–178).

[628]J. A. Aguilar, I. Al Samarai, A. Albert, et al. „Performance of the front-end electronics of the ANTARES neutrino telescope“. In: *Nuclear Instruments and Methods in Physics Research A* 622.1 (2010), pp. 59–73. DOI: 10.1016/j.nima.2010.06.225. arXiv: 1007.2549 [astro-ph.IM] (cit. on pp. 165, 168–170, 172, 174, 199, 205, 206).

[629]J. A. Aguilar, A. Albert, F. Ameli, et al. „Study of large hemispherical photomultiplier tubes for the ANTARES neutrino telescope“. In: *Nuclear Instruments and Methods in Physics Research A* 555.1-2 (2005), pp. 132–141. DOI: 10.1016/j.nima.2005.09.035. arXiv: physics/0510031 [physics.ins-det] (cit. on p. 167).

[630]M. Ageron, J. A. Aguilar, A. Albert, et al. „Studies of a full-scale mechanical prototype line for the ANTARES neutrino telescope and tests of a prototype instrument for deep-sea acoustic measurements“. In: *Nuclear Instruments and Methods in Physics Research A* 581.3 (2007), pp. 695–708. DOI: 10.1016/j.nima.2007.08.148 (cit. on pp. 168, 211).

[631]F. Feinstein and ANTARES Collaboration. „The analogue ring sampler: A front-end chip for ANTARES“. In: *Nuclear Instruments and Methods in Physics Research A* 504.1-3 (2003), pp. 258–261. DOI: 10.1016/S0168-9002(03)00773-3 (cit. on pp. 169, 177).

[632]J. A. Aguilar, I. Al Samarai, A. Albert, et al. „AMADEUS—The acoustic neutrino detection test system of the ANTARES deep-sea neutrino telescope“. In: *Nuclear Instruments and Methods in Physics Research A* 626 (2011), pp. 128–143. DOI: 10.1016/j.nima.2010.09.053. arXiv: 1009.4179 [astro-ph.IM] (cit. on p. 171).

[633]Harold Yepes Ramírez. „Characterization of the optical properties at the ANTARES site using the Optical Beacon system. Influence on the detector performance.“ PhD thesis. Valencia U., IFIC, 2014-05-03. URL: http://roderic.uv.es/handle/10550/35482 (cit. on p. 172).

[634]R Gurin and A Maslennikov. *ControlHost: Distributed Data Handling Package*. Technical report. CASPUR Inter-University, Computing Consortium, Rome, 1995. URL: http://www.nikhef.nl/pub/experiments/antares/software/Dispatcher/ControlHost.ps (cit. on p. 178).

[635]Rene Brun and Fons Rademakers. „ROOT — An object oriented data analysis framework“. In: *Nuclear Instruments and Methods in Physics Research A* 389.1 (1997), pp. 81–86. DOI: 10.1016/S0168-9002(97)00048-X (cit. on pp. 178, 231, 254, 259).

[636]M De Jong. „The ANTARES Trigger Software“. In: (2005). URL: https://cds.cern.ch/record/951361 (cit. on pp. 178, 180).

[637]B A P Van Rens. „The software trigger in ANTARES“. In: (2004). URL: https://cds.cern.ch/record/951345 (cit. on p. 180).

[638]Florian Folger. „Search for a diffuse cosmic neutrino flux using shower events in the ANTARES neutrino telescope“. doctoralthesis. Friedrich-Alexander-Universität Erlangen-Nürnberg (FAU), 2014, p. 272. URL: https://opus4.kobv.de/opus4-fau/files/5107/FlorianFolgerDissertation-1.pdf (cit. on p. 181).

[639]M De Jong. „Antares data formats“. In: (2004). URL: https://cds.cern.ch/record/951350 (cit. on p. 180).

[640]Erwin Lourens Visser. „Neutrinos from the Milky Way“. PhD thesis. Leiden U., 2015. URL: http://www.nikhef.nl/pub/services/biblio/theses_pdf/thesis_EL_Visser.pdf (cit. on p. 182).

[641]Dmitry Zaborov. „Coincidence rate from Potassium-40 seen with MILOM“. In: (2006). URL: https://cds.cern.ch/record/951238 (cit. on p. 180).

[642]Dmitry Zaborov. „The K-40 calibration method“. In: (2011). URL: https://cds.cern.ch/record/1401827 (cit. on p. 180).

[643]J Carr, S Escoffier, and D Zaborov. „Proposition for an alternative trigger based on the T3 cluster trigger“. In: (2007). URL: https://cds.cern.ch/record/1071192 (cit. on p. 180).

[644]M De Jong. „The Antares Trigger Parameters“. In: (2008). URL: https://cds.cern.ch/record/1150115 (cit. on p. 180).

[645]S Escoffier. „Performance of the T3 Triggers on MC Data“. In: (2008). URL: https://cds.cern.ch/record/1139412 (cit. on p. 180).

[646]P. Amram, S. Anvar, E. Aslanides, et al. „Background light in potential sites for the ANTARES undersea neutrino telescope“. In: *Astroparticle Physics* 13.2-3 (2000), pp. 127–136. DOI: 10.1016/S0927-6505(99)00118-8. arXiv: astro-ph/9910170 [astro-ph] (cit. on pp. 183, 189, 190, 201).

[647]P. Buford Price and Lars Bergström. „Optical properties of deep ice at the South Pole: scattering“. In: Appl. Opt. 36.18 (1997), pp. 4181–4194. DOI: 10.1364/AO.36.004181 (cit. on p. 184).

[648]P. Buford Price. „Implications of optical properties of ocean, lake, and ice for ultrahigh-energy neutrino detection“. In: Appl. Opt. 36.9 (1997), pp. 1965–1975. DOI: 10.1364/AO.36.001965 (cit. on p. 184).

[649]Harold Yepes-Ramirez and ANTARES Collaboration. „Water absorption length measurement with the ANTARES optical beacon system“. In: *Nuclear Instruments and Methods in Physics Research A* 626 (2011), S118–S119. DOI: 10.1016/j.nima.2010.04.124 (cit. on p. 186).

[650]Xiaohong Quan and Edward S. Fry. „Empirical equation for the index of refraction of seawater“. In: Appl. Opt. 34.18 (1995), p. 3477. DOI: 10.1364/AO.34.003477 (cit. on pp. 187–189).

[651]R. C. Millard and G. Seaver. „An index of refraction algorithm for seawater over temperature, pressure, salinity, density, and wavelength“. In: *Deep Sea Research A* 37.12 (1990), pp. 1909–1926. DOI: 10.1016/0198-0149(90)90086-B (cit. on pp. 187, 188).

[652]Roswell W. Austin and George Halikas. „The Index of Refraction of Seawater“. In: *SIO Ref. No. 76-1, Scripps Inst. Oceanogr., la Jolla* (Jan. 1976), p. 124. URL: https://escholarship.org/uc/item/8px2019m (cit. on p. 189).

[653]Steven H. D. Haddock, Mark A. Moline, and James F. Case. „Bioluminescence in the Sea“. In: *Annual Review of Marine Science* 2 (2010), pp. 443–493. DOI: 10.1146/annurev-marine-120308-081028 (cit. on p. 190).

[654]Christian Tamburini, Miquel Canals, Xavier Durrieu de Madron, et al. „Deep-Sea Bioluminescence Blooms after Dense Water Formation at the Ocean Surface“. In: *PLoS ONE* 8.7 (2013), e67523. DOI: 10.1371/journal.pone.0067523 (cit. on p. 190).

[655]R. B. Firestone, S. Y. F. Chu, and C. M. Baglin. „8th edition of the Table of Isotopes: 1998 Update“. In: *APS Division of Nuclear Physics Meeting Abstracts*. 1997, BD.11 (cit. on p. 190).

[656]John A. Cameron and Balraj Singh. „Nuclear Data Sheets for A=40“. In: *Nuclear Data Sheets* 102.2 (2004), pp. 293–513. DOI: 10.1016/j.nds.2004.06.001 (cit. on p. 190).

[657]A.G. Dickson and C. Goyet. „Handbook of methods for the analysis of the various parameters of the carbon dioxide system in sea water. Version 2“. In: *ORNL/CDIAC-74* (1994). DOI: 10.2172/10107773. URL: https://epic.awi.de/id/eprint/45689/ (cit. on p. 190).

[658]Javier Barrios Martí. „Search for cosmic sources in neutrino telescopes and time calibration in the ANTARES neutrino telescope.“ PhD thesis. Valencia U., IFIC, 2018. URL: http://roderic.uv.es/handle/10550/66597 (cit. on pp. 191, 239, 246).

[659]ANTARES Collaboration, CAU CEFREM Collaboration, P. Amram, et al. „Sedimentation and fouling of optical surfaces at the ANTARES site“. In: *Astroparticle Physics* 19.2 (2003), pp. 253–267. DOI: 10.1016/S0927-6505(02)00202-5. arXiv: astro-ph/0206454 [astro-ph] (cit. on pp. 192, 193).

[660]M. Ageron, J. A. Aguilar, A. Albert, et al. „The ANTARES optical beacon system“. In: *Nuclear Instruments and Methods in Physics Research A* 578.3 (2007), pp. 498–509. DOI: 10.1016/j.nima.2007.05.325. arXiv: astro-ph/0703355 [astro-ph] (cit. on pp. 195, 196).

[661]Juan Antonio Aguilar Sánchez. „Analysis of the Optical Beacon system and search for point-like sources in the ANTARES neutrino telescope“. PhD thesis. Valencia U., 2007. URL: http://antares.in2p3.fr/Publications/index.html (cit. on pp. 197–200).

[662]M. G. Kendall, A. Stuart, and J. K. Ord, eds. *Kendall's Advanced Theory of Statistics*. New York, NY, USA: Oxford University Press, Inc., 1987. ISBN: 0-195-20561-8 (cit. on p. 199).

[663]J. A. Aguilar, I. Al Samarai, A. Albert, et al. „Measurement of the atmospheric muon flux with a 4 GeV threshold in the ANTARES neutrino telescope“. In: *Astroparticle Physics* 33.2 (2010), pp. 86–90. DOI: 10.1016/j.astropartphys.2009.12.002. arXiv: 0910.4843 [astro-ph.HE] (cit. on p. 202).

[664]Bruny Baret and for the ANTARES collaboration. „Charge Calibration of the ANTARES high energy neutrino telescope“. In: *arXiv e-prints*, arXiv:0908.0810 (2009), arXiv:0908.0810. arXiv: 0908.0810 [astro-ph.IM] (cit. on pp. 204, 205).

[665]J. P. Gómez-González and ANTARES Collaboration. „Calibration systems of the ANTARES neutrino telescope“. In: *Nuclear Instruments and Methods in Physics Research A* 725 (2013), pp. 199–202. DOI: 10.1016/j.nima.2012.11.166. arXiv: 1204.5021 [astro-ph.IM] (cit. on pp. 204, 207).

[666]M De Jong. „The ARS AVC calibration“. In: (2005). URL: https://cds.cern.ch/record/951076 (cit. on p. 205).

[667]A Kouchner, J Aublin, E Delagnes, et al. „On the linearity response of the ARS charge channels“. In: (2007). URL: https://cds.cern.ch/record/1047054 (cit. on p. 206).

[668]Sotirios S Loucatos. „Correction of the differential non-linearity of the ADCs“. In: (2005). URL: https://cds.cern.ch/record/951149 (cit. on p. 206).

[669]P. Keller. „Acoustic Positioning System for the Deep-Sea ANTARES Neutrino Telescope“. In: *Sensor Technologies and Applications, International Conference on*. Los Alamitos, CA, USA: IEEE Computer Society, 2007, pp. 243–247. DOI: 10.1109/SENSORCOMM.2007.17. URL: https://doi.ieeecomputersociety.org/10.1109/SENSORCOMM.2007.17 (cit. on p. 209).

[670]Miguel Ardid and ANTARES Collaboration. „Positioning system of the ANTARES neutrino telescope“. In: *Nuclear Instruments and Methods in Physics Research A* 602.1 (2009), pp. 174–176. DOI: 10.1016/j.nima.2008.12.033 (cit. on p. 209).

[671]Teresa Montaruli. „The ANTARES project“. In: Proc. SPIE. Ed. by Peter W. Gorham. Vol. 4858. Society of Photo-Optical Instrumentation Engineers (SPIE) Conference Series. 2003, pp. 92–102. DOI: 10.1117/12.478949 (cit. on p. 210).

[672]Thierry Pradier. „The ANTARES Neutrino Telescope: first results“. In: *Proceedings, 43rd Rencontres de Moriond on Electroweak Interactions and Unified Theories: La Thuile, Italy, March 1-8, 2008*. 2008, pp. 423–430. arXiv: 0805.2545 [astro-ph] (cit. on pp. 210, 211).

[673]Teresa Montaruli and ANTARES Collaboration. „ANTARES Status Report“. In: *International Cosmic Ray Conference*. Vol. 3. International Cosmic Ray Conference. 2003, p. 1357. arXiv: physics/0306057 [physics.ins-det] (cit. on pp. 210, 211).

[674]I. A. Sokalski. „The ANTARES neutrino project“. In: *Physics of Atomic Nuclei* 67 (2004), pp. 1172–1176. DOI: 10.1134/1.1772454. arXiv: astro-ph/0310130 [astro-ph] (cit. on pp. 210, 211).

[675]J. D. Zornoza. „Status Report on the ANTARES Project“. In: *Fundamental Interactions*. Ed. by A. Astbury, B. A. Campbell, F. C. Khanna, and M. G. Vincter. 2005, pp. 339–343. DOI: 10.1142/9789812701961_0055 (cit. on p. 210).

[676]M. Circella and ANTARES Collaboration. „Toward the ANTARES Neutrino Telescope: Results from a Prototype Line“. In: *International Cosmic Ray Conference* 3 (2003), p. 1529 (cit. on pp. 210, 211).

[677]J. A. Aguilar, A. Albert, F. Ameli, et al. „First results of the Instrumentation Line for the deep-sea ANTARES neutrino telescope“. In: *Astroparticle Physics* 26.4-5 (2006), pp. 314–324. DOI: 10.1016/j.astropartphys.2006.07.004. arXiv: astro-ph/0606229 [astro-ph] (cit. on p. 211).

[678]Y. Becherini and Antares Collaboration. „Status report of the ANTARES experiment“. In: *Journal of Physics Conference Series*. Vol. 39. Journal of Physics Conference Series. 2006, pp. 444–446. DOI: 10.1088/1742-6596/39/1/116. arXiv: astro-ph/0603570 [astro-ph] (cit. on p. 211).

[679]B. Vallage and ANTARES Collaboration. „Status report on the ANTARES neutrino telescope“. In: *Journal of Physics Conference Series*. Vol. 120. Journal of Physics Conference Series. 2008, p. 062008. DOI: 10.1088/1742-6596/120/6/062008 (cit. on p. 211).

[680]Paschal Coyle. „The ANTARES Deep-Sea Neutrino Telescope: Status and First Results“. In: *arXiv e-prints*, arXiv:1002.0754 (2010), arXiv:1002.0754. arXiv: 1002.0754 [astro-ph.HE] (cit. on pp. 211, 212).

[681]Oleg Kalekin and ANTARES Collaboration. „The ANTARES underwater neutrino telescope“. In: *Journal of Physics Conference Series*. Vol. 160. Journal of Physics Conference Series. 2009, p. 012036. DOI: 10.1088/1742-6596/160/1/012036 (cit. on pp. 211, 212).

[682]HAWC Collaboration, A. U. Abeysekara, R. Alfaro, et al. „The HAWC Gamma-Ray Observatory: Design, Calibration, and Operation“. In: *arXiv e-prints*, arXiv:1310.0074 (2013), arXiv:1310.0074. arXiv: 1310.0074 [astro-ph.IM] (cit. on pp. 213–215, 217, 226).

[683]H. Le Vargas. „First scientific contributions from the High Altitude Water Cherenkov Observatory“. In: *J. Phys. Conf. Ser.* 639.1 (2015), p. 012011. DOI: 10.1088/1742-6596/639/1/012011 (cit. on p. 213).

[684]K. Malone. „First HAWC Spectra of Galactic Gamma-ray Sources Above 100 TeV and the Implications for Cosmic-ray Acceleration“. In: *36th International Cosmic Ray Conference (ICRC2019)*. Vol. 36. International Cosmic Ray Conference. 2019, p. 734. arXiv: 1908.07059 [astro-ph.HE] (cit. on p. 214).

[685]Mehr Un Nisa. „Probing Cosmic-ray Propagation with TeV Gamma Rays from the Sun Using the HAWC Observatory“. In: *PoS* ICRC2017 (2018), p. 340. DOI: 10.22323/1.301.0340. arXiv: 1708.03732 [astro-ph.HE] (cit. on p. 215).

[686]A. U. Abeysekara, R. Alfaro, C. Alvarez, et al. „Search for TeV Gamma-Ray Emission from Point-like Sources in the Inner Galactic Plane with a Partial Configuration of the HAWC Observatory“. In: ApJ 817.1, 3 (2016), p. 3. DOI: 10.3847/0004-637X/817/1/3. arXiv: 1509.05401 [astro-ph.HE] (cit. on pp. 216, 217, 219).

[687]Stefan Westerhoff. „First Light with the HAWC Gamma-Ray Observatory“. In: *PoS* EPS-HEP2013 (2013), p. 412. DOI: 10.22323/1.180.0412 (cit. on pp. 217, 218).

[688]D. Lennarz, I. Taboada, J. Wood, and HAWC Collaboration. „The HAWC GRB programme“. In: *6th International Symposium on High Energy Gamma-Ray Astronomy*. Vol. 1792. American Institute of Physics Conference Series. Jan. 2017, p. 050033. DOI: 10.1063/1.4968979 (cit. on p. 217).

[689]Z. Ren, R. Lauer, J. Matthews, and HAWC Collaboration. „Survey of nearby active galactic nuclei with the HAWC Observatory“. In: *35th International Cosmic Ray Conference (ICRC2017)*. Vol. 301. International Cosmic Ray Conference. 2017, p. 635. arXiv: 1708.05698 [astro-ph.HE] (cit. on p. 217).

[690]C. D. Rho, H. Ayala Solares, H. Zhou, and HAWC Collaboration. „Techniques for Measuring Galactic Diffuse Emission Flux and their Preliminary Results in Confused Regions“. In: *35th International Cosmic Ray Conference (ICRC2017)*. Vol. 301. International Cosmic Ray Conference. 2017, p. 741. arXiv: 1708.07273 [astro-ph.HE] (cit. on p. 217).

[691]HAWC Collaboration, A. U. Abeysekara, R. Alfaro, et al. „The HAWC Gamma-Ray Observatory: Dark Matter, Cosmology, and Fundamental Physics“. In: *arXiv e-prints*, arXiv:1310.0073 (2013), arXiv:1310.0073. arXiv: 1310.0073 [astro-ph.HE] (cit. on p. 217).

[692]H. Martínez-Huerta and HAWC Collaboration. „Potential constrains on Lorentz invariance violation from the HAWC TeV gamma-rays“. In: *35th International Cosmic Ray Conference (ICRC2017)*. Vol. 301. International Cosmic Ray Conference. 2017, p. 868. arXiv: 1708.03384 [astro-ph.HE] (cit. on p. 217).

[693]H. Martínez-Huerta, S. Marinelli, J. Linnemann, and J. Lundeen. „Constraints on Lorentz invariance violation using HAWC observations above 100 TeV“. In: *36th International Cosmic Ray Conference (ICRC2019)*. Vol. 36. International Cosmic Ray Conference. 2019, p. 738. arXiv: 1908.09614 [astro-ph.HE] (cit. on p. 217).

[694]A. U. Abeysekara, R. Alfaro, C. Alvarez, et al. „Observation of Small-scale Anisotropy in the Arrival Direction Distribution of TeV Cosmic Rays with HAWC“. In: ApJ 796.2, 108 (2014), p. 108. DOI: 10.1088/0004-637X/796/2/108. arXiv: 1408.4805 [astro-ph.HE] (cit. on p. 217).

[695]A. U. Abeysekara, R. Alfaro, C. Alvarez, et al. „Observation of Anisotropy of TeV Cosmic Rays with Two Years of HAWC“. In: ApJ 865.1, 57 (2018), p. 57. DOI: 10.3847/1538-4357/aad90c. arXiv: 1805.01847 [astro-ph.HE] (cit. on p. 217).

[696]A. U. Abeysekara, R. Alfaro, C. Alvarez, et al. „All-sky Measurement of the Anisotropy of Cosmic Rays at 10 TeV and Mapping of the Local Interstellar Magnetic Field“. In: ApJ 871.1, 96 (2019), p. 96. DOI: 10.3847/1538-4357/aaf5cc. arXiv: 1812.05682 [astro-ph.HE] (cit. on p. 217).

[697]T. N. Ukwatta, D. R. Stump, J. T. Linnemann, et al. „Primordial Black Holes: Observational characteristics of the final evaporation“. In: *Astroparticle Physics* 80 (2016), pp. 90–114. DOI: 10.1016/j.astropartphys.2016.03.007. arXiv: 1510.04372 [astro-ph.HE] (cit. on p. 217).

[698]K. Engel, A. Peisker, P. Harding, et al. „Setting Upper Limits on the Local Burst Rate Density of Primordial Black Holes Using HAWC“. In: *36th International Cosmic Ray Conference (ICRC2019)*. Vol. 36. International Cosmic Ray Conference. July 2019, p. 516 (cit. on p. 217).

[699]Stephen P. Martin. „A Supersymmetry Primer“. In: *Perspectives on Supersymmetry. Edited by KANE GORDON L. Published by World Scientific Publishing Co. Pte. Ltd., 1998. ISBN #9789812839657, pp. 1-98*. 1998, pp. 1–98. DOI: 10.1142/9789812839657_0001 (cit. on p. 217).

[700]Sidney Coleman. „Q-balls“. In: *Nuclear Physics B* 262.2 (1985), pp. 263–283. DOI: 10.1016/0550-3213(85)90286-X (cit. on p. 217).

[701]P. Karn. „Searching for Q-Balls with the High Altitude Water Cherenkov Observatory“. In: *APS California Section Meeting Abstracts*. Nov. 2012, H1.004 (cit. on p. 217).

[702]P. Karn. „A Search for Supersymmetric Q-balls with the High Altitude Water Cherenkov Observatory“. PhD thesis. University of California, Irvine, 2014 (cit. on p. 217).

[703]Leszek Roszkowski, Enrico Maria Sessolo, and Sebastian Trojanowski. „WIMP dark matter candidates and searches—current status and future prospects“. In: *Reports on Progress in Physics* 81.6, 066201 (2018), p. 066201. DOI: 10.1088/1361-6633/aab913. arXiv: 1707.06277 [hep-ph] (cit. on p. 217).

[704]A. U. Abeysekara, R. Alfaro, C. Alvarez, et al. „Sensitivity of HAWC to high-mass dark matter annihilations“. In: Phys. Rev. D 90.12, 122002 (2014), p. 122002. DOI: 10.1103/PhysRevD.90.122002. arXiv: 1405.1730 [astro-ph.HE] (cit. on p. 217).

[705]A. U. Abeysekara, A. Albert, R. Alfaro, et al. „Searching for dark matter sub-structure with HAWC“. In: J. Cosmology Astropart. Phys. 2019.7, 022 (2019), p. 022. DOI: 10.1088/1475-7516/2019/07/022. arXiv: 1811.11732 [astro-ph.HE] (cit. on p. 217).

[706]Lars Bergström, Torsten Bringmann, Martin Eriksson, and Michael Gustafsson. „Gamma Rays from Kaluza-Klein Dark Matter“. In: Phys. Rev. Lett. 94.13, 131301 (2005), p. 131301. DOI: 10.1103/PhysRevLett.94.131301. arXiv: astro-ph/0410359 [astro-ph] (cit. on p. 217).

[707]A. U. Abeysekara, R. Alfaro, C. Alvarez, et al. „The HAWC Real-time Flare Monitor for Rapid Detection of Transient Events“. In: ApJ 843.2, 116 (2017), p. 116. DOI: 10.3847/1538-4357/aa789f. arXiv: 1704.07411 [astro-ph.HE] (cit. on p. 218).

[708]A. Sandoval, R. Lauer, and J. Wood. „HAWC detection of increased TeV flux state for Markarian 501“. In: *The Astronomer's Telegram* 8922 (Apr. 2016) (cit. on p. 218).

[709]A. Biland, D. Dorner, R. Lauer, et al. „Enhanced and increasing activity in gamma rays and X-rays from the HBL Mrk421“. In: *The Astronomer's Telegram* 9137 (June 2016) (cit. on p. 218).

[710]J. Wood, I. Martinez, and R. Lauer. „Increased TeV gamma-ray activity from Mrk 421 on January 1-4“. In: *The Astronomer's Telegram* 9936 (Jan. 2017) (cit. on p. 218).

[711]I. Martinez, J. Wood, and R. Lauer. „HAWC detection of further increase in TeV gamma-ray flux from Mrk 421“. In: *The Astronomer's Telegram* 9946 (Jan. 2017) (cit. on p. 218).

[712]J. A. Garcia-Gonzalez and I. Martinez. „Enhanced Activity of Mrk 421 for an extended period over 30 days measured by HAWC“. In: *The Astronomer's Telegram* 12683 (Apr. 2019) (cit. on p. 218).

[713]C. Riviere, H. Fleischhack, and A. Sandoval. „HAWC detection of TeV emission near PSR B0540+23“. In: *The Astronomer's Telegram* 10941 (Nov. 2017) (cit. on p. 218).

[714]C. Brisbois, C. Riviere, H. Fleischhack, and A. Smith. „HAWC detection of TeV source HAWC J0635+070“. In: *The Astronomer's Telegram* 12013 (Sept. 2018) (cit. on p. 218).

[715]I. Martinez, I. Taboada, M. Hui, and R. Lauer. „HAWC gamma ray data prior to IceCube-170922A“. In: *The Astronomer's Telegram* 10802 (Sept. 2017) (cit. on p. 218).

[716]J. A. Garcia-Gonzalez, M. Gonzalez, I. Martinez, and HAWC Collaboration. „HAWC follow up for gamma-rays emission coincident with the position of AT2018cow“. In: *The Astronomer's Telegram* 11792 (June 2018) (cit. on p. 218).

[717]S. J. Smartt, P. Clark, K. W. Smith, et al. „ATLAS18qqn (AT2018cow) - a bright transient spatially coincident with CGCG 137-068 (60 Mpc)“. In: *The Astronomer's Telegram* 11727 (June 2018) (cit. on p. 218).

[718]I. Taboada. „HAWC TeV gamma-ray follow-up observation of the sky region of IceCube's multi-PeV neutrino-induced event“. In: *The Astronomer's Telegram* 7868 (Aug. 2015) (cit. on p. 218).

[719]S. Schoenen and L. Raedel. „Detection of a multi-PeV neutrino-induced muon event from the Northern sky with IceCube“. In: *The Astronomer's Telegram* 7856 (July 2015) (cit. on p. 218).

[720]J. Linnemann, P. Harding, J. Lundeen, S. Marinelli, and H. Martínez-Huerta. „The Spectrum of the Crab Nebula and Highest Energy Photons Measured by HAWC“. In: *36th International Cosmic Ray Conference (ICRC2019)*. Vol. 36. International Cosmic Ray Conference. 2019, p. 723. arXiv: 1908.11408 [astro-ph.HE] (cit. on pp. 220, 221).

[721]Hugo Alberto Ayala Solares. „AMON: TeV Gamma and Neutrino Coincidence Alerts from HAWC and IceCube subthreshold data“. In: *36th International Cosmic Ray Conference (ICRC 2019) Madison, Wisconsin, USA, July 24-August 1, 2019*. 2019. arXiv: 1908.05990 [astro-ph.HE] (cit. on p. 222).

[722]A. U. Abeysekara, A. Albert, R. Alfaro, et al. „Extended gamma-ray sources around pulsars constrain the origin of the positron flux at Earth“. In: *Science* 358.6365 (2017), pp. 911–914. DOI: 10.1126/science.aan4880. arXiv: 1711.06223 [astro-ph.HE] (cit. on pp. 222, 223).

[723]G. F. Bignami, P. A. Caraveo, and R. C. Lamb. „An identification for 'Geminga' (2CG 195+04) 1E 0630+178 - A unique object in the error box of the high-energy gamma-ray source“. In: ApJ 272 (Sept. 1983), pp. L9–L13. DOI: 10.1086/184107 (cit. on p. 222).

[724]A. A. Abdo, B. Allen, D. Berley, et al. „TeV Gamma-Ray Sources from a Survey of the Galactic Plane with Milagro“. In: ApJ 664 (Aug. 2007), pp. L91–L94. DOI: 10.1086/520717. arXiv: 0705.0707 (cit. on p. 222).

[725]Vincent Marandon, Armelle Jardin-Blicq, and Harm Schoorlemmer. „Latest news from the HAWC outrigger array“. In: *arXiv e-prints*, arXiv:1908.07634 (2019), arXiv:1908.07634. arXiv: 1908.07634 [astro-ph.IM] (cit. on p. 226).

[726]U. Barres de Almeida, G. Anton, Y. Becherini, et al. „Use of ANTARES optical modules in a high-altitude water Cherenkov observatory“. In: (2016). URL: http://irfu.cea.fr/Pisp/fabian.schussler/ewExternalFiles/AMIGO_2016-10-11.pdf (cit. on pp. 226, 227).

[727]Vikas Joshi and Armelle Jardin-Blicq. „HAWC High Energy Upgrade with a Sparse Outrigger Array“. In: *PoS* ICRC2017 (2018). [35,806(2017)], p. 806. DOI: 10.22323/1.301.0806. arXiv: 1708.04032 [astro-ph.IM] (cit. on p. 226).

[728]A. Jardin-Blicq and V. Joshi. „HAWC upgrade for multi-TeV γ-ray detection“. In: *6th International Symposium on High Energy Gamma-Ray Astronomy*. Vol. 1792. American Institute of Physics Conference Series. 2017, p. 070010. DOI: 10.1063/1.4969007. arXiv: 1610.08340 [astro-ph.IM] (cit. on p. 226).

[729]Andres Sandoval. „HAWC Upgrade with a Sparse Outrigger Array“. In: *PoS* ICRC2015 (2016), p. 977. DOI: 10.22323/1.236.0977. arXiv: 1509.04269 [astro-ph.IM] (cit. on p. 226).

[730]F Versari, LA Fusco, and A Margiotta. „Efficiency loss correction for atmospheric muon simulation“. In: (2017). URL: https://cds.cern.ch/record/2290909 (cit. on pp. 229, 235).

[731]L. A. Fusco and A. Margiotta. „The Run-by-Run Monte Carlo simulation for the ANTARES experiment“. In: *European Physical Journal Web of Conferences*. Vol. 116. European Physical Journal Web of Conferences. 2016, p. 02002. DOI: 10.1051/epjconf/201611602002 (cit. on pp. 229, 234, 235).

[732]D. Bailey. „Monte Carlo tools and analysis methods for understanding the ANTARES experiment and predicting its sensitivity to dark matter“. PhD thesis. Oxford U., 2002. URL: https://antares.in2p3.fr/Publications/thesis/2002/d-bailey-thesis.ps.gz (cit. on pp. 230, 232, 233).

[733]Kerstin Fehn. „Search for neutrinos from TANAMI observed AGN using Fermi lightcurves with ANTARES“. doctoralthesis. Friedrich-Alexander-Universität Erlangen-Nürnberg (FAU), 2015. URL: https://ecap.nat.fau.de/wp-content/uploads/2018/02/2015_Fehn_Dissertation.pdf (cit. on pp. 230, 234–236).

[734]David J L Bailey. „Genhen : Extension of "genneu" for high energy neutrino interactions“. In: (2000). URL: https://cds.cern.ch/record/951297 (cit. on pp. 230, 231).

[735]David J L Bailey. „Genhen v3r1 : Further optimisation for large energy ranges“. In: (2000). URL: https://cds.cern.ch/record/951298 (cit. on pp. 230, 231).

[736]David J L Bailey. „Genhen v5r1 : Software Documentation“. In: (2002). URL: https://cds.cern.ch/record/951318 (cit. on pp. 230, 231).

[737]G De Bonis. „GENHEN release v7r1 (... and some anticipations on the next release)“. In: (2014). URL: https://cds.cern.ch/record/1704358 (cit. on pp. 230, 231, 235).

[738]*FFREAD: Format Free Input Processing. Long Writeups I302; version 3.13*. CERN Program Library. Geneva: CERN, 1993. URL: https://cds.cern.ch/record/1107247 (cit. on p. 230).

[739]G. Ingelman, A. Edin, and J. Rathsman. „LEPTO 6.5 — A Monte Carlo generator for deep inelastic lepton-nucleon scattering“. In: *Computer Physics Communications* 101.1 (1997), pp. 108–134. DOI: 10.1016/S0010-4655(96)00157-9. arXiv: hep-ph/9605286 [hep-ph] (cit. on p. 231).

[740]Annalisa Labbate, Teresa Montaruli, and Igor A Sokalski. „GENHEN v6: ANTARES neutrino generator extension to all neutrino flavors and inclusion of propagation through the Earth“. In: (2004). URL: https://cds.cern.ch/record/951354 (cit. on p. 231).

[741]K Kuzmin, T Montaruli, and I A Sokalski. „GENHEN v6r3: implementation of the Glashow resonance and of MUSIC transport code“. In: (2004). URL: https://cds.cern.ch/record/951356 (cit. on p. 231).

[742]P. Antonioli, C. Ghetti, E. V. Korolkova, V. A. Kudryavtsev, and G. Sartorelli. „A three-dimensional code for muon propagation through the rock: MUSIC“. In: *Astroparticle Physics* 7.4 (1997), pp. 357–368. DOI: 10.1016/S0927-6505(97)00035-2. arXiv: hep-ph/9705408 [hep-ph] (cit. on p. 231).

[743]J. Brunner. *"GEASIM"*. http://antares.in2p3.fr/internal/software/geasim.html. [Online; accessed 20-September-2019]. 2000 (cit. on pp. 231, 235).

[744]René Brun, F Bruyant, Federico Carminati, et al. *GEANT: Detector Description and Simulation Tool; Oct 1994*. CERN Program Library. Long Writeup W5013. Geneva: CERN, 1993. DOI: 10.17181/CERN.MUHF.DMJ1. URL: https://cds.cern.ch/record/1082634 (cit. on p. 231).

[745]J Brunner. „Updated tag list for the new ANTARES event format“. In: (1999). URL: https://cds.cern.ch/record/951283 (cit. on pp. 232–234).

[746]J Brunner. „Antares simulations“. In: (2003). URL: https://cds.cern.ch/record/951343 (cit. on p. 234).

[747]G. Carminati, M. Bazzotti, A. Margiotta, and M. Spurio. „Atmospheric MUons from PArametric formulas: a fast GEnerator for neutrino telescopes (MUPAGE)“. In: *Computer Physics Communications* 179.12 (2008), pp. 915–923. DOI: 10.1016/j.cpc.2008.07.014. arXiv: 0802.0562 [physics.ins-det] (cit. on pp. 234, 235).

[748]D. Heck, J. Knapp, J. N. Capdevielle, G. Schatz, and T. Thouw. *CORSIKA: a Monte Carlo code to simulate extensive air showers.* 1998 (cit. on p. 234).

[749]J. Knapp and D. Heck. „Extensive air shower simulations with the CORSIKA code.“ In: *Nachr. Forschungszent. Karlsr* 30.1 (1998), pp. 27–37 (cit. on p. 234).

[750]T. S. Sinegovskaya and S. I. Sinegovsky. „Prompt muon contribution to the flux underwater“. In: Phys. Rev. D 63.9, 096004 (2001), p. 096004. DOI: 10.1103/PhysRevD.63.096004. arXiv: hep-ph/0007234 [hep-ph] (cit. on p. 234).

[751]Sergio Navas and Lee Thompson. „KM3 User Guide and Reference Manual“. In: (1999). URL: https://cds.cern.ch/record/951291 (cit. on p. 235).

[752]M de Jong. „The TriggerEfficiency program“. In: (2009). URL: https://cds.cern.ch/record/1160888 (cit. on p. 236).

[753]Boutayeb Bouhou. „Coincident searches between high energy neutrinos and gravitationnal waves with ANTARES, VIRGO and LIGO detectors“. Theses. Université Pierre et Marie Curie - Paris VI, Dec. 2012. URL: https://tel.archives-ouvertes.fr/tel-00819985 (cit. on pp. 237, 238, 241, 242).

[754]Aart Heijboer. „An algorithm for track reconstruction in ANTARES“. In: (2002). URL: https://cds.cern.ch/record/951316 (cit. on pp. 238, 240–242).

[755]J. A. Aguilar, I. Al Samarai, A. Albert, et al. „A fast algorithm for muon track reconstruction and its application to the ANTARES neutrino telescope“. In: *Astroparticle Physics* 34.9 (2011), pp. 652–662. DOI: 10.1016/j.astropartphys.2011.01.003. arXiv: 1105.4116 [astro-ph.IM] (cit. on pp. 238, 239).

[756]Aart Heijboer. „Reconstruction of Atmospheric Neutrinos in Antares“. In: *arXiv e-prints*, arXiv:0908.0816 (2009), arXiv:0908.0816. arXiv: 0908.0816 [astro-ph.IM] (cit. on pp. 238, 240).

[757]M. C. Charif. „Indirect Search for Dark Matter with the ANTARES Telescope“. Theses. Aix-Marseille Université, Sept. 2012. URL: https://tel.archives-ouvertes.fr/tel-00975918 (cit. on pp. 238–240).

[758]Zhengyou Zhang. *Parameter Estimation Techniques: A Tutorial with Application to Conic Fitting*. Research Report RR-2676. INRIA, Oct. 1995. URL: https://hal.inria.fr/inria-00074015 (cit. on p. 241).

[759]D Palioselitis. „Measurement of the atmospheric neutrino energy spectrum“. PhD thesis. Institute for High Energy Physics (IHEF), 2012. URL: http://dare.uva.nl/cgi/arno/show.cgi?fid=444188 (cit. on pp. 241, 245).

[760]S. Adrián-Martínez, A. Albert, I. Al Samarai, et al. „Measurement of the atmospheric ν_μ energy spectrum from 100 GeV to 200 TeV with the ANTARES telescope“. In: *European Physical Journal C* 73, 2606 (2013), p. 2606. DOI: 10.1140/epjc/s10052-013-2606-4. arXiv: 1308.1599 [astro-ph.HE] (cit. on pp. 245, 246).

[761]Luigi Antonio Fusco, Vladimir Kulikovskiy, and ANTARES Collaboration. „Measurement of the Atmospheric $\nu\mu$ Energy Spectrum with the Antares Neutrino Telescope“. In: *International Cosmic Ray Conference*. Vol. 33. International Cosmic Ray Conference. 2013, p. 3271 (cit. on pp. 245, 246).

[762]Fabian Schüssler and ANTARES Collaboration. „Energy Reconstruction in Neutrino Telescopes“. In: *International Cosmic Ray Conference*. Vol. 33. International Cosmic Ray Conference. 2013, p. 3394 (cit. on pp. 246, 247).

[763]Fabian Schussler. „Energy reconstruction of Antares events: the dE/dX energy estimator“. In: (2012). URL: https://cds.cern.ch/record/1482101 (cit. on pp. 246, 247, 252).

[764]The ANTARES Collaboration. „The Antares Collaboration : Contributions to the 33st International Cosmic Ray Conference (ICRC 2013, Rio de Janeiro)“. In: *arXiv e-prints*, arXiv:1312.4308 (2013), arXiv:1312.4308. arXiv: 1312.4308 [astro-ph.HE] (cit. on pp. 246, 247, 252).

[765]J Schnabel. „The ANNergy estimator - Using Artificial Neural Networks for muon energy reconstruction“. In: (2012). URL: https://cds.cern.ch/record/1497159 (cit. on pp. 246, 252).

[766]Jutta Schnabel. „Search for a cosmic neutrino flux from all neutrino flavours with ANTARES“. doctoralthesis. Friedrich-Alexander-Universität Erlangen-Nürnberg (FAU), 2019, p. 183. URL: https://opus4.kobv.de/opus4-fau/frontdoor/index/index/docId/11123 (cit. on pp. 247, 253).

[767]R. Barlow. „Extended maximum likelihood“. In: *Nuclear Instruments and Methods in Physics Research A* 297 (Dec. 1990), pp. 496–506. DOI: 10.1016/0168-9002(90)91334-8 (cit. on pp. 250–252).

[768]The ANTARES Collaboration. „Search for muon-neutrino emission from GeV and TeV gamma-ray flaring blazars using five years of data of the ANTARES telescope“. In: J. Cosmology Astropart. Phys. 2015.12, 014 (2015), p. 014. DOI: 10.1088/1475-7516/2015/12/014. arXiv: 1506.07354 [astro-ph.HE] (cit. on pp. 250, 252, 257, 259).

[769]A. Albert, M. André, G. Anton, et al. „Time-dependent search for neutrino emission from X-ray binaries with the ANTARES telescope“. In: J. Cosmology Astropart. Phys. 2017.4, 019 (2017), p. 019. DOI: 10.1088/1475-7516/2017/04/019. arXiv: 1609.07372 [astro-ph.HE] (cit. on pp. 250, 257, 259).

[770]Anne Oppelt. „Energy reconstruction“. In: (2001). URL: https://cds.cern.ch/record/951311 (cit. on p. 252).

[771]Sara Coutiño de León, Alberto Carramiñana Alonso, and Daniel Rosa-González. „Spectral analysis of Markarian 421 and Markarian 501 with HAWC“. In: *PoS* ICRC2017 (2018). [35,606(2017)], p. 606. DOI: 10.22323/1.301.0606. arXiv: 1708.04637 [astro-ph.HE] (cit. on pp. 254, 262).

[772]J. F. Beacom. „Supernova neutrinos and the neutrino masses.“ In: *Revista Mexicana de Fisica* 45.2 (1999), pp. 36–39. arXiv: hep-ph/9901300 [hep-ph] (cit. on p. 257).

[773]P. A. Oesch, G. Brammer, P. G. van Dokkum, et al. „A Remarkably Luminous Galaxy at z=11.1 Measured with Hubble Space Telescope Grism Spectroscopy“. In: ApJ 819.2, 129 (2016), p. 129. DOI: 10.3847/0004-637X/819/2/129. arXiv: 1603.00461 [astro-ph.GA] (cit. on p. 257).

[774]Ch Kraus, B. Bornschein, L. Bornschein, et al. „Final results from phase II of the Mainz neutrino mass searchin tritium {β} decay“. In: *European Physical Journal C* 40.4 (2005), pp. 447–468. DOI: 10.1140/epjc/s2005-02139-7. arXiv: hep-ex/0412056 [hep-ex] (cit. on p. 257).

[775]V. N. Aseev, A. I. Belesev, A. I. Berlev, et al. „Upper limit on the electron antineutrino mass from the Troitsk experiment“. In: Phys. Rev. D 84.11, 112003 (2011), p. 112003. DOI: 10.1103/PhysRevD.84.112003. arXiv: 1108.5034 [hep-ex] (cit. on p. 257).

[776]S. Adrián-Martínez, I. Al Samarai, A. Albert, et al. „Search for Cosmic Neutrino Point Sources with Four Years of Data from the ANTARES Telescope“. In: ApJ 760.1, 53 (2012), p. 53. DOI: 10.1088/0004-637X/760/1/53. arXiv: 1207.3105 [hep-ex] (cit. on p. 259).

[777]F. James and M. Roos. „Minuit - a system for function minimization and analysis of the parameter errors and correlations“. In: *Computer Physics Communications* 10 (Dec. 1975), pp. 343–367. DOI: 10.1016/0010-4655(75)90039-9 (cit. on p. 259).

[778]J. Neyman. „Outline of a Theory of Statistical Estimation Based on the Classical Theory of Probability“. In: *Philosophical Transactions of the Royal Society of London Series A* 236.767 (1937), pp. 333–380. DOI: 10.1098/rsta.1937.0005 (cit. on pp. 267, 301).

[779]Jeffrey D. Scargle, Jay P. Norris, Brad Jackson, and James Chiang. „Studies in Astronomical Time Series Analysis. VI. Bayesian Block Representations“. In: ApJ 764.2, 167 (2013), p. 167. DOI: 10.1088/0004-637X/764/2/167. arXiv: 1207.5578 [astro-ph.IM] (cit. on pp. 270, 271).

[780]Maurizio Spurio. „ANTARES constraints on a Galactic component of the IceCube cosmic neutrino flux“. In: *European Physical Journal Web of Conferences*. Vol. 121. European Physical Journal Web of Conferences. 2016, p. 05007. DOI: 10.1051/epjconf/201612105007. arXiv: 1501.01551 [astro-ph.HE] (cit. on p. 289).

[781]S. Coutiño de Leon, A. C. Alonso, D. Rosa-Gonzalez, and A. L. Longinotti. „Spectral analysis of the blazars Markarian 421 and Markarian 501 with the HAWC Gamma-Ray Observatory“. In: *36th International Cosmic Ray Conference (ICRC2019)*. Vol. 36. International Cosmic Ray Conference. 2019, p. 654. arXiv: 1909.01179 [astro-ph.HE] (cit. on pp. 307–309).

[782]A. A. Abdo, M. Ackermann, M. Ajello, et al. „Fermi Large Area Telescope Observations of Markarian 421: The Missing Piece of its Spectral Energy Distribution“. In: ApJ 736, 131 (Aug. 2011), p. 131. DOI: 10.1088/0004-637X/736/2/131. arXiv: 1106.1348 [astro-ph.HE] (cit. on p. 308).

[783]M. Petropoulou, S. Dimitrakoudis, P. Padovani, A. Mastichiadis, and E. Resconi. „Photohadronic origin of γ -ray BL Lac emission: implications for IceCube neutrinos“. In: MNRAS 448.3 (2015), pp. 2412–2429. DOI: 10.1093/mnras/stv179. arXiv: 1501.07115 [astro-ph.HE] (cit. on p. 308).

[784]Maria Petropoulou, Stefan Coenders, and Stavros Dimitrakoudis. „Time-dependent neutrino emission from Mrk 421 during flares and predictions for IceCube“. In: *Astroparticle Physics* 80 (2016), pp. 115–130. DOI: 10.1016/j.astropartphys.2016.04.001. arXiv: 1603.06954 [astro-ph.HE] (cit. on p. 315).

List of Figures

List of Tables

Glossary and Abbreviations

ACS Anti-Coincidence Shield

ADC Analogue-to-Digital Converters

AGILE Astro-rivelatore Gamma a Immagini LEggero

AGN Active Galactic Nuclei

ANITA ANtarctic Impulsive Transient Antenna

ANN Artificial Neural Network

ANTARES Astronomy with a Neutrino Telescope and Abyss environmental RE-Search project

AMADEUS ANTARES Modules for the Acoustic Detection Under the Sea

AMON Astrophysical Multimessenger Observatory Network

ARCA Astroparticle Research with Cosmics in the Abyss

ARGO-YBJ Astrophysical Radiation with Ground-based Observatory at YangBaJing

ARS Analog Ring Sampler

AS Acoustic Storeys

ASAS-SN All-Sky Automated Survey for SuperNovae

ASI Italian Space Agency

ATel Astronomer's Telegram

AVC Amplitude-to-Voltage Converter

BBH Binary Black Hole

BEST Baksan Experiment on Sterile Transitions

BH Black Hole

BL Lac BL-Lacertae

BNO Baksan Neutrino Observatory

BNS Binary Neutron Star

BSS Bottom String Socket

BUST Baksan Underground Scintillation Telescope

CC Charged Current

CDM Cold Dark Matter

CGRO Compton Gamma Ray Observatory

CKM Cabbibo-Kobayashi-Maskawa

CL Confidence Level

CMB Cosmic Microwave Background

CNO Carbon-Nitrogen-Oxygen

CORSIKA COsmic Ray SImulation for KAscade

CPT Charge, Parity, and Time symmetry

CR Cosmic Ray

CTA Cherenkov Telescope Array

DAQ Data Acquisition System

DF Discovery Flux

DIS Deep Inelastic Scattering

DM Dark Matter

DOM Digital Optical Module

DP Discovery Power

DUMAND Deep Underwater Muon and Neutrino Detector

DWDM Dense Wavelength Division Multiplexing

EAS Extensive Air Shower

EBL Extragalactic Background Light

EGCR ExtraGalactic Cosmic Ray

EGMF ExtraGalactic Magnetic Fields

EGRET Energetic Gamma Ray Experiment Telescope

EHE Extremely High Energy

EML Extended Maximum Likelihood

ES Elastic Scattering

ESA European Space Agency

ESS Engel-Seckel-Stanev

FACT First G-APD Cherenkov Telescope

***Fermi*-GBM** Fermi Gamma-ray Burst Monitor

***Fermi*-LAT** Fermi Large Area Telescope

FOCAS Faint Object Camera and Spectrograph

FOV Field of View

FPGA Field Programmable Gate Array

FSRQ Flat Spectrum Radio Quasar

FWHM Full Width at Half Maximum¨

GALLEX GALLium EXperiment

GC Galactic Centre

GCN Gamma-Ray Coordinate Network

GCR Galactic Cosmic Ray

GEANT GEometry ANd Tracking

GENHEN GENerator of High Energy Neutrinos

GGNT Gallium-Germanium Neutrino Telescope

GNN Global Neutrino Network

GP Ground Parameter

GPS Global Positioning System

GRB Gamma-Ray Burst

GSC Gas Slit Camera

GVD Gigaton Volume Detector

GW Gravitational Wave

GZK Greisen-Zatsepin-Kuzmin

HAWC High Altitude Water Cherenkov

HBL High-frequency peaked BL Lac

HE High Energy

HESE High Energy Starting Event

H.E.S.S. High Energy Stereoscopic System

HEASARC High Energy Astrophysics Science Archive Research Center

HST Hubble Space Telescope

HQE High-Quantum Efficiency

IACT Imaging Atmospheric Cherenkov Telescope

IC Inverse Compton

ICL IceCube Laboratory

IGMF Intergalactic Magnetic Field

IL Instrumentation Line

INR RAS Institute for Nuclear Research of the Russian Academy of Sciences

INTEGRAL INTernational Gamma-Ray Astrophysics Laboratory

IMB Irvine-Michigan-Brookhaven

IPN InterPlanetary Network

IR InfraRed

ISM InterStellar Medium

JB Junction Box

JEM/EUSO Japanese Experiment Module/Extreme Universe Space Observatory

KASCADE Karlsruhe Shower Core and Array Detector

KM3NeT Cubic Kilometre Neutrino Telescope

LAT Large Area Telescope

LBL Low-frequency peaked BL Lacertae

LCM Local Control Module

LED Light-Emitting Diode

LHAASO Large High Altitude Air Shower Observatory

LHC Large Hadron Collider

LIGO Laser Interferometer Gravitational-wave Observatory

LMC Large Magellanic Cloud

LNGS Laboratori Nazionali del Gran Sasso

LPB Local Power Box

LSD Liquid Scintillation Detector

LT Livetime

MACRO Monopole, Astrophysics and Cosmic Rays Observatory

MAGIC Major Atmospheric Gamma-Ray Imaging Cherenkov Telescopes

MAXI Monitor of All-sky X-ray Image

MAXI/GSC Monitor of All-sky X-ray Image Gas Slit Camera

MAXI/SSC Monitor of All-sky X-ray Image Solid-state Slit Camera

MC Monte Carlo

MDP Model Discovery Potential

MEOC Main Electro-Optical Cable

Milagro Milagro Gamma Ray Observatory

MILOM Mini Instrumentation Line with Optical Modules

MJD Modified Julian Day

ML Maximum Likelihood

MLCM Master Local Control Module

MoUs Memoranda of Understanding

MM MultiMessenger

MPR Mannheim-Protheroe-Rachen

MUPAGE Atmospheric MUons from PArametric formulas: a fast GEnerator for neutrino telescopes

MUSIC MUon SImulation Code

NARC Neutrino Array Radio Calibration

NASA National Aeronautics and Space Administration

NC Neutral Current

NN Neural Network

NS Neutron Star

NSF National Science Foundation

NIR Near Infrared

NLSy1 Narrow-Line Seyfert 1 Galaxy

NuSTAR Nuclear Spectroscopic Telescope Array

OB Optical Beacon

OM Optical Module

OMF Optical Module Frame

ORCA Oscillations Research with Cosmics in the Abyss

OSO-3 Third satellite of the Orbiting Solar Observatory program

OVRO Owens Valley Radio Observatory

PBH Primordial Black Hole

PDF Probability Density Function

PEX Pseudo EXperiment

PH Power Hut

PMNS Pontecorvo-Maki-Nakagawa-Sakata

PMT PhotoMultiplier Tube

PS Point Source

PSD Pulse Shape Discriminator

PSF Point Spread Function

PWN Pulsar Wind Nebula

QCD Quantum ChromoDynamics

QED Quantum ElectroDynamics

QSO Quasi-Stellar Object

Quasar QUAsi-StellAr Radiosource

RA/Dec Right Ascension/Declination

R&D Research and Development

RES Resonance

RICE Radio Ice Cherenkov Experiment

RMS Root Mean Square

SAGE Soviet–American Gallium Experiment

SALT Southern African Large Telescope

SALT/HRS Southern African Large Telescope High Resolution Spectrograph

SC Slow-Control

SCM String Control Module

SED Spectral Energy Distribution

SKA Square Kilometre Array

SM Standard Model

SMBH SuperMassive Black Hole

SN SuperNova

SNR SuperNova Remnant

SNU Solar Neutrino Unit

SPE Single PhotoElectron

SPM String Power Module

SPRAT SPectrograph for the Rapid Acquisition of Transients

SSC Synchrotron Self Compton

SSDC Space Science Data Center

SSM Standard Solar Model

Subaru/FOCAS Subaru Faint Object Camera and Spectrograph

SUSY SUperSYmmetry

Swift/BAT Swift Burst Alert Telescope

Swift/XRT Swift X-Ray Telescope

TA Telescope Array

TNS Transient Name Server

ToO Target of Opportunity

ToT Time Over Threshold

TS Test Statistic

TT Transit Time

TTS Transit Time Spread

TVC Time-to-Voltage Converter

UHBL Ultra-High-Frequency peaked BL Lacacertae

UHE Ultra-High Energy

UHECR Ultra-High Energy Cosmic Ray

UNO Mount Blanc Underground Neutrino Observatory

UT Universal Time

UTC Coordinated Universal Time

UV UltraViolet

VERITAS Very Energetic Radiation Imaging Telescope Array System

VHE Very High Energy

VLA Very Large Array

VLT Very Large Telescope

XRT X-Ray Telescope

QE Quasi-Elastic

W&B Waxman-Bahcall

WCD Water Cherenkov Detector

WF Wave Form

WIMP Weakly Interacting Massive Particle

Colophon

This thesis was typeset with LaTeX 2_ε. It uses the *Clean Thesis* style developed by Ricardo Langner. The design of the *Clean Thesis* style is inspired by user guide documents from Apple Inc.

Download the *Clean Thesis* style at http://cleanthesis.der-ric.de/.